



universität
wien

DISSERTATION

Titel der Dissertation

“Shock metamorphism and geochemistry of impactites
from the Bosumtwi impact structure:
A case study of shock-induced deformations and
transformations in quartz and associated methodology”

Verfasser

Mag. Ludovic Ferrière

angestrebter akademischer Grad

Doktor der Naturwissenschaften (Dr. rer. nat.)

Wien, im Dezember 2008

Studienkennzahl lt. Studienblatt:

A 091 431

Dissertationsgebiet lt. Studienblatt:

Geologie

Betreuer:

Univ.-Prof. Dr. Christian Koeberl



The author at the Tswaing impact structure (South Africa; August 2008).

**Dedicated to my parents, Didier and Isabelle Ferrière
and my grandparents, Guy and Jacqueline Ferrière
and Paul and Michèle Bremard.**

PREFACE:

The present thesis is the result of three full years of work conducted mainly at the Department of Lithospheric Research (University of Vienna) and essentially based on the investigation of impactite samples from the Bosumtwi impact structure (Ghana). The prime objective of my study was to characterize the petrography and geochemistry of impact breccias and basement rocks that were recovered in core LB-08A, which was drilled on the outer flank of the central uplift of the Bosumtwi crater during the 2004 International Continental Scientific Drilling Program (ICDP) drilling project. This work was done at the macroscopic scale for the general description of the samples and for the construction of a detailed lithostratigraphic column of the core, and at the microscope scale for the characterization of the different minerals and clasts forming the impactite samples. Using various techniques, such as the optical microscope, the universal stage (U-stage), transmission electron microscopy (TEM), scanning electron microscopy (SEM), and microRaman spectroscopy, it was possible to identify and to characterize shock metamorphism effects in minerals; the investigations were focused on shock-induced deformations and transformations in quartz (i.e., planar deformation features (PDFs), ballen quartz/cristobalite, toasted quartz) and melt particles, providing some constraints on shock pressures and temperatures. The mixing of target rocks and changes induced by post-impact hydrothermal activity were also evaluated, combining the petrographic characteristics of the samples with their major and trace element composition, as well as, C, Sr, and Nd isotopic composition of representative samples. Geochemical and isotopic data were obtained using instrumental neutron activation analysis (INAA), X-ray fluorescence (XRF) spectrometry, electron microprobe (EMP), and mass spectrometry (MS).

The thesis is divided into 10 chapters, with a general introduction on impact cratering (chapter 1), a review of shock metamorphism (chapter 2), a brief overview of the Bosumtwi crater (chapter 3), and an extended section about the methodology used (chapter 4). Besides, the other chapters represent manuscripts published (chapters 5–8) or submitted (chapter 9) in refereed journals. A last chapter, called Potpourri (chapter 10), presents further detailed investigations that were conducted subsequently and to complement the work in the publication chapters. Finally, most of the extensive chemical data are reported in the Appendices, as well as detailed descriptions of all LB-08A samples investigated. The main conclusions of the chapters 5–10 are summarized in the next section. Samples and thin sections described in this thesis are stored at the University of Vienna. All presented macro- and micro-photos, scanning electron microscopy, microprobe, cathodoluminescence, and TEM images, as well as all reported measurements were obtained by me unless noted otherwise.

Chapter 5 and 6 are articles published in a Bosumtwi special issue of *Meteoritics and Planetary Science* (MAPS; Vol. 42, No. 4/5) in which detailed petrographic and geochemical investigations done on 121 impactite samples from core LB-08A are reported.

Chapter 5 presents the lithostratigraphy of core LB-08A, as well as mineralogical and petrographic observations of the core samples. Investigation of the core shows that the central uplift is composed of fractured/brecciated metasediments (i.e., basement rocks), mainly fine-grained to gritty meta-graywacke, phyllite, and slate. Basement rocks are covered by about 25 m of polymict, clast-supported lithic breccia intercalated with suevite. The crater-fill suevite contains a lower proportion of melt particles and diaplectic quartz glass, as well as calcite clasts but no granite clasts, in contrast to suevite from outside the northern crater rim. Quartz grains with up to 4 sets of planar deformation features (PDFs), generally decorated with tiny fluid inclusions, were noted in impactites; the decoration of the PDFs argue for a rapid and intense hydrothermal alteration or an impact into a water- or volatile-rich target. The presence of melt particles in the crater-fill breccia is an indicator of shock pressures exceeding 45 GPa, whereas basement rocks have recorded pressures locally reaching 25-30 GPa.

Chapter 6 presents and discusses the major and trace element data of the different lithologies recovered in core LB-08A. It was shown that most of the variations of compositions in the different lithologies result from the initial compositional variations of the various target rock types, as well as from aqueous alteration processes, which have affected the different rocks. Crater-fill suevite display some differences in major (mainly in MgO, CaO, and Na₂O contents) and minor (mainly Cr and Ni) element abundances compared to the suevite from outside the northern crater rim. These differences likely represent the higher degree of alteration of crater-fill suevite, but also result from differences in the clast populations of the two suevite types. No evidence for a meteoritic component was detected in impact breccias.

Chapter 7 is the corrected proof of a paper that is in press in the journal "Science". This article discusses the findings and implications of detailed petrographic investigations of 18 meta-graywacke samples from core LB-08A, which are combined with results of numerical modeling of inelastic rock deformation and modification processes during uplift. The shock wave attenuation was characterized in the uppermost part of the central uplift and the pre-impact position of the drilled rocks in the target before crater modification was reconstructed. The results show that the shock attenuation amounts to ~5 GPa in the uppermost 200 m of basement rocks sampled in core LB-08A, and that these samples have been uplifted by about 1.2 to 1.5 km as a result of the edification of the central uplift. The results of this study further imply that for moderately sized craters the rise of the central uplift is dominated by brittle failure. It was also shown that the proportion of shocked quartz grains and the average number of PDF sets per grain provide a more sensitive indication of minor changes in shock pressure than PDF orientations.

Chapter 8 is a paper that is in press in the European Journal of Mineralogy (EJM; doi: 10.1127/0935-1221/2009/0021-1898). This article represents the first detailed investigation of ballen silica in impactites in an attempt to contribute to the understanding of the formation mechanism(s) of ballen quartz/cristobalite. Ballen silica were investigated from five impact structures (Bosumtwi, Chicxulub, Mien, Ries, and Rochechouart) and five types of ballen were distinguished. Coesite inclusions were also, for the first time, characterized within ballen α -cristobalite from the Bosumtwi crater. Investigations indicate

that ballen quartz/cristobalite result from back-transformation of shock-induced states, thus representing indirect evidence of shock metamorphism.

Chapter 9 is a manuscript currently in review in MAPS; it represents the first systematic and comparative study of U-stage measurements of PDFs in quartz. Implications for statistical significance and representation of results are discussed. The study shows that the precision of U-stage measurements depends mainly of the number of PDF sets investigated and that by following a strict measurement procedure, the reproducibility of U-stage measurements is good.

Chapter 10 presents and discusses several additional short studies performed on samples from core LB-08, such as SEM investigations of melt particles and calcite clasts from suevite samples, U-Pb dating of single detrital zircon grains from suevite and basement rocks, as well as whole-rock Sr-Nd isotopic analyses of suevite, phyllite, and meta-graywacke samples. Additionally, results of TEM investigations of the microtexture of PDF planes in quartz grains and the characterization of “toasted” quartz grains in impactite samples from the Bosumtwi are reported, and compared to investigations performed on impactites from the Chesapeake Bay impact structure. Complementary work performed on ballen silica from several impact structures is also presented.

ACKNOWLEDGEMENT:

I thank my main supervisor Christian Koeberl for supervising this thesis, for sharing a part of his experience, for his help in writing scientific papers, for financial support, for scientific discussions, and for the more than 2,000 emails received during the last three years. I would like to say sorry to the other candidates that have not been selected for this project, as it was a pleasure to work in Vienna, especially on this topic. Thank also for pleasant evenings and dinners together with Dona Jalufka and other colleagues, as I have discovered that a famous scientist can also be a “Gourmet cook”.

I greatly appreciate the help of W. Uwe Reimold (Museum of Natural History, Berlin, Germany) for valuable discussions, critical review of my work, and encouragement. I really appreciate the sharing of knowledge on shock metamorphism.

Dieter Mader (Univ. Vienna) is thanked for his every-day assistance, especially with the INAA and mass spectrometer, for encouragement, for discussions, and for the translation of my abstract into German.

I would like to thank also all the following persons for help, support, discussions, and assistance, because the achievement of this thesis would have been almost impossible without their contributions (names are listed in alphabetic order).

S. Augustin, A. Schreiber, and R. Wirth (GFZ, Potsdam, Germany) for the preparation of FIB TEM foils.

M. Bichler, H. Böck, E. Klapfer, H. Schachner, G. Steinhauser, J. Sterba, and M. Villa (Atominstut Vienna) for the irradiations of samples.

F. Brandstätter (Natural History Museum, Vienna) for assistance with SEM and CL work, as well as for discussions.

L. Coney (Wits Univ., Johannesburg, South Africa) for encouragement, discussion, and sharing experience of core samples from the Bosumtwi crater.

R. Conze, U. Harms, and T. Wöhrl (GFZ, Potsdam, Germany) for help and support with the core samples, notably during the time spent in the garage where cores are stored at the GFZ.

P. Czaja and L. Hecht (Museum of Natural History, Berlin, Germany) for technical assistance with the electron microprobe in Berlin.

S. Farrell-Turner (Wits Univ., Johannesburg, South Africa) for the XRF analyses.

W. Füzi (Univ. Vienna) and A. Mathebula (Wits Univ., Johannesburg, South Africa) for expert thin sections preparation.

R. Gibson (Wits Univ., Johannesburg, South Africa) for help with the first descriptions of some of my thin sections.

S. Gier (Univ. Vienna) for an XRD analysis.

A. Greshake (Museum of Natural History, Berlin, Germany) and H. Leroux (Univ. Lille, France) for assistance with the TEM.

Acknowledgement

M. Horschinegg and M. Thöni (Univ. Vienna) for Sr-Nd isotopic analyses of some Bosumtwi samples.

B.A. Ivanov (Russian Academy of Sciences, Moscow, Russia) for introducing me to the basics of numerical modeling and for collaborating work.

U. and E. Klötzli, F. Biedermann (Univ. Vienna), and C. Liang (Northwest Univ., China) for assistance with zircon preparation, U-Pb dating, and for discussions.

E. Libowitzky (Univ. Vienna), J.N. Rouzaud, and C. Le Guillou (both ENS, Paris, France) for assistance with the microRaman spectroscopic analyses.

J.R. Morrow (San Diego State Univ., USA) for discussions, interesting suggestions, encouragement, and works realized together with U-stage.

R.-T. Schmitt (Museum of Natural History, Berlin), J.-P. Lorand, and G. Carlier (both MNHN, Paris, France) for providing thin sections.

D. Boamah, M. Bourot-Denise, A. Deutsch, B.M. and M.H. French, E.P. Gurov R. Hewins, D. King, D. Kring, S. Luetke, G. Osinski, C. Perron, E. Robin, J. Spray, D. Stoeffler, A. Wittmann, and B. Zanda are thanked for interesting discussions and/or review of some of the publication chapters presented in this thesis.

I thank also F. Mikysek and A. Vogt for secretarial help, N. Irnberger for the printing of conference posters, and above all, the students and colleagues from our Department, mainly K. Bartosova, A. Dunford, T. Amgaa, F. Karikari, M. Hagos, A. Cernok, and T. H. Son, for assistance, discussions, and encouragement during the work on my thesis and also for nice evenings together. K. Bartosova is especially thanked for scientific and friendly discussions, help and encouragement, and for the numerous “cakes and tortes” offered for my long days sitting in the office. Students and colleagues from the Museum of Natural History of Berlin (Germany) and C. Alwmark (Univ. Lund, Sweden) are acknowledged for friendly discussions.

I would like also to thank the Barringer Crater Company for financial support, making it possible for me to attend international conferences to present my work and SYNTHESYS (DE-TAF-4172) for funding my research work at the Museum of Natural History of Berlin (Germany).

This study was supported by the Austrian FWF (P17194-N10 and P18862-N10) and the Austrian Academy of Sciences (project ICDP-490).

Drilling at Bosumtwi was supported by ICDP, the U.S. NSF-Earth System History Program under grant no. ATM-0402010, Austrian FWF (project P17194-N10), the Austrian Academy of Sciences, and by the Canadian NSERC.

ABSTRACT:

Two boreholes were drilled in the central part of the Bosumtwi impact crater (Ghana; 1.07 Ma; 10.5-km-diameter) during the 2004 International Continental Scientific Drilling Program (ICDP) drilling project: LB-08A from the outer flank of the central uplift and LB-07A from the deep crater moat. This thesis presents petrographic and chemical investigations of 121 impactites, mainly suevite and metasediments, from core LB-08A. Comparing core LB-07A and samples from outside the crater rim show that the crater-fill suevite contains a lower proportion of melt particles and diaplectic glass, as well as calcite clasts but no granite clasts, in contrast to fallout suevite.

Bosumtwi impactites contain quartz grains with up to 4 sets of planar deformation features (PDFs). PDFs planes are defined by dislocations and tiny fluid inclusions, indicating that impactites from the central uplift were subjected to intense hydrothermal alteration. Microprobe investigations show that toasted quartz contains abundant small vesicles that enhance scattering of transmitted light, and that some trace elements were expelled from the quartz's structure. Therefore, toasted quartz formed by vesiculation after pressure release.

Universal-stage investigations show that the proportion of shocked quartz grains and the average number of PDF sets per grain provide a more sensitive indication of minor changes in shock pressure than PDF orientations, and that the precision of U-stage measurements depends mainly of the number of PDF sets investigated. Combining micro-scale observations with numerical modeling of inelastic rock deformation and modification processes during uplift allowed reconstruction of the pre-impact position of the drilled rocks and revealed a shock attenuation by ~5 GPa in the uppermost 200-meters of the central uplift, and that central uplift formation is dominated by brittle failure.

Investigation of ballen silica from several impact structures distinguished five types of ballen, the presence of coesite within ballen α -cristobalite, and indicated that ballen quartz/cristobalite result from back-transformation of shock-induced states, thus representing indirect evidence of shock metamorphism.

ZUSAMMENFASSUNG:

Im Zuge des Bohrprojektes “2004 International Continental Scientific Drilling Programs (ICDP)” wurden zwei Bohrkerne im zentralen Bereich des Bosumtwi-Impaktkraters (Ghana; 1.07 Ma; 10.5 km Durchmesser) erbohrt: LB-08A in die äußeren Flanke der Zentralerhebung und LB-07A im tiefen Kratergraben. Diese Dissertation präsentiert petrographische und geochemische Untersuchungen von 121 Impaktiten des Bohrkerns LB-08A, hauptsächlich Suevite und Metasedimente. Im Vergleich zwischen Bohrkern LB-07A und mit Suevitproben außerhalb des Kraterlands haben die Suevite innerhalb des Kraters einen geringeren Anteil an Schmelzteilen, diaplektischem Glas und Kalzitklasten, aber keine Granitklasten.

Quarzkörner der Bosumtwi-Impaktite enthalten bis zu vier Gruppen an planaren Deformationsstrukturen (PDFs). Die PDF-Ebenen sind durch Dislokationen und winzige Flüssigkeitseinschlüsse definiert, was auf eine intensive (post-impakte) hydrothermale Alteration der Gesteine der Zentralerhebung hinweist. Mikrosonden-Analysen machen deutlich, dass sogenannte „geröstete“ Quarze reichliche kleine Bläschen enthalten, welche die Streuung des Durchlichts erhöhen, und dass einige Spurenelemente aus der Quarzkristallstruktur hinausgedrängt wurden. „Geröstete“ Quarze könnten daher durch Bläschenbildung nach der Druckentlastung gebildet worden sein.

Untersuchungen mit dem Universal-Drehtisch zeigen, dass der Anteil der geschockten Quarze und die durchschnittliche Anzahl der PDF-Gruppen pro Mineralkorn empfindlichere Indikatoren für geringe Änderungen in den Schockdrücken darstellen als die PDF-Orientierungen. Weiterhin ist die Präzision der U-Tisch Messungen vorwiegend von der Anzahl der untersuchten PDF-Sets abhängig. Die Kombination von Mikrobeobachtungen und numerischer Modellierung unelastischer Gesteinsdeformation und Modifikationsprozessen während des Aufstiegs der Zentralerhebung erlauben die Rekonstruktion der Prä-Einschlagsposition der erbohrten Gesteine und lassen eine Schockabschwächung von ~5 GPa innerhalb der obersten 200 Meter der Zentralerhebung, welche von sprödem Bruchverhalten dominiert ist, erkennen.

Untersuchungen an Ballensilikaten aus mehreren Impaktstrukturen führten zur Unterscheidung von fünf Ballen-Typen und zur Präsenz von Coesit in Ballen- α -Cristobalit, und sie zeigen, dass Ballenquarz/-cristobalit das Ergebnis einer Rücktransformation von schockinduzierten Zuständen ist, und stellt daher einen indirekten Hinweis auf Schockmetamorphose dar.

TABLE OF CONTENTS

<i>Preface</i>	iii
<i>Acknowledgement</i>	vii
<i>Abstract</i>	ix
<i>Zusammenfassung</i>	xi
Chapter 1: Introduction to impact cratering	1
1.1. General introduction	1
1.2. Types of impact craters	3
1.2.1. <i>Simple craters</i>	3
1.2.2. <i>Complex craters</i>	4
1.3. Cratering mechanics	4
1.3.1. <i>Contact and compression stage</i>	5
1.3.2. <i>Excavation stage</i>	5
1.3.3. <i>Modification stage</i>	7
References	7
Chapter 2: Review of shock metamorphism	11
2.1. Impactites	12
2.1.1. <i>Proximal impactites</i>	12
<u>2.1.1.1. <i>Shocked rocks</i></u>	12
<u>2.1.1.2. <i>Impact breccias</i></u>	13
2.1.1.2.1. <i>Monomict breccia</i>	13
2.1.1.2.2. <i>Lithic breccia</i>	13
2.1.1.2.3. <i>Suevite</i>	14
2.1.1.2.4. <i>Pseudotachylitic breccia</i>	14
<u>2.1.1.3. <i>Impact melt rocks</i></u>	15
2.1.2. <i>Distal impactites</i>	15
<u>2.1.2.1. <i>Tektites and microtektites</i></u>	15
<u>2.1.2.2. <i>Airfall beds</i></u>	16
2.2. Shock features	17
2.2.1. <i>Shatter cones</i>	17
2.2.2. <i>Deformations in quartz</i>	18
<u>2.2.2.1. <i>Planar microstructures</i></u>	18
2.2.2.1.1. <i>Planar fractures (PFs)</i>	18
2.2.2.1.2. <i>Planar deformation features (PDFs)</i>	19
<u>2.2.2.2. <i>Mosaicism</i></u>	20
<u>2.2.2.3. <i>Refractivity, birefringence, and density</i></u>	21
2.2.3. <i>Deformations in other minerals</i>	21
2.2.4. <i>Diaplectic glasses</i>	22
2.2.5. <i>Mineral and whole-rock melt</i>	23
2.2.6. <i>High-pressure polymorphs</i>	24
<u>2.2.6.1. <i>Coesite and Stishovite</i></u>	24
<u>2.2.6.2. <i>Impact diamonds</i></u>	25
2.2.7. <i>Post-shock features</i>	25

2.2.7.1. <i>Toasted quartz</i>	25
2.2.7.2. <i>Ballen quartz and cristobalite</i>	26
References	27
Chapter 3: The Bosumtwi impact structure	33
3.1. Geology of the crater	34
3.2. Geochemistry of country rocks and impactites from outside of the crater – Relationship with the Ivory Coast tektites	36
3.2.1. <i>Geochemistry of country rocks</i>	36
3.2.2. <i>Geochemistry of impactites and relationship of the Bosumtwi crater with the Ivory Coast tektite strewn field</i>	37
3.3. The 2004 ICDP drilling project	38
3.3.1. <i>Geological setting and stratigraphy of drill core LB-07A</i>	39
3.3.2. <i>Geological setting and stratigraphy of drill core LB-08A</i>	41
References	42
Chapter 4: Methodology	47
4.1. Samples	47
4.1.1. <i>Selection of samples</i>	47
4.1.2. <i>Sample preparation</i>	47
4.2. Analytical methods	48
4.2.1. <i>Optical microscope and universal stage (U-stage)</i>	48
4.2.1.1. <i>Preparation of the microscope for U-stage installation</i>	49
4.2.1.2. <i>Mounting of assembled U-Stage</i>	49
4.2.1.3. <i>Installation of the U-stage on the microscope</i>	49
4.2.1.4. <i>Calibration of the U-stage</i>	49
4.2.1.5. <i>Measurement of the c-axis and PDF orientations in quartz grains</i>	49
4.2.1.6. <i>Plotting measurements and data reduction</i>	51
4.2.2. <i>Instrumental Neutron Activation Analysis (INAA)</i>	52
4.2.2.1. <i>Source of neutrons – Irradiation</i>	52
4.2.2.2. <i>Gamma spectroscopy</i>	53
4.2.2.3. <i>Data processing and corrections</i>	54
4.2.2.4. <i>Sample preparation</i>	55
4.2.2.5. <i>Measurement</i>	56
4.2.3. <i>X-ray Fluorescence (XRF) spectrometry</i>	58
4.2.4. <i>Scanning Electron Microscopy (SEM)</i>	60
4.2.4.1. <i>General principle</i>	60
4.2.4.2. <i>X-ray spectrometers</i>	61
4.2.4.3. <i>SEM investigations</i>	62
4.2.5. <i>Cathodoluminescence (CL) spectroscopy</i>	62
4.2.6. <i>Transmission Electron Microscopy (TEM)</i>	64
4.2.6.1. <i>General principle</i>	64
4.2.6.2. <i>Sample preparation</i>	65
4.2.7. <i>Electron Microprobe (EMP)</i>	67
4.2.8. <i>MicroRaman spectroscopy</i>	68
4.2.8.1. <i>Fundamental on Raman spectroscopy</i>	68
4.2.8.2. <i>Instrumentation</i>	69
4.2.8.3. <i>Measurement</i>	69

4.2.9. Mass spectrometry (MS)	70
4.2.9.1. Isotope Ratio Mass Spectrometry (IRMS)	70
4.2.9.1.1. Instrumentation	71
4.2.9.1.2. Measurement	71
4.2.9.2. Isotope Dilution–Thermal Ionization Mass Spectrometer (ID-TIMS)	71
4.2.9.3. Laser Ablation Inductively Coupled Plasma Spectrometer (LA-ICP-MS)	72
References	73
Chapter 5:	77
<i>Drill core LB-08A, Bosumtwi impact structure, Ghana: Petrographic and shock metamorphic studies of material from the central uplift (Ferrière et al., 2007, MAPS 42:611–633)</i>	
Chapter 6:	101
<i>Drill core LB-08A, Bosumtwi impact structure, Ghana: Geochemistry of fallback breccia and basement samples from the central uplift (Ferrière et al., 2007, MAPS 42:689–708)</i>	
Chapter 7:	121
<i>Shock metamorphism of Bosumtwi impact crater rocks, shock attenuation, and uplift formation (Ferrière et al., 2008, Science, in press)</i>	
Chapter 8:	143
<i>Characterization of ballen quartz and cristobalite in impact breccias: new observations and constraints on ballen formation (Ferrière et al., 2009, EJM, doi: 10.1127/0935-1221/2009/0021-1898)</i>	
Chapter 9:	159
<i>Systematic study of universal-stage measurements of planar deformation features in shocked quartz: Implications for statistical significance and representation of results (Ferrière et al., 2009, MAPS, in revision)</i>	
Chapter 10: Potpourri	185
10.1. Geochemistry of various minerals, melt particles, and bulk analyses of samples from the drill core LB-08A	185
10.2. U-Pb zircon ages and Sr-Nd isotopic composition of samples from drill core LB-08A	197
10.3. Transmission electron microscope observations of planar deformation features in quartz from the Bosumtwi and the Chesapeake Bay impact structures	203
10.4. “Toasted” quartz in impactites – Origin revisited	208
10.4.1. Previous work	208

<i>10.4.2. Results and Discussion</i>	208
<i>10.4.3. Conclusions</i>	213
10.5. New observations of ballen quartz and cristobalite	215
References	218

Appendices 223

<i>Appendix A: Details of investigated samples from drill core LB-08A</i>	225
<i>Appendix B: Major and trace element composition for samples from drill core LB-08A</i>	228
<i>Appendix C: Petrographic descriptions of LB-08A drill core samples</i>	240
<i>Appendix D: SEM quantitative energy dispersive X-ray analyses of mineral clasts and melt particles in suevite samples from the Bosumtwi crater (Ghana)</i>	265
<i>Appendix E: Isotope ratios and U-Pb ages of zircons from suevite and meta-graywacke samples from drill core LB-08A</i>	270
<i>List of Publications</i>	273
<i>Curriculum Vitae</i>	277

CHAPTER 1: Introduction to impact cratering

1.1. General introduction:

Impact cratering is now widely accepted as a major geological process, largely due to the Apollo program and other missions of exploration of the solar system. The discovery of evidence for a large impact event in sediments from the Cretaceous-Tertiary boundary, as well as the collision of the comet Shoemaker-Levy 9 on the surface of Jupiter, in 1994, have also contributed to recognize that hypervelocity asteroidal or cometary collision of objects with the Earth is a significant process. Impact cratering differs mainly from other surface geological processes (such as volcanism) by the extreme pressures, temperatures, and high strain rates involved, and by the almost instantaneous nature of the impact process. Impact structures are observed at the surface of all solid planetary bodies, including asteroids and planets with icy surface. However, on Earth, only a few impact structures are easily distinguishable, because of the constant renewing of its surface by plate tectonics and erosion, and due to the deposition of sediments, or the oceans and forest which cover craters. Currently, only 174 impact structures are definitively recognized on Earth (see Figure 1-1; Earth Impact Database, 2008), but many other impact structures that must exist have not yet been discovered. Some more or less circular structures are presently considered to be of uncertain origin (see, e.g., Rajmon, 2006; Reimold, 2007), however their recognition and confirmation as new impact structures will need to be supported by evidence of unambiguous shock deformation or traces of extraterrestrial matter (see for details the chapter 2).

The terrestrial cratering record is biased towards young and large craters, mainly due to resurfacing and alteration processes, but in addition, some country of the world are quasi non-investigated because of wars and/or non-existing access facilities. The oldest craters known on Earth are the Dhala crater, between 1.6-2.5 Gyr old (Pati et al., 2008), the Suavjärvi crater, about 2.4 Gyr old (however, this age is not yet well constrained) (Mashchak and Naumov, 1996), and the Vredefort Dome, 2.02 Gyr old (Kamo et al., 1997). On the contrary, the youngest craters known are Sikhote Alin, formed in 1947 and only 27 m in diameter (Earth Impact Database, 2008) and Wabar, about 290 ± 38 years old and ~ 116 m in diameter (Prescott et al., 2004). An even younger “small impact crater” have been formed very recently, on the 15 of September 2007, the Carancas crater (Peru), about 13.5 m in diameter (e.g., Brown et al., 2008). However, no large impact crater was formed during the last thousands years on Earth, and only numerical modeling and explosive experiments combined with detailed investigations of impact structures can be used for the understanding of cratering processes. In nature, an in-depth view of the final impact structure is possible because of the differential levels of erosion of the different impact structures around the world. In addition, drilling campaigns have also recovered samples from several impact structures.

The study of a large number of impact structures on the Moon and more recently on Mars, Venus, and Mercury have permitted to better characterize morphological aspects of the different types of craters. On Earth, two morphologically different types of craters are

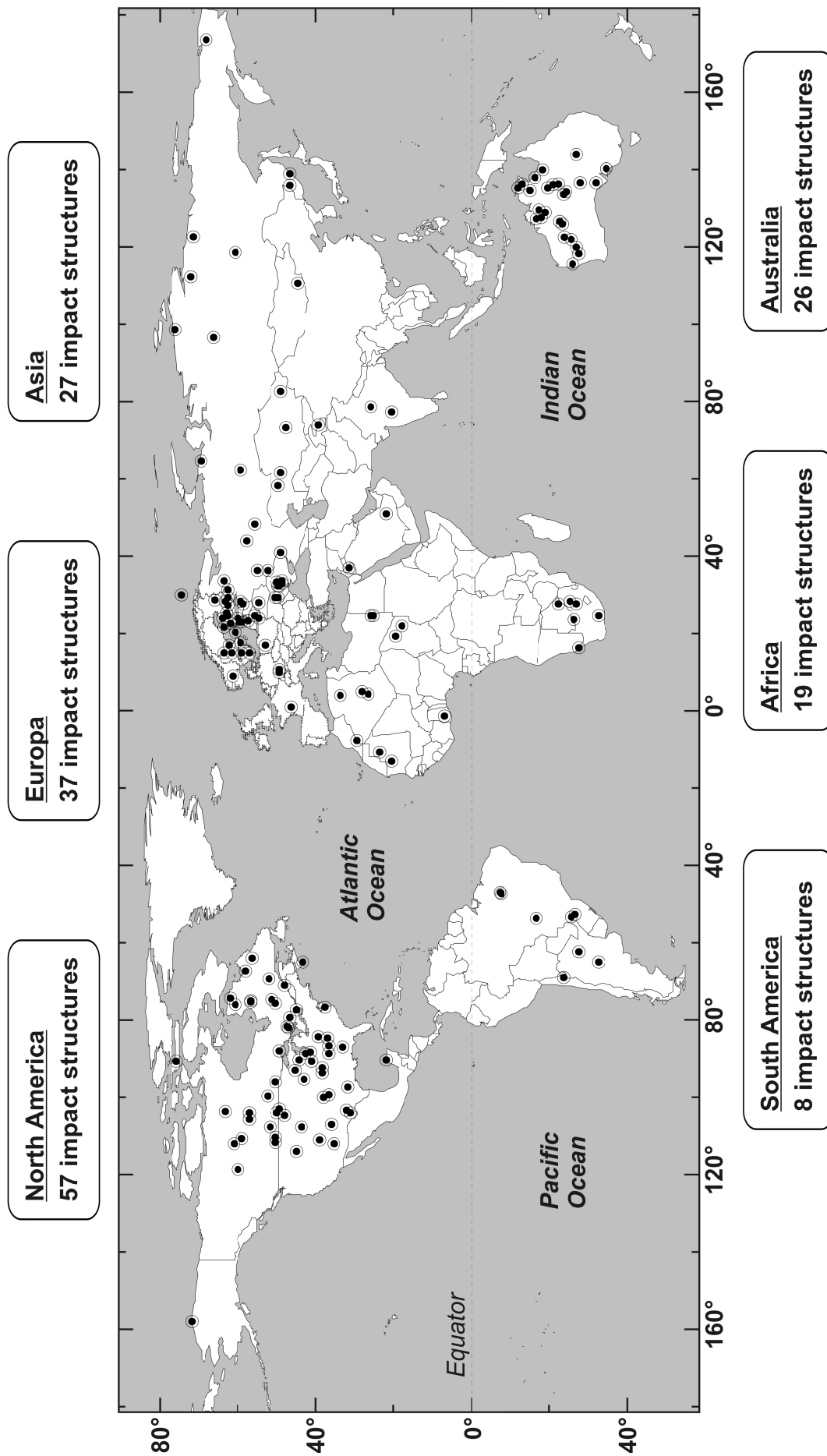


Figure 1-1. Distribution of impact structures on Earth. Location of 174 currently known impact structures is reported. Data from Earth Impact Database (2008). Arkeno 1 and 2 (Libya) and Calvin (Michigan, U.S.A) craters are note reported as no definite evidence for meteorite impact origin have been founded so far for these structures. Two recently discovered impact structures (not yet included in the Earth Impact Database) are also shown, Dhala (India) [Pati et al., 2008] and Waqf as Suwwan (Jordanania) [Salameh et al., 2008].

known, the simple impact craters and the complex impact craters (see, e.g., Roddy, 1977; Melosh, 1989; French, 1998). On other planets, larger structures, ranging from a few hundreds to thousands kilometers, have been observed, the so-called multi-ring basins (e.g., Melosh, 1989; Spudis, 1993). The Chicxulub crater (Mexico) is considered by some authors to be a terrestrial multi-ring basin (e.g., Morgan and Warner, 1999).

1.2. Types of impact craters:

1.2.1. Simple craters

Simple craters are bowl-shaped craters (Figure 1-2) with diameters of up to 2-4 km, depending of the target rocks (these diameters values are only valid for terrestrial craters as the change-over diameter between simple and complex crater is also dependent of the gravity). The transition between simple and complex crater is observed at lower diameter for sedimentary rocks (around 2 km) than for crystalline rocks (around 4 km; Grieve, 1987). The crater depth, or distance between crater rim and crater floor, is about one third of the crater diameter; this is true only for well preserved craters. Rim height is about four percent of the crater diameter (Melosh, 1989). The crater is generally filled by impact breccia, the so-called “breccia lens” or “crater-fill breccia” (e.g., French, 1998).

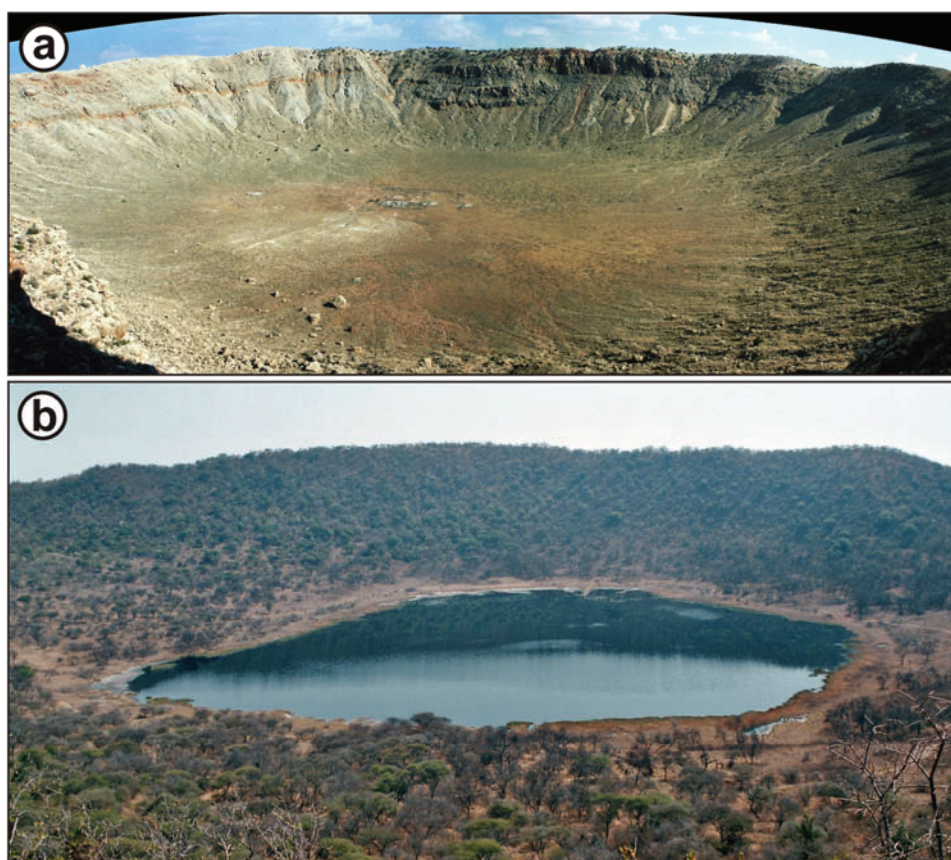


Figure 1-2. Examples of well preserved simple impact structures; the Meteor Crater and the Tswaing, about 1.2 and ~1 km in diameter, respectively. a) Meteor Crater (or Barringer Meteorite Crater) occurs in Paleozoic-Mesozoic sedimentary rocks, in Arizona (U.S.A.) and was formed about 50 ka. b) Tswaing crater (or Pretoria Saltpan crater) occurs in granite and was formed about 220 ka.

1.2.2. Complex craters

Complex craters are characterized by a central uplift, a flat floor, and inward collapse around the rim (see Figure 1-3). On Earth, the diameter of complex impact craters is larger to about 2 to 4 km (Grieve, 1987); complex craters start to form on the Moon for diameters around 15-20 km (e.g., Howard, 1974). The central uplift is composed of rocks that originated below the crater floor. It represents a stratigraphic uplift of about one-tenth of the crater diameter (see, e.g., Melosh, 1989; Cintala and Grieve, 1998). Like for simple craters, complex craters are filled by a mixture of rock and mineral clasts, both shocked and unshocked, together with impact melt and material slumped in the crater from the walls and crater rim. Detailed study of the texture and composition of the different units forming the crater-fill breccia can permit the reconstruction of the successive phases of the crater formation and modification. This approach need however to be combined with numerical modeling (see Stöffler et al., 2004).

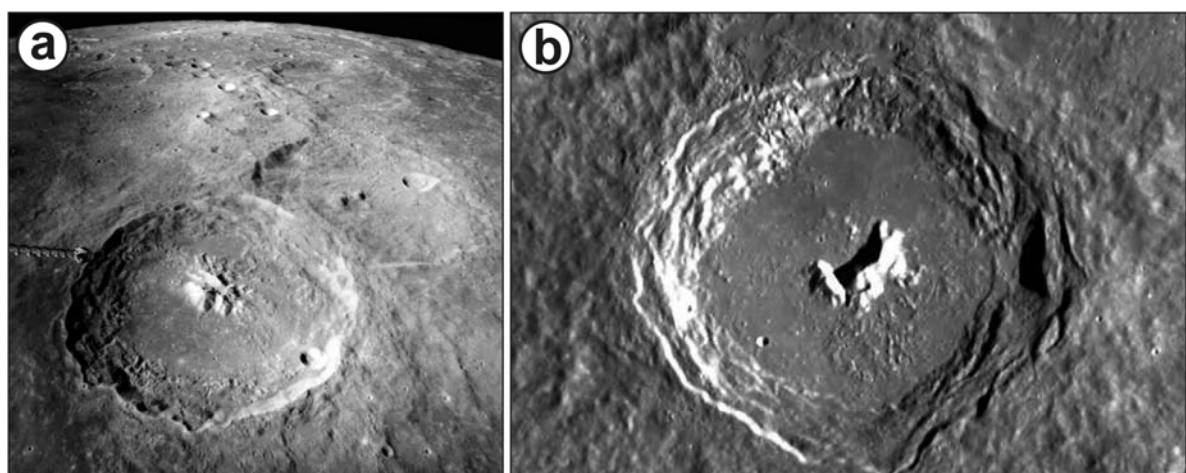


Figure 1-3. Examples of complex impact structures on the Moon with well-preserved central uplift and terraced walls. a) The about 100 km diameter Theophilus impact crater (NASA; Apollo 16 image AS16-M-0692); b) The about 120 km diameter Pythagoras impact crater (ESA/Space-X photograph; SMART-1).

1.3. Cratering mechanics:

The time necessary to the formation of an impact crater, depending on the size of the impact event, is of the order of a few seconds to some minutes (e.g., Melosh, 1989; Ivanov and Artemieva, 2002); however it can take up to few hours for the proximal ejecta to be completely deposited. Target rocks are deformed and fractured, partially melted and vaporized as a result of a catastrophic burst of energy. Asteroid and comets collided the Earth at hypervelocity, between about 10 to 72 km/s (e.g., Melosh, 1989). Small bodies of a few meters across normally disintegrate in the atmosphere and only in rare cases, a fragment survives and reaches the ground at low speed (not more than a few hundreds m/s). Such a rock, which may excavate a small hole, rarely much wider than the rock itself, is called a meteorite. Larger asteroidal or cometary bodies are not significantly decelerated in the atmosphere and hit the Earth's surface at cosmic velocity. As a result of this collision,

an impact crater is formed. The formation of an impact crater (i.e., cratering process) is a continuous process which is generally subdivided into three main stages (for a review, see, e.g., Gault et al., 1968; Grieve, 1987; Melosh, 1989; French, 1998): the contact and compression, excavation, and modification stages (Figure 1-4).

1.3.1. Contact and compression stage

The contact and compression stage begins when the projectile contacts the ground surface (i.e., target surface). At this instant the projectile is stopped, penetrating not more than 2 times its diameter, and its kinetic energy is transferred to the target rocks in the form of, e.g., shock waves. Shock waves are generated at the contact point between projectile and target's surface, and propagate simultaneously, into the target rocks and into the projectile itself. When the shock wave reaches the upper surface of the projectile, it is reflected back into the projectile; this wave is called rarefaction wave or tensional wave (Figure 1-4). Consequently, the projectile is very quickly decompressed and most of it is melted and/or vaporized. Only in some cases fragments of the projectile were recovered within or around the crater. The passage of the shock wave and of the subsequent rarefaction wave through the target rocks also results in the melting and vaporization of a large volume of target material. The shock pressures, in excess of 100 GPa close to the impact point, attenuate with distance from the point of impact, as shock waves decrease in energy density during propagation in the target rocks. Consequently, a variety of shock effects are produced in rock-forming minerals and the relative spatial distribution of these shock transformations and deformations, formed at different pressures and temperatures in autochthonous rocks (i.e., basement rocks), can be used to estimate maximum shock pressures and, thus, the rate of shock attenuation (see for details the publication chapter 7). Shock pressures between 10 to 50 GPa can be reached at several kilometers depth in the case of large impact structures. At even greater distances from the impact point, the shock waves eventually become seismic waves or elastic waves; Pressures of about 1-2 GPa are reached (e.g., Kieffer and Simonds, 1980), not enough to produce any shock transformations, causing brecciation and faulting of the rocks (French, 1998).

The contact and compression stage is extremely brief as it is over in no more than a second (e.g., Melosh, 1989). The crater itself forms during the subsequent stage, the so-called excavation stage (Figure 1-4).

1.3.2. Excavation stage

The excavation stage, which immediately follows the contact and compression stage, is dominated by complex interactions between the outward-directed shock waves and the downward-directed rarefaction waves with the target, leading to the formation of the so-called transient crater or transient cavity. The excavation starts when tensional stress exceeds the mechanical strength of the target rocks. Rocks are fractured and shattered, moving in various directions, mainly upwards and out in the upper excavated zone and mainly down and outwards in the lower zone of the transient cavity. The opening of the transient cavity stops when shock and rarefaction waves are not energetic enough to eject

material beyond the cavity rim. The transient crater, typically 20-30 times larger than the projectile diameter (e.g., French, 1998), shows an uplifted rim. During the excavation stage, the material in the excavated zone is ejected beyond the transient cavity rim, forming impact ejecta. The material in the displaced zone remains within the transient cavity, forming crater fill impactites (Figure 1-4). The entire excavation stage takes seconds to minutes to be completed, depending upon the crater size. About 6 seconds are necessary to excavate a 1-km-diameter crater, while a 200-km-diameter crater is excavated in about one minute and thirty seconds (Melosh, 1989; French, 1998).

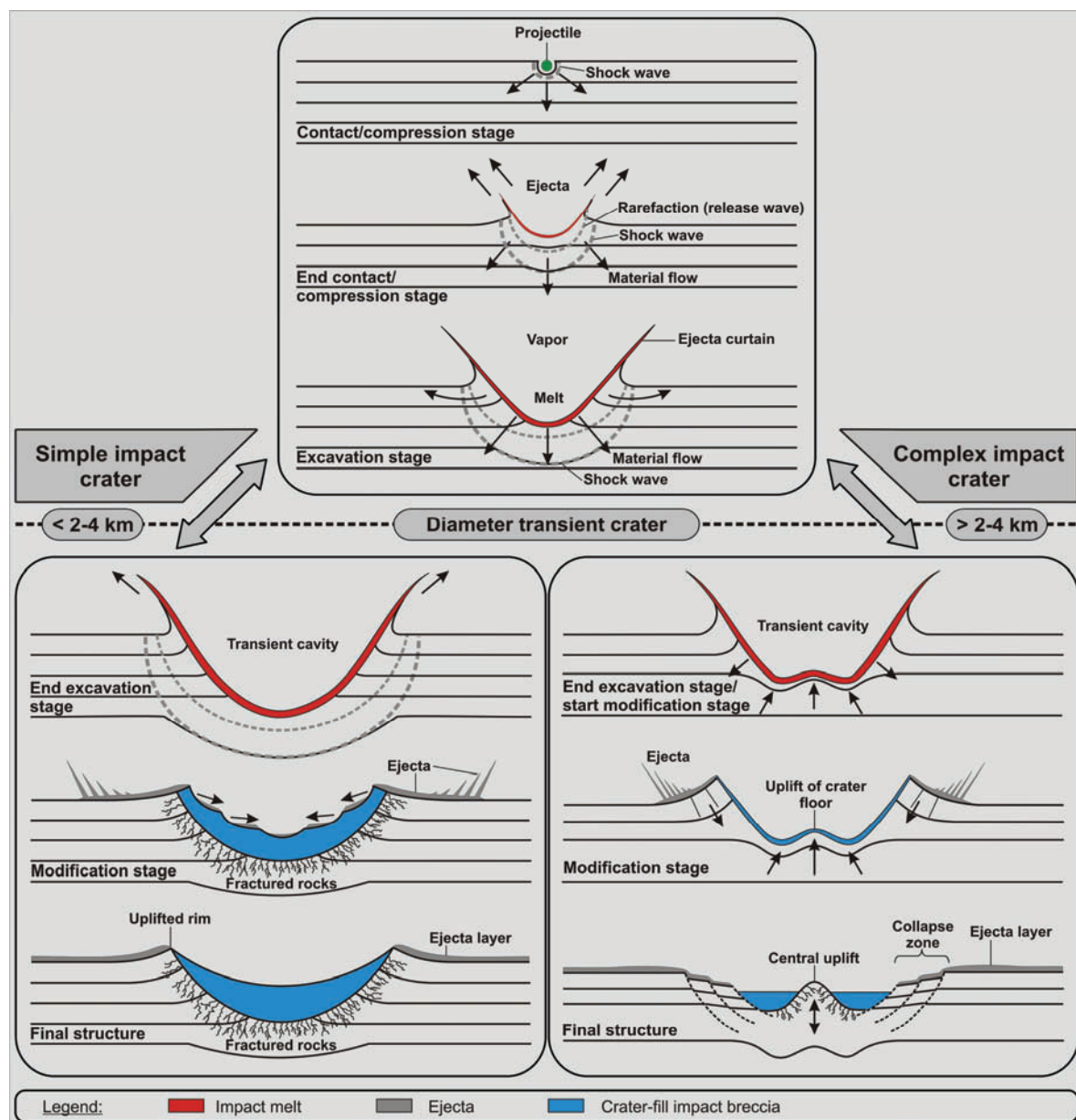


Figure 1-4. Cross-section diagrams showing the different stages of formation of an impact structure. At small diameters (i.e. diameter <2–4 km), a simple impact crater forms, when for diameters >2–4 km, the initial transient crater is unstable and a complex impact crater forms. The first stage, so-called contact/compression stage, as well as the starting excavation stage is depicted on a unique series of cross-section for both, simple and complex impact craters, as these stages of formation are almost identical in the two cases. See text for discussion on the different stages of formation (modified after French, 1998).

1.3.3. Modification stage

The modification stage begins soon as the transient cavity reaches its maximum dimension. The magnitude of modifications is mainly function of the gravity of the impacted planet (or asteroid) and it depends also of the crater size. Major readjustments of the transient cavity occur for the formation of complex craters, while the bowl-shaped transient crater is quasi not modified in the case of simple craters. Two competing processes act during the modification stage; downward-directed gravitational collapse of the inner rim and uplift of the transient crater floor. The initially steep walls of the transient crater collapsed under gravitational forces forming characteristic terraces. Concerning the development of the central uplift, it occurs by displacements along faults as a brittle component in the case of moderately sized impact structures (such as for Bosumtwi; 10.5-km-diameter), whereas in the case of larger impact structures central uplifts involve fluidization and/or large differential movements of target blocks (see for details the publication chapter 7).

The modification stage takes typically only a few minutes to be completed, even though further readjustments of the crater, can take years or even millions of years, as a result of sedimentation within the crater, seismic readjustments, and/or erosion processes. In addition, rock-forming minerals are modified by impact-associated hydrothermal activity and weathering (e.g., Naumov, 2005).

References

- Brown P., ReVelle D. O., Silber E. A., Edwards W. N., Arrowsmith S., Jackson L. E. Jr., Tancredi G., and Eaton D. 2008. Analysis of a crater-forming meteorite impact in Peru. *Journal of Geophysical Research* 113:E09007, doi:10.1029/2008JE003105.
- Cintala M. J. and Grieve R. A. F. 1998. Scaling impact melting and crater dimensions: Implications for the lunar cratering record. *Meteoritics and Planetary Science* 33:889–912.
- Earth Impact Database 2008. <http://www.unb.ca/passc/ImpactDatabase/> (accessed 29 September 2008).
- French B. M. 1998. *Traces of catastrophe: A handbook of shock-metamorphic effects in terrestrial meteorite impact structures*. LPI Contribution #954. Houston, Texas: Lunar and Planetary Institute. 120 p.
- Gault D. E., Quaide W. L., and Oberbeck V. R. 1968. Experimental and analytical studies of crystalline damage useful for the recognition of impact structures. In *Shock metamorphism of natural materials*, edited by French B. M. and Short N. M. Baltimore: Mono Book Corporation. pp. 87–99.

Grieve R. A. F. 1987. Terrestrial impact structures. *Annual Reviews of Earth Planetary Science* 15:245–270.

Howard K. A. 1974. Fresh lunar impact craters: Review of variations with size. Proceedings, 5th Lunar Science Conference. pp. 61–69.

Ivanov B. A. and Artemieva N. A. 2002. Numerical modeling of the formation of large impact craters. In *Catastrophic events and mass extinctions: Impacts and beyond*, edited by Koeberl C. and MacLeod K. G. GSA Special Paper #356. Boulder, Colorado: Geological Society of America. pp. 619–630.

Kamo S. L., Reimold W. U., Krogh T. E., and Colliston W. P. 1997. A 2.023 Ga age for the Vredefort impact event and a first report of shock metamorphosed zircons in pseudotachylitic breccias and Granophyre. *Earth and Planetary Science Letters* 144:369–387.

Kieffer S. W. and Simonds C. H. 1980. The role of volatiles and lithology in the impact cratering process. *Reviews of Geophysics and Space Physics* 76:5449–5473.

Mashchak M. S. and Naumov M. V. 1996. The Suavjärvi structure: An early Proterozoic impact site on the Fennoscandian shield (abstract). 27th Lunar and Planetary Science Conference. pp. 825–826.

Melosh H. J. 1989. *Impact cratering—A geological process*. New York: Oxford University Press. 245 p.

Morgan J. and Warner M. 1999. Chicxulub; the third dimension of a multi-ring impact basin. *Geology* 27:407–410.

Naumov M.V. 2005. Principal features of impact-generated hydrothermal circulation systems: mineralogical and geochemical evidence. *Geofluids* 5:165–184.

Pati J. K., Reimold W. U., Koeberl C., and Pati P. 2008. The Dhala structure, Bundelkhand craton, Central India – Eroded remnant of a large Paleoproterozoic impact structure. *Meteoritics and Planetary Science* 43:1383-1398.

Prescott J. R., Robertson G. B., Shoemaker C., Shoemaker E. M., and Wynn J. 2004. Luminescence dating of the Wabar meteorite craters, Saudi Arabia. *Journal of Geophysical Research* 109, E01008, doi:10.1029/2003JE002136.

Rajmon D. 2006. Suspected Earth impact sites (abstract #2372). 37th Lunar and Planetary Science Conference. CD-ROM.

Reimold W. U. 2007. The impact crater Bandwagon (Some problems with the terrestrial impact cratering record). *Meteoritics and Planetary Science* 42:1467–1472.

Roddy D. J. 1977. Large-scale impact and explosion craters: Comparisons of morphological and structural analogs. In *Impact and explosion cratering*, edited by Roddy D. J., Pepin R. O., and Merrill R. B. New York: Pergamon Press. pp. 185–246.

Salameh E., Khoury H., Reimold W. U., Schneider W., and Kenkmann T. 2008. First large meteorite impact structure discovered in the middle east: Jebel Waqf As Suwwan, Jordan (abstract #3106). Large Meteorite Impacts and Planetary Evolution (LMI IV) Meeting, Vredefort Dome, South Africa.

Spudis P. D. 1993. The geology of multi-ring impact basins: The Moon and other planets. Cambridge: Cambridge University Press. 263 p.

Stöffler D., Artemieva N. A., Ivanov B. A., Hecht L., Kenkmann T., Schmitt R.-T., Tagle R. A., and Wittmann A. 2004. Origin and emplacement of the impact formations at Chicxulub, Mexico, as revealed by the ICDP deep drilling at Yaxcopoil-1 and by numerical modeling. *Meteoritics and Planetary Science* 39:1035–1067.

CHAPTER 2: Review of shock metamorphism

Recognition and confirmation of impact structures need to be supported by evidence of shock effects in minerals (such as planar deformation features in quartz, stishovite, etc.) and/or by siderophile-element anomalies (e.g., iridium contents, osmium isotopes). Crater morphology is not a sufficient argument, because a variety of circular features can be formed by completely different geological processes (e.g., volcanism or salt diapir).

Shock effects or shock-metamorphic effects is a term that covers all types of shock-induced changes, such as formation of planar microstructures, phase transformations, decomposition of minerals, melting, and vaporization of rock-forming minerals. These irreversible changes are produced when rocks are subjected to shock pressures above their Hugoniot elastic limit (HEL). This limit is defined as “the critical shock pressure at which a solid yields under the uniaxial strain of a plane shock wave” (Stöffler, 1972). The HEL of quartz is mostly in the range of 5–8 GPa and of about 1–10 GPa for most geological materials (e.g., Stöffler, 1972; Stöffler and Langenhorst, 1994). In nature, at the surface of the Earth, only hypervelocity impacts can generate such high shock pressures. For comparison, pressure and temperature fields of endogenic metamorphism and shock metamorphism are reported in Figure 2-1.

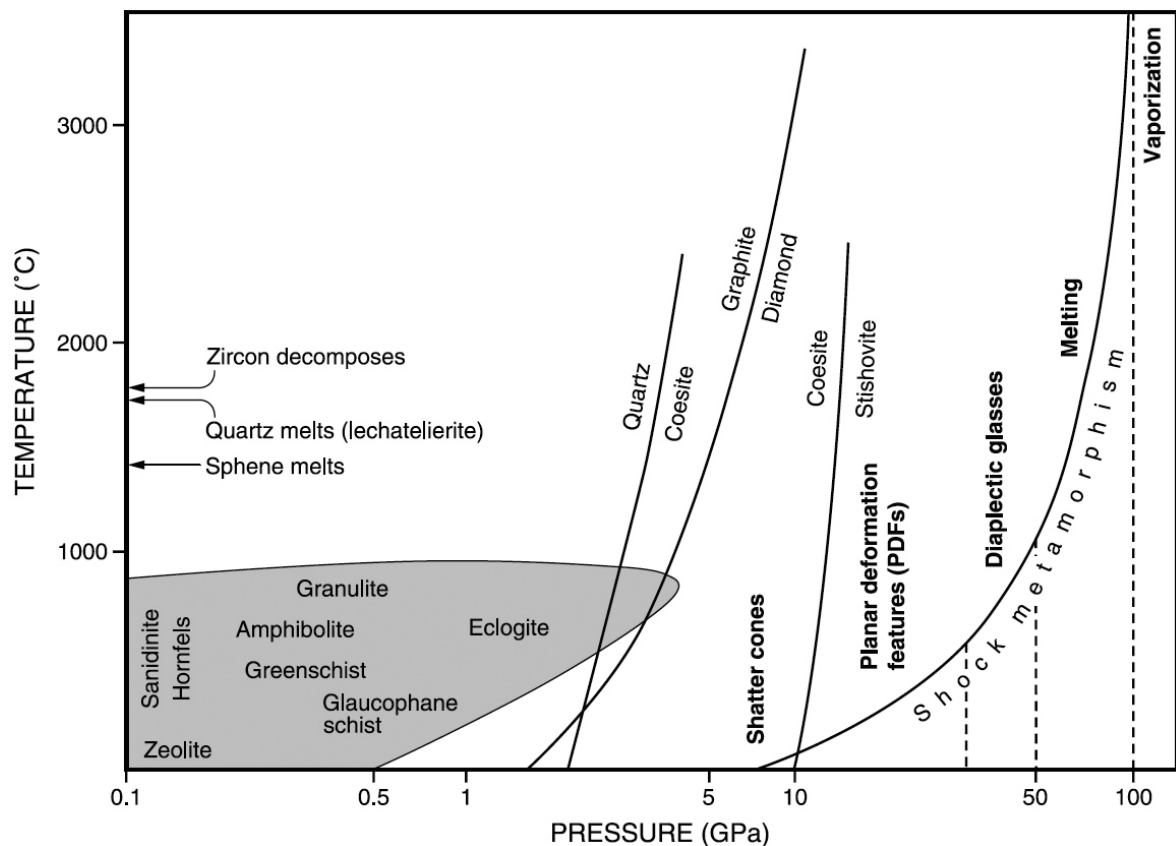


Figure 2-1. Pressure and temperature fields of endogenic metamorphism and shock metamorphism. Onset pressures of specific shock effects in the rocks and minerals are indicated by vertical dashed lines. The exponential curve on the right (noted “Shock metamorphism”) shows the relation between pressure and post-shock temperature for shock metamorphism of granitic rocks (from French, 1998).

A great diversity of shock effects in minerals are known, and have been abundantly described, mostly for quartz, in the literature during the last forty years (see, e.g., French and Short, 1968; Engelhardt and Bertsch, 1969; Stöffler, 1972; Stöffler and Langenhorst, 1994; Grieve et al., 1996; French, 1998; Montanari and Koeberl, 2000; Langenhorst, 2002; and references therein). A review of shock effects in minerals is provided in the following sections; in addition two examples of post-shock (thermal) effects, namely toasted quartz and ballen silica, are also discussed.

Minerals subjected to shock metamorphism occur in different petrographic assemblages and in different rock types. Depending on the nature (i.e., lithology) and on properties of the target rock(s), function of the level of erosion of the crater and of the magnitude of the hypervelocity impact, etc., the full spectrum of diagnostic features is not necessary present in all impact structures. The different rocks affected (or produced) by one or more hypervelocity impact(s) are called “impactites” (see, e.g., the reviews by French, 1998; Stöffler and Grieve, 2007). The classification and definition of the various impactites is complex and always discussed, nevertheless, using basic criteria, such as “microstructure, degree of shock metamorphism, and lithological components”, Stöffler and Grieve (2007) have defined the main types of impactites. Using additional criteria, such as “the mode of occurrence with respect to the parent impact crater and to the geological or structural setting of the impactites”, the same authors have established a subclassification of the main types of impactites. As the name of the different rock types described in this thesis follow this classification, an illustrated overview of the classification by Stöffler and Grieve (2007) is presented. Definitions for each type of impactite is reported and discussed, as some specific points need to be clarified.

2.1. Impactites:

Impactite is defined as “rock produced by impact metamorphism”, including “shocked rocks, impact breccias, impact melt rocks, (micro)tektites and impactoclastic airfall beds” (Stöffler and Grieve, 2007). The two main types of impactites occurring on Earth (i.e., impactites from single impacts) are subdivided into proximal and distal impactites. The so-called “impactites from multiple impacts” (Stöffler and Grieve, 2007) are not discussed as only terrestrial impactites were investigated.

2.1.1. Proximal impactites

Proximal impactites are subdivided into shocked rocks, impact breccias, and impact melt rocks.

2.1.1.1. Shocked rocks:

Shocked rocks are defined as “non-brecciated rocks, which show unequivocal effects of shock metamorphism, exclusive of whole rock melting” (Stöffler and Grieve, 2007). Shocked rocks are further subclassified into “progressive stage of shock metamorphism” (Stöffler and Grieve, 2007). For each of the different types of lithologies, such as quartzofeldspathic, basaltic-gabbroic, sandstone, etc., the subclassification is

somewhat different, as each rock type is modified (i.e., altered) differently at the same peak pressure. Detailed tables for several different lithologies are given by Stöffler and Grieve (2007).

2.1.1.2. Impact breccias:

According to Stöffler and Grieve (2007), impact breccias are subdivided into three subgroups, namely, monomict breccia, lithic breccia, and suevite. This subdivision is based on the degree of mixing of the different target lithologies and on the occurrence of melt particles (Stöffler and Grieve, 2007). Pseudotachylitic breccia is not included in the list of the different types of impact breccias, but it should be added to this list, as an additional subtype of impact breccia.

2.1.1.2.1. Monomict breccia:

The monomict (impact) breccia is, according to Stöffler and Grieve (2007), “a cataclasite produced by impact and displaying weak or no shock metamorphism”. This definition is in fact not fully correct, as it is impossible in absence of evidences of shock metamorphism to differentiate a monomict breccia from a conventional cataclasite formed by tectonic. The term of monomict breccia was only used in the present work for breccia containing only a single lithology of lithic clasts and displaying shock metamorphism. Monomict breccia occurs usually in the “(par)autochthonous floor of an impact crater” or as clasts/blocks “within polymict impact breccia” (Stöffler and Grieve, 2007).

2.1.1.2.2. Lithic breccia:

The lithic (impact) breccia is a polymict impact breccia with clastic matrix containing mineral and lithic clasts, but lacking cogenetic impact melt particles (see Figure 2-2a; Stöffler and Grieve, 2007). The different clasts are excavated from different regions of the target rock section, transported, mixed, and deposited inside or around the impact crater or injected, as dykes, into the target rocks (Stöffler and Grieve, 2007). In the rare case of single lithology target, a lithic breccia can be monomict.

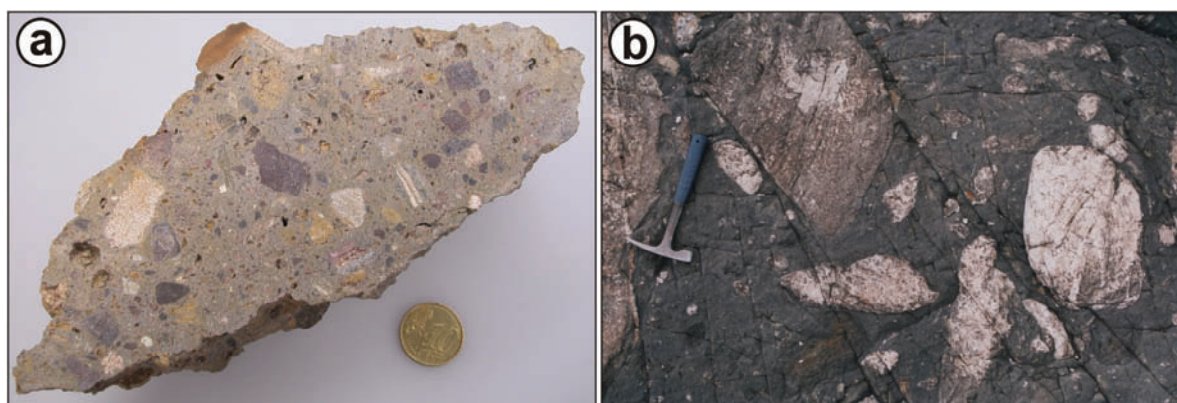


Figure 2-2. Macrophotographs of impactites. a) Typical hand specimen of polymict lithic impact breccia from the Rochechouart crater (France). Note that various clast lithologies are visible in a grayish clastic matrix. b) Exposure view of pseudotachylitic breccia from the Sudbury impact structure (Canada). The view shows a mixture of large angular and rounded blocks of quartzite in a dark matrix.

2.1.1.2.3. *Suevite:*

Suevite (or suevite breccia, or suevitic breccia) is defined as a “polymict impact breccia with particulate matrix containing lithic and mineral clasts in all stages of shock metamorphism including cogenetic impact melt particles which are in a glassy or crystallized state” (see Figure 2-3; Stöffler and Grieve, 2007). The name of suevite, originally used for impactites from the Ries, have been generalized, and is now used for the description of similar rocks occurring within or outside of the crater rim, such as at Bosumtwi (see Figure 2-3). In some impact structures, dykes of suevite are reported (such as at Bosumtwi).

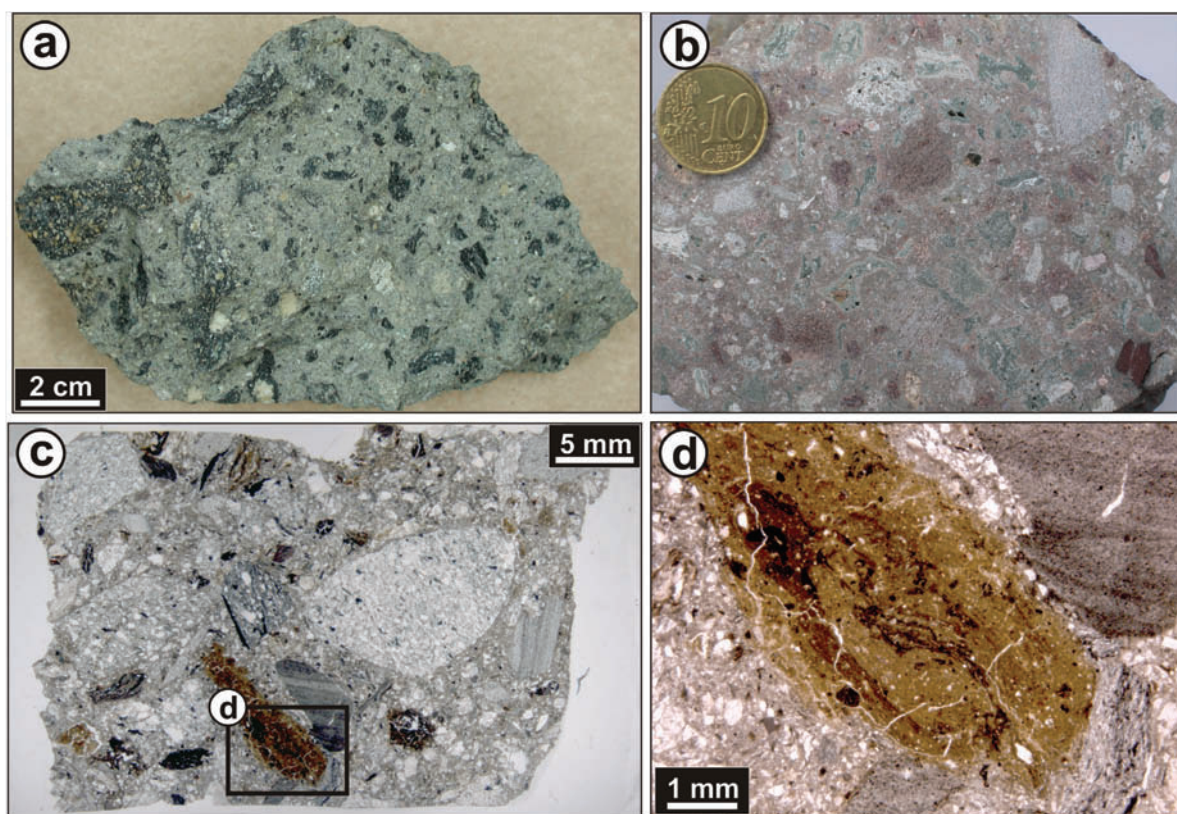


Figure 2-3. Macrophotographs (a-b) and microphotographs (c-d; in plane-polarized light) of suevite samples. a) Typical suevite from the Ries crater (Germany) with irregular and contorted fragments of glass (dark). b) Suevite sample from the Rochechouart crater (France); melt fragments are mainly grey. c) Thin section microphotograph of a suevite dike sample from the Bosumtwi crater (sample CAN-31; depth = 440.32 m). A large melt particle (brown) is visible (enlarged in [d]); other tiny melt particles are barely visible on the lower left side of the photograph. d) Enlarged part of (c) showing details of an altered melt particle with flow structures and undigested grains (mainly quartz).

2.1.1.2.4. *Pseudotachylitic breccia:*

Pseudotachylitic breccia (or pseudotachylite, or pseudotachylite-like breccia, or impact pseudotachylite) contains unshocked and shocked mineral and lithic clasts in a fine-grained aphanitic (or crystalline) matrix (see Figure 2-2b). Clasts are both, rounded and angular, and range from submicroscopic to pluri-meters in size. Typically pseudotachylitic breccia occurs as irregular dike-like bodies, such as at Vredefort (South Africa) or at

Sudbury (Canada). Pseudotachylitic breccia is debated to be the result of shock melting, friction melting, or decompression melting (for more information, see, e.g., Reimold, 1995; French, 1998; Reimold and Gibson, 2005).

2.1.1.3. Impact melt rocks:

Impact melt rock (or impact melt breccia) is a “crystalline, semihyaline, or hyaline rock solidified from impact melt and containing variable amounts of clastic debris of different degree of shock metamorphism” (see Figure 2-4; Stöffler and Grieve, 2007). Impact melt rocks can be subdivided according to the content of clasts (Stöffler and Grieve, 2007), namely, clast-rich, clast-poor, and clast-free; or subdivided according to the degree of crystallinity (French, 1998), namely, holohyaline (glassy), hypocrystalline (mixture of glassy and crystalline), and holocrystalline (completely crystalline). Impact melt rock occurs generally within the crater, forming large bodies, sill-like bodies or dike-like bodies penetrating the basement rocks (e.g., French, 1998).

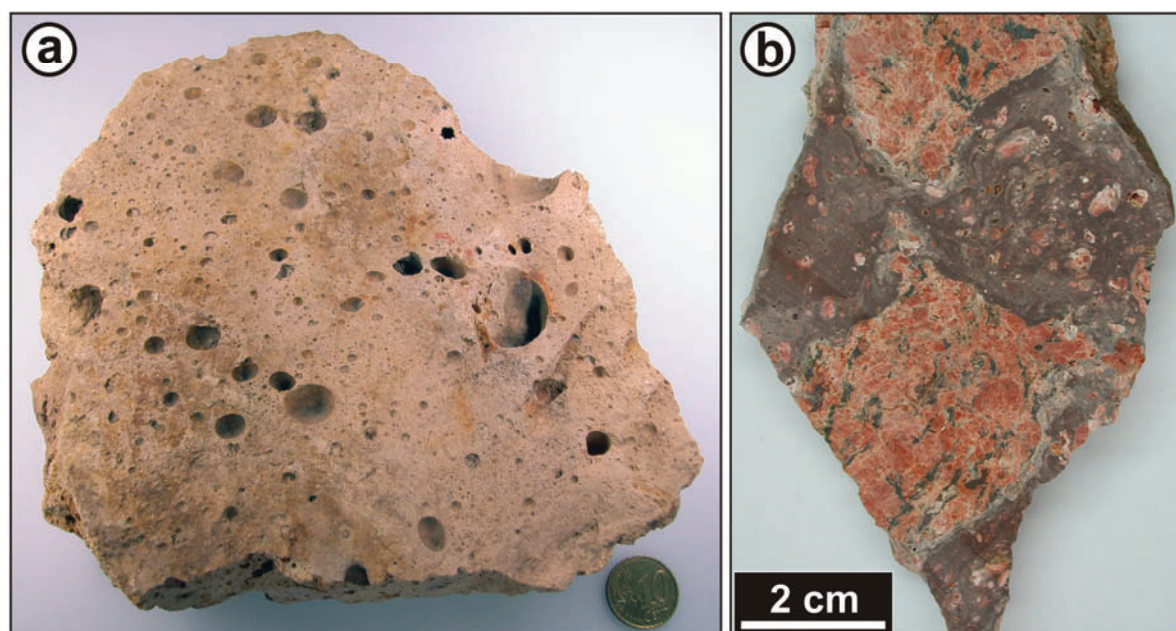


Figure 2-4. Macrophotographs of impact melt rock. a) Vesicular impact melt rock from the Rochechouart crater (France). b) Clast-rich impact melt rock from the Siljan crater (Sweden). Note the irregular shape of the target granite clasts (red) in the fine brownish matrix.

2.1.2. Distal impactites

Two types of distal impactites are distinguished in the literature (see, e.g., Stöffler and Grieve, 2007), the consolidated ones, namely tektites and microtektites, and the unconsolidated ones, the so-called airfall beds.

2.1.2.1. Tektites and microtektites

Tektites and microtektites are natural glasses, mostly dark green to black in color (see Figure 2-5), and display a variety of shapes. By definition, microtektites are smaller

than 1 mm in size and tektites are larger than 1 mm; some tektites are several centimeters in size (see, e.g., the reviews by O'Keefe, 1963; Koeberl, 1994). Three main groups of tektites have been defined: splash form tektites, aerodynamically shaped tektites, and Muong Nong-type (or layered) tektites. Four tektites strewn fields are known, namely, the North American, Central European, Ivory Coast, and Australasian strewn fields (O'Keefe, 1963). Microtektites occur in deep-sea sediments, in the North American, Ivory Coast, and Australasian strewn fields (see, e.g., Glass, 1967). Recently, microtektites were also described from Antarctica, in a possibly new strewn field, named Victoria Land Transantarctic strewn field (Folco et al., 2008), which might be associated with the Australasian field.

In some cases, relict minerals occur in tektites, such as zircon, rutile, corundum, quartz, chromite, etc. (e.g., Glass, 1970, 1972). Lechatelierite, coesite, and high-temperature breakdown products, such as baddeleyite, have been also characterized in tektites (e.g., Chao, 1963). The impact origin of tektites has been solved only recently, mainly based on geochemical data (e.g., Koeberl and Shirey, 1993) and petrological data. Tektites are formed by melting of terrestrial surficial material during hypervelocity impact. The Ivory Coast tektites (see Figure 2-5) are associated with the Bosumtwi crater, the Central European tektites with the Ries, and the North American tektites with the Chesapeake Bay crater (e.g., Koeberl, 1994). The Australasian strewn field, only ~0.79-0.80 Ma old (see, Glass and Koeberl, 2006) Ma, has so far no impact structure associated. For more information on tektites and microtektites, see, e.g., O'Keefe, 1963; Barnes, 1990; Glass, 1990; Koeberl, 1994.

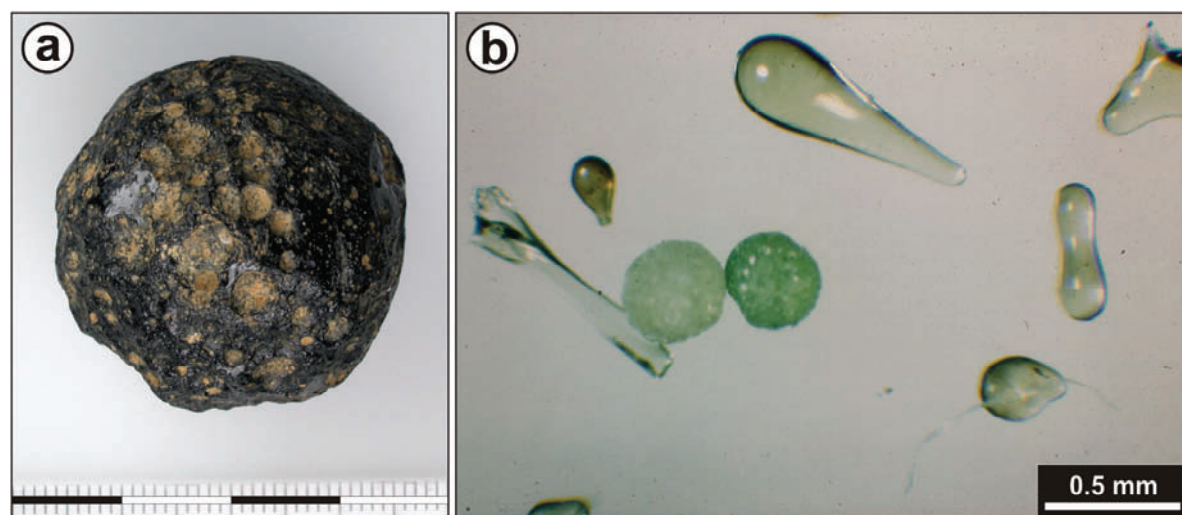


Figure 2-5. Photographs of tektite and microtektites. a) Spherical tektite from the Ivory Coast strewn field (scale bar in cm; sample n°528, MNHN, Paris). b) Microtektites with large variety of shapes from the Australasian tektite strewn field (photo courtesy B. P. Glass).

2.1.2.2. Airfall beds:

Airfall beds are “pelitic sediment with melt spherules, shocked and unshocked clasts” (Stöffler and Grieve, 2007). However, the term of *impactoclastic airfall bed* should be preferred, as the term of airfall bed is already used for the description of pyroclastic

debris layers or ash beds. The Cretaceous-Tertiary boundary, associated with the formation of the Chicxulub impact structure, is one of the best examples of impactoclastic airfall bed (see, e.g., the review by Kring, 2007).

2.2. Shock features:

2.2.1. Shatter cones

Shatter cones are the only distinctive shock-deformation feature (i.e., diagnostic evidence of hypervelocity impact) that can be seen with the naked eye (e.g., Dietz, 1960, 1968; French, 1998). These meso- to macro-scale features, consisting of conical striated fracture surfaces, are best developed in fine-grained lithologies (such as limestone; see Figure 2-6), but can also be observed in coarser-grained lithologies, such as crystalline rocks, in which it is however poorly developed. By definition, shatter cones are “distinctive curved, striated fractures that typically form partial to complete cones” (French, 1998).

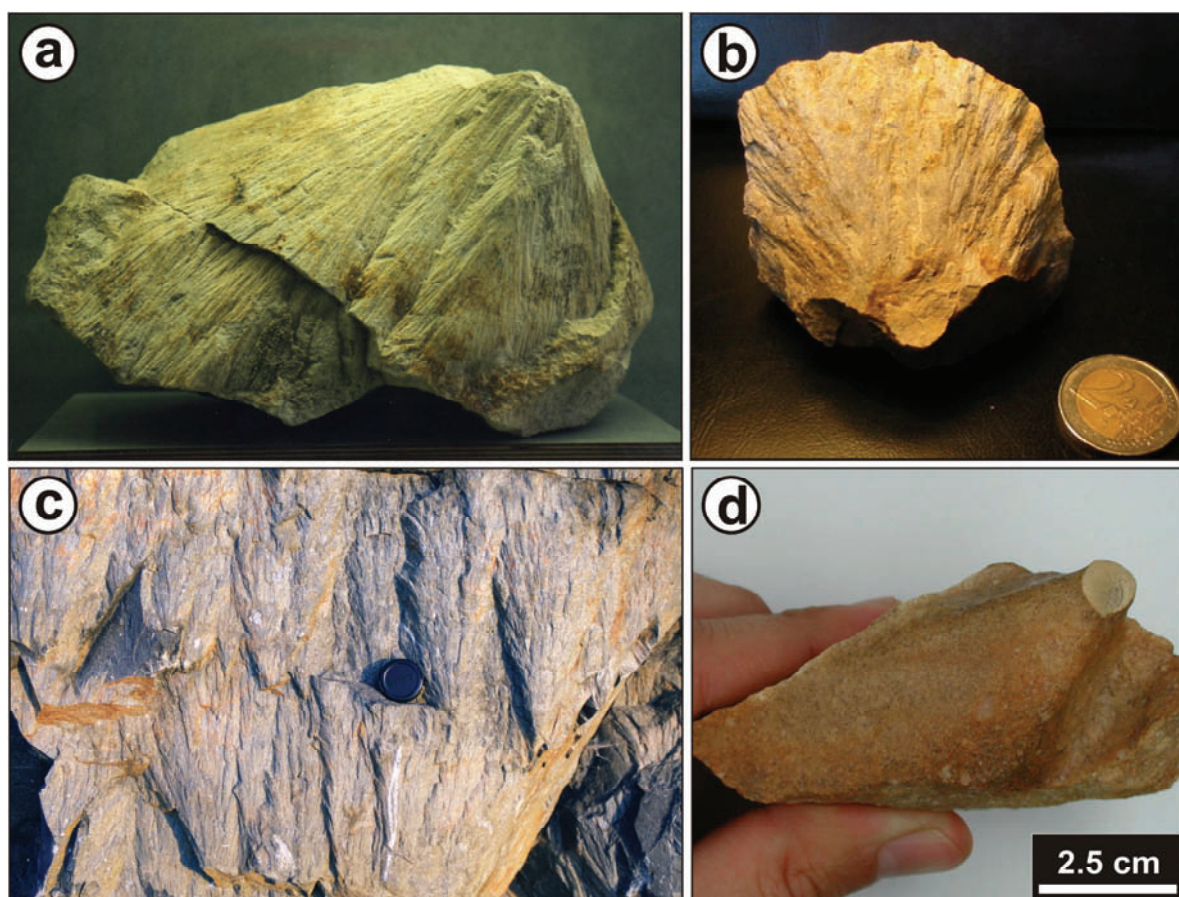


Figure 2-6. Macrophotographs of shatter cones (a-c) and ventifacts (d) for comparison. a) Typical shatter cone developed in fine-grained limestone from the Steinheim crater (Germany). b) Hand specimen of shatter cone from the Eagle Butte crater (Canada). c) Exposure view of shatter cones from the Sudbury structure (Canada). Note that cone surfaces show the typical divergence of striae away from the cone apex. d) Typical ventifacts developed in quartzitic breccia (sample from the GKCF02 structure, Egypt). Note the presence of a clast at the apex of the cone.

Shatter cones occur usually in the central part of the impact structures and in a few rare cases, isolated fragments/clasts of shatter cones have been found in impact breccias (e.g., at the Haughton crater, Canada). The distribution of shatter cones at an impact site has also been used as a parameter for estimating the original size of a structure, particularly for old and eroded impact sites, as they occur generally below the crater floor or in the central uplifts of large structures.

The formation of shatter cones, widely accepted as unequivocal proof of a meteorite impact crater, is still not completely resolved (see, e.g., Baratoux and Melosh, 2003; Sagy et al., 2004; Wieland et al., 2006), but current formation hypotheses suggest that shatter cones originate very early during the impact process. It is generally accepted that shatter cones form at relatively low shock pressures, typically between about 2 and 10 GPa (e.g., French, 1998). At the microscopic scale, PFs and/or PDFs occur in minerals, mostly from the cone surfaces (e.g., Wieland et al., 2006).

2.2.2. Deformations in quartz

2.2.2.1. Planar microstructures:

Upon shock compression, quartz develops irregular fractures (which are not diagnostic shock effects) and planar microstructures. Planar microstructures in quartz are divided into planar fractures (PFs) and planar deformation features (PDFs; see, e.g., French and Short, 1968; Engelhardt and Bertsch, 1969; Stöffler and Langenhorst, 1994; Grieve et al., 1996; French, 1998). Both planar microstructures are crystallographically controlled and therefore, PFs and PDFs are oriented parallel to rational crystallographic planes. As quartz belongs to the hexagonal crystal system, four numbers (hki), the so-called Miller-Bravais indices, are used for the identification of the planes in the crystal. The numbers (hki) represent the inverse plane intercepts along the a_1 , a_2 , a_3 , and c axes, respectively (see, e.g., Bloss, 1971).

2.2.2.1.1. Planar fractures (PFs):

Planar fractures are parallel, thin open fissures, generally greater than 3 μm wide and spaced more than 15-20 μm apart (see Figure 2-7). According to different authors, this spacing between PFs can vary of a few micrometers; spacing more than 5-20 μm according to Langenhorst (2002), more than 10 μm apart for Morrow (2007), between 15-20 μm or more according to French (1998), and about 20 μm or more according to Stöffler and Langenhorst (1994), Grieve et al. (1996), and Montanari and Koeberl (2000). The PFs are oriented parallel to rational crystallographic planes, such as (0001) and $\{10\bar{1}1\}$, and occasionally to $\{10\bar{1}3\}$. The PFs often control and/or limit the distribution of adjacent PDF sets, what have been used to prove that PF formation predates PDF formation in a given quartz crystal grain (see, e.g., Engelhardt and Bertsch, 1969; Stöffler and Langenhorst, 1994).

Formed at pressures of ~5-8 GPa, PFs are not regarded as unambiguous evidence of shock metamorphism, as they also occur, rarely, in quartz grains from non-impact settings (e.g., French, 1998).

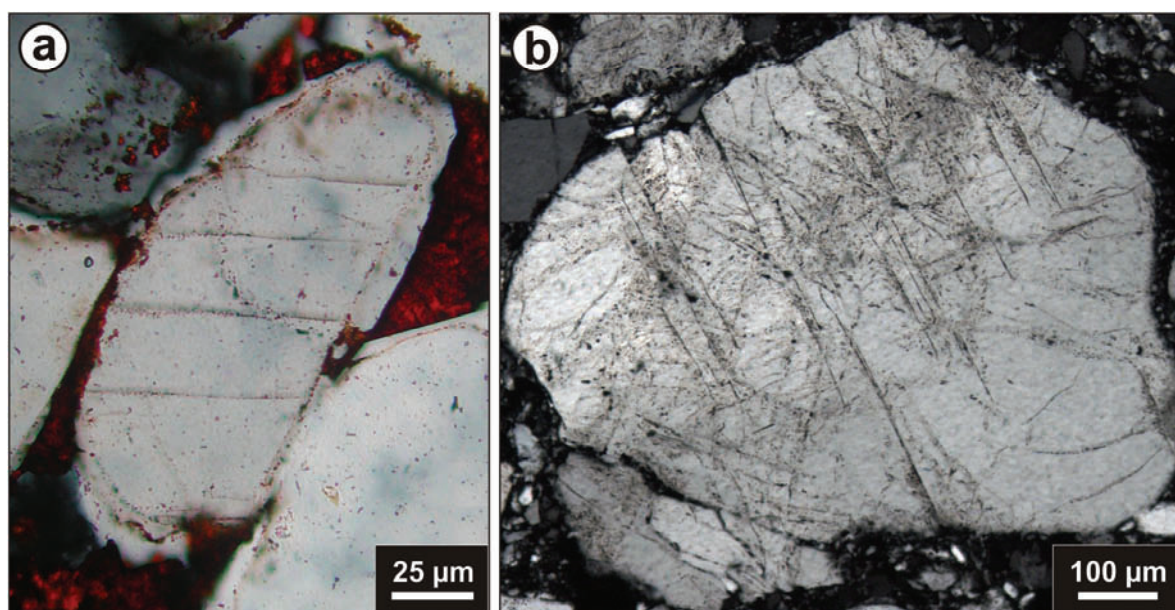


Figure 2-7. Microphotographs (in cross-polarized light) of quartz grains with planar fractures. a) Authigenic quartz grain with 1 set of regularly spaced PFs (sandstone sample from the Libyan Desert Glass strewn field, Egypt). b) Quartz grain with 1 prominent set of planar fractures; other irregular fractures are also visible in the grain (sample OR-10; Aorounga crater, Chad).

2.2.2.1.2. Planar deformation features (PDFs):

Planar deformation features in quartz grains, which developed over the pressure range of 5-10 to ~35 GPa (see Stöffler and Langenhorst, 1994; French, 1998; and references therein), are one of the best criterion for the identification of new impact structures. In contrast to PFs, PDFs are not open fractures. PDFs are commonly composed of narrow, individual planes of amorphous material that are less than 2 µm thick, comprising straight, parallel sets spaced 2-10 µm apart (e.g., Engelhardt and Bertsch, 1969; Stöffler and Langenhorst, 1994). Generally occurring as multiple sets per grain, and often in more than one crystallographic orientation, PDFs are either decorated or non-decorated (Figure 2-8). The PDFs are generally decorated with tiny fluid inclusions or bubbles, usually less than 2 µm in diameter, which greatly facilitate their detection at the scale of the optical microscope. Decorated PDFs are considered secondary features, in which the decorations formed by post-shock annealing and aqueous alteration of non-decorated amorphous PDFs (e.g., Stöffler and Langenhorst, 1994; Grieve et al., 1996; Leroux, 2005).

The PDFs are preferentially oriented parallel to rational crystallographic planes, such as $\{10\bar{1}3\}$, $\{10\bar{1}2\}$, (0001), $\{10\bar{1}1\}$, $\{11\bar{2}2\}$, $\{11\bar{2}1\}$, $\{21\bar{3}1\}$, $\{51\bar{6}1\}$, $\{10\bar{1}0\}$, and $\{11\bar{2}0\}$, and more rarely to other planes (see for details the publication chapter 9); the measurement of PDF orientations is possible using transmission electron microscopy (TEM; e.g., Goltrant et al., 1991), as well as with the spindle stage (e.g., Bohor et al., 1987), or using the universal stage technique (see chapter 4 for details on this technique). As specific orientations of PDFs in quartz are formed at different shock pressures (e.g., Hörz, 1968; Müller and Défourneaux, 1968; Huffman and Reimold, 1996), several authors, e.g., Robertson and Grieve (1977), Grieve et al. (1990), and Dressler et al. (1998), have derived

average shock pressure values for a given sample, based on the assignation of fixed values of pressure to each individual PDF orientation. For discussion on this method and limitations, see chapter publication 9.

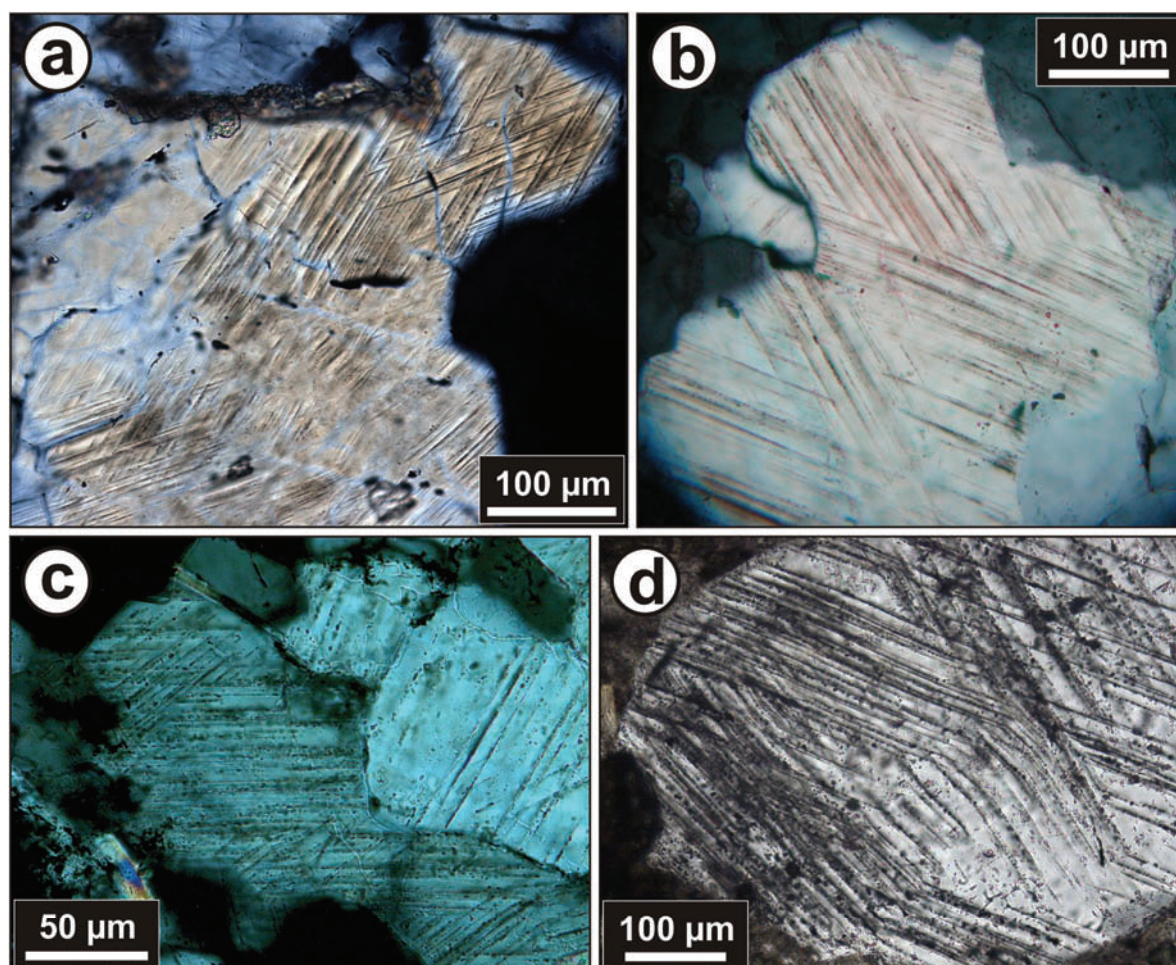


Figure 2-8. Microphotographs of quartz grains with PDF sets. a) Quartz grain with two relatively non-decorated PDF sets. Quartzite clast in suevite from the Bosumtwi (sample KR8-006; depth = 240.36 m). b) Quartz grain with two PDF sets. Meta-graywacke sample from the Bosumtwi (sample KR8-080; depth = 384.54 m). c) Two sets of decorated PDFs in a quartz grain from a meta-graywacke sample from the Bosumtwi (sample KR8-070; depth = 364.12 m). d) Quartz grain with two PDF sets. Fragmental dike breccia sample from the Manson crater (USA; sample M8-516.3; depth = 157.37 m). Microphotographs (a-c) taken in cross-polarized light and (d) in plane-polarized light.

Because PDFs cannot be clearly resolved under the optical microscope, the TEM is also used for characterization of their microstructure (see our TEM investigations on PDFs in quartz from the Bosumtwi and from the Chesapeake Bay craters in chapter 10).

2.2.2.2. Mosaicism:

Mosaicism is characterized by an irregular or mottled optical extinction pattern, which is distinctly different from undulatory extinction (common in tectonically deformed quartz). A crystal showing mosaicism comprises several smaller sub-domains with slightly

different optical axes (see, e.g., Dachille et al., 1968; Stöffler, 1972; Stöffler and Langenhorst, 1994), as a result of the distortion (i.e., plastic deformation) of the lattice into small domains that are rotated by low angles against each other. Deformation bands and/or PFs and PDFs are generally associated with mosaicism (e.g., Stöffler, 1972). In addition, mosaicism, while mainly described for quartz, is also observed in various other rock-forming minerals, such as olivine or pyroxene.

Mosaicism can be semi-quantitatively characterized by X-ray diffraction study of the degree of asterism in a single crystal. As, shock-induced polycrystallinity, such type of X-ray diffraction study can be useful for the characterization of shock pressure recorded by minerals. However, no correlation between pressure and degree of mosaicism is valid if minerals where recrystallized during secondary thermal metamorphism (Stöffler, 1972).

2.2.2.3. Refractivity, birefringence, and density:

Optical properties, such as refractivity and birefringence of quartz, have been intensively investigated in the past, see, e.g., reviews by Stöffler, 1974; Stöffler and Langenhorst, 1994. It was shown that with increasing shock pressure, the birefringence and the refractive index, both decrease simultaneously, until the amorphous state (i.e., diaplectic glass) is reached. Similarly, there is a decrease of the density of quartz with increasing shock pressure, from its normal value of 2.650 ± 0.002 to values as low as 2.280 ± 0.002 g/cm³ for shocked quartz (Langenhorst and Deutsch, 1994). The same authors show that this significant drop in density, between 25 and 35 GPa, depends on the pre-shock temperature, as well as on the direction of the shock wave relative to the c-axis of the quartz crystal.

2.2.3. Deformations in other minerals

Shock-induced deformations occur in all minerals; deformations that largely depend on the crystal structure and on the composition of the mineral (Langenhorst, 2002). Mainly two types of microstructures are formed, namely planar microstructures (i.e., PFs and PDFs) and deformation bands (i.e., kink bands and mechanical twins). These features have been poorly investigated and characterized in other minerals than quartz, possibly due to the complexity of such features in other minerals and/or because of the obliteration of these features by secondary alteration.

Aside from quartz, deformations in feldspar are most often reported in the literature (e.g., Stöffler, 1972; French, 1998), as PFs or more frequently PDFs, in both, plagioclase and alkali-feldspar. Similarly, PDFs have been observed in olivine, pyroxene, amphibole, sillimanite, garnet, apatite, etc. (Stöffler, 1972; French, 1998; Langenhorst, 2002). Decorated PDFs have been also observed in feldspar and in amphibole (Stöffler, 1972).

Kink bands are frequently observed in mica, for example in muscovite and in biotite (see Figure 2-9), but also in other minerals, as in graphite (Stöffler, 1972). Typically, kink bands formed in sheet silicates, without specific orientation relative to the rational crystallographic planes. As kink bands are also observed in minerals from non-impact

settings (such as in tectonically deformed rocks), they cannot be used as a diagnostic criterion for the impact origin of a structure.

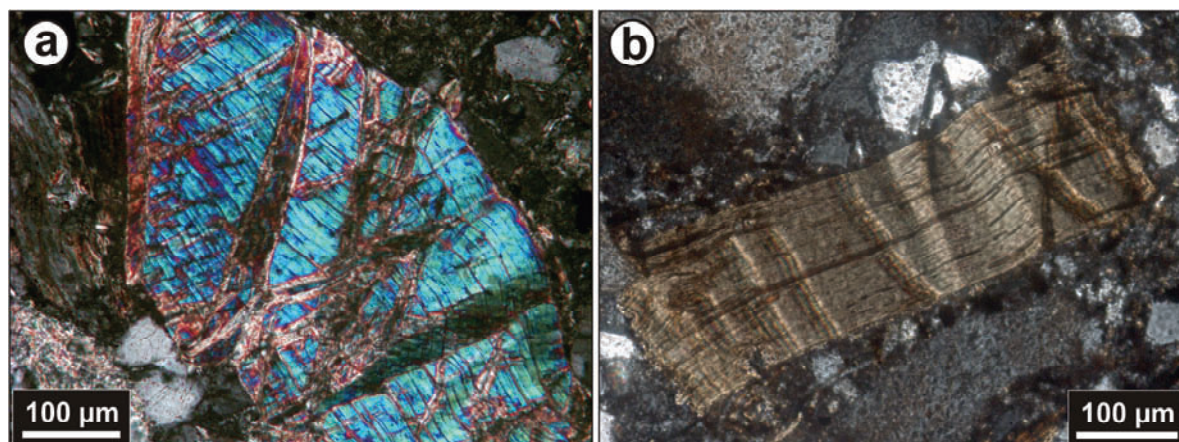


Figure 2-9. Microphotographs (in cross-polarized light) of kink-banding in mica. a) Kink bands in a muscovite clast; suevite sample from the Chesapeake Bay crater (USA; sample CB6-100; depth = 1427.01 m). b) Kink bands in a biotite clast; polymict impact breccia sample from the Rochechouart crater (France).

Mechanical twins are mainly observed in pyroxene, amphibole, sphene, and ilmenite, and more rarely in plagioclase. These twins appear as sets of parallel bands, submicroscopic to some 10 μm in width (Stöffler, 1972). Little is actually known about shock deformation of calcite, but calcite can develop mechanical twins. In addition, as mentioned above, mosaicism is also observed in several minerals, such as in olivine or in pyroxene.

2.2.4. Diaplectic glasses

In the high-pressure regime, at shock pressures higher than about 35 GPa, diaplectic glass start to form (e.g., Stöffler, 1972; Stöffler and Langenhorst, 1994; French, 1998; and references therein). Diaplectic glass forms without melting by solid-state transformation, generally from framework minerals, such as quartz or feldspar, as other minerals (such as biotite or pyroxene) tend to oxidize or to decompose. Diaplectic glass is amorphous, the pre-shock morphology and texture of the mineral is preserved, and flow structures or vesicles are absent (see Stöffler and Langenhorst, 1994). Two types of diaplectic glasses are often reported in the literature, namely, diaplectic quartz glass and maskelynite (i.e., diaplectic plagioclase feldspar glass). Both glasses are formed in the same range of pressure. Typically, diaplectic glasses have a refractive index and a density that decrease with increasing shock intensity. Thermal annealing experiments have shown that at temperature above 1200°C, diaplectic quartz glass starts to recrystallize (see, e.g., Rehfeldt-Oskierski, 1986), forming ballen α -cristobalite. As a result, in some impactites, diaplectic quartz glass is missing, but either ballen α -cristobalite or ballen α -quartz is present.

2.2.5. Mineral and whole-rock melt

Melting of individual minerals starts at around 50 GPa (Stöffler, 1972) and at around 60 GPa for the whole-rock. The melts have approximately the same composition as the original minerals or mixture of minerals. Melt is present as coherent sheets in large impact structures (as at the Popigai crater), as fragments/particles in suevite, and as glass bombs in ejecta (e.g., at the Ries crater). Melt particles are generally vesicular, with flow structures, and frequently contain minerals or lithic fragments undigested in the groundmass (see Figure 2-10). Both, impact glasses (quenched melt) and melt particles are commonly altered to secondary minerals, such as clay minerals, zeolites, and chalcedony.

Commonly observed in impactites, lechatelierite is a monomineralic quartz melt that forms at very high temperatures (above 1700 °C) without necessarily requiring high shock pressures. Lechatelierite occurs in nature only in fulgurites and in impactites (e.g., Stöffler and Langenhorst, 1994; and references therein).

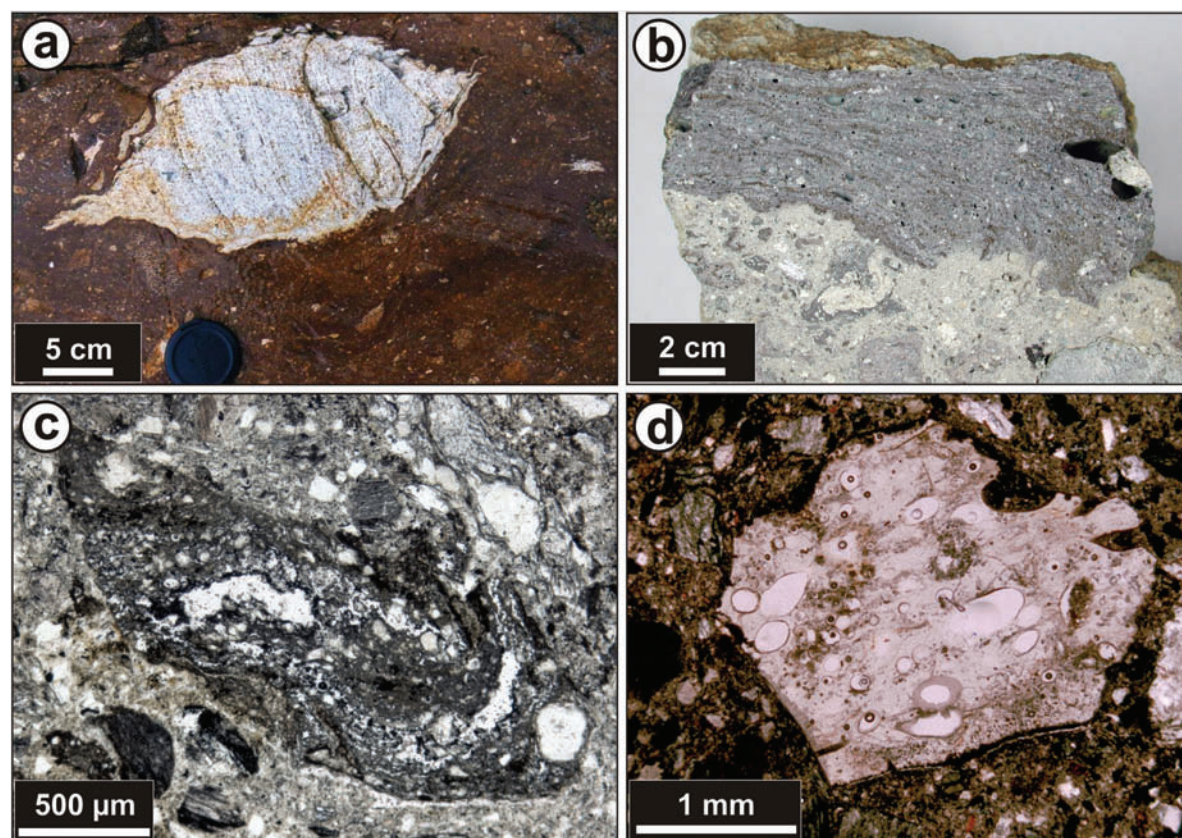


Figure 2-10. Macrophotographs (a-b) and microphotographs (c-d; in plane-polarized light) of impact breccia samples with prominent melt particles. a) Aerodynamically-shaped (fish-shaped) melt particle in an impact melt breccia sample from the Manicouagan crater (Canada). b) A large melt particle with flow structure in a suevite sample from the Bosumtwi crater (sample from outside the northern crater rim). c) Vesicular, subangular, melt particle in suevite from Bosumtwi (sample KR8-004; depth = 239.65 m). d) Highly vesicular, shard-like, melt glass fragment in suevite from Bosumtwi (sample LB-39a; from outside the crater rim).

2.2.6. High-pressure polymorphs

High-pressure phases are commonly reported in impactites (e.g., Stöffler, 1972), as coesite and stishovite (from quartz), diamond (from graphite), jadeite (from plagioclase), majorite (from pyroxene), reidite (from zircon), and ringwoodite (from olivine). However, some of them, such as coesite and diamond, are not exclusively formed during shock metamorphism, as they are also products of endogenic processes.

2.2.6.1. Coesite and Stishovite:

The high-pressure polymorphs of quartz, namely, coesite and stishovite, formed upon shock compression and are metastably preserved in rocks that experienced peak pressure ranges between 30-60 GPa and 12-45 GPa, respectively (e.g., Stöffler and Langenhorst, 1994). However, recent investigations (Lakshtanov et al., 2007) have shown that aluminum and possibly hydrogen content in these phases have a large effect on the stability fields of coesite and stishovite. Both polymorphs occur usually in impactites within diaplectic quartz glass (see Figure 2-11), along grain boundaries, or in association with PDFs (Stöffler 1971; Stähle et al, 2008; and references therein).

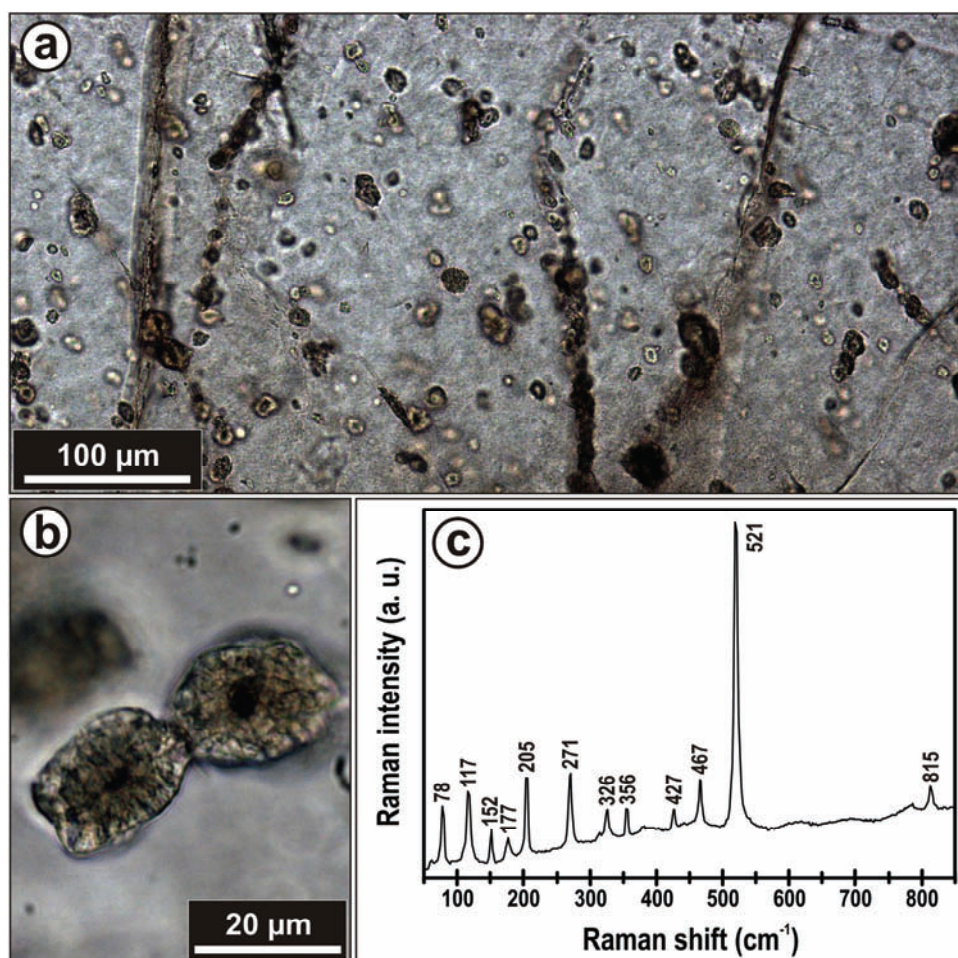


Figure 2-11. Microphotographs (a-b; in plane-polarized light) and associated microRaman spectrum (c) of coesite. a) Coesite aggregates (green to brown clusters) within diaplectic quartz glass from suevite (Bosumtwi crater; sample LB-44B; from outside the crater rim). b) Enlarged view of two aggregates of coesite from the same sample. c) Typical Raman spectrum of one of the illustrated aggregate of coesite.

Small polycrystalline aggregates of coesite (up to ~200 μm in size), colorless to brownish, have been characterized in impactites from only a few impact structures, including Meteor Crater (Chao et al., 1960), the Ries (Shoemaker and Chao, 1961), and Bosumtwi (Littler et al., 1961). At Meteor Crater and at the Ries, stishovite was also detected. The identification of these two polymorphs was used for establishing the impact origin of the Ries crater (Shoemaker and Chao, 1961).

Stishovite has been so far only identified in meteorites and in impact related rocks (see, e.g., the review by Gillet et al., 2007), but post-stishovite is one of the main constituents of the basaltic layer of subducting slabs and it may also occur in the lower mantle and at the core-mantle boundary (see, e.g., Lakshtanov et al., 2007; Liu et al., 2007). Occurrence of coesite is frequently reported in kimberlites or in ultra-high pressure metamorphic rocks, but can be distinguished easily from coesite in impactites by the different petrographic assemblages. It is important to note that under static equilibrium conditions, where reaction rates are slower and kinetic factors less important, coesite forms at pressures superior to 2 GPa and stishovite starts to form around 7-8 GPa (Heaney et al., 1994; and references therein).

2.2.6.2. Impact diamonds:

Impact diamonds were first discovered in impactites from the Popigai structure, Siberia (Masaitis et al., 1972) and were later found at the Ries crater (Rost et al., 1978), and in a few other impact structures. The graphite, occurring in the target rocks (e.g., graphite-bearing gneiss) of these impact structures, is transformed into diamonds during the very short time of the shock compression. As a result, impact diamonds are defect-rich and some features of the precursor graphite are inherited (see, e.g., Koeberl et al., 1997).

2.2.7. Post-shock features

2.2.7.1. Toasted quartz:

The term of “toasted” quartz was used first by Short and Gold (1993) in an abstract, for the description of quartz grains showing an orange-brown to grayish-reddish brown appearance, and in reference to the aspect of “toasted bread” (see Figure 2-12). Toasted quartz was then studied in more details by Short and Gold (1996) and Whitehead et al. (2002). Such type of quartz is considered to be a post-shock feature, probably the result of “hydrothermal or other post-shock modification” for Short and Gold (1996) or resulting of “the exsolution of water from glass, primarily along PDFs, during heat-driven recrystallization” for Whitehead et al. (2002). Both studies have also shown that toasted quartz have a higher albedo than untoasted quartz, visible in hand samples. In addition, Whitehead et al. (2002) noted that “no compositional origin for the browning is evident”. The brownish appearance of quartz is, according to Whitehead et al. (2002), caused by a high proportion of very tiny fluid inclusions that are principally located along decorated PDFs.

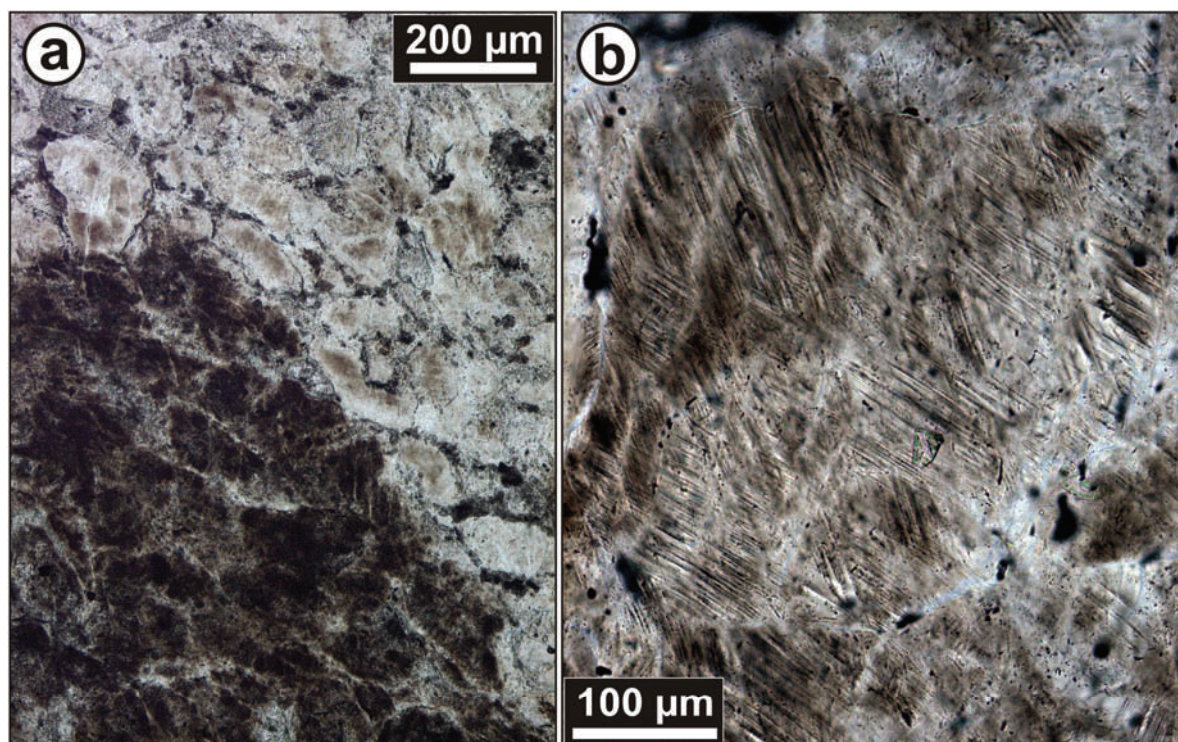


Figure 2-12. Microphotographs (in plane-polarized light) of quartz grains toasting. a) Detail of a toasted region (lower left side of the photograph) and untoasted region of a sandstone clast; conglomerate sample from the Chesapeake Bay crater (USA; sample CB6-125b; depth = 1522.72 m). b) Toasted quartz grain with two PDF sets; quartzite clast in suevite from the Bosumtwi crater (sample KR8-006; depth = 240.36 m).

More recently toasted quartz has been also reported in shocked quartz from the late Eocene impact ejecta layer at Massignano, Italy (Glass et al., 2004), and within an impact ejecta layer containing Australasian microtektites (Glass and Koeberl, 2006). New observations and investigations on toasted quartz grains are reported in chapter 10.

2.2.7.2. Ballen quartz and cristobalite:

Ballen silica, with either α -quartz or α -cristobalite structure, occurs as independent clasts or within diaplectic quartz glass or lechatelierite inclusions (see Figure 2-13). Ballen are more or less spheroidal, in some cases elongate (ovoid), bodies that range in size from 8 to 214 μm , and either intersect or penetrate each other or abut each other (see chapter publication 8). The occurrence of so-called ballen quartz has been reported from about one in five of the known terrestrial impact structures, mostly from clasts in impact melt rock and, more rarely, in suevite. Different types of ballen silica have been described and characterized (Bischoff and Stöffler, 1984; chapter publication 8).

The formation of ballen involves an impact-triggered solid-solid transition from α -quartz to diaplectic quartz glass, followed by the formation at high temperature of ballen of β -cristobalite and/or β -quartz, and finally back-transformation to α -cristobalite and/or α -quartz; or a solid-liquid transition from quartz to lechatelierite followed by nucleation and crystal growth at high temperature. As ballen quartz/cristobalite result of back-

transformations from shock-induced states, ballen silica cannot be considered direct evidence of shock metamorphism, but represents indirect evidence. See the publication chapter 8 and chapter 10 for more details.

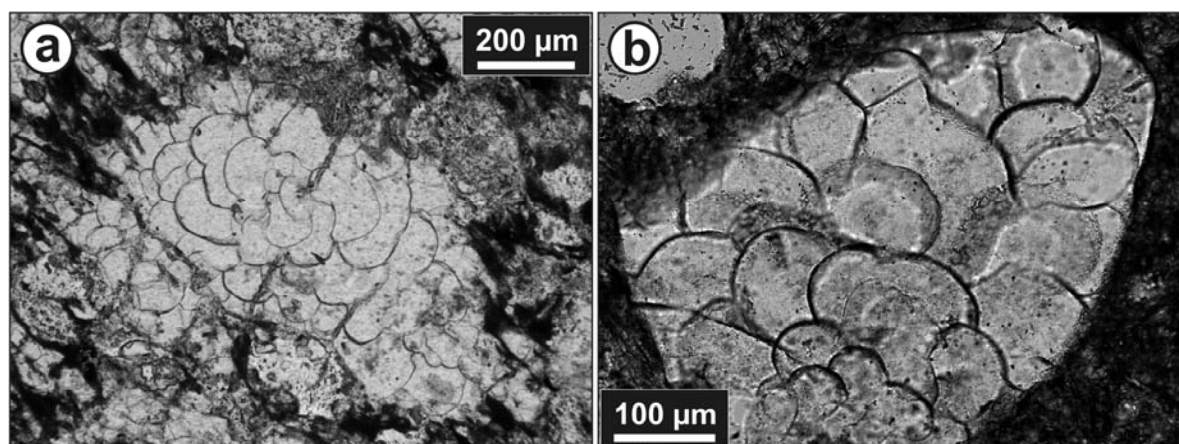


Figure 2-13. Microphotographs (in plane-polarized light) of ballen silica. a) Elongate ovoid (crescent) to roundish α -cristobalite ballen in suevite from the Bosumtwi (sample BH1-0790). b) Ballen α -quartz with varied ballen sizes (smaller ones on the lower part of the photograph) in a diaplectic quartz clast in a glassy impact melt rock from the Wanapitei crater (Canada).

References

Baratoux D. and Melosh H. J. 2003. The formation of shatter cones by shock wave interference during impacting. *Earth and Planetary Science Letters* 216:43–54.

Barnes V. E. 1990. Tektites research 1936–1990. *Meteoritics and Planetary Science* 25:149–159.

Bischoff A. and Stöffler D. 1984. Chemical and structural changes induced by thermal annealing of shocked feldspar inclusions in impact melt rocks from Lappajärvi crater, Finland. *Journal of Geophysical Research* 89:B645–B656.

Bloss F. D. 1971. *Crystallography and crystal chemistry: an introduction*. New York: Holt, Rinehart, and Winston. 545 p.

Bohor B. F., Modreski P. J., and Foord E. E. 1987. Shocked quartz in the Cretaceous-Tertiary boundary clays: Evidence for a global distribution. *Science* 236:705–708.

Chao E. C. T. 1963. The petrographic and chemical characteristics of tektites. In *Tektites*, edited by O’Keefe J. A. Chicago: University of Chicago Press. pp. 51–94.

Chao E. C. T., Shoemaker E. M., and Madsen B. M. 1960. First natural occurrence of coesite. *Science* 132:220–222.

Dachille F., Gigl P., and Simons P. Y. 1968. Experimental and analytical studies of crystalline damage useful for the recognition of impact structures. In *Shock metamorphism of natural materials*, edited by French B. M. and Short N. M. Baltimore: Mono Book Corporation. pp. 555–569.

Dietz R. S. 1960. Meteorite impact suggested by shatter cones in rock. *Science* 131:1781–1784.

Dietz R. S. 1968. Shatter cones in cryptoexplosion structures. In *Shock metamorphism of natural materials*, edited by French B. M. and Short N. M. Baltimore: Mono Book Corporation. pp. 267–285.

Dressler B. O., Sharpton V. L., and Schuraytz B. C. 1998. Shock metamorphism and shock barometry at a complex impact structure: State Islands, Canada. *Contributions to Mineralogy and Petrology* 130:275–287.

Engelhardt W. v. and Bertsch W. 1969. Shock induced planar deformation structures in quartz from the Ries crater, Germany. *Contributions to Mineralogy and Petrology* 20:203–234.

Folco L., Rochette P., Perchiazzi N., D'Orazio M., Laurenzi M. A., and Tiepolo M. 2008. Microtektites from Victoria Land Transantarctic Mountains. *Geology* 36:291–294.

French B. M. 1998. *Traces of catastrophe: A handbook of shock-metamorphic effects in terrestrial meteorite impact structures*. LPI Contribution #954. Houston, Texas: Lunar and Planetary Institute. 120 p.

French B. M. and Short N. M. 1968. *Shock Metamorphism of Natural Materials*. Baltimore: Mono Book Corporation. 644 p.

Gillet P., El Goresy A., Beck P., and Chen M. 2007. High-pressure mineral assemblages in shocked meteorites and shocked terrestrial rocks: Mechanisms of phase transformations and constraints to pressure and temperature histories. In *Advances in high-pressure mineralogy*, edited by Ohtani E. GSA Special Paper #421. Boulder, Colorado: Geological Society of America. pp. 57–82.

Glass B. P. 1967. Microtektites in deep sea sediments. *Nature* 214:372–374.

Glass B. P. 1970. Zircon and chromite crystals in Muong Nong-type tektite. *Science* 169:766–769.

Glass B. P. 1972. Crystalline inclusions in a Muong Nong-type indochinite. *Earth and Planetary Science Letters* 16:23–26.

Glass B. P. 1990. Tektites and microtektites: key facts and inferences. *Tectonophysics* 171:393–404.

Glass B. P. and Koeberl C. 2006. Australasian microtektites and associated impact ejecta in the South China Sea and the Middle Pleistocene supereruption of Toba. *Meteoritics and Planetary Science* 41:305–326.

Glass B. P., Liu S., and Montanari A. 2004. Impact ejecta in upper Eocene deposits at Massignano, Italy. *Meteoritics and Planetary Science* 39:589–597.

Goltrant O., Cordier P., and Doukhan J.-C. 1991. Planar deformation features in shocked quartz; a transmission electron microscopy investigation. *Earth and Planetary Science Letters* 106:103–115.

Grieve R. A. F., Coderre J. M., Robertson P. B., and Alexopoulos J. 1990. Microscopic planar deformation features in quartz of the Vredefort structure: Anomalous but still suggestive of an impact origin. *Tectonophysics* 171:185–200.

Grieve R. A. F., Langenhorst F., and Stöffler D. 1996. Shock metamorphism of quartz in nature and experiment: II. Significance in geoscience. *Meteoritics and Planetary Science* 31:6–35.

Heaney P. J., Prewitt C. T., and Gibbs G. V. 1994. *Silica: physical behavior, geochemistry and materials applications*. Reviews in Mineralogy 29. Washington DC: Mineralogical Society of America. 606 p.

Hörz F. 1968. Statistical measurements of deformation structures and refractive indices in experimentally shock loaded quartz. In *Shock Metamorphism of Natural Materials*, edited by French B. M. and Short N. M. Baltimore: Mono Book Corporation. pp. 243–253.

Huffman A. R. and Reimold W. U. 1996. Experimental constraints on shock-induced microstructures in naturally deformed silicates. *Tectonophysics* 256:165–217.

Koeberl C. 1994. Tektite origin by hypervelocity asteroidal or cometary impact: Target rocks, source craters, and mechanisms. In *Large Meteorite Impacts and Planetary Evolution*, edited by Dressler B. O., Grieve R. A. F., and Sharpton V. L. GSA Special Paper #293. Boulder, Colorado: Geological Society of America. pp. 133–151.

Koeberl C. and Shirey S. B. 1993. Detection of a meteoritic component in Ivory Coast tektites with rhenium-osmium isotopes. *Science* 261:595–598.

Koeberl C., Masaitis V. L., Shafranovsky G. I., Gilmour I., Langenhorst F., and Schrauder M. 1997. Diamonds from the Popigai impact structure, Russia. *Geology* 25:967–970.

Kring D. A. 2007. The Chicxulub impact event and its environmental consequences at the Cretaceous–Tertiary boundary. *Palaeogeography, Palaeoclimatology, Palaeoecology* 255:4–21.

Lakshtanov D. L., Sinogeikin S. V., Litasov K. D., Prakapenka V. B., Hellwig H., Wang J., Sanches-Valle C., Perrillat J.-P., Chen B., Somayazulu M., Li J., Ohtani E., and Bass J. D. 2007. The post-stishovite phase transition in hydrous alumina-bearing SiO₂ in the lower mantle of the earth. *Proceedings of the National Academy of Sciences of the United States of America* 104:13588–13590.

Langenhorst F. 2002. Shock metamorphism of some minerals: Basic introduction and microstructural observations. *Bulletin of the Czech Geological Survey* 77:265–282.

Langenhorst F. and Deutsch A. 1994. Shock experiments on pre-heated α - and β -quartz: I. Optical and density data. *Earth and Planetary Science Letters* 125:407–420.

Leroux H. 2005. Weathering features in shocked quartz from the Ries impact crater, Germany. *Meteoritics and Planetary Science* 40:1347–1352.

Little J., Fahey J. J., Dietz R. S., and Chao E. C. T. 1961. Coesite from the Lake Bosumtwi crater, Ashanti, Ghana (abstract). *Geological Society of America Special Paper* #68. pp. 218.

Liu L., Zhang J., Green II H. W., Jin Z., and Bozhilov K. N. 2007. Evidence of former stishovite in metamorphosed sediments, implying subduction to >350 km. *Earth and Planetary Science Letters* 263:180–191.

Masaitis V. L., Futergendler S. I., and Gnevushev M. A. 1972. Diamonds in impactites of the Popigai meteorite crater. *Zapiski Vsesoyuznogo Mineralogicheskogo Obshchestva* 101:108–112 (in Russian).

Montanari A. and Koeberl C. 2000. *Impact stratigraphy: the Italian record*. Lectures notes in earth sciences 93. Heidelberg: Springer Verlag. 364 p.

Morrow J. R. 2007. Shock-metamorphic petrography and microRaman spectroscopy of quartz in upper impactite interval, ICDP drill core LB-07A, Bosumtwi impact crater, Ghana. *Meteoritics and Planetary Science* 42:591–609.

Müller W. F. and Défourneaux M. 1968. Deformationsstrukturen im Quarz als Indikator für Stosswellen: Eine experimentelle Untersuchung an Quarz-Einkristallen. *Zeitschrift für Geophysik* 34:483–504.

O'Keefe J. A. 1963. *Tektites*. Chicago: University of Chicago Press. 228 p.

- Rehfeldt-Oskierski A. 1986. Stosswellenexperimente an quartz-einkristallen und thermisches Verhalten von diaplektischen Quarzglasern. Unpubl. PhD thesis, University of Münster, Germany, 145 p.
- Reimold W. U. 1995. Pseudotachylite in impact structures – Generation by friction melting and shock brecciation?: A review and discussion. *Earth-Science Reviews* 39:247–264.
- Reimold W. U. and Gibson R. L. 2005. “Pseudotachylites” in large impact structures. In *Impact Tectonics*. Impact Studies, vol. 6, edited by Koeberl C. and Henkel H. Heidelberg: Springer. pp. 1–53.
- Robertson P. B. and Grieve R. A. F. 1977. Shock attenuation at terrestrial impact structures. In *Impact and explosion cratering*, edited by Roddy D. J., Pepin R. O., Merrill R. B. New York: Pergamon Press. pp. 687–702.
- Rost R., Dolgov Y. A., and Vishnevsky S. A. 1978. Gases in inclusions of impact glass in the Ries crater, West Germany and finds of high-pressure carbon polymorphs. *Doklady Akademia Nauk SSSR* 241:695–698 (in Russian).
- Sagy A., Fineberg J., and Reches Z. 2004. Shatter cones: branched, rapid fractures formed by shock impact. *Journal of Geophysical Research* 109, B10209, doi:10.1029/2004JB003016.
- Shoemaker E. M. and Chao E. C. T. 1961. New evidence for the impact origin of the Ries Basin, Bavaria, Germany. *Journal of Geophysical Research* 66:3371–3378.
- Short N. M. and Gold D. P. 1993. Petrographic analysis of selected core materials from the Manson (Iowa) impact structure (abstract). *Meteoritics and Planetary Science* 28:A436–437.
- Short N. M. and Gold D. P. 1996. Petrography of shocked rocks from the central peak at the Manson impact structure. In *The Manson impact structure, Iowa: anatomy of an impact crater*, edited by Koeberl C. and Anderson R. R. GSA Special Paper #302. Boulder, Colorado: Geological Society of America. pp. 245–265.
- Stähle V., Altherr R., Koch M., and Nasdala L. 2008. Shock-induced growth and metastability of stishovite and coesite in lithic clasts from suevite of the Ries impact crater (Germany). *Contributions to Mineralogy and Petrology* 155:457–472.
- Stöffler D. 1971. Coesite and stishovite in shocked crystalline rocks. *Journal of Geophysical Research* 76:5474–5488.

Stöffler D. 1972. Deformation and transformation of rock-forming minerals by natural and experimental shock processes: I. Behavior of minerals under shock compression. *Fortschritte der Mineralogie* 49:50–113.

Stöffler D. 1974. Deformation and transformation of rock-forming minerals by natural and experimental processes: II. Physical properties of shocked minerals. *Fortschritte der Mineralogie* 51:256–289.

Stöffler D. and Grieve R. A. F. 2007. Impactites, Chapter 2.11. In *Metamorphic rocks: a classification and glossary of terms, Recommendations of the International Union of Geological Sciences*, edited by Fettes D. and Desmons J. Cambridge: Cambridge Univ. Press. pp. 82–92 + Glossary.

Stöffler D. and Langenhorst F. 1994. Shock metamorphism of quartz in nature and experiment: I. Basic observation and theory. *Meteoritics and Planetary Science* 29:155–181.

Whitehead J., Spray J. G., and Grieve R. A. F. 2002. Origin of “toasted” quartz in terrestrial impact structures. *Geology* 30:431–434.

Wieland F., Reimold W. U., and Gibson R. L. 2006. New observations on shatter cones in the Vredefort impact structure, South Africa, and evaluation of current hypotheses for shatter cone formation. *Meteoritics and Planetary Science* 41:1737–1759.

CHAPTER 3: The Bosumtwi impact structure

The Bosumtwi impact structure, centered at 06°30'N, 01°25'W, is situated in the Ashanti region, in Ghana, West Africa (Figure 3-1). It is a well-preserved 1.07 Myr old complex impact structure, 10.5 km in diameter, with a pronounced rim and small central uplift (e.g., Scholz et al., 2002; Koeberl and Reimold, 2005). Topographic studies have revealed the occurrence, outside of the crater rim, of a slight, near-circular depression (at about 1.5 km from the rim crest), and an outer ring of minor topographic elevation (10-20 m high) with a diameter of about 20 km (Figure 3-2; Jones et al., 1981; Reimold et al., 1998; Wagner et al., 2002). The crater is actually almost entirely filled by Lake Bosumtwi, which is ~8 km diameter and up to ~80 m deep at its center. The Bosumtwi impact structure is also associated with the Ivory Coast tektites, on the basis of the geographical location of the tektite strewn field, as well as identical ages and matching chemical and isotopic compositions of the tektites and the Bosumtwi crater rocks (Schnetzler et al., 1966, 1967; Gentner et al., 1967, 1969; Kolbe et al., 1967; Jones, 1985; Koeberl et al., 1997).

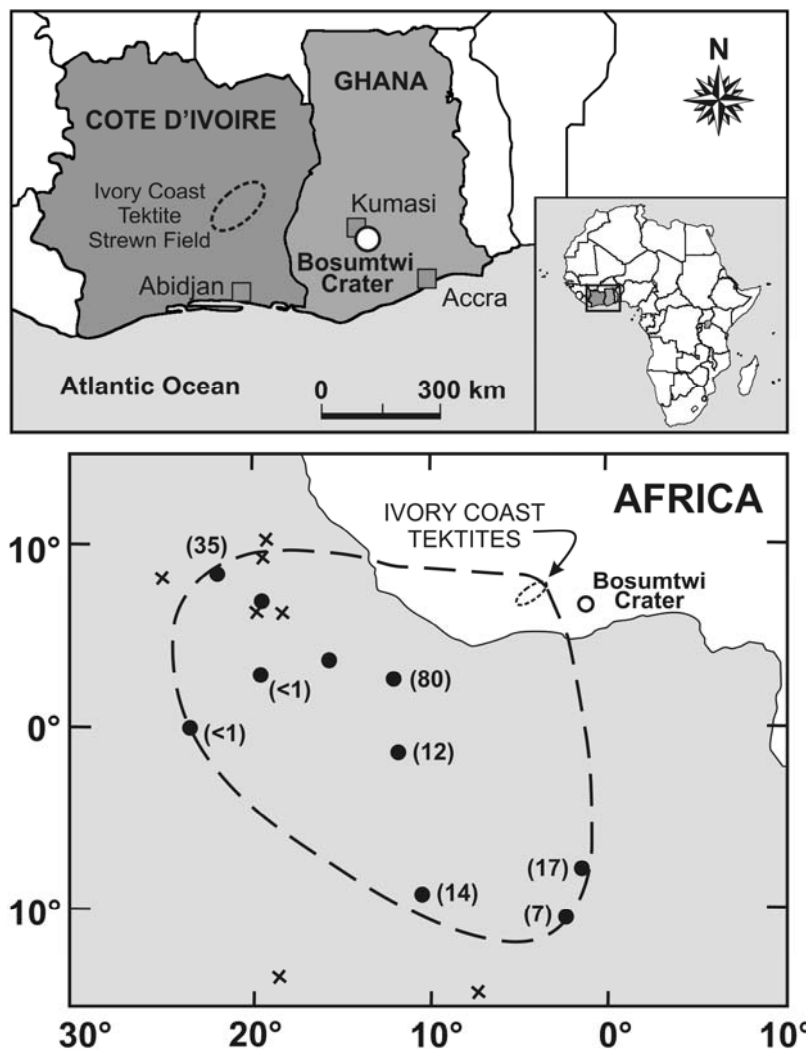


Figure 3-1. Location map of the Bosumtwi impact structure, Ghana, and its relation to the Ivory Coast tektite strewn field and to the offshore microtektite strewn field. Deep-sea cores in which microtektites were found are indicated with full circles; the numbers associated indicate the integrated numbers of microtektites per cm² (after Glass et al., 1991). No microtektites were found at deep-sea cores marked with an "x".

The first evidence for an impact origin of the Bosumtwi structure was identified in the 1960s, including the discovery of coesite (Littler et al., 1961) and of baddeleyite (El

Goresy et al., 1968). Later, PDFs in quartz and feldspar were found in suevite outside of the northern crater rim (e.g., Koeberl et al., 1998; Boamah and Koeberl, 2003, 2006; Koeberl and Reimold, 2005). The crater was recently the subject of an international and multidisciplinary drilling project by the International Continental Scientific Drilling Program (ICDP; see below and Koeberl et al., 2007a, for more information).

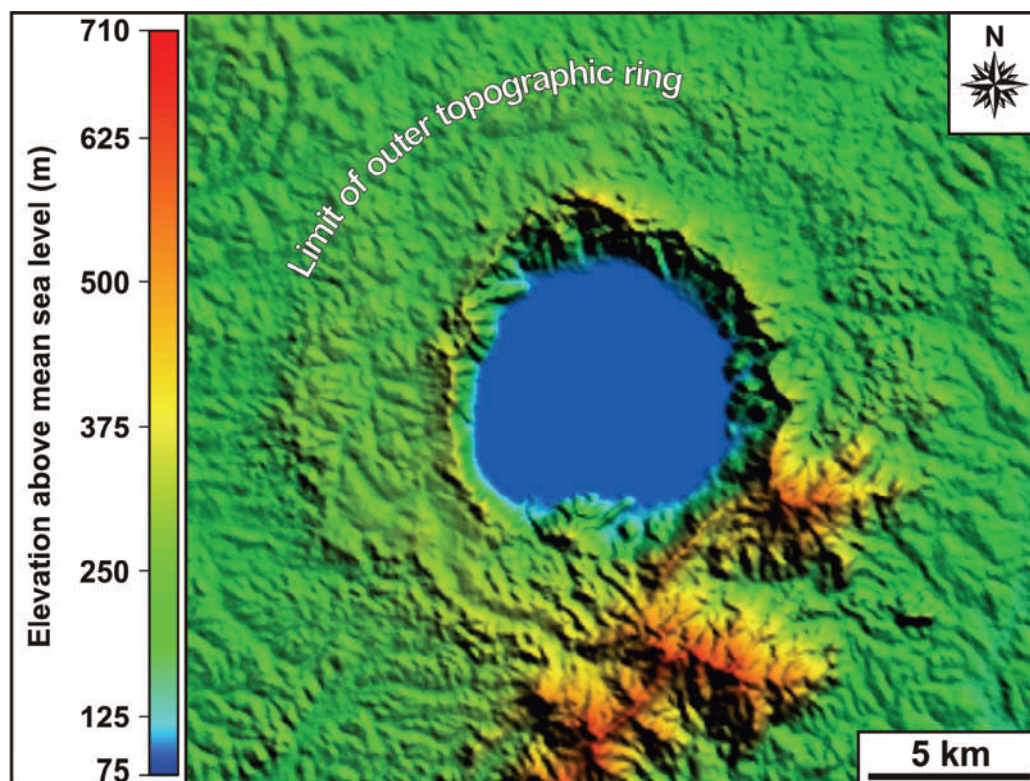


Figure 3-2. Projection of the Shuttle Radar Topography Mission (SRTM) data, showing the regional topography around the Bosumtwi crater, with the faint outer ring feature and the Obuoum Range visible at the bottom center of the image. SRTM data available online (<http://www2.jpl.nasa.gov/srtm/>, accessed 3 March 2008).

3.1. Geology of the crater:

First geological investigations around Lake Bosumtwi were made in the 1930s (Junner, 1937) and completed later in the 1960s (e.g., Woodfield, 1966; Moon and Mason, 1967; Jones et al., 1981). Recently, additional mapping was carried out, including descriptions of new outcrops revealed by recent road construction (see, Koeberl and Reimold, 2005) and observations obtained from shallow drilling on the rim and outside of the northern crater rim (Boamah and Koeberl, 2003).

The Bosumtwi impact structure was excavated in lower greenschist facies metasediments of the Early Proterozoic, 2.1-2.2 Gyr old, Birimian Supergroup (Jones et al., 1981; Wright et al., 1985; Leube et al., 1990). The Birimian Supergroup consists of two units that were formed almost contemporaneously (e.g., Leube et al., 1990; Hirdes et al., 1996); a unit composed mostly of metasedimentary rocks, including interbedded phyllites and meta-tuffs together with meta-graywackes, quartzitic graywackes, shales, phyllites,

schists, and slates (e.g., Junner, 1937); and a unit of metavolcanic rocks composed of hornblende-actinolite schists, calcite-chlorite schists, mica schists, and amphibolites, occurring to the southeast of the crater (e.g., Woodfield, 1966; Moon and Mason, 1967; Reimold et al., 1998).

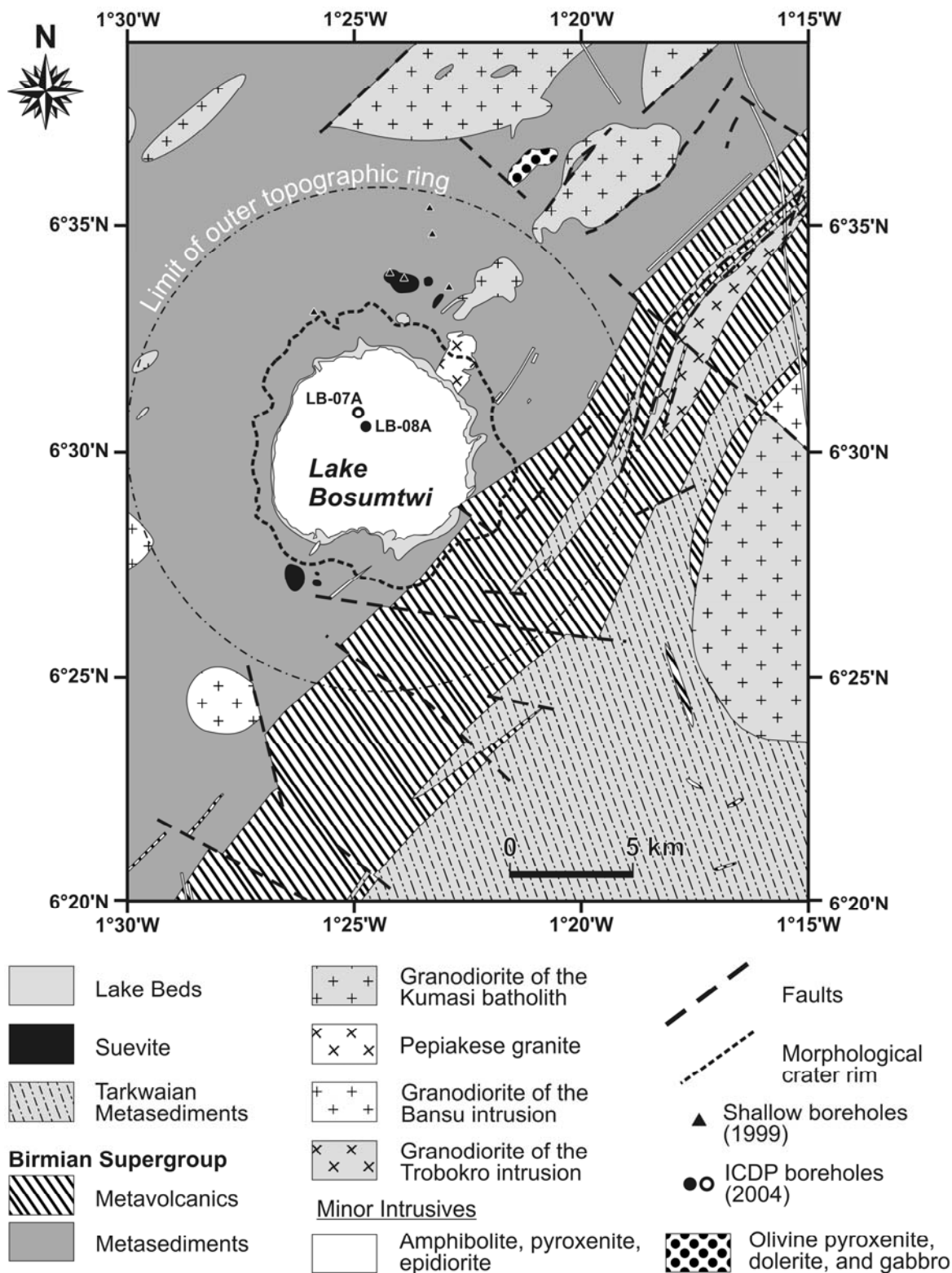


Figure 3-3. Schematic geological map of the Bosumtwi impact structure and surroundings (after Koeberl and Reimold, 2005).

Tarkwaian clastic sedimentary rocks, which are regarded as the detritus of Birimian rocks (Leube et al., 1990), occur to the east and southeast of the crater (see Figure 3-3). The age of 2.0–2.3 Gyr, determined using Sm/Nd isotopic data, for these Birimian rocks (Taylor et al., 1992), was recently better constrained to about 2.10–2.15 Gyr by Feybesse et al. (2006).

A variety of intrusive bodies has also been observed around the crater and in the crater rim (see Figure 3-3), including Proterozoic granitic intrusions, weathered granitic dikes, other granitoid dikes, and dolerite and amphibolite dikes (e.g., Junner, 1937; Woodfield, 1966; Moon and Mason, 1967; Jones, 1985; Reimold et al., 1998). Some of these intrusions seem to be correlated with the Papiakese and Kumasi granitoid intrusions (Woodfield, 1966; Moon and Mason, 1967). In the northeast sector of the crater, Papiakese granite occur, showing a variety of lithologies, including hornblende diorite, biotite-muscovite granite, and an almost pure albite rock (Jones, 1985; Koeberl et al., 1998). In the immediate environs of the crater, several outcrops of breccia are present (e.g., Junner, 1937; Woodfield, 1966; Moon and Mason, 1967), widely exposed, but it is not clear whether or not all these breccias are impact-related (Reimold et al., 1998). Based on composition and texture, Boamah and Koeberl (2003) distinguished three types of impact breccia at the Bosumtwi crater: an autochthonous monomict breccia; a probable allochthonous polymict lithic impact breccia; and suevite. Monomict breccia occurs along the northern crater rim and consists of angular fragments of different sizes, irregularly distributed, and cemented in a matrix of the same materials (Boamah and Koeberl, 2003). Suevites occur outside of the northern and southern crater rim, at about 250 m to 2 km from the crater rim crest (Koeberl and Reimold, 2005), and contain abundant impact glass and melt fragments, and a variety of clasts (such as meta-graywacke, phyllite, shale, and granite) up to about 40 cm in size (Boamah and Koeberl, 2003, 2006).

3.2. Geochemistry of country rocks and impactites from outside of the crater – Relationship with the Ivory Coast tektites:

Several country rocks and impact breccia samples from outside the crater have been analyzed for their major and trace element compositions (e.g., Jones, 1985; Koeberl et al., 1998, Boamah and Koeberl, 2003; Dai et al., 2005; Karikari et al., 2007), and some samples were also analyzed for their O, Sr, and Nd isotopic compositions (e.g., Schnetzler et al., 1966; Kolbe et al., 1967; Shaw and Wasserburg, 1982; Koeberl et al., 1998).

3.2.1. Geochemistry of country rocks

As country rocks at Bosumtwi display a large variety of lithologies, such as meta-graywacke, phyllite, shale, granite dikes, and Papiakese granite, a good characterization of the different possible target rocks is necessary in order to model the composition of the different impact breccias and to compare with Ivory Coast tektites and microtektites compositions. The chemical composition for major and trace elements of the different country rocks and of the Ivory Coast tektites is reported in the publication chapter 6 (Table

1). Large variations in chemical composition are noticeable between the different country rocks and also between individual samples, such as for the Papiakese granite samples (Koeberl et al., 1998). Shales are distinct from phyllite and meta-graywacke in that they have lower silica and higher aluminum, iron, and magnesium contents. Papiakese granites are also very different from the other samples, with chromium, cobalt, and nickel contents nearly 3-5 times higher than for the granite dike samples (see publication chapter 6, Table 1). In addition, all country rocks show an elevated siderophile element contents, which is attributed to the sulfide minerals associated with the Birmanian hydrothermal alteration (see, e.g., Karikari et al., 2007; and references therein). Differences in oxygen and strontium isotopic composition were also noted by Koeberl et al. (1998) for the different rocks types.

The chemical composition of country rocks was recently compared with the chemical composition of target rocks recovered during the 2004 ICDP drilling project (see publication chapter 6 and Coney et al., 2007a). Additional Sr and Nd isotopic compositions of target rocks recovered during the 2004 ICDP drilling project, including phyllite and meta-graywacke samples, are also reported and discussed in the publication chapter 10.

3.2.2. Geochemistry of impactites and relationship of the Bosumtwi crater with the Ivory Coast tektite strewn field

Fallout suevites and tektites were investigated mostly for the detection of a possible meteoritic component. El Goresy (1966) reported the presence of microscopic metallic spherules in glass fragments from suevite, which yielded a composition very similar to the composition of kamacite in some iron meteorites. The Ivory Coast tektites were identified as having been produced by the Bosumtwi event. The first suggestion for such a connection was based on the geographical proximity of the tektite strewn field relatively to the Bosumtwi impact structure (see Figure 3-1). This suggestion was then supported by similarities in chemical compositions (e.g., Schnetzler et al., 1967; Jones, 1985; Koeberl et al., 1998), similar isotopic characteristics for the tektites and Bosumtwi country rocks (Schnetzler et al., 1967; Lippolt and Wasserburg, 1966; Shaw and Wasserburg, 1982; Koeberl et al., 1998), and similar ages of tektites and Bosumtwi impact glasses (e.g., Gentner et al., 1964, 1967; Kolbe et al., 1967; Storzer and Wagner, 1977; Koeberl et al., 1997). The question of a meteoritic component in the tektites was raised by Palme et al. (1978), who measured the concentrations of siderophile elements in one Ivory Coast tektite and they found that the iridium and osmium contents were significantly higher than terrestrial crustal values. However, only Koeberl and Shirey (1993), using Re-Os isotope systematics, have provided a definite evidence of the presence of a meteoritic component, of up to 0.6%, in Ivory Coast tektites. In addition, using chromium isotopic composition of tektites, Koeberl et al. (2007b) were able to characterize the ordinary chondritic composition of the impactor.

However, no definite evidence for the presence of a meteoritic component in fallout suevites has been established to date (e.g., Boamah and Koeberl, 2003; Dai et al., 2005; McDonald et al., 2007; Karikari et al., 2007). The same is true for suevites recovered during the 2004 ICDP drilling project (i.e., fallback suevite; see publication chapter 6; McDonald et al., 2007; Goderis et al., 2007; Coney et al., 2007a). The chemical composition of

fallback suevite is compared with fallout suevite in the publication chapter 6. Nevertheless, differences in the chemical compositions between the fallback and fallout suevites do not allow a clear separation of what is the result of the impact itself and what was induced by secondary alteration processes. Both suevite types (i.e., fallback and fallout suevites) are altered, melt particles are generally devitrified; the original glass is in most cases altered to phyllosilicate minerals (see, e.g., publication chapter 6 and Karikari et al., 2007). The matrix of suevite samples contains also evidences of post-impact alteration, such as the presence of smectite, chlorite, and calcite and iron oxides filling micro-fractures (see publication chapter 6 and Karikari et al., 2007).

3.3. The 2004 ICDP drilling project:

Because the Bosumtwi crater is filled with a lake and a 1 Myr section of lacustrine sediments, no direct observation of the central part of the structure is possible. The global image of the structure was established by remote sensing and geophysical studies (Plado et al., 2000; Karp et al., 2002; Wagner et al., 2002; Pesonen et al., 2003). The first information on the sublake structure was obtained from aerogeophysical studies (Pesonen et al., 1998, 2003) and seismic investigations (Scholz et al., 2002). A small central uplift, previously only hypothesized (e.g., Jones et al., 1981; Plado et al., 2000), was revealed recently by seismic investigations (Scholz et al., 2002). The central uplift has an apparent diameter of 1.9 km and a maximum height of about 130 m above the surrounding moat (Scholz et al., 2002). However, to obtain information about the subsurface structure, to provide groundtruth for geophysical studies, and to obtain rock samples of the not exposed portion of the crater, drilling was necessary.

The drilling was achieved within the framework of an international and multidisciplinary drilling project led by the International Continental Scientific Drilling Program (ICDP) (see the review by Koeberl et al., 2007a). The ICDP drilling project had two major scientific goals: to obtain a 1 Myr paleoenvironmental record from post-impact sediments and to acquire hardrock samples from the crater moat and central uplift of the crater. During this project, a total of 16 drill cores were obtained at six locations within the lake, including 14 sediment cores and two impactite cores. Drilling, geophysical studies, and logging were done between June and October 2004 (see Koeberl et al., 2007a). Drilling operations were performed using the DOSECC/ICDP GLAD800 lake drilling system (see Figure 3-4a). All details concerning drilling operations, including general organization, obtaining permissions for drilling, drilling conditions, etc., are reported in detail in the review by Koeberl et al. (2007a).

The two impactites cores, LB-07A and LB-08A, were drilled into the crater fill and underlying basement in the deep crater moat and on the outer flank of the central uplift, respectively (Figure 3-5). Their locations, 6°30'50''N, 1°24'55''E for LB-07A and 6°30'33''N, 1°24'45''E for LB-08A, are situated on lines of seismic surveys that were made during the preparation phase of the drilling project (see e.g., Karp et al., 2002; Scholz et al., 2002; Koeberl et al., 2007a).



Figure 3-4. Photographs taken during the 2004 ICDP drilling project. a) General view of the GLAD800 drilling barge on Lake Bosumtwi (photo courtesy C. Koeberl). b) Example of core box (number 14; drill core LB-08A) showing metasediments, mainly meta-graywacke and some phyllite and slate (darker units) at the bottom of the image. Starting and ending depths of the cored section are also indicated, at the upper left and lower right, respectively.

The core sections, with a diameter of 6 cm, were then sent to the ICDP headquarters (GeoForschungsZentrum [GFZ] in Potsdam, Germany), where scanning and documentation of the cores was done between December 2004 and January 2005 (Figure 3-4b). Core images, scanning data, and core descriptions are available online (<http://bosumtwi.icdp-online.org>; accessed 23 September 2008). Core boxes are currently stored and accessible at the ICDP headquarters.

3.3.1. Geological setting and stratigraphy of drill core LB-07A

Core LB-07A, drilled in the deep crater moat surrounding the central uplift (Figure 3-5), was recovered at depths between 333.38 and 545.08 m (below lake level) and represents 211.7 m of core. Depending on the rock types, core recovery ranged from 10 to 100 %, with an average of 65 % (Coney et al., 2007b). A schematic lithostratigraphic column of drill core LB-07A is presented in Figure 3-5b; a detailed lithostratigraphic column is reported in Coney et al. (2007b). This drill core displays several different lithologies: polymict lithic impact breccia, monomict lithic breccia, suevite, shale, slate, phyllite, schist, and meta-graywacke. Drill core LB-07A was divided into three units by Coney et al. (2007b): an upper impactite unit (from 333.38 to 415.67 m) composed of polymict lithic impact breccia alternating with suevite, a lower impactite unit (from 415.37 and 470.55 m) consisting

mainly of monomict impact breccia of meta-graywacke and minor intercalations of shale, and a basement section (from 470.55 to 545.08 m) consisting of highly disaggregated metasediments, mainly altered shale and meta-graywacke. In addition, suevite dykes occurs in the lower impactite unit and in the basement section (see Figure 3-5b), as well as an intercalation of a granophyric-textured lithology at 487.12-487.42 m (see Coney et al., 2007b).

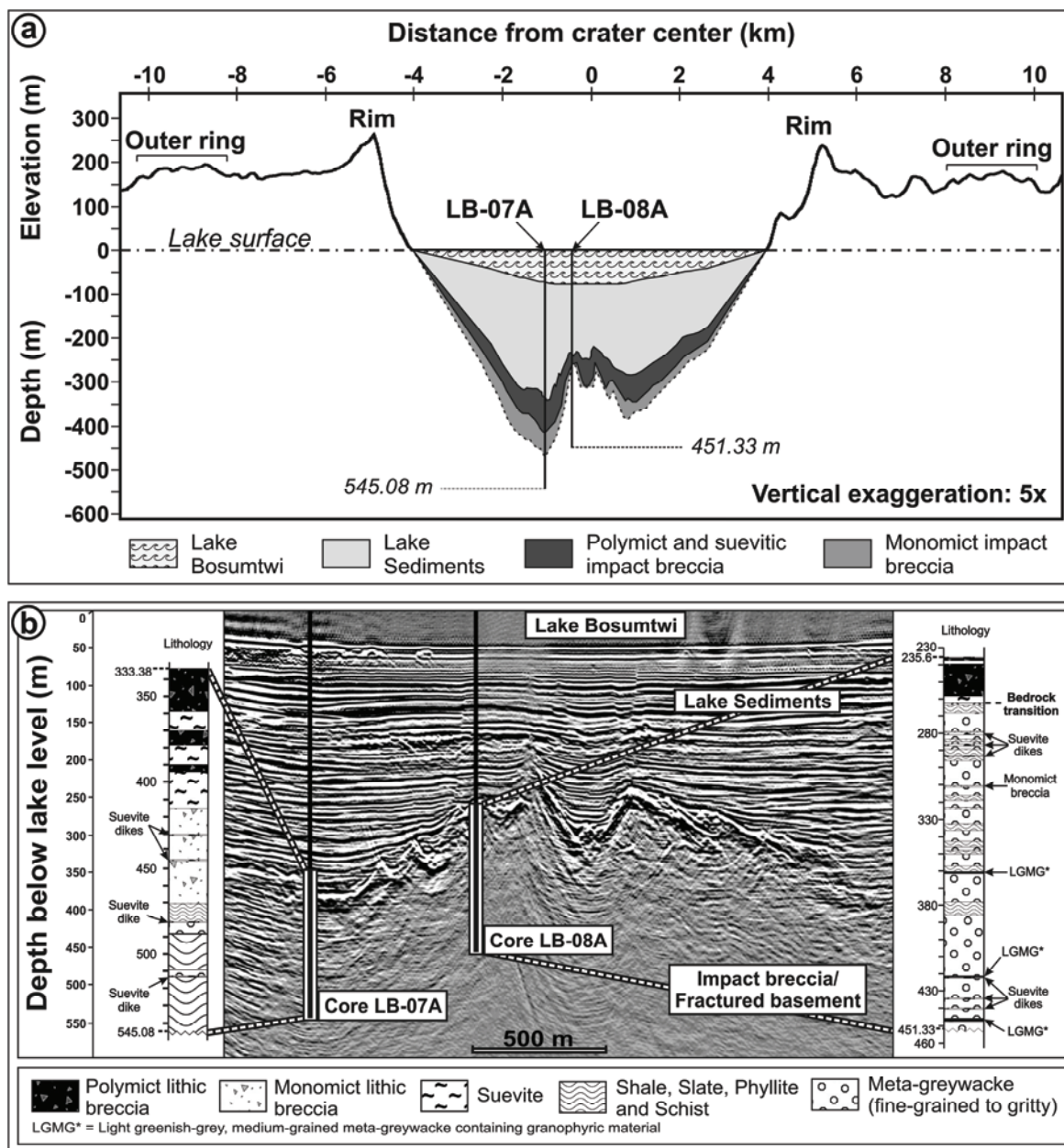


Figure 3-5. a) Cross-section of the Bosumtwi impact structure, based on the SRTM data for the regional topography of the exposed portion of the crater (profile from west to east) and on seismic reflection data (profile from northwest to southeast; after Scholz et al., 2002) for the central part of the crater. Location of boreholes LB-07A and LB-08A are given. The volume of lake sediments is based on seismic reflection data. The distribution of “polymict and suevitic impact breccia” and “monomict impact breccia” is based on observations of cores LB-07A and LB-08A (Coney et al., 2007b; Ferrière et al., 2007) as well as seismic reflections. Depths and elevations are relative to lake level. **b)** Schematic lithostratigraphic columns of drill cores LB-07A and LB-08A superimposed on a northwest to southeast seismic profile (from Scholz et al., 2002).

Detailed petrographic investigations on samples from core LB-07A are reported in Coney et al. (2007b) and Morrow (2007); their major observations and conclusions can be summarized as follows:

*Impactites in core LB-07A are mainly composed of meta-graywacke clasts and in lower proportion of altered shales.

*A carbonate target component, unknown in fallout suevite, occurs in suevite from core LB-07A, and granite clasts are extremely rare.

*Basement rocks (i.e., target rocks) in core LB-07A are dominated by altered shales.

*The high-pressure silica polymorph coesite occur in fallback suevite within diaplectic glass.

*Quartz grains with 1 to 4 PDF sets are common to abundant in impactite samples.

*Quartz grains are commonly toasted and PDFs are generally decorated.

*A lower amount of melt is observed within fallback suevite than in fallout suevite.

Regarding shock pressures, Coney et al. (2007b) estimate that the bulk of the suevite from core LB-07A is derived from the <35 GPa shock zone of the transient crater, when Morrow (2007) estimates that shock pressures of 20 GPa were generally reached and exceeding 40-45 GPa in rare cases in the upper impactite. In addition, based on the presence of decorated PDFs, toasted quartz, and distribution of melt, Morrow (2007) suggested a water- or volatile-rich target for the Bosumtwi impact event.

3.3.2. Geological setting and stratigraphy of drill core LB-08A

Core LB-08A, drilled on the outer flank of the central uplift (Figure 3-5), was recovered at a depth between 235.6 and 451.33 m and represents 215.7 m of core. Depending on the rock types and alteration level of the rocks, core recovery ranged from 40 to 115 %, with an average of 93 % (see publication chapter 5). A schematic lithostratigraphic column of drill core LB-08A is presented in Figure 3-5b; a detailed lithostratigraphic column is reported in the publication chapter 5. As for core LB-07A, detailed petrographic and geochemical investigations were conducted on samples from core LB-08A; results of these investigations are presented in publication chapters 5, 6, and 7. Deutsch et al. (2007) also performed petrographic investigations on samples taken from core LB-08A; they provide a lithostratigraphic column that is similar to the one reported in Figure 3-5b.

Drill core LB-08A displays a variety of lithologies, including suevite, polymict lithic impact breccia, monomict lithic impact breccia, slate, phyllite, and meta-graywacke. The core can be divided into two main parts: the uppermost 25 meters that are composed of polymict lithic impact breccia (clast-supported) intercalated with suevite, and the other part of the core (between 262 to 451 m), which is dominated by fractured metasediment, locally intersected by monomict lithic breccia and suevite dikelets (see Figure 3-5b and the publication chapter 5). The upper part of the core, between 235.6 and 262 m, has been interpreted as a fallback impact breccia deposit and the lower part of the core, between 262 and 451 m, is considered to be a section of the crater basement, which has been shocked and fractured in situ during the formation of the impact crater (see for details the publication chapters 5 and 7).

For details on all scientific investigations that result from the 2004 ICDP drilling project, the reader is invited to look at the special issue of *Meteoritics & Planetary Science* (MAPS, volume 42, Nr 4/5) devoted to the Bosumtwi impact structure that was published in 2007.

References

Boamah D. and Koeberl C. 2003. Geology and geochemistry of shallow drill cores from the Bosumtwi impact structure, Ghana. *Meteoritics and Planetary Science* 38:1137–1159.

Boamah D. and Koeberl C. 2006. Petrographic studies of “fallout” suevite from outside the Bosumtwi impact structure, Ghana. *Meteoritics and Planetary Science* 41: 1761–1774.

Coney L., Gibson R. L., Reimold W. U., and Koeberl C. 2007a. Lithostratigraphic and petrographic analysis of ICDP drill core LB-07A, Bosumtwi impact structure, Ghana. *Meteoritics and Planetary Science* 42:569–589.

Coney L., Reimold W. U., Gibson R. L., and Koeberl C. 2007b. Geochemistry of impactites from ICDP borehole LB-07A, Bosumtwi impact structure, Ghana. *Meteoritics and Planetary Science* 42:667–688.

Dai X., Boamah D., Koeberl C., Reimold W. U., Irvine G., and McDonald I. 2005. Bosumtwi impact structure, Ghana: Geochemistry of impactites and target rocks, and search for a meteoritic component. *Meteoritics and Planetary Science* 40:1493–1511.

Deutsch A., Luetke S., and Heinrich V. 2007. The ICDP lake Bosumtwi impact crater scientific drilling project (Ghana): Core LB-08A litho-log, related ejecta, and shock recovery experiments. *Meteoritics and Planetary Science* 42:635–654.

El Goresy A. 1966. Metallic spherules in Bosumtwi crater glasses. *Earth and Planetary Science Letters* 1:23–24.

El Goresy A., Fechtig H., and Ottemann T. 1968. The opaque minerals in impactite glasses. In *Shock Metamorphism of Natural Materials*, edited by French B. M. and Short N. M. Baltimore: Mono Book Corporation. pp. 531–554.

Ferrière L., Koeberl C., and Reimold W. U. 2007. Drill core LB-08A, Bosumtwi impact structure, Ghana: Petrographic and shock metamorphic studies of material from the central uplift. *Meteoritics and Planetary Science* 42:611–633.

Feybesse J.-L., Billa M., Guerrot C., Duguey E., Lescuyer J.-L., Milesi J.-P., and Bouchot V. 2006. The paleoproterozoic Ghanaian province: Geodynamic model and ore controls, including regional stress modeling. *Precambrian Research* 149:149–196.

Gentner W., Lippolt H. J., and Müller O. 1964. Das Kalium-Argon-Alter des Bosumtwi Krateres in Ghana und die chemische Beschaffenheit seiner Gläser. *Zeitschrift für Naturforschung* 19A:150–153.

Gentner W., Kleinmann B., and Wagner G. A. 1967. New K-Ar and fission track ages of impact glasses and tektites. *Earth and Planetary Science Letters* 2:83–86.

Gentner W., Storzer D., and Wagner G. A. 1969. New fission track ages of tektites and related glasses. *Geochimica et Cosmochimica Acta* 33:1075–1081.

Glass B. P., Kent D. V., Schneider D. A., and Tauxe L. 1991. Ivory Coast microtektite strewn field: Description and relation to the Jaramillo geomagnetic event. *Earth and Planetary Science Letters* 107:182–196.

Goderis S., Tagle R., Schmitt R. T., Erzinger J., and Claeys P. 2007. Platinum group elements provide no indication of a meteoritic component in ICDP cores from the Bosumtwi crater, Ghana. *Meteoritics and Planetary Science* 42:731–741.

Hirdes W., Davis D. W., Lüdtkke G., and Konan G. 1996. Two generations of Birimian (Paleoproterozoic) volcanic belts in northeastern Côte d’Ivoire (West Africa): consequences for the “Birimian controversy”. *Precambrian Research* 80:173–191.

Jones W. B. 1985. Chemical analyses of Bosumtwi crater target rocks compared with the Ivory Coast tektites. *Geochimica et Cosmochimica Acta* 48:2569–2576.

Jones W. B., Bacon M., and Hastings D. A. 1981. The Lake Bosumtwi impact crater, Ghana. *Geological Society of America Bulletin* 92:342–349.

Junner N. R. 1937. The geology of the Bosumtwi caldera and surrounding country. *Gold Coast Geological Survey Bulletin* 8:1–38.

Karikari F., Ferrière L., Koeberl C., Reimold W. U., and Mader D. 2007. Petrography, geochemistry, and alteration of country rocks from the Bosumtwi impact structure, Ghana. *Meteoritics and Planetary Science* 42:513–540.

Karp T., Milkereit B., Janle P., Danuor S. K., Pohl J., Berckhemer H., and Scholz C. A. 2002. Seismic investigation of the Lake Bosumtwi impact crater: Preliminary results. *Planetary and Space Science* 50:735–742.

Koeberl C. and Reimold W. U. 2005. Bosumtwi impact crater, Ghana (West Africa): An updated and revised geological map, with explanations. *Jahrbuch der Geologischen Bundesanstalt, Wien (Yearbook of the Austrian Geological Survey)* 145:31–70 (+ 1 map, 1:50,000).

Koeberl C. and Shirey S. B. 1993. Detection of a meteoritic component in Ivory Coast tektites with rhenium-osmium isotopes. *Science* 261:595–598.

Koeberl C., Bottomley R. J., Glass B. P., and Storzer D. 1997. Geochemistry and age of Ivory Coast tektites and microtektites. *Geochimica et Cosmochimica Acta* 61:1745–1772.

Koeberl C., Reimold W. U., Blum J. D., and Chamberlain C. P. 1998. Petrology and geochemistry of target rocks from the Bosumtwi impact structure, Ghana, and comparison with Ivory Coast tektites. *Geochimica et Cosmochimica Acta* 62:2179–2196.

Koeberl C., Milkereit B., Overpeck J. T., Scholz C. A., Amoako P. Y. O., Boamah D., Danuor, S. K., Karp T., Kueck J., Hecky R. E., King J., and Peck J. A. 2007a. An international and multidisciplinary drilling project into a young complex impact structure: The 2004 ICDP Bosumtwi impact crater, Ghana, drilling project – An overview. *Meteoritics and Planetary Science* 42:483–511.

Koeberl C., Shukolyukov A., and Lugmair G. W. 2007b. Chromium isotopic studies of terrestrial impact craters: Identification of meteoritic components at Bosumtwi, Clearwater East, Lappajärvi, and Rochechouart. *Earth and Planetary Science Letters* 256:534–546.

Kolbe P., Pinson W. H., Saul J. M., and Miller E. W. 1967. Rb-Sr study on country rocks of the Bosumtwi crater, Ghana. *Geochimica et Cosmochimica Acta* 31:869–875.

Leube A., Hirdes W., Mauer R., and Kesse G. O. 1990. The Early Proterozoic Birimian Supergroup of Ghana and some aspects of its associated gold mineralization. *Precambrian Research* 46:139–165.

Lippolt H. J. and Wasserburg G. J. 1966. Rubidium-Strontium-Messungen an Gläsern vom Bosumtwi-Krater und an Elfenbeinküsten-Tektiten. *Zeitschrift für Naturforschung* 21A:226–231.

Little J., Fahey J. J., Dietz R. S., and Chao E. C. T. 1961. Coesite from the Lake Bosumtwi crater, Ashanti, Ghana (abstract). *Geological Society of America Special Paper* #68. pp. 218.

McDonald I, Peucker-Ehrenbrink B., Coney L., Ferrière L., Reimold W. U., and Koeberl C. 2007. Search for a meteoritic component in drill cores from the Bosumtwi impact structure, Ghana: Platinum group elements contents and osmium isotopic characteristics. *Meteoritics and Planetary Science* 42:743–753.

Moon P. A. and Mason D. 1967. The geology of ¼° field sheets 129 and 131, Bompata S. W. and N. W. *Ghana Geological Survey Bulletin* 31:1–51.

Morrow J. R. 2007. Shock-metamorphic petrography and microRaman spectroscopy of quartz in upper impactite interval, ICDP drill core LB-07A, Bosumtwi impact crater, Ghana. *Meteoritics and Planetary Science* 42:591–609.

Palme H., Janssens M. J., Takahashi H., Anders E., and Hertogen J. 1978. Meteorite material at five large impact craters. *Geochimica et Cosmochimica Acta* 42:313–323.

Pesonen L. J., Koeberl C., Ojamo H., Hautaniemi H., Elo S., and Plado J. 1998. Aerogeophysical studies of the Bosumtwi impact structure, Ghana (abstract). *Geological Society of America Abstracts with Programs* 30(7):A190.

Pesonen L. J., Koeberl C., and Hautaniemi H. 2003. Airborne geophysical survey of the Lake Bosumtwi meteorite impact structure (Southern Ghana) – Geophysical maps with descriptions. *Jahrbuch der Geologischen Bundesanstalt, Vienna (Yearbook of the Austrian Geological Survey)* 143:581–604.

Plado J., Pesonen L. J., Koeberl C., and Elo S. 2000. The Bosumtwi meteorite impact structure, Ghana: A magnetic model. *Meteoritics and Planetary Science* 35:723–732.

Reimold W. U., Brandt D., and Koeberl C. 1998. Detailed structural analysis of the rim of a large, complex impact crater: Bosumtwi crater, Ghana. *Geology* 26:543–546.

Schnetzler C. C., Pinson W. H., and Hurley P. M. 1966. Rubidium-Strontium age of the Bosumtwi crater area, Ghana, compared with the age of the Ivory Coast tektites. *Science* 151:817–819.

Schnetzler C. C., Philpotts J. A., and Thomas H. H. 1967. Rare earth and barium abundances in Ivory Coast tektites and rocks from the Bosumtwi crater area, Ghana. *Geochimica et Cosmochimica Acta* 31:1987–1993.

Scholz C. A., Karp T., Brooks K. M., Milkereit B., Amoako P. Y. O., and Arko J. A. 2002. Pronounced central uplift identified in the Bosumtwi impact structure, Ghana, using multichannel seismic reflection data. *Geology* 30:939–942.

Shaw H. F. and Wasserburg G. J. 1982. Age and provenance of the target materials for tektites and possible impactites as inferred from Sm-Nd and Rb-Sr systematics. *Earth and Planetary Science Letters* 60:155–177.

Storzer D. and Wagner G. A. 1977. Fission track dating of meteorite impacts. *Meteoritics* 12: 368–369.

Taylor P. N., Moorbath S., Leube A., and Hirdes W. 1992. Early Proterozoic crustal evolution in the Birimian of Ghana: Constraints from geochronology and isotope geochemistry. *Precambrian Research* 56:97–111.

Wagner R., Reimold W. U., Brandt D. 2002. Bosumtwi impact crater, Ghana: A remote sensing investigation. In *Meteorite impacts in Precambrian shields*, edited by Plado J. and Pesonen L. J. Impact Studies, vol. 2. Heidelberg: Springer-Verlag. Pp. 189–210.

Woodfield P. D. 1966. The geology of the $\frac{1}{4}^{\circ}$ field sheet 91, Fumso N. W. *Ghana Geological Survey Bulletin* 30:1–66.

Wright J. B., Hastings D. A., Jones W. B., and Williams H. R. 1985. *Geology and Mineral Resources of West Africa*. London: Allen & Unwin. 187 p.

CHAPTER 4: Methodology

For the study of the samples, a large number of techniques were employed, including standard methods (such as optical microscopy, universal stage [U-stage], or scanning electron microscope [SEM]), but also high precision analytical methods were used, as instrumental neutron activation analysis (INAA), X-ray fluorescence (XRF) spectroscopy, electron microprobe (EMP), and mass spectroscopy. Some samples were additionally investigated using microRaman spectroscopy, transmission electron microscopy (TEM), and cathodoluminescence (CL). A review of the different techniques employed for the investigations is provided in the following sections.

4.1. Samples:

4.1.1. Selection of samples

As mentioned above (see section about the 2004 ICDP drilling project; chapter 3), most of the investigated samples were obtained by drilling of the outer flank of the central uplift of the Bosumtwi impact structure (drill core LB-08A). Additional suevite samples from outside of the crater rim were also used for comparison (see chapter 10). The same samples from outside of the crater rim were investigated in detail for the work on ballen cristobalite (see chapter 8 for details). Several thin sections of samples from a number of impact structures were also studied for the characterization of the different types of ballen quartz-cristobalite (for information, see publication chapter 8 and chapter 10). In addition, three thin sections (a meta-greywacke clast in breccia [BOS-3; from the Bosumtwi crater], a biotite-gneiss [M8-427.7; from the Manson crater], and a sandstone [AUS-90-43-2; from the Gosses Bluff crater]) were investigated, using U-stage, for the publication chapter 9.

Concerning samples from drill core LB-08A, a total of 121 core samples, with masses ranging from 30 to 500 g, were selected during the sampling party at the GeoForschungsZentrum (GFZ) in Potsdam, Germany. Samples were cut at the GFZ and mailed to Vienna. Sample labeling, as given by the operational support group of the ICDP at the GFZ (e.g., SR0002B0001-4-25,35) was simplified to KR8- (initials for Koeberl-Reimold and 8 for core LB-08A) and a number; the sample number generally increasing with the depth of recovery. However, as the original labeling contains some essential information (see Figure 4-1), as the sample run number, box number, row number, and the distance (in centimeters) of the core sample from the beginning of the considered run, this information was extracted and is reported in Appendix A.

4.1.2. Sample preparation

Representative aliquots of the different samples, weighing about 20 to 30 g, were crushed in polyethylene wrappers and powdered in a mechanical agate mill for bulk chemical analysis. Special attention was paid to avoid clasts larger than 5 mm in diameter for the impact breccia samples, to obtain relatively representative compositions. The full

results of INAA and XRF analyses are reported in Appendix B; average compositions of the different lithologies are presented in the publication chapter 6.

Thin sections were prepared for petrographic studies (concise descriptions are presented in the publication chapter 5; detailed petrographic descriptions of the samples are reported in Appendix C) and polished thin sections for SEM and EMP analyses (compositions of minerals and melt particles are reported in Appendix D).

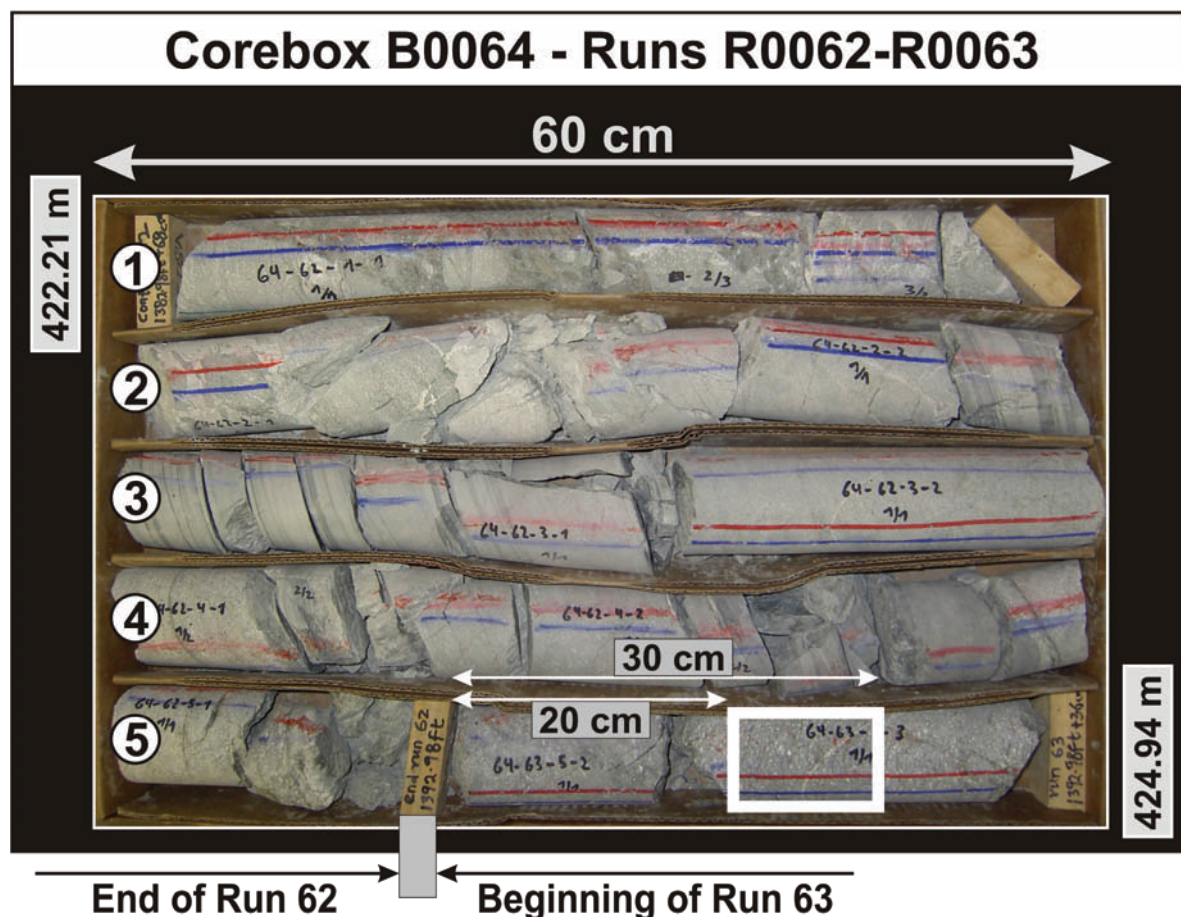


Figure 4-1. Example of core box (number 64) containing runs 62 and 63, from which sample KR8-108 (or SR0063B0064-5-20.30) was selected. Sample location is indicated by the white rectangle. Row numbers (from 1 to 5) are noted on the left side of the image, as well as the respective distances of the core sample from the beginning of the core run. Starting and ending depths (below lake level) of the total cored section are also indicated.

4.2. Analytical methods:

4.2.1. Optical microscope and universal stage (U-stage)

All thin sections and polished thin sections were examined with an optical microscope in both transmitted and reflected light. Modal composition analyses were performed on several thin sections; some sections were also selected for scanning electron microscopy (SEM), cathodoluminescence (CL), electron microprobe studies, and microRaman spectroscopy.

Universal-stage (U-stage) microscope analysis was performed on several thin sections for determining the crystallographic orientations of planar deformation features (PDFs) in quartz. More information on U-stage can be found in, e.g., Reinhard (1931), Emmons (1943); these references were used for the elaboration of the present notice of use of the U-stage (supplementary information on the use of U-stage was provided by B. M. French; written commun.).

4.2.1.1. Preparation of the microscope for U-stage installation:

- * Remove all standard microscope objectives.
- * Install U-stage objectives into opposite sockets (two magnifications are available: 10x and 30x).
- * Lock microscope stage with index at 0°/360°.

4.2.1.2. Mounting of assembled U-Stage:

The assembly U-Stage is composed of four components (from bottom up; see Figure 4-2):

- Lower hemisphere (circular) – Ref#: n=1.554.
- Circular glass plate.
- Thin section.
- Upper hemisphere (rectangular) – Ref#: n=1.554.

[Lower and upper hemispheres are selected to match index of quartz (n=1.554)]

- * Attach the circular glass plate to the lower hemisphere using one drop of glycerine.
- * Insert the assemblage into the center of the inner disk and adjust in function.
- * Add a drop of glycerine and place the thin section on top of the glass plate (top-side up).
- * Add a drop of glycerine and place the upper hemisphere on the thin section.
- * Lock carefully the assembly using the two screws.

4.2.1.3. Installation of the U-stage on the microscope:

- * Lift U-stage onto microscope stage with the large wheel at right (see Figure 4-2).
- * Fixation of the U-stage (two screws).
- * Lock the outer vertical stage with index 10°/10° (by using the screw located inside the large wheel at right).

4.2.1.4. Calibration of the U-stage:

- * Center U-stage objectives.
- * Center U-stage on microscope stage.
- * Adjust vertical elevation of stage.

4.2.1.5. Measurement of the c-axis and PDF orientations in quartz grains:

Move the thin section until the selected quartz grain is under crosshairs (remembering that only the central part of the section is accessible for measurement).

Measurement of c-axis orientations:

First of all, check that all settings are set to 0° . Turn the inner vertical stage until extinction of the grain (if the grain shows undulose extinction [variable c-axis orientation in different parts of the grain], be sure to do the measurement of the c-axis that refer to the PDF that needs to be measured). Two possibilities of extinctions are possible: N-S or E-W.

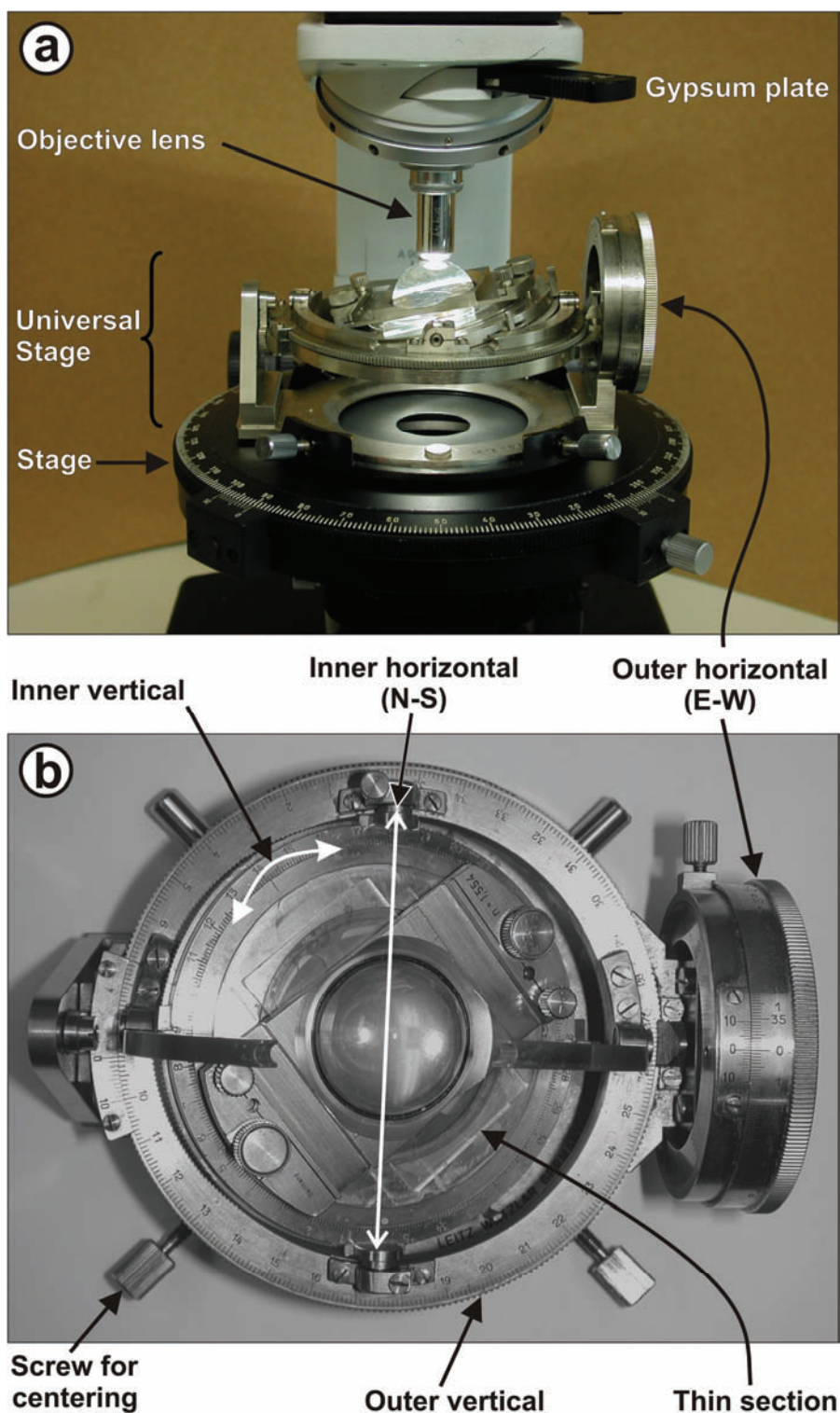


Figure 4-2. Photographs of a four axis universal stage at the Department of Lithospheric Research (University of Vienna). a) General view of the U-stage mounted on the microscope. b) A closer view of the U-stage showing the different components.

For the measurement, the c-axis should be oriented E-W. To check for c-axis orientation, use the gypsum plate (see Figure 4-2). When the grain is at extinction, rotate microscope stage clockwise of about 30° . Then, insert the gypsum plate; if the grain becomes gray/yellow, it is okay, the grain was originally oriented E-W [if the grain becomes blue/green, it is not okay; the inner vertical stage should be turned till next extinction]. After that, remove gypsum plate and rotate back microscope stage to the initial position. Now, rotate outer horizontal stage (the large wheel at right; see Figure 4-2) about 20 to 40° (until grain comes out of extinction and becomes as bright as possible). Then, rotate inner horizontal stage until grain is again at extinction (or maximum extinction position). Check by rotating again outer horizontal stage. Finally, return microscope stage to zero and record observations for c-axis (azimuth and inclination).

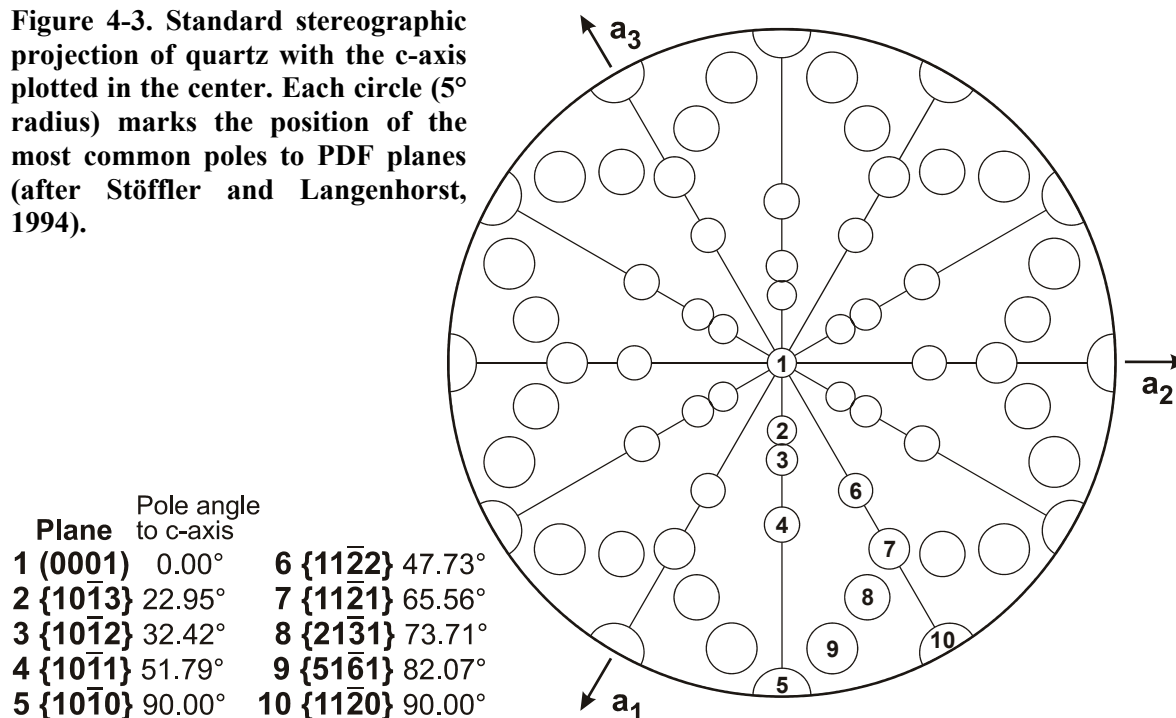
Determine orientations of PDF sets:

Rotate inner vertical stage until set of PDF is oriented parallel to N-S crosshairs, then rotate inner horizontal stage until a set of PDF appears at maximum sharpness (both, plane- or cross-polarized light can be used). Finally, record observations for PDF sets (azimuth and inclination).

4.2.1.6. Plotting measurements and data reduction:

When measurements of c-axis and of the poles perpendicular to planes of all PDFs are completed, data are plotted on a stereographic Wulff net. Then, finally, the planes measured are indexed using a standard stereographic projection template (SPT; see Figure 4-3), which displays the possible pole orientations of common PDF planes within a 5° envelope of measurement error (e.g., Engelhardt and Bertsch (1969); Stöffler and Langenhorst (1994); Grieve et al. (1996); Langenhorst (2002)). This SPT (see Figure 4-3) allows the indexing of ten typical PDF crystallographic orientations in quartz.

Figure 4-3. Standard stereographic projection of quartz with the c-axis plotted in the center. Each circle (5° radius) marks the position of the most common poles to PDF planes (after Stöffler and Langenhorst, 1994).



4.2.2. Instrumental Neutron Activation Analysis (INAA):

This method is a sensitive multi-element analytical technique, which allows precise determination of major, minor, and trace elements abundances from powder or whole samples. This non-destructive method permits the simultaneous determination of up to 40 elements with high precision (see Table 4-1) and without any chemical treatment.

For INAA, samples are irradiated by neutrons (mostly thermal neutrons), commonly within a nuclear reactor. Thus, a naturally occurring stable isotope is transformed, in a neutron capture reaction, into a short-lived radioactive isotope that undergoes radioactive decay – mostly β -decay combined with the emission of a photon, either an X-ray or a γ -ray. Specific isotopes can be then identified from the energies of the emitted γ -rays, which are characteristic for a particular isotope. The amount of the isotopes present is determined by measuring the intensities of the γ -rays. The counting is done during several cycles (three cycles for the present study), as the γ -spectrum changes with time as a result of the different half-lives of the various nuclides occurring in the samples. The quantification of the elements is finally achieved by comparing the different γ -spectra with the reference materials.

For detailed information on the INAA method, see e.g., Ehmann and Vance (1991), Koeberl (1993, 1995), Gill (1997).

A brief description of the source of neutrons used for this study is provided, as well as information on the instrumentation suitable for the detection of γ -rays. In addition, data processing and corrections, sample preparation, and measurement, is discussed.

4.2.2.1. Source of neutrons – Irradiation:

Different sources can be used for the irradiation with neutrons, such as nuclear reactors, accelerators, or radioisotopic emitters, but nuclear reactors with their high fluxes of neutrons from uranium fission are most commonly used in routine INAA. A research reactor, the 250 kW TRIGA Mark II type (at the Atomic Institute of the Austrian Universities, Vienna, Austria), was used for irradiation of our samples.

The probability of the interaction of a neutron with a target nuclide is called the neutron capture cross section (σ). The capture cross section is function of the neutron energy. The activity of an isotope, which depends on the half-life of the intermediate nucleus, can be expressed by the following equation:

$$A = n \cdot \phi \cdot \sigma \cdot \left(1 - e^{-\ln 2 \frac{t_{irr}}{t_{1/2}}}\right)$$

where n is the number of atoms of the target, Φ is the neutron flux, σ is the neutron capture cross section, t_{irr} is the irradiation time, and $t_{1/2}$ is the half-life of the indicator nuclide.

A neutron flux of about $2 \cdot 10^{12} \text{ n.cm}^{-2} \cdot \text{s}^{-1}$ was used during the irradiation of the samples in the Triga reactor.

Table 4-1. Typical precision of INAA analyses (in relative %) at the University of Vienna. Data obtained by at least 10 replicate analyses of international geological standard reference materials.

Na (wt%)	2
K (wt%)	5
Sc	2
Cr	3
Fe (wt%)	4
Co	2
Ni	15
Zn	3
As	10
Rb	2
Sr	5
Zr	10
Sb	5
Cs	2
Ba	10
La	2
Ce	3
Nd	5
Sm	2
Eu	2
Gd	5
Tb	2
Tm	5
Yb	2
Lu	2
Hf	2
Ta	2
W	10
Ir (ppb)	Below detection limit 1 ppb
Au (ppb)	15
Th	2
U	10

All data in ppm, except as listed.
Data from Son and Koeberl (2005).

4.2.2.2. Gamma spectroscopy:

To measure γ -rays emitted by the samples, a semiconductor detector is used with a digital signal processor (DSP) connected to a multichannel-analyzer (MCA) with computed-based data evaluation (see Figure 4-4). High purity HpGe semiconductor detectors are employed, operating at liquid nitrogen temperatures to minimize electronic noise and to avoid damage of the lithium layer in the germanium crystals. A digital signal processor (DSP) receives voltage pulses from the pre-amplifier that collects signals from the detector, and then, the signal is stored in a memory channel of the multichannel analyzer (MCA). Every channel (from 4096 or 8192) of the MCA stores the signal of a certain energy; the amount of signals give a peak.

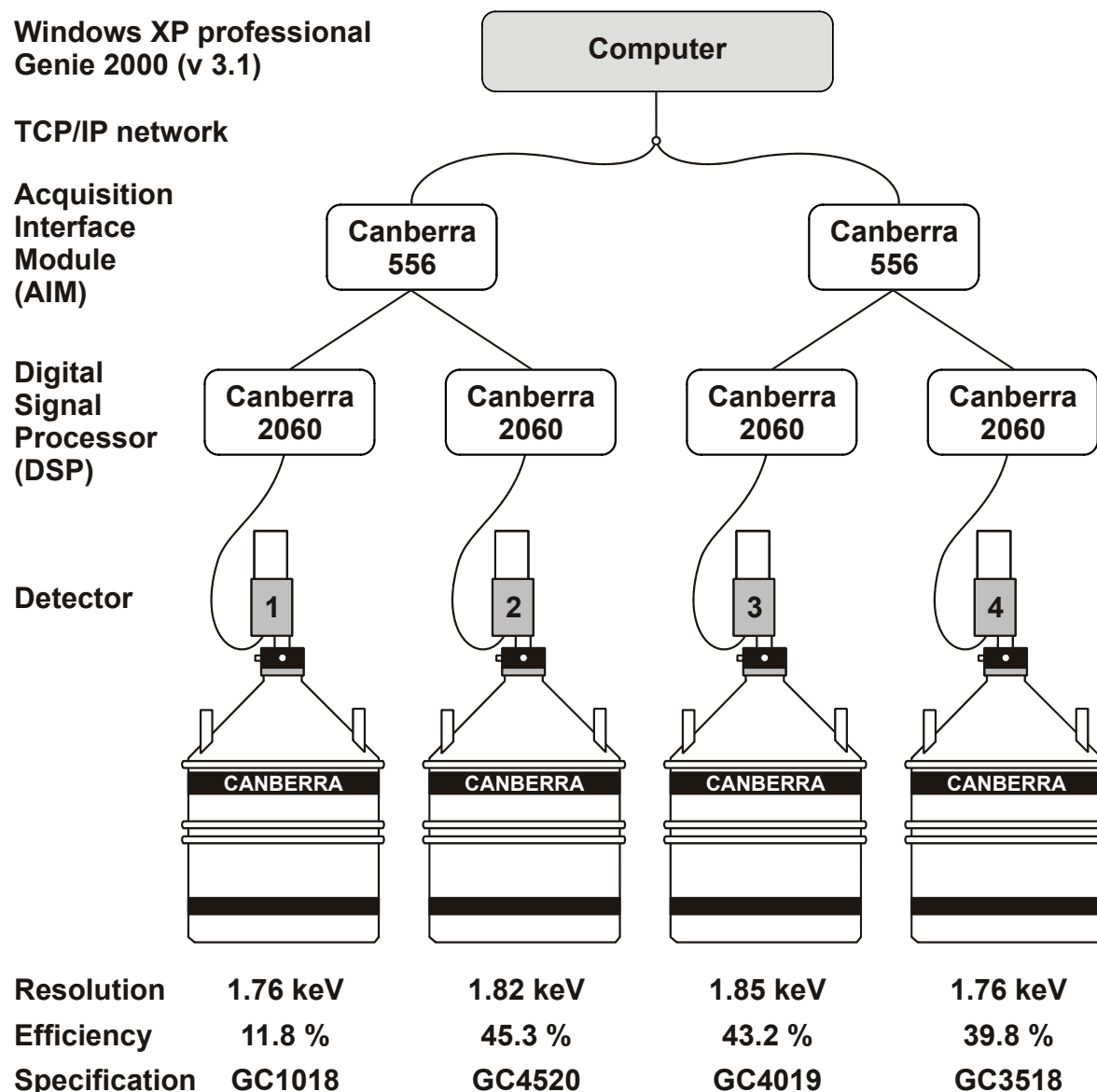


Figure 4-4. Configuration of the INAA system at the Department of Lithospheric Research (University of Vienna).

4.2.2.3. Data processing and corrections:

For determination of the concentration of the different elements present in the investigated samples, and after background subtraction and peak-area calculation, several corrections are necessary; namely: decay time correction, dead time correction, normative time correction, geometry correction, and flux correction. Samples and standards are not measured simultaneously, thus, a recalculation to a normative time is necessary for comparison. This operation is called the decay time correction (f_z):

$$f_z = e^{\ln 2 \frac{\Delta t}{t_{1/2}}}$$

were Δt is the decay time and $t_{1/2}$ is the half-life of the indicator nuclide.

The dead time correction (f_p), which is done automatically during signal processing, results from the high count rates and represents the time of losses due to electronic overflow in the DSP. In addition, the different measuring times and the varying decay rates of the nuclides have to be corrected, as the activity of samples and standards is decreasing with time. This correction, called normative time correction (f_n), is done following this equation:

$$f_n = \frac{1 - e^{-\ln 2 \frac{t_{std}}{t_{1/2}}}}{1 - e^{-\ln 2 \frac{t_{sample}}{t_{1/2}}}}$$

where t_{std} is the measurement time of the standard and t_{sample} is the measurement time of the sample.

A geometry correction (f_g) needs to be applied if the measurement geometry (i.e., the distance between the sample and detector) is changed during measurement of individual samples in a batch. In some cases, a flux correction (f_f) is also necessary, if the neutron flux that the samples were subjected to during irradiation in the reactor was heterogeneous; the flux correction can be done as the position of each sample and standard during the irradiation is known.

Finally, after all these corrections, the concentration of each element is calculated using the following equation:

$$c_{sample} = c_{std} \frac{W_{std} \cdot A_{sample}}{W_{sample} \cdot A_{std}}$$

where c is the concentration of the element, W is the weight of the element, and A is the peak area.

4.2.2.4. Sample preparation:

For the analyses, about 160 mg of each sample powder and about 90 mg of international rock standards, was used. Three international standard materials were used: the carbonaceous chondrite Allende (Smithsonian Institution, Washington, USA; Jarosewich et al., 1987), granite AC-E (Centre de Recherche Pétrographique et Géochimique, Nancy, France; Govindaraju, 1994), and granite G-2 (USGS; Govindaraju, 1994).

Samples were weighed into polyethylene capsules, heat sealed, and checked if watertight. Then, 20 to 25 vials were packed together into aluminum foil and were placed into a plastic tube for irradiation. The relative positions of the vials were noted for the neutron flux correction. Finally, after irradiation and a cooling period of about four days,

the samples vials were decontaminated in solutions of diluted HCl, diluted NaOH, and distilled water. After drying, the samples were measured.

4.2.2.5. Measurement:

The gamma spectroscopy system at the Department of Lithospheric Research (University of Vienna) has four independent HpGe detectors with relative efficiencies between ~12 and 45 % and energy resolutions between 1.76 and 1.85 keV (see Figure 4-4). The measurements were done during three counting cycles, L1, L2, and L3, respectively, because of the different half-life of the nuclides (Table 4-2). The first counting period (L1) started 4 days after irradiation, with counting time of at least one hour for each sample (depending on the composition and of the activity of the sample); the second one (L2) started about 10 days after irradiation, with counting time of about three hours; and the last counting period (L3) started about one month after the irradiation, with counting time between 12 and 24 hours. After the measurements were completed, the spectra were calibrated, and a peak search procedure was performed. Finally, the concentrations of the elements were calculated using the PC-based Neutron Activation Analysis Software (PNAA v1.1).

The contents of additional elements were determined by X-ray Fluorescence (XRF) Spectrometry (see XRF section for details); the Fe, Na, K, Cr, Co, Ni, Zn, Rb, Sr, Zr, and Ba concentrations were determined by both, XRF and INAA methods.

Table 4-2. Elements determined by INAA. Indicator isotopes are reported as well as energy lines, half-lives, and measuring cycles.

Element	Indicator isotope	Energy lines [keV]	Half-life $T_{1/2}$	Measurement cycle
Na	²⁴ Na	1368.6	14.96 h	L1
K	⁴² K	1524.7	12.36 h	L1
Sc	⁴⁶ Sc	889.3; 1120.5	83.79 d	L2, L3
Cr	⁵¹ Cr	320.1	27.70 d	L2, L3
Fe	⁵⁹ Fe	192.3; 1099.2; 1291.6	44.50 d	L2, L3
Co	⁶⁰ Co	1173.2; 1332.5	5.27 y	L3
Ni	⁵⁸ Co	810.8	70.82 d	L2, L3
Zn	⁶⁵ Zn	1115.5	244.26 d	L3
As	⁷⁶ As	559.1	26.32 h	L1
Br	⁸² Br	554.3; 776.5	35.30 h	L1
Sr	⁸⁵ Sr	514.0	64.84 d	L2, L3
Rb	⁸⁶ Rb	1076.6	18.63 d	L2, L3
Zr	⁹⁵ Zr	724.2; 756.7	64.02 d	L2, L3
Sb	¹²⁴ Sb	1691.0	60.0 d	L3
	¹²² Sb	564.1	2.70 d	L1
Cs	¹³⁴ Cs	795.8	2.06 y	L3
Ba	¹³¹ Ba	496.3	11.50 d	L2, L3
La	¹⁴⁰ La	328.8; 487.0; 1596.2	1.68 d	L1, L2
Ce	¹⁴¹ Ce	145.4	32.50 d	L2, L3
Nd	¹⁴⁷ Nd	91.1; 531.0	10.98 d	L2
Sm	¹⁵³ Sm	103.2	46.27 h	L1, L2
Eu	¹⁵² Eu	121.8; 1408.0	13.54 y	L2, L3
Gd	¹⁵³ Gd	97.4; 103.2	241.6 d	L3
Tb	¹⁶⁰ Tb	298.6; 897.4; 966.2; 1178.0	72.3 d	L2, L3
Tm	¹⁷⁰ Tm	84.3	128.6 d	L2, L3
Yb	¹⁷⁵ Yb	282.5; 396.3	4.18 d	L1, L2
	¹⁶⁹ Yb	177.2; 198.0	32.03 d	L1, L2
Lu	¹⁷⁷ Lu	208.4	6.73 d	L1, L2
Hf	¹⁸¹ Hf	482.2	42.39 d	L2, L3
Ta	¹⁸² Ta	67.7; 222.1; 1221.4; 1231	114.43 d	L2, L3
W	¹⁸⁷ W	685.8	23.72 h	L1
Ir	¹⁹² Ir	299.0; 308.5; 316.5; 468.1	73.83 d	L3
Au	¹⁹⁸ Au	411.8	2.70 d	L1
Th	²³³ Pa	300.3; 312.2	26.97 d	L2, L3
U	²³⁹ Np	228.2; 277.6	2.36 d	L1

Energy lines and half lives are from Firestone and Shirley (1996); "h" for hour, "d" for day, and "y" for year.

4.2.3. X-ray Fluorescence (XRF) spectrometry:

X-ray fluorescence (XRF) spectrometry is a standard technique widely used for bulk chemical analysis. The concentrations of major and minor elements, as well as of some trace elements can be determined using this highly accurate and reproducible technique. An XRF spectrometer consists of an X-ray tube (primary radiation source), a sample holder, a primary collimator (to parallelize the emitted photons), an analyzing crystal, a second collimator, and a detector (see Figure 4-5).

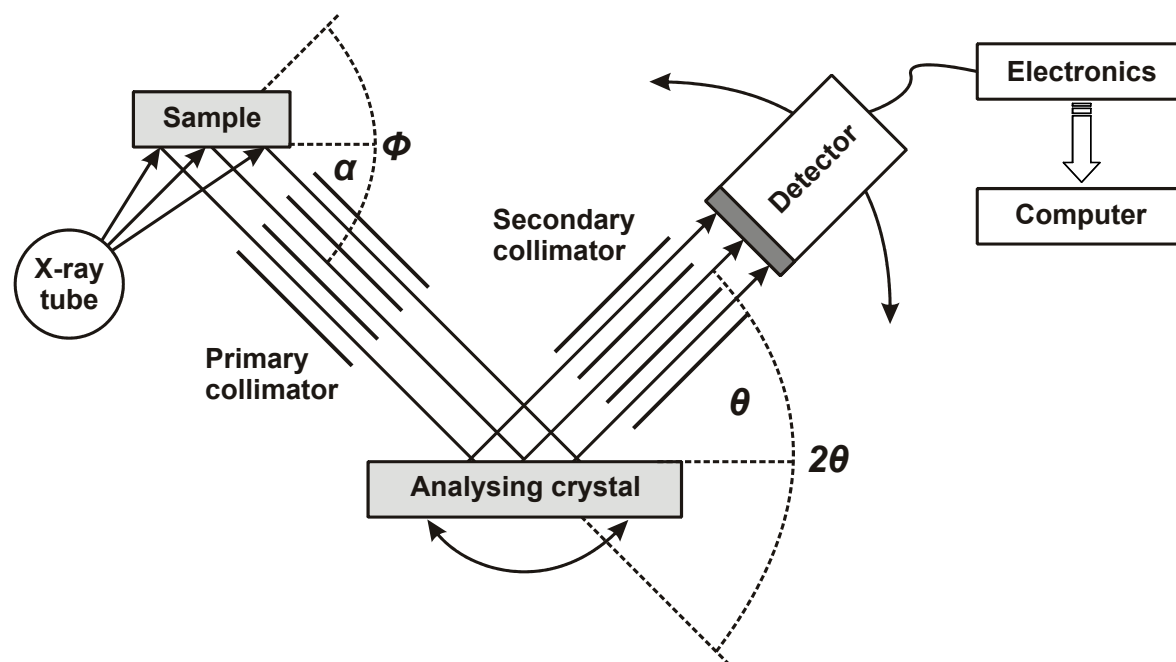


Figure 4-5. Schematic diagram of a typical XRF spectrometer (after Gill, 1997).

The atoms of the sample are irradiated with high-energy X-ray photons using an X-ray tube. Thus, electrons of the strongest bound electronic orbitals are ejected from electron shells near the nucleus of the atoms. The resulting free positions are filled by electrons of the outer orbitals (in respect to restore the atoms to a more stable state), a process which is accompanied by the emission of secondary X-rays (fluorescent X-rays). Because each element has a unique set of energy levels, each element produces fluorescent X-rays at a unique set of energies. The energy of emitted fluorescent X-rays is determined by the difference between the two binding energies of the corresponding shells. The secondary X-rays are collimated to a parallel beam and spectrally divided, with an analyzing crystal (i.e., a synthetic crystal), to a spectrum. The diffracted X-rays are further collimated and only a parallel beam of X-rays reaches the detector (see Figure 4-5). The secondary collimator and the detector, coupled to the analyzing crystal, can move around the rotation axis of the analyzing crystal (i.e., Rowland circle). This mechanism, which allows measurement of the rotation angle, is called a goniometer. Only fluorescent X-rays with wavelength (λ) satisfying the Bragg equation ($n\lambda = 2d \sin\theta$) are reflected from the analyzing crystal into the detector. In the Bragg equation, n is an integer, d is the lattice spacing of the analyzing crystal, and θ is the Bragg angle.

For quantification, the wavelength and intensities of the emitted X-rays are compared with reference standards. For detailed information on XRF spectrometry, see e.g., Potts (1987), Gill (1997); these two references were used for the compilation of the present summary.

Standard XRF spectrometry was used at the University of the Witwatersrand, Johannesburg (South Africa) for the determination of the contents of the major element oxides (SiO_2 , TiO_2 , Al_2O_3 , Fe_2O_3 , MnO , MgO , CaO , Na_2O , K_2O , and P_2O_5) and the trace elements abundances (V, Cr, Co, Ni, Cu, Zn, Rb, Sr, Y, Zr, Nb, and Ba). Sample powders were prepared in two different forms: as a glass bead made from sample powder fused with lithium metaborate or tetraborate for major element analysis, and as a pressed powder disc for trace element analysis. Samples were measured with a Philips PW 1400 XRF spectrometer. Precision and accuracy values are reported in Table 4-3.

Table 4-3. Typical precision and accuracy of XRF analyses at the University of the Witwatersrand (Johannesburg, South Africa). Data obtained by 5 replicate analyses of international geological standard reference materials.

	Standard deviation	Absolute error
SiO_2	0.41	-0.04
TiO_2	0.07	-0.04
Al_2O_3	0.41	-0.22
Fe_2O_3	0.07	-0.03
MnO	0.01	-0.01
MgO	0.17	-0.05
CaO	0.06	0.004
Na_2O	0.10	0.06
K_2O	0.07	-0.002
P_2O_5	0.02	-0.02
V	8	4.0
Cr	15	8.1
Co	3	1.8
Ni	6	-1.8
Cu	4	0.1
Zn	2	-0.1
Rb	8	-2.6
Sr	4	-1.4
Y	2	-0.2
Zr	5	1.9
Nb	1	-2.2
Ba	13	-2.3

Standard deviation and absolute error for major elements in wt% and trace elements in ppm. The standard deviation is calculated by summing the squares of the individual deviations from the mean, taking the square root of this sum, and dividing by the number of degrees of freedom (which is n-1). For the absolute error, the negative sign is retained as it indicates that the experimental result is smaller than the accepted value.

4.2.4. Scanning Electron Microscopy (SEM):

Scanning electron microscopy (SEM) is a routine technique, mainly used for the acquisition of high magnification images, secondary electron (SE) or back-scattered electron (BSE) images. When equipped with an X-ray analyzer, a SEM can be used for semi-quantitative chemical analyses. An SEM consists of an electron gun, an electron column (consisting of condenser and objective lens), a specimen chamber, and an X-ray analyzer (see Figure 4-6). An electron image is formed by bombardment of the surface of a specimen using a beam of accelerated electrons. More information on SEM can be found in, e.g., Potts (1987), Potts et al. (1995), Gill (1997), Watt (1997); these references were used for the preparation of the following review.

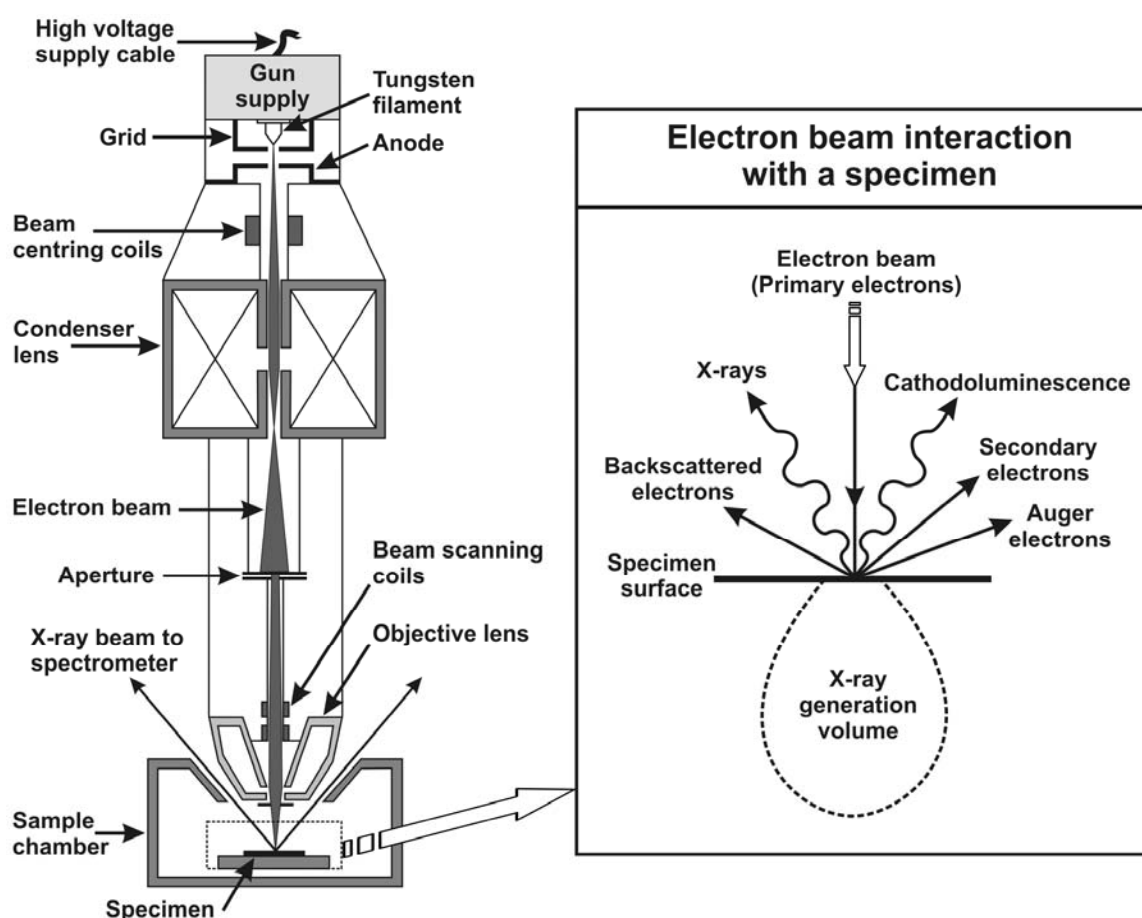


Figure 4-6. Schematic cross-section of an electron column (modified from Potts, 1987) with representation of the photon and charged particle emission produced by electron beam interaction with a specimen (modified from Watt, 1997).

4.2.4.1. General principle:

An electron beam, with typically kinetic energy in the range of 15-30 keV, is emitted from an electron gun (usually made of tungsten). The beam current, emerging from the anode, is focused by condenser lenses and then passes through pairs of scanning coils (Figure 4-6). After that, the primary electron beam passes through the objective lens, which

controls the focus of the beam, and finally interacts with the specimen. The interaction volume, pear shaped or hemispherical and representing only a few cubic micrometers, depends mainly of the kinetic energy of the electron beam, the atomic number, and the density of the sample. The electrons interact with the specimen by elastic and inelastic scattering; a fraction of the incident electrons are absorbed whereas others are scattered. Back-scattered electrons, secondary electrons, Auger electrons, X-rays, cathodoluminescence, and other radiations are produced (Figure 4-6).

Secondary electrons (i.e., low energy electrons, < 50 eV) are ejected in an ionized state from atoms of a thin surface layer and provide information on the surface of the sample. These electrons are used to produce the so-called SE images; images with detailed information on the topography of the sample. The images, previously captured by photography from a high resolution cathode ray tube, are now digitally captured and displayed on a computer monitor.

Back-scattered electrons are produced by elastic interaction of the primary electron beam with the sample. The number of back-scattered electrons increases with the mean atomic number (Z) of the sample, and consequently, BSE images provide compositional information (i.e., distribution of different elements in the sample). On the images, bright areas correspond to regions where the mean atomic number is high (i.e., many electrons are back-scattered), and dark areas where the mean atomic number is low. However, back-scattering is also influenced by the surface topography of the sample; therefore polished sections are usually preferred.

Characteristic X-rays are also produced (see the X-ray Fluorescence spectrometry section), possessing wavelengths and energies specific to the elements from which they are emitted, and can be used for chemical analysis of the sample. The chemical composition is determined by comparing the intensities of characteristic X-rays from the sample with the intensities from reference standards. Specific X-ray wavelengths are selected and counted by an X-ray analyzer.

4.2.4.2. X-ray spectrometers:

Two types of X-ray analyzers are commonly used, separating the components of the X-ray spectrum, either on the basis of photon energy for the energy dispersive X-ray spectrometer (EDS), or by separating wavelengths for the wavelength dispersive spectrometer (WDS). Both types of spectrometers have benefits and disadvantages, and differences in term of detector efficiency and resolution.

The EDS uses a solid state semi-conductor detector to electronically sorts and measures X-rays with respect to their energies. It is mainly used for qualitative analyses, as it allows recording a full spectrum very quickly. However, EDS is not sensitive enough to reveal X-rays peaks from most minor and trace elements. Energy dispersive element peaks are broader than those obtained with a WDS. The WDS uses Bragg diffraction to sort X-rays by their wavelengths. Only one selected wavelength of the incoming X-rays reaches the detector, allowing better measurement accuracy than using EDS. The minimum detection limit is also lower using WDS than with EDS.

4.2.4.3. SEM investigations:

Polished thin sections were carbon-coated and examined at the Department of Mineralogy, Natural History Museum, Vienna (Austria) on a JEOL JSM 6400 SEM equipped with an energy-dispersive X-ray (ED) analyzer. Sections were examined in SE and BSE modes. Semi-quantitative chemical analyses were done on several polished thin section to determine the composition of the different minerals and the composition of melt particles. Analyses were carried out using a KEVEX SuperDry Si(Li) detector linked to a VANTAGE EDS system. The operating conditions for all investigations were 15 kV accelerating voltage and ~1.2 nA beam current. The diameter of the interaction volume in the sample was of about 2 μm for a beam diameter of about 0.1 μm before interaction with the sample. The analytical results were automatically normalized to 100 wt%. The standardless EDX analyses have a precision of about 3 rel% and accuracies of ≤ 10 rel%. Detection limits are about 0.2 - 0.5 wt% for major elements.

4.2.5. Cathodoluminescence (CL) spectroscopy:

Cathodoluminescence (CL) is mostly used in the geosciences for the identification of growth zonations (e.g., in zircons (Figure 4-7), in quartz, or in carbonate minerals) or to provide information on impurities, defects in crystals, or for trace element content distribution in a crystal. When a sample is bombarded with high-energy electrons, visible light (i.e., photons) is emitted, a phenomenon known as cathodoluminescence (see section about SEM, Figure 4-6). The intensity of CL emissions is function of the density of electron traps in a crystal. Even though the fundamental causes of CL emissions are not totally understood, two kinds of luminescence centers (i.e., electron traps) are recognized: extrinsic and intrinsic luminescence centers. Extrinsic luminescence is caused by impurities or defects (so called activators) that absorb energy and emit optical photons. Activators are ions that substitute for cations in the structure of a mineral (e.g., Mn^{2+} can substitute for Ca^{2+} and Mg^{2+} in carbonate minerals). Intrinsic luminescence is caused by structural imperfections (as poor ordering or shock damage), by nonstoichiometry of a mineral, or by impurities.

Two types of CL analytical systems are commonly used; a CL detector attached to an SEM (or to an electron microprobe or to a transmission electron microscope), or an optical cathodoluminescence microscope. An SEM-CL system was used for the present investigation, a system that consists of a retractable parabolic mirror (collecting the luminescence), a monochromator, and a photomultiplier (PMT) detector (for the measurement of the number of photons) and a monochromator. The signal from the PMT is then amplified and displayed on a monitor. For detailed information on cathodoluminescence spectroscopy, see e.g., Marshall (1988), Pagel et al. (2000), Boggs and Krinsley (2006); these references were used for the preparation of this review.

The polished thin sections were examined with an Oxford Mono-CL system attached to a JEOL JSM 6400 SEM at the Department of Mineralogy, Natural History Museum, Vienna (Austria). The operating conditions for all SEM-CL investigations were

15 kV accelerating voltage, 1.2 nA beam current, and monochromator grating with 1200 lines/mm; CL images were obtained from areas of approximately $450 \times 450 \mu\text{m}$, with scanning times of about 1 min.

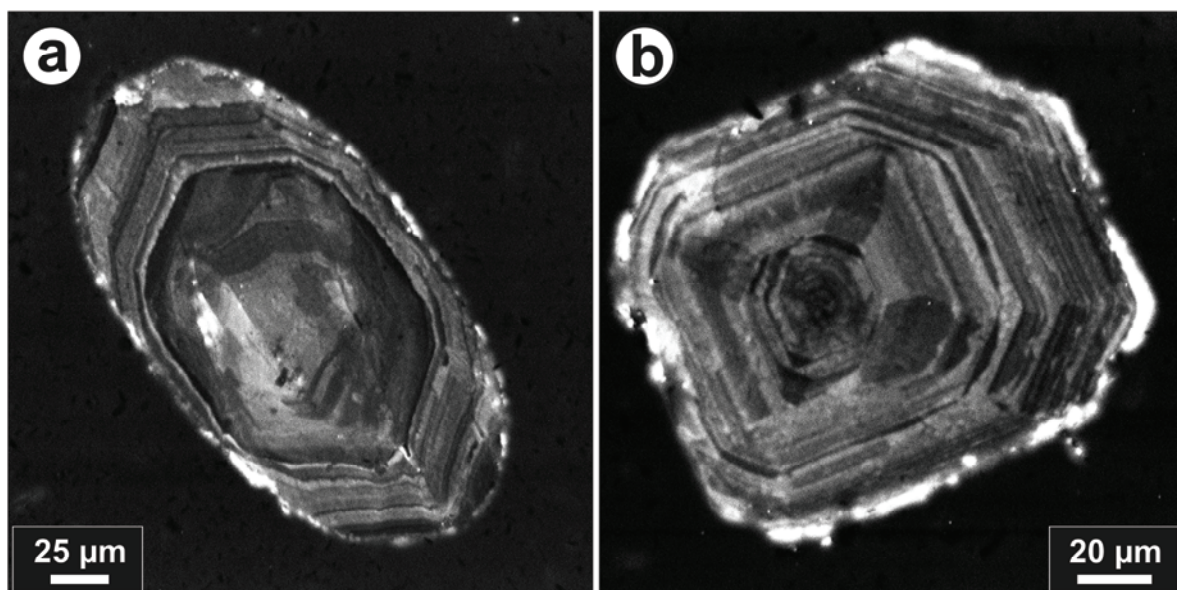


Figure 4-7. Typical cathodoluminescence images of zircons from sample KR8-109 (meta-graywacke from the Bosumtwi crater). Note the overgrowth rims around the inherited magmatic core in (a).

4.2.6. *Transmission Electron Microscopy (TEM):*

Transmission electron microscopy (TEM) investigations require electron-transparent specimens. Formerly, specimens were prepared using argon ion milling, but during the last fifteen years, a new technique is more often used: the focused ion beam (FIB) sample preparation technique. This technique, used for the preparation of some of the present samples, is described in the following section, after a short review on TEM. More information on TEM can be found in, e.g., Williams and Carter (1996), Watt (1997), Fultz and Howe (2002); these references were used for the preparation of the present review.

4.2.6.1 General principle:

A TEM instrument operates on the same principle than a light microscope, but uses electrons, as an SEM, instead of light; electrons are transmitted through the sample. One of the characteristic of the TEM is that using short wavelength (~ 1 nm) a very high magnification image can be obtained; it is possible to image minerals at the atomic scale. The essential components of a standard TEM are shown in a schematic cross-section (Figure 4-8). An electron gun (i.e., heated tungsten filament) emits the electrons that travel through the vacuum in the column of the microscope. The beam of accelerated electrons is then focused using electromagnetic lenses and it interacts with the sample, mostly by diffraction.

The intensity of the diffraction depends on the orientation of the planes of atoms in a crystal, relative to the electron beam. Some electrons are scattered, depending on the angle between the electron beam and the sample. Goniometers stages permit to tilt the sample, and a rotation of 360° around the lens axis is also possible, creating a variety of diffraction conditions. Finally, an electron image is formed, called “high contrast” or “bright field” image, by hitting of the unscattered electrons on a fluorescent screen. Alternatively, the aperture can be moved to allow only diffracted electrons to hit the screen, producing a “dark field” image.

The screen is coated with a phosphor that luminesces green when bombarded by electrons. The image of the structure of the sample is then visible as variations of darkness according to the electron density. This image directly visible on the fluorescent screen can be captured using a camera (film and digital camera were both used for the present study).

Crystallographic information can be also obtained by selected-area electron diffraction. This is possible as the electron beam, after diffraction by the sample, forms a miniature diffraction pattern in the back focal plane of the objective lens. This diffraction pattern can be enlarged and projected on the screen, and an image of this pattern can be recorded. Using the diffraction pattern, lattice spacings can be measured.

In addition, information on the elemental composition of the sample were obtained with the TEM, as both TEM used for our study were equipped with an energy-dispersive X-ray spectrometer (see the SEM section for details on X-ray detector).

Transmission Electron Microscope investigations were performed using a 200 kV PHILIPS CM 20 STEM equipped with a TRACOR Northern energy-dispersive X-ray detector sensitive to elements with atomic numbers >5 at the Museum of Natural History,

Humboldt-University, Berlin (Germany), and using a 200 kV JEOL 200 CX electron microscope at the Laboratoire de Structure et Propriétés de l'Etat Solide, University of Lille, Villeneuve d'Ascq, (France). Conventional bright-field imaging techniques were used to observe and characterize microstructural characteristics of PDFs in quartz, individual ballen quartz and cristobalite, as well as coesite in diaplectic quartz glass.

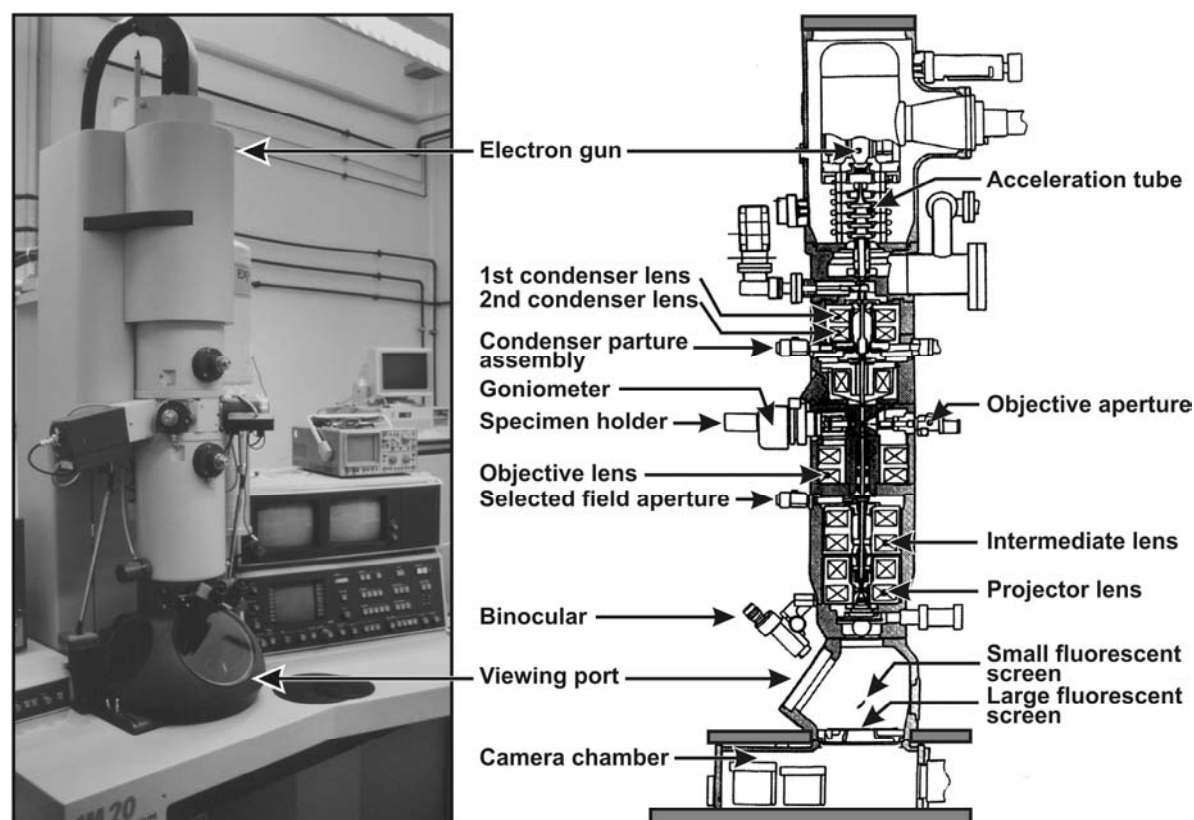


Figure 4-8. Photograph of the PHILIPS CM 20 STEM used in Berlin and cross-section showing the principal components of the TEM instrument (modified from Fultz and Howe, 2002).

4.2.6.2. Sample preparation:

Two different techniques were used for sample preparation for TEM investigations; argon ion milling at the Laboratoire de Structure et Propriétés de l'Etat Solide, University of Lille (Villeneuve d'Ascq, France) and the FIB technique at the GFZ in Potsdam (Germany), using a FEI, FIB200.

For both methods, suitable areas of interest for TEM investigations were selected, using an optical microscope. For the argon ion milling technique, standard thin sections were used; copper grids were glued on selected regions prior to their removal. Then these areas were thinned using ion milling (with Ar⁺ ions) and finally the preparation was deposited on a thin layer of carbon (i.e., specimen support grids). This technique allows the preparation of wedge-shaped samples with non-uniform thickness; in addition, the precise location of interest is not easily sampled.

For the FIB sample preparation, as for the argon ion milling technique, suitable areas for TEM investigations were selected; however, polished thin sections are preferred.

The FIB technique is a site-specific sample preparation technique that can produce TEM foils of 15-20 x 5-15 μm extent and about 100-200 nm thickness. The following description of the method has been summarized from papers by Overwijk et al. (1993), Wirth (2004, 2008), Lee et al. (2007). The FIB machine is somewhat similar to a SEM, as it uses a focused beam of gallium ions (Ga-ions), instead of a focused beam of electrons, to image the sample, which is kept in a vacuum. The Ga-ions, which are bombarded onto the sample, are from a liquid metal source. The milling process is fully automated and only compensation for beam shift or sample drift is necessary during the milling sequence. In that respect, after location of the area where the TEM foil will be cut, two crosses are milled and used as reference points on the sample surface. Then, a 1–2 μm layer of platinum (Pt) is deposited on the surface, in order to protect the area from the ion beam, where the foil will be cut. After that, two large trenches are milled in front and in the back of the Pt strap (Figure 4-9). The progress of the sputtering process is monitored by acquiring secondary electron images.

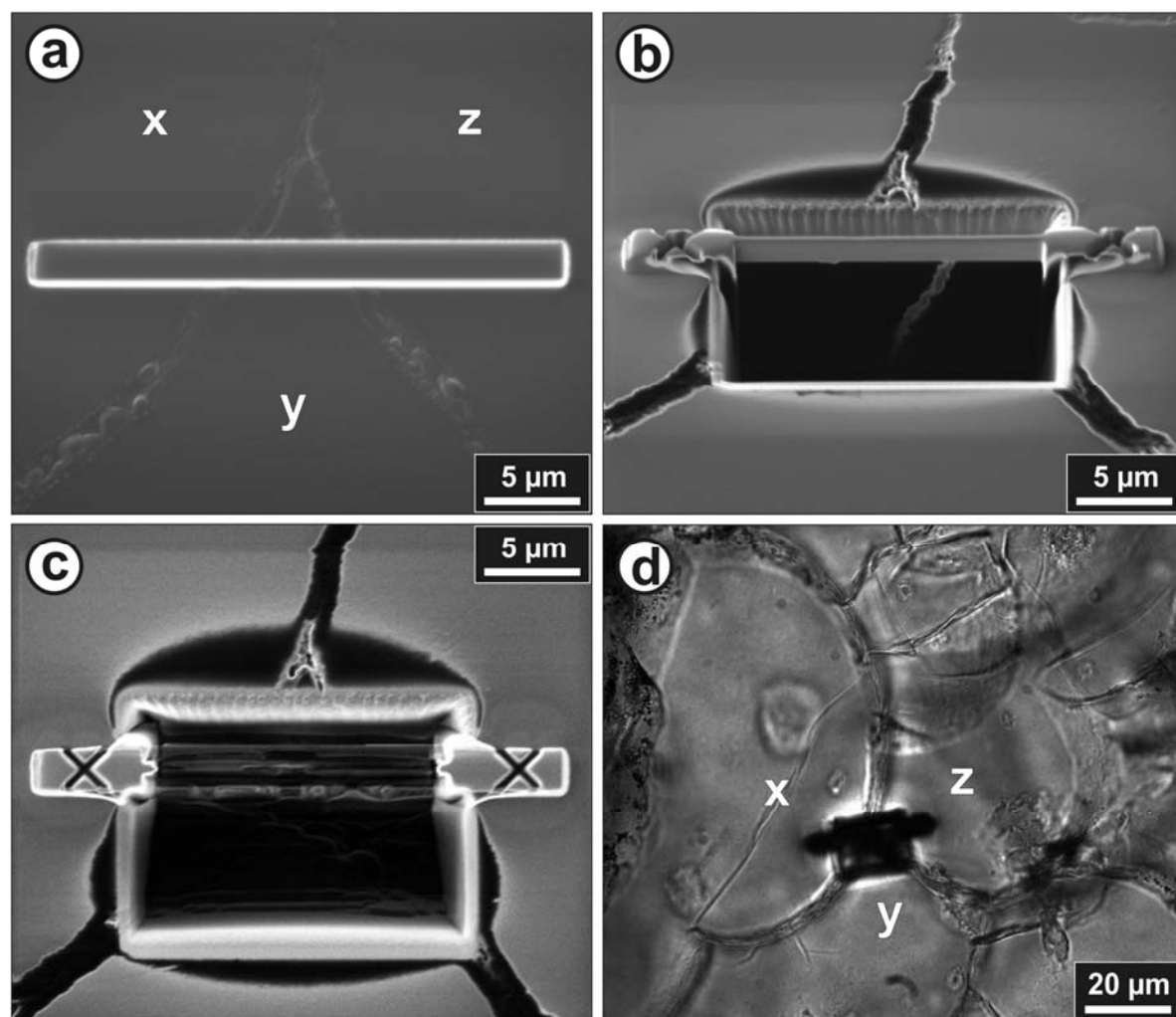


Figure 4-9. Images of FIB based TEM foil preparation. a) SE image of the platinum strap deposited on the sample surface. b) SE image of the FIB milled trenches. c) SE image of the TEM foil cut free. The two reference crosses milled are also visible. d) Microphotograph (in plane-polarized light) showing the area sampled using FIB (sample LB-44B; ballen cristobalite from the Bosumtwi). The three ballen in contact with each other are marked “x”, “y”, and “z” for orientation.

These trenches are stepped, gradually increasing in depth towards the cross-sectional area of interest and the overlying Pt strap. After completion of the large trenches, milling is continued with a reduced beam size and ion current. The slice is gradually thinned down to ~500 nm. The sample is then tilted at about 45° and the foil is cut free on both sides and at its base. Only a thin strap of Pt is preserved at the top of the foil to fix it in its position for final polishing. Milling is achieved with smaller beam and reduced Ga-ion current until the final thickness is attained; then, the foil is cut free (Figure 4-9). Finally, the sample is removed from the FIB device and transferred to an optical microscope for lift-out the foil from its excavation site. This operation is done using a special manipulator and a glass needle. The foil is finally deposited on the carbon membrane of the standard TEM Cu-grid. A standard TEM foil can be milled in a fully automated process in about 4 h.

4.2.7. *Electron Microprobe (EMP):*

Electron microprobe (EMP) is the most widely used technique for non-destructive in-situ X-ray microanalysis investigations. This analytical technique has a high spatial resolution and sensitivity. As for an SEM, the EMP measures the intensity of characteristic X-rays generated by electron bombardment, from which the chemical composition is determined. The principle for EMP analysis is the same as for an SEM (see SEM section for details), however, an EMP have normally three, four, or five WDS, which are situated around the electron column. This configuration allows simultaneous measurement of different elements. The chemical composition of a sample is determined by comparing the intensity of X-rays from reference standards with intensity from the investigated sample. More information on EMP can be found in, e.g., Potts (1987), Potts et al. (1995), Gill (1997), Watt (1997).

Electron microprobe investigations were performed using a JEOL JXA-8500F Electron Probe Microanalyzer (EPMA) equipped with five WDS and one EDS, at the Museum of Natural History, Humboldt-University, Berlin (Germany). The instrument operates at low accelerating voltages (between 1 to 30 kV) over a wide range of probe currents (from 10pA to 500nA). A minimum beam size of about 40 nm is obtained at 10 kV accelerating voltage and 10 nA beam current. Quantitative analysis can be made for elements from Be to U with detection limits depending on the mean atomic number of the sample and on X-ray counting times. Detection limits for the different measured elements are reported together with the results of our investigations in chapter 10. The instrument was used for the study of toasted quartz grains.

4.2.8. MicroRaman spectroscopy:

Raman spectroscopy is a non-destructive method, widely used for the identification of minerals or inclusions in minerals. It is a powerful and extremely fast acquisition method that allows identification of matter and even different polymorphs by vibrational spectra, providing also information on the degree of order of minerals, melts, or glasses. Specimens of very small dimensions can be investigated (less than a few micrometers in size) without any specific sample preparation.

A MicroRaman spectrometer consists of a laser (i.e., light source), an optical microscope (used to illuminate the sample and for the collection of the Raman scattered light), a filter set (holographic notch or edge filters), a monochromator (for the spectral analysis of the light), and a detector (usually a charge-coupled device [CCD]) (see Figure 4-10). More information on Raman spectroscopy can be found in, e.g., McMillan (1989), Laserna (1996), Turell and Corset (1996); these references were used for the preparation of the present review.

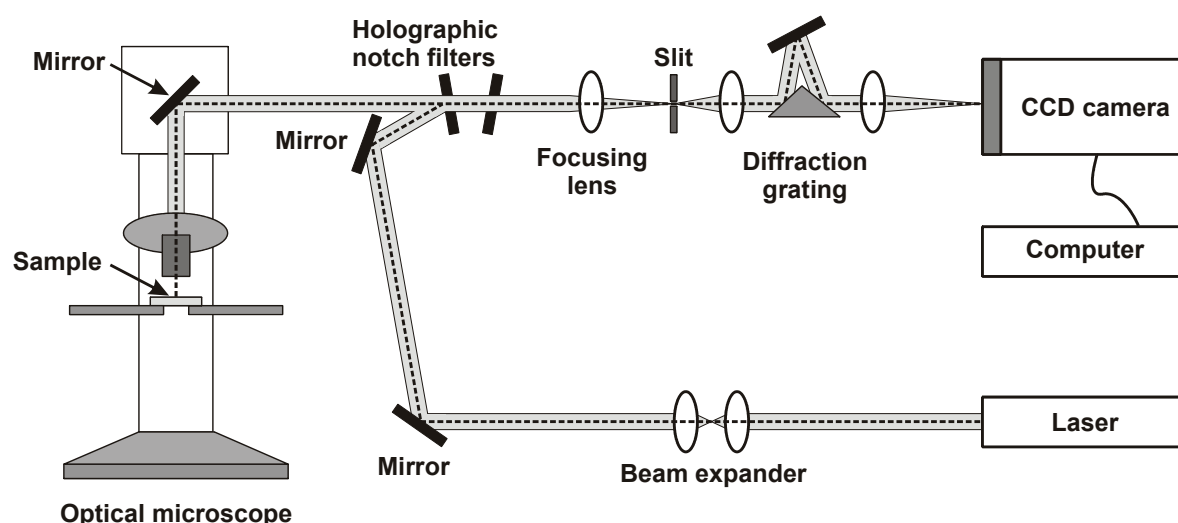


Figure 4-10. Schematic diagram of the Renishaw RM1000 confocal microRaman spectrometer used at the Institute of Mineralogy and Crystallography (University of Vienna).

4.2.8.1. Fundamental on Raman spectroscopy:

When a substance (a solid in the present case) is illuminated by a monochromatic beam of light, about 10^{-3} of the incident intensity is scattered elastically (i.e., Rayleigh scattering) and about 10^{-6} of the incident intensity is scattered inelastically (i.e., Raman scattering). The Raman scattering results from an energy exchange between the incident light and the vibrational levels of the substance illuminated. This exchange or shift in frequency is characteristic of the vibrational species that cause the scattering. Raman data are generally given as wavenumber (cm^{-1}) shifts from the incident light.

4.2.8.2. Instrumentation:

First of all, the laser is reflected by a holographic filter and then, the laser beam is focused on the sample, using a conventional optical microscope. Subsequently, the back-scattered light passes through the microscope objective lens and through the same holographic filter and an additional holographic filter (Figure 4-10). The holographic notch filters are used to block the Rayleigh scattered line. A portion of the incident light is also reflected towards the sample. After that, the Raman scattered light is focused on the entrance slit of the monochromator, where the scattered beam is dispersed as a function of wavelength. This action is performed by an optical diffraction grating. The Raman signal is finally collected by the CCD detector. The use of confocal microscope optics allows to perform spatial- and depth-resolved measurements.

4.2.8.3. Measurement:

Raman spectra were obtained with a Renishaw RM1000 confocal edge filter-based microRaman spectrometer with a 20 mW, 632.8 nm He-Ne-laser excitation system, a grating with 1200 lines/mm, and a thermoelectrically cooled CCD array detector at the Institute of Mineralogy and Crystallography, University of Vienna, Vienna (Austria). Spectra were obtained in the range from 30 to 1000 cm^{-1} , with generally a 300 seconds acquisition time. The spectral resolution of the system (apparatus function) was 3 - 4 cm^{-1} and the wavenumber accuracy was better than $\pm 1 \text{ cm}^{-1}$ (both calibrated with the Rayleigh line and the 520.5 cm^{-1} line of a silicon standard). The Raman spectra were taken in confocal mode from $3 \times 3 \times 3 \text{ }\mu\text{m}$ sample volumes using a Leica DMLM microscope and a Leica 50 \times /0.75 objective. Instrument control and data acquisition were done with the Grams/32 software (Thermo Galactic Corporation). For phase identification, reference spectra from Caltech, California Institute of Technology (USA), were used (http://minerals.gps.caltech.edu/files/raman/Caltech_data/index.htm, accessed 12 October 2007).

4.2.9. Mass spectrometry (MS)

Mass spectrometry (MS) is an analytical method used for the measurement of isotope ratios to very high precision and with very low detection limits. The principle is based on the fact that ionized atoms can be sorted according to their mass-to-charge ratio using a magnetic field. Typically, a mass spectrometer is divided into three parts: a source (or ionization source), a mass analyzer (i.e., a magnet), and an ion collector (see Figure 4-11). As different types of mass spectrometer were used for our investigations, only the general principle is described here; detailed information on the specific mass spectrometers used are reported in the following sub-sections.

First of all, the sample or salt is ionized and the resulting ionized gas is accelerated by a high voltage field. The ions are then deflected according to their mass-to-charge ratio, using a magnetic field, within a mass analyzer. However, it is important to note that isobars (i.e., atoms with the same mass number but with different atomic numbers) cannot be separated by this technique, and for that reason, in some cases, chemical separation of the elements is necessary before starting the measurements. Finally, the ions reach the collector slit which consists of an electron multiplier detector or of Faraday cup(s). The collector records either the charge induced or the current produced by the ions impacting its surface. After amplification, the signal is passed to the computer for isotope ratios calculations. More information on mass spectrometry can be found in, e.g., Potts (1987), Gill (1997), de Groot (2004); these references were used for the elaboration of this review.

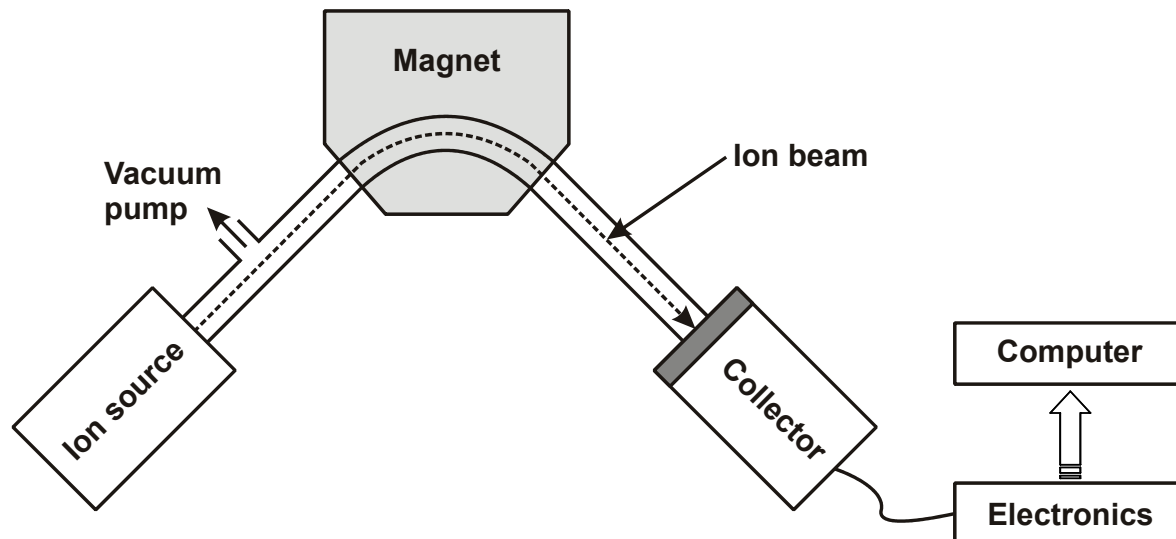


Figure 4-11. Schematic diagram of the main components of a mass spectrometer (after Gill, 1997).

4.2.9.1. Isotope Ratio Mass Spectrometry (IRMS)

The isotope ratio mass spectrometry (IRMS) technique is commonly used for the determination of stable isotope ratios. Carbon isotopic compositions and carbon contents were measured at the Department of Lithospheric Research (University of Vienna), using a Carla Erba NC 2500 elemental analyzer coupled to a Micromass Optima IRMS. For the

present study the continuous flow inlet system was used to couple the elemental analyzer to the mass spectrometer. This system uses a carrier gas (helium) to transport the sample gas into the ion source.

4.2.9.1.1. Instrumentation:

The powder samples, weighed into tin capsules, are placed into the autosampler carousel of the elemental analyzer and are combusted in a flash combustion reaction. The resulting sample gasses are swept in a continuous flow of helium (He) through a reduction reactor, then dehydrated using a chemical trap, and finally chromatographically separated in a chromatographic column. Individual gaseous species are separated as a function of retention time, and the separated CO₂ is introduced in the IRMS.

The Micromass Optima IRMS consists of an ion optics system, an ion source, an ion collector (i.e., Faraday cups), and a sample inlet system. First, the electrons are emitted by thermal extraction from a rhenium wire filament, and then, these electrons either collide with gas molecules and combine to produce charged ions, or for a majority of them, are collected in an electron trap, providing a constant flow of electrons through the source. Finally, after ionization and acceleration, ions are separated according to their mass-to-charge ratio prior to their detection by the ion collector consisting of three Faraday cups. The collected ions are converted to an electric current and after amplification, the signal is sent to the computer. Note that the reference gas used for isotopic calibration was supplied from a CO₂ bottle.

4.2.9.1.2. Measurement:

Carbon isotopic compositions and carbon contents were determined for 14 samples, including shale, slate, phyllite, and a melt particle from drillcore LB-08A (Bosumtwi crater). From each sample, 0.5 to 6.5 mg of powder, mostly from clasts that were drilled out or from whole rock samples, was weighed into tin capsules. Each powder sample was analyzed three times, resulting in precisions of the measurements that ranged from 1.20 to 2.11 ‰. Replicate analyses of graphite (USGS24) and of carbonatite (NBS18) standards were used to determine the accuracy; measured precision of 0.43 ‰ for USGS24 and of 0.46 ‰ for NBS18. Information on samples and results are reported in chapter 10. Sample isotope ratios reported are relative to the Vienna Pee Dee Belemnite (V-PDB) standard, a Cretaceous marine fossil which has an absolute ratio of ¹³C/¹²C of 0.0112371 ± 0.0000090 (Chang and Li, 1990).

4.2.9.2. Isotope Dilution–Thermal Ionization Mass Spectrometer (ID-TIMS):

Whole-rock Rb-Sr and Sm-Nd isotope analyses were performed at the Department of Lithospheric Research (University of Vienna) using an isotope dilution–thermal ionization mass spectrometer (ID-TIMS). Before starting the analyses, a chemical separation of the elements Rb, Sr, Sm, and Nd was done. The sample digestion was performed in tightly closed Savillex® beakers, using a 5:1 mixture of ultrapure HF and

HClO₄, for 3-4 weeks at ~100 °C on a hot plate. Then, after acid evaporation, repeated treatment of the residue using 5.8 N HCl resulted in clear solutions. The Sr and REE fractions were extracted using AG®50W-X8 (200–400 mesh, Bio-Rad) resin and 2.5/4.0 N HCl. Nd was separated from the REE fraction using teflon-coated HdEHP, and 0.18 N, as elution media. Maximum total procedural blanks were <100 pg for Nd, and <1 ng for Sr. After that, Sr and Nd IC samples were loaded on a Re double filament and measured using a ThermoFinnigan Triton instrument.

A ⁸⁷Sr/⁸⁶Sr ratio of 0.710253±0.000006 (n=4) was determined for the NBS987 (Sr) and a ¹⁴³Nd/¹⁴⁴Nd ratio of 0.511844±0.000003 (n=4) was determined for the La Jolla (Nd) international standards during our investigations. Within-run mass fractionation was corrected for ¹⁴⁶Nd/¹⁴⁴Nd=0.7219.

Results are presented in chapter 10 with uncertainties on the Sr and Nd isotope ratios quoted as 2σ_m. Errors on the ¹⁴⁷Sm/¹⁴⁴Nd ratio are given as ±5.0%, representing maximum errors; regression calculation is based on these uncertainties. Age errors are given at the 2σ level. Isotopic ratios are expressed in ε notation where εNd is the measured deviation in parts in 10⁴ of the ¹⁴³Nd/¹⁴⁴Nd ratio from the present-day chondritic uniform reservoir (CHUR) value of 0.512638 (Faure, 1986):

$$\varepsilon^{Nd} = \left[\frac{\left(\frac{^{143}\text{Nd}}{^{144}\text{Nd}} \right)_{\text{sample}}}{0.512638} - 1 \right] \times 10^4$$

ε^{Sr} is the measured deviation in parts in 10⁴ of the ⁸⁷Sr/⁸⁶Sr ratio from the unfractionated mantle reservoir (UR) reference of 0.7045 (Faure, 1986):

$$\varepsilon^{Sr} = \left[\frac{\left(\frac{^{87}\text{Sr}}{^{86}\text{Sr}} \right)_{\text{sample}}}{0.7045} - 1 \right] \times 10^4$$

4.2.9.3. Laser Ablation Inductively Coupled Plasma Spectrometer (LA-ICP-MS):

Zircon U-Pb dating were performed at the State Key Laboratory of Continental Dynamics (Northwest University, China) using a laser ablation inductively coupled plasma spectrometer (LA-ICP-MS). Three samples from the core LB-08A (Bosumtwi crater), a suevite (KR8-004) and two meta-graywacke (KR8-032 and KR8-109), were crushed, then sieved, and finally heavy minerals were concentrated using methylene iodide. Zircons to be dated were hand picked under a binocular, mounted in epoxy, and polished. All mounted grains (about 140 in total) were then documented using cathodoluminescence (at the Department of Mineralogy, Natural History Museum, Vienna), prior to measurements, in respect to identify pristine areas for analysis and to determine if multiple age components (i.e., core and overgrowths) occur (see Figure 4-7). A total of 31 laser spot analyses in 21

zircon grains were performed. The obtained isotope ratios and U-Pb ages are reported in Appendix E.

The spot size and frequency were, 30 μm and 10 Hz, respectively. Each spot analysis consisted of about 30s background acquisition and 40s sample data acquisition. Five to seven sample analyses were followed by measurement of three international standards; Harvard zircon 91500, NIST SRM 610, and Australian Macquarie University zircon GJ1. The isotopic ratios $^{207}\text{Pb}/^{206}\text{Pb}$, $^{206}\text{Pb}/^{238}\text{U}$, and $^{207}\text{Pb}/^{235}\text{U}$ were calculated using GLITTER 4.0 (Macquarie University, Australia) and corrected using Harvard zircon 91500 as external standard. For the evaluation of U-Pb isotopes of Harvard zircon 91500, the Australian Macquarie University zircon GJ1 was used as external standard. Analytical techniques, standards, instrumentation, and data correction are described in detail by Liu et al. (2007). Ages were calculated using Isoplot 3 (Ludwig, 2002).

References

- Boggs S., Jr. and Krinsley D. 2006. *Application of cathodoluminescence imaging to the study of sedimentary rocks*. Cambridge: Cambridge University Press. 165 p.
- Chang T. L. and Li W. 1990. A calibrated measurement of the atomic weight of carbon. *Chinese Science Bulletin* 35:290–296.
- de Groot P. A. 2004. *Handbook of stable isotope analytical techniques*. Amsterdam: Elsevier. 1234 p.
- Ehmann W. D. and Vance D.E. 1991. *Radiochemistry and nuclear methods of analysis*. New York: John Wiley and Sons. 531 p.
- Emmons R. C. 1943. The universal stage (with five axes of rotation). *Geological Society of America Memoir* 8, 205 p.
- Engelhardt W. v. and Bertsch W. 1969. Shock induced planar deformation structures in quartz from the Ries crater, Germany. *Contributions to Mineralogy and Petrology* 20:203–234.
- Faure G. 1986. *Principles of isotope geology*, 2nd ed. New York: John Wiley and Sons. 589 p.
- Firestone R. B. and Shirley V. S. 1996. *Table of Isotopes*, 8th ed. (volume I and II). New York: John Wiley & Sons.
- Fultz B. and Howe J. 2002. *Transmission electron microscopy and diffractometry of material*, 2nd ed. New York: Springer. 748 p.

Gill R. 1997. *Modern analytical geochemistry: an introduction to quantitative chemical analysis techniques for earth, environmental and materials scientists*. Longman: Harlow. 329 p.

Govindaraju K. 1994. 1994 compilation of working values and sample description for 383 geostandards. *Geostandards Newsletter* 18:1–158.

Grieve R. A. F., Langenhorst F., and Stöffler D. 1996. Shock metamorphism of quartz in nature and experiment: II. Significance in geoscience. *Meteoritics and Planetary Science* 31:6–35.

Jarosewich E., Clarke R. S. J., and Barrows J. N. 1987. The Allende meteorite reference sample. *Smithsonian Contributions to Earth Sciences* 27:1–49.

Koeberl C. 1993. Instrumental neutron activation analysis of geochemical and cosmochemical samples: a fast and reliable method for small sample analysis. *Journal of Radioanalytical and Nuclear Chemistry* 168:47–60.

Koeberl C. 1995. Neutron activation analysis. In *Methods and instrumentations: results and recent developments*, Advanced mineralogy, Vol 2, edited by Marfunin A. S. Berlin, Heidelberg, New York: Springer-Verlag. pp. 322–329.

Langenhorst F. 2002. Shock metamorphism of some minerals: Basic introduction and microstructural observations. *Bulletin of the Czech Geological Survey* 77:265–282.

Laserna J. J. 1996. *Modern techniques in Raman spectroscopy*. Chichester: John Wiley & Sons. 427 p.

Lee M. R., Brown D. J., Smith C. L., Hodson M. E., MacKenzie M., and Hellmann R. 2007. Characterization of mineral surfaces using FIB and TEM: a case study of naturally weathered alkali feldspars. *American Mineralogist* 92:1383–1394.

Liu X.-M., Gao S., Diwu C.-R., Yuan H.-L., and Hu Z.-C. 2007. Simultaneous *in-situ* determination of U-Pb age and trace elements in zircon by LA-ICP-MS in 20 µm spot size. *Chinese Science Bulletin* 52:1257-1264.

Ludwig K. 2002. Isoplot/Ex version 2.49. A geochronological toolkit for Microsoft Excel. Berkeley Geochronological Center Special Publication.

Marshall D. J. 1988. *Cathodoluminescence of geological materials*. Boston: Unwin Hyman. 146 p.

McMillan P. F. 1989. Raman spectroscopy in mineralogy and geochemistry. *Annual Review of Earth and Planetary Sciences* 17:255–283.

Overwijk M. H. F., van den Heuvel F. C., and Bulle-Lieuwma C. W. T. 1993. Novel scheme for the preparation of transmission electron microscopy specimens with a focused ion beam. *Journal of Vacuum Science and Technology B* 11:2021–2024.

Pagel M., Barbin V., Blanc P., and Ohnenstetter D. 2000. *Cathodoluminescence in geosciences*. Berlin: Springer Verlag. 514 p.

Potts P. J. 1987. *A handbook of silicate rock analysis*. Glasgow: Blackie. 622 p.

Potts P. J., Bowles J. F. W., Reed S. J. B., and Cave M. R. 1995. *Microprobe techniques in the earth sciences*. London: Chapman & Hall. 419 p.

Reinhard M. 1931. *Universaldrehtischmethoden*. Basel, Switzerland: Birkhäuser. 118 p.

Son T. H. and Koeberl C. 2005. Chemical variation within fragments of Australasian tektites. *Meteoritics and Planetary Sciences* 40:805–815.

Stöffler D. and Langenhorst F. 1994. Shock metamorphism of quartz in nature and experiment: I. Basic observation and theory. *Meteoritics and Planetary Science* 29:155–181.

Turrell G. and Corset J. 1996. *Raman microscopy: developments and applications*. London: Academic Press. 463 p.

Watt I. M. 1997. *The principles and practice of electron microscopy*, 2nd ed. Cambridge: Cambridge University Press. 484 p.

Williams D. B. and Carter C. B. 1996. *Transmission electron microscopy: a textbook for materials science*. New York: Springer. 729 p.

Wirth R. 2004. Focused Ion Beam (FIB): a novel technology for advanced application of micro- and nanoanalysis in geosciences and applied mineralogy. *European Journal of Mineralogy* 16:863–876.

Wirth R. 2008. Focused Ion Beam (FIB) combined with SEM and TEM: advanced analytical tools for studies of chemical composition, microstructure and crystal structure in geomaterials on a nanometre scale. *Chemical Geology* (in press).



Drill core LB-08A, Bosumtwi impact structure, Ghana: Petrographic and shock metamorphic studies of material from the central uplift

Ludovic FERRIÈRE^{1*}, Christian KOEBERL¹, and Wolf Uwe REIMOLD²

¹Department of Geological Sciences, University of Vienna, Althanstrasse 14, A-1090 Vienna, Austria

²Mineralogy, Museum of Natural History, Humboldt University, Invalidenstrasse 43, D-10115 Berlin, Germany

*Corresponding author. E-mail: ludovic.ferriere@univie.ac.at

(Received 28 August 2006; revision accepted 29 December 2006)

Abstract—During a recent drilling project sponsored by the International Continental Scientific Drilling Program (ICDP), two boreholes (LB-07A and LB-08A) were drilled into the crater fill of the Bosumtwi impact structure and the underlying basement, into the deep crater moat and the outer flank of the central uplift, respectively. The Bosumtwi impact structure in Ghana (West Africa), which is 10.5 km in diameter and 1.07 Myr old, is largely filled by Lake Bosumtwi.

Here we present the lithostratigraphy of drill core LB-08A (recovered between 235.6 and 451.33 m depth below lake level) as well as the first mineralogical and petrographic observations of samples from this core. This drill core consists of approximately 25 m of polymict, clast-supported lithic breccia intercalated with suevite, which overlies fractured/brecciated metasediment that displays a large variation in lithology and grain size. The lithologies present in the central uplift are metasediments composed dominantly of fine-grained to gritty meta-graywacke, phyllite, and slate, as well as suevite and polymict lithic impact breccia. The suevites, principally present between 235.6 and 240.5 m and between 257.6 and 262.2 m, display a fine-grained fragmental matrix (about 39 to 45 vol%) and a variety of lithic and mineral clasts that include meta-graywacke, phyllite, slate, quartzite, carbon-rich organic shale, and calcite, as well as melt particles, fractured quartz, unshocked quartz, unshocked feldspar, quartz with planar deformation features (PDFs), diaplectic quartz glass, mica, epidote, sphene, and opaque minerals). The crater-fill suevite contains calcite clasts but no granite clasts, in contrast to suevite from outside the northern crater rim.

The presence of melt particles in suevite samples from the uppermost 25 meters of the core and in suevite dikelets in the basement is an indicator of shock pressures exceeding 45 GPa. Quartz grains present in suevite and polymict lithic impact breccia abundantly display 1 to (rarely) 4 sets of PDFs per grain. The shock pressures recorded by the PDFs in quartz grains in the polymict impact breccia range from 10 to ~30 GPa. We also observed a decrease of the abundance of shocked quartz grains in the brecciated basement with increasing depth. Meta-graywacke samples from the basement are heterogeneously shocked, with shock pressures locally ranging up to 25–30 GPa. Suevites from this borehole show a lower proportion of melt particles and diaplectic quartz glass than suevites from outside the northern crater rim (fallback impact breccia), as well as a lack of ballen quartz, which is present in the external breccias. Similar variations of melt-particle abundance and shock-metamorphic grade between impact-breccia deposits within the crater and fallout impact breccia outside the crater have been observed at the Ries impact structure, Germany.

INTRODUCTION

The 1.07 Myr old Bosumtwi impact structure, centered at 06°30'N, 01°25'W, is located in Ghana, West Africa (Fig. 1). It is a well-preserved, complex impact structure 10.5 km in diameter with a pronounced rim and a small central uplift (Scholz et al. 2002; Koeberl and Reimold 2005). The

Bosumtwi impact structure is also associated with the Ivory Coast tektites, on the basis of the geographical location of the tektite strewn field, as well as identical ages and matching chemical and isotopic composition of the tektites and the Bosumtwi crater rocks (Koeberl et al. 1997 and references therein). The crater was excavated in lower greenschist facies metasediments of the 2.1–2.2 Gyr Birimian Supergroup

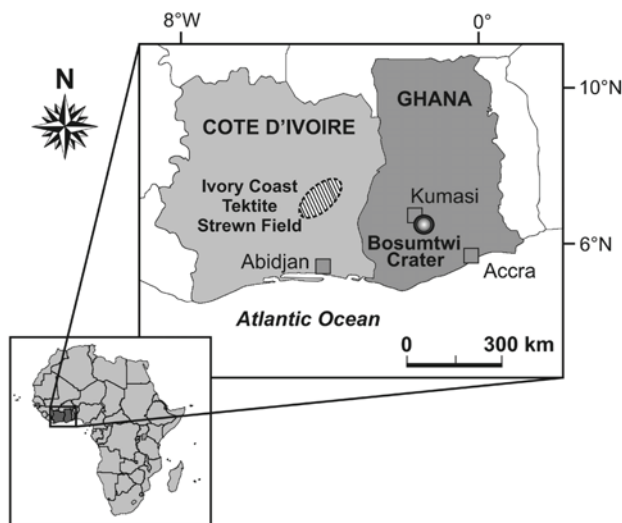


Fig. 1. The geographical location of the Bosumtwi impact crater, Ghana, in relation to the Ivory Coast tektite strewn field (after Koeberl et al. 1998).

(Wright et al. 1985; Leube et al. 1990) and is almost entirely filled by Lake Bosumtwi, which is 8 km in diameter. The lake sediments have accumulated a 1 Myr long paleoclimate record since the impact event. Bosumtwi was recently the subject of an international and multidisciplinary drilling project by the International Continental Scientific Drilling Program (ICDP) (for more information, see below; Koeberl and Reimold 2005; Coney et al. 2006; Ferrière et al. 2006; Koeberl et al. 2006; Koeberl et al. 2007; Coney et al. 2007).

In the present paper, we report on the lithostratigraphy and mineralogy of drill core LB-08A and provide a brief comparison with observations on samples from outside the crater as well as observations at the Ries crater, Germany. Preliminary results were reported in an abstract by Ferrière et al. (2006).

GEOLOGICAL SETTING

First geological investigations around Lake Bosumtwi were made in the 1930s (Junner 1937) and completed later in the 1960s (Woodfield 1966; Moon and Mason 1967; Jones et al. 1981). Recently, additional mapping was carried out to complete and update older observations, which includes descriptions of new outcrops revealed by recent road construction (Koeberl and Reimold 2005). This new geological map also summarizes observations obtained from shallow drilling on and outside of the northern crater rim (Boamah and Koeberl 2003). This work provided a good geological perspective of the crater rim and the region around the crater, but because samples from the crater fill were not accessible due to the lake and lake sediments, that part of the crater remained unknown. The first information on the sublake structure was obtained from aerogeophysical studies

(Pesonen et al. 1998, 2003) and seismic investigations (Scholz et al. 2002); the latter revealed the presence of a small central uplift, which was previously only hypothesized.

The crater was excavated in lower greenschist facies metasediments of the 2.1–2.2 Gyr Birimian Supergroup (Wright et al. 1985; Leube et al. 1990). The rocks from this supergroup were previously separated into Lower and Upper Birimian units, dominated by metasediments and metavolcanics, respectively (Junner 1937), but this subdivision has recently been abandoned (Koeberl and Reimold 2005). These rocks are an assemblage of metasediments that comprises phyllites, meta-tuffs, meta-graywackes, quartzitic meta-graywackes, schists (see Coney et al. 2007), shales, and slates. Birimian metavolcanic rocks occur to the southeast of the crater and Tarkwaian clastic sedimentary rocks (detritus of Birimian rocks) occur to the east and southeast of the crater (Koeberl and Reimold 2005). A variety of intrusive bodies has also been observed around the crater, including Proterozoic granitic intrusions, weathered granitic dikes, other granitoid dikes, and dolerite and amphibolite dikes (e.g., Junner 1937; Woodfield 1966; Moon and Mason 1967; Reimold et al. 1998). Some of these intrusions seem to be correlated with the Pepiakese and Kumasi intrusive bodies (Woodfield 1966; Moon and Mason 1967). Several outcrops of breccia were described from around the crater (e.g., Junner 1937; Woodfield 1966; Moon and Mason 1967), but it is not clear whether or not all these breccias are impact-related (Reimold et al. 1998). On the basis of composition and texture, Boamah and Koeberl (2003) distinguished three types of impact breccia at the Bosumtwi crater: an autochthonous monomict breccia, a probable allochthonous polymict lithic impact breccia, and a suevitic breccia. Monomict breccia occurs along the northern crater rim and consists of angular fragments of different sizes, irregularly distributed and cemented in a matrix of the same materials (Boamah and Koeberl 2003). Previously suevite has been found outside of the northern and southern crater rim (at about 250 m to 2 km from the crater rim crest) (Koeberl and Reimold 2005); this suevite contains abundant impact-melt fragments and a variety of clasts (meta-graywacke, phyllite, shale, granite) up to about 40 cm in size (Boamah and Koeberl 2003, 2006).

THE 2004 ICDP DRILLING PROJECT

The ICDP drilling project had two major scientific goals: to obtain a 1-million-year paleoenvironmental record from post-impact sediments and to acquire hardrock samples from the central uplift and crater moat of the largest young impact structure known on Earth. During this project, sixteen drill cores were obtained at six locations in the lake. Drilling, geophysical studies, and logging were done between June and October 2004 (see Koeberl et al. 2007). Fourteen sediment cores were drilled for paleoenvironmental studies and two

impactite cores (LB-07A and LB-08A) were drilled for impact crater investigations. Note that all sample depths used in this paper represent depths below lake level. These two boreholes (LB-07A and LB-08A) were drilled into the crater fill and underlying basement to depths of 545.08 m in the deep crater moat and to 451.33 m depth on the outer flank of the central uplift, respectively. Their locations, 6°30'50"N, 1°24'55"E for LB-07A and 6°30'33"N, 1°24'45"E for LB-08A, are situated on lines of seismic surveys that were made during the preparation phase of the drilling project (Karp et al. 2002; Scholz et al. 2002).

In this study we focus on core LB-08A, which was recovered at a depth between 235.6 and 451.33 m and represents 215.7 m of core with a diameter of 6 cm. The core sections are stored at the ICDP headquarters (GeoForschungsZentrum [GFZ] in Potsdam, Germany) in 73 boxes. Depending on the rock types and alteration level of the rocks, core recovery ranged from 40 to 115%, with an average of 93%. Cores were scanned and documented in December 2004 and January 2005 at the GFZ. Core images, scanning data, and detailed core descriptions are available online at <http://bosumtwi.icdp-online.org>.

SAMPLES AND EXPERIMENTAL METHODS

One hundred and twenty one samples were taken from core LB-08A, covering depths from 235.77 m (KR8-001) to 451.23 m (KR8-125) (see Appendix 1 for depths of all the samples). Samples were selected to encompass the complete variety of different lithologies present. The petrographic characteristics of the samples, including shock metamorphic effects, were studied by optical and electron microscopy. For this purpose, 174 unoriented thin sections (representing 53 impact breccia and 121 metasediment samples) were prepared from the 121 samples and investigated by optical microscopy. In addition, 12 polished thin sections were prepared for electron microscopy. Electron microscopy, including mineral analysis by energy-dispersive spectrometry (EDX), was done with a JEOL JSM 6400 instrument at the Naturhistorisches Museum, Vienna, Austria, at 15 kV acceleration voltage and with a beam current of about 2 nA. The EDX analyses have a precision of about 3 rel% and a detection limit of about 0.1 wt% for major elements. In addition, electron microprobe analyses were obtained at the Commissariat à l'Énergie Atomique (CEA), Gif-sur-Yvette, France, using a JEOL JSM 840 scanning electron microscope (SEM) associated with an energy-dispersive spectrometer (EDS). Chemical analyses were done at 15 kV acceleration voltage with 1 nA sample current and a beam diameter of 1 µm. Multi-element spectra obtained from the SEM/EDS-ACC system were compared to a series of pure reference spectra, and X-ray absorption and fluorescence effects were corrected using the ZAF program supplied by Princeton Gamma Tech (PGT). The precision is about 5 rel% and the detection limit is 0.1 wt%.

For each sample, lithology, minerals present, and shock effects in these minerals were assessed qualitatively. In addition, modal analyses of 9 suevite thin sections (from samples between 235.77 and 260.49 m) were made by point-counting. The petrographic "point-counting" method used in this study is not the one traditionally used (e.g., Chayes 1949), but an alternative method based on estimation of the true values of areal fractions. This new method was employed because of the counting error due to the large particle size (lithic and mineral clasts). In this method, the area of the whole thin section was subdivided into adjacent cells of 2.4 × 1.5 mm (equivalent to a rectangle in the field of view of the microscope at a magnification of 50×). Each one of those "cells" was further subdivided into three smaller rectangles of identical size (1.5 × 0.8 mm, i.e., an area of 1.2 mm²). The type of clast/aggregate(s) in each of these rectangles was determined and their number was counted. Only clasts and aggregates with long dimensions ≥0.8 mm were counted as such, and anything smaller than this limit was considered to be "matrix." This method is intermediate between the traditional petrographic modal analysis (e.g., Chayes 1949) and digital image analysis of thin section microphotographs. The reason for choosing this technique was the large size of the clasts in the suevites; thus it is only applicable to rocks with populations of large clasts. Between 566 and 676 areas of 1.2 mm² were counted per thin section.

Measurements of the crystallographic orientations of planar deformation features (PDFs) in quartz grains (e.g., Stöffler and Langenhorst 1994; Grieve et al. 1996) with a four-axis universal stage (U-stage; cf. Reinhard 1931; Emmons 1943) were made in individual quartz grains of 10 thin sections. The optic axis and the pole to a PDF plane were determined, and PDFs were indexed in a stereonet with the c-axis in the center (Engelhardt and Bertsch 1969; Stöffler and Langenhorst 1994; Langenhorst 2002). The PDF poles were indexed with Miller indices (hkil) for quartz using the technique described in Stöffler and Langenhorst (1994). Five Raman spectra were determined in two samples with a Renishaw Invia Raman spectrometer at the Laboratoire de Géologie (ENS-Paris, France) to confirm the occurrence of carbon and the carbon organization-state in a specific clast population present in suevite samples. An excitation wavelength of 514 nm was used on a 20 mW Ar laser. The laser beam was focused by a microscope equipped with a LEICA 50× magnification objective, leading to a spot diameter of 1 micrometer. Acquisition time was 10 s for all measurements.

RESULTS

Core LB-08A—Introduction and Terminology

Based on our macroscopic and microscopic observations (Appendix 1), we constructed a detailed lithostratigraphic column of drill core LB-08A (Fig. 2). This drill core displays

a variety of lithologies: polymict breccia, monomict lithic breccia, slate, phyllite, and meta-graywacke. It can also be divided into two main parts: the uppermost 25 meters that are composed of polymict lithic impact breccia (clast-supported) intercalated with suevite, and the other part of the core (between 262 to 451 m), which is dominated by fractured/brecciated metasediment, locally intersected by monomict lithic breccia and suevite dikelets (Fig. 2). Metasediment displays a large variation in lithology (slate, phyllite, and meta-graywacke) and grain size (from fine-grained to gritty meta-graywacke). In order of abundance, the LB-08A drill core intersected about 65% meta-graywacke, 21% slate and phyllite, 13.5% polymict breccia, and 0.5% monomict lithic breccia (estimations based on our macroscopic core descriptions).

Our classification of the various rock types follows definitions by Stöffler and Grieve (1994) for impact breccia, and Jackson (1997) and Brodie et al. (2004) for metasediments. Suevite is defined as a “polymict impact breccia with clastic matrix containing lithic and mineral clasts in various stages of shock metamorphism including cogenetic impact melt particles which are in a glassy or crystallized state” (Stöffler and Grieve 1994). Polymict lithic impact breccia contains shocked and unshocked clasts from more than one precursor lithology in a clastic matrix, but lacks cogenetic melt particles. Monomict lithic impact breccia is defined as a “cataclasite produced by impact and generally displaying weak or no shock metamorphism; occurs in the (par)autochthonous basement of an impact crater or as clasts (up to the size of blocks and megablocks) within allochthonous impact breccias” (Stöffler and Grieve 1994). Schist is “the systematic root term covering all rocks with a well-developed schistosity including slates and phyllites” (Brodie et al. 2004). Slate is “a compact, fine-grained metamorphic rock that possesses slaty cleavage and hence can be split into slabs and thin plates. Most slate was formed from shale” (Jackson 1997). Phyllite is “a metamorphosed rock, intermediate in grade between slate and mica schist. Minute crystals of graphite, sericite, chlorite impart a silky sheen to the surface of cleavage (or schistosity). Phyllites commonly exhibit corrugated cleavage surfaces” (Jackson 1997). Graywacke is “a dark gray firmly indurated coarse-grained sandstone that consists of poorly sorted angular to subangular grains of quartz and feldspar, with a variety of dark rock and mineral fragments embedded in a compact clayey matrix and containing an abundance of very fine-grained illite, sericite, and chloritic minerals” (Jackson 1997). In this paper, we use the term “meta-graywacke,” because all graywacke is metamorphosed.

Detailed Lithostratigraphy of Core LB-08A

Polymict Lithic Impact Breccia

Polymict lithic impact breccia intercalated with suevite (Fig. 3a) is present between 235.6 to 262 m. The polymict

lithic impact breccia is clast-supported and consists of angular to subrounded rock fragments of a variety of sizes (from <1 to >6 cm, the diameter of the core). These fragments represent three different lithologies, in order of decreasing abundance: meta-graywacke, phyllite, and slate. Thin section observations (see Appendix 1 for detailed descriptions of all samples) confirm the presence of these fragment types, but also the occurrence of quartzitic fragments (up to 6 vol% in KR8-008; depth = 244.45 m). The matrix is fine-grained and grayish in color, consisting of small lithic fragments and metasedimentary minerals, as well as secondary minerals such as phyllosilicates. The abundance of matrix varies from less than 1 vol% (e.g., in KR8-009; depth = 244.87 m) to 5 vol% (e.g., in KR8-015 and KR8-017; depth = 250.74 m and 251.74 m, respectively), and up to 48 vol% (in KR8-008; depth = 244.45 m). Polymict lithic breccia samples are altered (e.g., KR8-009; depth = 244.87 m); most of the biotite (present principally in meta-graywacke clasts) is altered to chlorite and some feldspar to sericite (with presence of cloudiness). This alteration is variable in the samples (from 50 to 80 vol% of feldspar altered to sericite) and no trend of increasing or decreasing alteration degree with depth was observed. The alteration is localized preferentially along fractures. Aggregates of very fine-grained calcite, veinlets, and veins are frequently observed in polymict lithic impact breccia (e.g., KR8-022; depth = 256.81 m), and also some cracks/fractures are filled with iron oxides, pyrite, and rutile (e.g., KR8-024; depth = 259.14 m). Calcite veinlets, as well as fractures filled with iron oxides, are irregularly distributed through the polymict lithic impact breccia and represent less than 5 vol% of the core.

Suevite

General Aspects: The polymict lithic impact breccia between 235.6 to 262 m is intercalated with suevite. Suevite is not easily distinguished from polymict lithic breccia at the macroscopic scale (Figs. 3b and 3c) due to the low abundance of melt particles and their small size. On a macroscopic scale in hand specimen, the melt particle abundance in the suevite appears to be <1 vol%, but microscopic studies of thin sections yields higher values of up to about 15 vol%. Suevite samples have a grayish, fine-grained fragmental matrix and consist of rock and mineral clasts and of secondary minerals like smectite, chlorite, and calcite, in the form of very fine-grained aggregates or micro-veinlets. Matrix accounts for 39 to 45 vol% of the total suevite (Fig. 4; Table 1). A variety of lithic and mineral clasts, with sizes up to 5 cm, is present: meta-graywacke, phyllite, slate, quartzite, carbon-rich organic shale, and calcite. Furthermore, there are melt particles, fractured quartz, unshocked quartz, unshocked feldspar, quartz with PDFs, diaplectic quartz glass, micas, epidote, sphene, and opaque minerals. For more details about the clast distribution in the top 25 meters of the core, see Fig. 4 and Table 1.

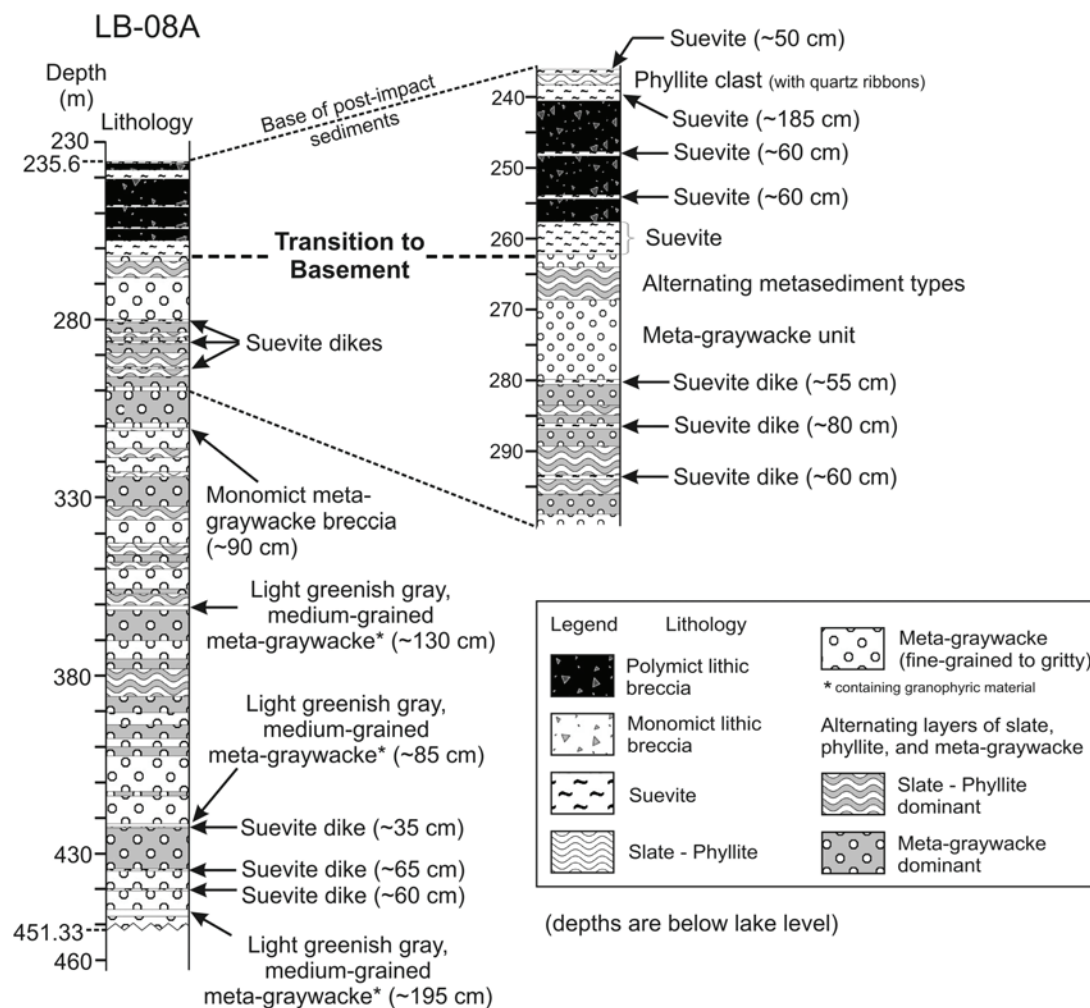


Fig. 2. A detailed lithostratigraphic column of drill core LB-08A. The uppermost 25 m are composed of clast-supported polymict lithic impact breccia intercalated with suevite (interpreted as fallback breccia). The lower part of the core is composed of an alternating sequence of metasediment with (in order of decreasing abundance) meta-graywacke (dominant), phyllite, and slate; locally monomict lithic breccia; light greenish gray, medium-grained meta-graywacke (with granophyric material); and suevite dikelets in the metasediment. Metasediment displays a large variation in lithology and grain size. This second part of the core, between 262 to 451 m, represents the basement that has been shocked and fractured during the impact crater formation. The transition to basement is at a depth of about 262 m below lake level.

Lithic Clasts, Melt Particles, and Diaplectic Quartz Glass:

Meta-graywacke clasts display a variety of grain sizes (from fine- to medium-grained, and rarely to gritty) and also a variety of textures that include meta-graywacke with strong mylonitic fabric, sheared meta-graywacke, and undeformed meta-graywacke. The abundance of the meta-graywacke clasts in the suevite ranges from ~17.5 vol% to more than 42 vol% of the total suevite in samples between 235.77 to 260.49 m depth (Fig. 4; Table 1). Meta-graywacke clasts are more altered in the uppermost 5 meters.

Point-counting confirms that lithic clasts in suevite are dominated by meta-graywacke and that the clasts are seemingly irregularly distributed throughout the suevite section. Phyllite and slate clasts are more or less abundant (from ~5 to 30 vol%), and the phyllite clasts frequently display crenulation.

Carbon-rich shale clasts (Fig. 5) are only present in the uppermost few meters of the core (in samples KR8-001, KR8-003, KR8-004, KR8-005, and KR8-012), with a slightly decreasing abundance with increasing depth (from 7 to 2 vol%) (Fig. 4; Table 1). The presence of carbon in the clast population termed “carbon-rich shale clast” was confirmed by Raman spectra obtained for four carbon-rich shale clasts in two samples (KR8-003 and KR8-005; depths = 238.90 and 240.04 m, respectively). The Raman spectra display a typical carbon signature with one intrinsic band (G-band, 1582 cm^{-1}) originating from the lattice vibration of graphite, in addition to a defect-induced band (D-band, 1355 cm^{-1}) (Fig. 5). The intensity ratios between these two bands (used to evaluate the structural ordering of carbonaceous matter) (see Wopenka and Pasteris [1993] for more information) indicate that the carbon is not well organized.

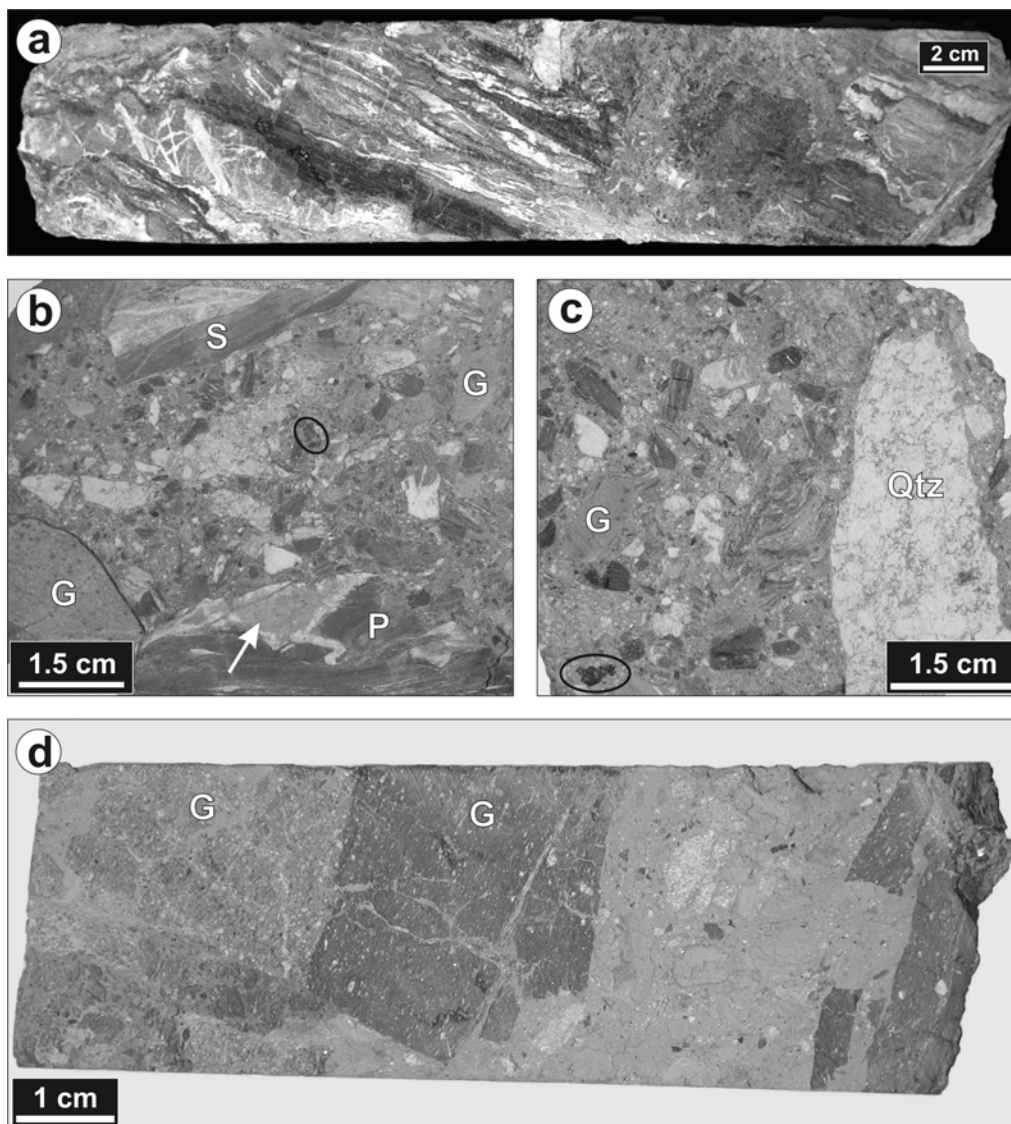


Fig. 3. Macrophotos. a) Polymict lithic impact breccia. Sample KR8-011; depth = 247.46 m. b) Suevite with variety of lithic clasts: meta-graywacke (G), phyllite (P), and slate (S), glass (arrow), melt particles (see ellipse), carbon-rich organic shale, quartzite, and calcite. Sample KR8-001; depth = 235.77 m. c) Suevite (similar to [b]), but with a prominent quartzite (Qtz) clast and a distinct melt particle (see ellipse). Sample KR8-003; depth = 238.90 m. d) Strongly altered suevite with prominent meta-graywacke clasts (fine- to medium-grained) and secondary phyllosilicates. Sample KR8-043; depth = 296.94 m.

Quartz, feldspar, and calcite fragments (mainly with angular shape) are also present in the suevite, with average abundances of 2 vol%, 1 vol%, and <1 vol%, respectively (Fig. 4; Table 2). Feldspar grains frequently display polysynthetic twinning displaced along microfaults that could be tectonic or impact derived. Several calcite grains display anomalously dense cleavage and some planar fractures (Fig. 11a), up to four different directions per calcite grain. These planar fractures in calcite are not yet understood, but could represent impact-induced deformation.

Melt particles, which are usually not observed in hand specimen, are rare in the suevite samples (Fig. 3), comprising ~6 vol% on average in suevite from 235.77 to 260.49 m, with

maximum abundances of 10–15 vol% observed in samples KR8-004, KR8-005, and KR8-026 (Fig. 4; Table 1). Mostly devitrified melt particles, in which the original glass is rarely preserved, occur at various stages of alteration, from partially to completely transformed to secondary phyllosilicates (Figs. 6a and 7). Melt particles are subangular, or subrounded to irregular, in shape, and most have sizes between 100 μm and 0.5 cm; the largest melt particle observed is ~1 cm, in sample KR8-004; depth = 239.65 m. Some lithic quartz clasts are common within melt particles (Figs. 6a and 7). These quartz fragments, most of them shocked, display planar fractures (PFs) and PDFs with altered, originally likely amorphous material (Fig. 7).

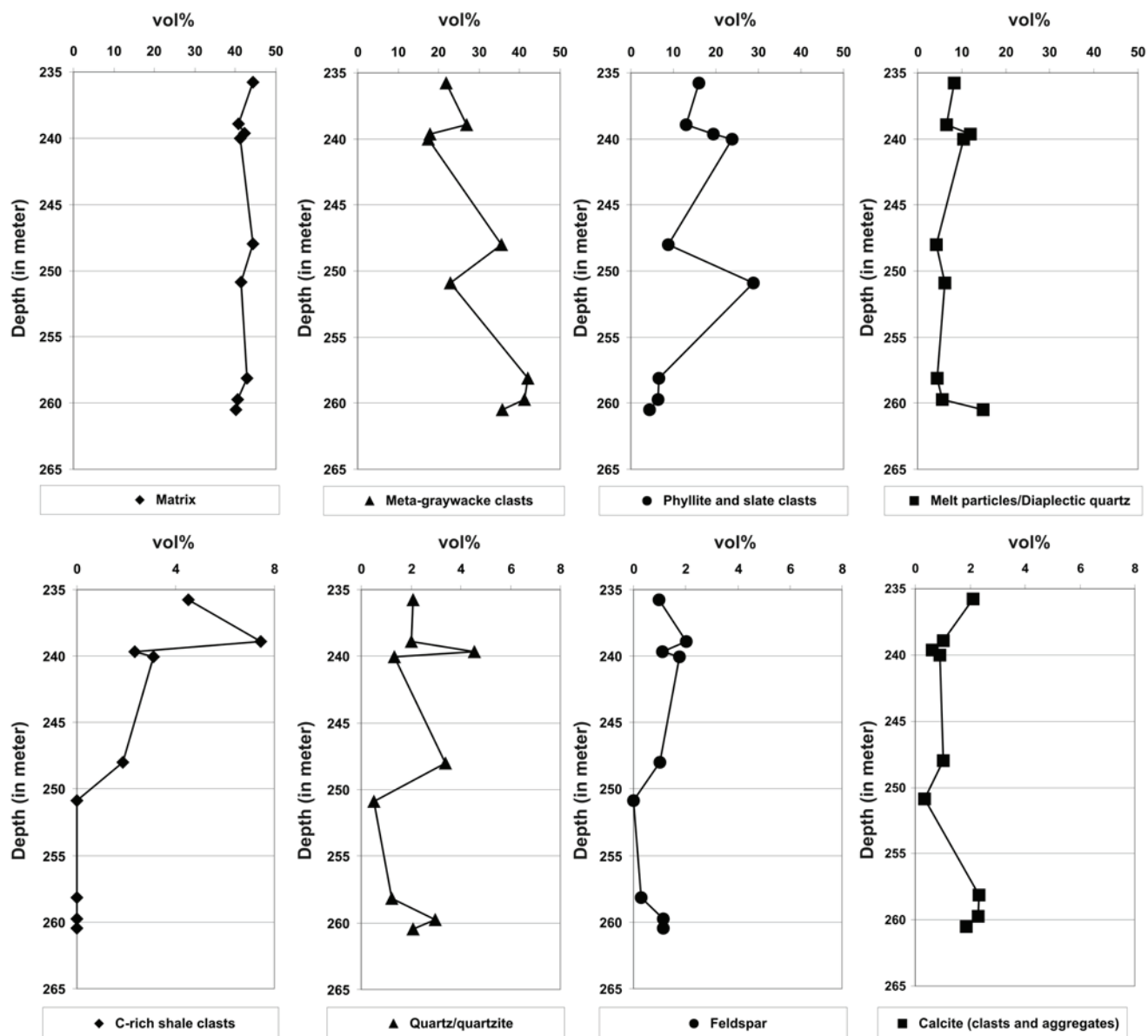


Fig. 4. Modal compositions (vol%) of nine suevite samples from core LB-08A between 235.77 and 260.49 m (between 566 and 676 areas of 1.2 mm² were counted per thin section).

Diaplectic quartz glass (Fig. 8) has only been observed in the uppermost 5 m of suevite (in KR8-001 and KR8-005; depths = 235.77 and 240.04 m, respectively). Two diaplectic quartz glass fragments present in KR8-001 (2 and 8 mm in size, respectively) contain altered silicate and residual quartz grains that display PFs where the originally amorphous material is altered only in part.

Shock Petrographic Study: Shock-metamorphic effects in rocks are the main characteristics by which an impact origin is assigned to a circular geological structure (e.g., Stöffler and Langenhorst 1994; Huffman and Reimold 1996; French 1998; Montanari and Koeberl 2000). In the case of Bosumtwi, the

first evidence for an impact origin came from findings of NiFe-rich spherules (e.g., El Goresy et al. 1968) and of the high-pressure quartz polymorph coesite (Littler et al. 1961). Later, PDFs in quartz and feldspar were found in suevite outside of the northern crater rim (e.g., Koeberl et al. 1998; Boamah and Koeberl 2003; Koeberl and Reimold 2005).

A variety of shock-petrographic effects has been observed in suevite samples from core LB-08A, including melt particles, diaplectic quartz glass, and PDFs in quartz grains.

Quartz grains with PFs and PDFs (commonly 1, 2, or 3 sets; rarely 4 sets) are present in suevite. Some of these quartz grains have a grayish brown appearance in plane-polarized light (Figs. 9a and 9b), with patches containing micrometer-

Table 1. Modal compositions (vol%) of nine suevite samples from core LB-08A between 235.77 and 260.49 m (counting of 566 to 676 areas of 1.2 mm² per thin section). Only clasts/aggregates with long dimensions ≥ 0.8 mm were counted. Any clast/aggregate or crystal smaller than this size limit was counted as matrix.

Sample	KR8-01	KR8-03	KR8-04	KR8-05	KR8-12	KR8-16	KR8-23	KR8-25	KR8-26
Depth (m)	235.77	238.90	239.65	240.04	248.00	250.89	258.14	259.74	260.49
Matrix	44.3	40.8	42.2	41.3	44.4	41.4	42.8	40.5	40.0
Meta-graywacke clasts	21.8	26.9	17.9	17.5	35.5	22.8	42.0	41.2	35.7
Phyllite and slate clasts	16.0	13.1	19.3	23.8	8.8	28.9	6.6	6.4	4.4
Melt particles and diaplectic quartz	8.2	6.6	11.9	10.4	4.2	6.1	4.5	5.6	14.8
C-rich shale clasts	4.5	7.5	2.4	3.1	1.9	0	0	0	0
Quartz/quartzite	2.1	2.0	4.6	1.3	3.4	0.5	1.2	3.0	2.1
Feldspar	1.0	2.0	1.1	1.8	1.0	0	0.3	1.2	1.2
Calcite (clasts and aggregates)	2.1	1.0	0.6	0.9	1.0	0.3	2.3	2.3	1.9

size fluid inclusions; this has been described as a “toasted appearance” (Short and Gold 1996; Whitehead et al. 2002). Other quartz grains display PDFs decorated with numerous small fluid inclusions (Fig. 9). Traditionally, decorated PDFs are considered secondary features, formed by annealing and aqueous alteration of non-decorated amorphous PDFs (Grieve et al. 1996; Leroux 2005). The crystallographic orientations of 151 sets of PDFs in 82 quartz grains (methods in, e.g., Stöffler and Langenhorst 1994; Grieve et al. 1996) were analyzed on 5 thin sections of suevite (KR8-001, KR8-003, KR8-004, KR8-005, and KR8-006; depth = 235.77, 238.90, 239.65, 240.04, and 240.36 m, respectively; Table 2a). The frequency of indexed PDFs versus angle between c-axis and PDFs, with only indexed planes (Grieve et al. 1996), is shown in Fig. 10a. Between 60 to 68 rel% of all the poles to the PDF planes measured are oriented about 23° to the c-axis, corresponding to the $\omega\{10\bar{1}3\}$ orientation that is diagnostic of shock metamorphism (e.g., Stöffler and Langenhorst 1994; Grieve et al. 1996). Planes parallel to the $\{2241\}$, $\{11\bar{2}2\}$, $\{10\bar{1}1\}$, $\{10\bar{1}2\}$, and $\{11\bar{2}1\}$ orientations are also present (between 2 and 8 rel%) and only about 10 rel% of the measured sets could not be indexed. Only a very small component (<2 rel%) of basal PDFs was found. More detail on the shock effects in quartz, as determined by transmission electron microscopy (TEM) analysis, will be presented elsewhere. No PDFs were observed in feldspar grains.

Basement Rocks

General Aspects: Most of the core recovered from 262 to 451.33 m consists of an alternating sequence of metasediments, in order of decreasing abundance: meta-graywacke (dominant), phyllite, and slate. Suevite dikelets (3 dikelets between 279.5 and 298 m and 3 other dikelets between 418 and 440 m; up to 80 cm thick), monomict meta-graywacke breccia (between 310 and 311 m), and a distinct light greenish gray, medium-grained meta-graywacke (containing granophyric material) are also present in the basement (Fig. 2). Basement rocks display a high number of

fractures that are irregularly distributed throughout the basement rocks. Quartz veinlets and veins (from the millimeter-scale to 25 cm thickness; KR8-111, depth = 432.03 m) are also present and irregularly distributed in the lower part of the core. Locally meta-graywacke is completely brecciated (e.g., presence of monomict meta-graywacke breccia, between 310 and 311 m), and in other parts, meta-graywacke samples display diskings (possibly related to drilling; e.g., in between 269 and 272 m; Deutsch et al. 2007).

Meta-graywacke: Meta-graywacke is light to dark gray in color and occurs with a large variability of grain size, from fine-grained to gritty (Fig. 12; Appendix 1). The term gritty is used for grain sizes larger than 5 mm. This variability of grain size is noted in hand specimen as well as at the thin-section scale (Fig. 13), which makes it difficult to construct a lithostratigraphic column at a reasonable scale. Meta-graywacke samples show undeformed, sheared, brecciated, and mylonitic textures (Appendix 1) and are mainly composed of (in order of decreasing abundance): quartz, feldspar, muscovite, chlorite/biotite, calcite, and accessory minerals (in order of decreasing abundance: epidote, pyrite, sphene, apatite, zircon, rutile, allanite). In most of the samples, biotite is altered to chlorite. Some meta-graywacke samples have significant carbonate content, in the form of numerous aggregates of very fine-grained calcite, veinlets, and veins (e.g., KR8-053 and KR8-122, depths = 316.97 and 446.69 m, respectively) (Appendix 1), with variable amounts in each sample (see variations with depth of CaO abundances measured in bulk samples) (Ferrière et al. 2007). meta-graywacke samples display also a variability of relative abundances of quartz, feldspar, and mica, which is difficult to quantify by optical observations alone, but the variations in the abundances of silica and aluminum measured in bulk samples (see Ferrière et al. 2007) illustrates such compositional variations throughout the core. Quartz grains frequently show microfractures and undulatory extinction. Feldspar grains also display some cracks and are commonly altered to sericite. Most meta-graywacke samples are shocked (PFs and PDFs in quartz grains; see details below).

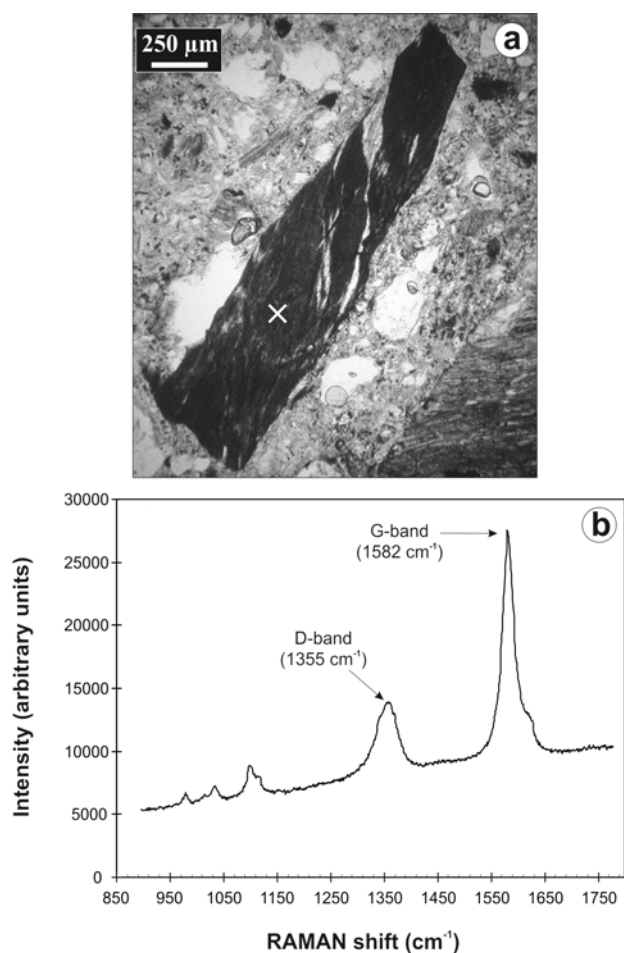


Fig. 5. a) A microphotograph of a carbon-rich shale clast in suevite (white cross indicates the area of the Raman spectroscopic measurement); sample KR8-004, depth = 239.65 m (plane-polarized light). b) A typical Raman spectrum from the carbon-rich shale clast, with one intrinsic band (G-band, 1582 cm^{-1}) originating from lattice vibration of graphite, and an additional defect-induced band (D-band, 1355 cm^{-1}). The intensity ratio between the G-band and the D-band is used to evaluate the structural ordering of carbonaceous matter (see Wopenka and Pasteris [1993] for more information).

Monomict meta-graywacke breccia is present at a depth between 310 and 311 m (Fig. 2) and is composed of meta-graywacke fragments (clast size from 1 to 10 cm) of variable grain size, from fine- to medium-grained. Only one sample from this monomict meta-graywacke breccia (KR8-049; depth = 310.23 m) was studied. It is locally sheared and, in order of decreasing abundance, is composed mainly of quartz, feldspar, muscovite, chlorite, epidote, sphene, and opaque minerals (pyrite and rutile). Aggregates of fine-grained calcite are abundant in the monomict meta-graywacke breccia.

We distinguish three units of a light greenish gray, medium-grained meta-graywacke that occur at 360.15, 421.6, and 445.8 m depth, at thicknesses of approximately 130, 85, and 195 cm, respectively (Fig. 2). These three units are concordant with the metasediment hosts and have been

Table 2a. Abundance of PDF sets in quartz grains from suevite samples (KR8-001, KR8-003, KR8-004, KR8-005, and KR8-006; depths = 235.77, 238.90, 239.65, 240.04, and 240.36 m, respectively).

Sets of planes	No. of grains	Percent (rel%)
1	28	34.2
2	43	52.4
3	7	8.5
4	4	4.9
151	82	100

151 planes were measured from 82 grains; plane /grain ratio (P/G = 1.70).

Table 2b. Abundance of PDF sets in quartz grains from meta-graywacke samples (KR8-029, KR8-030, KR8-031, and KR8-032; depths = 271.43, 272.00, 273.99, and 274.99 m, respectively).

Sets of planes	No. of grains	Percent (rel%)
1	24	40.7
2	29	49.1
3	5	8.5
4	1	1.7
101	59	100

101 planes were measured from 59 grains; plane /grain ratio (P/G = 1.71).

distinguished from the other meta-graywacke units (described before) by the characteristic light greenish gray color, easily discernible in hand specimen, and due to the abundance of chlorite. The first unit (at 360.15 m) is in part “pulverized” and more fractured than the two other units at depths of 421.6 and 445.8 m, which are rather less fractured. Some veinlets of quartz and calcite (up to 1 cm thick) are present with traces of pyrite in their interiors. At the microscopic scale, these light greenish gray, medium-grained meta-graywacke samples (KR8-069, KR8-106, KR8-121, and KR8-122a; depths = 361.18, 421.88, 446.02, and 447.14 m, respectively) exhibit mainly (in order of decreasing abundance) feldspar, chloritoid, quartz, muscovite, sphene, and opaque minerals. Cuneiform intergrowths of quartz and feldspar (granophyric material) have been observed, and calcite in the form of local aggregates and/or pods is present. The four samples have the same mineral composition, but only one sample (KR8-069; depth = 361.18 m) contains quartz grains with PDFs (1 or 2 sets; some with a toasted appearance). This observation of shocked quartz grains was made on one sample (KR8-069) that was taken from the “pulverized” and strongly fractured unit at 361.18 m.

Phyllite and Slate: Phyllite and slate are gray to black in hand specimen, very fine- to fine-grained, well-banded, and folded (Fig. 14). Phyllite and slate are frequently associated and interbedded with fine- to medium-grained meta-graywacke in core (e.g., between 375 and 385 m) and hand specimen (e.g., KR8-109; depth = 425.24 m) (Fig. 12b), but also at the microscopic scale (e.g., KR8-063; depth = 343.57 m). Slate samples are more friable than phyllite samples.

These two lithologies are rare among our samples

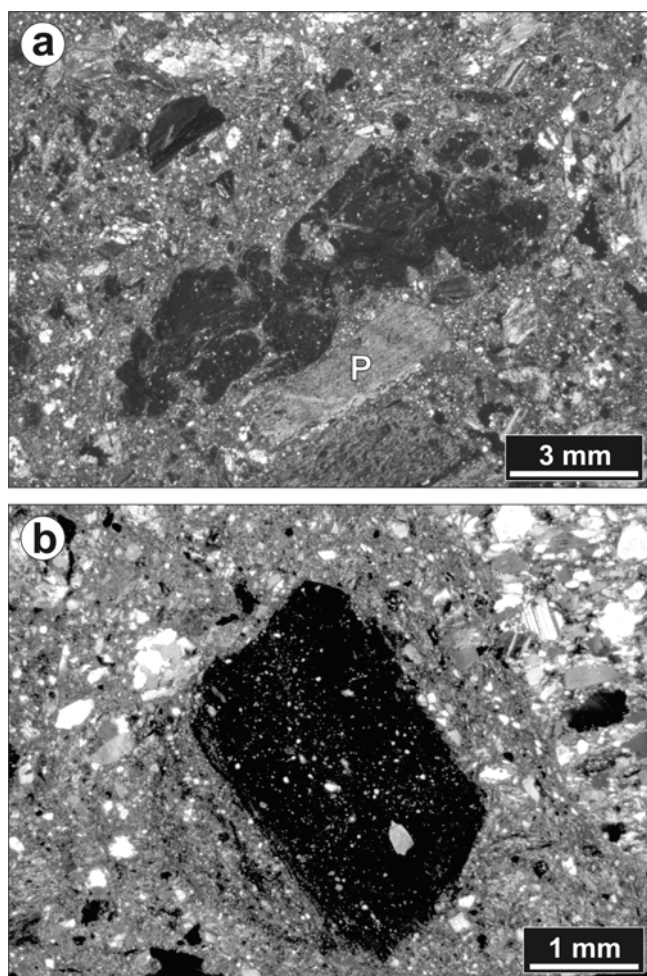


Fig. 6. Microphotographs (cross-polarized light) of melt particles in suevite. a) A mostly devitrified and irregular melt particle close to a phyllite clast (P). Sample KR8-004; depth = 239.65 m. b) A subangular melt particle (dark fragment) with small quartz clasts. Sample KR8-113; depth = 434.59 m.

(KR8-028, KR8-046, and KR8-063; depths = 266.18, 303.25, and 343.57 m, respectively) (Appendix 1). Microscopic observations on phyllite and slate samples showed that these two lithologies, in order of decreasing abundance, are mainly composed of mica (mainly muscovite and sericite) and quartz, with variable amounts of feldspar, chlorite, biotite, rutile, sphene, and pyrite. At the microscopic scale, minor fracturing frequently transects the rock; some of these microfractures are filled with iron oxides. Veinlets of granoblastic quartz, as well as primary calcite pods, are frequently observed. Shock metamorphic effects, mainly PFs but also some rare PDFs, have been observed in quartz grains from quartz veinlets that cross-cut phyllite and slate samples (e.g., KR8-063; depth = 343.57 m), which indicates that the veinlets predate the impact event.

Shock Petrographic Study: Basement rocks display a large heterogeneity of shock effects in quartz grains. The

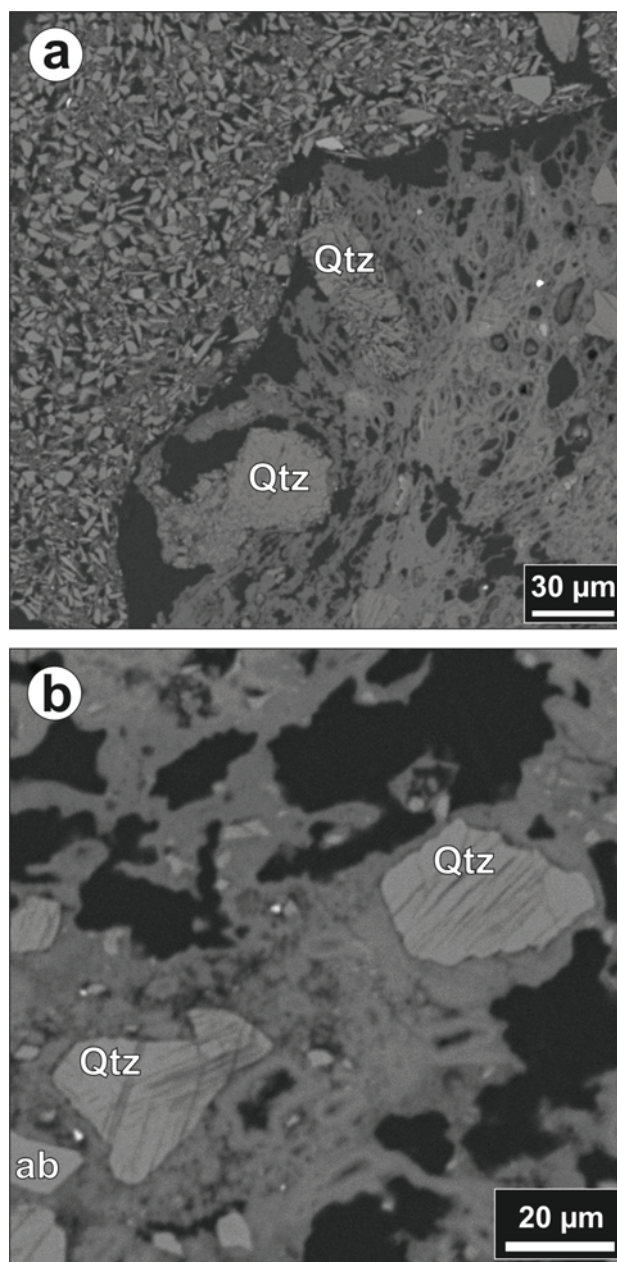


Fig. 7. Backscattered electron images showing the texture of two altered melt particles in suevite. a) Subangular lithic quartz grains in argillaceous matrix (left) and subrounded to subangular quartz grains embedded in argillaceous matrix (right). b) Shocked quartz grains embedded in argillaceous matrix with albite grains (ab); argillaceous matrix is dominated by illite. Sample KR8-004; depth = 239.65 m.

abundance of shocked quartz (with PFs and PDFs) in meta-graywacke samples is variable, from abundant (up to 38% of all quartz grains, in KR8-029 and KR8-032; depths = 271.43 and 274.99 m, respectively), many (up to 20%, in KR8-066 and KR8-067; depths = 353.95 and 356.59 m, respectively), to few (less than 5%) or not observed (for example, in KR8-125; depth = 451.23 m). See Appendix 1 for more detail. A detailed description of each sample allows us to

answer the question of the different response to shock effects for the different meta-graywacke samples (an apparent function of the grain size and of the relative abundances of quartz grains). Our observations revealed an apparent decrease of the number of shocked quartz grains with increasing depth. Even though meta-graywackes with similar grain sizes were used for this estimate, our conclusions need to be substantiated using a larger number of samples from more than three different depth intervals. Shocked quartz grains observed in meta-graywacke samples display PFs and PDFs (1, 2, or rarely 3 to 4 sets), some of which are decorated (Figs. 9b, 9c, and 9d). In some instances, the quartz grains are toasted (Figs. 9a and 9b). The crystallographic orientations of 155 PDF orientations in 89 quartz grains were analyzed on five thin sections of four meta-graywacke samples (KR8-029, KR8-030, KR8-031, and KR8-032; depths = 271.43, 272.00, 273.99, and 274.99 m, respectively) (Table 2b). More than 80% of all the poles to the PDF planes measured are oriented at $\sim 23^\circ$ to the c-axis (corresponding to the $\omega\{10\bar{1}3\}$ orientation). Less than 4% of planes parallel to the $\{2241\}$ orientation are present. Not more than 1% of the measured sets represent basal PDFs. The frequency of indexed PDF sets versus angle between c-axis and PDFs is shown in Fig. 10b.

Some feldspar grains display fractures or polysynthetic twinning displaced along microfaults; these features are preferentially observed in meta-graywacke, which also contains numerous shocked quartz grains (e.g., KR8-033; depth = 277.03 m). Several calcite grains show fractures, microfaults, and curved twins (e.g., KR8-108; depth = 424.78 m; Fig. 11b).

Suevite Dikelets

Suevite dikelets in metasediment occur between 279.5 and 298 m (three suevite dikelets of about 55 cm thickness at 280 m, 80 cm at 286 m, and 60 cm at 293.4 m), and between 418 and 440 m (three more suevite dikelets of about 35 cm thickness at 422.5 m, 65 cm at 434.3 m, and 60 cm at 440 m). In addition, thin suevite intercalations up to ~ 3 cm thick are present (e.g., at 418.05 m and around the suevite dikelet at 440 m) (Fig. 15). These suevite occurrences display a greenish gray, fine-grained fragmental matrix, consisting of rock and mineral fragments, and secondary smectite (mainly) and chlorite. Angular clasts of meta-graywacke, quartzite, phyllite, and slate occur. This greenish gray color of the suevite samples is due to the abundance of secondary phyllosilicates that results from the alteration of melt particles but also of matrix (Fig. 3d). Microscopic observations also reveal the presence of calcite fragments and of meta-graywacke clasts of the previously described "light greenish gray, medium-grained meta-graywacke" in suevite dikelet samples KR8-041, KR8-042, KR8-043, and KR8-107 from depths of 293.79, 293.97, 296.94, and 422.36 m, respectively.

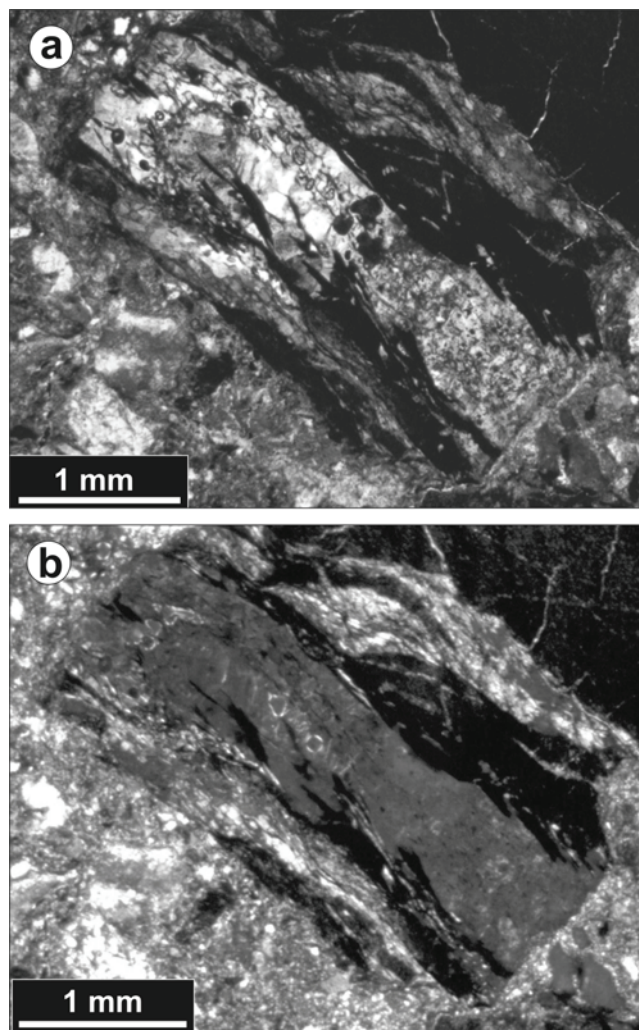


Fig. 8. A microphotograph of diaplectic quartz glass in suevite: (a) plane-polarized light and (b) cross-polarized light. Sample KR8-001; depth = 235.77 m.

Melt particles (Fig. 6b) are subangular to subrounded in shape and have sizes between 100 μm and 1 cm (in sample CAN-31, depth = 440.32 m). Melt particles present in suevite dikelets are mostly devitrified and altered to secondary phyllosilicates (Fig. 3d).

SUMMARY AND DISCUSSION

Core LB-08A can be subdivided into two major parts: the uppermost 25 m are composed of polymict lithic impact breccia (clast-supported) intercalated with suevite units (Fig. 2), and the lower part is composed of fractured/brecciated metasediment between 262 to 451 m, dominated by meta-graywacke (locally monomict lithic breccia), and intersected by a few suevite dikelets (Fig. 2). Because of the irregular distribution of melt particles in the upper 25 m of the core, the whole unit might be called a melt-poor suevite.

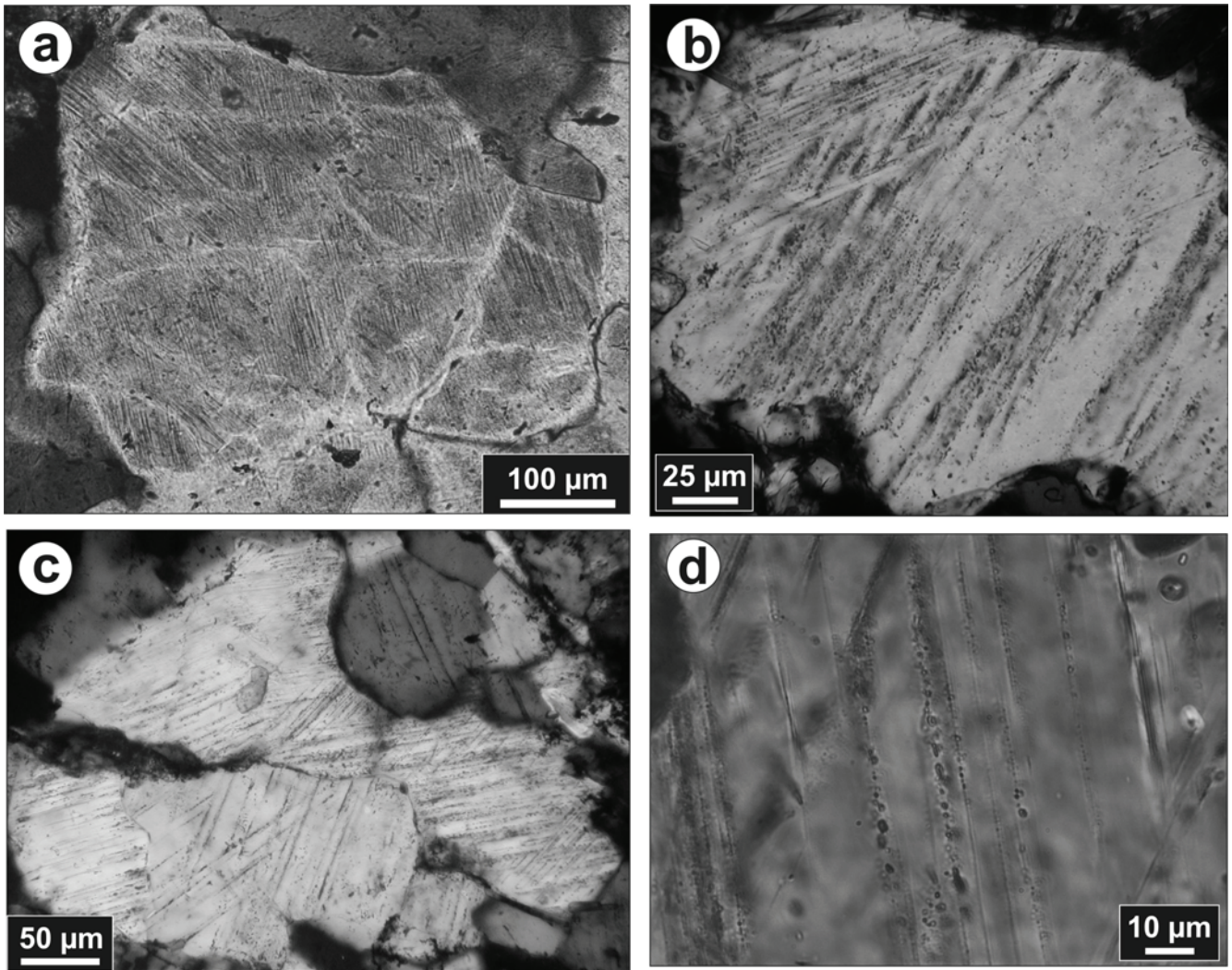


Fig. 9. Microphotographs in cross-polarized light. a) PDFs in quartz (locally toasted) from a quartzite clast in suevite. Sample KR8-006; depth = 240.36 m. b) Decorated PDFs in partially toasted quartz grains; medium-grained meta-graywacke. Sample KR8-056; depth = 326.78 m. c) Decorated PDFs in quartz grains; mylonitic medium-grained meta-graywacke. Sample KR8-070; depth = 364.12 m. d) Decorated (with numerous small fluid inclusions) PDFs in quartz grains; medium-grained meta-graywacke. Sample KR8-098; depth = 410.74 m.

However, our distinction between polymict lithic breccia and suevite is based on thin-section observations. This part of the core most likely represents fallback impact breccia. A deposition of this unit by slump processes is unlikely because after the formation of the crater—and even today—this location was topographically higher than the surrounding crater fill. Diaplectic quartz glass fragments are only present in the uppermost five meters of the core. It is not clear why diaplectic quartz glass fragments do not occur in all of the suevitic breccia parts of the fallback deposit.

The lower part of the core represents the basement that has been shocked and fractured during impact crater formation. The transition from impact breccia to basement is located at a depth of about 262 m below lake level. The basement is composed of an alternating sequence of metasediment with (in order of decreasing abundance)

meta-graywacke (dominant), phyllite, and slate, with local occurrences of monomict lithic breccia, light greenish gray medium-grained meta-graywacke with granophyric material, and some suevite dikelets. The metasediment displays a large variation in lithology and grain size, from fine-grained to gritty, at the macroscopic and microscopic scales, which is normally typical of turbiditic deposits. The observations made during this study are in favor of a single structural unit; no major discontinuity has been observed in the lower part of the core.

The suevite dikelets observed in the metasediment (up to 80 cm thick; between 279.5 and 298 m, and between 418 and 440 m) are probably the result of injection of material into fractures. It is not clear whether, in addition to local fragments, material from all stratigraphic levels of the target was included in the suevite dikelets. However, the

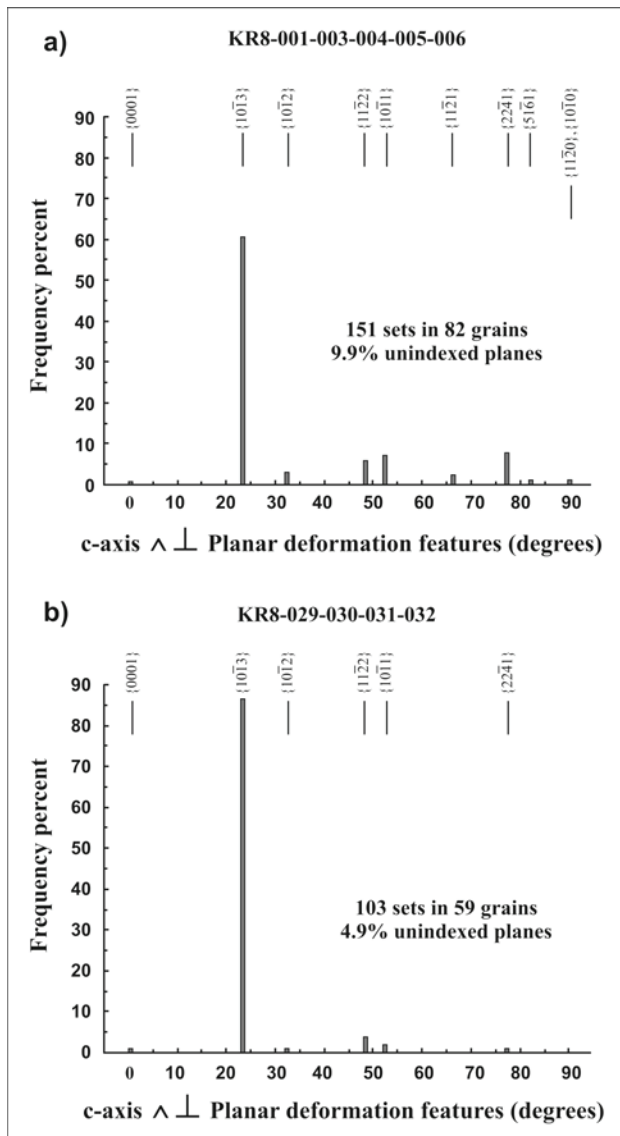


Fig. 10. Histograms of the frequency percent of uniquely indexed PDFs in quartz grains from (a) 5 suevite samples with depths between 235.77 and 240.36 m; and (b) 4 meta-graywacke samples from the basement with depths between 271.43 and 274.99 m. Note the very low frequency of basal (0001) PDFs. See text for details.

large variety of clast populations and presence of melt particles favors incorporation of material from the uppermost levels. It is also not clear whether the fractures into which the material was injected predate the impact event or were caused by it.

Shock Petrographic Characteristics of the Fallback Impact Breccia and of the Basement Samples, Drill Core LB-08A

Quartz grains with PFs and PDFs (commonly 1, 2, or 3 sets; rarely 4 sets) in suevite samples frequently display a toasted appearance (Short and Gold 1996; Whitehead et al.

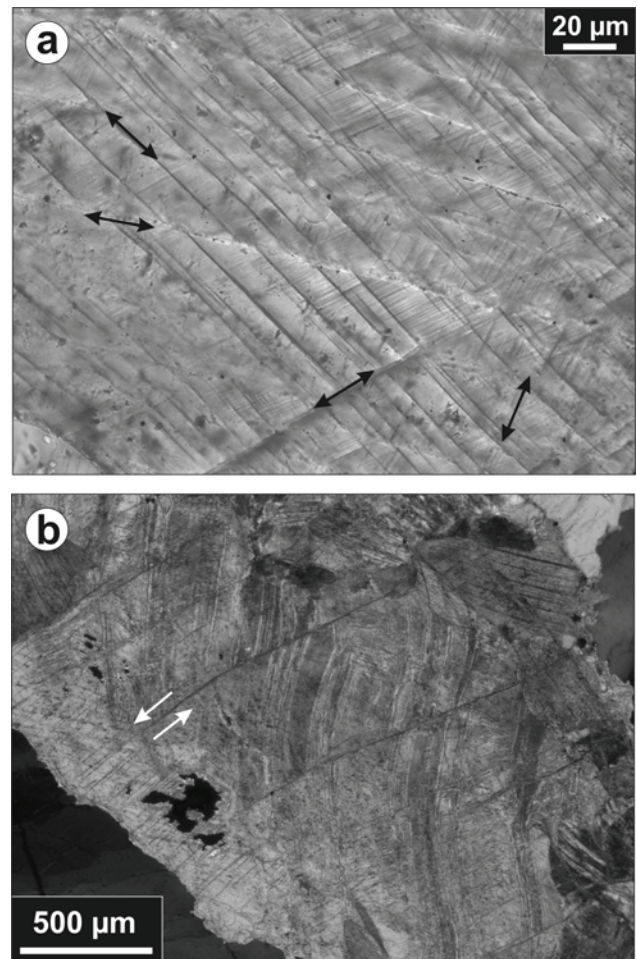


Fig. 11. Microphotographs of calcite grains. a) Grains with anomalous number of microfeatures (twins, cleavages, or planar fractures? Up to 4 different orientations). Suevite sample KR8-006; depth = 240.36 m (plane-polarized light). b) Grains with fractures, microfaults, and curved twins. Meta-graywacke sample KR8-108; depth = 424.78 m (cross-polarized light).

2002). Some PDFs in quartz grains are decorated with numerous small fluid inclusions. Normally, decorated PDFs are considered secondary features, in which the decorations formed by post-shock annealing and aqueous alteration of non-decorated amorphous PDFs (e.g., Grieve et al. 1996; Leroux 2005). For this reason, the presence of decorated PDFs is surprising in the case of the Bosumtwi impact structure, which is only 1.07 Myr old. However, recent shock experiments (Kenkmann et al. 2006) show that it is possible to produce decorated PDFs in “wet” experiments (A. Deutsch and T. Kenkmann, personal communication), i.e., in experiments with target rocks saturated in water (Kenkmann et al. 2006). Observations of decorated PDFs in Bosumtwi samples argue for an impact into a water-rich metasedimentary target or, possibly, rapid post-impact alteration.

Orientations of PDF sets in quartz grains from suevite

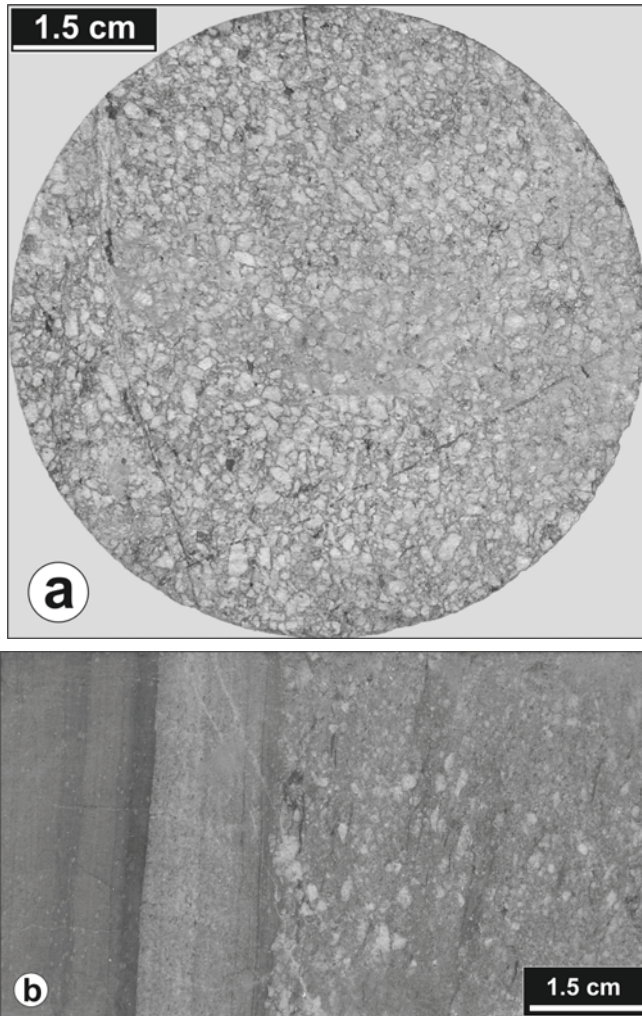


Fig. 12. Macrophotos. a) A core cross-section of gritty meta-graywacke. Sample KR8-029; depth = 271.43 m. b) Metasediment with large variation in grain size; from phyllite (left part), fine-grained meta-graywacke to medium-grained meta-graywacke (right part). Sample KR8-109; depth = 425.24 m.

samples show that planes parallel to $\{10\bar{1}3\}$ are most abundant among the orientations of PDFs measured (up to 68 rel%) and that only a very small proportion of basal PDFs was found, which is in agreement with observations by Boamah and Koeberl (2006) on suevite from the northern outer sector of the impact structure. Such a frequency distribution of PDF orientations argues for shock pressures of at least 16 GPa (Grieve and Robertson 1976; Robertson et al. 1968; Huffman and Reimold 1996; French 1998), whereas shock pressures of up to 35 GPa in the top 5 m of the suevite are indicated by the presence of diaplectic quartz glass (e.g., Grieve et al. 1996), and the presence of melt particles in suevite indicates pressures higher than 45 GPa (e.g., French 1998). This heterogeneity of the shock levels in the suevite represents thorough mixing of variably shocked (and melted) target components.

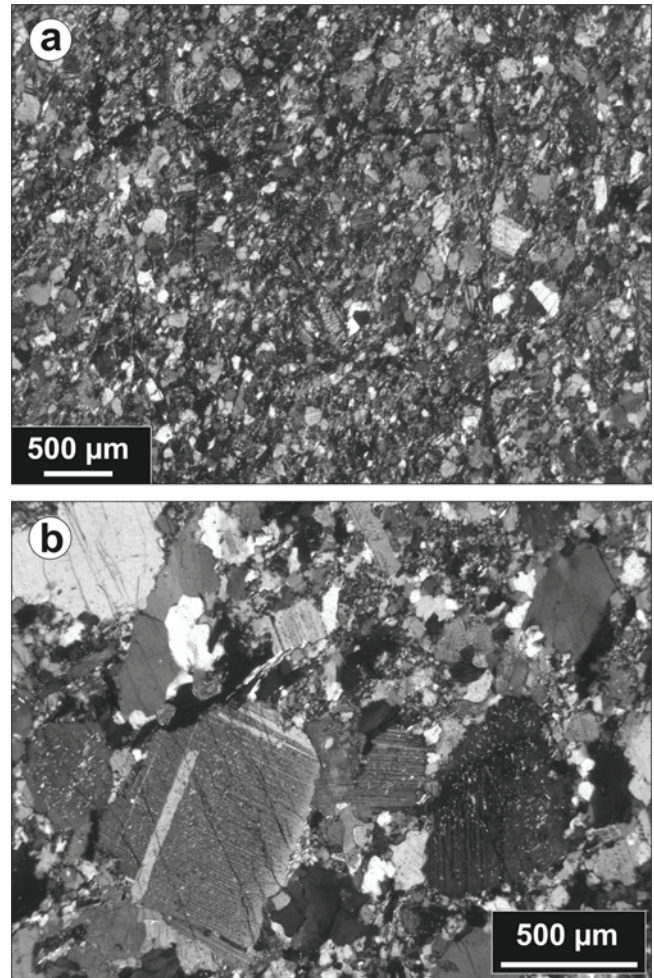


Fig. 13. Microphotographs (cross-polarized light). a) Sheared, fine-grained meta-graywacke cut by fine fractures. Sample KR8-027; depth = 263.76 m. b) Altered medium-grained to gritty meta-graywacke (partially annealed) with mainly fragments of feldspar and quartz. Sample KR8-123; depth = 447.96 m.

Fractured and locally completely brecciated (presence of monomict meta-graywacke breccia; between 310 and 311 m) basement rocks display evidence of shock metamorphism, such as the presence of PFs and PDFs in quartz grains within meta-graywacke samples. The ratio of shocked to unshocked quartz grains in meta-graywacke seemingly decreases with depth, which can be related to shock pressure attenuation with distance from shock wave origin. On the basis of the different measurements of the poles to the PDF planes in quartz grains from meta-graywacke samples, largely dominated by planes parallel to $\{10\bar{1}3\}$ and low amount of planes parallel to $\{22\bar{4}1\}$, as well as the presence of up to 3 (or rarely 4) sets of PDFs in quartz grains, we have estimated that the intensity of shock pressure was highly heterogeneous in the basement, but shock pressures attained locally up to 25–30 GPa (Huffman and Reimold 1996; French 1998).

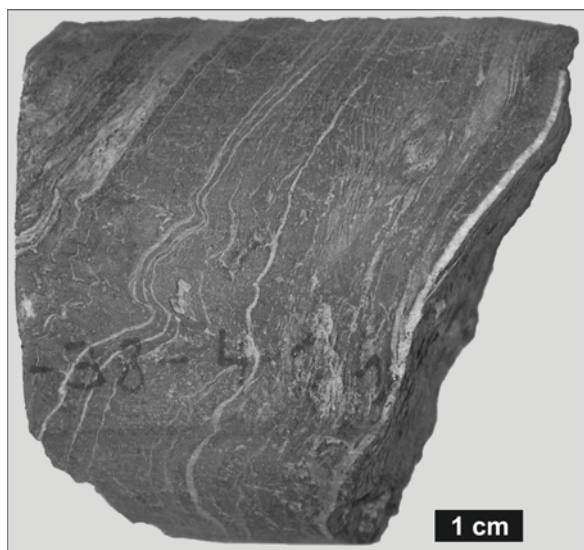


Fig. 14. A macrophoto of deformed phyllite with quartz laminae. Sample KR8-064; depth = 348.43 m.

Alteration of the Rocks in Drill Core LB-08A

A variety of alteration effects has been observed in samples from the central uplift: alteration of plagioclase to sericite, biotite to chlorite, fractures filled with iron oxides, pyrite, and calcite veinlets and aggregates of secondary calcite. Alteration of plagioclase to sericite and biotite to chlorite took place mostly prior to the impact event, because rocks outside the crater show the same alteration features (Woodfield 1966; Moon and Mason 1967). Most of the fracture fills of iron oxides and pyrite flakes in the basement samples seem to be post-impact alteration features: the presence of calcite veinlets and aggregates in suevite samples from the fallback deposit indicates that they are secondary features likely resulting from hydrothermal circulation after the impact event (Kontny and Just 2006; Kontny et al. 2007). We have not observed by microscopic observation any systematic change in the distribution of calcite veinlets and aggregates with depth throughout the core, but CaO abundances measured in bulk samples (see Ferrière et al. 2007) show a weak trend of increasing abundances with depth. The majority of impact-melt particles in our fallback suevite samples, as well as in suevite dikelets in the basement, are devitrified and transformed to secondary phyllosilicates. The matrix of polymict impact breccia also contains an abundance of very fine-grained phyllosilicates, which is consistent with post-impact hydrothermal alteration.

Comparison with the Main Observations from Drill Core LB-07A

The LB-07A core, which was drilled into the deep crater moat, shows a number of differences compared to core LB-08A in terms of lithostratigraphy and also in terms of

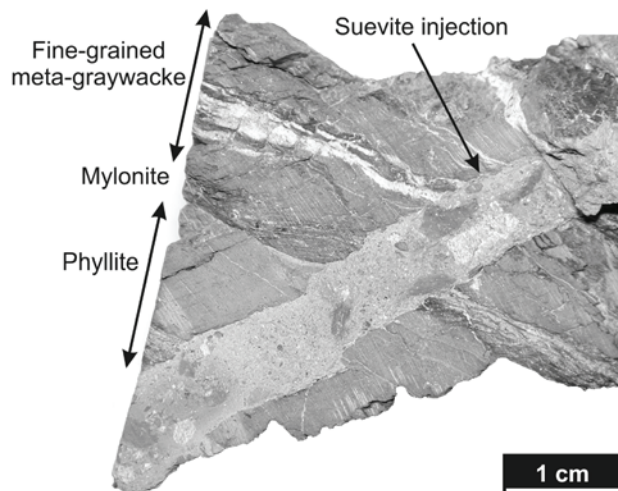


Fig. 15. A macrophoto of an altered suevite injection (~0.8 cm thick) in fine-grained metasediment (phyllite to fine-grained meta-graywacke, locally mylonitized and brecciated). Sample ADE-8A; depth = 418.05 m.

shock (Coney et al. 2007; Koeberl et al. 2007). In comparison with core LB-08A, which was subdivided into two major sections (this study), three sequences have been distinguished for the core LB-07A (Coney et al. 2007). The first 80 m of the core, termed “upper impactite” by Coney et al. (2007) (from 333.38 to 415.67 m in depth), consists of an alternating sequence of suevite and lithic impact breccias, underlain by the so-called “lower impactite,” which consists mostly of monomict lithic breccia (about 55 m), followed by the basement rocks (from 470.55 to 545.08 m in depth), and an assemblage of low-grade metapelites (including shale, schist, and phyllite), meta-graywacke, and minor meta-sandstone, quartzite, and thin carbonate strata (Coney et al. 2007).

These observations from core LB-07A indicate that at about 615 m to the northwest of the location of the core LB-08A, the thickness of the polymict impact breccia sequence is about three times greater. This major difference between the two cores could be the result of the transport during the crater modification stage, with material sliding off the top of the central uplift, or it could be the result of enhanced erosion of the top of the central uplift. The fact that the central part of the central uplift is collapsed (e.g., Scholz et al. 2002) indicates that some form of transport and material movement has taken place. The polymict lithic breccias in the upper sections of both cores may in fact represent debris flows off the central uplift and/or off the crater rim. This would explain the alternation of lithic breccia and suevite.

Concerning the occurrence of monomict impact breccia, just ~1 m of this lithology has been found in core LB-08A (this study) in comparison with ~55 m in core LB-07A (Coney et al. 2007). The basement underneath the crater seems to be heterogeneous, as metasediments observed in

core LB-07A are dominated by fine-grained rocks (mostly shale, schist, and phyllite) compared to the metasediments observed in the core LB-08A, which are mostly composed of fine- to medium-grained meta-graywacke. No gritty meta-graywacke has been observed in core LB-07A and, in turn, no shale and schist have been found in core LB-08A (this study; Deutsch et al. 2007).

In terms of shock petrography, both impactite sequences (in cores LB-07A and LB-08A) contain melt particles, which are more or less altered. Rare glass fragments have been found only in the top five meters of the fallback impact breccia in core LB-08A (this study), in comparison with the apparent absence of glass fragments in the upper impactite sequence in core LB-07A (Coney et al. 2007).

Comparison with Suevite from Outside the Crater

Melt particles and diaplectic quartz glass are present in suevite from the central uplift (Ferrière et al. 2006; this study), which is similar to suevites from outside the northern crater rim (Koeberl et al. 2002; Boamah and Koeberl 2003, 2006). However, melt particles and diaplectic quartz are rarer (about 6 vol%, with a maximum abundance of 10–15 vol% observed at the thin-section scale) and smaller (largest melt particle observed of ~1 cm) in suevite from the central uplift than in suevite from outside the northern crater rim; the abundance of impact-melt fragments in this suevite ranges from 15 vol% (Boamah and Koeberl 2003, 2006) to 60 vol% (Koeberl et al. 2002), and the size of the fragments is also up to more than ten times larger in suevite from outside the northern crater rim (up to 40 cm in diameter) (Koeberl and Reimold 2005). In addition, suevites from outside the crater rim contain coesite (Littler 1961), baddeleyite (the high-temperature decomposition product of zircon; El Goresy et al. 1968), and ballen quartz (Boamah and Koeberl 2003, 2006). Based on the presence of a sizable melt component in suevite from outside the crater rim and in suevite from the central uplift, shock pressures exceeding in both cases 45 GPa (according to Huffman and Reimold 1996; French 1998) can be assumed. However, it is clear that the relative amount of shocked and melted material in suevites from the central uplift is lower than in suevite from outside the northern crater rim.

Calcite clasts in suevite samples from the fallback deposit and also in suevite injected into the basement (also Coney et al. 2007) have not been observed before in polymict impact breccia from the Bosumtwi crater. Interestingly, we did not find any granite clasts in the suevite in core LB-08A, in contrast to suevite from outside the northern crater rim, which contains an up to 3 vol% component of granitic clasts (Boamah and Koeberl 2003, 2006; Koeberl et al. 2002).

The differences between suevite from the central uplift and suevite from outside the northern crater rim should represent differences in the ejection and deposition modes. To confirm these hypotheses, further detailed study of suevite

deposits from the north side of the crater structure and of suevites from the occurrences to the south of the crater should be carried out.

Comparison with Observations at the Ries Impact Crater

Our observations of melt-particle abundance, i.e., lower melt-particle abundance in the fallback relative to the fallout breccia deposits, and distribution appear to be very similar to observations made at the Ries crater. Ries crater fallout suevite differs distinctly from the Ries fallback suevite with respect to volume, shape, and grain size of melt products and to volume and type of sedimentary rock inclusions, areal distribution, and thickness (Stöffler 1977; Stöffler et al. 1977).

Implications for Numerical Modeling

We have demonstrated in this study that the central uplift from Bosumtwi crater consists of fractured rocks, which are, at the location of borehole LB-08A, covered with about 25 m of polymict impact breccia. Neither in core LB-08A nor in core LB-07A (Coney et al. 2007) is there any significant amount of melt-rich suevite breccia or an indication of a coherent impact-melt lens, which was assumed to be present with a thickness of at least 200 m in the central part of the crater based on earlier geophysical and numerical modeling (Jones et al. 1981; Plado et al. 2000; Artemieva et al. 2004). The magnetic anomaly located in the northern part of the lake was previously interpreted to result from a melt-rich suevite layer (Jones et al. 1981; Plado et al. 2000), which has now been shown to be absent. How these observations compare with numerical investigations of tektite formation and deposition (Artemieva 2002) is not yet clear. Our study confirms that impact into metasedimentary target, especially into a wet metasedimentary target, produces only a limited amount of melt, which is widely and finely dispersed into the central part of the crater and under the form of large blobs outside of the crater rim. Whether or not oblique impact could have played a role is to be further investigated. Refined numerical modeling on the basis of these new observations may help to better understand the formation of the Bosumtwi crater.

CONCLUSIONS

The central uplift of the Bosumtwi impact structure was sampled for the first time during the 2004 ICDP drilling project, and here we present the first lithological, petrographic, mineralogical, and shock-petrographic observations on the rocks from drill core LB-08A. We have studied 174 thin sections by optical microscopy and 12 polished thin sections by electron microscopy from 121 samples covering the total depth range of the core, from 235.6 to 451.33 m below lake level.

Our main observations and conclusions are:

1. The uppermost 25 m of core LB-08A represent a fallback sequence containing melt particles, which indicates pressures >45 GPa, and diaplectic quartz glass, only observed in the top five meters, which indicates pressures of up to 35 GPa. The second part of the core, between 262 to 451 m, represents in situ heterogeneously shocked and fractured basement, with shock pressures locally reaching 25–30 GPa.
2. Melt particles and diaplectic quartz glass are rare in suevite from the central uplift in comparison with suevite samples from the northern part of the crater.
3. Observations of decorated PDFs in Bosumtwi samples argue for an impact into a water-bearing metasedimentary target or, possibly, rapid post-impact alteration.
4. The present study of samples from the central uplift, with comparison to observations on samples from outside the northern crater rim, yielded results that are concordant with observations from the Ries crater.

A more detailed optical and electron microscopic study of shocked minerals in all core units, as well as analyses of the proportion of shocked and unshocked quartz grains present in a variety of grain sizes from meta-graywacke samples and also of the relative abundance of quartz and feldspar grains throughout the basement, is in progress.

Acknowledgments—Drilling was funded by ICDP, the U.S. NSF, the Austrian FWF, the Canadian NSERC, and the Austrian Academy of Sciences. We are grateful to DOSECC for the drilling operations. This work was supported by the Austrian FWF (P17194-N10, to C. K.). We are grateful to F. Brandstätter (Natural History Museum, Vienna, Austria) and E. Robin (CEA, Gif-sur-Yvette, France) for assistance with electron microscopy and microprobe work, to J. N. Rouzaud and C. Le Guillou (both ENS, Paris, France) for assistance for Raman measurements, and to A. Deutsch and S. Luetke (both University of Muenster, Germany), and L. Coney and R. Gibson (University of the Witwatersrand, Johannesburg, South Africa) for constructive discussions. We are grateful to J. Morrow and D. Kring for constructive reviews.

Editorial Handling—Dr. Bernd Milkereit

REFERENCES

- Artemieva N. A. 2002. Tektite origin in oblique impact: Numerical modeling. In *Impacts in Precambrian shields*, edited by Plado J. and Pesonen L. New York: Springer-Verlag, pp. 257–276.
- Artemieva N. A., Karp T., and Milkereit B. 2004. Investigating the Lake Bosumtwi impact structure: Insight from numerical modeling. *Geochemistry Geophysics Geosystems* 5, doi:10.1029/2004GC000733.
- Boamah D. and Koeberl C. 2003. Geology and geochemistry of shallow drill cores from the Bosumtwi impact structure, Ghana. *Meteoritics & Planetary Science* 38:1137–1159.
- Boamah D. and Koeberl C. 2006. Petrographic studies of fallout suevite from outside the Bosumtwi impact structure, Ghana. *Meteoritics & Planetary Science* 41:1761–1774.
- Brodie K., Fettes D., Harte B., and Schmid R. 2004. Structural terms including fault rock terms. http://www.bgs.ac.uk/scmr/docs/paper_3/scmr_struc2.pdf.
- Chayes F. 1949. A simple point counter for thin-section analysis. *American Mineralogist* 34:1–11.
- Coney L., Reimold W. U., Koeberl C., and Gibson R. L. 2006. Mineralogical and geochemical investigations of impact breccias in the ICDP borehole LB-07A, Bosumtwi impact structure, Ghana (abstract #1279). 37th Lunar and Planetary Science Conference. CD-ROM.
- Coney L., Gibson R. L., Reimold W. U., and Koeberl C. 2007. Lithostratigraphic and petrographic analysis of ICDP drill core LB-07A, Bosumtwi impact structure, Ghana. *Meteoritics & Planetary Science* 42. This issue.
- Deutsch A., Luetke S., and Heinrich V. 2007. The ICDP Lake Bosumtwi impact crater scientific drilling project (Ghana): Core LB-08A litho-log, related ejecta, and shock recovery experiments. *Meteoritics & Planetary Science* 42. This issue.
- El Goresy A., Fechtig H., and Ottemann T. 1968. The opaque minerals in impactite glasses. In *Shock metamorphism of natural materials*, edited by French B. M. and Short N. M. Baltimore: Mono Book Corp. pp. 531–554.
- Emmons R. C. 1943. *The universal stage (with five axes of rotation)*. GSA Memoir #8. New York: Geological Society of America. 205 p.
- Engelhardt W. von and Bertsch W. 1969. Shock-induced planar deformation structures in quartz from the Ries crater, Germany. *Contributions to Mineralogy and Petrology* 20:203–234.
- Ferrière L., Koeberl C., Reimold W. U., and Gibson R. L. 2006. First mineralogical observations and chemical analyses of core LB-08A from the central uplift of the Bosumtwi impact structure, Ghana: Comparison with suevite from outside the crater (abstract #1845). 37th Lunar and Planetary Science Conference. CD-ROM.
- Ferrière L., Koeberl C., Reimold W. U., and Mader D. 2007. Drill core LB-08A, Bosumtwi impact structure, Ghana: Geochemistry of fallback breccia and basement samples from the central uplift. *Meteoritics & Planetary Science* 42. This issue.
- French B. M. 1998. *Traces of catastrophe: A handbook of shock-metamorphic effects in terrestrial meteorite impact structures*. LPI Contribution #954. Houston: Lunar and Planetary Institute. 120 p.
- Grieve R. A. F. and Robertson P. B. 1976. Variations in shock deformation at the Slate Islands impact structure, Lake Superior, Canada. *Contributions to Mineralogy and Petrology* 58:37–49.
- Grieve R. A. F., Langenhorst F., and Stöffler D. 1996. Shock metamorphism of quartz in nature and experiment: II. Significance in geoscience. *Meteoritics & Planetary Science* 31: 6–35.
- Huffman A. R. and Reimold W. U. 1996. Experimental constraints on shock-induced microstructures in naturally deformed silicates. *Tectonophysics* 256:165–217.
- Jackson J. A. 1997. *Glossary of geology*, 4th ed. Alexandria, Virginia: American Geological Institute. 769 p.
- Jones W. B., Bacon M., and Hastings D. A. 1981. The Lake Bosumtwi impact crater, Ghana. *Geological Society of America Bulletin* 92:342–349.
- Junner N. R. 1937. The geology of the Bosumtwi caldera and surrounding country. *Gold Coast Geological Survey Bulletin* 8: 1–38.

- Karp T., Milkereit B., Janle P., Danuor S. K., Pohl J., Berckhemer H., and Scholz C. A. 2002. Seismic investigation of the Lake Bosumtwi impact crater: Preliminary results. *Planetary and Space Science* 50:735–742.
- Kenkmann T., Thoma K., and the MEMIN team 2006. Hypervelocity impact into dry and wet sandstone (abstract). *Geophysical Research Abstracts* 8:A-02389.
- Koerberl C. and Reimold W. U. 2005. Bosumtwi impact crater, Ghana (West Africa): An updated and revised geological map, with explanations. *Jahrbuch der Geologischen Bundesanstalt, Wien* (Yearbook of the Austrian Geological Survey). 145:31–70 (+1 map, 1:50,000).
- Koerberl C., Bottomley R. J., Glass B. P., and Storzer D. 1997. Geochemistry and age of Ivory Coast tektites and microtektites. *Geochimica et Cosmochimica Acta* 61:1745–1772.
- Koerberl C., Reimold W. U., Blum J. D., and Chamberlain C. P. 1998. Petrology and geochemistry of target rocks from the Bosumtwi impact structure, Ghana, and comparison with Ivory Coast tektites. *Geochimica et Cosmochimica Acta* 62:2179–2196.
- Koerberl C., Denison C., Ketcham R. A., and Reimold W. U. 2002. High-resolution X-ray computed tomography of impactites. *Journal of Geophysical Research* 107, doi:10.1029/2001JE001833.
- Koerberl C., Milkereit B., Overpeck J. T., Scholz C. A., Reimold W. U., Amoako P. Y. O., Boamah D., Claeys P., Danuor S. K., Deutsch A., Hecky R. E., King J., Newsom H., Peck J., and Schmitt D. R. 2006. An international and multidisciplinary drilling project into a young complex impact structure: The 2004 ICDP Bosumtwi impact crater, Ghana, drilling project—An overview (abstract #1859). 37th Lunar and Planetary Science Conference. CD-ROM.
- Koerberl C., Milkereit B., Overpeck J. T., Scholz C. A., Amoako P. Y. O., Boamah D., Danuor S., Karp T., Kueck J., Hecky R. E., King J. W., and Peck J. A. 2007. An international and multidisciplinary drilling project into a young complex impact structure. The 2004 ICDP Bosumtwi Crater Drilling Project—An overview. *Meteoritics & Planetary Science* 42. This issue.
- Kontny A. and Just J. 2006. Magnetic mineralogy and rock magnetic properties of impact breccias and crystalline basement rocks from the BCDP-drillings 7A and 8A (abstract #1343). 37th Lunar and Planetary Science Conference. CD-ROM.
- Kontny A., Elbra T., Just J., Pesonen L. J., Schleicher A., and Zolk J. 2007. Petrography and shock-related remagnetization of pyrrhotite in drill cores from the Bosumtwi Crater Drilling Project, Ghana. *Meteoritics & Planetary Science* 42. This issue.
- Langenhorst F. 2002. Shock metamorphism of some minerals: Basic introduction and microstructural observations. *Bulletin of the Czech Geological Survey* 77:265–282.
- Leroux H. 2005. Weathering features in shocked quartz from the Ries impact crater, Germany. *Meteoritics & Planetary Science* 40:1347–1352.
- Leube A., Hirdes W., Mauer R., and Kesse G. O. 1990. The Early Proterozoic Birimian Supergroup of Ghana and some aspects of its associated gold mineralization. *Precambrian Research* 46:139–165.
- Littler J., Fahey J. J., Dietz R. S., and Chao E. C. T. 1961. Coesite from the Lake Bosumtwi crater, Ashanti, Ghana. GSA Special Paper #68. Boulder, Colorado: Geological Society of America. 218 p.
- Montanari A. and Koerberl C. 2000. *Impact stratigraphy: The Italian record*. Lecture Notes in Earth Sciences, vol. 93. Heidelberg: Springer-Verlag. 364 p.
- Moon P. A. and Mason D. 1967. The geology of ¼° field sheets 129 and 131, Bompata S. W. and N. W. *Ghana Geological Survey Bulletin* 31:1–51.
- Pesonen L. J., Koerberl C., Ojamo H., Hautaniemi H., Elo S., and Plado J. 1998. Aerogeophysical studies of the Bosumtwi impact structure, Ghana (abstract). *Geological Society of America Abstracts with Programs* 30:A190.
- Pesonen L. J., Koerberl C., and Hautaniemi H. 2003. Airborne geophysical survey of the Lake Bosumtwi meteorite impact structure (southern Ghana)—Geophysical maps with descriptions. *Jahrbuch der Geologischen Bundesanstalt, Vienna* (Yearbook of the Austrian Geological Survey) 143:581–604.
- Plado J., Pesonen L. J., Koerberl C., and Elo S. 2000. The Bosumtwi meteorite impact structure, Ghana: A magnetic model. *Meteoritics & Planetary Science* 35:723–732.
- Reimold W. U., Brandt D., and Koerberl C. 1998. Detailed structural analysis of the rim of a large, complex impact crater: Bosumtwi crater, Ghana. *Geology* 26:543–546.
- Reinhard M. 1931. *Universaldrehtischmethoden*. Basel, Switzerland: Birkhäuser. 118 p.
- Robertson P. B., Dence M. R., and Vos M. A. 1968. Deformation in rock-forming minerals from Canadian craters. In *Shock metamorphism of natural materials*, edited by French B. M. and Short N. M. Baltimore: Mono Book Corp. pp. 433–452.
- Scholz C. A., Karp T., Brooks K. M., Milkereit B., Amoako P. Y. O., and Arko J. A. 2002. Pronounced central uplift identified in the Bosumtwi impact structure, Ghana, using multichannel seismic reflection data. *Geology* 30:939–942.
- Short N. M. and Gold D. P. 1996. Petrography of shocked rocks from the central peak at the Manson impact structure. GSA Special Paper #302. Boulder, Colorado: Geological Society of America. pp. 245–265.
- Stöffler D. 1977. Research drilling Nördlingen 1973: Polymict breccias, crater basement, and cratering model of the Ries impact structure. *Geologica Bavarica* 75:443–458.
- Stöffler D. and Grieve R. A. F. 1994. Classification and nomenclature of impact metamorphic rocks: A proposal to the IUGS subcommission on the systematics of metamorphic rocks. In *ESF Scientific Network on Impact Cratering and Evolution of Planet Earth, Post-Östersund Newsletter*, edited by Montanari A. and Smit J. pp. 9–15.
- Stöffler D. and Langenhorst F. 1994. Shock metamorphism of quartz in nature and experiment: I. Basic observation and theory. *Meteoritics* 29:155–181.
- Stöffler D., Ewald U., Ostertag R., and Reimold W. U. 1977. Research drilling Nördlingen 1973 (Ries): Composition and texture of polymict breccias. *Geologica Bavarica* 75:163–189.
- Whitehead J., Spray J. G., and Grieve R. A. F. 2002. Origin of “toasted” quartz in terrestrial impact structures. *Geology* 30:431–434.
- Wopenka B. and Pasteris J. D. 1993. Structural characterization of kerogens to granulites-facies graphite: Applicability of Raman spectroscopy. *American Mineralogist* 78:533–577.
- Woodfield P. D. 1966. The geology of the ¼° field sheet 91, Fumso N. W. *Ghana Geological Survey Bulletin* 30:1–66.
- Wright J. B., Hastings D. A., Jones W. B., and Williams H. R. 1985. *Geology and mineral resources of West Africa*. London: Allen & Unwin. 187 p.

APPENDIX

Appendix 1. Detailed petrographic descriptions (rock name, minerals present, etc.) and depths of the 121 samples documented for this study. This table is based on optical microscopic observations of 174 thin sections.

Sample no.	Depth (m)	Petrographic description
KR8-001	235.77	Suevite with a variety of lithic and mineral clasts: meta-graywacke, phyllite, slate, melt particles (partially or completely devitrified), carbon-rich organic shale, diaplectic quartz glass, and calcite; quartz grains show some PFs and PDFs (1 or 2 sets; one quartz grains with 3 sets)
KR8-002	236.40	Phyllite (clast) with quartzitic laminae/ribbon quartz; local development of crenulation cleavage; no obvious shock effects; similar to KR8-007
KR8-003	238.90	Suevite; very similar to KR8-001 in composition and appearance (but no diaplectic quartz glass seen); a few quartz grains with 1 or 2 sets of PDFs
KR8-004	239.65	Suevite with a variety of lithic and mineral clasts: phyllite and slate, mylonitic meta-graywacke, quartzite, melt particles (in a few cases with flow structure and vesicles), and carbon-rich organic shale clasts (few in comparison with KR8-001 and KR8-003); many melt particles (one large one, ~1 cm in the longest dimension); some quartz grains with PDFs (1 or 2 sets); fractures filled with iron oxides and calcite aggregates
KR8-005	240.04	Suevite with a variety of lithic and mineral clasts: phyllite (similar to KR8-002, with large ribbon quartz) and slate, melt particles (brown or black in color and with vesicles), mylonitic meta-graywacke, carbon-rich organic shale, quartzite, calcite, and diaplectic quartz glass; quartz grains show some PFs and PDFs (1 or 2 sets; one quartz grains with 3 sets)
KR8-006	240.36	Quartzite clast in suevite; plenty of PDFs (1, 2, 3, and 4 sets) in quartz grains partially or totally toasted; presence of cracks filled by calcite; a small part of the section comprises suevite
KR8-007	241.94	Phyllite (clast) with quartzitic laminae/ribbon quartz; presence of chlorite veinlets (aligned parallel to the foliation); no trace of shock deformation; very similar to KR8-002
KR8-008	244.45	Strongly altered polymict lithic breccia (clasts supported) with a variety of clasts: meta-graywacke (some mylonitic), phyllite and slate, and quartzite
KR8-009	244.87	Altered polymict lithic breccia (clast supported); faulted clasts of phyllite and slate with quartzitic beds and breccia veins (matrix-poor); phyllite and slate (dominant), quartzite, meta-graywacke (minor) clasts; some of the quartz grains show undulatory extinction and few PFs and PDFs (1 or 2 sets)
KR8-010	245.58	Altered polymict lithic breccia with injected suevitic breccia (vein)
KR8-011	247.46	Altered polymict lithic breccia; composed mainly of mylonitic meta-graywacke, quartzite, and phyllite and slate clasts; many PFs and PDFs (1 or 2 sets, one grain with 3 sets) in quartz grains; calcite aggregates occur
KR8-012	248.00	Suevite with a variety of clasts: mylonitic meta-graywacke, phyllite and slate (fine-grained, well-foliated and with locally development of crenulation cleavage), melt particles (devitrified), quartzite, and carbon-rich organic shale and calcite (minor); some calcite aggregates occur
KR8-013	248.80	Altered polymict lithic breccia; composed mainly of mylonitic meta-graywacke, quartzite, and phyllite and slate clasts; many PFs and PDFs (1 or 2 sets) in quartz grains (locally toasted); calcite aggregates and elongated opaque crystals occur; similar to KR8-011
KR8-014	249.30	Suevite (matrix dominate) with a variety of lithic and mineral clasts: altered meta-graywacke, phyllite and slate, melt particles (gray to brown in color), quartzite, and calcite; few PFs and PDFs with 1 set (only 3 quartz grains with 2 sets of PDFs each)
KR8-015	250.74	Altered polymict lithic breccia (clasts supported); composed of two different clast types, phyllite (and slate) and mylonitic meta-graywacke; lots of the quartz grains are fractured, a few show undulatory extinction, and a few others PFs and PDFs (1 or 2 sets)
KR8-016	250.89	Strongly altered polymict lithic breccia with injected suevitic breccia (veinlet); composed of a variety of clasts: phyllite and slate (with development of crenulation cleavage), mylonitic meta-graywacke, melt particles (brown in color) that are completely devitrified, and quartzite; alteration mainly around the suevitic breccia veinlet
KR8-017	251.74	Altered polymict lithic breccia (clasts supported); composed of two different clast types, phyllite (and slate) and mylonitic meta-graywacke; some of the quartz grains show cracks, PFs, and PDFs (1 or 2 sets); very similar to KR8-015
KR8-018	253.04	Altered polymict lithic breccia (clast-supported); composed of two different clast types, phyllite (and slate) and mylonitic meta-graywacke; aggregates of small opaque minerals and tabular opaque crystals occur; few calcite aggregates; very similar to KR8-015 and KR8-017
KR8-019	253.56	Altered polymict lithic breccia with injected suevitic breccia veinlets; composed of meta-graywacke clasts (dominant), few melt particles (altered), phyllite and slate, and calcite clasts; very few PFs (no PDFs seen); abundant calcite aggregates and veinlets
KR8-021	255.65	Altered polymict lithic breccia (clast-supported); few quartz grains show PFs (no PDFs seen); many calcite aggregates and veinlets; very similar to KR8-015, KR8-017, and KR8-018
KR8-022	256.81	Altered polymict lithic breccia (clast-supported); presence of a tiny suevitic veinlet mostly composed of melt particles, isotropic quartz grains, and quartz grains with undulatory extinction); many calcite aggregates and veinlets; no PDFs seen; sample very similar to KR8-015, KR8-017, KR8-018, and KR8-021

Appendix 1. *Continued.* Detailed petrographic descriptions (rock name, minerals present, etc.) and depths of the 121 samples documented for this study. This table is based on optical microscopic observations of 174 thin sections.

Sample no.	Depth (m)	Petrographic description
KR8-023	258.14	Suevite with a variety of clasts: meta-graywacke (medium-grained meta-graywacke dominant) to mylonitic meta-graywacke, slate and phyllite, melt particles (brown in color), quartzite, and minor calcite; few quartz grains (some partially toasted) show PFs (no PDFs seen); a few feldspar crystals are recrystallized (myrmekitic intergrowths of quartz and feldspar)
KR8-024	259.14	Altered polymict lithic breccia (clast-supported); composed of two different clast types, mylonitic meta-graywacke as well as faulted phyllite (and slate); unusual outline (step-like; possibly result of faulting) of phyllite in contact with mylonitic meta-graywacke; very few quartz grains show PFs (no PDFs seen); fine-grained breccia veinlets (suevite?); many opaque grains
KR8-025	259.74	Suevite with a variety of clasts: meta-graywacke (fine- to medium-grained; some are mylonitic or sheared), quartzite, slate, phyllite, melt particles brown to black in color, and few calcite clasts; very few quartz grains with PFs (no PDFs seen); some calcite and opaque minerals aggregates occur
KR8-026	260.49	Suevite with a variety of lithic and mineral clasts: phyllite, fine- to medium-grained meta-graywacke (some are mylonitic), melt particles (brown or black in color), quartzite, slate, and calcite; many quartz grains show PDFs (1 or 2 sets), generally decorated, and some quartz grains are partially toasted; a few feldspar crystals are recrystallized with spherulitic texture (myrmekitic intergrowths of quartz and feldspar); large opaque minerals (pyrite)
KR8-027	263.76	Sheared, fine-grained meta-graywacke; some quartz grains show PFs and PDFs (few grains with 2 sets of PDFs each); calcite veins, veinlets, and aggregates occur
KR8-028	266.18	Very fine-grained metasediment (slate); a few PDFs in quartz (1 set); opaque minerals (pyrite) occur; sample very similar to KR8-046
KR8-029	271.43	Gritty meta-graywacke; plenty of PDFs in quartz (1, 2, or rarely 3 sets; one grain with 4 sets)
KR8-030	272.00	Gritty meta-graywacke; plenty of PDFs in quartz (1 or 2 sets); very similar to KR8-029
KR8-031	273.99	Gritty meta-graywacke; plenty of PDFs in quartz (1, 2, or rarely 3 sets)
KR8-032	274.99	Medium-grained to gritty meta-graywacke; plenty of PDFs (1, 2, or 3 sets) in quartz grains that are partially toasted
KR8-033	277.03	Medium-grained meta-graywacke; lots of PDFs in quartz (1 or 2 sets), some are decorated, and some partially toasted; shock-induced twinning in plagioclase
KR8-034	277.89	Mylonitic, medium-grained to gritty meta-graywacke (locally brecciated); lots of PDFs in quartz (1 or 2 sets), some decorated, and some grains are partially toasted
KR8-035	280.30	Altered suevite with a variety of lithic and mineral clasts: meta-graywacke (sheared or mylonitic), quartzite, phyllite and slate (some clasts displays crenulation cleavage), altered melt particles (gray to brown in color), and calcite clasts; quartz grains show cracks, some grains display PDFs (1 or 2 sets), and a few are toasted
KR8-036	281.32	Mylonitic, medium-grained meta-graywacke; abundant PDFs in quartz (1 or 2 sets); some quartz grains are partially toasted
KR8-037	283.50	Mylonitic, medium-grained meta-graywacke; many PDFs in quartz (1 or 2 sets)
KR8-038	283.74	Brecciated meta-graywacke locally mylonized; lots of PDFs in quartz (1 or 2 sets); some quartz grains are partially toasted
KR8-039	286.17	Strongly altered suevite with a variety of lithic and mineral clasts: abundant melt particles (gray to brown in color), meta-graywacke (some mylonitic), quartzite, phyllite and slate, and calcite clasts
KR8-040	290.47	Suevite with a variety of lithic and mineral clasts: meta-graywacke clast (altered, weakly sheared fine-grained meta-graywacke principally), phyllite, melt particles (mostly brown in color), and calcite; only very few quartz grains display PFs (only one grain with 1 set of PDFs)
KR8-041	293.79	Suevite with a variety of lithic and mineral clasts: phyllite, slate, shocked medium-grained meta-graywacke, chloritoid-rich meta-graywacke, melt particles (brown in color), quartzite, and calcite clasts; a few quartz grains show PFs or PDFs (1 set)
KR8-042	293.97	Suevite (with a prominent phyllite clast) with a variety of lithic and mineral clasts: phyllite and slate, meta-graywacke (mainly mylonitic and some chloritoid-rich meta-graywacke), brown melt particles, quartzite, and calcite
KR8-043	296.94	Strongly altered suevite with a variety of lithic and mineral clasts: phyllite and slate, meta-graywacke (mylonitic, fine- to medium-grained meta-graywacke and some chloritoid-rich meta-graywacke), melt particles (brown in color), quartzite, and calcite; a few quartz grains with PDFs (1 or 2 sets)
KR8-045	300.41	Weakly sheared, heterogranular meta-graywacke (fine- to medium-grained); quartz grains show cracks and some are partially isotropic; some quartz grains with PDFs, generally decorated (1 or 2 sets), and some grains are partially toasted; a few quartz grains display broad, sometimes planar fluid inclusion trails
KR8-046	303.25	Very fine-grained slate; a small quartz veinlet with few quartz grains with PFs and PDFs; sample very similar to KR8-028
KR8-047	305.71	Alternating slate and sheared, fine-grained meta-graywacke; quartz grains show fracturing, some PFs, and a few PDFs (1 set) that are generally decorated
KR8-048	307.30	Altered protomylonitic medium-grained meta-graywacke, locally cataclastic; few PFs and PDFs; allanite and zircon occur; numerous penetrative fractures filled by iron oxides and/or by chlorite; presence of calcite aggregates

Appendix 1. *Continued.* Detailed petrographic descriptions (rock name, minerals present, etc.) and depths of the 121 samples documented for this study. This table is based on optical microscopic observations of 174 thin sections.

Sample no.	Depth (m)	Petrographic description
KR8-049	310.23	Medium-grained meta-graywacke breccia, locally sheared or cataclastic; some PFs and a few PDFs (1 set); many calcite aggregates occur
KR8-050	310.99	Heterogranular meta-graywacke; few PFs (no PDFs seen) in quartz grains; abundant calcite aggregates
KR8-051	312.40	Medium-grained to gritty meta-graywacke; quartz and feldspar grains show a lot of cracks; very few quartz grains with decorated PFs and only one grain with 1 set of decorated PDFs; calcite aggregates occur
KR8-052	315.75	Weakly sheared medium-grained meta-graywacke; a few quartz grains with decorated PFs (only one toasted quartz grain with 2 sets of PDFs); fractures filled with iron oxides and calcite occur
KR8-053	316.97	Sheared medium-grained meta-graywacke breccia; many decorated PFs and PDFs (1 or 2 sets) in partially or totally toasted quartz grains; abundant calcite veins and aggregates
KR8-054	320.62	Altered, fractured, mylonitic medium-grained meta-graywacke; a few decorated PFs and PDFs (1 set, only one grain with 2 sets) in partially toasted quartz grains; many penetrative fractures filled with iron oxides; similar to KR8-070
KR8-056	326.78	Medium-grained meta-graywacke (locally sheared); many quartz grains partially or totally toasted with decorated PFs and PDFs (1 or 2 sets); penetrative fractures filled with iron oxides
KR8-057	330.08	Altered, weakly sheared, medium-grained meta-graywacke, locally cataclastic; a few quartz grains with PFs and PDFs (1 set); low shock degree (~10 GPa); local cataclasis and veining filled with chlorite and epidote; many fractures filled with iron oxides; calcite aggregates
KR8-059	333.51	Mature heterogranular meta-graywacke, locally annealed, and brecciated; a lot of quartz grains with PDFs (1, 2, and 3 sets), some partially toasted; some penetrative fracturing
KR8-060	337.33	Sheared, fine-grained meta-graywacke (locally brecciated); a few quartz grains with decorated PFs and only two grains with PDFs (1 set); low shock degree (~5–6 GPa); calcite veins and aggregates occur
KR8-061	341.17	Unshocked heterogranular meta-graywacke; one penetrative fracture filled by iron oxides cut through the section; no diagnostic shock indicators
KR8-062	341.86	Sheared medium-grained meta-graywacke; a few quartz grains show decorated PFs and only one grain with PDFs (1 set); small calcite aggregates occur
KR8-063	343.57	Well-banded, fine-grained metasediment (bands of phyllite, slate, and fine-grained meta-graywacke); a lot of quartz grains with PFs and some with PDFs (1 or 2 sets); tabular opaque crystals and calcite pods occur
KR8-064	348.43	Phyllite with shocked quartz veins; very nice crenulation cleavage; many quartz grains show decorated PDFs (1 or 2 sets); cracks partially filled with iron oxides; many opaque minerals (pyrite)
KR8-065	352.31	Weakly sheared, heterogranular meta-graywacke; some PFs and PDFs (1 or 2 sets), some with decoration, in quartz grains
KR8-066	353.95	Altered, sheared, fractured, heterogranular meta-graywacke; many PDFs (1 or 2 sets); a large quartz vein cut through the section; penetrative fractures filled by iron oxides and chlorite occur
KR8-067	356.59	Weakly sheared, fractured, heterogranular meta-graywacke; many decorated PFs and PDFs (1 or 2 sets) in quartz grains, some partially toasted; many fractures filled with iron oxides
KR8-068	359.44	Altered, gritty meta-graywacke, locally cataclastic; a lot of PDFs (1 or 2 sets) in quartz grains (some partially toasted); many penetrative fractures filled by iron oxides and chlorite
KR8-069	361.18	Shocked (and somewhat brecciated) light greenish gray (chloritoid-rich), medium-grained meta-graywacke with granophyric material; some quartz grains with PDFs (1 or 2 sets) and some toasted; many graphic intergrowths of quartz and feldspar; calcite aggregates occur; very similar to KR8-106, KR8-121, and KR8-122a, but shocked
KR8-070	364.12	Mylonitic medium-grained meta-graywacke; a lot of PDFs (1 or 2 sets) in quartz grains (some partially toasted)
KR8-071	368.97	Mylonitic, medium-grained to gritty meta-graywacke, locally brecciated (annealed), and weakly shocked; few quartz grains with decorated PFs and PDFs (1 set); some fractures filled by iron oxides and chlorite
KR8-072	370.96	Sheared, fine- to medium-grained meta-graywacke; weakly shocked (<5 GPa); some quartz grains with subplanar fractures or PFs and a few with PDFs (1 set)
KR8-073	371.07	Medium-grained meta-graywacke; weakly shocked (<5 GPa); some quartz grains with subplanar fractures or PFs and a few with PDFs (1 set)
KR8-074	375.24	Medium-grained meta-graywacke; a lot of quartz grains with PFs and PDFs (1 or 2 sets); very similar to KR8-073, but shocked to a higher degree
KR8-075	377.78	Mylonite; unshocked
KR8-076	379.70	Weakly sheared medium-grained to gritty meta-graywacke (locally cataclastic); a few quartz grains with PDFs (1 set), some partially toasted; many fractures filled with secondary phyllosilicate minerals
KR8-077	380.98	Sheared fine-grained meta-graywacke; some quartz grains with decorated PFs and PDFs (1 or 2 sets), partially toasted; one mylonitic intercalation; minor fracturing; similar to KR8-072
KR8-078	382.17	Medium-grained to gritty meta-graywacke, partially annealed and locally cataclastic; no obvious shock effects
KR8-079	384.06	Weakly sheared heterogranular meta-graywacke; microfractures mostly filled with opaque minerals and phyllosilicate minerals; calcite veins; unshocked

Appendix 1. *Continued.* Detailed petrographic descriptions (rock name, minerals present, etc.) and depths of the 121 samples documented for this study. This table is based on optical microscopic observations of 174 thin sections.

Sample no.	Depth (m)	Petrographic description
KR8-080	384.54	Alternation of fine-grained metasediments (phyllite, slate, and meta-graywacke) with a wide quartzitic vein (~1 cm thick); many decorated PFs and PDFs in quartz (1 or 2 sets); plenty of calcite (veinlets and pods)
KR8-081	387.36	Weakly shocked and weakly sheared medium-grained meta-graywacke; a few quartz grains with PFs and PDFs (1 set; only 1 quartz grain seen with 2 sets); a large calcite vein and some calcite aggregates occur
KR8-082	387.78	Altered, sheared, weakly shocked, fine- to medium-grained meta-graywacke; some decorated PFs and PDFs (1 set; only one quartz grain with 2 sets) in quartz grains (some partially toasted); many cracks and fractures (some penetrative) filled by calcite, iron oxides, and chlorite; calcite aggregates occur
KR8-083	389.25	Altered, fractured, medium-grained to gritty meta-graywacke; only two quartz grains with 1 set of PFs each; several large penetrative fractures filled by iron oxides; some calcite veins and aggregates occur; no obvious shock effects
KR8-084	390.00	Slate/phyllite; no shock deformation
KR8-085	392.65	Altered, fractured, medium-grained to gritty meta-graywacke; only 4 quartz grains show decorated PFs; many fractures filled with iron oxides and chlorite
KR8-086	393.07	Altered, weakly shocked, heterogranular meta-graywacke; many quartz grains display decorated PFs (only 2 grains with decorated PDFs, 1 and 2 sets, respectively); some calcite aggregates occur
KR8-087	394.30	Altered medium-grained meta-graywacke; many PFs and some decorated PDFs (1 or 2 sets) in quartz grains (some partially toasted); a large penetrative fracture with halo of secondary calcite; abundant chlorite
KR8-088	395.25	Fine- to medium-grained meta-graywacke (weakly shocked); a few quartz grains show irregular fluid inclusion trails; a lot of calcite aggregates and veinlets; no obvious shock effects
KR8-089	397.30	Shocked medium-grained meta-graywacke partially brecciated; quartz grains display some decorated PFs and PDFs (1 set), some grains are partially toasted; calcite veinlets and aggregates occur; several fractures filled with iron oxides; few quartz grains contain rutile fibers
KR8-090	398.80	Weakly sheared, fine- to medium-grained meta-graywacke; no trace of shock deformation
KR8-091	400.35	Altered gritty meta-graywacke, fractured, and locally brecciated; some quartz grains with decorated PFs and PDFs (two quartz grains with 2 sets of decorated PDFs); many fractures (shock fracturing?) filled with chlorite and iron oxides
KR8-092	403.00	Altered medium-grained meta-graywacke; few quartz grains with decorated PFs and PDFs (1 set; only 2 grains seen with 2 sets); minor fracturing; calcite veinlets and aggregates occur
KR8-093	403.64	Altered gritty meta-graywacke locally cataclastic and fractured; only two quartz grains with PFs; numerous penetrative fractures, filled or not with iron oxides and chlorite; no obvious shock effects
KR8-094	404.18	Gritty meta-graywacke; a few quartz grains with PFs
KR8-095	405.34	Altered, fractured, and mylonitic fine-grained meta-graywacke; weakly shocked; mica-rich shear bands cut by a vein (impact breccia?); many fractures filled with iron oxides and/or secondary calcite; two quartz grains with shear fractures and PFs
KR8-096	406.31	Medium-grained meta-graywacke, locally brecciated, and fractured; some quartz grains with PFs and a few with PDFs (1 or 2 sets); several fractures (shock compression resulted?)
KR8-097	409.67	Altered sheared medium-grained to gritty meta-graywacke (locally annealed); no obvious shock effects
KR8-098	410.74	Medium-grained meta-graywacke (fractured); quartz grains (partially toasted) display decorated, curved, or subplanar fractures, sometimes PFs and PDFs (1 or 2 sets); a lot of fractures; a few quartz grains contain rutile fibers
KR8-099	412.92	Gritty meta-graywacke (fractured, locally brecciated, and weakly sheared); quartz grains display sets of subplanar fractures (some decorated), some PFs, and very few PDFs (1 set); many fractures filled with iron oxides
KR8-100	412.74	Unshocked, sheared, heterogranular meta-graywacke; calcite aggregates occur; no shock deformation
KR8-101	414.28	Altered gritty meta-graywacke; a few quartz grains with PFs; minor fractures filled by iron oxides; a few calcite aggregates occur
KR8-102	416.84	Monomict meta-graywacke breccia (sheared medium-grained meta-graywacke); quartz grains display rare decorated PFs and PDFs (1 set); some fractures and secondary calcite veinlets and aggregates occur
KR8-103	417.39	Heterogranular (from medium-grained to gritty) meta-graywacke and suevite; few quartz grains show decorated PFs (only one grain with 1 set of PDFs); calcite aggregates occur; suevite with mainly meta-graywacke clasts, besides, quartz, feldspar, melt particles, and calcite clasts
KR8-104	417.60	Altered, fine-grained meta-graywacke (locally cataclastic); a few quartz grains are partially toasted and display decorated PFs (only three grains with 1 set of PDFs); calcite aggregates occur
ADE-8a	418.05	Altered suevite veinlet (~1 cm thick) in fine metasediment (from phyllite to fine-grained meta-graywacke, locally mylonitic); a variety of lithic and mineral clasts: fine- to medium-grained meta-graywacke (altered), melt particles (brown in color), quartz, and calcite; few quartz grains displays PFs and only two quartz grains with decorated PDFs (1 set)
KR8-106	421.88	Light greenish gray (chloritoid-rich), medium-grained meta-graywacke with granophyric material; cuneiform-shaped intergrowths of quartz in feldspar; many calcite aggregates and veins occur; no distinct shock deformation; very similar to KR8-69, KR8-121, and KR8-122a

Appendix 1. *Continued.* Detailed petrographic descriptions (rock name, minerals present, etc.) and depths of the 121 samples documented for this study. This table is based on optical microscopic observations of 174 thin sections.

Sample no.	Depth (m)	Petrographic description
KR8-107	422.36	Altered suevite with a variety of lithic and mineral clasts: melt particles (brown in color, very heterogeneous in shape, from subangular to rounded), light gray (chloritoid-rich) medium-grained meta-graywacke (similar to KR8-106), meta-graywacke, quartz, slate and phyllite, and calcite; a few quartz grains display decorated PFs and PDFs (1 set); many calcite aggregates occur
KR8-108	424.78	Shocked heterogranular (form fine-grained to gritty) meta-graywacke (partially sheared) with a thick (~1.5 cm) quartz vein; several decorated PFs and PDFs (1 or 2 sets) in quartz grains (some are partially toasted); a large shocked quartz vein occur, cross-cut by calcite aggregates and veinlets (chlorite is also associated); a large pyrite flake
KR8-109	425.24	Gritty meta-graywacke; one quartz grains with shear fractures (penetrative fracturing); a few quartz grains show curved and subplanar PFs; fractures filled by iron oxides occur; pyrite infill of a cataclastic zone
KR8-110	429.31	Altered, shocked, brecciated, medium-grained meta-graywacke; several decorated PFs and PDFs (1 or 2 sets) in quartz grains (a few are partially toasted); calcite veinlets and aggregates occur; many fractures filled by calcite or chlorite
KR8-111	432.03	Quartz, shocked, fractured, and locally cataclastic (large vein); several fractures occur and show preferential orientations (subparallel fractures); many PFs and PDFs (1 or 2 sets) in quartz grains (locally toasted); some part of the section display cataclastic quartz (angular quartz fragments)
KR8-112	434.33	Suevite with a variety of lithic and mineral clasts: meta-graywacke (altered), slate and phyllite, quartz, calcite, and melt particles; clasts are small in size (2 mm maximum); only two quartz grains show PFs
KR8-113	434.59	Suevite with a variety of lithic and mineral clasts: fine- to medium-grained meta-graywacke (dominant, more or less altered, some show calcite veinlets and/or fractures filled with iron oxides), melt particles (brown in color; variety of shape), slate and phyllite, quartz, and calcite; a few quartz grains show decorated PFs or PDFs (1 set)
KR8-114	434.75	Suevite with a variety of lithic and mineral clasts: fine- to medium-grained meta-graywacke (more or less altered), melt particles (brown in color), slate and phyllite, quartz, and calcite; a few quartz grains show decorated PFs and only 2 grains seen with decorated PDFs (1 set); very similar to KR8-113, but with meta-graywacke clasts less abundant
KR8-115	437.37	Unshocked, altered, fine- to medium-grained meta-graywacke; calcite aggregates occur; no distinct shock deformation
KR8-117	439.87	Altered medium-grained to gritty meta-graywacke; some quartz grains with PFs and PDFs (1 or 2 sets); several opaque minerals (pyrite); a lot of chlorite; a sliver of impact breccia (suevite veinlet?)
CAN-31	440.32	Altered suevite with a variety of lithic and mineral clasts: fine- to medium-grained altered meta-graywacke, melt particles (brown in color, a large particle of ~1 cm), slate and phyllite, quartz, and calcite; a few quartz grains display PFs
KR8-119	441.87	Altered gritty meta-graywacke; a few quartz grains with PFs (no PDFs seen); penetrative fracturing filled by iron oxides, chlorite, or calcite; calcite aggregates occur
KR8-120	442.11	Altered mylonitic medium-grained meta-graywacke; some quartz grains show PDFs (1 or 2 sets); a lot of fractures filled by chlorite or calcite; a breccia veinlet cutting through the section
KR8-121	446.02	Light greenish gray (chloritoid-rich), medium-grained meta-graywacke, partially sheared, and with granophyric material; cuneiform-shaped intergrowths of quartz and feldspar; calcite aggregates; unshocked; very similar to KR8-069, KR8-106, and KR8-122a
KR8-122	446.69	Altered, weakly shocked, medium-grained meta-graywacke with intense cataclasis (locally brecciated); shock fracturing (shock pressure <8 GPa); a lot of calcite aggregates occur; no PDFs seen
KR8-122a	447.14	Light greenish gray (chloritoid-rich), medium-grained meta-graywacke, partially sheared, and with granophyric material; cuneiform-shaped intergrowths of quartz in feldspar (or poikiloblastic nature); abundant calcite aggregates and chloritoid; no shock recorded; very similar to KR8-069, KR8-106, and KR8-121
KR8-123	447.96	Altered medium-grained to gritty meta-graywacke (partially annealed); many fractures filled with calcite and chlorite; no PDFs (only 3 or 4 quartz grains with PFs)
KR8-124	449.12	Altered sheared heterogranular meta-graywacke (in part brecciated); many calcite aggregates occur; fractures filled with iron oxides; no distinct shock deformation
KR8-125	451.23	Weakly sheared medium-grained to gritty meta-graywacke; calcite aggregates; no diagnostic shock indicators



Drill core LB-08A, Bosumtwi impact structure, Ghana: Geochemistry of fallback breccia and basement samples from the central uplift

Ludovic FERRIÈRE^{1*}, Christian KOEBERL¹, Wolf Uwe REIMOLD², and Dieter MADER¹

¹Department of Geological Sciences, University of Vienna, Althanstrasse 14, A-1090 Vienna, Austria

²Museum of Natural History (Mineralogy), Humboldt University, Invalidenstrasse 43, D-10115 Berlin, Germany

*Corresponding author. E-mail: ludovic.ferriere@univie.ac.at

(Received 16 September 2006; revision accepted 01 January 2007)

Abstract—The 1.07 Myr old Bosumtwi impact structure in Ghana (West Africa), which measures 10.5 km in diameter and is largely filled by Lake Bosumtwi, is associated with one of four currently known tektite strewn fields. Two boreholes were drilled to acquire hard-rock samples of the deep crater moat and from the flank of the central uplift (LB-07A and LB-08A, respectively) during a recent ICDP-sponsored drilling project.

Here we present results of major and trace element analysis of 112 samples from drill core LB-08A. This core, which was recovered between 235.6 and 451.33 m depth below lake level, contains polymict lithic breccia intercalated with suevite, which overlies fractured/brecciated metasediment. The basement is dominated by meta-graywacke (from fine-grained to gritty), but also includes some phyllite and slate, as well as suevite dikelets and a few units of a distinct light greenish gray, medium-grained meta-graywacke.

Most of the variations of the major and trace element abundances in the different lithologies result from the initial compositional variations of the various target rock types, as well as from aqueous alteration processes, which have undeniably affected the different rocks.

Suevite from core LB-08A (fallback suevite) and fallout suevite samples (from outside the northern crater rim) display some differences in major (mainly in MgO, CaO, and Na₂O contents) and minor (mainly Cr and Ni) element abundances that could be related to the higher degree of alteration of fallback suevites, but also result from differences in the clast populations of the two suevite populations. For example, granite clasts are present in fallout suevite but not in fallback breccia, and calcite clasts are present in fallback breccia and not in fallout suevite. Chondrite-normalized rare earth element abundance patterns for polymict impact breccia and basement samples are very similar to each other.

Siderophile element contents in the impact breccias are not significantly different from those of the metasediments, or compared to target rocks from outside the crater rim. So far, no evidence for a meteoritic component has been detected in polymict impact breccias during this study, in agreement with previous work.

INTRODUCTION

The 1.07 Myr old, well-preserved Bosumtwi impact structure (centered at 06°30'N, 01°25'W) is situated in the Ashanti region of Ghana, West Africa. It is a complex impact structure, 10.5 km in diameter, with a pronounced rim and a small central uplift (Scholz et al. 2002). The crater is mostly filled by Lake Bosumtwi, which is ~8 km in diameter. The Bosumtwi impact structure is also associated with the Ivory Coast tektites, on the basis of the geographical location of the tektite strewn field, as well as identical ages and matching

chemical and isotopic compositions of the tektites and the Bosumtwi crater rocks (Schnetzler et al. 1966, 1967; Gentner et al. 1967, 1969; Kolbe et al. 1967; Jones 1985; Koeberl et al. 1997). Bosumtwi was recently the subject of an international and multidisciplinary drilling project by the International Continental Scientific Drilling Program (ICDP; see below and Koeberl et al. 2007 for more information).

Here, we present results of major and trace element analysis of 112 samples from drill core LB-08A. We also provide a brief comparison of chemical data for LB-08A (fallback breccia and basement) samples with those for

Bosumtwi target rocks and suevite from the fallout deposit sampled to the north of the crater structure.

GEOLOGICAL SETTING AND SAMPLES

Geological Setting and Previous Work

Geological investigations around Lake Bosumtwi were first performed in the 1930s (Junner 1937) and continued in the 1960s (Woodfield 1966; Moon and Mason 1967; Jones et al. 1981). A new geological map (Koeberl and Reimold 2005) summarizes the results of these early studies but also includes observations on new outcrops revealed by recent road construction as well as observations obtained from shallow drilling on and beyond the northern crater rim (Boamah and Koeberl 2003). The crater was formed in lower greenschist facies metasediments of the 2.1–2.2 Gyr Birimian Supergroup (Wright et al. 1985; Leube et al. 1990). The Birimian Supergroup rocks consist of an assemblage of metasediments, including phyllites, meta-tuffs, meta-graywackes, quartzitic meta-graywackes, shales, and slates (Koeberl and Reimold 2005). Proterozoic granitic intrusions, weathered granitoid dikes, and dolerite and amphibolite dikes are also present in the region around the crater (e.g., Junner 1937; Woodfield 1966; Moon and Mason 1967; Reimold et al. 1998). Numerous outcrops of breccia were identified in the environs of the crater (e.g., Junner 1937; Woodfield 1966; Moon and Mason 1967), but it is not clear whether or not all breccias are impact-related (Reimold et al. 1998). On the basis of composition and texture, Boamah and Koeberl (2003) distinguished three types of impact breccia at the Bosumtwi crater: an autochthonous monomict breccia (occurs on the northern part of the crater rim), a probably allochthonous polymict lithic impact breccia (also to the north of the crater rim), and a suevitic breccia (occurs to the north and south of the crater and along the northern crater rim; contains impact melt fragments and a variety of country rock clasts [meta-graywacke, phyllite, shale, and granite] of up to about 40 cm in size).

Target rocks from outside the crater rim and suevite samples from the crater rim were analyzed earlier for their major and trace element compositions (Koeberl et al. 1998; Boamah and Koeberl 2003; Dai et al. 2005; soils from the environs of the Bosumtwi crater were also analyzed for their elemental abundances by Boamah and Koeberl [2002]), and some samples were analyzed for their O, Sr, and Nd isotopic compositions (Koeberl et al. 1998).

Drill Core LB-08A

The core LB-08A was drilled on the outer flank of the central uplift, into the crater fill and underlying basement, to a depth of 451.33 m. Located in the northwestern part of the uplift structure (6°30'33"N, 1°24'45"E), the drilling was

situated on seismic survey lines that were established during the preparation phase of the drilling project (see Koeberl et al. 2007 for more information). The central uplift was identified on multichannel seismic reflection profiles; it has an apparent diameter of 1.9 km and a maximum height of about 130 m above the surrounding moat (e.g., Scholz et al. 2002).

The drill core displays a variety of lithologies (in order of decreasing abundance): meta-graywacke, slate, phyllite, polymict impact breccia, and monomict lithic impact breccia. The distinction and characterization of the different rock types is based on petrographic observations, and the classification follows definitions by Stöffler and Grieve (1994) for impact breccia, and Jackson (1997) and Brodie et al. (2004) for metasediments (more details are provided in Ferrière et al. 2007). The core can be divided into two main parts: the uppermost 25 m that are composed of polymict lithic impact breccia (clast-supported) intercalated with suevite (containing melt fragments), and the other part of the core (between 262 to 451 m) which is dominated by autochthonous, fractured/brecciated metasediment, which is locally brecciated (monomict lithic breccia) and intersected by suevite dikelets.

The upper part of the core, between 235.6 and 262 m (Fig. 1), has been interpreted as a fallback impact breccia deposit (Ferrière et al. 2007). This suevite has a fine-grained fragmental matrix (39 to 45 vol%) and contains a variety of lithic clasts and mineral fragments: meta-graywacke, phyllite, slate, quartzite, carbon-rich organic shale, and calcite, as well as impact-melt particles, diaplectic quartz glass, unshocked quartz, fractured quartz, quartz with shock-characteristic planar deformation features (PDFs; up to 4 sets of different orientations), phyllosilicate minerals, epidote, sphene, and opaque minerals.

The lower part of the core (Fig. 2), between 262 and 451 m, represents the crater basement, which has been shocked (as shown by, e.g., the presence of PDFs in quartz grains) and fractured in situ during the formation of the impact crater (for more information on drill core LB-08A, see Ferrière et al. 2007). The sharp transition from impact breccia to basement is located at a depth of ~262 m below lake level. The basement is composed of an alternating sequence of metasediment comprising (in order of decreasing abundance) meta-graywacke (dominant), phyllite, and slate, with locally occurring monomict lithic breccia, light greenish gray, medium-grained meta-graywacke (which contains some clasts of granophyric material), and suevite dikelets (likely injections into the metasediment, up to 80 cm thick; occurring between 279.5 and 298 m and between 418 and 440 m). The metasediment displays a large variation in lithology and grain size (from fine-grained to gritty; Ferrière et al. 2007).

Samples from the central uplift display a variety of alteration effects: alteration of plagioclase to sericite, biotite

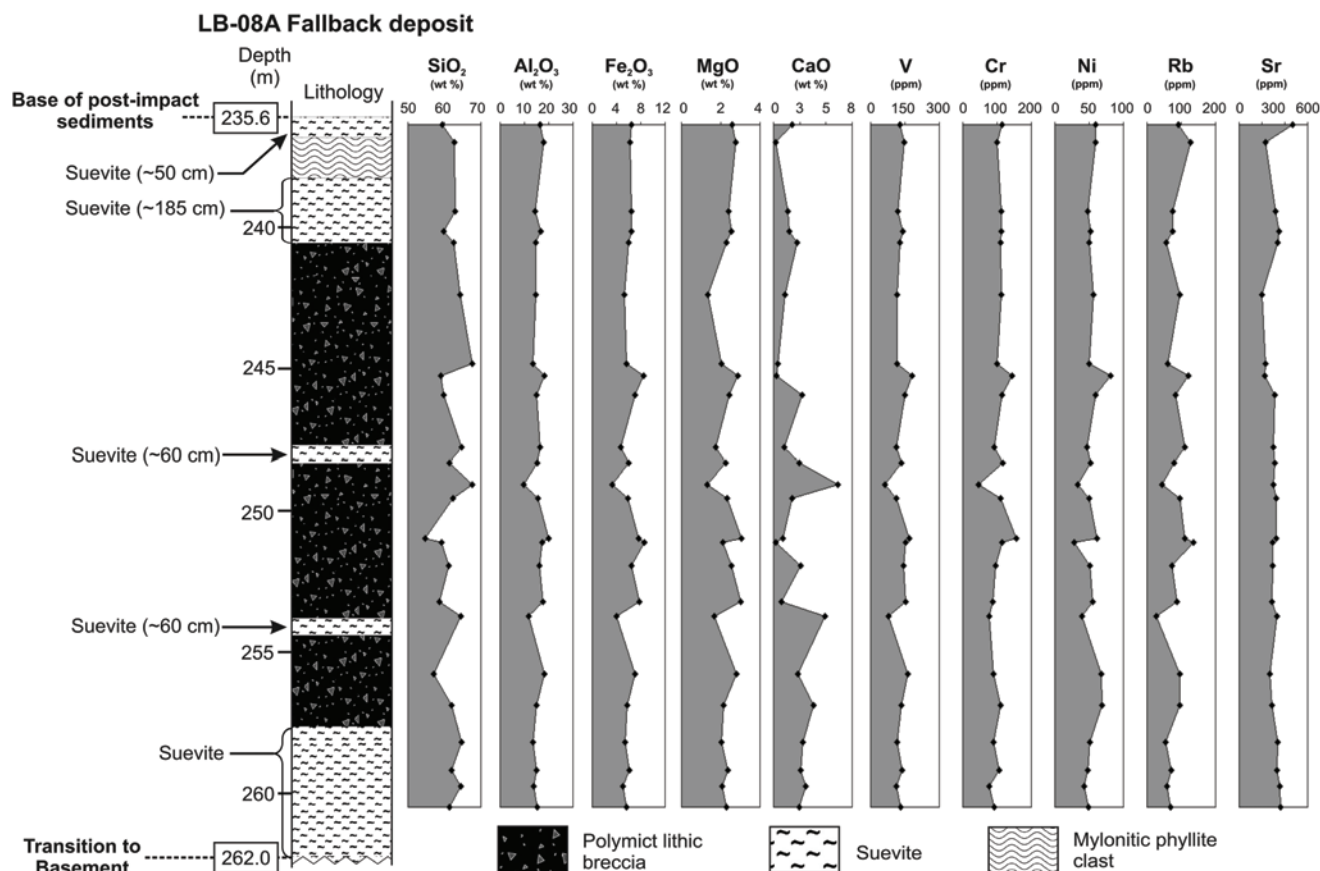


Fig. 1. Lithostratigraphy of the uppermost part (fallback deposit; between 235.6 to 262 m) of core LB-08A into the central uplift of the Bosumtwi impact structure, comparing the variations of concentrations of some major (SiO₂, Al₂O₃, Fe₂O₃, MgO, and CaO) and trace (V, Cr, Ni, Rb, and Sr) elements with depth.

to chlorite, fractures that are filled with iron oxides, secondary pyrite, and secondary calcite veinlets and aggregates, and the matrices of polymict impact breccias are composed to a large degree of very fine-grained phyllosilicates (Ferrière et al. 2007). Calcite veinlets and aggregates in suevite samples from the fallback deposit have been interpreted as the result of hydrothermal circulation in the rock after the impact event (Ferrière et al. 2007). No systematic change regarding the intensity of secondary alteration throughout the core has been identified in that detailed petrographic study.

Samples

One hundred and twenty one samples, comprising all lithologies present, were taken from core LB-08A, between 235.77 m (KR8-001) and 451.23 m (KR8-125) depth, in order to cover the complete variety of different lithologies present in the core (Ferrière et al. 2007). One hundred and twelve samples, comprising polymict lithic impact breccia (13 samples), suevite (20 samples), meta-graywacke (67 samples), slate-phyllite (8 samples), and light greenish gray meta-graywacke (4 samples) were analyzed.

EXPERIMENTAL METHODS

Samples with masses ranging from 30 to 500 g were taken from drill core LB-08A during the sampling party at the GeoForschungsZentrum (GFZ) in Potsdam, Germany, where the core is kept at ICDP headquarters. Samples were cut at the GFZ and mailed to Vienna. Representative aliquots weighing about 20 to 30 g of these samples were crushed in polyethylene wrappers and powdered in a mechanical agate mill for bulk chemical analysis. Special attention was paid to avoid clasts larger than 5 mm in diameter for the impact breccia samples, to obtain relatively representative compositions. Due to the variable abundance of matrix (from less than 2 to 48 vol%) in the polymict lithic impact breccia samples (Ferrière et al. 2007), and also due to the occurrence of some clasts larger than the core diameter, some minor heterogeneities can result from the restrictions of the sample preparation.

The contents of major and trace elements (V, Cr, Co, Ni, Cu, Zn, Rb, Sr, Y, Zr, Nb, and Ba) were determined by standard X-ray fluorescence (XRF) spectrometry at the University of the Witwatersrand, Johannesburg (South

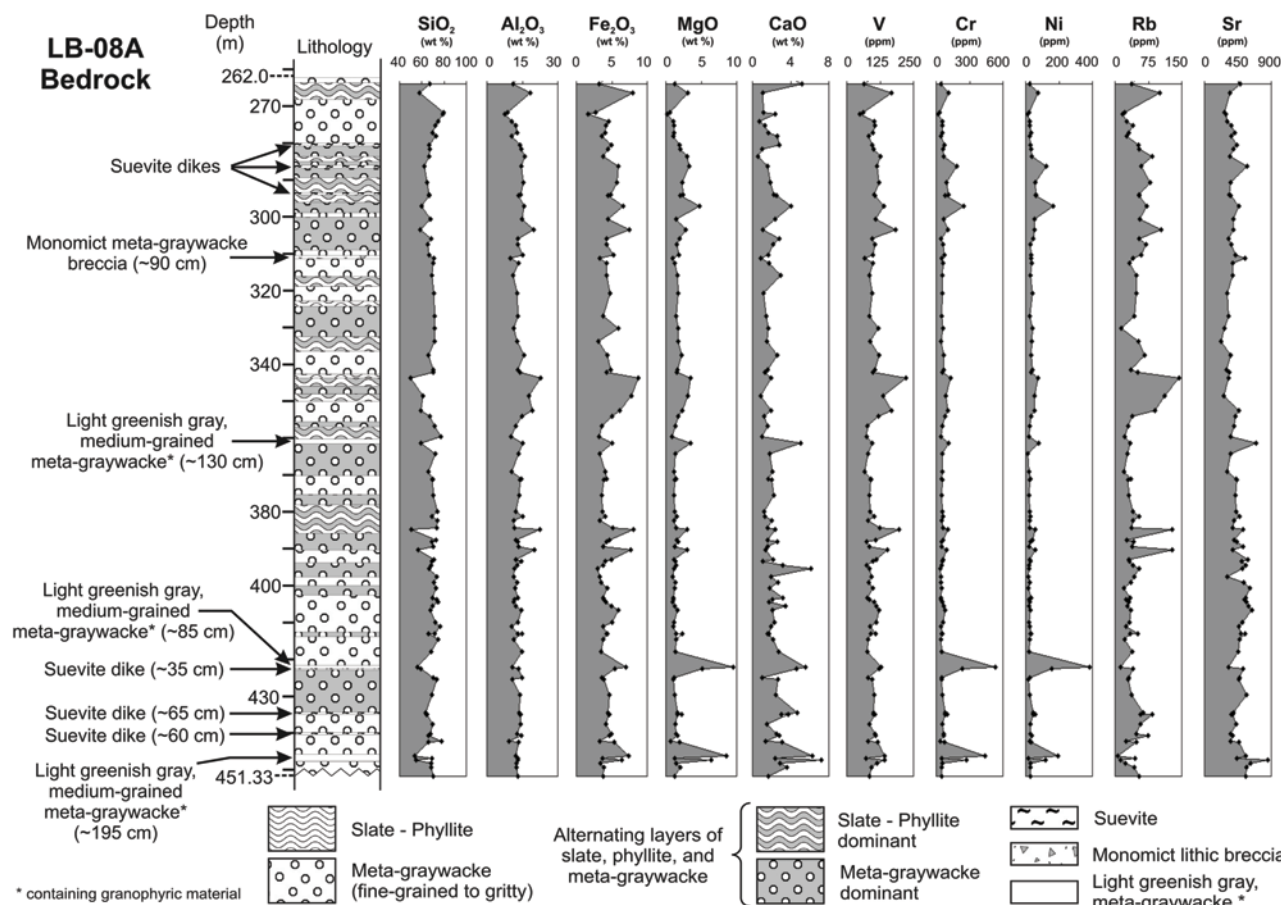


Fig. 2. Lithostratigraphy of the basement section (between 262 to 451.33 m) of core LB-08A into the central uplift of the Bosumtwi impact structure, comparing the variation of concentrations of some major (SiO_2 , Al_2O_3 , Fe_2O_3 , MgO , and CaO) and trace (V, Cr, Ni, Rb, and Sr) elements with depth.

Africa). Precision and accuracy values are (in wt%) about 0.4 for SiO_2 , 0.03 for TiO_2 , 0.2 for Al_2O_3 and MgO , 0.1 for Fe_2O_3 , CaO and K_2O , 0.01 for MnO and P_2O_5 , and 0.3 for Na_2O (for more details, see Reimold et al. 1994).

Abundances of some major elements (Fe, Na, and K) and other trace elements (Sc, Cr, Co, Ni, Zn, As, Se, Br, Rb, Sr, Zr, Sb, Cs, Ba, Hf, Ta, Th, and U), including the rare earth elements (REE), were determined by instrumental neutron activation analysis (INAA) at the Department of Geological Sciences, University of Vienna (Austria). About 160 mg of each sample powder and about 90 mg of several international rock standards: the carbonaceous chondrite Allende (Smithsonian Institution, Washington, USA; Jarosewich et al. 1987), granite ACE (Centre de Recherche Pétrographique et Géochimique, Nancy, France; Govindaraju 1994), and granite G-2 (USGS; Govindaraju 1994) were sealed in polyethylene capsules. Samples and standards were irradiated together in the 250 kW Triga reactor of the Atomic Institute of the Austrian Universities for 8 hours at a neutron flux of $2.10^{12} \text{ n} \cdot \text{cm}^{-2} \cdot \text{s}^{-1}$. More details on instrumentation, as well as accuracy and precision values of our method, have been

described in, e.g., Koeberl (1993) and Son and Koeberl (2005). For all samples, the Fe, Na, K, Cr, Co, Ni, Zn, Rb, Sr, Zr, and Ba concentrations were determined by both XRF and INAA.

RESULTS

The major and trace element contents of the 112 LB-08A samples are summarized in the form of average compositions for each different lithology (Table 1). Individual data are not listed here, but will be published elsewhere. To allow discussion of the general geochemical patterns of the samples investigated in this study, the contents of some major (SiO_2 , Al_2O_3 , Fe_2O_3 , MgO , and CaO) and trace (V, Cr, Ni, Rb, and Sr) elements have been plotted against depth in the uppermost part (fallback deposit) and the basement section of core LB-08A, and are shown in Figs. 1 and 2, respectively. These specific trace elements have been selected because of the extent of their relative abundance variations between the various lithologies and also within each lithological type. Elements the abundances of which show significant

Table 1. The average and range of compositions of analyzed samples from borehole LB-08A, compared to those of fallout suevites, target rocks, and Ivory Coast tektites.^a

	Suevite (n = 20)		Polymict lithic impact breccia (n = 13)		Meta-graywacke (n = 67)		Phyllite-slate (n = 8)	
	Average	Range	Average	Range	Average	Range	Average	Range
SiO ₂	63.16 ± 2.44	59.01–66.79	61.44 ± 3.92	54.80–67.74	70.68 ± 3.18	65.49–79.73	57.85 ± 5.19	50.14–64.41
TiO ₂	0.55 ± 0.09	0.43–0.70	0.63 ± 0.15	0.28–0.81	0.41 ± 0.07	0.15–0.57	0.69 ± 0.15	0.40–0.95
Al ₂ O ₃	14.65 ± 1.01	13.33–16.68	15.70 ± 2.84	9.64–20.12	12.67 ± 1.72	7.47–15.99	19.20 ± 2.68	14.59–22.86
Fe ₂ O ₃	5.49 ± 0.74	4.44–6.63	6.34 ± 1.65	3.31–8.64	4.07 ± 0.73	1.64–5.93	7.39 ± 1.11	5.25–8.71
MnO	0.06 ± 0.01	0.05–0.09	0.07 ± 0.02	0.03–0.10	0.05 ± 0.02	0.03–0.17	0.06 ± 0.02	0.04–0.10
MgO	2.50 ± 0.93	1.62–5.16	2.31 ± 0.54	1.30–3.04	1.39 ± 0.41	0.24–2.99	2.82 ± 0.63	1.33–3.45
CaO	2.67 ± 0.98	1.38–4.72	2.19 ± 1.88	0.20–6.14	2.05 ± 0.94	0.60–6.14	1.26 ± 0.65	0.23–2.35
Na ₂ O	2.94 ± 0.36	2.05–3.58	2.73 ± 0.62	1.85–4.00	3.77 ± 0.71	2.30–5.61	2.37 ± 0.60	1.75–3.30
K ₂ O	1.67 ± 0.36	0.87–2.37	2.08 ± 0.69	0.77–2.93	0.99 ± 0.39	0.29–2.25	2.94 ± 0.94	1.08–4.03
P ₂ O ₅	0.11 ± 0.02	0.08–0.15	0.12 ± 0.04	0.04–0.21	0.09 ± 0.02	0.03–0.15	0.18 ± 0.13	0.08–0.44
LOI	5.25 ± 0.87	3.67–7.01	5.25 ± 1.03	3.15–6.81	3.10 ± 1.61	1.53–9.44	4.90 ± 2.10	3.76–9.99
Total	99.06		98.86		99.26		99.66	
Sc	14.0 ± 2.6	9.7–18.2	17.9 ± 5.3	7.2–25.4	8.2 ± 1.8	3.1–13.2	20.5 ± 3.5	16.9–26.6
V	117 ± 14	96–142	135 ± 35	63–180	93 ± 16	50–127	166 ± 34	117–222
Cr	115 ± 51	71–249	103 ± 28	46–156	54 ± 11	21–79	105 ± 13	86–130
Co	17 ± 4	12–26	18 ± 6	8–27	10 ± 2	3–15	22 ± 4	17–27
Ni	65 ± 37	31–165	53 ± 15	28–82	27 ± 8	11–52	61 ± 9	53–76
Cu	27 ± 9	11–43	41 ± 21	8–90	24 ± 16	2–83	44 ± 12	28–64
Zn	66 ± 11	50–84	74 ± 19	43–103	43 ± 9	11–64	94 ± 12	82–111
As	14.3 ± 12.5	3.73–51.9	10.7 ± 8.0	1.35–24.9	4.09 ± 3.71	0.09–14.1	10.9 ± 11.8	0.91–29.3
Rb	67 ± 15	39–97	86 ± 31	28–135	38 ± 13	14–84	117 ± 17	97–143
Sr	387 ± 72	314–575	291 ± 32	226–329	434 ± 100	225–638	333 ± 103	203–522
Y	16 ± 4	12–23	21 ± 5	13–28	11 ± 2	7–17	20 ± 3	16–25
Zr	126 ± 15	103–152	134 ± 24	76–164	117 ± 21	56–171	122 ± 9	112–132
Nb	3.8 ± 0.7	3–5	4.7 ± 0.9	3–6	3.3 ± 0.4	3–4	5.5 ± 0.8	5–7
Sb	0.40 ± 0.16	0.22–0.69	0.36 ± 0.23	0.08–1.01	0.36 ± 0.24	0.03–0.98	0.38 ± 0.14	0.20–0.57
Cs	4.30 ± 1.42	2.50–7.31	4.34 ± 1.63	1.66–7.29	2.29 ± 0.85	1.00–5.74	5.76 ± 1.19	3.74–7.58
Ba	626 ± 124	322–803	742 ± 267	258–1129	537 ± 163	244–972	1023 ± 232	612–1279
La	20.5 ± 3.3	15.1–27.0	18.5 ± 4.7	9.2–25.4	19.3 ± 4.52	11.6–33.0	20.0 ± 2.4	17.1–25.2
Ce	42.4 ± 6.7	32.0–59.2	38.9 ± 10.4	16.8–51.8	38.9 ± 7.91	23.7–64.2	43.7 ± 5.0	38.8–53.1
Nd	20.8 ± 4.0	14.2–30.3	19.4 ± 5.5	9.4–26.1	16.7 ± 3.15	11.7–25.9	20.9 ± 2.4	18.2–25.5
Sm	3.91 ± 0.78	2.57–5.63	3.97 ± 1.00	1.74–5.67	2.95 ± 0.49	1.86–4.25	4.25 ± 0.48	3.72–4.97
Eu	1.13 ± 0.19	0.74–1.52	1.07 ± 0.27	0.47–1.54	0.89 ± 0.13	0.55–1.20	1.22 ± 0.20	1.00–1.57
Gd	3.36 ± 0.45	2.74–4.09	3.27 ± 0.85	1.87–5.12	2.52 ± 0.61	1.04–4.08	4.14 ± 1.20	2.84–5.87
Tb	0.49 ± 0.11	0.27–0.70	0.54 ± 0.12	0.32–0.75	0.39 ± 0.11	0.19–0.65	0.61 ± 0.13	0.46–0.84
Tm	0.23 ± 0.05	0.15–0.34	0.31 ± 0.08	0.20–0.45	0.17 ± 0.03	0.11–0.23	0.28 ± 0.04	0.22–0.32
Yb	1.50 ± 0.31	1.10–2.11	2.09 ± 0.55	1.26–3.11	1.12 ± 0.17	0.64–1.63	1.83 ± 0.22	1.50–2.13
Lu	0.24 ± 0.04	0.18–0.31	0.33 ± 0.09	0.20–0.50	0.18 ± 0.03	0.10–0.27	0.29 ± 0.04	0.23–0.36
Hf	3.12 ± 0.35	2.49–3.65	3.35 ± 0.71	1.61–4.29	3.07 ± 0.71	1.20–5.09	3.00 ± 0.19	2.75–3.24

Table 1. *Continued.* The average and range of compositions of analyzed samples from borehole LB-08A, compared to those of fallout suevites, target rocks, and Ivory Coast tektites.^a

	Suevite (n = 20)		Polymict lithic impact breccia (n = 13)		Meta-graywacke (n = 67)		Phyllite-slate (n = 8)	
	Average	Range	Average	Range	Average	Range	Average	Range
Ta	0.32 ± 0.05	0.23–0.42	0.36 ± 0.09	0.17–0.49	0.30 ± 0.08	0.13–0.58	0.56 ± 0.23	0.31–0.95
W	2.70 ± 1.51	0.08–6.17	3.30 ± 1.44	0.73–6.11	1.84 ± 1.59	0.05–5.45	3.00 ± 1.05	1.73–4.18
Th	3.17 ± 0.65	1.95–4.84	3.31 ± 0.61	2.28–3.95	2.91 ± 0.67	1.58–4.42	3.63 ± 0.33	3.27–4.18
U	1.39 ± 0.68	0.71–3.25	1.42 ± 0.83	0.61–3.02	1.07 ± 0.57	0.26–3.36	1.02 ± 0.34	0.65–1.50
K/U	12,018 ± 4946	3877–20,958	15,751 ± 8611	2117–30,685	9518 ± 5467	2245–28,896	27,716 ± 14,327	5996–49,525
Zr/Hf	40.4 ± 3.7	34.6–52.2	40.3 ± 2.9	36.2–47.1	38.7 ± 4.15	26.1–47.1	40.6 ± 2.3	35.6–43.1
La/Th	6.57 ± 0.84	5.25–8.40	5.71 ± 1.47	2.36–7.90	6.69 ± 0.85	3.80–9.01	5.52 ± 0.62	4.53–6.57
Hf/Ta	9.94 ± 0.92	8.01–11.3	9.50 ± 1.42	7.60–12.7	10.6 ± 2.23	6.05–16.4	6.13 ± 2.41	3.25–9.96
Th/U	2.77 ± 1.18	0.93–5.36	3.04 ± 1.52	0.76–5.42	3.25 ± 1.43	0.82–10.6	3.89 ± 1.19	2.64–5.40
La _N /Yb _N	9.51 ± 2.00	5.49–12.4	6.34 ± 2.12	2.64–10.5	11.8 ± 2.61	4.82–18.5	7.50 ± 1.47	6.33–10.4
Eu/Eu*	0.98 ± 0.05	0.91–1.09	0.91 ± 0.07	0.80–1.03	1.01 ± 0.11	0.81–1.51	0.88 ± 0.06	0.82–0.95
CIA	56	47–63	60	38–73	54	41–69	67	64–73

^aMajor element data in wt%, trace element data in ppm. All Fe as Fe₂O₃. n = number of samples; N = chondrite-normalized (Taylor and McLennan 1985); chemical index of alteration (CIA) = (Al₂O₃/[Al₂O₃ + CaO + Na₂O + K₂O]) × 100 in molecular proportions. All ratios are the average of the ratios calculated for each samples.

Table 1. *Continued.* The average and range of compositions of analyzed samples from borehole LB-08A, compared to those of fallout suevites, target rocks, and Ivory Coast tektites.^a

	Metasediments ^b (n = 75)		Light greenish gray meta-graywacke (n = 4)		Fallout suevite (n = 11) ^c		Meta-graywacke and phyllite (n = 7) ^d		Granite dike (n = 2) ^d		Pepiakese granite (n = 3) ^d		Ivory Coast tektites ^d	
	Average	Range	Average	Range	Average	Range	Average	Range	Average	Range	Average	Range	Average	Range
SiO ₂	69.17 ± 5.34	50.14–79.73	55.91 ± 2.59	53.49–59.48	63.58 ± 3.01	66.75 ± 1.77	68.74 ± 0.50	57.81 ± 6.28	67.58					
TiO ₂	0.44 ± 0.12	0.15–0.95	0.65 ± 0.05	0.58–0.68	0.64 ± 0.07	0.66 ± 0.07	0.50 ± 0.00	0.46 ± 0.34	0.56					
Al ₂ O ₃	13.44 ± 2.79	7.47–22.86	12.81 ± 1.83	10.78–15.12	15.58 ± 1.15	15.27 ± 1.31	15.91 ± 0.18	16.45 ± 2.42	16.74					
Fe ₂ O ₃	4.44 ± 1.30	1.64–8.71	6.45 ± 1.01	5.05–7.34	6.58 ± 2.24	6.37 ± 0.62	3.97 ± 0.31	6.09 ± 3.97	6.16					
MnO	0.05 ± 0.02	0.03–0.17	0.10 ± 0.01	0.08–0.11	0.11 ± 0.05	0.028 ± 0.009	0.014 ± 0.013	0.067 ± 0.047	0.06					
MgO	1.56 ± 0.63	0.24–3.45	6.97 ± 2.66	3.48–9.48	1.43 ± 0.54	2.12 ± 0.25	1.44 ± 0.36	6.63 ± 4.61	3.46					
CaO	1.96 ± 0.93	0.23–6.14	6.02 ± 0.93	5.06–7.19	1.39 ± 0.61	0.19 ± 0.13	0.31 ± 0.01	4.36 ± 2.94	1.38					
Na ₂ O	3.62 ± 0.81	1.75–5.61	2.54 ± 1.28	0.96–3.62	1.73 ± 0.53	2.26 ± 0.95	4.14 ± 0.49	6.04 ± 4.14	1.90					
K ₂ O	1.22 ± 0.77	0.29–4.03	0.50 ± 0.54	0.12–0.88	1.27 ± 0.38	1.80 ± 0.61	1.92 ± 0.15	0.67 ± 0.43	1.95					
P ₂ O ₅	0.10 ± 0.05	0.03–0.44	0.15 ± 0.03	0.13–0.19	0.09 ± 0.03	0.06 ± 0.03	0.06 ± 0.00	0.10 ± 0.08						
LOI	3.30 ± 1.73	1.53–9.99	8.07 ± 1.53	5.78–8.90	7.68 ± 2.22	4.25 ± 0.59	2.98 ± 0.33	1.48 ± 0.71	0.002					
Total	99.30	100.2	100.2	100.1	100.1	99.76	99.98	100.15	99.79					
Sc	9.6 ± 4.4	3.1–26.6	17.2 ± 4.1	11.9–20.4	15.3 ± 5.3	15.5 ± 2.0	9.76 ± 0.02	17.5 ± 11.6	14.7					
V	102 ± 30	50–222	127 ± 22	95–143	120 ± 45	134 ± 13	91 ± 1	110 ± 54						
Cr	60 ± 20	21–130	339 ± 187	110–531	373 ± 615	165 ± 25	127 ± 30	517 ± 352	244					
Co	10.9 ± 4.6	3–27	31 ± 13	15–41	19.9 ± 12.7	12.1 ± 5.4	9.66 ± 3.74	30.4 ± 19.4	26.7					
Ni	31 ± 13	11–76	194 ± 137	76–386	106 ± 108	48 ± 15	49 ± 24	172 ± 114	157					

Table 1. *Continued.* The average and range of compositions of analyzed samples from borehole LB-08A, compared to those of fallout suevites, target rocks, and Ivory Coast tektites.^a

	Metasediments ^b (n = 75)		Light greenish gray meta-graywacke (n = 4)		Fallout suevite (n = 11) ^c		Meta-graywacke and phyllite (n = 7) ^d		Granite dike (n = 2) ^d		Pepiakese granite (n = 3) ^d		Ivory Coast tektites ^d	
	Average	Range	Average	Range	Average	Range	Average	Range	Average	Range	Average	Range	Average	Range
Cu	25.7 ± 16.6	2–83	13 ± 9	6–19	24 ± 21	6–19	15.5 ± 7.5	6–19	10.7 ± 7.7	6–19	24.3 ± 15.1	6–19	24.3 ± 15.1	6–19
Zn	49 ± 18	11–111	76 ± 12	61–88	73 ± 16	61–88	104 ± 13	61–88	82 ± 5	61–88	90 ± 59	61–88	90 ± 59	61–88
As	5.03 ± 5.64	0.09–29.3	84.7 ± 67.3	23.1–161	3.1 ± 1.0	23.1–161	7.00 ± 5.91	23.1–161	14.9 ± 12.3	23.1–161	12.7 ± 6.9	23.1–161	12.7 ± 6.9	23.1–161
Rb	47.3 ± 28.3	14–143	17 ± 13	5–35	51.4 ± 17.7	5–35	65.2 ± 26.2	5–35	69.9 ± 18.7	5–35	22.4 ± 19.4	5–35	22.4 ± 19.4	5–35
Sr	424 ± 104	203–638	608 ± 223	328–854	301 ± 56	328–854	152 ± 40	328–854	342 ± 31	328–854	377 ± 44	328–854	377 ± 44	328–854
Y	12 ± 3	7–25	12 ± 1	11–13	16 ± 2	11–13	19 ± 5	11–13	11 ± 1	11–13	11 ± 6	11–13	11 ± 6	11–13
Zr	118 ± 21	56–171	90 ± 14	78–109	122 ± 19	78–109	143 ± 12	78–109	129 ± 10	78–109	82 ± 21	78–109	82 ± 21	78–109
Nb	3.6 ± 0.9	3–7	3	3–3	8.0 ± 2.6	3–3	5.7 ± 0.8	3–3	3.7 ± 0.3	3–3	1.8 ± 1.3	3–3	1.8 ± 1.3	3–3
Sb	0.36 ± 0.22	0.03–0.98	1.59 ± 1.90	0.30–4.39	0.33 ± 0.16	0.30–4.39	0.20 ± 0.06	0.30–4.39	0.18 ± 0.04	0.30–4.39	0.42 ± 0.16	0.30–4.39	0.42 ± 0.16	0.30–4.39
Cs	2.69 ± 1.40	1.00–7.58	1.08 ± 0.62	0.48–1.93	3.71 ± 3.78	0.48–1.93	3.27 ± 1.48	0.48–1.93	4.22 ± 1.49	0.48–1.93	0.87 ± 0.46	0.48–1.93	0.87 ± 0.46	0.48–1.93
Ba	599 ± 241	244–1320	155 ± 161	46–387	563 ± 83	46–387	454 ± 112	46–387	605 ± 109	46–387	226 ± 117	46–387	226 ± 117	46–387
La	19.4 ± 4.3	11.6–33.0	12.7 ± 2.2	10.5–15.9	18.9 ± 5.1	10.5–15.9	23.4 ± 8.3	10.5–15.9	18.8 ± 4.0	10.5–15.9	15.6 ± 8.2	10.5–15.9	15.6 ± 8.2	10.5–15.9
Ce	39.5 ± 7.8	23.7–64.2	28.8 ± 5.8	23.8–37.2	38.8 ± 8.5	23.8–37.2	34.8 ± 11.8	23.8–37.2	39.4 ± 7.3	23.8–37.2	32.0 ± 14.9	23.8–37.2	32.0 ± 14.9	23.8–37.2
Nd	17.2 ± 3.3	11.7–25.9	16.3 ± 4.3	12.5–22.5	18.2 ± 4.8	12.5–22.5	26.5 ± 10.8	12.5–22.5	19.8 ± 6.4	12.5–22.5	17.5 ± 9.2	12.5–22.5	17.5 ± 9.2	12.5–22.5
Sm	3.10 ± 0.63	1.86–4.97	3.28 ± 0.64	2.81–4.17	3.53 ± 0.74	2.81–4.17	5.06 ± 1.68	2.81–4.17	3.74 ± 0.25	2.81–4.17	3.58 ± 1.87	2.81–4.17	3.58 ± 1.87	2.81–4.17
Eu	0.93 ± 0.18	0.55–1.57	0.95 ± 0.12	0.78–1.06	1.07 ± 0.18	0.78–1.06	1.29 ± 0.41	0.78–1.06	1.03 ± 0.14	0.78–1.06	1.19 ± 0.49	0.78–1.06	1.19 ± 0.49	0.78–1.06
Gd	2.72 ± 0.87	1.04–5.87	2.66 ± 0.46	2.18–3.08	2.92 ± 0.95	2.18–3.08	4.80 ± 1.73	2.18–3.08	3.40 ± 0.00	2.18–3.08	3.07 ± 1.45	2.18–3.08	3.07 ± 1.45	2.18–3.08
Tb	0.42 ± 0.13	0.19–0.84	0.47 ± 0.09	0.40–0.60	0.47 ± 0.10	0.40–0.60	0.73 ± 0.27	0.40–0.60	0.59 ± 0.02	0.40–0.60	0.47 ± 0.22	0.40–0.60	0.47 ± 0.22	0.40–0.60
Tm	0.18 ± 0.04	0.11–0.32	0.17 ± 0.02	0.15–0.20	0.33 ± 0.13	0.15–0.20	0.35 ± 0.11	0.15–0.20	0.22 ± 0.03	0.15–0.20	0.20 ± 0.09	0.15–0.20	0.20 ± 0.09	0.15–0.20
Yb	1.20 ± 0.28	0.64–2.13	1.13 ± 0.13	0.98–1.30	1.57 ± 0.28	0.98–1.30	2.14 ± 0.46	0.98–1.30	1.13 ± 0.05	0.98–1.30	1.18 ± 0.54	0.98–1.30	1.18 ± 0.54	0.98–1.30
Lu	0.19 ± 0.05	0.10–0.36	0.17 ± 0.02	0.15–0.21	0.23 ± 0.04	0.15–0.21	0.29 ± 0.05	0.15–0.21	0.16 ± 0.01	0.15–0.21	0.14 ± 0.07	0.15–0.21	0.14 ± 0.07	0.15–0.21
Hf	3.08 ± 0.68	1.20–5.09	2.34 ± 0.20	2.14–2.60	3.22 ± 0.24	2.14–2.60	4.04 ± 0.36	2.14–2.60	3.66 ± 0.12	2.14–2.60	1.88 ± 0.91	2.14–2.60	1.88 ± 0.91	2.14–2.60
Ta	0.33 ± 0.14	0.13–0.95	0.25 ± 0.14	0.17–0.46	0.30 ± 0.08	0.17–0.46	0.42 ± 0.11	0.17–0.46	0.28 ± 0.09	0.17–0.46	0.19 ± 0.08	0.17–0.46	0.19 ± 0.08	0.17–0.46
W	1.97 ± 1.57	0.05–5.45	3.89 ± 0.06	3.84–3.93	2.94 ± 0.61	3.84–3.93	0.64 ± 0.16	3.84–3.93	0.84 ± 0.04	3.84–3.93	0.54 ± 0.17	3.84–3.93	0.54 ± 0.17	3.84–3.93
Th	2.99 ± 0.67	1.58–4.42	1.75 ± 0.20	1.54–2.01	2.94 ± 0.61	1.54–2.01	3.94 ± 0.56	1.54–2.01	3.10 ± 0.27	1.54–2.01	2.21 ± 2.09	1.54–2.01	2.21 ± 2.09	1.54–2.01
U	1.06 ± 0.54	0.26–3.36	2.02 ± 2.22	0.76–5.34	1.05 ± 0.58	0.76–5.34	1.35 ± 0.15	0.76–5.34	1.75 ± 0.11	0.76–5.34	0.74 ± 0.53	0.76–5.34	0.74 ± 0.53	0.76–5.34
K/U	11,622 ± 8993	2245–49,525	1337 ± 44	1306–1368	10,568	1306–1368	11,389 ± 4357	1306–1368	9245 ± 1314	1306–1368	10,800 ± 7108	1306–1368	10,800 ± 7108	1306–1368
Zr/Hf	38.9 ± 4.0	26.1–47.1	38.1 ± 3.9	32.8–41.9	37.9	32.8–41.9	35.5 ± 3.7	32.8–41.9	35.4 ± 3.9	32.8–41.9	51.9 ± 19.6	32.8–41.9	51.9 ± 19.6	32.8–41.9
La/Th	6.56 ± 0.90	3.80–9.01	7.21 ± 0.56	6.65–7.86	6.54	6.65–7.86	6.15 ± 2.49	6.65–7.86	6.00 ± 0.77	6.65–7.86	10.9 ± 5.79	6.65–7.86	10.9 ± 5.79	6.65–7.86
Hf/Ta	10.0 ± 2.66	3.25–16.4	10.5 ± 3.32	5.66–13.1	11.6	5.66–13.1	10.1 ± 2.48	5.66–13.1	14.5 ± 4.08	5.66–13.1	12.7 ± 7.26	5.66–13.1	12.7 ± 7.26	5.66–13.1
Th/U	3.32 ± 1.41	0.82–10.6	1.53 ± 0.83	0.33–2.23	3.34	0.33–2.23	2.95 ± 0.51	0.33–2.23	1.79 ± 0.27	0.33–2.23	2.67 ± 0.91	0.33–2.23	2.67 ± 0.91	0.33–2.23
La _N /Yb _N	11.3 ± 2.82	4.82–18.5	7.75 ± 2.06	6.63–10.8	8.19	6.63–10.8	7.30 ± 1.93	6.63–10.8	11.2 ± 1.95	6.63–10.8	13.7 ± 13.2	6.63–10.8	13.7 ± 13.2	6.63–10.8
Eu/Eu*	0.99 ± 0.11	0.81–1.51	0.99 ± 0.07	0.92–1.08	1.10	0.92–1.08	0.83 ± 0.14	0.92–1.08	0.88 ± 0.09	0.92–1.08	1.16 ± 0.13	0.92–1.08	1.16 ± 0.13	0.92–1.08
CIA	55	41–73	46	41–49	70	41–49	72	41–49	63	41–49	47	41–49	47	41–49

^aMajor element data in wt%, trace element data in ppm. All Fe as Fe₂O₃; n = number of samples; N = chondrite-normalized (Taylor and McLennan 1985); chemical index of alteration (CIA) = (Al₂O₃/Al₂O₃ + CaO + Na₂O + K₂O) × 100 in molecular proportions. All ratios are the average of the ratios calculated for each sample.^bAverage of 68 meta-graywacke and 8 phyllite-slate samples.^cData from Boamah and Koebel (2003).^dData from Koebel et al. (1998).

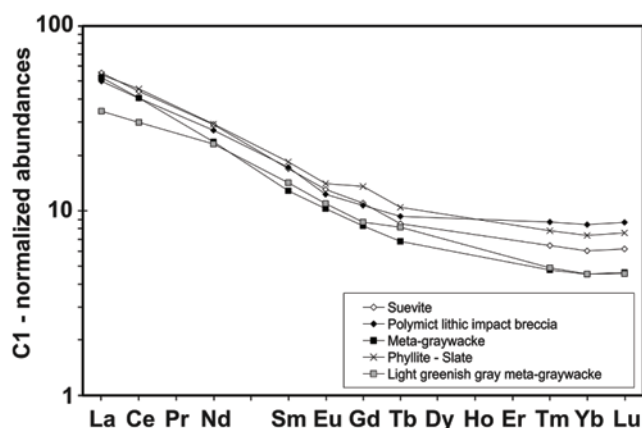


Fig. 3. Chondrite (C1)-normalized rare earth element distribution patterns for the averages of the various lithologies of core LB-08A. The ranges and patterns for the impact breccias and the various target rocks are very similar, indicating that no significant component that is not represented in the basement section contributed to the impact breccia mixtures and also that post-impact alteration was limited and did not lead to any significant REE anomalies. Normalization factors from Taylor and McLennan (1985).

variations, as well as those that are of geochemical importance, are shown in Figs. 1 and 2 and are discussed here. The chondrite-normalized REE distribution patterns of the averages of the different lithologies in core LB-08A are shown in Fig. 3. In addition, we also present Harker diagrams (Fig. 4) showing the variations in major element contents for all the lithologies present in core LB-08A (suevite, polymict lithic impact breccia, meta-graywacke, phyllite-slate, and light greenish gray meta-graywacke), together with the average value for suevite from outside the northern crater rim (after Boamah and Koeberl 2003). Figure 5 contains the binary diagrams of the abundances of trace elements Ba, Cs, and Rb (in ppm) against K_2O contents (in wt%), showing the relation of the contents of these elements to the abundance of potassic phases in samples from core LB-08A. Figure 6 displays the elemental compositions of the average fallback suevite (from core LB-08A) major and trace element contents normalized to the average fallout suevite composition from outside the northern crater rim.

Major Element Contents

The compositions of the five main lithologies (suevite, polymict lithic impact breccia, meta-graywacke, slate-phyllite, and light greenish gray meta-graywacke [LGMG]) all show substantial variations within each lithology, and also have significant differences between them, especially for SiO_2 , Al_2O_3 , Fe_2O_3 , MgO, and CaO contents (Figs. 1 and 2; Table 1). Meta-graywacke samples display the highest SiO_2 content (70.7 wt% on average; std. dev. = 3.18 wt%) of the five lithologies analyzed and can be easily discriminated from phyllite and slate samples, which have an average SiO_2

content of about 57.8 wt%. Phyllite and slate samples have higher Fe_2O_3 and Al_2O_3 contents than meta-graywacke. Compared to all the other lithologies, the LGMG samples have higher CaO and LOI values (Table 1) and also a very high MgO content. Suevite and polymict lithic impact breccia samples have both very similar SiO_2 contents (63.2 and 61.4 wt% on average, respectively).

In the fallback breccia deposit (between 235.6 and 262 m, see Fig. 1), samples display significant differences for the SiO_2 and CaO contents, from 54.80 to 68.43 wt% and from 0.20 to 6.14 wt%, respectively, and substantial variation for the Al_2O_3 , Fe_2O_3 , and MgO contents. The same is true for the lithologies in the basement section (between 262 to 451 m; see Fig. 2), where the sample compositions also vary within a substantial range, especially for the SiO_2 , Al_2O_3 , Fe_2O_3 , MgO, and CaO contents. LGMG samples have higher MgO and CaO contents compared to the other lithologies (significant peaks in Fig. 2). The other significant peaks observed for both Fe_2O_3 and Al_2O_3 contents in Fig. 2 result from the presence of phyllite and slate samples.

Trace Element Contents

Some significant variation of trace element contents between lithologies and also within lithological types has been observed (Figs. 1 and 2; Table 1). In the following sections, elements are separated according to their geochemical behavior.

Lithophile and Chalcophile Elements

The abundances of the lithophile elements Ba, Rb, and Sr vary by about an order of magnitude between different samples, with Sr showing less variation than Ba and Rb. The different lithologies have variable Ba contents (also variable within lithological types), but the averages for suevite (626 ppm on average), polymict lithic impact breccia (742 ppm on average), and meta-graywacke (537 ppm on average) are fairly similar to each other. The Ba content of the phyllite-slate samples varies by about a factor of two and on average these rocks have a Ba content that is about ten times higher than that of the LGMG samples (1023 versus 155 ppm). The largest variation in Ba content of any of the lithologies is shown by the polymict lithic breccias.

The Rb content is also variable in the different lithologies (Figs. 1 and 2). Suevite and polymict lithic impact breccia samples have similar contents (67 and 86 ppm, respectively), whereas a higher content is observed in phyllite-slate samples (117 ppm on average), compared to a lower one in meta-graywacke and LGMG samples (38 and 17 ppm, respectively). The Sr content is very variable in the different lithologies and also within lithologies, with higher abundances observed in LGMG samples, and lower abundance in polymict lithic impact breccia. The Sr content is higher (on average) in suevite than in polymict lithic impact breccia.

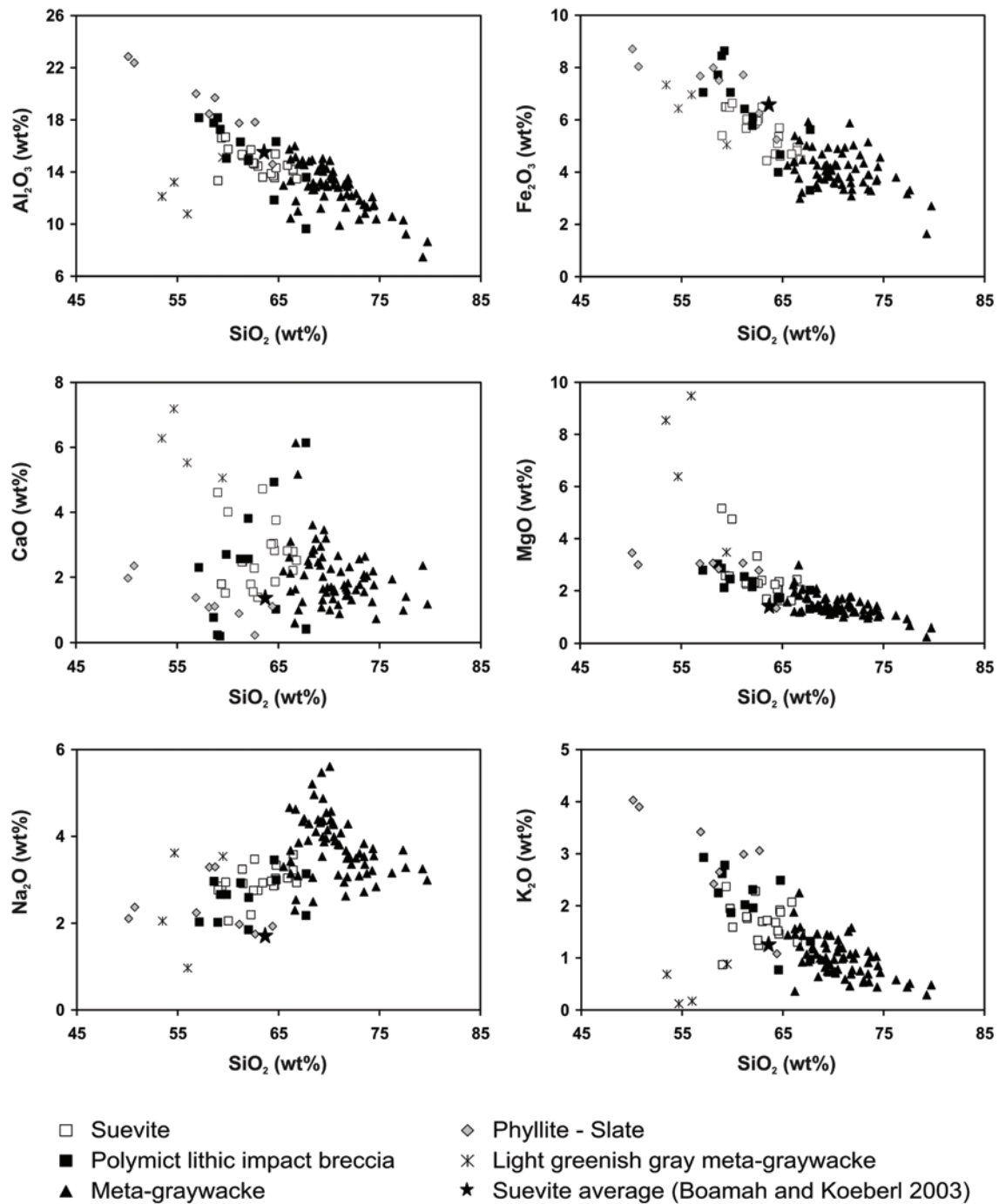


Fig. 4. Harker diagrams for the contents of the major oxides of Al, Fe, Ca, Mg, Na, and K, plotted versus silica content, for suevite, polymict lithic impact breccia, meta-graywacke, phyllite-slate, and light greenish gray meta-graywacke samples from core LB-08A. These data are compared with the average values for suevite from outside the northern crater rim (from Boamah and Koeberl 2003).

The contents of the chalcophile elements Cr, Cu, and Zn show less variation than the lithophile elements discussed above. Chromium contents are very similar for suevite, polymict lithic impact breccia, and phyllite-slate samples (on average), with a wider range for suevite samples. Two suevite samples, KR8-043 and KR8-107 (depths = 296.94 and 422.36 m, respectively) have Cr content about 2.5 times

higher than the other suevite samples (significant peaks in Fig. 2). The LGMG samples have a high Cr content (339 ppm on average; maximum Cr content of 531 ppm, significant peaks in Fig. 2) in comparison with the other lithologies. Thus the Cr content is about 6 times higher in LGMG than in other meta-graywacke samples. The Cu contents are in about the same range for suevite and meta-

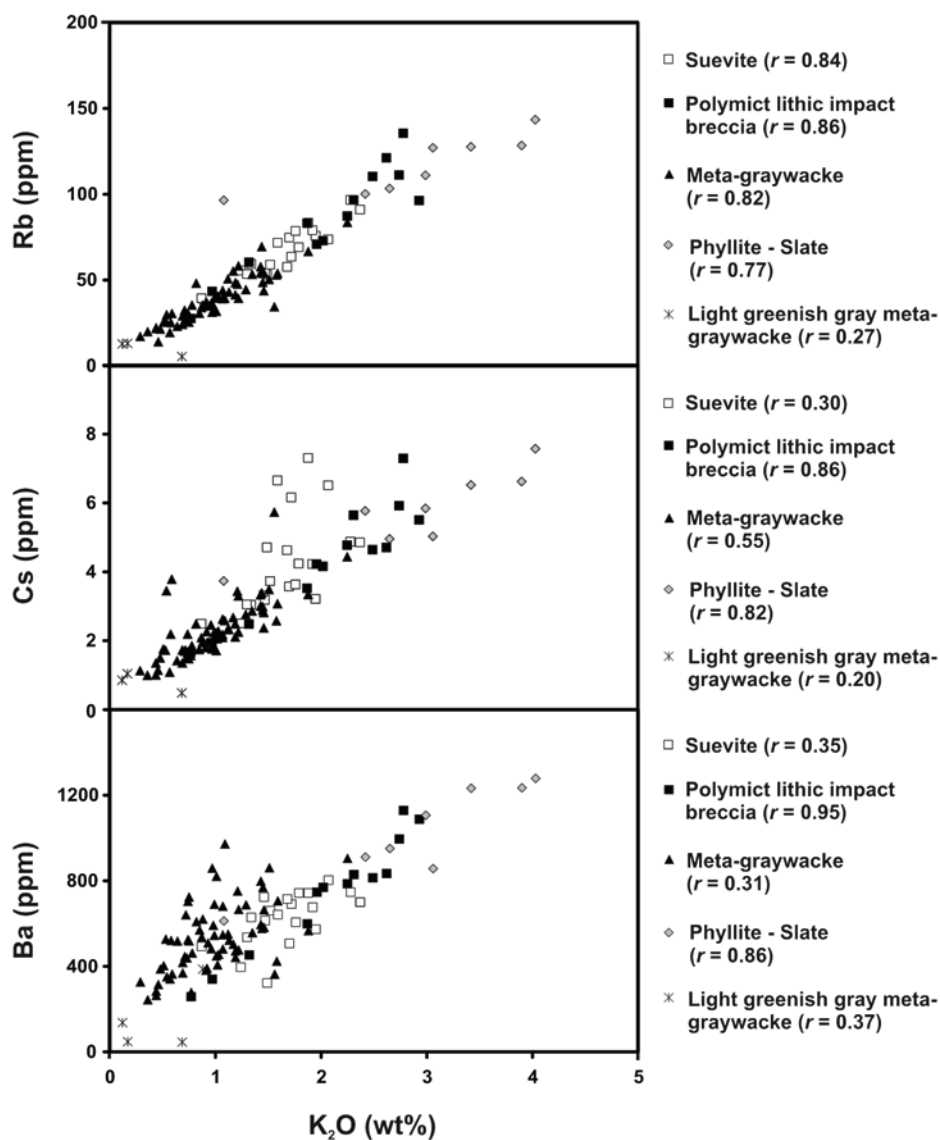


Fig. 5. Binary diagrams comparing the abundances of the trace elements Ba, Cs, and Rb (in ppm) with those of K_2O content (in wt%), showing the degree of correlation between the abundances of these elements for the different lithologies present in core LB-08A (r = correlation coefficient).

graywacke samples (about 25 ppm on average) and higher in both polymict lithic impact breccia and phyllite-slate samples (41 and 44 ppm on average, respectively). The Zn contents in suevite, polymict lithic impact breccia, and LGMG samples are somewhat similar (between 66 to 76 ppm on average), higher in phyllite-slate samples (94 ppm in average) and lower in meta-graywacke samples (43 ppm in average).

Siderophile Elements

The Co and Ni contents are very similar for suevite, polymict lithic impact breccia, and phyllite-slate samples (on average), with higher standard deviations for suevite samples (Table 1). The LGMG samples have higher Co and Ni

contents (31 and 194 ppm on average, respectively) than the other lithologies (up to 41 and 386 ppm, respectively, significant peaks like for Cr content in Fig. 2). The Ni content is about 7 times higher in LGMG than in meta-graywacke samples. The Co and Ni contents are two times lower in meta-graywacke samples than in phyllite-slate samples. The two suevite samples (at 296.94 and 422.36 m, respectively) that display higher Cr content than the other suevite samples (discussed earlier) have also Ni content about three times higher than the other suevite samples (significant peaks in Fig. 2). Gold contents are generally very high compared to average crustal abundances (e.g., Taylor and McLennan 1985), and Ir contents are below the detection limit (of about 1 to 2 ppb) for all samples.

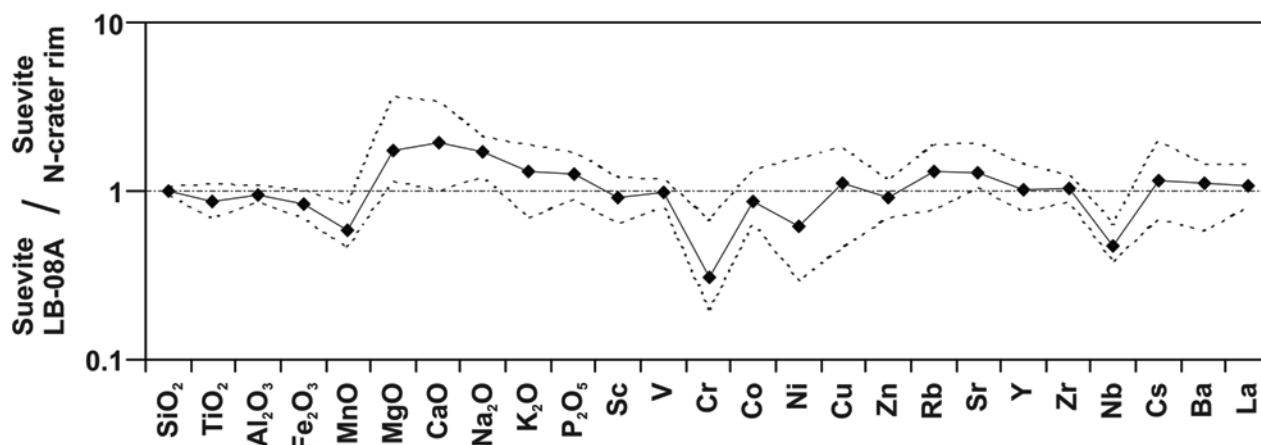


Fig. 6. Major and trace element contents for the average composition of suevites in core LB-08A, normalized to the average composition of suevite from outside the northern crater rim (Boamah and Koeberl 2003). Dashed lines indicate the maximum range of the ratios.

Rare Earth Elements (REE)

As shown in Fig. 3, the chondrite-normalized distribution patterns for the rare earth elements (REE) for all samples from core LB-08A are quite similar to each other and the ranges of contents for all lithologies overlap. All samples are enriched in both light rare earth elements (LREE) and heavy rare earth elements (HREE) relative to chondritic values. Only phyllite and slate samples and some of the meta-graywacke samples display minor, mostly negative Eu anomalies, which are not visible on Fig. 3 due to averaging the 67 meta-graywacke samples (Table 1). No Ce anomaly is evident in the analyzed samples.

Correlation Coefficients and Factor Analysis

To investigate correlations between the abundances of different chemical elements in the various lithologies present in core LB-08A, a correlation matrix, containing correlation coefficients between different pairs of major and trace elements, was calculated (Fig. 7). In addition, the compositions of 100 LB-08A samples, of different lithologies (suevite, polymict lithic impact breccia, and meta-graywacke, respectively) were analyzed by factor analysis using the SPSS program (version 11.0), to detect more complex interactions between the different chemical elements. Factor analysis is one of the best methods to reduce observed associations between numerous variables to a small number of fundamental “factors.” These “factors” identify groups of elements that behave in similar ways, and are, in most cases, indicative of specific geochemical processes. The abundance data were recalculated using a logarithmic transformation. For the factor analysis, we used the classical principal factor analysis (PFA) option and the method of factor rotation called “varimax” (orthogonal rotations, i.e., the rotated factors are not correlated). For more information about practical aspects, possibilities, and problems of factor analysis in geochemistry,

see, e.g., Reimann et al. (2002). The results of the factor analysis are summarized in Figs. 8 and 9, where the x-axis corresponds to the variance for the whole data set for each factor and the y-axis shows the factor loadings of the different chemical elements considered. These figures display the different factors, which account for about 80 to 90% of the total variance of major and trace elements considered, but also the relative importance (or loading) of each element within each factor. It is clear that, for example, the variance of Fe_2O_3 , TiO_2 , Zn, and V is quasi-exclusively controlled by factor 1 in the three lithologies (Figs. 8 and 9). Moreover, in the three lithologies, the siderophile elements, such as Ni, Cr, and Co, are totally controlled by factors 1 and 2. Factor 3 in the case of the meta-graywacke samples (Fig. 9) has high loadings for the variables Na_2O and Sr, and is interpreted to represent the variation of feldspar contents. In suevite samples, factor 3 is highly loaded by Ba, K_2O , and Rb, and is interpreted to represent the variations of K-feldspar. Factors 4 and 5 in suevite and meta-graywacke samples, and factors 3 and 4 in polymict lithic impact breccia samples, respectively, have very high loadings for the variables MnO, CaO, and LOI (also P_2O_5 and Sr in suevite and in polymict lithic impact breccia samples, respectively). Mainly because of the high loading of LOI in these factors (Figs. 8 and 9), this parameter has an important role and suggests that these factors are mainly controlled by secondary processes.

Mixing Calculations

In order to model the compositions of suevite and polymict lithic impact breccia lithologies, we performed a series of mixing calculations, using the Harmonic Least-Squares (HMX) mixing calculation program (Stöckelmann and Reimold 1989). The average compositions of the three principal target groups used in the calculations are given in Table 1. For additional information on the refinement control

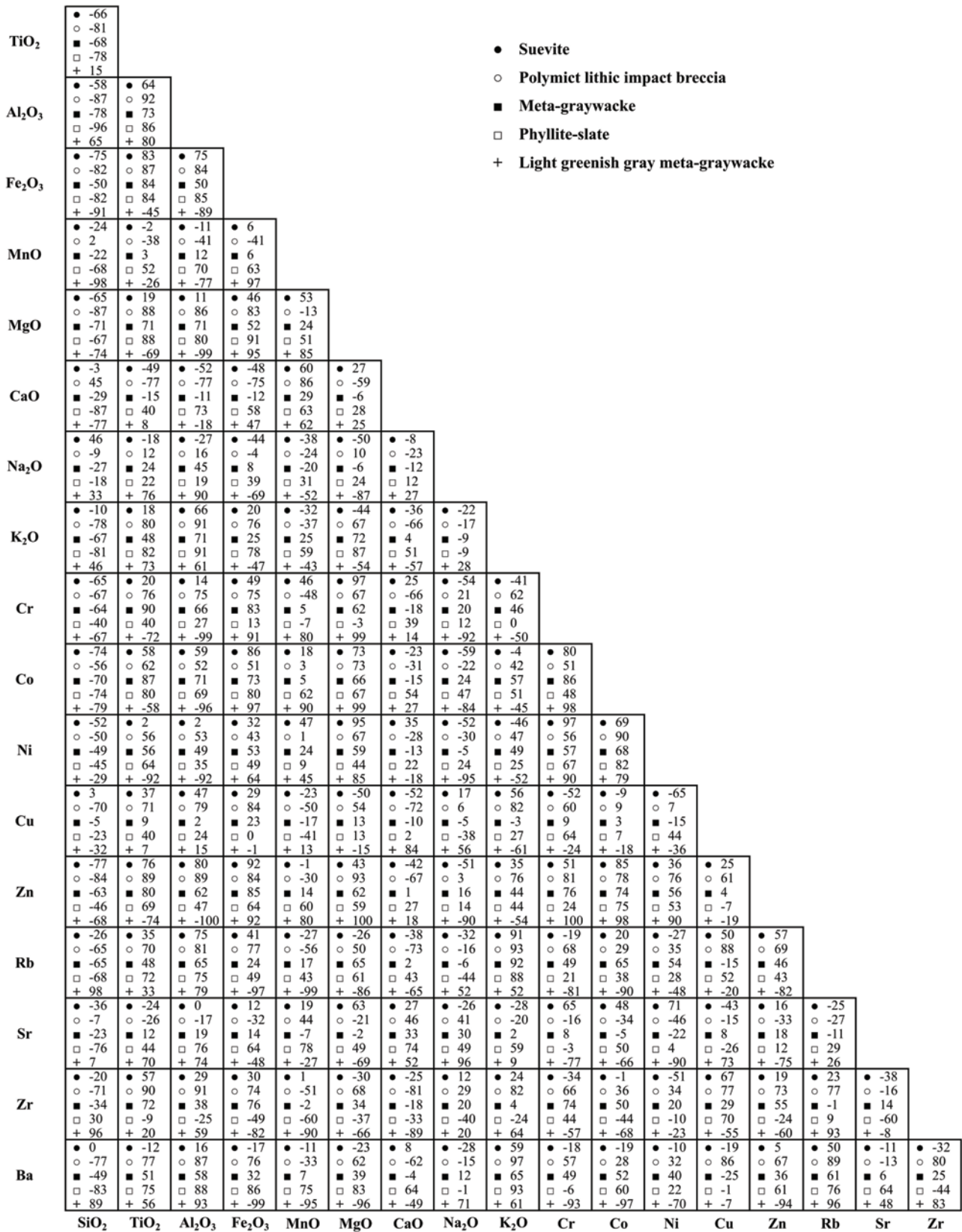


Fig. 7. Correlation coefficient r for various element pairs for the five different lithologies of this drill core (all r values are multiplied by 100). The same pair of elements can show positive as well as negative correlation, depending on rock types.

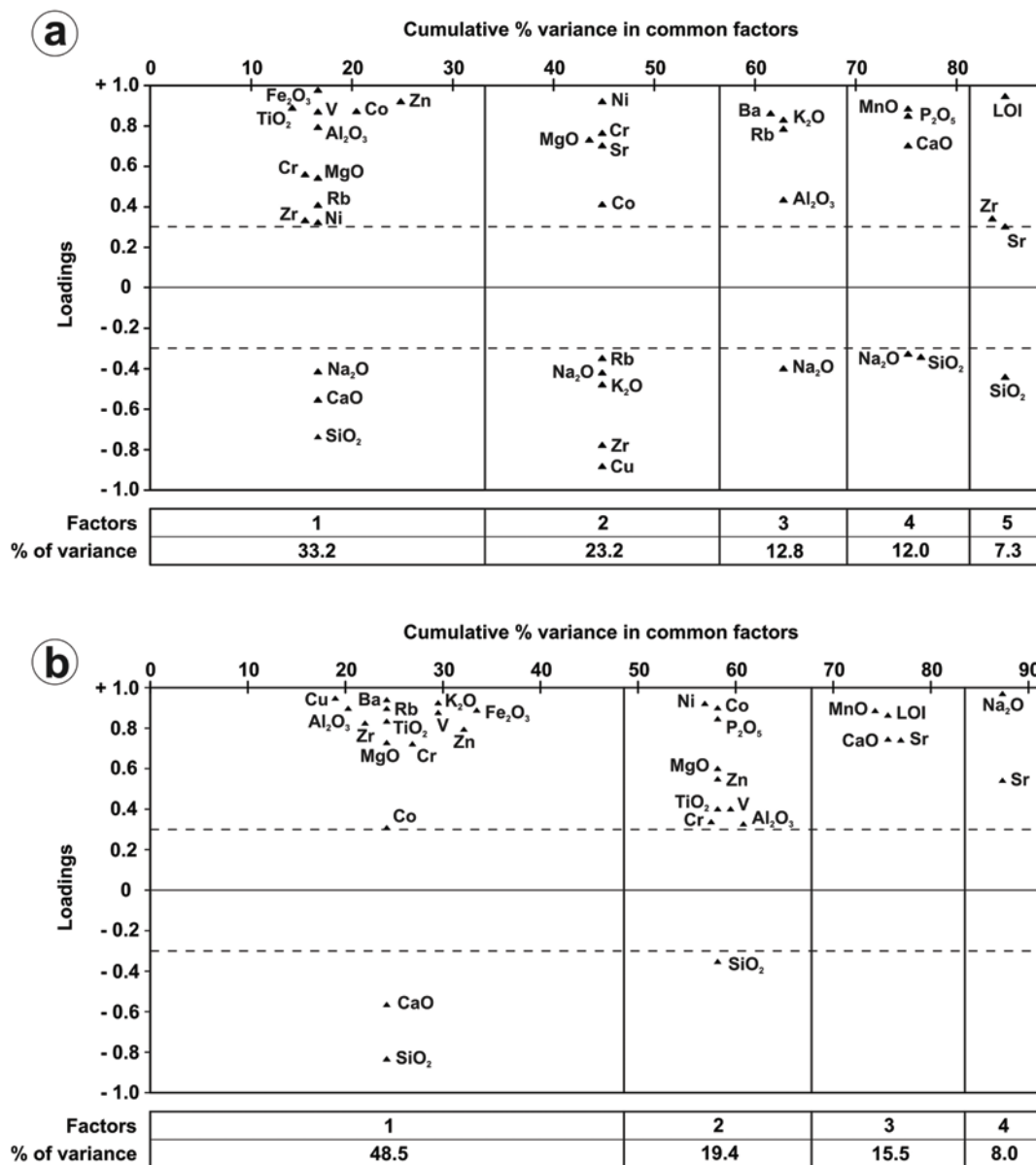


Fig. 8. A graphical representation of the factors extracted from factor analysis (principal factor analysis [PFA], Varimax rotation) for (a) suevite and (b) polymict lithic impact breccia samples. Number of elements = 21; number of samples = 20 for (a) and 13 for (b). The triangles represent the load factor for each element; loadings below 0.3 are not plotted here (they are considered as not significant). The width of the rectangles is proportional to the variance of each factor.

parameters for the purpose of setting different constraints on the mixing calculations, see Stöckelmann and Reimold (1989). Four calculation runs were performed, with major elements only, and others with major elements in combination with some trace elements that are different in abundance from component to component (i.e., the lithologies). Results are summarized in Table 2. Addition of the alkali elements and some trace elements to the calculations did not change the results appreciably (by not more than of a few percent of variation) (Table 2). The mobility of the alkali elements, which could be the result of post-impact alteration, seems to

have no effects on the mixing calculations. The discrepancy factors, which indicate the validity of the results (goodness of fit of the mixing calculations), are excellent in all reported calculation runs (Table 2). The observed and calculated mixture compositions for suevite and polymict lithic impact breccia lithologies are compared in Table 3. In both cases, the calculations yield results that are in good agreement with the petrographic observations (Ferrière et al. 2007): the target-rock components of suevite samples are dominated by meta-graywacke and phyllite-slate, with a very small proportion of LGMG. However, it seems that the abundance of the LGMG

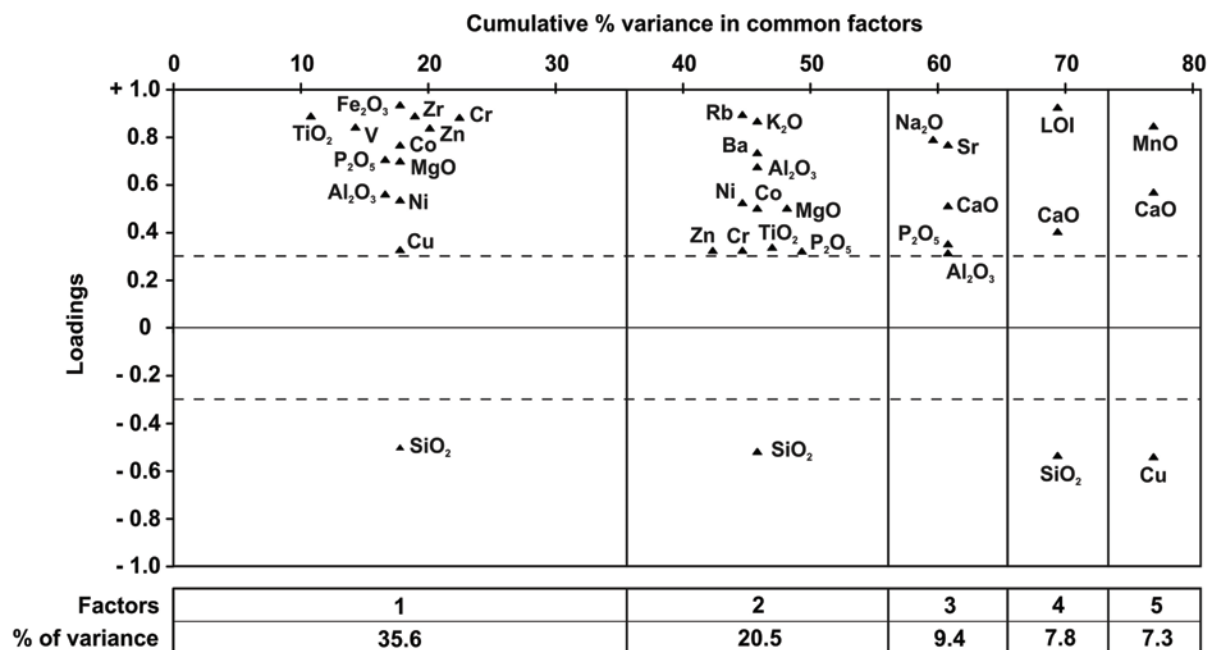


Fig. 9. A graphical representation of the factors extracted from factor analysis (principal factor analysis [PFA], Varimax rotation) for meta-graywacke samples. Number of elements = 21; number of samples = 67. The triangles represent the load factor for each element; loadings below 0.3 are not plotted here (they are considered as not significant). The width of the rectangles is proportional to the variance of each factor.

Table 2. The results of HMX mixing calculations to reproduce Bosumtwi suevite and polymict lithic impact breccia compositions from contributions from the different lithologies actually identified in the LB-08A drill core.

	Target rock components			Discrepancy factor
	Meta-graywacke	Phyllite-slate	Light greenish gray meta-graywacke	
Suevite [1]	48.9 ± 1.4	34.6 ± 1.4	16.5 ± 1.4	0.33
Suevite [2]	50.9 ± 1.4	31.4 ± 1.6	17.7 ± 1.4	0.21
Suevite [3]	49.4 ± 1.1	34.6 ± 1.2	16.1 ± 1.0	0.28
Suevite [4]	49.2 ± 1.2	35.2 ± 1.3	15.6 ± 1.2	0.32
Polymict lithic breccia [1]	35.7 ± 2.0	60.8 ± 2.3	3.4 ± 1.2	0.44
Polymict lithic breccia [2]	36.1 ± 2.6	61.0 ± 3.1	2.9 ± 1.3	0.38
Polymict lithic breccia [3]	35.3 ± 1.8	60.3 ± 2.1	4.4 ± 0.7	0.42
Polymict lithic breccia [4]	33.5 ± 1.8	63.4 ± 1.9	3.1 ± 0.9	0.45

Run numbers: [1] all major elements, except Mn and P, components total 100%; [2] major elements, except Mn, Na, K, and P, components total 100%; [3] as in run 1 but including Cr and Ni; [4] as in run 1 but including Sc and Th; mixing proportions given in %. Discrepancy factor = goodness of fit (a lower number is best). Harmonic mixing calculations after Stöckelmann and Reimold (1989). Average of target-rock compositions from Table 1.

lithology is overestimated in the calculated suevite mixture composition. The mixing calculations with the polymict lithic breccia composition yielded the highest proportion of the phyllite-slate components (about 60%) in comparison to the ~36% of the meta-graywacke components.

DISCUSSION

In the Harker diagrams (Fig. 4), the data for all lithologies (except the LGMG samples) show a clear inverse correlation between the contents of SiO₂ and the other major oxides: Al₂O₃, Fe₂O₃, MgO, and K₂O, but not for Na₂O. The different lithologies show scattered distributions, which are clearly evident for meta-graywacke and phyllite-slate samples, and

with some overlap between suevite and polymict lithic impact breccia samples. This overlap is due to the fact that both suevite and polymict lithic impact breccia are derived from a mixture of similar target rocks (mainly meta-graywacke, phyllite, and slate; Ferrière et al. 2007). No significant correlation between the SiO₂ and CaO contents (Fig. 4) is evident for suevite, polymict lithic impact breccia, and meta-graywacke samples, which could be evidence for overprint from a secondary, post-impact calcium carbonate component. Curiously, the SiO₂ and CaO contents show a normal correlation in phyllite-slate and LGMG samples (Figs. 4 and 7), which is not yet understood. We have also observed a tendency of increasing CaO content in meta-graywacke samples with increasing depth in the lower part of the basement

section (in between 320 and 451 m) (Fig. 2), which might be due to an increase in the abundance of secondary calcite veinlets and aggregates with depth. This tendency has not been yet confirmed by microscopic observations of the distribution of calcite veinlets and aggregates with depth in the meta-graywacke samples from the basement (Ferrière et al. 2007).

The LGMG samples have higher CaO and LOI values than all other lithologies (Table 1; Fig. 4), which could be related to the presence of significant amounts of calcite pods in the LGMG samples (in agreement with observations by Ferrière et al. 2007). The LOI values are about two times higher for LGMG samples than for the other lithologies (8.07 wt% on average), which indicate the presence of a significant amount of volatiles (water, calcium carbonate). High LOI values are consistent with alteration, which agrees with the petrographic determination of significant amounts of chlorite in the LGMG samples (Ferrière et al. 2007).

In comparison with all the lithologies present in core LB-08A, LGMG samples also have very high MgO contents of about 7 wt% (Table 1; Fig. 4), five times higher than the content in the meta-graywacke and about three times higher than in the other lithologies. This high MgO abundance could be related to abundant chlorite (Ferrière et al. 2007) present in the LGMG samples. Interestingly, the MgO content is about two times higher in two suevite samples (KR8-043 and KR8-107; depths = 294.94 and 422.36 m, respectively; Fig. 4) than in other suevite samples. These observations are in agreement with the presence of clasts of the LGMG lithology (that contains abundant chlorite) in the KR8-043 and KR8-107 suevite samples, as shown by Ferrière et al. (2007).

The Na₂O content in meta-graywacke samples (3.77 wt% on average) is slightly higher than the contents in the “meta-graywacke and phyllite lithology” from outside the crater (2.26 wt% on average; Table 1), and the Na₂O abundance varies from 2.30 to 5.61 wt% within the meta-graywacke lithology. These variations of the Na₂O content can be mainly credited to the variable albite abundances in the different meta-graywacke samples (Ferrière et al. 2007).

The Rb content is clearly correlated with K₂O content (Figs. 5 and 7) in all the samples from core LB-08A (except for LGMG samples; correlation coefficient of 0.57), suggesting that this element is mostly incorporated in potassic phases (such as K-feldspar and some phyllosilicate minerals). The Cs and Ba contents do not correlate well with the K₂O contents in suevite, meta-graywacke, and LGMG samples. On the other hand, the Cs and Ba contents show good correlations with the K₂O, Al₂O₃, and Fe₂O₃ content in polymict lithic impact breccia and phyllite-slate samples (Figs. 5 and 7), suggesting that Cs and Ba elements are mainly incorporated in K-feldspar and phyllosilicate minerals (e.g., Shaw 1956).

The Sr contents vary for the different lithologies and within lithological types (Table 1) and are higher in suevite than in polymict lithic impact breccia (387 and 291 ppm on average, respectively). Strontium concentrations are in part

Table 3. A comparison of measured suevite and polymict lithic impact breccia compositions with those obtained from the mixing calculations.

	Suevite		Polymict lithic breccia	
	Calc. (Run 1)	$\Delta_{\text{obs-calc}}$	Calc. (Run 1)	$\Delta_{\text{obs-calc}}$
SiO ₂	63.43	-0.27	61.93	-0.49
TiO ₂	0.55	<0.01	0.60	0.03
Al ₂ O ₃	14.78	-0.13	16.41	-0.71
Fe ₂ O ₃	5.58	-0.09	6.21	0.13
MgO	2.74	-0.24	2.40	-0.09
CaO	2.49	0.18	1.74	0.45
Na ₂ O	3.00	-0.55	2.83	-0.10
K ₂ O	1.64	0.03	2.13	-0.05

All data in wt%. $\Delta_{\text{obs-calc}}$ = observed value (Table 1) minus calculated value.

controlled by plagioclase abundance (Rollinson 1993; however, no specific difference of plagioclase abundance in polymict impact breccia samples has been noted by Ferrière et al. 2007).

The REE patterns (Fig. 3) for all lithologies are very similar, and, indeed, the ranges of the REE contents of the various lithologies overlap. This indicates that the breccias do not contain a significant amount of any exotic lithologies that are not represented by the basement lithologies present in core LB-08A. None of the lithologies show any significant negative Eu anomalies (except a very slight negative Eu anomaly for phyllite-slate samples, of about 0.88 on average), which is typical for Archean crustal rocks, according to Taylor and McLennan (1985). The average Eu/Eu* values for all lithologies are between about 0.90 and 1.00. The Eu anomalies for some of the lithologies vary somewhat (e.g., 0.8 to 1.5 for metasediments in general), but for most samples the deviations from the average values are very small. The chondrite-normalized REE distribution pattern for the average meta-graywacke, as shown in Fig. 3, does not indicate a negative Eu anomaly because the average value is indistinguishable from unity. Variations of the Eu/Eu* value are commonly associated with varying abundances of feldspar (mainly plagioclase; Nance and Taylor 1977), but might be also result from the presence of some accessory minerals (Taylor and McLennan 1985). Petrographic observations of meta-graywacke samples from core LB-08A (Ferrière et al. 2007) have shown a large variation in the relative abundance of the different minerals (major minerals, but also accessory minerals) that make up meta-graywacke samples, which could explain the observed variation of the Eu/Eu* values. The highest La and Ce contents in meta-graywacke samples in comparison with LGMG samples (Fig. 3) can be due to the presence of some accessory minerals in meta-graywacke samples (such as allanite) (Ferrière et al. 2007).

The slightly different patterns for heavy rare earth elements (HREE) (Fig. 3) in suevite and polymict lithic

breccia may be due to the mixture of the various target rock types at somewhat different proportions. The La_N/Yb_N values range from 2.64 to 18.5 (with an average La_N/Yb_N value that is two times higher in meta-graywacke samples than in the other lithologies), which can be the result of the original mixing of the different minerals which constitute samples, or the effect of REE fractionation due to alteration processes. The absence of significant Ce anomalies indicates that post-impact aqueous alteration was either not particularly severe, or did not involve large volumes of fluids percolating through the breccia units.

The chemical index of alteration (CIA) (Table 1) is, in average, very similar for suevite, polymict impact breccia, and meta-graywacke (CIA = 56, 60, and 54, respectively), somewhat higher for phyllite-slate samples (CIA = 67) and lower for LGMG samples (CIA = 46). Suevite, polymict lithic impact breccia, and meta-graywacke samples display a large variation of the CIA values, which suggest some variation in the degree of alteration for the various samples, and possibly also because of the presence of heavy minerals, such as zircon.

As noted above, the abundances of the chalcophile and siderophile elements chromium, vanadium, nickel, and cobalt vary between the different lithologies, but also within lithological types (Table 1). Cobalt is well correlated with the Fe_2O_3 content in most lithologies (not correlated well in polymict lithic impact breccia samples) (Fig. 7), suggesting that this element is mainly incorporated in sulfide minerals (such as pyrite), biotite, and chlorite minerals. Chromium and nickel contents are also rather well correlated with the MgO abundance (correlation coefficients between 0.85 and 0.99) (Fig. 7) in both suevite and LGMG samples, which can again be explained by these elements being contained mainly in phyllosilicate minerals, as well as in sulfide minerals such as pyrite (Ferrière et al. 2007) or pyrrhotite (Kontny and Just 2006). The large standard deviations on the average Cr and Ni contents for suevite samples (std. dev. = 57 and 31 ppm, respectively) are mainly due to the presence of two suevite samples, KR8-043 and KR8-107 (depths = 296.94 and 422.36 m, respectively), which have Cr contents more than twice the average suevite value (249 and 238 ppm, respectively), compared to about 115 ppm on average (significant peaks in Fig. 2) and Ni contents about three times that of the average suevite (165 and 156 ppm, respectively, compared to 50 ppm on average). The presence of LGMG clasts in these two suevite samples (Ferrière et al. 2007) can explain these abnormally higher Cr and Ni contents in comparison to the average of Cr and Ni abundances for suevite (significant peaks in Fig. 2). This observation indicates that local rock fragments (only transported a few centimeters; angular clasts) are incorporated into the suevite dikelets (see also Ferrière et al. 2007). These authors also noticed that these suevite dikelets are more severely altered (abundant phyllosilicate minerals) than the surrounding metasediments.

The siderophile element data show similar abundances

for polymict impact breccia and for phyllite-slate samples (Table 1), as well as for the meta-graywacke samples. The observation that the various impact breccias do not show any anomalous enrichment in the siderophile element contents compared to the target rocks, indicates that there is no immediate evidence for the presence of a meteoritic component. This is in agreement with previous work by Dai et al. (2005), who studied platinum group elements in impactites from outside the crater and have not detected the presence of a meteoritic component in Bosumtwi impactites. These results by Dai et al. (2005) also confirm the high indigenous abundances of the siderophile elements, and these authors concluded that elemental data alone cannot be used to verify the presence of a meteoritic component in Bosumtwi crater rocks. On the other hand, Koeberl and Shirey (1993) found an extraterrestrial component in Ivory Coast tektites and Bosumtwi impact glass (isolated from suevites), using the Os isotopic method method; this was confirmed by Cr isotopic studies by Koeberl et al. (Forthcoming). Numerical modeling of the formation of Bosumtwi (Artemieva et al. 2004) predicted that the extraterrestrial material should be heterogeneously distributed within the crater with 0.1% or less of a projectile component in samples from inside the crater. Artemieva et al. (2004) also predicted that there is a higher probability of finding a projectile component in downrange distal ejecta (to the west-southwest of the crater center, according to the position of the Ivory Coast tektites strewn field) and also a substantial amount in proximal ejecta near the crater rim in a downrange direction (Artemieva et al. 2004). These predictions are partially in accordance with our observations, as well as those of Dai et al. (2005) and Koeberl and Shirey (1993). However, the absence of any significant melt-rich-suevite layer in the central part of the crater (Ferrière et al. 2007), which was assumed to be present based on geophysical as well as numerical modeling (Jones et al. 1981; Plado et al. 2000; Artemieva et al. 2004), is noticeable.

Comparison with Chemical Data for Fallout Impact Breccia

For comparison of chemical data for suevite samples from core LB-08A (fallback breccia) and chemical data for suevite from outside the northern crater rim (fallout breccia; cf. Boamah and Koeberl 2003) we use, in addition to the Harker diagrams (Fig. 4), a diagram showing the contents in average suevite (from core LB-08A) normalized to contents in suevite from outside the northern crater rim (Fig. 6). In both Boamah and Koeberl (2003) and this study, the concentrations were determined by the same methods.

Fallback suevites from LB-08A core and fallout suevite have identical SiO_2 contents (63.2 and 63.6 wt% on average, respectively). Regarding the other major elements, the TiO_2 , Al_2O_3 , and Fe_2O_3 contents are very similar in both suevite

populations (Fe_2O_3 contents are slightly lower in fallback suevite); the MnO, MgO, CaO, and Na_2O contents are very different in both suevite types (this regards the average compositions as well as the maxima and minima) (Fig. 6). Specifically, the MnO content is lower in fallback suevite than in fallout suevite samples, whereas the MgO, CaO, and Na_2O contents are higher in fallback suevite than in fallout suevite samples. The K_2O and P_2O_5 contents are slightly higher in fallback suevite from core LB-08A, but still within the range of contents in fallout suevite samples. These differences in some major element abundances can be the result of a difference in clast populations in both suevite populations (calcite clasts are present in fallback breccia and not in fallout suevite, and granite clasts are present in fallout suevite and not in fallback breccia; Ferrière et al. 2007) or might suggest a higher post-impact aqueous alteration in suevite samples from core LB-08A than in fallout suevite samples.

The trace element contents in both suevite populations are very similar (Fig. 6), with the exception of the abundances of Cr, Nb, and Ni. The Ni content is lower in fallback suevite than in fallout suevite samples, but the ranges overlap (31 to 165 ppm versus 52 to 423 ppm, respectively). Chromium and Nb are relatively depleted in fallback suevite from core LB-08A, by factors of 3 and 2, respectively, compared to fallout suevite. This enrichment of Cr and Ni in fallout suevite (in comparison with fallback suevite) could be due to a difference in clast populations that constitute both suevite samples. For example, granite clasts have been observed in suevite from outside the northern crater rim (up to 3 vol% of granitic clasts) (Boamah and Koeberl 2003, 2006) but not in suevite from core LB-08A (Ferrière et al. 2007), and only rare granite clasts, observed in suevite from core LB-07A (Coney et al. 2007). However, the contents of Cr and Ni in a few granite dike samples analyzed by Koeberl et al. (1998) are too low and cannot explain the enrichment in these elements in fallout suevite. On the other hand, the Pepiakese granite (Table 1) (Koeberl et al. 1998) shows high Cr and Ni contents (517 and 172 ppm on average, respectively), but cannot explain the enrichment observed for these elements in fallout suevite (at least about 40 mass% of Pepiakese granite mix into the fallout suevite is necessary to explain these values, which is not realistic). The MnO content in Pepiakese granite (0.067 wt% on average [Koeberl et al. 1998]) seems also to be too low to explain the enrichment in MnO in fallout suevite (in comparison with fallback suevite). Thus, for the time being we cannot readily explain the difference in Cr and Ni contents between the fallback and fallout suevites.

In terms of implications for the understanding of excavation and depositional processes, the differences in the chemical compositions between the fallback and fallout suevites do not allow a clear separation between what is the result of the impact itself and what was induced by secondary alteration processes.

Comparison with Chemical Data for Target Rocks Outside the Crater Rim

The target rocks at Bosumtwi include a variety of lithologies, mainly meta-graywacke, phyllite, shale, granite dikes, and Pepiakese granite (chemical data for each target rocks lithologies are reported in Table 1 for comparison; data from Koeberl et al. 1998). In the basement section of core LB-08A, granite dikes and Pepiakese granite of the target rock types (found in the wider crater region) are definitely absent, and shale occurs only in the form of clasts in the top of the fallback breccia deposit. Earlier papers have not distinguished, as in our study, between meta-graywacke and phyllite samples, but presented an average composition of both lithologies (“graywacke-phyllite” lithology; Table 1; data in Koeberl et al. 1998). To allow a comparison between metasediments in core LB-08A and metasediments from outside the crater rim, we have calculated an average composition for all the metasediments present in core LB-08A (Table 1).

The major element composition of the average graywacke-phyllite from outside the crater rim is within the range of composition of the metasediments from core LB-08A. However, on average, the CaO and Na_2O contents are significantly higher in metasediment from core LB-08A, whereas the Al_2O_3 , Fe_2O_3 , and MgO contents are slightly higher in graywacke-phyllite from outside the crater rim (Table 1). The higher Al_2O_3 , Fe_2O_3 , and MgO contents in graywacke-phyllite from outside the crater rim can easily be explained by the fact that a larger number of phyllite samples (having a high content of phyllosilicate minerals) was used in the calculation of the average metasediment from outside the crater rim than in the respective calculation for core LB-08A. The slightly lower SiO_2 content observed for the average of data for metasediment samples from outside the crater rim confirms this higher proportion of phyllite. However, the difference in meta-graywacke and phyllite proportions for the average calculation cannot explain the higher CaO and Na_2O contents observed in metasediment from core LB-08A. These differences in the CaO and Na_2O contents could be the signature of secondary alteration, which affected the basement after the impact event, or simply a result of the original mixing of the different metasediments.

Chromium contents in metasediment from outside the crater rim are more than 1.5 times higher than in the phyllite-slate sample average from core LB-08A and also higher than the maximum Cr content observed in phyllite-slate from core LB-08A (Table 1). Chromium contents are correlated with TiO_2 and Fe_2O_3 abundances in meta-graywacke samples from core LB-08A (Fig. 7), which argues in favor of the localization of the Cr element in magnetite.

Regarding the other trace elements, metasediment compositions from core LB-08A are similar to the composition of the metasediment from outside the crater rim,

except for Sr, which has an abundance three to four times higher in metasediment from core LB-08A. This difference in Sr content might be due to a higher aqueous alteration of samples from core LB-08A than of target rock samples, or to a difference of plagioclase abundance (Rollinson 1993).

During this study we have observed a slight Eu anomaly in phyllite-slate and also in meta-graywacke samples (the Eu anomaly present in several meta-graywacke samples isn't visible on Fig. 3, due to the averaging), similar to the Eu anomaly that was observed in "shale" and "graywacke-phyllite" lithologies (Boamah and Koeberl 2003; Dai et al. 2005) from the target rocks.

SUMMARY AND CONCLUSIONS

A large number of samples of polymict impact breccia (33 samples) and metasediment (79 samples) from the central uplift of the Bosumtwi crater were analyzed for their major and trace element composition.

Five different lithologies have been distinguished on the basis of petrographic observations (Ferrière et al. 2007), comprising polymict lithic impact breccia, suevite, meta-graywacke, slate-phyllite, and light greenish gray meta-graywacke; all these lithologies show significant differences between them, especially for SiO₂, Al₂O₃, Fe₂O₃, MgO, and CaO contents and also substantial variations within lithological types. Suevite and polymict lithic impact breccia samples have both very similar SiO₂ contents (63.2 and 61.4 wt% on average, respectively), in between the SiO₂ content of meta-graywacke samples (70.7 wt% on average) and the SiO₂ content of phyllite-slate samples (57.8 wt% on average). A clear inverse correlation between the contents of SiO₂ and the other major oxides: Al₂O₃, Fe₂O₃, MgO, and K₂O (except for Na₂O) is observed for all lithologies (except for the LGMG samples). The distributions scatter due to the fact that both types of polymict impact breccia are derived from a mixture of target rocks (mainly meta-graywacke and phyllite-slate). No correlation of the SiO₂ and CaO contents for suevite, polymict lithic impact breccia, and meta-graywacke samples have been observed, which might suggest a contribution of a post-impact calcium carbonate component. The CaO content in meta-graywacke samples, which show a tendency of increasing with depth in the lower part of the basement section, can be the result of an increase in the abundance of secondary calcite veinlets and aggregates with depth.

Significant variation of trace element contents between lithologies and also within lithological types has been observed, mainly for Rb, Cs, Ba, and Sr contents. The Cr, Co, and Ni contents are very similar for suevite, polymict lithic impact breccia, and phyllite-slate samples (about 105, 20, and 60 ppm on average, respectively), two times lower in meta-graywacke samples (54, 10, and 27 ppm on average, respectively) and clearly higher in LGMG samples (339, 31, and 194 ppm on average, respectively). Those abundances in Cr, Co, and Ni contents are mainly the result of the

localization of these elements in sulfide minerals (such as pyrite and pyrrhotite grains), as well as in phyllosilicate minerals.

The REE patterns, somewhat similar for all samples from core LB-08A, show enrichment in both LREE and HREE relative to chondritic values. The slightly different patterns observed for HREE in suevite and polymict lithic breccia could result from the mixture of the various target rock types at somewhat different proportions. Only the phyllite and slate samples and some meta-graywacke samples display a slight Eu anomaly.

This study also shows the possibility to clearly distinguish the different metasediment lithologies, on the basis of their compositions, using the major element abundances and Sc, Cr, Co, Ni, and Zn contents, which are noticeably distinct for these lithologies.

Our main conclusions are:

1. Most of the variations of the major and trace element abundances within each lithology results from variations in the proportions of the mineral constituents of those rocks. However, aqueous alteration processes have definitely affected the different rocks from the core LB-08A, which is shown by the CIA values (from 41 to 73) and by the presence of secondary calcium carbonates; this is in agreement with petrographic observations.
2. The chemical compositions of both the suevite and the polymict lithic breccia from core LB-08A can be closely approximated using the HMX mixing calculation program. A mixture of about 50 wt% meta-graywacke, 34 wt% phyllite-slate, and 16 wt% of LGMG for the suevite composition, and a higher proportion of phyllite-slate (~60%) with ~36% of meta-graywacke for the polymict lithic breccia, have been calculated, and those results are in good agreement with the petrographic observations.
3. Fallback suevite (suevite from core LB-08A) and fallout suevite samples display some differences in major element abundances, mainly in the MgO, CaO, and Na₂O contents that could be related to the higher degree of alteration of samples from fallback suevite than fallout suevite samples. Some differences in the clast populations of the two suevite facies (no granite clasts have been observed in samples from core LB-08A and no calcite clasts in fallout suevite), can also induce some variations of major and trace element abundances.
4. No significant difference exists between the chondrite-normalized REE patterns for the different lithologies studied in core LB-08A and the fallout suevite and target rocks from outside the crater rim, suggesting that the major constituents of both suevite populations represent the same target rock types.
5. No evidence for a meteoritic component has been detected during this study (similar siderophile element contents observed for polymict impact breccia and for

phyllite-slate samples), which is in agreement with previous works. Complementary analyses, such as platinum group element analyses and related isotopic studies, are necessary to investigate any possible extraterrestrial component in fallback breccia.

Acknowledgments—Drilling at Bosumtwi was supported by the International Continental Scientific Drilling Program (ICDP), the U.S. NSF-Earth System History Program under grant no. ATM-0402010, Austrian FWF (project P17194-N10), the Austrian Academy of Sciences, and by the Canadian NSERC. We are grateful to DOSECC, Inc., for the drilling operations. This work was supported by the Austrian FWF (P17194-N10, to C. K.). We appreciate the help of H. Böck, M. Villa, M. Bichler, and G. Steinhauser (Atominstitut Vienna) with the irradiations. We are grateful to D. Kring and G. Osinski for constructive reviews.

Editorial Handling—Dr. Bernd Milkereit

REFERENCES

- Artemieva N. A., Karp T., and Milkereit B. 2004. Investigating the Lake Bosumtwi impact structure: Insight from numerical modeling. *Geochemistry Geophysics Geosystems* 5, doi:10.1029/2004GC000733.
- Boamah D. and Koeberl C. 2002. Geochemistry of soils from the Bosumtwi impact structure, Ghana, and relationship to radiometric airborne geophysical data. In *Meteorite impacts in Precambrian shields*, edited by Plado J. and Pesonen L. Impact Studies, vol. 2. Heidelberg: Springer. pp. 211–255.
- Boamah D. and Koeberl C. 2003. Geology and geochemistry of shallow drill cores from the Bosumtwi impact structure, Ghana. *Meteoritics & Planetary Science* 38:1137–1159.
- Boamah D. and Koeberl C. 2006. Petrographic studies of “fallout” suevite from outside the Bosumtwi impact structure, Ghana. *Meteoritics & Planetary Science* 41:1761–1774.
- Brodie K., Fettes D., Harte B., and Schmid R. 2004. Structural terms including fault rock terms. http://www.bgs.ac.uk/scmr/docs/paper_3/scmr_struc2.pdf. Accessed 16 March 2007.
- Coney L., Gibson R. L., Reimold W. U., and Koeberl C. 2007. Lithostratigraphic and petrographic analysis of ICDP drill core LB-07A, Bosumtwi impact structure, Ghana. *Meteoritics & Planetary Science* 42. This issue.
- Dai X., Boamah D., Koeberl C., Reimold W. U., Irvine G., and McDonald I. 2005. Bosumtwi impact structure, Ghana: Geochemistry of impactites and target rocks, and search for a meteoritic component. *Meteoritics & Planetary Science* 40: 1493–1511.
- Ferrière L., Koeberl C., and Reimold W. U. 2007. Drill core LB-08A, Bosumtwi impact structure, Ghana: Petrographic and shock metamorphic studies of material from the central uplift. *Meteoritics & Planetary Science* 42. This issue.
- Gentner W., Kleinmann B., and Wagner G. A. 1967. New K-Ar and fission track ages of impact glasses and tektites. *Earth and Planetary Science Letters* 2:83–86.
- Gentner W., Storzer D., and Wagner G. A. 1969. New fission track ages of tektites and related glasses. *Geochimica et Cosmochimica Acta* 33:1075–1081.
- Govindaraju K. 1994. 1994 compilation of working values and sample description for 383 geostandards. *Geostandards Newsletter* 18:1–158.
- Jackson J. A. 1997. *Glossary of geology*, 4th edition. Alexandria, Virginia: American Geological Institute. 769 p.
- Jarosewich E., Clarke R. S. J., and Barrows J. N. 1987. The Allende meteorite reference sample. *Smithsonian Contributions to Earth Sciences* 27:1–49.
- Jones W. B. 1985. Chemical analyses of Bosumtwi crater target rocks compared with the Ivory Coast tektites. *Geochimica et Cosmochimica Acta* 48:2569–2576.
- Jones W. B., Bacon M., and Hastings D. A. 1981. The Lake Bosumtwi impact crater, Ghana. *Geological Society of America Bulletin* 92:342–349.
- Junner N. R. 1937. The geology of the Bosumtwi caldera and surrounding country. *Gold Coast Geological Survey Bulletin* 8: 1–38.
- Koeberl C. 1993. Instrumental neutron activation analysis of geochemical and cosmochemical samples: A fast and proven method for small samples analysis. *Journal of Radioanalytical and Nuclear Chemistry* 168:47–60.
- Koeberl C. and Reimold W. U. 2005. Bosumtwi impact crater, Ghana (West Africa): An updated and revised geological map, with explanations. *Jahrbuch der Geologischen Bundesanstalt, Wien (Yearbook of the Austrian Geological Survey)* 145:31–70 (+1 map, 1:50,000).
- Koeberl C. and Shirey S. B. 1993. Detection of a meteoritic component in Ivory Coast tektites with rhenium-osmium isotopes. *Science* 261:595–598.
- Koeberl C., Bottomley R. J., Glass B. P., and Storzer D. 1997. Geochemistry and age of Ivory Coast tektites and microtektites. *Geochimica et Cosmochimica Acta* 61:1745–1772.
- Koeberl C., Reimold W. U., Blum J. D., and Chamberlain C. P. 1998. Petrology and geochemistry of target rocks from the Bosumtwi impact structure, Ghana, and comparison with Ivory Coast tektites. *Geochimica et Cosmochimica Acta* 62:2179–2196.
- Koeberl C., Milkereit B., Overpeck J. T., Scholz C. A., Amoako P. Y. O., Boamah D., Danuor S., Karp T., Kueck J., Hecky R. E., King J. W., and Peck J. A. 2007. An international and multidisciplinary drilling project into a young complex impact structure: The 2004 ICDP Bosumtwi Crater Drilling Project—An overview. *Meteoritics & Planetary Science* 42. This issue.
- Koeberl C., Shukolyukov A., and Lugmair G. W. Forthcoming. Chromium isotopic studies of terrestrial impact craters: Identification of meteoritic components at Bosumtwi, Clearwater East, Lappajärvi, and Rochechouart. *Earth and Planetary Science Letters*.
- Kolbe P., Pinson W. H., Saul J. M., and Miller E. W. 1967. Rb-Sr study on country rocks of the Bosumtwi crater, Ghana. *Geochimica et Cosmochimica Acta* 31:869–875.
- Kontny A. and Just J. 2006. Magnetic mineralogy and rock magnetic properties of impact breccias and crystalline basement rocks from the BCDP-drillings 7A and 8A (abstract #1343). 37th Lunar and Planetary Science Conference. CD-ROM.
- Leube A., Hirdes W., Mauer R., and Kesse G. O. 1990. The Early Proterozoic Birimian Supergroup of Ghana and some aspects of its associated gold mineralization. *Precambrian Research* 46: 139–165.
- Moon P. A. and Mason D. 1967. The geology of ¼° field sheets 129 and 131, Bompata S. W. and N. W. *Ghana Geological Survey Bulletin* 31:1–51.
- Nance W. B. and Taylor S. R. 1977. Rare earth element patterns and

- crustal evolution—II. Archean sedimentary rocks from Kalgoorlie, Australia. *Geochimica et Cosmochimica Acta* 41: 225–231.
- Plado J., Pesonen L. J., Koeberl C., and Elo S. 2000. The Bosumtwi meteorite impact structure, Ghana: A magnetic model. *Meteoritics & Planetary Science* 35:723–732.
- Reimold W. U., Koeberl C., and Bishop J. 1994. Roter Kamm impact crater, Namibia: Geochemistry of basement rocks and breccias. *Geochimica et Cosmochimica Acta* 58:2689–2710.
- Reimold W. U., Brandt D., and Koeberl C. 1998. Detailed structural analysis of the rim of a large, complex impact crater: Bosumtwi crater, Ghana. *Geology* 26:543–546.
- Reimann C., Filzmoser P., and Garrett R. G. 2002. Factor analysis applied to regional geochemical data: Problems and possibilities. *Applied Geochemistry* 17:185–206.
- Rollinson H. R. 1993. *Using geochemical data: Evaluation, presentation, interpretation*. Harlow, United Kingdom: Longman. 352 p.
- Schnetzler C. C., Pinson W. H., and Hurley P. M. 1966. Rubidium-strontium age of the Bosumtwi crater area, Ghana, compared with the age of the Ivory Coast tektites. *Science* 151:817–819.
- Schnetzler C. C., Philpotts J. A., and Thomas H. H. 1967. Rare earth and barium abundances in Ivory Coast tektites and rocks from the Bosumtwi crater area, Ghana. *Geochimica et Cosmochimica Acta* 31:1987–1993.
- Scholz C. A., Karp T., Brooks K. M., Milkereit B., Amoako P. Y. O., and Arko J. A. 2002. Pronounced central uplift identified in the Bosumtwi impact structure, Ghana, using multichannel seismic reflection data. *Geology* 30:939–942.
- Shaw D. M. 1956. Geochemistry of polytic rocks. Part II: Major elements and general geochemistry. *GSA Bulletin* 67:919–934.
- Son T. H. and Koeberl C. 2005. Chemical variation within fragments of Australasian tektites. *Meteoritics & Planetary Science* 40: 805–815.
- Stöckelmann D. and Reimold W. U. 1989. The HMX mixing calculation program. *Mathematical Geology* 21:853–860.
- Taylor S. R. and McLennan S. M. 1985. *The continental crust: Its composition and evolution*. Oxford: Blackwell Scientific Publications. 312 p.
- Woodfield P. D. 1966. The geology of the ¼° field sheet 91, Fumso N. W. *Ghana Geological Survey Bulletin* 30:1–66.
- Wright J. B., Hastings D. A., Jones W. B., and Williams H. R. 1985. *Geology and mineral resources of West Africa*. London: Allen & Unwin. 187 p.
-

Shock Metamorphism of Bosumtwi Impact Crater Rocks, Shock Attenuation, and Uplift Formation

Ludovic Ferrière¹, Christian Koeberl^{1*}, Boris A. Ivanov², Wolf Uwe Reimold³

¹*Department of Lithospheric Research, University of Vienna, Althanstrasse 14, A-1090 Vienna, Austria.*

²*Institute for Dynamics of Geospheres, Russian Academy of Sciences, Leninsky Prospect 38-1, 119334 Moscow, Russia.*

³*Museum of Natural History (Mineralogy), Humboldt University, Invalidenstrasse 43, D-10115 Berlin, Germany.*

**To whom correspondence should be addressed. E-mail: christian.koeberl@univie.ac.at
Tel.: +43-1-4277-53110; fax: +43-1-4277-9534.*

Science, In Press, Corrected Proof, Available online 12 December 2008

Shock wave attenuation rate and formation of central uplifts are not precisely constrained for moderately sized complex impact structures. The distribution of shock metamorphism in drilled basement rocks from the 10.5-kilometer-diameter Bosumtwi crater, and results of numerical modeling of inelastic rock deformation and modification processes during uplift, constrained with petrographic data, allowed reconstruction of the pre-impact position of the drilled rocks and revealed a shock attenuation by ~5 gigapascals in the uppermost 200 meters of the central uplift. The proportion of shocked quartz grains and the average number of planar deformation feature sets per grain provide a sensitive indication of minor changes in shock pressure. The results further imply that for moderately sized craters the rise of the central uplift is dominated by brittle failure.

During the contact and compression phase of hypervelocity impact, a spherical shock wave is generated, propagates through the target rocks (1), and is attenuated rapidly with increasing distance. Consequently, a variety of shock effects are produced in rock-forming minerals, including formation of planar deformation features (PDFs) and high-pressure phases. The relative spatial distribution of these shock transformations and deformations formed at different pressures and temperatures [e.g., (2, 3)] in autochthonous rocks, at the scale of the impact structure, can be used to estimate maximum shock pressures and, consequently, the rate of shock attenuation. However, many parameters such as rock type as well as lithological contrasts, texture, fabric, grain size, preshock orientation of grains, porosity, and volatile content, influence the shock levels attained locally. Furthermore, and typical in the case of complex impact structures (i.e., craters with diameters ≥ 2 to 4 km on Earth) (4), the original position and distribution of the shocked rocks is modified when, because of gravitational instability of the transient cavity rim, rebound of the crater floor leads to formation of a central uplift. Redistribution of rock is also associated with the collapse of the initially oversteepened central uplift (5).

There have been several efforts to estimate shock wave decay, mainly from nuclear and explosion crater studies or by numerical modeling [e.g., (6–8)]. Few studies have tried

to quantify shock pressure distribution in simple (9) and complex impact structures (9–16) [see supporting online material (SOM text)] by using the frequency of shock-induced deformations in quartz grains from samples taken along profiles across the erosion surface of an impact structure. Only three investigations have explored the relative vertical decay of recorded shock pressure in complex impact structures, two for the ~40-km-diameter Puchezh-Katunki impact structure (13, 15) and another for the ~65-km-diameter Kara crater (11).

We characterized the shock wave attenuation in the uppermost part of the central uplift of the Bosumtwi impact structure, a moderately sized (10.5-km diameter) and well preserved complex impact structure [e.g., (17)], and attempted to reconstruct the original position of the sampled section in the target before crater modification. This is possible by combining petrographic investigations (at the microscale) with modeling of inelastic rock deformation (at the mesoscale) and modification processes during uplift (at the megascale). This approach allows us to constrain shock wave attenuation and rock deformation during central uplift formation.

We studied drill core samples from the central part of the structure retrieved in the 2004 International Continental Scientific Drilling Program (ICDP) Bosumtwi drilling project (18–20) (SOM text). The central uplift extends ~130 m above the crater moat, is ~1.9 km wide (21), and is composed of metasedimentary rocks [mostly metagreywacke (MGW) and shale] (19). Two cores were retrieved by the ICDP project: core LB-08A from the outer flank of the central uplift and core LB-07A from the deep crater moat (Fig. 1 and SOM text).

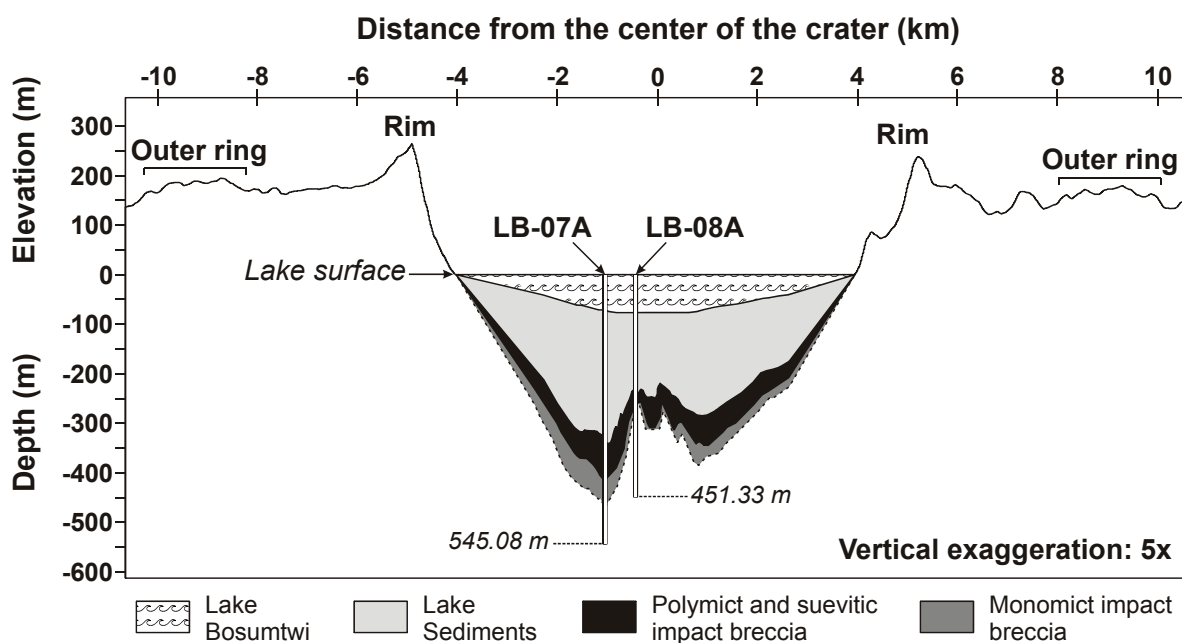


Figure 1. Cross section of the Bosumtwi impact structure, based on Shuttle Radar Topography Mission (SRTM) data for the regional topography of the exposed portion of the crater (profile from west to east) and on a northwest-southeast seismic reflection profile (21) across the central crater. Location of boreholes LB-07A and LB-08A are given. The volume of lake sediments is based on seismic reflection data. The distribution of “polymict and suevitic impact breccia” and “monomict impact breccia” is based on observations from cores LB-07A and LB-08A (19, 20), as well as interpretations of seismic reflection data. Depths and elevations are relative to lake level. SRTM data were available online (www2.jpl.nasa.gov/srtm/; accessed 3 March 2008).

To derive the distribution of shock metamorphic effects with depth, we studied 18 MGW samples from 271.4 to 451.2 m depth in core LB-08A (Fig. 1), recording modal analysis and shock deformation properties of 8991 quartz grains (22) (table S1 and S2). We determined 1056 crystallographic orientations of sets of PDFs in 602 quartz grains (table S3), because predominance of specific orientations of PDFs in quartz has long been considered to indicate different shock pressures [e.g., (23)].

The abundance of shocked quartz grains (i.e., quartz grains with planar fractures and/or PDFs) decreases with increasing depth (for PDFs, cf. Fig. 2). We interpret this decrease to reflect the variation of shock pressure in the uppermost part of the central uplift.

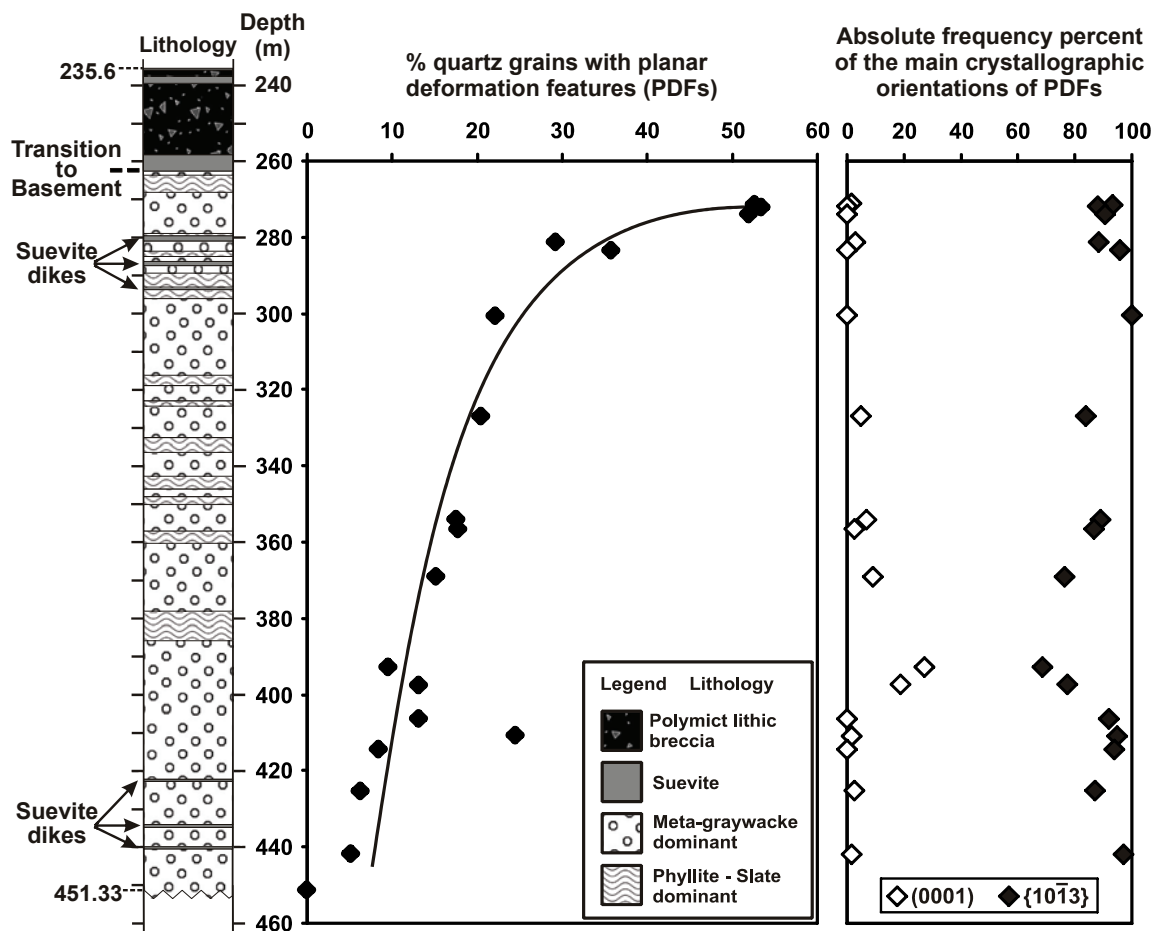


Figure 2. Simplified lithostratigraphic column for drill core LB-08A [after (19)] and PDF data for 18 MGW samples from the basement section. The abundance of quartz grains with PDFs relative to the total number of quartz grains is shown (left, solid diamond) and, on the right, the absolute frequency percent of the two main PDF crystallographic orientations (open diamond symbols for basal PDF and solid diamonds for $\omega\{10\bar{1}3\}$ crystallographic orientation data) in quartz grains, as measured on a universal stage.

Similarly, the average number of PDF sets per quartz grain (N) decreases steadily with depth, from ~ 2.1 at 271 m depth to ~ 1.6 at 442 m (Fig. 3). We interpret the decrease of N as evidence of the shock pressure attenuation with distance from shock wave origin.

No clear change was evident over this interval in the relative frequencies of the main crystallographic orientations of PDF sets in quartz grains with increasing depth (Fig. 2 and Table S3). Most of the poles to the PDF planes correspond to the $\omega\{10\bar{1}3\}$ orientation,

and only a few, typically less than 5 relative-percent (rel%) of the orientation data obtained per section, correspond to basal [i.e., parallel to (0001)] planes. Only two samples, KR8-85 and KR8-89, from 390 to 400 m depth, show a higher proportion of basal PDF, at about 27 and 19 rel%, respectively (Table S3). These two MGW samples originated just below a 10-m-thick layer of comparatively fine-grained metasedimentary rocks (phyllite and slate; Fig. 2); thus, it is possible that shock wave interference at the transition from metapelite to MGW resulted in the local formation of a larger proportion of basal PDFs [basal PDFs are formed at lower pressures (from 8 to 10 GPa) than $\omega\{10\bar{1}3\}$ orientations (>10 GPa); e.g., (2)]. However, about 50% of the basal PDFs measured in these two samples occur in association with $\omega\{10\bar{1}3\}$ PDF (i.e., dual sets of PDFs in the same quartz grain), which indicates relatively high shock pressures. Thus, minor variations of the relative proportions of crystallographic orientations of PDF sets in quartz grains with depth cannot be used to quantify the slight attenuation of the shock pressure along the ~200 m-long bedrock section investigated here. Because the relative proportion of shocked quartz grains, as well as the number of PDF sets per quartz grain, steadily decrease with depth (Figs. 2 and 3), we infer that the shock wave was attenuated but not by much.

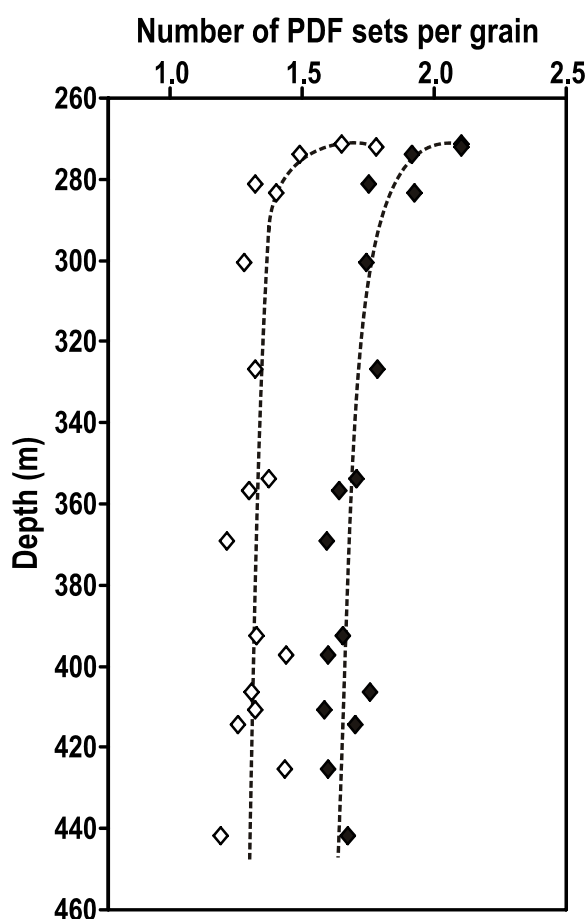


Figure 3. Average number of PDF sets per host quartz grain (N) in MGW samples from the uppermost ~ 200 m of basement drilled in the central uplift of the Bosumtwi impact structure. For both methods, that is, with use of a petrographic microscope (under horizontal stage examination; open diamonds) and with the U-stage (solid diamonds), N values follow the same trend of decreasing abundance of PDF sets per grain with increasing depth.

On the basis of the relative abundances of quartz grains with PDFs, the presence of multiple sets of PDFs in quartz grains (up to four sets), and the occurrence of various PDF set orientations, we estimate that the studied section experienced peak shock pressures of up to ~25 to 30 GPa [e.g., (2, 24–25)]. The upper limit of peak shock pressure (i.e., 30 GPa) is further constrained by the lack of isotropization of the quartz grains, which typically begins

at this shock pressure [e.g., (2)]. The estimated pressure range is much too low for either partial or total shock melting of the whole rock, which is in agreement with macroscopic and microscopic observations on these metasedimentary rocks that have preserved their preimpact texture (19) (SOM text). Thus, the rise of the central uplift was not facilitated by shock-induced plasticity, and brittle failure was dominant. This finding is also supported by the presence of abundant faults in the central uplift, as indicated by reflection seismic data (21).

To further evaluate the apparent shock attenuation, we calculated the expected shock pressure attenuation and reconstructed the preimpact position of the investigated section of the central uplift by numerical modeling, by using a variant of the SALEB numerical code (26) (SOM text). To model the crater and central uplift properly, we did a direct parametric fit of our model to the observed crater geometry, without usage of scaling relations for the crater size (SOM text and Fig. S3). After modeling, tracers in the vicinity of the exact location of the two drill holes were identified (allowing the tracking of their initial positions), and lastly the position of the top of the “model core” was defined by the maximum recorded shock pressure of 30 GPa (based on our petrographic investigations). Then, the initial position of these tracers was plotted (Fig. 4). Our calculations show that, despite quite similar present-day depths, the initial depth of rocks in the crater moat (core LB-07A) was above that of the rocks in the central uplift corehole (Fig. 4). This specific displacement of the target rocks during crater modification is interesting because it indicates that rocks occurring in the outer flank of the central uplift were originally more deeply buried than the basement rocks drilled below the deep crater moat and, thus, were subjected to somewhat lower shock pressures. Thus, before estimating shock attenuation in complex impact structures, it is important to consider the differential movements of the target rocks, which cause changes in the spherical shock-attenuation scheme. The numerical model (Fig. 4 and SOM text) indicates that the samples investigated in core LB-08A have been uplifted by about 1.2 to 1.5 km. By using the relationship $SU = 0.086 D^{1.03}$ (27) (where D is the crater diameter), we estimated the amount of structural uplift (SU) for the Bosumtwi central uplift at about 1 km, in good agreement with the modeling result.

Taking into account the uplift of target rocks, the calculated apparent shock attenuation along the about 200 m of investigated core is ~5 to 10 GPa (Fig. S4). On the basis of the general absence of changes in the statistics of PDF orientations, a maximum shock attenuation of 5 GPa seems to be the more realistic value.

The percentage of shocked quartz grains and the number of PDF sets per grain are more sensitive indicators of minor changes in shock pressure than pure PDF orientation statistics. The combination of detailed petrographic investigation and numerical modeling indicates that both of these approaches are essential to reconstruct the preimpact position of rocks and to characterize properly the shock pressure distribution at the scale of an impact structure. Our observations suggest that, in the case of the 10.5-km-diameter Bosumtwi impact structure, the uppermost rocks of the central uplift experienced shock pressures below 30 GPa, whereas pressures up to 40 to 45 GPa were recorded for the about four times larger Puchezh-Katunki impact structure (15). Shock attenuation in the uppermost part of a central uplift has been, for the first time, constrained by detailed shock degree profiling at the micro-scale.

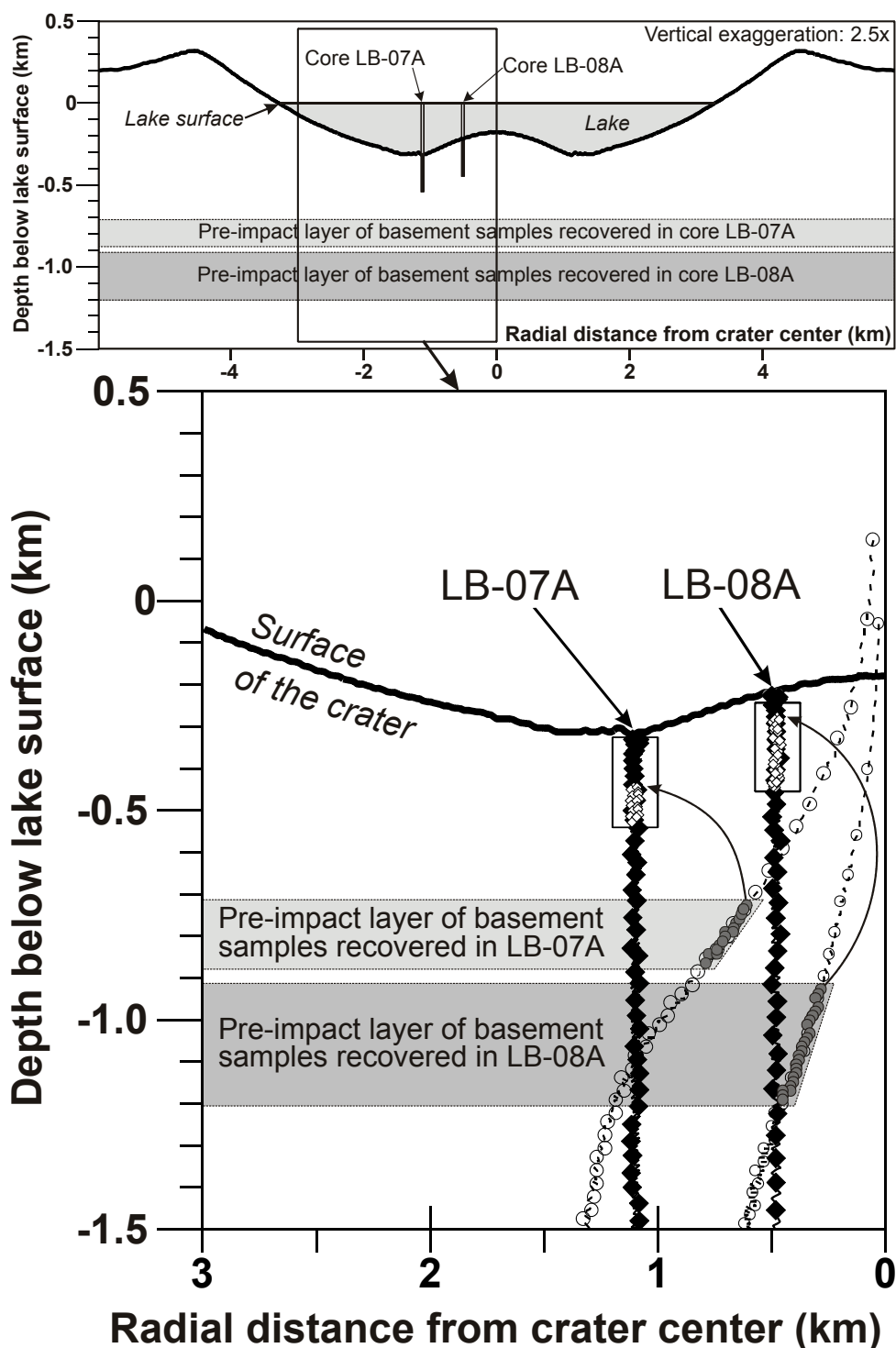


Figure 4. Calculated crater profile with enlarged inner part showing initial and final positions of rocks recovered in drill cores LB-07A (from the crater moat) and LB-08A (from the outer flank of the central uplift). Solid diamonds show final positions of tracers (0.48 and 1.1 km radial distance from crater center), whereas open circles indicate their initial positions in the pre-impact target stratigraphy. Gray dots and open diamonds show, respectively, the initial and final positions of basement samples (i.e., investigated MGW samples in core LB-08A) recovered in drill cores. Solid diamonds above open diamonds represent the modeled impact breccia. Locations of drill cores are indicated by large open rectangles. Model run with ANEOS (ANalytical Equation Of State) granite (28), an impact velocity of 20 km s^{-1} , and a residual friction (μ) of 0.4. For comparison of the calculated and the actual cross sections of the Bosumtwi crater, see fig. S3.

Numerical modeling of this section of the central uplift has then established where this section of the central uplift was located before uplift formation, which was only possible once the shock regime had been established by micropetrography. The results imply that, for moderately sized impact craters, the rise of the central uplift is dominated by brittle failure, whereas in the case of larger impact structures, and also depending on rock properties, the uplifted, relatively stronger shocked rocks may behave in a more ductile manner.

References and Notes

1. D. Stöffler, *Fortschr. Mineral.* **49**, 50 (1972).
2. D. Stöffler, F. Langenhorst, *Meteorit. Planet. Sci.* **29**, 155 (1994).
3. R. A. F. Grieve, F. Langenhorst, D. Stöffler, *Meteorit. Planet. Sci.* **31**, 6 (1996).
4. R. A. F. Grieve, *Annu. Rev. Earth Planet. Sci.* **15**, 245 (1987).
5. H. J. Melosh, *Impact Cratering—A Geological Process* (Oxford Univ. Press, New York, 1989).
6. J. T. Cherry, F. L. Petersen, in *Peaceful Nuclear Explosions* (International Atomic Energy Agency, Vienna, 1970), pp. 241–325.
7. T. J. Ahrens, J. D. O’Keefe, in *Impact and Explosion Cratering*, D. J. Roddy, R. O. Pepin, R. B. Merrill, Eds. (Pergamon, New York, 1977), pp. 639–656.
8. N. K. Mitani, *J. Geophys. Res.* **108**, 5003 (2003).
9. P. B. Robertson, R. A. F. Grieve, in *Impact and Explosion Cratering*, D. J. Roddy, R. O. Pepin, R. B. Merrill, Eds. (Pergamon, New York, 1977), pp. 687–702.
10. R. A. F. Grieve, P. B. Robertson, *Contrib. Mineral. Petrol.* **58**, 37 (1976).
11. L. V. Sazonova, N. N. Karotaeve, G. Y. Ponomarev, A. I. Dabizha, in *Impactites*, A. A. Marakushev, Ed. (Moscow State Univ., Moscow, 1981), pp. 93–133.
12. R. A. F. Grieve, J. M. Coderre, P. B. Robertson, J. Alexopoulos, *Tectonophysics* **171**, 185 (1990).
13. V. I. Fel’dman, L. V. Sazonova, S. I. Kotel’nikov, *Dokl. Akad. Nauk SSSR* **349**, 658 (1996).
14. B. O. Dressler, V. L. Sharpton, B. C. Schuraytz, *Contrib. Mineral. Petrol.* **130**, 275 (1998).
15. V. L. Masaitis, L. A. Pevzner, *Deep Drilling in the Impact Structure: Puchezh-Katunki, Russia* (VSEGEI, St. Petersburg, 1999).
16. R. L. Gibson, W. U. Reimold, *Geol. Soc. Am. Spec. Pap.* **384**, 329 (1996).
17. C. Koeberl, W. U. Reimold, *Yearb. Austrian Geol. Surv.* **145**, 31 (2005).
18. C. Koeberl *et al.*, *Meteorit. Planet. Sci.* **42**, 483 (2007).
19. L. Ferrière, C. Koeberl, W. U. Reimold, *Meteorit. Planet. Sci.* **42**, 611 (2007).
20. L. Coney, R. L. Gibson, W. U. Reimold, C. Koeberl, *Meteorit. Planet. Sci.* **42**, 569 (2007).
21. C. A. Scholz *et al.*, *Geology* **30**, 939 (2002).
22. Materials and methods are available as supporting material on *Science Online*.

23. F. Hörz, in *Shock Metamorphism of Natural Materials*, B. M. French, N. M. Short, Eds. Mono, Baltimore, 1968), pp. 243–253.
24. A. R. Huffman, W. U. Reimold, *Tectonophysics* **256**, 165 (1996).
25. B. M. French, *Traces of Catastrophe: A Handbook of Shock-Metamorphic Effects in Terrestrial Meteorite Impact Structures* [LPI Contribution No. 954, Lunar and Planetary Institute (LPI), Houston, TX, 1998].
26. B. Ivanov, *Solar Sys. Res.* **39**, 381 (2005).
27. M. J. Cintala, R. A. F. Grieve, *Meteorit. Planet. Sci.* **33**, 889 (1998).
28. E. Pierazzo, A. M. Vickery, H. J. Melosh, *Icarus* **127**, 408 (1997).
29. Drilling was funded by ICDP, NSF, the Austrian Fonds zur Förderung der wissenschaftlichen Forschung (FWF), the Canadian Natural Sciences and Engineering Research Council, and the Austrian Academy of Sciences. We thank DOSECC for the drilling operations. This work was supported by the Austrian FWF (grants P17194-N10 and P18862-N10) and the Austrian Academy of Sciences. B. I. was supported by the Russian Foundation for Basic Science (RFBR grant 08-05-00908-a), and U. R.'s research is supported by the German Science Foundation (Deutsche Forschungsgemeinschaft) and Humboldt University of Berlin.

Supporting Online Material

[www.sciencemag.org/cgi/content/full/322/5908\[PAGE\]/DC1](http://www.sciencemag.org/cgi/content/full/322/5908[PAGE]/DC1)

Materials and Methods

SOM text

Figs. S1 to S4

Tables S1 to S4

References

23 September 2008; accepted 10 November 2008

10.1126/science.1166283

Supporting Online Material

Materials and Methods:

Eighteen thin sections of meta-graywacke (MGW) samples from the basement rock depth interval from 271.43 m (KR8-029) to 451.23 m (KR8-125) of core LB-08A were prepared. Special attention was paid to avoid significant variation in grain size between the different MGW samples.

The MGW samples are light to dark gray in color and mostly medium-grained (grain size range from ~200 to 600 μm). Note that samples KR8-029, KR8-030, KR8-031, KR8-101, KR8-109, and KR8-119 are relatively coarser-grained, with grain sizes up to a few millimeters. However, these samples do not show any different results from the medium-grained samples, in terms of either abundance of shocked quartz grains or orientation statistics of planar deformation features (PDFs). Most of the MGW samples do not show pre-impact deformation; only a few (KR8-045, KR8-066, KR8-067, and KR8-125) are sheared or display a mylonitic texture (KR8-036, KR8-037, and KR8-071), but these samples do not show any different results from the other samples. Meta-graywacke consists of poorly sorted mineral grains/fragments embedded in a compact matrix mostly composed of very fine-grained secondary minerals, such as chlorite and sericite. Petrographic descriptions of the samples are reported in Ferrière et al. (*S1*); modal analyses are reported in Table S1.

Our investigations were carried out using an optical microscope and a four-axis universal stage (U-stage; cf. *S2*) following three distinct steps:

- 1) Standard thin-section point counting techniques (e.g., *S3*) were applied to establish quantitative modal compositions. The modal analysis was done by counting ~960 points, on average, per thin section (with a total of 15892 points evaluated for the eighteen sections). The whole area of each thin section was investigated with 0.3 mm spaces between points and 0.9 mm between traverses. Microscope magnification for this work was 312.5 x. Mineral grains less than 50 μm apparent diameter were counted as matrix. Results are reported in Table S1.

- 2) The same thin sections were then subjected to a systematic analysis of the properties of quartz grains; e.g., unshocked, shocked (with planar fractures [PFs] and PDFs), number of sets of PF and PDF, respectively, presence of PDF decoration, toasted appearance, etc (Table S2). Only quartz grains with sizes larger than 50 μm were examined along traverses spaced at 1.2 mm. For each thin section, about 500 quartz grains were investigated.

- 3) The crystallographic orientations of 1056 PDF sets in 602 PDF-bearing quartz grains were measured by U-stage, on seventeen thin sections of MGW (no PDF were observed in quartz grains from sample KR8-125; depth = 451.2 m) following the methods described by, e.g., Engelhardt and Bertsch (*S4*), Stöffler and Langenhorst (*S5*), and Grieve et al. (*S6*). The number of measured PDF is restricted to the surface area that can be investigated with the U-stage (usually about one third of the section). The optic axis orientation and that of the pole to a PDF plane were determined, and PDF were indexed in a stereonet with the c-axis

placed into the center (e.g., *S4*, *S5*). The PDF poles were indexed with Miller-Bravais indices (*hkl*) for quartz following techniques outlined in, e.g., Engelhardt and Bertsch (*S4*) and Stöffler and Langenhorst (*S5*), and only between 0 and 5.6 rel% of all the measured sets in the different samples could not be indexed. To allow comparison between the different samples (without the influence of the number of unindexed PDFs planes on the proportion of the various orientations), the unindexed PDF planes were subtracted from the total number of measured PDFs for each sample. Data in absolute frequency percent (i.e., corrected for unindexed PDFs) are reported in Table S3. The reported data represent the totality of PDF orientations measured in all quartz grains, including the grains with 1, 2, 3, and 4 sets; to control the robustness of our data, absolute frequency of indexed PDFs was also recalculated using only measurements of PDF orientations measured in quartz grains with 2 sets and no significant differences were observed.

Supporting online text:

Previous studies on shock pressure distribution in impact structures

In most previous studies of shock pressure distribution in impact structures (e.g., *S7–S11*), authors used a method similar to that developed by Grieve and Robertson (*S12*). This method derives average shock pressure values for a given sample based on the assignation of fixed values of pressure to each individual PDF orientation, namely, 7.5 GPa for PDF parallel to $c(0001)$, 10 GPa for PDF parallel to $\omega\{10\bar{1}3\}$, 14 GPa for PDF parallel to $\{22\bar{4}1\}$, $r/z\{10\bar{1}1\}$, and $\xi\{11\bar{2}2\}$, and 16 GPa for PDF parallel to $\pi\{10\bar{1}2\}$. Average shock pressure is then calculated on the basis of proportions of different PDF orientations.

A problem with this approach is that other typical crystallographic orientations of PDFs in shocked quartz (as $m\{10\bar{1}0\}$, $s\{11\bar{2}1\}$, $\rho\{21\bar{3}1\}$, $x\{51\bar{6}1\}$, $a\{11\bar{2}0\}$, etc.) (*S5*) are ignored, and it is not clear how these orientations of PDFs enter into the calculation of average pressure values. It is also not clear how co-existing orientations (e.g., c and π) enter these counting statistics – as these indicators of lower and moderate shock pressures may well form at the same pressure – in the example case more likely at the higher end of the range given by these two orientations. There are also studies that show that the onset of double orientation development is more likely at ca. 15 GPa (e.g., *S13*). In addition, these studies did not provide sufficient descriptions and characteristics of the investigated samples, when differences in lithology, texture, fabric, grain size, porosity, etc., in the investigated lithologies, as well as rheological contrasts between adjacent lithologies and/or different degrees of brittle deformation can significantly influence the development of PDFs in quartz. Furthermore, only limited numbers of quartz grains and only few PDF set orientations were measured, raising questions about how representative these results are.

Brief description of the Bosumtwi impact structure

The Bosumtwi impact structure, located in Ghana, West Africa, is a well-preserved, complex, young impact structure, with a pronounced rim and small central uplift (e.g., *S14–*

S15). The structure has a rim-to-rim diameter of about 10.5 km. The crater, only 1.07 Myr old, was excavated in lower greenschist facies metasediments of the 2.1-2.2 Gyr Birimian Supergroup, and is now filled almost entirely by Lake Bosumtwi of 8 km diameter (*S15*; and references therein). In addition to earlier remote sensing and geophysical, as well as limited surface-based, studies, a recent international and multidisciplinary drilling project by the International Continental Scientific Drilling Program (ICDP) (see *S16* for review) led to the recovery of two drill cores from the crater fill and underlying basement. Cores LB-07A and LB-08A (Fig. 1) were retrieved from the deep crater moat and the outer flank of the central uplift, respectively. The annular moat is filled with over 135 m of lithic and suevitic impact breccia. A well-defined, faulted, collapsed central uplift occurs near the north-central part of the crater (*S17*). The central uplift, composed of metasedimentary rocks overlain by about 25 m of fallback impact breccia (*S1*, *S18*), reaches ~130 m above the crater moat and is ~1.9 km wide (*S17*).

Geological setting and stratigraphy of drill core LB-08A

As noted above, the Bosumtwi impact structure was mostly excavated in lower greenschist-facies supracrustal rocks of the Birimian Supergroup, an assemblage of metasedimentary rocks that comprise phyllites, meta-tuffs, meta-graywackes, quartzitic meta-graywackes, schists, shales, and slates (e.g., *S15*).

In this study we focus on core LB-08A (Fig. 1), which was recovered from 235.6 to 451.33 m, representing 215.7 m of core with a diameter of 6 cm. All depths indicated are depths below lake level. Initial descriptions of drill core LB-08A were reported by Deutsch et al. (*S18*) and Ferrière et al. (*S1*). According to these authors, core LB-08A can be subdivided into two parts: the uppermost 25 m, composed of polymict lithic impact breccia (clast-supported) intercalated with suevite units, and the lower part composed of fractured/brecciated metasedimentary rocks between 262 to 451 m, dominated by MGW units alternating with phyllite and slate and intersected by a few suevite dikelets. The upper 25 m of the core most likely represent fallback impact breccia superimposed on the basement rocks that have been shocked and then uplifted during impact crater formation (*S1*).

In comparison, core LB-07A, drilled only 615 m northwest of the drill site for core LB-08A (Fig. 1), is composed of a thick section of impact breccia (333.4–470.6 m depth) overlying basement rocks (mostly metapelites and some MGW), from 470.6 m to the total drilling depth of 545.1 m (*S19*).

Petrographic investigations

1) Modal analyses:

The modal compositions for the MGW samples are reported in volume% in Table S1. Quartz comprises an overall estimated 43 vol%, and typically, feldspar (K-feldspar and plagioclase) grains/fragments account for about 30 vol%, with some variation between samples (see Table S1). The matrix represents, on average, about 10 vol%, with significant variations, from 2.7 vol% (in KR8-125) to 26.5 vol% (in KR8-36).

Table S1. Modal analyses (in vol%) by optical microscopy on thin sections of eighteen meta-graywacke samples from the basement, drill core LB-08A, Bosumtwi impact structure^a.

Sample (KR8-#)	29	30	31	36	37	45	56	66	67	71	85	89	96	98	101	109	119	125	
Depth (m)	271.4	272.0	274.0	281.3	283.5	300.4	326.8	354.0	356.6	369.0	392.7	397.3	406.3	410.7	414.3	425.2	441.9	451.2	Average
Quartz	46.4	43.5	40.5	34.9	42.5	37.3	45.6	39.8	50.9	44.9	35.0	46.9	37.0	43.4	46.0	45.7	52.4	42.2	43.0
Feldspar	K	23.7	27.8	18.9	22.3	14.4	20.3	22.6	17.1	16.8	24.4	10.3	21.2	18.7	18.5	12.7	15.3	17.6	18.8
	P	10.8	10.9	13.7	8.6	6.5	12.9	8.2	9.0	13.5	13.7	9.8	13.1	12.2	14.8	11.7	9.1	14.1	11.3
Total	34.5	38.7	32.5	31.0	20.8	33.2	27.1	30.8	26.1	30.3	38.1	20.0	34.2	31.0	33.2	24.4	24.4	31.7	30.1
Matrix ^b	6.5	6.0	7.4	26.5	17.6	13.3	10.3	12.8	6.1	4.3	14.3	15.1	16.6	11.6	7.6	8.1	5.5	2.7	10.7
Biotite	n.d.	n.d.	n.d.	x	x	x	x	x	x	n.d.	n.d.	x	x	n.d.	n.d.	3.9	x	x	0.3
Chlorite	4.7	3.2	9.4	1.7	10.4	2.9	4.2	7.5	4.6	8.5	6.4	3.5	3.2	2.4	6.2	5.1	7.3	8.8	5.6
Muscovite	1.3	2.2	2.3	1.4	4.2	1.5	5.1	2.9	3.5	2.1	2.3	3.3	1.4	1.7	x	x	0.9	3.3	2.2
Chert	0.6	1.7	1.1	n.d.	1.2	1.5	1.1	x	1.0	1.8	0.6	0.6	n.d.	1.6	n.d.	1.4	1.6	1.7	1.0
Calcite	3.6	2.5	1.2	2.2	x	2.9	0.8	3.0	4.8	3.0	0.6	5.1	1.9	0.8	1.2	2.0	5.8	7.2	2.7
Opaque minerals	1.7	1.5	4.1	1.9	n.d.	1.8	1.0	2.1	1.1	2.0	1.8	3.2	1.4	2.5	0.5	1.0	1.9	1.9	1.7
Other minerals ^c	0.6	0.8	1.5	x	2.7	5.3	4.5	0.7	1.8	3.1	1.0	2.1	3.9	5.0	5.0	7.9	x	0.5	2.6
Total Counts	1413	1827	1352	1150	1204	714	708	1155	909	1039	877	779	567	827	644	692	694	754	961

^aK = alkali feldspar; P = plagioclase; x = traces (<0.5 vol%); n.d. = none detected.^bMatrix represents all grains smaller than 50 µm.^cIncluding epidote, amphibole, sphene, apatite, zircon, and allanite (in relative order of decreasing abundance).

In addition, MGW contains (with decreasing abundance): chlorite, calcite, muscovite, opaque minerals (mostly pyrite), chert clasts, biotite, epidote, amphibole, sphene, apatite, zircon, and allanite (Table S1). Chlorite is generally present as a secondary alteration product after biotite. No specific or discernible trends with depth in the relative abundance of the different populations of minerals have been observed.

2) Properties of quartz grains and occurrence of shocked quartz:

Ferrière et al. (S1) noted that most of the MGW from the basement (i.e., in core LB-08A) is shocked (occurrence of PFs and PDFs in quartz grains). Quartz occurs mostly as single crystals (rarely as polycrystalline clasts) and frequently shows micro-fractures and undulatory extinction. Our investigations of the properties of ~9000 quartz grains in eighteen MGW samples (see Table S2) indicate that quartz grains with undulatory extinction are irregularly distributed through the central uplift interval. Shocked quartz grains observed in MGW display PFs and PDFs (1, 2, 3, and rarely 4 sets; Fig. S1); about 50 rel%, on average, of the PDFs are decorated with numerous small fluid inclusions (Table S2). Traditionally decorated PDFs are considered “secondary” features, formed by annealing and aqueous alteration of non-decorated amorphous PDFs (e.g., S6, S20).

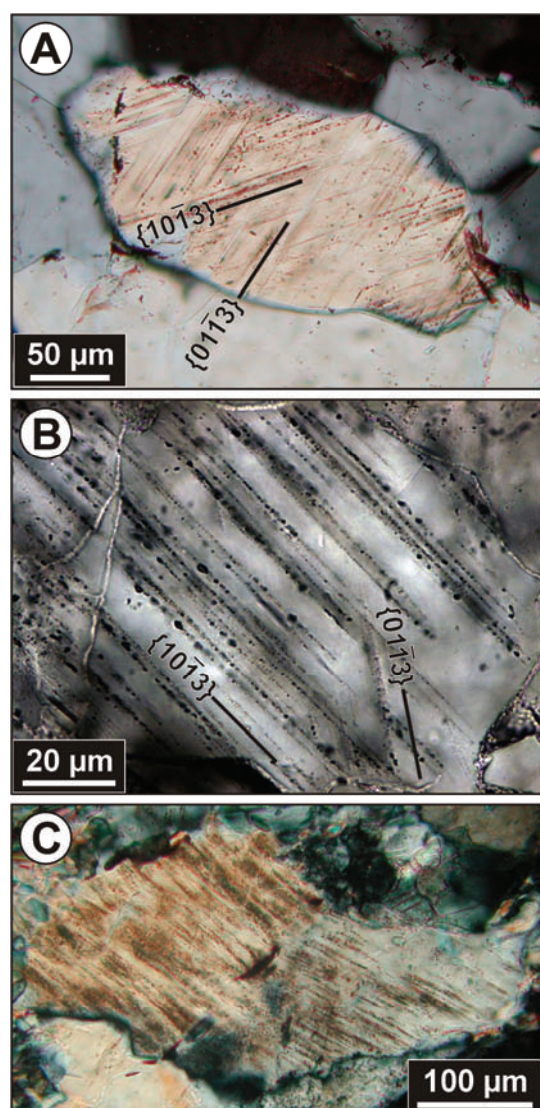


Figure S1. Microphotographs of shocked quartz grains in meta-graywacke. a) Quartz grain with 2 sets of PDFs. Sample KR8-067; depth = 356.59 m (cross-polarized light). b) Decorated (with numerous tiny fluid inclusions) PDFs in a quartz grain (2 sets). Sample KR8-056; depth = 326.78 m (plane-polarized light). c) Typical quartz grains showing the toasted appearance. Sample KR8-098; depth = 410.74 m (cross-polarized light).

In some instances, the quartz grains have a grayish brown appearance (Fig. S1c), with patches containing micrometer-sized fluid inclusions (too small to be resolved with the petrographic microscope); this has been described as “toasted appearance” (S21, S22). About 20 rel% of the shocked quartz grains show this “toasted appearance” (Table S2). The abundance of decorated PDFs and of toasted quartz grains does not seem to be dependent on depth. However, the relative abundances of quartz grains with decorated PDFs and of those with “toasted appearance” indicate a relatively good correlation ($r = 0.80$; Fig. S2).

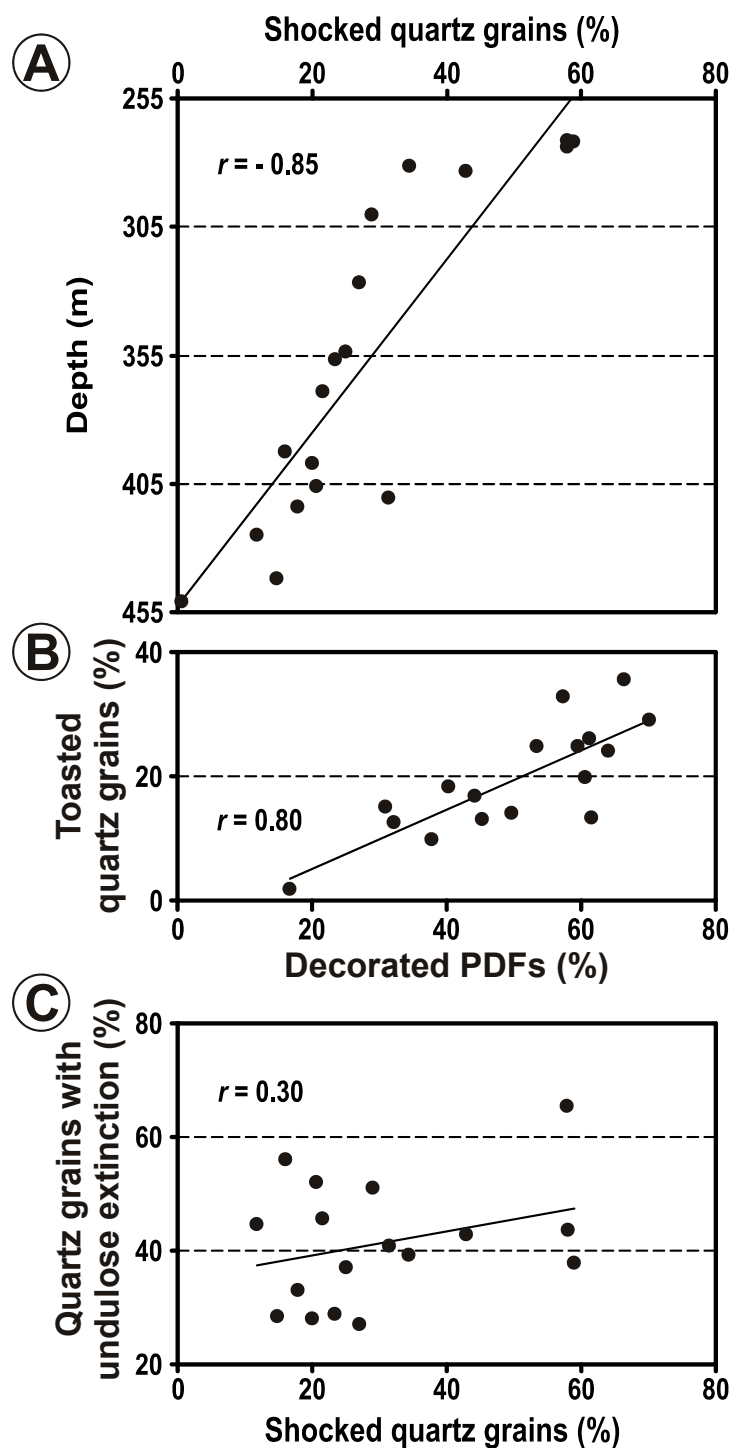


Figure S2. Binary diagrams showing the degree of correlation between: a) the location of the samples in LB-08A drill core (i.e., depth; in meters) and the relative abundance of shocked quartz grains (i.e., quartz grains with PFs and PDFs; in %); b) the relative abundance of toasted quartz grains and those with decorated PDFs (in %); c) the relative abundance of quartz grains that show undulose extinction and the abundance of shocked quartz grains (in %). No correlation is observed between the proportion of quartz grains with undulose extinction and the proportion of shocked quartz grains.

Table S2. Results from point-counting of quartz grain properties in eighteen meta-graywacke samples from the basement, drill core LB-08A, Bosumtwi impact structure, in comparison with PDF set abundances determined using universal stage^a.

Sample (KR8-#)	29	30	31	36	37	45	56	66	67	71	85	89	96	98	101	109	119	125	
Depth (m)	271.4	272.0	274.0	281.3	283.5	300.4	326.8	354.0	356.6	369.0	392.7	397.3	406.3	410.7	414.3	425.2	441.9	451.2	Total
Grains counted	508	521	566	520	490	501	533	520	564	519	511	556	374	522	461	476	407	442	8991
	% relative to total No. of quartz grains within sample																		
Unshocked	42	41	42	66	57	71	73	75	77	78	84	80	79	69	82	88	85	99	
Shocked	58	59	58	34	43	29	27	25	23	22	16	20	21	31	18	12	15	<1	
	% relative to total No. of shocked quartz grains within sample																		
PF	9.2	9.4	10.4	15.1	16.7	23.4	24.3	30.0	24.2	29.5	40.2	34.2	36.4	22.0	52.4	46.4	65.0	100	
PDF	90.8	90.6	89.6	84.9	83.3	76.6	75.7	70.0	75.8	70.5	59.8	65.8	63.6	78.0	47.6	53.6	35.0	n.d.	
	% relative to total No. of quartz grains with PDFs examined within sample																		
PDF sets	1	43	38	54	68	62	72	68	63	71	78	67	69	68	74	57	81	81	Average
	2	51	46	42	31	37	28	32	37	28	22	33	41	31	32	43	19	19	N/A 64.2
	3	6	14	3	<1	2	n.d.	n.d.	n.d.	1	n.d.	n.d.	1	n.d.	n.d.	n.d.	n.d.	n.d.	N/A 34.0
	4	<1	1	n.d.	n.d.	n.d.	n.d.	n.d.	n.d.	n.d.	n.d.	n.d.	n.d.	n.d.	n.d.	n.d.	n.d.	n.d.	N/A 1.6
Avg. No. PDF sets/grain	1.65	1.78	1.49	1.32	1.40	1.28	1.32	1.37	1.30	1.22	1.33	1.44	1.31	1.32	1.26	1.43	1.19	1.19	N/A 0.1
	% relative to total No. of shocked quartz grains within sample																		
Decorated PDF	53	31	66	50	60	64	70	45	61	62	40	61	44	57	38	32	17	17	Average
Toasted	25	15	36	14	25	24	29	13	20	13	18	26	17	33	10	13	2	2	N/A 50
Undulose extinction	65	38	44	39	43	51	27	37	29	46	56	28	52	41	33	45	28	28	N/A 20
Grain mosaicism	15	34	19	1	9	<1	2	2	2	2	2	<1	n.d.	1	n.d.	4	n.d.	n.d.	N/A 41
	No. PDF sets; % relative to total No. of quartz grains with PDFs examined within sample; determined using universal stage																		
PDF sets	1	21	24	21	30	26	42	38	41	47	46	45	46	47	40	48	42	42	Average
	2	52	48	66	65	59	44	47	48	43	49	45	49	47	50	44	49	49	N/A 37.9
	3	24	21	13	5	13	12	13	11	11	5	10	6	17	6	10	8	9	N/A 49.7
	4	3	7	n.d.	n.d.	3	2	2	n.d.	n.d.	n.d.	n.d.	n.d.	n.d.	n.d.	n.d.	n.d.	n.d.	N/A 11.4
Avg. No. PDF sets/grain	2.10	2.10	1.91	1.75	1.92	1.74	1.79	1.70	1.64	1.59	1.66	1.60	1.76	1.58	1.70	1.60	1.67	1.67	N/A 1.0

^aQuartz grains with diameter < 50 μm were not counted.

Abbreviations: n.d. = none detected; N/A = not applicable.

On the other hand, quartz grains that display mosaicism occur mostly in samples from the top of the core; up to 34 % of the shocked quartz grains show mosaicism in sample KR8-030 (Table S2). According to Stöffler and Langenhorst (S5), mosaicism is defined as a “highly irregular mottled optical extinction pattern” and is “distinctly different from undulatory extinction”. Mosaicism results of the distortion of the lattice into small domains that are rotated by low angles against each other; it is an indicator of pressure on the order of ~30 GPa (e.g., S5).

It is obvious from Table S2 that the number of shocked quartz grains decreases with increasing depth; Fig. S2 shows a good correlation between the number of shocked quartz grains and depth ($r = -0.85$). About 60 % of the quartz grains are shocked in the samples from between 270 and 275 m depths, about 25 vol% in the samples from between 350 and 370 m depths, and less than 15 vol% in the samples from the last 20 m of the core (Fig. 2; Table S2). Concurrently, a decrease of the abundance of PDF sets per grain with depth is observed (Fig. 3; Table S2). The higher abundance of PDF sets per grain is partly caused by the presence of quartz grains with 3 to 4 sets of PDFs which occur only in samples from the uppermost part of the core (Table S2).

3) Orientations of planar deformation features in quartz:

A large proportion, from 69 to 100 rel% (for the various thin sections; see Table S3), of all the poles to the PDF planes measured are oriented at ~23° to the c-axis, corresponding to the $\omega\{10\bar{1}3\}$ orientation. Only a small proportion of basal PDF [parallel to (0001)] was found, typically less than 5 rel% per section, with the notable exception of two samples, KR8-85 and KR8-89, from between 390 and 400 m, in which up to 27 rel% of basal PDFs occur (Table S3). However, about 50% of the basal PDFs measured in these two samples occur in association with other PDF orientations in the same quartz grain; similar proportion, ~40% in average, of the basal PDFs measured in all the other samples occur in association with other PDF orientations in the same grain. Other measured PDF orientations, which rarely occur at more than 5 rel% per section, include (in relative order of decreasing abundance) $\rho\{2\bar{1}3\}$, $\pi\{10\bar{1}2\}$, $x\{5\bar{1}6\}$, $r/z\{10\bar{1}1\}$, $s\{11\bar{2}1\}$, $\xi\{11\bar{2}2\}$, $m\{10\bar{1}0\}$, and $a\{11\bar{2}0\}$. These orientations do not represent more than 1.5 rel% of all measurements (see Table S3).

PDF sets not observable under horizontal stage examination are visible when using a U-stage. Figure 3 clearly shows the systematically higher average number of PDF sets per grains (denoted N) when determined with the U-stage. Those higher N values closely follow the same trend as the values of N directly calculated from our analysis of the properties of quartz grains systematic analyses (Fig. 3); this systematic shift in the N values, on average, 28 ± 9 rel% higher when determined with the U-stage, confirms that the results of our U-stage measurements are statistically representative of the complete thin sections (even though only a restricted part of the section can be investigated using the U-stage). For comparison, the abundance of PDF sets as determined using the U-stage is reported in the bottom part of the Table S2. In U-stage observations, quartz grains with 2 PDF sets account for ~50 rel%, whereas they represent only one third of the total in horizontal stage examinations (see Table S2).

Table S3. Indexed PDF crystallographic orientations in quartz grains in meta-graywacke samples from the basement section of drill core LB-08A^a. Data given as absolute frequency values (recalculated to 100% without unindexed PDF orientations)^b.

Sample	Depth (m)	c {0001}	PDF crystallographic orientations										Total number of measured sets	
			ω {10 $\bar{1}$ 3}	π {10 $\bar{1}$ 2}	r, z {10 $\bar{1}$ 1}	m {10 $\bar{1}$ 0}	ξ {11 $\bar{2}$ 2}	s {11 $\bar{2}$ 1}	a {11 $\bar{2}$ 0}	x {51 $\bar{6}$ 1}	ρ {21 $\bar{3}$ 1}			
KR8-29	271.43	1.7	93.3	3.3	n.d.	n.d.	1.7	n.d.	n.d.	n.d.	n.d.	n.d.	n.d.	60
KR8-30	272.00	n.d.	87.9	3.4	5.2	n.d.	1.7	1.7	n.d.	n.d.	n.d.	n.d.	n.d.	58
KR8-31	273.99	n.d.	90.7	1.2	n.d.	1.2	n.d.	2.3	2.3	n.d.	n.d.	2.3	2.3	86
KR8-36	281.32	2.9	88.2	n.d.	n.d.	n.d.	n.d.	2.9	2.9	1.5	1.5	1.5	2.9	68
KR8-37	283.50	n.d.	95.8	1.4	1.4	n.d.	1.4	n.d.	n.d.	n.d.	n.d.	n.d.	n.d.	71
KR8-45	300.41	n.d.	100	n.d.	n.d.	n.d.	n.d.	n.d.	n.d.	n.d.	n.d.	n.d.	n.d.	75
KR8-56	326.78	5.0	83.8	1.3	1.3	n.d.	1.3	n.d.	n.d.	n.d.	1.3	1.3	6.3	80
KR8-66	353.95	6.7	88.9	n.d.	n.d.	2.2	n.d.	2.2	n.d.	n.d.	n.d.	n.d.	n.d.	45
KR8-67	356.59	2.6	86.8	1.3	5.3	n.d.	1.3	1.3	n.d.	n.d.	1.3	1.3	1.3	76
KR8-71	368.97	9.1	76.4	n.d.	1.8	n.d.	n.d.	1.8	n.d.	n.d.	7.3	7.3	3.6	55
KR8-85	392.65	27.1	68.8	2.1	n.d.	n.d.	n.d.	n.d.	n.d.	n.d.	n.d.	n.d.	2.1	48
KR8-89	397.30	18.9	77.4	1.9	n.d.	n.d.	n.d.	n.d.	n.d.	n.d.	1.9	1.9	n.d.	53
KR8-96	406.31	n.d.	92.0	n.d.	n.d.	n.d.	n.d.	2.0	n.d.	n.d.	4.0	4.0	2.0	50
KR8-98	410.74	1.8	94.7	n.d.	1.8	n.d.	n.d.	1.8	n.d.	n.d.	n.d.	n.d.	n.d.	57
KR8-101	414.28	n.d.	93.9	6.1	n.d.	n.d.	n.d.	n.d.	n.d.	n.d.	n.d.	n.d.	n.d.	33
KR8-109	425.24	2.6	87.2	n.d.	2.6	n.d.	n.d.	n.d.	2.6	n.d.	2.6	2.6	2.6	39
KR8-119	441.87	1.5	97.1	n.d.	n.d.	n.d.	n.d.	n.d.	n.d.	n.d.	n.d.	n.d.	1.5	68
All samples combined		4.7	88.4	1.3	1.1	0.2	0.5	1.0	1.0	0.1	1.3	1.3	1.4	1022

^aMethod described in, e.g., Engelhardt and Bertsch (S4), Stöffler and Langenhorst (S5), and Grieve et al. (S6).

^bRecalculating without unindexed PDF orientations allows comparison between the different samples; from 0 to 5.5 rel% of the measured PDF orientations could not be indexed.
n.d. = none detected.

Numerical modeling

Numerical modeling allows to record any desirable variable for any location within an impact crater and for all times during the crater formation process (e.g., S23). Here we used the Simplified Arbitrary Lagrangian-Eulerian code, version B (SALEB; S24), as also used by Artemieva et al. (S25), but with an extended range of model parameter variation. In contrast to Artemieva et al. (S25), we made a direct parametric fit of our model to the observed crater geometry, without usage of scaling relations for the crater size. In addition, we made the fit to the actual position of the central uplift, below the rim level, without assumption of bulking.

Calculations were done for a vertical impact of a spherical projectile. To model the mechanical properties of the projectile and of the Bosumtwi target (projectile is assumed to be made of the same material as the target), we used the tabulated ANEOS equation of state for Westerly granite (S26) and the Tillotson EOS fitted to the granite Hugoniot for the range below 100 GPa. In addition, available ANEOS equations of state for dunite and calcite were also tested. Acoustic fluidization (AF) model parameters (see Table S4) were tuned to reproduce the depth and width of the central uplift.

Table S4. Main parameters used in the acoustic fluidization (AF) model.

Equation of state	ANEOS granite	Tillotson EOS granite
Friction coefficient of totally damaged material	0.4	0.55
AF model switch on time, s	3	4
AF model decay time, s	6	6.4
AF model limiting velocity, m.s ⁻¹	100	300

Our best model was obtained for the model parameters listed in Table S4. Model crater profiles for two model runs (of a total of about two dozen) compared to the observed crater cross-section of the Bosumtwi crater are presented in Fig. S3. Each model run starts with the impact and stops 75 seconds after the impact. Mass-less Lagrangian tracers imbedded into each cell (with sizes of 12 × 12 m or of 14 × 14 m) record shock pressure and the material motion through the Eulerian grid. The projectile has a resolution of 27 cells per projectile radius (CPPR) for models with an impact velocity of 10 kms⁻¹ and of 18 CPPR for models with an impact velocity of 20 kms⁻¹.

After modeling, tracers in the vicinity of the exact location of the two drill holes were identified, allowing the reconstruction of their initial positions. As the model is too crude to exactly represent the real rock displacements, we used a comparative approach, comparing model results and observations. All tracers in a zone of about 20 m (comparable with the cell size of 12 × 12 m), at the correct radial distances from the crater center (0.48 and 1.1 km for LB-08A and LB-07A, respectively), were listed, and finally, the position of the top of the “model core” was defined by the maximum recorded shock pressure of 30 GPa (pressure estimate based on our petrographic investigations). The bottom part of the “model cores” was defined by a tracer identified 200 m below the position of the 30 GPa level in the “model core” for core LB-08A, and at about 100 m below the 30 GPa level for core LB-07A. Then, the initial position of these tracers was plotted (Fig. 4), showing which layers of the target were sampled by the “model cores”.

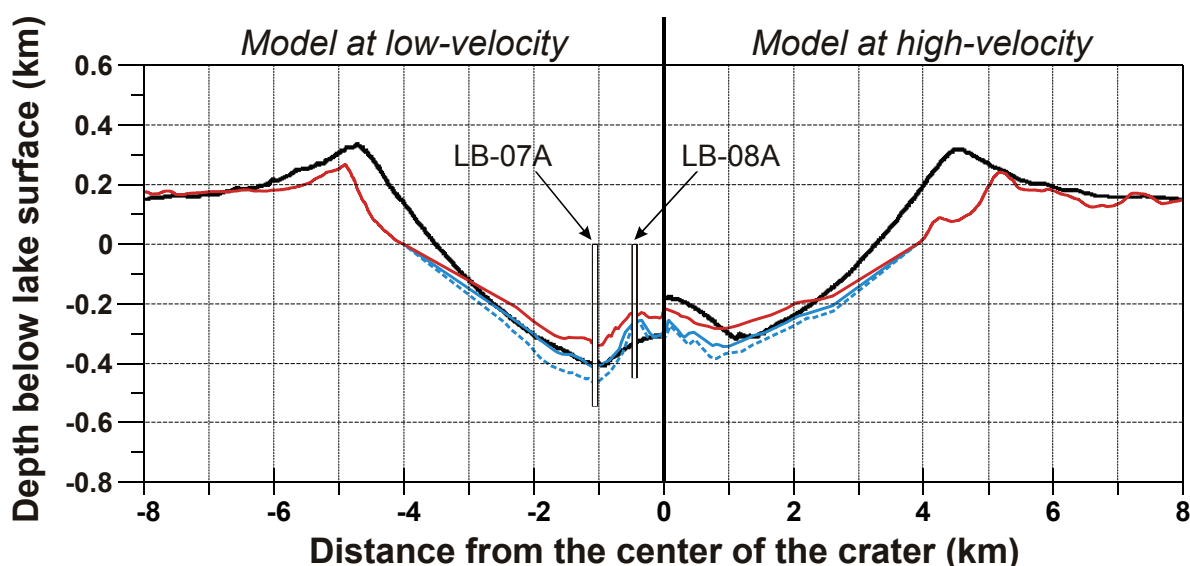


Figure S3. Model crater profiles (black curves; using ANEOS granite equation of state for target and projectile) versus observed (i.e., actual) crater profile (red and solid blue lines for the apparent and true crater profiles, respectively, and dashed blue line for the lower limit of the monomict impact breccia). Note the difference between modeled and actual crater profile around the rim, which can be explained by post-impact erosion. Models of impact at low-velocity (left, $v_{\text{imp}} = 10 \text{ km s}^{-1}$, $D_{\text{proj}} = 0.648 \text{ km}$, $\delta = 2630 \text{ kg m}^{-3}$) and at high-velocity (right, $v_{\text{imp}} = 20 \text{ km s}^{-1}$, $D_{\text{proj}} = 0.432 \text{ km}$, $\delta = 2630 \text{ kg m}^{-3}$) are compared. In both runs, residual friction (μ) = 0.4, the fraction of the maximum particle velocity ($C_{\text{vib}} = 0.15$, and decay time ($\tau_{\text{dec}} = 6 \text{ s}$). The ratio of projectile diameters is chosen to keep the “late stage equivalency” $D_{\text{proj}} \times v_{\text{imp}}^{0.58}$ constant. In both runs the apparent crater diameter is about 9 km. Location of boreholes LB-07A and LB-08A is given.

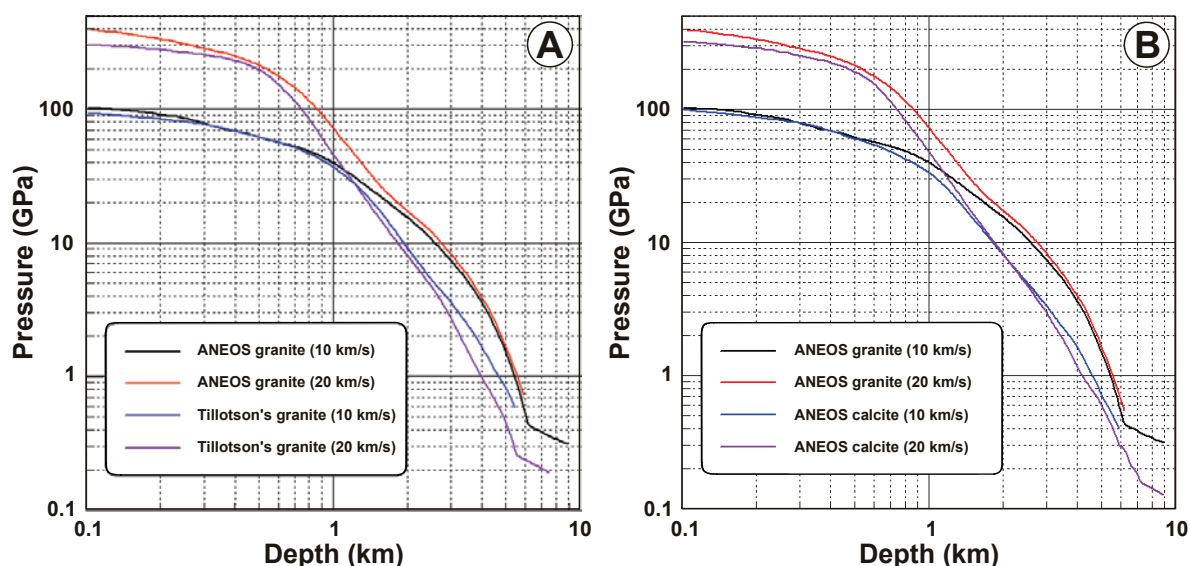


Figure S4. Comparison of the shock pressure decay along the vertical center line for different materials and impact velocities. In all cases, targets and projectiles are made of the same material. The ANEOS granite case is shown as a reference in comparison with (a) Tillotson's EOS for granite and (b) ANEOS calcite. The 10 km s^{-1} projectiles have diameters of 0.648 km, whereas 20 km s^{-1} projectiles have diameters of 0.432 km.

To estimate the level of confidence of our modeling, several dozen model runs were calculated, varying the parameters of the target material as well as the impact velocity. We find that our modeling is robust, as for all model runs the same relative positions of rocks in cores LB-07A and LB-08A were observed. We have also noted that the shock pressure decay is slightly different for low- and high-velocity projectiles (Fig. S4).

Supporting references

- S1. L. Ferrière, C. Koeberl, W. U. Reimold, *Meteorit. Planet. Sci.* **42**, 611–633 (2007).
- S2. R. C. Emmons, *The Universal Stage* (GSA Memoir **8**, GSA, New York, 1943).
- S3. F. Chayes, *Am. Mineral.* **34**, 1–11 (1949).
- S4. W. v. Engelhardt, W. Bertsch, *Contrib. Mineral. Petrol.* **20**, 203–234 (1969).
- S5. D. Stöffler, F. Langenhorst, *Meteorit. Planet. Sci.* **29**, 155–181 (1994).
- S6. R. A. F. Grieve, F. Langenhorst, D. Stöffler, *Meteorit. Planet. Sci.* **31**, 6–35 (1996).
- S7. P. B. Robertson, R. A. F. Grieve, in *Impact and explosion cratering*, D. J. Roddy, R. O. Pepin, R. B. Merrill, Eds. (Pergamon Press, New York, 1977), pp. 687–702.
- S8. L. V. Sazonova, N. N. Karotaeve, G. Y. Ponomarev, A. I. Dabizha, in *Impactits*, A. A. Marakushev, Ed. (Moscow State University, Moscow, 1981), pp. 93–133 (in Russian).
- S9. R. A. F. Grieve, J. M. Coderre, P. B. Robertson, J. Alexopoulos, *Tectonophysics* **171**, 185–200 (1990).
- S10. V. I. Fel'dman, L. V. Sazonova, S. I. Kotel'nikov, *Dokl. Akad. Nauk SSSR* **349**, 658–660 (1996).
- S11. B. O. Dressler, V. L. Sharpton, B. C. Schuraytz, *Contrib. Mineral. Petrol.* **130**, 275–287 (1998).
- S12. R. A. F. Grieve, P. B. Robertson, *Contrib. Mineral. Petrol.* **58**, 37–49 (1976).
- S13. A. R. Huffman, W. U. Reimold, *Tectonophysics* **256**, 165–217 (1996).
- S14. C. A. Scholz *et al.*, *Geology* **30**, 939–942 (2002).
- S15. C. Koeberl, W. U. Reimold, *Yearb. Austrian Geol. Surv.* **145**, 31–70 (2005).
- S16. C. Koeberl *et al.*, *Meteorit. Planet. Sci.* **42**, 483–511 (2007).
- S17. C. A. Scholz, T. Karp, R. P. Lyons, *Meteorit. Planet. Sci.* **42**, 549–560 (2007).
- S18. A. Deutsch, S. Luetke, V. Heinrich, *Meteorit. Planet. Sci.* **42**, 635–654 (2007).
- S19. L. Coney, R. L. Gibson, W. U. Reimold, C. Koeberl, *Meteorit. Planet. Sci.* **42**, 569–589 (2007).
- S20. H. Leroux, *Meteorit. Planet. Sci.* **40**, 1347–1352 (2005).
- S21. N. M. Short, D. P. Gold, *GSA Spec. Pap.* **302**, 245–265 (1996).
- S22. J. Whitehead, J. G. Spray, R. A. F. Grieve, *Geology* **30**, 431–434 (2002).
- S23. G. S. Collins, H. J. Melosh, B. A. Ivanov, *Meteorit. Planet. Sci.* **39**, 217–231 (2004).
- S24. The original code was developed at Los Alamos Nat. Lab by A.A. Amsden *et al.*, *LAL Report LA-8095* (1980). The code has been advanced to treat multimaterial cells with Eulerian advection by B. Ivanov, *LPSC XXXIII*, abs. #1286 (2002). Material strength models were described by Collins *et al.*, *Meteorit. Planet. Sci.* **34**,

- 217–31 (2004), the acoustic fluidization model by Wünnemann and Ivanov, *Planet. Space Sci.* **51**, 831–845 (2003), and verification of the code by modeling of 3 very large terrestrial impact craters was presented by B. Ivanov, *Solar Sys. Res.* **39**, 381–409 (2005).
- S25. N. Artemieva, T. Karp, B. Milkereit, *Geochem., Geophys., Geosyst.* **5**, doi:10.1029/2004GC000733 (2004).
- S26. E. Pierazzo, A. M. Vickery, H. J. Melosh, *Icarus* **127**, 408–423 (1997).

Characterisation of ballen quartz and cristobalite in impact breccias: new observations and constraints on ballen formation

LUDOVIC FERRIÈRE^{1,*}, CHRISTIAN KOEBERL¹ and WOLF UWE REIMOLD²

¹ Department of Lithospheric Research, University of Vienna, Althanstrasse 14, A-1090 Vienna, Austria

*Corresponding author, e-mail: ludovic.ferriere@univie.ac.at

² Museum of Natural History (Mineralogy), Humboldt-University, Invalidenstrasse 43, D-10115, Berlin, Germany

Abstract: Ballen quartz and cristobalite in impactite samples from five impact structures (Bosumtwi, Chicxulub, Mien, Ries, and Rochechouart) were investigated by optical microscopy, scanning electron microscopy (SEM), cathodoluminescence (CL), transmission electron microscopy (TEM), and Raman spectroscopy to better understand ballen formation. The occurrence of so-called “ballen quartz” has been reported from about one in five of the known terrestrial impact structures, mostly from clasts in impact melt rock and, more rarely, in suevite. “Ballen silica”, with either α -quartz or α -cristobalite structure, occurs as independent clasts or within diaplectic quartz glass or lechatelierite inclusions. Ballen are more or less spheroidal, in some cases elongate (ovoid) bodies that range in size from 8 to 214 μm , and either intersect or penetrate each other or abut each other. Based mostly on optical microscopic observations and Raman spectroscopy, we distinguish five types of ballen silica: α -cristobalite ballen with homogeneous extinction (type I); ballen α -quartz with homogeneous extinction (type II), with heterogeneous extinction (type III), and with intraballen recrystallisation (type IV); chert-like recrystallized ballen α -quartz (type V). For the first time, coesite has been identified within ballen silica – in the form of tiny inclusions and exclusively within ballen of type I.

The formation of ballen involves an impact-triggered solid-solid transition from α -quartz to diaplectic quartz glass, followed by the formation at high temperature of ballen of β -cristobalite and/or β -quartz, and finally back-transformation to α -cristobalite and/or α -quartz; or a solid-liquid transition from quartz to lechatelierite followed by nucleation and crystal growth at high temperature. The different types of ballen silica are interpreted as the result of back-transformation of β -cristobalite and/or β -quartz to α -cristobalite and/or to α -quartz with time. In nature, ballen silica has not been found anywhere else but associated with impact structures and, thus, these features could be added to the list of impact-diagnostic criteria.

Key-words: ballen quartz, α -cristobalite, silica, shock metamorphism, impact structure.

1. Introduction

1.1. Historical background and previous studies of ballen quartz

So-called “ballen quartz” was first observed in 1890, in impact melt rock from the Mien impact structure (Holst, 1890). At this time, the impact origin of Mien was not yet confirmed and consequently these rocks were associated with some kind of volcanic activity. Ballen quartz was described to occur in the form of “rounded, egg shaped or elongated batches, consisting of aggregates of elongated lamellae” (Holst, 1890).

Similar features were described much later by McIntyre (1968) from impactites of the Clearwater impact structures and by Engelhardt (1972) from the Ries. The first detailed study of these features was reported by Carstens (1975), who concluded that the ballen texture represented pseudomorphs after cristobalite that had replaced lechatelierite initially formed by shock-induced thermal transformation

of quartz. Carstens (1975) also suggested that ballen “formed as the result of the tensile stresses set up by the high-low inversion of cristobalite being associated with a volume shrinkage of about 7 %”. Bischoff & Stöffler (1984) found that ballen represented recrystallized diaplectic quartz glass that had undergone the transition to cristobalite and then to α -quartz. They recognized three types of “ballen quartz”: (a) ballen with optically homogeneous extinction ($\sim 30\text{--}45$ GPa), (b) ballen with different crystallographic orientations ($\sim 45\text{--}55$ GPa), and (c) ballen with intraballen-recrystallisation (>50 GPa). This is based on optical characteristics of coexisting shock-deformed quartz and feldspar grains, and assigned specific shock pressures to the shock metamorphic stages experienced by the quartz grains now converted to ballen silica.

“Ballen quartz” has since been observed in samples from many other impact structures (see Table 1), but not many detailed descriptions and characterisations have been published, except for ballen from Popigai (Whitehead *et al.*, 2002) and from Wanapitei (Dressler *et al.*, 1997),

Table 1. Impact structures in which ballen have been observed so far. Structures with asterisk (*) are those for which thin section samples were investigated here.

Structure name	Location	Diameter (km)	Age (Ma)	Host rock/Types of ballen	Reference
Boltysh	Ukraine	24	65.17 ± 0.64	Microcrystalline melt rock	Grieve <i>et al.</i> , 1987
Bosumtwi*	Ghana	10.5	1.07	Suevite (type I)	<i>e.g.</i> , Boamah & Koeberl, 2006; Ferrière <i>et al.</i> , 2006; this study
Chesapeake Bay	Virginia, U.S.A.	85	35.5 ± 0.3	Suevite (types III and IV)	Bartosova <i>et al.</i> , 2007
Chicxulub*	Yucatan, Mexico	180	64.98 ± 0.05	Suevite and impact melt rock (type IV)	<i>e.g.</i> , Stöffler <i>et al.</i> , 2004; Tuchscherer <i>et al.</i> , 2004; Wittmann <i>et al.</i> , 2004; this study
Clearwater East	Quebec, Canada	26	290 ± 20	Impact melt rock	McIntyre, 1968
Clearwater West	Quebec, Canada	36	290 ± 20	Impact melt rock	McIntyre, 1968; Phinney <i>et al.</i> , 1978
Deep Bay	Saskatchewan, Canada	13	99 ± 4	Intensively shocked granite	Short, 1970
Dellen	Sweden	19	89.0 ± 2.7	Impact melt rock	Carstens, 1975
Dhala	India	15	>1600; <2500	Impact melt rock	Pati <i>et al.</i> , in press
El'gygytgyn	Russia	18	3.5 ± 0.5	Impact melt rock (type I)	<i>e.g.</i> , Gurov <i>et al.</i> , 2005
Gow	Saskatchewan, Canada	4	<250	Impact melt rock	Thomas <i>et al.</i> , 1977
Ilynets	Ukraine	8.5	378 ± 5	Shock-melted granitoid clasts (in breccia)	Gurov <i>et al.</i> , 1998
Jänisjärvi	Russia	14	700 ± 5	Cryptocrystalline melt breccia	<i>e.g.</i> , Müller <i>et al.</i> , 1990
Kara	Russia	65	70.3 ± 2.2	Impact melt rock	Schmieder & Buchner, 2007
Lappajärvi	Finland	23	73.3 ± 5.3	Clast-poor impact melt rock (types II, III, and IV)	Carstens, 1975; Bischoff & Stöffler, 1984
Manicouagan	Quebec, Canada	100	214 ± 1	Impact melt breccia	Schmieder & Buchner, 2007
Mien*	Sweden	9	121.0 ± 2.3	Impact melt rock (types I, II, III, and IV)	Holst, 1890; Carstens, 1975; this study
Mistastin	Labrador, Canada	28	36.4 ± 4	Impact melt rock	Grieve, 1975
Morokweng	South Africa	70	145.0 ± 0.8	Partially annealed granite	Reimold <i>et al.</i> , 1999
New Quebec	Quebec, Canada	3.44	1.4 ± 0.1	Impact melt rock	Marvin & Kring, 1992
Popigai	Russia	100	35.7 ± 0.2	Impact melt rock (types I, II, III, and IV)	<i>e.g.</i> , Vishnevsky & Montanari, 1999; Whitehead <i>et al.</i> , 2002
Ries*	Germany	24	15.1 ± 0.1	Impact melt rock from Pölsingen and Amerbach (types IV and V)	<i>e.g.</i> , Engelhardt, 1972; Osinski, 2004; this study
Rochechouart*	France	25	214 ± 8	Impact melt rock (types III, IV, and V)	Ferrière & Koeberl, 2007; this study
Sääksjärvi	Finland	6	~560	Cryptocrystalline melt breccia	<i>e.g.</i> , Müller <i>et al.</i> , 1990
Saint Martin	Manitoba, Canada	40	220 ± 32	Impact melt rock	Phinney <i>et al.</i> , 1978
Suvasvesi N	Finland	4	<1000	Impact melt rock	Pesonen <i>et al.</i> , 1996
Tenoumer	Mauritania	1.9	0.0214 ± 0.0097	Impact melt rock	French <i>et al.</i> , 1970; French, 1998
Ternovka (Terny)	Ukraine	11	280 ± 10	Impact melt rock	Schmieder & Buchner, 2007
Tswaing	South Africa	1.13	0.220 ± 0.052	Suevitic gravel	Montanari & Koeberl, 2000
Wanapitei	Ontario, Canada	7.5	37.2 ± 1.2	Glassy impact melt rock (types III and IV)	Grieve & Ber, 1994; Dressler <i>et al.</i> , 1997
Zapadnaya	Ukraine	3.2	165 ± 5	Suevite and impact melt rock	<i>e.g.</i> , Gurov <i>et al.</i> , 2002

Diameter and age data from Earth Impact Database (2008).

where some information on the different types of ballen are reported. Ballen with a “toasted appearance” somewhat similar to what has been described for shocked quartz

grains (*e.g.*, Short & Gold, 1996) have been described from Popigai (Whitehead *et al.*, 2002), from Wanapitei (Dressler *et al.*, 1997), and more recently from Dhala (Pati *et al.*,

in press). Alpha-quartz, α -cristobalite, and α -tridymite were identified, using X-ray diffraction techniques, in ballen-quartz-bearing melt rocks from Popigai (Vishnevsky & Montanari, 1999; Whitehead *et al.*, 2002).

Short (1970) was able to reproduce ballen-like features experimentally, after annealing of a slab of experimentally shocked (at ~ 40 GPa) quartzite at 1450 °C for 24 h, producing “ovoid to arcuate microstructures” within grains of diaplectic silica glass. In these experiments, an embryonic stage of “ballen quartz” formed already in the specimens annealed at 1200 °C. Short (1970) concluded that “ballen quartz” was formed by recrystallisation of glassy material at high temperatures. Similar annealing experiments with diaplectic quartz glass by Rehfeldt-Oskierski (1986) arrived at comparable results, with a minimum annealing temperature of 1150 °C for ballen to develop. Ballen formed at 1150 and 1300 °C were 0.2 – 0.3 mm and 0.5 – 1.0 mm in size, respectively. Polycrystalline ballen with individual crystals of 0.1 – 0.4 mm in size were also produced (Rehfeldt-Oskierski, 1986). In addition, the occurrences of “patches of faint planar fractures” (Short, 1970) or “relics of planar deformation features (PDFs)” (Rehfeldt-Oskierski, 1986) within the annealed samples are mentioned, as observed by these workers through optical microscopy.

1.2. Occurrence of ballen quartz and cristobalite

Ballen silica has been reported from about one in five of the known terrestrial impact structures (Table 1), mostly from impact melt rock and, more rarely, from suevite samples. These occurrences include the Bosumtwi, Chicxulub, Mien, Ries, and Rochechouart impact structures, from which samples have been investigated here (Fig. 1). We present a detailed study of 27 thin sections of samples from these impact sites, to contribute to the understanding of the so far still uncertain formation mechanism(s) of “ballen quartz”.

2. Samples and geological background for studied impact structures

Our classification of the various rock types follows definitions by Stöffler & Grieve (2007). Impactite is defined as “rock produced by impact metamorphism”, including “shocked rocks, impact breccias, impact melt rocks, (micro)tektites and impactoclastic air fall beds” (Stöffler & Grieve, 2007). Suevite (or suevite breccia) is defined as a “polymict impact breccia with particulate matrix containing lithic and mineral clasts in all stages of shock metamorphism including cogenetic impact melt particles which are in a glassy or crystallized state” (Stöffler & Grieve, 2007).

Distinction between “diaplectic quartz glass” and “lechatelierite” is based on morphology, as it is generally accepted that diaplectic quartz glass preserves pre-shock morphology of crystals, whereas the morphology of lechatelierite inclusions is determined by the surface tension of the liquid (*e.g.*, Engelhardt & Stöffler, 1968). Where the terms “cristobalite”

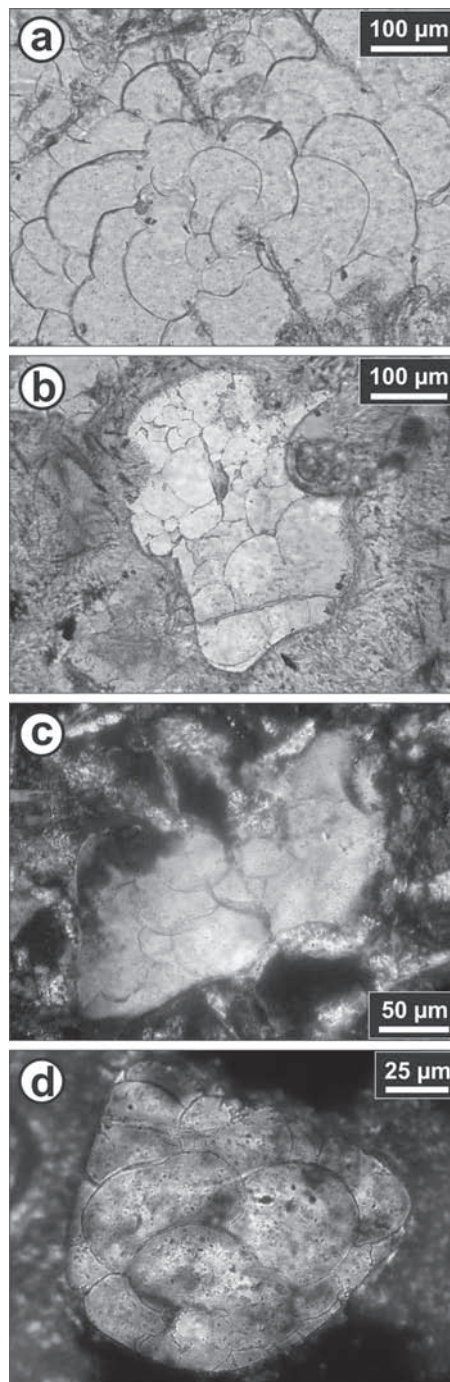


Fig. 1. Microphotographs of ballen silica from various impact structures. (a) Elongate ovoid (crescent) to roundish α -cristobalite ballen in suevite from Bosumtwi (sample BH1-0790). (b) Ballen α -quartz with varied ballen sizes in a lechatelierite clast in impact melt rock from Mien. The melt matrix is mostly composed of feldspar, pyroxene, and opaque microlites, with interstitial mesostasis (sample RD_01). (c) Ballen α -quartz in a lechatelierite clast in impact melt rock from Rochechouart (sample 215_5). (d) Roundish to ovoid ballen α -quartz in suevite from Chicxulub (sample Yax-1_808.87m). Microphotographs (a) and (b) taken in plane-polarized light, (c) and (d) in cross-polarized light.

and “quartz” are referred, for example with respect to historical observations, it is understood that the low-temperature polymorphs “ α -cristobalite” and “ α -quartz” are meant.

2.1. Bosumtwi impact structure (Ghana)

The 1.07 Ma old Bosumtwi crater in Ghana (West Africa) is a well-preserved complex impact structure, 10.5 km in diameter (*e.g.*, Koeberl & Reimold, 2005). Suevite occurs outside of the northern and southern crater rim and contains abundant impact-melt fragments and a variety of clasts up to about 40 cm in size (Boamah & Koeberl, 2006). Coherent impact melt rock has not been found yet at Bosumtwi. “Ballen quartz” was observed in some samples from suevite deposits outside the crater rim (Boamah & Koeberl, 2006; Karikari *et al.*, 2007). Recent work on suevite samples from the deep crater moat and the central uplift of the structure, from the LB-O7A and LB-O8A boreholes of the International Continental Scientific Drilling Program (ICDP), have, to date, not revealed the presence of ballen silica (Coney *et al.*, 2007; Ferrière *et al.*, 2007). For this study, we have investigated seven thin sections of suevite samples (BH1-0790, BH1-0790b, BH1-0800, LB-40B, LB-44B, LB-44B2, and LB-48) from the deposit outside the northern crater rim (located 6°33.9' N and 1°23.9' W).

2.2. Chicxulub impact structure (Mexico)

The 65 Ma old Chicxulub impact structure located on the Yucatán Peninsula, Mexico, has a diameter of ~180–195 km (*e.g.*, Hildebrand *et al.*, 1991). Actually covered by post-impact Tertiary sediments, the structure is only accessible by drilling or geophysical techniques. The 1511 m deep ICDP Yaxcopoil-1 (Yax-1) borehole allowed to recover 795 m of post-impact sediments, 100 m of allochthonous polymict impact breccia (mainly suevite), and more than 600 m of displaced target rocks with impact-induced dike breccias (Stöffler *et al.*, 2004). Rare “ballen quartz” in silica inclusions was mentioned in some samples of the allochthonous polymict impact breccia (*e.g.*, Stöffler *et al.*, 2004; Tuchscherer *et al.*, 2004; Wittmann *et al.*, 2004). We investigated six thin sections of samples from the Yax-1 drill core (suevite samples from 808.87, 842.51, 852.80, 860.25, and 889.32 m depth; and a brecciated impact melt rock sample from 875.35 m depth).

2.3. Mien impact structure (Sweden)

The Mien impact structure, 121 ± 2.3 Ma old, has a diameter of about 9 km. It is located in the Transscandinavian Granite Porphyry Belt, in southeastern Sweden (Åström, 1998). Boulders of impactite (mostly impact melt rock), first described as rhyolite of volcanic origin (Holst, 1890), occur to the south of Lake Mien as glacial deposits and on the island of Ramsö. Mien impact melt rock is vesicular and consists mainly of feldspar crystals with intersertal texture, quartz grains and aggregates, pyroxene, hematite, rutile, and

ilmenite, with interstices filled by a brownish devitrified mesostasis. Quartz inclusions, partially resorbed along the edges, are generally relict phases that display either PDFs or “ballen quartz”. We studied five thin sections of impact melt rock from the glacial deposits south of Lake Mien (Mien_01; 02; 02b; RD_01; RD_02).

2.4. Ries impact structure (Germany)

The Ries impact structure, 24 km in diameter and 14.3 ± 0.2 Ma old (Buchner *et al.*, 2003), is a well-preserved complex impact structure in Bavaria (*e.g.*, Pohl *et al.*, 1977). “Ballen quartz” has been observed only in Ries impact melt rock (Engelhardt, 1972), mainly in samples from Polsingen and Amerbach (*e.g.*, Carstens, 1975; Osinski, 2004). Three thin sections of impact melt rock from Polsingen (R_POL_1; R_POL_2; SIE_9766) were investigated. Polsingen melt rock is reddish in colour, vesicular, and contains abundant shocked clasts of crystalline basement rocks. The groundmass consists mainly of feldspar phenocrysts, quartz, and cryptocrystalline oxides with an interstitial glassy mesostasis.

2.5. Rochechouart impact structure (France)

The 214 ± 8 Ma old (Kelley & Spray, 1997) Rochechouart impact structure occurs in the northwest of the French Massif Central and has a diameter of about 25 km (*e.g.*, Kraut, 1970; Kraut & French, 1971; Lambert, 1977). Four impactite types have been recognized (*e.g.*, Kraut, 1970; Kraut & French, 1971): impact melt rock, two types of suevite, and one type of polymict lithic breccia. “Ballen quartz” in impactite from the Rochechouart structure was only found recently in impact melt rock (Ferrière & Koeberl, 2007). It is a vesicular impact melt rock, which consists mainly of feldspar and pyroxene laths in a matrix of devitrified glass. Rare clasts of shocked quartz and feldspar occur, and a few recrystallized quartz clasts show ballen texture. Six thin sections of impact melt rock were investigated (215_2; 3; 3b; 4; 5; B – Muséum National d’Histoire Naturelle, Paris, France).

3. Experimental Methods

The 27 thin sections of impact melt rock and suevite were examined with an optical microscope in both transmitted and reflected light. Some sections were then selected for scanning electron microscopy (SEM), cathodoluminescence (CL), and micro-Raman spectroscopy. One sample (LB-44B sample, from Bosumtwi) was investigated using transmission electron microscopy (TEM).

The sections were carbon-coated and examined with an Oxford Mono-CL system attached to a JEOL JSM 6400 scanning electron microscope at the Department of Mineralogy, Natural History Museum, Vienna, Austria. The operating conditions for all SEM-CL investigations were 15 kV accelerating voltage, 1.2 nA beam current, and

monochromator grating with 1200 lines/mm; CL images were obtained from areas of approximately $450 \times 450 \mu\text{m}$, with scanning times of about 1 min.

Raman spectra were obtained with a Renishaw RM1000 confocal edge filter-based micro-Raman spectrometer with a 20 mW, 632.8 nm He-Ne-laser excitation system, a grating with 1200 lines/mm, and a thermoelectrically cooled CCD array detector at the Institute of Mineralogy and Crystallography, University of Vienna, Vienna, Austria. Spectra were obtained in the range from 30 to 1000 cm^{-1} , with a 300 s acquisition time. The spectral resolution of the system (apparatus function) was 4.5 cm^{-1} and the wavenumber accuracy was better than $\pm 1 \text{ cm}^{-1}$ (both calibrated with the Rayleigh line and the 520.5 cm^{-1} line of a silicon standard). The Raman spectra were taken in confocal mode from $3 \times 3 \times 3 \mu\text{m}$ sample volumes, using a Leica DMLM microscope and a Leica $50 \times /0.75$ objective, from polished thin section surfaces. Instrument control and data acquisition were done with the Grams/32 software (Thermo Galactic Corporation). For phase identification, reference spectra from Caltech, California Institute of Technology, USA were used (http://minerals.gps.caltech.edu/files/raman/Caltech_data/index.htm accessed 12 October 2007).

The Focused Ion Beam (FIB) technique was used for the preparation of a TEM foil at the GeoForschungsZentrum (GFZ) Potsdam (Germany). A FIB foil of $15 \times 5 \mu\text{m}$ extent and about 150 nm thickness was prepared following the method described by Wirth (2004). Transmission electron microscopy was done with a 200 kV PHILIPS CM 20 STEM equipped with a TRACOR Northern energy-dispersive X-ray detector sensitive to elements with atomic numbers >5 at the Museum of Natural History, Humboldt-University, Berlin (Germany). Conventional bright-field imaging techniques were used to observe and characterize microstructural characteristics of individual ballen.

4. Results

Based mostly on optical microscopic observations and Raman investigation, we recognize five different types of ballen: α -cristobalite ballen with homogeneous extinction (type I); ballen α -quartz with homogeneous extinction (type II), with heterogeneous extinction (type III), and with intraballen recrystallisation (type IV); chert-like recrystallized ballen α -quartz (type V; Table 2).

4.1. Optical microscopic observations

Results of the microscopic examination of ballen from these different impact structures are reported separately for each location, in order to distinguish the particularities of ballen from each of these impact sites. General views of ballen from some of our samples are illustrated in Fig. 1. Figure 2 shows impressions of α -cristobalite ballen in a large silica clast. Different types of ballen quartz/cristobalite are presented in Fig. 3.

Table 2. Classification of the different types of ballen according to their microscopic properties and respective characteristics.

Type	Proposed name	Characteristics
I	Alpha-cristobalite ballen with homogeneous extinction	All ballen are isotropic in cross-polarized light; coesite occurs in the form of tiny inclusions within ballen
II	Ballen quartz with homogeneous extinction	All individual ballen have common extinction
III	Ballen quartz with heterogeneous extinction	Each individual ballen has homogeneous extinction
IV	Ballen quartz with intraballen recrystallisation	Intraballen polycrystallinity; heterogeneous extinction within single ballen
V	Chert-like recrystallized ballen quartz	Ballen are completely recrystallized; rims of individual ballen not easily distinguished in cross-polarized light

Note that all types of ballen quartz are made of alpha-quartz.

4.1.1. Bosumtwi samples

Ballen silica occurs in Bosumtwi samples only in impact melt clasts within suevite samples. It occurs in both diaplectic quartz glass (Fig. 2) and lechatelierite inclusions (Fig. 1a and 4). Ballen display a variety of shapes, from circular to oval or crescent shaped (Fig. 1a, 2, and 3a, b). All individual ballen are composed of α -cristobalite (confirmed with Raman spectroscopy), are isotropic in cross-polarized light (Fig. 3b), and have sharp outlines due to the marginal presence of phyllosilicate minerals (Fig. 2f; phyllosilicates cannot be resolved using optical microscopy but have been characterized by TEM analysis, see below). Only ballen silica of type I has been observed in Bosumtwi samples (Table 2). Most of the ballen contain one or several highly refractive, light green, tiny inclusions (Fig. 2e) that were confirmed as coesite by Raman spectroscopy. Ballen diameters range from 8 to $214 \mu\text{m}$, with an average diameter of $50 \mu\text{m}$ ($n = 478$; 18 clasts). The ballen size distribution is also highly variable from inclusion to inclusion, ranging from inclusions with ballen of similar size to inclusions with a large variation of ballen sizes. However, we have observed a decrease of the average diameter of ballen with increasing number of ballen loops in a given inclusion. No correlations seem to exist between the number of ballen per inclusion and the area of the entire inclusion, and between the average radius of ballen and the inclusion area. Large ballen occur in some inclusions preferentially within peripheral areas, but can also be concentrated in the centre of silica inclusions in other cases.

To complete our observations on ballen at the Bosumtwi impact structure, two polished thin sections (LB-44B and LB-44B2; oriented perpendicular to each other) of the same large (22 mm) silica clast were investigated (Fig. 2). In both thin sections, ballen have more or less

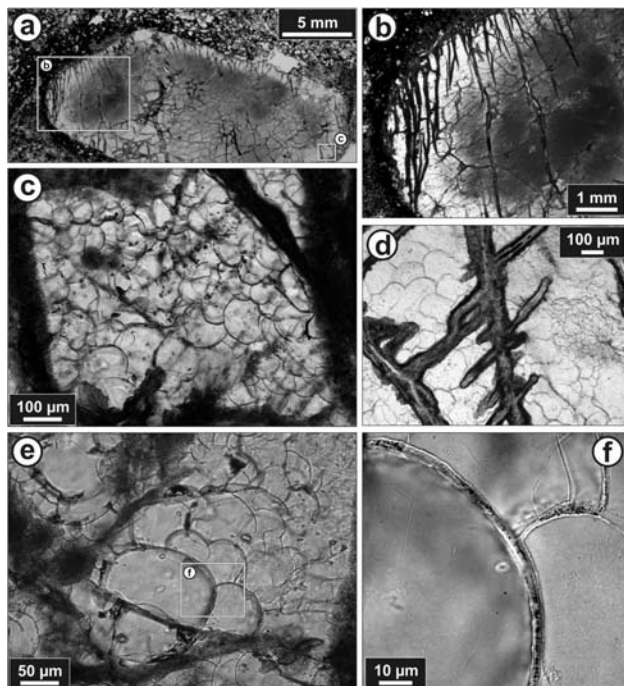


Fig. 2. Microphotographs (in plane-polarized light) of α -cristobalite ballen (type I) in suevite from Bosumtwi (sample LB-44B). (a) General view of a large, shocked silica clast. Primary shape of the quartz grain is preserved. (b) Enlarged part of the silica clast (a) showing the transition from the brownish core (coesite) to the transparent diaplectic quartz glass with fractures and abundant α -cristobalite ballen. (c) Enlarged part of (a) with roundish α -cristobalite ballen (like “bunches of grapes”) surrounded by fractures/veinlets of in part altered coesite (dark). (d) Fractures/veinlets of altered coesite with secondary α -quartz in the peripheral zone and α -cristobalite ballen in between. (e) A close-up view of well-developed α -cristobalite ballen. Tiny inclusions/grains of coesite (greenish inclusions with high relief) occur within individual ballen. (f) Higher magnification view of the boundary between several ballen, filled here with phyllosilicate.

roundish shapes, which allows us to visualize ballen as spheroidal bodies. This large silica clast which does not show any indications of deformation or flow in the fluid state (Fig. 2a) is composed of remnants of diaplectic quartz glass, α -cristobalite ballen, and coesite (Fig. 2 and 5a–c). Diaplectic quartz glass is crosscut by several fractures/veinlets that are greenish to brownish in colour (Fig. 2). The fractures contain some phyllosilicate minerals as well as coesite, which is largely recrystallized to secondary α -quartz. Coesite occurs also as highly refractive, light green aggregates (up to 30 μm) within the diaplectic quartz glass (Fig. 5a, b; as also described earlier by *e.g.*, Stöffler, 1971; French, 1998; Stähle *et al.*, 2008). Very well developed α -cristobalite ballen occur mainly at the fringe of the silica clast (Fig. 2c), but also along fractures in the inner part of the clast (Fig. 2d). In addition, ballen at the embryonic stage have been observed along fractures and within diaplectic quartz glass (Fig. 5a, b).

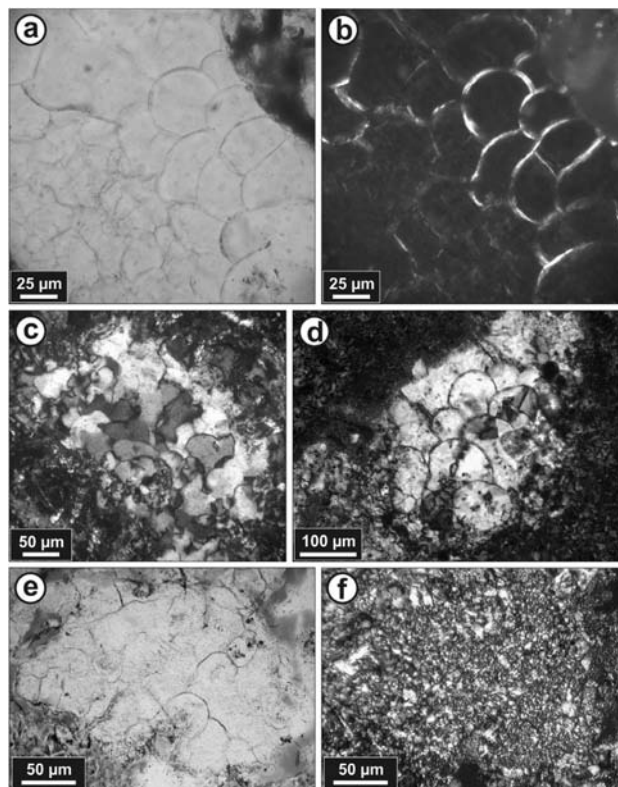


Fig. 3. Microphotographs of various types of ballen quartz/cristobalite. (a) Plane-polarized light and (b) cross-polarized light microphotographs of α -cristobalite ballen (type I) in a lechatelierite clast in suevite from Bosumtwi (sample LB-40B). All individual ballen have common extinction. (c) Ballen α -quartz with heterogeneous extinction (different optical orientations; type III) in a lechatelierite clast in impact melt rock from Rochechouart (sample 215_B; cross-polarized light). Note that each individual ballen has homogeneous extinction. (d) Ballen α -quartz with intraballen recrystallisation (type IV) in a lechatelierite clast in impact melt rock from the Ries (sample SIE-9766; cross-polarized light). Note the intraballen polycrystallinity and the resulting heterogeneous extinction within single ballen. (e) Plane-polarized light and (f) cross-polarized light microphotographs of chert-like recrystallized ballen α -quartz (microcrystalline quartz; type V) in a lechatelierite clast in impact melt rock from Rochechouart (sample 215_3). Note that rims of individual ballen are not easily distinguished in cross-polarized light.

4.1.2. Chicxulub samples

Ballen quartz from the Chicxulub impact structure occurs mostly in lechatelierite inclusions (rarely in diaplectic quartz glass) in suevite samples, as well as in the so-called brecciated impact melt rock (unit 5 of Stöffler *et al.*, 2004). Ballen are mainly circular or ovoid in shape (Fig. 1d), with a maximum size measured of 105 μm , and all display heterogeneous extinction of ballen (type IV; Table 2). They exclusively consist of α -quartz. One particularity of the ballen quartz from Chicxulub is that frequently ballen are not obvious when using an optical microscope, possibly because of the absence of phyllosilicate minerals at the margin of the ballen.

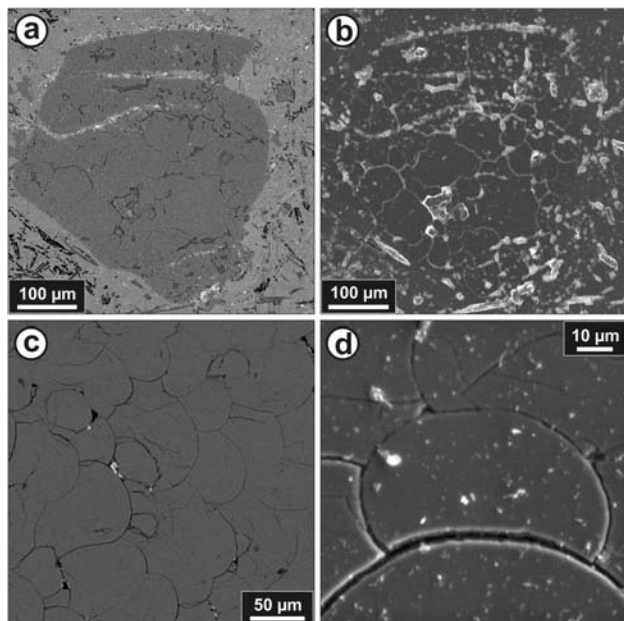


Fig. 4. Backscattered electron (BSE) and secondary electron (SE) images of typical ballen silica. (a) BSE and (b) SE images of an inclusion of lechatelierite displaying ballen α -quartz in a partly crystalline matrix. The sharp boundary between the inclusion and the matrix is obvious. Sample Mien-02. (c) BSE image of ballen at higher magnification showing the very homogeneous composition of individual ballen made of pure SiO_2 . Sample LB-44B. (d) SE image showing the "contact zone" between individual ballen. Note that the boundary appears empty, whereas in many other cases, phyllosilicate minerals occur. Sample LB-44B.

4.1.3. Mien samples

Ballen α -quartz and α -cristobalite occur in Mien impact melt rock samples, mostly in lechatelierite inclusions (Fig. 1b and 4a, b). Most of the ballen are oval to circular in shape and show a large variation in size, from about 22 to 138 μm . Ballen are of types I, II, III, and IV (Table 2); α -cristobalite ballen (type I) occur only associated with ballen α -quartz of type II in the same inclusions. Frequently, a dark "glass-rich" halo surrounds the ballen silica inclusions in the melt matrix, but no resorption of the silica inclusion at the contact zone is visible. Ballen silica also occurs within porphyroclasts of granitoid melt, with tail edges made of feldspar glass. Other porphyroclasts contain partially fused quartz grains that display PDFs. Rare quartz glass inclusions with both, ballen silica and crystalline relic areas with PDFs have been observed.

4.1.4. Ries samples

In Ries samples, ballen quartz occurs in clasts within impact melt rock and in most cases shows intraballen recrystallisation (type IV; Fig. 3d). Ballen α -quartz of type V (Table 2) has been observed as well. No α -cristobalite ballen has been observed in our Ries samples. Most ballen are circular in shape, but some oval ones occur as well (Fig. 5d). The maximum size measured is 168 μm . No

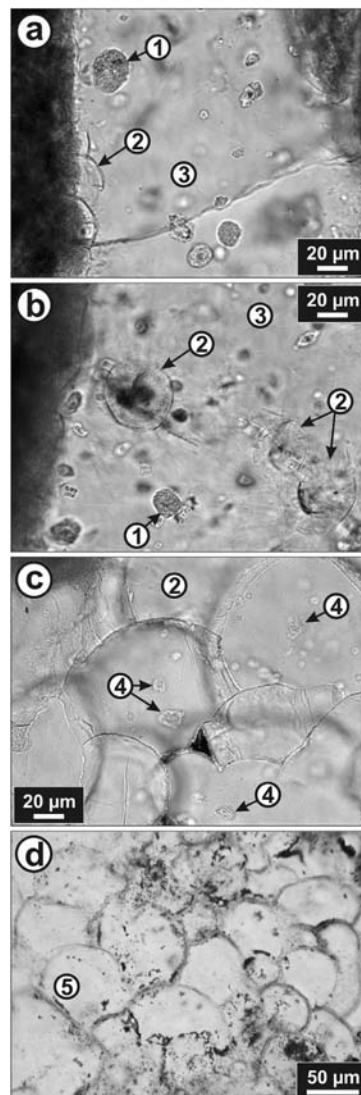


Fig. 5. Microphotographs (in plane-polarized light) of some silica phases investigated with a micro-Raman spectrometer. (a–b) Aggregates/clusters of coesite [1] and incipient development of α -cristobalite ballen [2] in diaplectic quartz glass [3]. (c) Alpha-cristobalite ballen [2] with a few minute inclusions of coesite \pm α -quartz [4]. (d) Ballen made of α -quartz [5] in a lechatelierite clast in impact melt rock. All microphotos are from sample LB-44B (from Bosumtwi), with the exception of (d) from sample SIE-9766 (from the Ries). See corresponding spectra in Fig. 7.

ballen silica has been recognized so far in suevites from either within or outside of the Ries.

4.1.5. Rochechouart samples

Three different types of ballen quartz occur in clasts in impact melt rock from the Rochechouart impact structure, namely types III, IV, and V (Table 2). Ballen α -quartz with intraballen recrystallisation (type IV; Fig. 3c) and chert-like recrystallized ballen α -quartz (type V; Fig. 3e, f) are the

most common types. No α -cristobalite ballen have been observed in our Rochechouart samples. Most of the ballen are oval shaped (Fig. 1c), and rarely circular. Typically, ballen range in size from about 15 to 90 μm . Regarding the chert-like recrystallized ballen α -quartz, rims of individual ballen are not easily distinguished in cross-polarized light.

4.2. Scanning electron microscope and cathodoluminescence observations

The SEM and CL investigations (Fig. 4) show that individual ballen are homogeneous in composition and made of pure SiO_2 (Fig. 4c). The typical pattern of ballen silica is visible in both backscattered electron (BSE) and secondary electron (SE) images (Fig. 4a, b). The BSE image (Fig. 4a) clearly shows the irregular shape of lechatelierite inclusions in a partly crystalline matrix (mainly feldspar crystals in black). The boundaries between ballen appear darker on BSE images, due mostly to the presence of phyllosilicate minerals and/or empty space. The sharp “contact zone” between individual ballen is shown in an SE image at higher magnification (Fig. 4d). Ballen silica does not show distinct CL signatures, reflecting the homogeneity in composition of the ballen, even at the trace-element level.

4.3. Micro-Raman spectroscopy

Silica shows abundant polymorphism as a function of pressure and temperature conditions (Fig. 6). Polymorphs can be easily distinguished using Raman spectroscopy (*e.g.*, Boyer *et al.*, 1985; Stähle *et al.*, 2008; and references therein). During our investigations, α -quartz, diaplectic quartz glass, α -cristobalite, and coesite have been characterized.

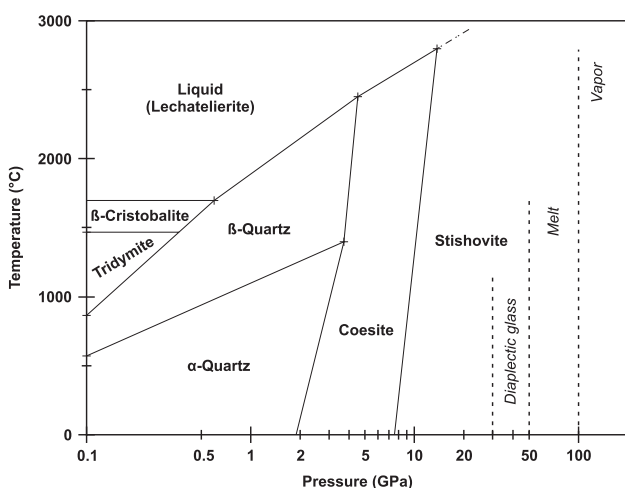


Fig. 6. Combined low and high P - T phase diagram of SiO_2 based on static compression experiments for low-pressure transitions (values from Heaney, 1994) and shock experimental data for high-pressure transformations (data from Cohen & Klement, 1967; Jackson, 1976; Kanzaki, 1990). The coesite-stishovite-liquid triple point is after Zhang *et al.* (1993). Approximate threshold pressure for formation of specific shock effects are indicated by vertical dashed lines (after French, 1998).

Corresponding Raman spectra from our natural samples are shown in Fig. 7.

Characteristic Raman spectra of α -cristobalite have been acquired for ballen from the Mien and Bosumtwi

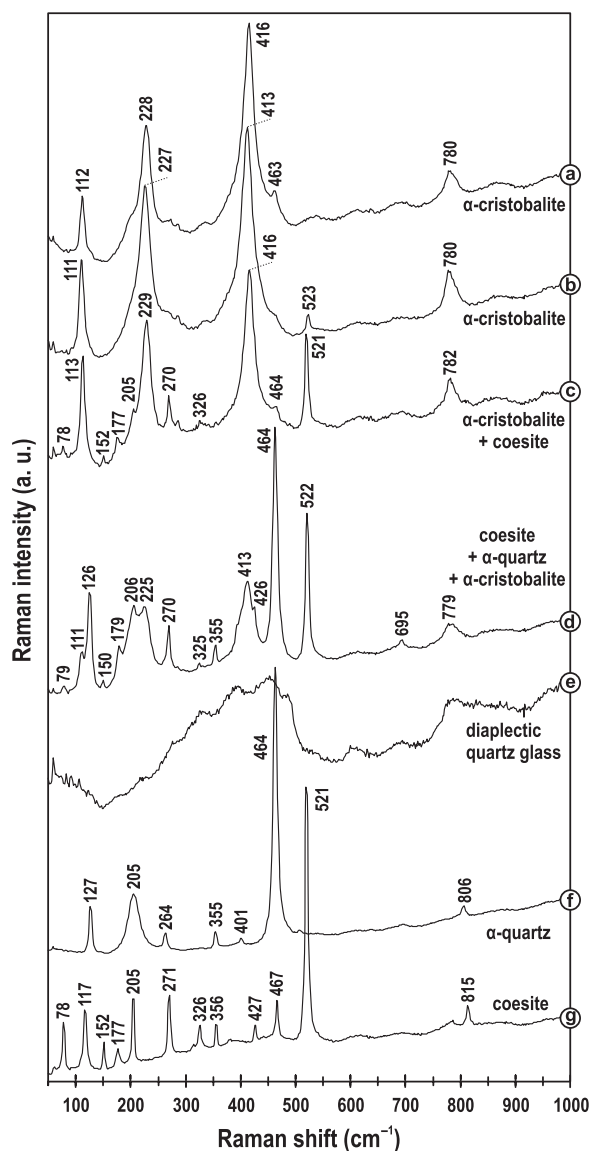


Fig. 7. Selected micro-Raman spectra of different silica phases characteristic of, or associated with, ballen silica. The numbers denote peak positions in cm^{-1} . (a) Alpha-cristobalite spectrum of individual ballen from Mien (sample Mien_02b). (b) Typical α -cristobalite spectrum of individual ballen from Bosumtwi (sample LB-44B2). (c–d) Spectra of minute intra-ballen inclusions, (c) α -cristobalite + coesite spectrum (sample LB-44B) and (d) coesite + α -quartz + α -cristobalite spectrum (sample LB-44B2). (e) Diaplectic quartz glass spectrum. The relatively high background is due to the high degree of amorphisation (sample LB-44B2). (f) Typical α -quartz spectrum (sample SIE-9766 from the Ries). Identical α -quartz spectra were obtained for individual ballen from the other impact structures investigated in this study (with the notable exception of the Bosumtwi samples, for which all ballen were found to be composed of α -cristobalite). (g) Spectrum of an aggregate of coesite illustrated in Fig. 5a (sample LB-44B).

impact structures (Fig. 7a, b, respectively) and show the four peaks typical for α -cristobalite at 111–113, 227–229, 413–416, and 780–782 cm^{-1} (e.g., Bates, 1972). All the ballen in Bosumtwi samples consist of α -cristobalite. However, in the case of the Mien samples, only a few α -cristobalite ballen have been observed together with ballen made of α -quartz, occurring in the same silica inclusion. Ballen from the other investigated impact structures are only composed of α -quartz and have a typical α -quartz Raman signature easily identified based on its intense Raman line at 464 cm^{-1} (Fig. 7f).

Raman spectra of different portions of the same ballen were acquired and show no significant differences, indicating the absence of intraballen variations (in agreement with the SEM results). Some α -cristobalite ballen (type I) contain coesite in the form of tiny, highly refractive, and light green intraballen inclusions (Fig. 5c). These inclusions display the characteristic Raman peaks of coesite, but the bands of α -cristobalite and/or α -quartz occur in these spectra as well (Fig. 7b, c). The mixture of coesite \pm α -cristobalite results from the minimum size of the Raman light beam, which is somewhat larger than the analyzed coesite crystals. The occurrence of α -quartz together with coesite within cristobalite ballen can be explained by the presence of some remnant quartz crystals due to initial shock heterogeneity on the sub-crystal scale, or alternatively by partial back-transformation of coesite to α -quartz. For comparison, Raman spectra of a coesite aggregate and of the host diaplectic quartz glass are also shown (Fig. 7g, e, respectively).

4.4. Transmission electron microscopy

The TEM observations on a FIB foil, cut across the triple junction between three α -cristobalite ballen, revealed that ballen are formed of numerous highly twinned crystals with different crystallographic orientations (Fig. 8). Crystals display polysynthetic twinning with extremely thin twin lamellae and sharp angular contacts between them (Fig. 9). Individual crystals of α -cristobalite are up to 2 μm long. The observed complex twinning and very small size of the crystals are typical for α -cristobalite that has been back-transformed from high temperature β -cristobalite (e.g., Deer *et al.*, 2004). The contact zones of the investigated α -cristobalite ballen are marked by the occurrence of fibrous material (*i.e.*, phyllosilicates), which probably precipitated in interstices between individual silica ballen or resulted from the aqueous alteration of glass phases. Energy-dispersive X-ray microanalysis showed that these phyllosilicates are Al- and Fe-rich (Al/Si ratio \sim 0.4–0.5; Al/Fe ratio \sim 2.2–2.3) and contain a minor amount of Ca (Fig. 9). Based on X-ray diffraction analysis, this badly crystallized phyllosilicate material, with basal d-spacing increasing from 14 to 16.5 \AA after saturation with ethylene glycol, probably belongs to the smectite group (Fe-smectite?) (S. Gier, Unir. Vienna, pers. comm.).

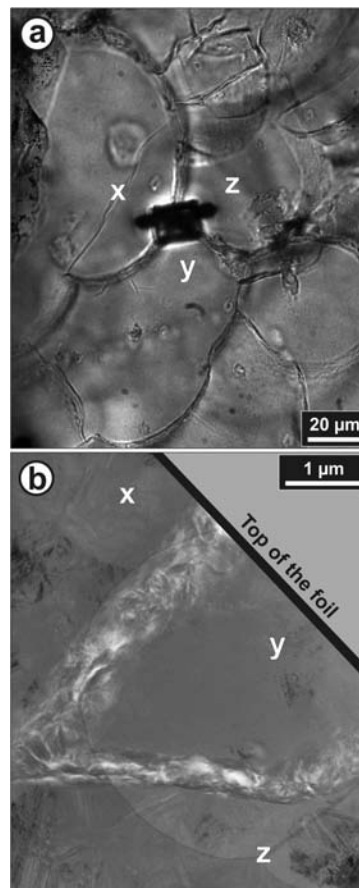


Fig. 8. (a) Microphotograph (in plane-polarized light) with the exact location of the FIB preparation of the TEM foil. The three ballen in contact are noted “x”, “y”, and “z” for orientation. (b) Overview TEM bright field image of the upper part of the TEM foil. Fibrous material (phyllosilicate mineral) occurs between ballen made of pure SiO_2 . The light grey network shown in the background corresponds to the carbon grid supporting the specimen. Sample LB-44B from the Bosumtwi crater.

5. Discussion and summary

5.1. Ballen characteristics and occurrences

Ballen are not cracks or vacuoles, but more or less spheroidal bodies, like grapes, which interpenetrate each other or abut each other. Ballen appear to be spheroids and not lamellae (previously proposed by Holst, 1890; Short, 1970), because under the microscope, no “flat” ballen were observed after investigation of clasts from which thin sections with different orientations had been prepared. “Ballen texture” has been described in the literature as a fish-scale pattern (e.g., Whitehead *et al.*, 2002; Osinski, 2004; Schmieder & Buchner, 2007), but this comparison is not appropriate, because fish-scales are layered lamellae, whereas ballen are spheroids, and they also do not overlap each other.

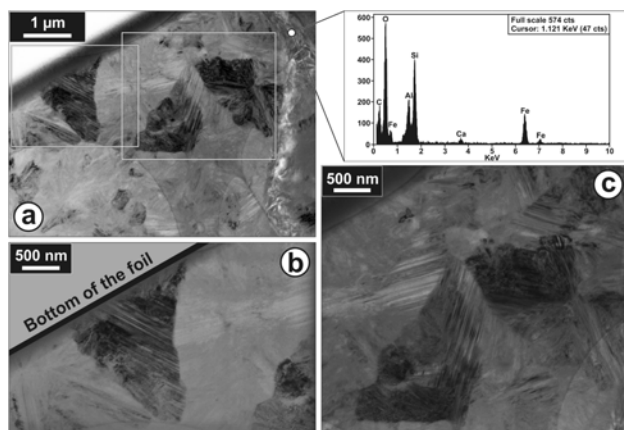


Fig. 9. TEM bright field photomicrographs of α -cristobalite ballen from Bosumtwi (sample LB-44B). (a) General view of a portion of a ballen composed of poly-twinned crystals of α -cristobalite with different orientations. The light grey network shown in this image corresponds to the carbon grid supporting the specimen. The fibrous material filling space between ballen is visible at the right part of the image. The corresponding energy dispersive X-ray spectrum is included. (b–c) Enlarged parts of the general view (a) showing the typical microtexture and arrangement of α -cristobalite crystals forming individual ballen. Note the prominent twin lamellae of the crystals and the sharp angular contact between the crystals.

Individual ballen show a sharp rim, clearly visible with the optical microscope or the SEM. Average ballen are typically about 50 μm wide, but the overall size variation, from 8 to 214 μm , is much larger. The size distribution from inclusion to inclusion (*i.e.*, diaplectic quartz glass or lechatelierite inclusion) is also highly variable, ranging from inclusions with ballen of homogeneous size to inclusions with a large ballen size variation. Large ballen may in some inclusions occur preferentially in the peripheral area, but they may also be present in the central part of a silica inclusion.

Optical observations and Raman spectroscopy have revealed the occurrence of tiny, often light green to brownish inclusions of coesite within ballen of type I (Fig. 2e and 5c; Table 2). Concerning ballen of types II, III, IV, and V (Table 2), no coesite inclusions have been observed so far, but tiny internal defects occur within ballen α -quartz.

Ballen are composed of two polymorphs of silica, α -cristobalite and α -quartz, and more rarely coesite occurs in the form of tiny intraballen inclusions in α -cristobalite ballen (so far only observed/preserved in ballen from the Bosumtwi; Fig. 2e and 5c). Tridymite was also identified by X-ray diffraction in ballen-quartz-bearing melt rocks from the Popigai structure (Vishnevsky & Montanari, 1999; Whitehead *et al.*, 2002), but not in any of our samples. Moreover, considering that tridymite was not observed in situ in ballen and without proper details regarding its relation to other polymorphs of silica, it is difficult to interpret the occurrence of tridymite in ballen silica.

The TEM investigations confirmed the presence of phyllosilicates between individual ballen. We interpret these phyllosilicates as evidence of fluid circulation; possibly, these phyllosilicate minerals filled void spaces between individual ballen.

The presence of relics of PDFs within “ballen quartz”, described from experimentally produced ballen (*e.g.*, Rehfeldt-Oskierski, 1986), has not been found in any of our samples. However, quartz glass clasts with both ballen silica and crystalline relic areas with PDFs have been observed (*e.g.*, at the Mien impact structure). Ballen with a “toasted appearance”, somewhat similar to what has been described for shocked quartz grains (*e.g.*, Short & Gold, 1996), have been noted in impact melt samples from the Popigai (Whitehead *et al.*, 2002) and Dhala (Pati *et al.*, in press) impact structures but not in our samples.

Ballen silica occurs in impact melt rock, as well as in suevite, and in both cases, ballen are irregularly distributed at the sample scale.

5.2. Ballen formation and phase transformation processes

Shock transformation and deformation of quartz have been studied extensively (*e.g.*, Stöffler & Langenhorst, 1994; Grieve *et al.*, 1996; and references therein). It is well known that diaplectic glass starts to form in the solid state in the form of distinct lamellae (*i.e.*, PDFs) along crystallographic orientations (from ~ 10 GPa; *e.g.*, Stöffler & Langenhorst, 1994). At higher pressures (~ 35 GPa), quartz is totally amorphized and forms so-called diaplectic quartz glass (Fig. 6). Quartz melts at higher pressure (~ 50 GPa). However, lechatelierite (the mono-mineralic quartz melt) can form at very high temperatures (above 1700 $^{\circ}\text{C}$), without necessarily requiring high shock pressures (Fig. 6). Lechatelierite occurs in nature only in fulgurites (*e.g.*, Rogers, 1928, 1946) and in impactites (*e.g.*, Stöffler & Langenhorst, 1994; and references therein).

During our investigations, ballen have been observed in both diaplectic quartz glass and lechatelierite inclusions. This means that two processes of formation of ballen are operative: (1) a solid-solid transition, from α -quartz to diaplectic quartz glass and then formation/crystallisation at high temperature of ballen of β -cristobalite and/or β -quartz states, and finally back-transformation to α -cristobalite and/or α -quartz, and (2) a solid-liquid transition, from α -quartz to lechatelierite and then nucleation and growth of β -cristobalite and/or β -quartz ballen at high temperatures that are then back-transformed to α -cristobalite and/or α -quartz.

Ballen at the embryonic stage have been observed at the edges of grains and along fractures (Fig. 2 and 5a), but also around inclusions and other defects preserved in the glass (Fig. 5b). These observations are in good agreement with the fact that defects or impurities are essential for inducing the nucleation of β -cristobalite (*e.g.*, Shoval *et al.*, 1997).

The tiny inclusions of coesite observed within α -cristobalite ballen (Fig. 2e and 5c) also represent possible nuclei for the nucleation of β -cristobalite ballen.

Pure silica is readily transformed into β -cristobalite at temperatures between 1470 and 1710 °C (Fig. 6); however, in natural silica minerals this transformation has been observed at comparatively lower temperatures between 1100–1600 °C (*e.g.*, Shoval *et al.*, 1997). This may be due to the presence of trace elements. In addition, water content and pressure conditions affect the temperature range. In high-temperature annealing experiments with diaplectic quartz glass, “ballen like” features started to form at about 1200 °C (Short, 1970; Rehfeldt-Oskierski, 1986).

Concerning the ballen types II, III, IV, and V (see Table 2), all composed of α -quartz, it is probable that these ballen, originally formed as β -cristobalite or β -quartz, were then back-transformed to α -quartz with time. Beta-cristobalite, which is only metastable at ambient temperature, slowly converts to the quartz structure with time (*e.g.*, Heaney, 1994). The occurrence of α -cristobalite ballen (type I), together with ballen α -quartz in the same silica inclusions from the Mien impact structure, is considered as evidence that the transformation from α -cristobalite to α -quartz has taken place. In addition, the observation that only α -cristobalite ballen occur at the relatively young (1.07 Ma old) Bosumtwi crater seems to support this interpretation. In terms of volume change, the transformation of cristobalite phases to α -quartz corresponds to a volume shrinkage of about 12 % (at atmospheric pressure; *e.g.*, Hemley *et al.*, 1994; and references therein). The transformation of cristobalite phases to α -quartz and the conditions (*e.g.*, velocity, water content, stress, etc) of this transformation evidently influence the formation of the different types (II, III, IV, and V) of ballen silica. However, we assume that these differences are mostly a function of the respective P - T conditions and velocity of the transformation of cristobalite phases to α -quartz. The volume changes resulting from the transformation of cristobalite polymorphs to α -quartz can also influence the orientations of nuclei (Wheeler *et al.*, 2001), inducing some misorientations of the resulting α -quartz crystals within ballen. In addition, post-impact alteration processes have also affected ballen silica, illustrated by the presence of phyllosilicate minerals in between ballen.

Nevertheless, it is not clear whether post-impact alteration processes (*e.g.*, hydrothermal alteration) directly influence microstructures of the different “ballen quartz” types. The exact conditions of formation for the different types of ballen (types II, III, IV, and V) are still unclear. Some annealing experiments and detailed petrographic observations of the resulting ballen-like features are necessary to better understand the transformation of cristobalite polymorphs to α -quartz and the various textures and microstructures observed in natural ballen. In addition, the observed size ranges and heterogeneous size distributions of ballen within silica inclusions, as well as the variety of ballen shapes, must have implications regarding

ballen formation. As discussed previously, impurities are necessary for the nucleation of β -cristobalite (*e.g.*, Shoval *et al.*, 1997), and consequently the distribution of ballen within silica clasts is mostly influenced by the distribution of initial impurities or other lattice defects, as nucleation sites. On the other hand, temperature gradients across clasts and cooling rates will influence the size ranges of ballen within silica inclusions. The different shapes of ballen observed during our study can either be the result of growing under stress conditions, or a function of the characteristics of the nuclei.

The occurrence of ballen quartz/cristobalite in suevite samples, such as at the Bosumtwi and at the Chicxulub impact structures, has interesting implications in terms of timing of formation and for the quantification of the cooling history of suevite deposits. We have shown that the different types of ballen are mostly a function of the P - T conditions, and that is why the occurrence of the different types of ballen (as at the Bosumtwi; exclusively of type I) in suevite samples can possibly be used as a tracer of these conditions (*i.e.*, remnant temperature of suevite deposits). The maximum size of ballen can also give some information on the duration of the conditions permitting the growth of ballen. However, as already discussed for the effects of post-impact alteration processes on the different types of ballen, further annealing experiments are necessary.

5.3. Ballen quartz/cristobalite – evidence for shock metamorphism?

Quartz is one of the most commonly used indicator minerals for shock metamorphism, as well as for pressure calibration. Quartz displays a wide variety of shock-induced mechanical deformations and transformations: PFs, PDFs, mosaicism, transformation to coesite and stishovite, amorphisation (*i.e.*, formation of diaplectic glass), and melting (*e.g.*, Stöffler, 1971; Stöffler & Langenhorst, 1994; Grieve *et al.*, 1996; Huffman & Reimold, 1996; Stähle *et al.*, 2008; and references therein).

Our observations have shown that ballen quartz/cristobalite is formed from diaplectic quartz glass and lechatelierite, nucleating at high temperatures (Fig. 6). Obviously, the formation of ballen silica requires special conditions, because otherwise such features would be abundant in volcanic rocks.

Recently, in an abstract, Schmieder & Buchner (2007) suggested that “ballen quartz” might not be restricted to impactites, claiming that similar features could occur in volcanic rocks and in fulgurites. It is well known (*e.g.*, Rogers, 1928; Deer *et al.*, 2004) that β -cristobalite, a high-temperature polymorph of silica, is common in acidic volcanic rocks, usually in the form of minute octahedrons, radiating clusters, spherical aggregates, or spherulites intergrown with feldspar. Schmieder & Buchner (2007) referred to a paper by Swanson *et al.* (1989) that mentions the occurrence of poikilitic cristobalite filling the space between feldspar fibres in obsidian. Ballen-like features were, however, not mentioned by Swanson *et al.* (1989).

Cristobalite in this case appears to have nucleated after feldspar, individual crystals of cristobalite are very small ($<10\ \mu\text{m}$), and the presence of coesite was not reported. The particular petrographic contexts of occurrence of these cristobalite “crystals”, as well as their characteristics, are very different from α -cristobalite ballen (type I) described in our study. In addition, in the case of silica glass (*i.e.*, obsidian) inclusions that occur in volcanic rocks, obsidian is not composed of pure SiO_2 , but contains a certain amount of other oxides such as Al_2O_3 , K_2O , or NaO . Ballen quartz/cristobalite has so far only been observed within pure SiO_2 inclusions (*i.e.*, diaplectic quartz glass and lechatelierite) in impactites.

Concerning the alleged occurrence of ballen-like features in fulgurites formed in quartz-rich sand, Schmieder & Buchner (2007) referred to a paper by Rogers (1946), where the occurrence of cristobalite is mentioned, but the presence of ballen-like features was actually not described. Mostly made of silica glass (*i.e.*, lechatelierite), sand fulgurites show remnants of quartz grains and abundant vesicles (generally empty) within a glassy matrix. Rarely cristobalite occurs in the external part of the fulgurite (*e.g.*, Rogers, 1946), but, so far, no α -cristobalite or α -quartz ballen have been described from fulgurites. Considering also the extremely short duration of the high-temperatures (above $1700\ \text{°C}$; Essene & Fisher, 1986) involved in the formation of sand fulgurites, it is not conceivable that cristobalite crystals can develop more than a few micrometers in size. The slower cooling rate within high-temperature impactites might be a requirement to form ballen. As in the case of cristobalite in volcanic rocks, the context of occurrence of cristobalite in sand fulgurites is, in any case, not comparable to α -cristobalite ballen in impactites.

We have shown that ballen silica occurs exclusively within diaplectic quartz glass and lechatelierite inclusions (*i.e.*, pure silica glass), phases that form at high shock pressures, namely ~ 35 and ~ 50 GPa, respectively (Fig. 6; *e.g.*, Stöffler & Langenhorst, 1994). Moreover, the temperature must have exceeded ~ 1200 – $1400\ \text{°C}$, according to annealing experiments by Short (1970) and Rehfeldt-Oskierski (1986). Only shock metamorphism can reach these P – T conditions at the Earth’s surface. However, as ballen quartz/cristobalite are the result of back-transformations from shock-induced states, ballen silica cannot be considered direct evidence of shock metamorphism; however, its occurrence is restricted to impact-derived rocks and, thus, its presence should be added to the list of impact-characteristic criteria.

6. Conclusions

Investigation of α -quartz and α -cristobalite ballen in 27 thin sections from five different impact structures (Bosumtwi, Chicxulub, Mien, Ries, and Rochechouart), combined with literature data, has shown that ballen

occur within diaplectic quartz glass and lechatelierite inclusions, not only in impact melt rock but also in suevite. Our observations show that two processes of formation are operating: (1) a solid-solid transition, from α -quartz to diaplectic quartz glass and then formation of ballen loops made of β -cristobalite and/or β -quartz, and (2) formation by nucleation and crystal growth at high temperatures after lechatelierite formation. In addition, our investigations have indicated that ballen, originally made of β -cristobalite and/or β -quartz, are back-transformed to α -cristobalite and to α -quartz with time. Coesite inclusions were also, for the first time, observed and characterized within ballen silica.

Five types of ballen have been distinguished: α -cristobalite ballen with homogeneous extinction (type I); ballen α -quartz with homogeneous extinction (type II), with heterogeneous extinction (type III), and with intra-ballen recrystallisation (type IV); chert-like recrystallized ballen α -quartz (type V).

Since more than 20 years, “ballen quartz” has on occasion been used as a “shock pressure indicator” (*e.g.*, Dressler *et al.*, 1997; Whitehead *et al.*, 2002), based on the occurrence of the three different types of ballen as described by Bischoff & Stöffler (1984). Our observations indicate that the interpretation of shock pressures cannot be based only on the occurrence of different types of ballen silica, because the different types of ballen are the result from post-impact transformations.

Nevertheless, the presence of ballen quartz/cristobalite provides some constraint on shock pressure which must have exceeded ~ 35 GPa (pressure of formation of diaplectic quartz glass; *e.g.*, Stöffler & Langenhorst, 1994; and references therein), as well as on temperature at ballen formation, which must have exceeded $1200\ \text{°C}$ (based on annealing experiments by Short, 1970 and Rehfeldt-Oskierski, 1986).

Acknowledgements: This work was supported by the Austrian Science Foundation (FWF), grant P18862-N10, and the Austrian Academy of Sciences. We are grateful to F. Brandstätter (Natural History Museum, Vienna, Austria) for assistance with SEM and CL work, to E. Libowitzky (University of Vienna, Austria) for assistance with the micro Raman spectroscopic analyses, S. Gier (University of Vienna, Austria) for an XRD analysis, to S. Augustin and R. Wirth (GFZ, Potsdam, Germany) for the FIB preparation, and to A. Greshake (Museum of Natural History, Humboldt-University, Berlin, Germany) for assistance with the TEM. Thanks also to J-P. Lorand and G. Carrier (Muséum National d’Histoire Naturelle, Paris, France) and to R.-T. Schmitt (Museum of Natural History, Humboldt-University, Berlin, Germany) for providing thin sections from the Rochechouart and Ries craters, respectively, H. Reyss (SAF, Paris, France) and E. Dransart (EMTT, Francheville, France) for the samples from Mien crater, C. Alwmark (University of Lund, Sweden) for providing and translating the reference by Holst (1890), and B. and M.H.

French, E.P., Gurov, J., Morrow, D., Stöffler, and A. Wittmann for helpful and constructive discussions. We thank J. Spray and two anonymous reviewers for constructive comments on an earlier version of this manuscript.

References

- Åström, K. (1998): Seismic signature of the Lake Mien impact structure, southern Sweden. *Geophys. J. Int.*, **135**, 215–231.
- Bartosova, K., Ferrière, L., Koeberl, C., Reimold, W.U., Gibson, R., Schmitt, R.T. (2007): Lithological, petrographical, and geochemical investigations of suevite from the Eyreville core, Chesapeake Bay impact structure. *Geol. Soc. Am. Abstr. Prog.*, **39**, A451.
- Bates, J.B. (1972): Raman spectra of α and β cristobalite. *J. Chem. Phys.*, **57**, 4042–4047.
- Bischoff, A. & Stöffler, D. (1984): Chemical and structural changes induced by thermal annealing of shocked feldspar inclusions in impact melt rocks from Lappajärvi crater, Finland. *J. Geophys. Res.*, **89**, B645–B656.
- Boamah, D. & Koeberl, C. (2006): Petrographic studies of fallout suevite from outside the Bosumtwi impact structure, Ghana. *Meteorit. Planet. Sci.*, **41**, 1761–1774.
- Boyer, H., Smith, D.C., Chopin, C., Lasnier, B. (1985): Raman microprobe (RMP) determinations of natural and synthetic coesite. *Phys. Chem. Minerals*, **12**, 45–48.
- Buchner, E., Seyfried, H., van den Bogaard, P. (2003): $^{40}\text{Ar}/^{39}\text{Ar}$ laser probe age determination confirms the Ries impact crater as the source of glass particles in Graupensand sediments (Grimmelfingen Formation, North Alpine Foreland Basin). *Int. J. Earth Sci.*, **92**, 1–6.
- Carstens, H. (1975): Thermal history of impact melt rocks in the Fennoscandian shield. *Contrib. Mineral. Petrol.*, **50**, 145–155.
- Cohen, L.H. & Klement, W.K., Jr. (1967): High-low quartz inversion: determination to 35 kilobars. *J. Geophys. Res.*, **73**, 4245–4251.
- Coney, L., Gibson, R.L., Reimold, W.U., Koeberl, C. (2007): Lithostratigraphic and petrographic analysis of ICDP drill core LB-07A, Bosumtwi impact structure, Ghana. *Meteorit. Planet. Sci.*, **42**, 569–589.
- Deer, W.A., Howie, R.A., Wise, W.S., Zussman, J. (2004): Rock-forming minerals. Framework silicates: silica minerals, feldspaths and the zeolites, The Geological Society, London, Vol. 4B, 2nd edition, 982 p.
- Dressler, B.O., Crabtree, D., Schuraytz, B.C. (1997): Incipient melt formation and devitrification at the Wanapitei impact structure, Ontario, Canada. *Meteorit. Planet. Sci.*, **32**, 249–258.
- Earth Impact Database. (2008): <http://www.unb.ca/passc/ImpactDatabase/> (accessed 15 December 2007).
- Engelhardt, W. von (1972): Shock produced rock glasses from the Ries crater. *Contrib. Mineral. Petrol.*, **36**, 265–292.
- Engelhardt, W. von & Stöffler, D. (1968): Stages of shock metamorphism in the crystalline rocks of the Ries Basin (Germany). in “Shock metamorphism of natural materials”, B.M. French, N.M. Short, eds., Mono Book Corp., Baltimore, 159–168.
- Essene, E.J. & Fisher, D.C. (1986) Lightning strike fusion: extreme reduction and metal-silicate liquid immiscibility. *Science*, **234**, 189–193.
- Ferrière, L. & Koeberl, C. (2007): Ballen quartz, an impact signature: new occurrence in impact melt breccia at Rochechouart-Chassenon impact structure, France. *Meteorit. Planet. Sci.*, **42**, Suppl, A46.
- Ferrière, L., Koeberl, C., Reimold, W.U. (2006): Ballen quartz in impact glass from the Bosumtwi impact crater, Ghana. *Meteorit. Planet. Sci.*, **41**, Suppl, A54.
- Ferrière, L., Koeberl, C., Reimold, W.U. (2007): Drill core LB-08A, Bosumtwi impact structure, Ghana: petrographic and shock metamorphic studies of material from the central uplift. *Meteorit. Planet. Sci.*, **42**, 611–633.
- French, B.M. (1998): *Traces of catastrophe: a handbook of shock-metamorphic effects in terrestrial meteorite impact structures*. LPI Contrib. No 954, Lunar and Planetary Institute, Houston, 120 p.
- French, B.M., Hartung, J.B., Short, N.M., Dietz, R.S. (1970): Tenoumer crater, Mauritania: age and petrologic evidence for origin by meteorite impact. *J. Geophys. Res.*, **75**, 4396–4406.
- Grieve, R.A.F. (1975): Petrology and chemistry of the impact melt at Mistastin Lake crater, Labrador. *Geol. Soc. Am. Bull.*, **86**, 1617–1629.
- Grieve, R.A.F. & Ber, T.J. (1994): Shocked lithologies at the Wanapitei impact structure, Ontario, Canada. *Meteorit. Planet. Sci.*, **29**, 621–631.
- Grieve, R.A.F., Reny, G., Gurov, E.P., Ryabenko, V.A. (1987): The melt rocks of the Boltysk impact crater, Ukraine, USSR. *Contrib. Mineral. Petrol.*, **96**, 56–62.
- Grieve, R.A.F., Langenhorst, F., Stöffler, D. (1996): Shock metamorphism of quartz in nature and experiment: II. Significance in geoscience. *Meteorit. Planet. Sci.*, **31**, 6–35.
- Gurov, E.P., Koeberl, C., Reimold, W.U. (1998): Petrography and geochemistry of target rocks and impactites from the Ilyinets Crater, Ukraine. *Meteorit. Planet. Sci.*, **33**, 1317–1333.
- Gurov, E.P., Gurova, E.P., Sokur, T.M. (2002): Geology and petrography of the Zapadnaya impact crater in the Ukrainian shield. in “Impacts in Precambrian shields”, J. Plado, L.J. Pesonen, eds. Impact studies 2, Springer-Verlag, Heidelberg, 173–188.
- Gurov, E.P., Koeberl, C., Reimold, W.U., Brandstätter, F., Amare, K. (2005): Shock metamorphism of siliceous volcanic rocks of the El’gygytyn impact crater (Chukotka, Russia). in “Large meteorite impacts III”, T. Kenkmann, F. Hörz, A. Deutsch, eds. *Geol. Soc. Am. Spec. Paper*, **384**, 391–412.
- Heaney, P.J. (1994): Structure and chemistry of the low-pressure silica polymorphs. in “Silica: physical behavior, geochemistry and materials applications”, P.J. Heaney, C.T. Prewitt, G.V. Gibbs, eds. Mineral. Soc. Am., Washington DC. *Rev. Mineral.*, **29**, 1–40.
- Hemley, R.J., Prewitt, C.T., Kingma, K.J. (1994): High-pressure behavior of silica. in “Silica: physical behavior, geochemistry and materials applications”, P.J. Heaney, C.T. Prewitt, G.V. Gibbs, eds. Mineral. Soc. Am., Washington DC. *Rev. Mineral.*, **29**, 41–81.
- Hildebrand, A.R., Penfield, G.T., Kring, D.A., Pilkington, M., Camargo Zanoaguera, A., Jacobsen, S.B. (1991): Chicxulub crater: a possible Cretaceous/Tertiary boundary impact crater on the Yucatán Peninsula, Mexico. *Geology*, **19**, 867–871.
- Holst, N.O. (1890): Ryoliten vid sjön Mien. Sveriges Geologiska Undersökning. Serie C, Avhandlingar och uppsatser, No 110. Stockholm, 50 p. (in Swedish).
- Huffman, A.R. & Reimold, W.U. (1996): Experimental constraints on shock-induced microstructures in naturally deformed silicates. *Tectonophys.*, **256**, 165–217.
- Jackson, I. (1976): Melting of silica isotypes SiO_2 , BeF_2 and GeO_2 at elevated pressures. *Phys. Earth Planet. Int.*, **13**, 218–231.
- Kanzaki, M. (1990): Melting of silica up to 7 GPa. *J. Am. Ceram. Soc.*, **73**, 3706–3707.

- Karikari, F., Ferrière, L., Koeberl, C., Reimold, W.U., Mader, D. (2007): Petrography, geochemistry, and alteration of country rocks from the Bosumtwi impact structure, Ghana. *Meteorit. Planet. Sci.*, **42**, 513–540.
- Kelley, S.P. & Spray, J.G. (1997): A late Triassic age for the Rochechouart impact structure, France. *Meteorit. Planet. Sci.*, **32**, 629–636.
- Koeberl, C. & Reimold, W.U. (2005): Bosumtwi impact crater, Ghana (West Africa): an updated and revised geological map, with explanations. *Jb. Geol. Bundesanstalt, Wien*, **145**, 31–70.
- Kraut, F. (1970): Über ein neues Impaktit-vorkommen im Gebiete von Rochechouart-Chassenon (Départements Haute Vienne und Charente, Frankreich). *Geol. Bavarica*, **61**, 428–450.
- Kraut, F. & French, B.M. (1971): The Rochechouart meteorite impact structure, France: preliminary geological results. *J. Geophys. Res.*, **76**, 5407–5413.
- Lambert, P. (1977): Les effets des ondes de choc naturelles et artificielles, et le cratère d'impact de Rochechouart (Limousin – France). Unpublished Habilitation Thesis, University of Paris Sud, Centre d'Orsay, France, 176 p. (in French).
- Marvin, U.B. & Kring, D.A. (1992): Authentication controversies and impactite petrography of the New Quebec crater. *Meteorit. Planet. Sci.*, **27**, 585–595.
- McIntyre, D.B. (1968): Impact metamorphism at Clearwater lake, Quebec. in “Shock metamorphism of natural materials”, B.M. French, N.M. Short, eds. Mono Book Corp., Baltimore, 363–366.
- Montanari, A. & Koeberl, C. (2000): Impact stratigraphy: the Italian record. Lectures notes in earth sciences 93, Springer Verlag, Heidelberg, 364 p.
- Müller, N., Hartung, J.B., Jessberger, E.K., Reimold, W.U. (1990): ⁴⁰Ar-³⁹Ar ages of Dellen, Jänisjärvi, and Sääksjärvi impact craters. *Meteorit. Planet. Sci.*, **25**, 1–10.
- Osinski, G.R. (2004): Impact melt rocks from the Ries structure, Germany: an origin as impact melt flows? *Earth Planet. Sci. Lett.*, **226**, 529–543.
- Pati, J.K., Reimold, W.U., Koeberl, C., Pati, P. (in press): The Dhala structure, Bundelkhand craton, central India – eroded remnant of a large Paleoproterozoic impact structure. *Meteorit. Planet. Sci.*
- Pesonen, L.J., Lehtinen, M., Deutsch, A., Elo, S., Lukkarinen, H. (1996): New geophysical and petrographic results of the Suvasvesi N impact structure, Finland (abstract). *Lunar Planet. Sci. Conf.*, **XXVII**, 1021–1022.
- Phinney, W.C., Simonds, C.H., Cochran, A., McGee, P.E. (1978): West clearwater, Quebec impact structure, part II: petrology. *Proc. Lunar Planet. Sci. Conf.*, **IX**, 2659–2693.
- Pohl, J., Stöffler, D., Gall, H., Ernstson, K. (1977): The Ries impact crater. in “Impact and explosion cratering”, D.J. Roddy, R.O. Pepin, R.B. Merrill, eds. Pergamon, New York, 343–404.
- Rehfeldt-Oskierski, A. (1986): Stosswellenexperimente an Quarzeinkristallen und thermisches Verhalten von diaplektischen Quarzglasern. Unpublished Ph.D. Thesis, University of Münster, Germany, 145 p. (in German).
- Reimold, W.U., Koeberl, C., Brandstätter, F., Kruger, F.J., Armstrong, R.A., Bootsman, C. (1999): Morokweng impact structure, South Africa: geologic, petrographic, and isotopic results, and implications for the size of the structure. in “Large meteorite impacts and planetary evolution II”, B.O. Dressler, V.L. Sharpton, eds., *Geol. Soc. Am. Spec. Paper*, **339**, 61–90.
- Rogers, A.G. (1928): Natural history of the silica minerals. *Am. Mineral.*, **13**, 73–92.
- (1946): Sand fulgurites with enclosed lechatelierite from river-side country, California. *J. Geol.*, **54**, 117–122.
- Schmieder, M. & Buchner, E. (2007): Is “ballen quartz” diagnostic for shock metamorphism? *Geochim. Cosmochim. Acta*, **71**, A897.
- Short, N.M. (1970): Progressive shock metamorphism of quartzite ejecta from the Sedan nuclear explosion crater. *J. Geol.*, **78**, 705–723.
- Short, N.M. & Gold, D.P. (1996): Petrography of shocked rocks from the central peak at the Manson impact structure. in “The Manson impact structure, Iowa: anatomy of an impact crater”, C. Koeberl, R.R. Anderson, eds. *Geol. Soc. Am. Spec. Paper*, **302**, 245–265.
- Shoval, S., Champagnon, B., Panczer, G. (1997): The quartz-cristobalite transformation in heated chert rock composed of micro and crypto-quartz by micro-Raman and FT-IR spectroscopy methods. *J. Therm. Anal.*, **50**, 203–213.
- Stähle, V., Altherr, R., Koch, M., Nasdala, L. (2008): Shock-induced growth and metastability of stishovite and coesite in lithic clasts from suevite of the Ries impact crater (Germany). *Contrib. Mineral. Petrol.*, **155**, 457–472.
- Stöffler, D. (1971): Coesite and Stishovite in shocked crystalline rocks. *J. Geophys. Res.*, **76**, 5474–5488.
- Stöffler, D. & Grieve, R.A.F. (2007): Impactites, Chapter 2.11. in “Metamorphic rocks: a classification and glossary of terms, Recommendations of the International Union of Geological Sciences”, D. Fettes, J. Desmons, eds., Cambridge Univ. Press, Cambridge, 82–92, Glossary.
- Stöffler, D. & Langenhorst, F. (1994): Shock metamorphism of quartz in nature and experiment: I. Basic observation and theory. *Meteorit. Planet. Sci.*, **29**, 155–181.
- Stöffler, D., Artemieva, N.A., Ivanov, B.A., Hecht, L., Kenkmann, T., Schmitt, R.T., Tagle, R.A., Wittmann, A. (2004): Origin and emplacement of the impact formations at Chicxulub, Mexico, as revealed by the ICDP deep drilling at Yaxcopoil-1 and by numerical modeling. *Meteorit. Planet. Sci.*, **39**, 1035–1067.
- Swanson, S.E., Naney, M.T., Westrich, H.R., Eichelberger, J.C. (1989): Crystallization of Obsidian Dome, Inyo Domes, California. *Bull. Volcanol.*, **51**, 161–176.
- Thomas, M.D., Innes, M.J.S., Dence, M.R., Grieve, R.A.F., Robertson, P.B. (1977): Gow Lake, Saskatchewan: evidence for an origin by meteorite impact. *Meteoritics*, **12**, A370–371.
- Tuchscherer, M.G., Reimold, W.U., Koeberl, C., Gibson, R.L., de Bruin, D. (2004): First petrographic results on impactites from the Yaxcopoil-1 borehole, Chicxulub structure, Mexico. *Meteorit. Planet. Sci.*, **39**, 899–930.
- Vishnevsky, S. & Montanari, A. (1999): Popigai impact structure (Arctic Siberia, Russia): geology, petrology, geochemistry, and geochronology of glass-bearing impactites. in “Large meteorite impacts and planetary evolution II”, B.O. Dressler, V.L. Sharpton, eds., *Geol. Soc. Am. Spec. Paper*, **339**, 19–59.
- Wheeler, J., Prior, D.J., Jiang, Z., Spiess, R., Trimby, P.W. (2001): The petrological significance of misorientations between grains. *Contrib. Mineral. Petrol.*, **141**, 109–124.
- Whitehead, J., Grieve, R.A.F., Spray, G. (2002): Mineralogy and petrology of melt rocks from the Popigai impact structure, Siberia. *Meteorit. Planet. Sci.*, **37**, 623–647.

Wirth, R. (2004): Focused Ion Beam (FIB): a novel technology for advanced application of micro- and nanoanalysis in geosciences and applied mineralogy. *Eur. J. Mineral.*, **16**, 863–876.

Wittmann, A., Kenkmann, T., Schmitt, R.T., Hecht, L., Stöffler, D. (2004): Impact-related dike breccia lithologies in the ICDP drill core Yaxcopoil-1, Chicxulub impact structure, Mexico. *Meteorit. Planet. Sci.*, **39**, 931–954.

Zhang, J., Liebermann, R.C., Gasparik, T., Herzberg, C.T., Fei, Y. (1993): Melting and subsolidus relations of SiO₂ at 9–14 GPa. *J. Geophys. Res.*, **98**, 19785–19793.

Received 15 July 2008

Modified version received 30 July 2008

Accepted 1 September 2008

Systematic study of universal-stage measurements of planar deformation features in shocked quartz: Implications for statistical significance and representation of results

Ludovic Ferrière ^{1*}, Jared R. Morrow ², Tsolmon Amgaa ¹, and Christian Koeberl ¹

¹*Department of Lithospheric Research, University of Vienna, Althanstrasse 14, A-1090 Vienna, Austria*

²*Department of Geological Sciences, San Diego State University, 5500 Campanile Drive, San Diego, California 92182-1020, USA*

**corresponding author: ludovic.ferriere@univie.ac.at*

Submitted to: Meteoritics and Planetary Science, September 06, 2008

Abstract:

The presence of shocked quartz is one of the key lines of evidence for the impact origin of rocks. The study of the crystallographic orientations of planar deformation features (PDF) in shocked quartz constrains the peak shock pressure that these grains have experienced. So far no systematic and comparative studies of the various orientation measurement methods and their bias have been available. Therefore, three shocked-quartz-bearing thin sections (meta-greywacke clast in breccia, biotite-gneiss, and sandstone) were independently analyzed by three operators (two experienced and one inexperienced) using a four-axis universal-stage (U-stage) microscope, in order to evaluate the quality, precision, repeatability, and representativeness of U-stage measurements. Based on the indexing of PDF sets using a new version of the commonly used stereographic projection template, the study of 1751 PDF set orientations in 666 quartz grains in three different shocked rocks shows that differences in abundance and orientation of various PDF sets, as measured by the three separate operators, is rather limited.

The precision of U-stage measurements depends mainly of the number of PDF sets investigated, as the ability level of the operator (experienced versus inexperienced) is only responsible for minor deviations in the number of unindexed planes. The frequency percent of dominant PDF planes may vary by up to 20 percentage points (pp) or 81% within a given crystallographic orientation when only 25 sets are measured. Where 100 PDF sets are measured, however, this deviation in dominant orientations is reduced to about 7 pp or 28%. We recommend the use of a new stereographic projection template, which plots the pole orientations of four additional commonly occurring PDF sets, as it can allow indexing of up to 8% more PDF planes; these are planes that would previously be considered unindexed and potentially regarded as errors of measurement.

Our results suggest that by following a strict measurement procedure, the reproducibility of U-stage measurements is good and the results of different studies can be readily compared. However, it is critical that published PDF orientation histograms clearly

define what type of frequency measurement is used, whether or not unindexed PDF sets are included in the frequency calculations, the numbers of grains and sets analyzed, and the relative proportions of each PDF set population that are combined in the histograms. This information appears to be essential for effectively comparing datasets from different studies.

1. Introduction:

Universal-stage (U-stage) microscope analysis is a standard technique used for determining the crystallographic orientations of planar deformation features (PDFs) in quartz. Detection of these shock-metamorphic features and the distribution of their orientations in quartz are crucial diagnostic evidence for proving the impact origin of many geological structures.

Upon shock compression, quartz develops irregular fractures (which are not diagnostic shock effects) and regular planar microstructures, as planar fractures (PFs) and PDFs, which are both produced during shock metamorphism (e.g., French and Short 1968; Engelhardt and Bertsch 1969; Alexopoulos et al. 1988; Stöffler and Langenhorst 1994; Grieve et al. 1996; French 1998). Planar fractures are parallel open fissures with a typical spacing of more than 15-20 μm apart. These differ from PDFs, which are commonly composed of narrow, individual planar elements of amorphous material that are less than 2 μm thick, comprising straight, parallel sets spaced 2-10 μm apart (e.g., Engelhardt and Bertsch 1969; Stöffler and Langenhorst 1994). Both PFs and PDFs are oriented parallel to rational crystallographic planes of low Miller indices (i.e., "low" refers to the Miller indices being small numbers; see Table 1). Miller indices consist of three numbers (hkl) representing the inverse of axial unit distances of the plane intercepts along each of the crystallographic axes (a, b, and c axes, respectively). In the case of hexagonal systems (as for quartz), four numbers ($hkil$), the so-called Miller-Bravais indices, are used. These numbers represent the inverse plane intercepts along the a_1 , a_2 , a_3 , and c axes, respectively (see, e.g., Bloss 1971). The combination of these three or four numbers uniquely identifies the three-dimensional orientation of planes in the crystal. The notation $\{hkil\}$ denotes all planes that are equivalent to ($hkil$) by the symmetry of the crystal. For the commonly formed planar microstructure orientations in shocked quartz, a letter symbol (ϵ , ω , π , etc.) can be substituted for, or used in conjunction with, the Miller-Bravais notation (Table 1; e.g., Stöffler and Langenhorst 1994; Langenhorst, 2002).

Previous studies have shown that PFs are parallel usually to (0001) and $\{10\bar{1}1\}$, and occasionally to $\{10\bar{1}3\}$, whereas PDFs are parallel commonly to $\{10\bar{1}3\}$, $\{10\bar{1}2\}$, (0001), $\{10\bar{1}1\}$, $\{11\bar{2}2\}$, $\{11\bar{2}1\}$, $\{2\bar{1}31\}$, $\{5\bar{1}61\}$, $\{10\bar{1}0\}$, and $\{11\bar{2}0\}$, and more rarely to other planes listed in Table 1 (e.g., Stöffler and Langenhorst 1994). The measurement of PDF orientations is possible using transmission electron microscopy (TEM; e.g., Goltrant et al. 1991), as well as with the spindle stage (e.g., Bohor et al. 1987), but only the U-stage technique allows a large number of PDF sets to be measured and potentially indexed both efficiently and inexpensively.

Universal-stage measurements have been performed in impact geology for about 40 years; however, the quality, precision, repeatability, and representativeness of the measurements (in terms of personal and laboratory biases) for a given sample have not been thoroughly tested. For these reasons, three shocked-quartz-bearing thin sections (BOS-3, a meta-greywacke clast in breccia from Bosumtwi crater; M8-427.7, a biotite-gneiss from Manson crater; and AUS-90-43-2, a sandstone from Gosses Bluff crater) were independently analyzed by each of three operators (two experienced and one inexperienced) using a four-axis U-stage mounted on an optical microscope.

This paper presents our results, based on the indexing of the PDF planes using a new version of the commonly used stereographic projection template, comparing measurements obtained on the same three thin sections by three operators, which allows discussion regarding the statistical meaning and reproducibility of U-stage measurements. These results expand on earlier preliminary data reported in abstract form by Ferrière et al. (2008).

2. Experimental methods and representation of the measurements:

Prior to describing our measurements, it is necessary to briefly review the method of measuring PDF orientations using the U-stage microscope, as well as discussing some definitions and the plotting and representation of data. Determination of the crystallographic orientations of PDFs in quartz grains with a U-stage microscope (see, e.g., Reinhard 1931; Emmons 1943 for general information) is done in four main steps: (1) determination of the optic or c-axis of the grain studied; (2) measurement of the poles perpendicular to planes of all PDFs visible in the grain investigated; (3) plotting, on a stereographic Wulff net, the optic axis and poles to all PDF planes; and (4) indexing, where possible, the planes measured using a standard stereographic projection template (SPT), which displays the possible pole orientations of common PDF planes within a 5° envelope of measurement error (e.g., Engelhardt and Bertsch 1969; Stöffler and Langenhorst 1994; Grieve et al. 1996; Langenhorst 2002).

This conventional method has been used for about 40 years and was also used for our investigations. However, the SPT (as reported in, e.g., Engelhardt and Bertsch 1969; Stöffler and Langenhorst 1994), which allows the indexing of ten typical PDF crystallographic orientations in quartz, is modified herein. As shown in Table 1, four other characteristic crystallographic orientations of PDFs in quartz, which have been identified but do not appear in the commonly used SPT (references above), are $\{22\bar{4}1\}$, $\{31\bar{4}1\}$, $t\{40\bar{4}1\}$, and $k\{51\bar{6}0\}$. For this reason, a new version of the stereographic projection template (denoted NSPT) that includes these additional orientations is presented (Fig. 1). As in previous versions of the SPT, the additional orientations in the NSPT are depicted as poles to PDF planes within a 5° envelope of error (Fig. 1).

In the present study, each operator received a stereographic Wulff net, the NSPT, a formatted Excel spreadsheet, and a standardized set of instructions. Operators were asked to determine, following conventional measurement methods (described above), the

crystallographic orientations of a maximum number of measurable PDFs, where possible excluding PFs, contained within ~50-100 quartz grains in each thin section. In addition, the analyses were “blind”, in that each operator selected grains without prior knowledge of the specific grains measured by the other workers. Each operator was instructed to plot the PDF plane orientations manually on the stereographic Wulff net, and then to index the planes to Miller-Bravais indices $\{hki\}$ for quartz using the NSPT (available online at <http://meteoritics.org/Online%20Supplements.htm>). To allow a detailed statistical evaluation, each operator reported the polar angle values between the quartz c-axis and poles to the planes of PDFs, as well as the assigned specific Miller-Bravais indices for each set measured, in an Excel spreadsheet. All data were then compiled, recalculated, and plotted by the lead author.

U-stage measurement data are commonly reported in publications using two different types of histograms, one where the number (or frequency) of uncorrected polar angle values are plotted into bins of 2–5° or a second where polar angle values are uniquely indexed within a 5° range of error and assigned to specific crystallographic indices (see, e.g., Grieve et al. 1996 for discussion). Frequently, no information is given on the exact methodology used for the measurements, how the data were recalculated, the number of sets measured, etc. In addition, tables including the raw data used to construct histograms are mostly not included. However, for understanding the quality of the data, it is critical that published PDF orientation histograms clearly define which version of frequency measurement is used (i.e., relative or absolute frequency; Engelhardt and Bertsch 1969), whether or not unindexed PDF sets are included in the frequency calculations, and the total numbers of grains and sets used in the calculations.

The definition of the relative and absolute frequency of PDF orientations is given by Engelhardt and Bertsch (1969) and clarified by D. Stöffler (written commun., 2008):

relative frequency $f_{hki} = q_{hki} / p_{hki} \times 100 (\%)$

absolute frequency $F_{hki} = q_{hki} / Q \times 100 (\%)$

where q_{hki} is the actual number of symmetrically equivalent planes observed in n quartz grains, p_{hki} the maximum number of symmetrically equivalent planes potentially observable in n quartz grains (i.e., number of symmetrically equivalent planes multiplied by n , the number of measured quartz grains, see Table 1), and Q the total number of all sets of PDFs, indexed and unindexed, observed in n quartz grains of a thin section. It is important to note that, because of the p_{hki} term, the total relative frequency can be much less than, or exceed, 100% (Table 1). According to these definitions, it seems that absolute frequency has been most widely used in previous published histograms, although, as noted above, this is often not specified.

3. Samples:

Three shocked-quartz-bearing thin sections of different lithologies and from distinct impact structures were independently investigated by each of three operators. Petrographic characteristics of the three investigated samples, which include a meta-greywacke clast in breccia (BOS-3), a biotite-gneiss (M8-427.7), and a sandstone (AUS-90-43-2), are

summarized in Table 2. The different samples were selected principally because of the abundance of PDF-bearing quartz grains in their respective thin sections and also in order to cover a wide possible variety of target lithologies that typically occur in documented impact structures.

In samples BOS-3 and M8-427.7, numerous quartz PDFs are decorated with tiny fluid inclusions (Fig. 2), while in sample AUS-90-43-2, primarily only non-decorated PDFs occur. This difference is potentially important, as decorated PDFs are more easily detected and measured as compared to the less visible, non-decorated PDFs. A number of quartz grains in the three samples display blocky, undulatory extinction, which can reduce the precision of the measurements because of uncertainty in the c-axis orientation. In addition, many quartz grains in samples BOS-3 and M8-427.7 have a grayish-brown appearance in plane-polarized light, with patches containing micrometer-scale fluid inclusions; these quartz grains have been described as “toasted” (Short and Gold 1996; Whitehead et al. 2002). In some cases, PDFs are partially masked in toasted quartz grains and are difficult to discern and measure.

4. Results and discussion:

The crystallographic orientations of 1751 PDF sets in 666 quartz grains were measured on three thin sections, one section each from samples BOS-3, M8-427.7, and AUS-90-43-2 (Table 3). For comparison, results are reported in both relative and absolute frequency. Histograms showing the proportion of angles, binned at 5°, between the c-axis and poles to PDF planes in quartz grains from the three samples, as determined by each of the three operators, are shown in Fig. 3. The unindexed plane sets, which could not be assigned using the NSPT, are also reported in Fig. 3 in order to evaluate if they show a preferred range of orientations. Usually, unindexed PDF orientations are considered to be the result of measurement or plotting errors (e.g., Langenhorst 2002) and they are normally ignored and rarely discussed. However, in several cases as observed by the two experienced operators, some of the unindexed plane sets are undoubtedly PDFs that cannot be indexed, even if the measurement and plotting operation is repeated several times. We have noted that the poles to the unindexed PDF planes are concentrated principally with angles of 10–30° relative to the c-axis (Fig. 3). Additional examination of these unindexed PDFs, e.g., using TEM techniques, is probably warranted.

As reported in Table 3, the proportion of unindexed planes is nearly identical for the two experienced operators, ranging from 7–8% for the three thin sections investigated, whereas this proportion is variable for the inexperienced operator, ranging from 8.5–15.5%. It is evident that observer ability had an influence on the resulting number of unindexed planes.

To allow consistent comparison of results, the data were recalculated to 100% without including unindexed PDF orientations in order to prevent the skewing of plane distributions. Histograms of the absolute frequency percent of indexed PDF sets versus angle between the c-axis and poles to PDF planes for the three samples, as determined by the different operators, are shown in Fig. 4. The three samples investigated have noticeably different distributions of PDF orientations: the dominant PDF orientations (>10%) are

$\{10\bar{1}3\}$ and $\{10\bar{1}2\}$ for sample BOS-3; $\{10\bar{1}3\}$ for M8-427.7; and (0001) and $\{10\bar{1}3\}$ for AUS-90-43-2 (Fig. 4). Planes parallel to the $\{10\bar{1}1\}$, $\{11\bar{2}2\}$, $\{11\bar{2}1\}$, $\{2\bar{1}3\}$, $\{5\bar{1}6\}$, $\{22\bar{4}1\}$, $\{3\bar{1}4\}$, $\{40\bar{4}1\}$, $\{10\bar{1}0\}$, $\{11\bar{2}0\}$, and $\{5\bar{1}60\}$ orientations are also present (Table 3; Fig. 4), but in lower proportions.

Surprisingly, no major difference in distribution of PDF orientations occurs from operator to operator; the average standard deviation of the orientation measurements between the three operators is between 1.2% and 1.4% for the three samples, with a maximum standard deviation of 4.1% for the $\{10\bar{1}3\}$ -equivalent crystallographic orientation in sample M8-427.7 (Fig. 4). It is important to note that a large number of PDFs sets were measured by each operator (between 127 and 267 for each thin section), which is not the case in many previous studies, where generally <50 and sometimes <20 PDF sets were measured.

Our study also shows that the average number of PDF sets per grain in a sample (denoted N; including all measured PDF orientations, both indexed and unindexed) varies from operator to operator, even though the same thin sections were investigated (Figs. 4–5; Table 3). Interestingly, the difference in the N values between the operators is nearly constant for each thin section (Fig. 5). However, this difference does not seem to be directly influenced by the observer experience. The total number of grains measured can influence N in the case of non-homogeneously shocked rock; an unintentional “selection” of the more heavily shocked grains can be another explanation.

With respect to the comparison of datasets from different studies and from different investigators, we have introduced a new term, “N*” (Fig. 4; Table 3), which is defined as the average number of indexed PDF sets per grain in a sample, where unindexed PDF orientations are excluded from the calculations. Values of N* are lower than values of N for any given sample (Table 3), but trends similar to those based on values of N are observed.

Regarding the number of measured PDF sets within individual grains (i.e., 1–8 sets per grain in this study), some inter-operator differences are noticed (Fig. 6; Table 3). For the experienced operators, a more or less “normal distribution” of the different PDF set abundances is observed, whereas a somewhat “bimodal distribution” is seen for the inexperienced operator. As noted for the values of N or N*, the proportions of the different PDF set populations are possibly influenced by the total number of grains measured, as well as by an unintentional “selection” of the grains investigated. Nevertheless, as grains with 6–8 PDF sets were almost exclusively identified and measured by the inexperienced operator, it is not excluded that this operator possibly measured grains with multiple crystallographic domains and considered these domains to be within a single monocrystalline grain with one c-axis, instead of within polycrystalline subunits containing multiple c-axes. A closer look at the plane measurements for these grains shows that about 22% of the PDF sets are unindexed. Thus, it seems that the distribution of the PDF set abundances within a thin section should more closely correspond to a “normal distribution”. Plots similar to those in Fig. 6 can then be used to evaluate the reliability of the U-stage measurements.

4.1. Sample size versus index distribution

Due to the limitations of the U-stage attachment, usually only about one third of the thin section area can be investigated. However, as some samples contain hundreds if not

thousands of grains showing PDFs, the investigator will have to stop after a certain number of measurements, having covered only part of the thin section. It is, therefore, difficult to avoid an unintentional “selection” of the grains investigated. Nevertheless, as shown in Fig. 7, in which the measured number of PDF sets per individual grain are reported in chronological order for each operator, a more or less “saw tooth” distribution is observed, indicating that no apparent selection bias was applied. These distribution patterns also show that the total number of grains measured may influence the reliability of the values of N or N^* . Predictably, better precision is obtained through the investigation of a larger number of grains.

In order to evaluate the influence of number of grains investigated and number of PDF sets measured on the resulting distribution of the indexed PDF sets, we generated several histogram plots for each sample investigated, considering the first 25, the first 50, and the first 100 PDF sets measured (Fig. 8). For each sample, measurements of single investigators are compared to the compiled group data, which are taken as a reference. It is obvious that larger differences in the frequency percent of indexed PDF orientations occur when considering only the first 25 PDF sets measured. When using only the first 25 measurements, the frequency percent of dominant PDF planes may vary by up to 20 percentage point (pp) or 81% between the reference and single operator values (Fig. 8). When considering the first 50 PDF sets measured, the maximum difference observed is about 12 pp or 48% for the dominant PDF orientations, and when considering the first 100 PDF sets measured, the maximum difference in dominant PDF orientations is of about 7 pp or 28% (Fig. 8). Regarding the other, less common PDF set orientations, which represent individually <10% of the total, the precision is even lower than for the dominant orientations. Thus, the presence or absence and abundance of these “accessory” orientations may be quite variable with smaller numbers of measurements. Based on these results, it is evident that a relationship exists between the number of PDF sets measured in a thin section and the reliability and precision of the results.

4.2. Biases due to methodology

We have shown that besides the dominant PDF orientations ((0001) , $\{10\bar{1}3\}$, and $\{10\bar{1}2\}$), several other “accessory” PDF orientations are present (Table 3; Fig. 4). Individually, these “accessory” PDF orientations do not represent more than 10%, but in total they represent 12–25 absolute frequency percent based on our measurements using the NSPT. Effectively, the use of the NSPT (Fig. 1), which includes the positions of four additional, typical high-index PDFs, may allow a reduction in the percentage of unindexed PDFs by a factor of about 2; these PDF planes probably would have been considered as unindexed using the SPT.

To evaluate the robustness of the typically used histogram, i.e., the one showing the combination of all PDF set populations, the absolute frequency of indexed PDFs was also recalculated using only measurements from quartz grains with one and two PDF sets (Fig. 9). In our study, histograms constructed from grains with three or more PDF sets are similar to those based on two sets; therefore, only histograms based on grains with two sets are shown (Fig. 9).

All histograms for both samples BOS-3 and M8-427.7 are relatively similar. However, larger variations are visible in the histograms based on one PDF set than in histograms based on two sets, when these first two plots are compared to the histograms combining all PDF set populations (Fig. 9). For sample AUS-90-43-2, the histogram based on quartz grains with only one set of PDFs is very different compared to the histograms based on grains with two sets of PDFs and on all PDF set populations. For this sample, the PDFs parallel to (0001) represent a dominant orientation, and apparently the proportion of quartz grains with one set of PDFs has an overriding influence on the combined index distribution pattern.

Based on these observations, it would seem useful to evaluate the robustness of future published PDF orientation histograms by plotting separately the measurements for the different PDF set populations. In addition to the number of investigated grains and sets, number of unindexed grains, etc., the relative proportion of each PDF set population that is combined into the published summary PDF orientation histogram should also be reported.

4.3. Influence on shock barometry

As specific orientations of PDFs in quartz are formed at different shock pressures (e.g., Hörz 1968; Müller and Défourneaux 1968; Huffman and Reimold 1996), several authors, e.g., Robertson and Grieve (1977), Grieve et al. (1990), and Dressler et al. (1998), have evaluated shock barometry using a method developed by Grieve and Robertson (1976). This method consists of the calculation of average shock pressure values for each investigated sample, based on laboratory shock experiments that bracket the pressure ranges associated with individual PDF orientations or assemblages of orientations. For summaries of this method and references see, e.g., Stöffler and Langenhorst (1994) and Grieve et al. (1996); however, DeCarli et al. (2002) provide a cautionary discussion regarding the potential limitations of this technique. In the Grieve and Robinson (1976) study, a value of 7.5 GPa was assigned for PDF orientations parallel to (0001), 10.0 GPa for PDF orientations parallel to $\{10\bar{1}3\}$, 14.0 GPa for PDF orientations parallel to $\{22\bar{4}1\}$, $\{10\bar{1}1\}$, and $\{11\bar{2}2\}$, and 16.0 GPa for PDF orientations parallel to $\{10\bar{1}2\}$ (see Grieve and Robertson 1976 for more details on the method). In their study, the U-stage technique was used to measure the orientations of PDF sets in 14–20 grains, containing 2–78 (average = 44) sets, per sample. A somewhat different pressure calibration scheme was proposed by Stöffler and Langenhorst (1994), based on characteristic combinations of PF and PDF orientations; four progressive stages of shock are defined and supported by experimental observations. For example, at pressures of 12–20 GPa, PDF orientations parallel to $\{10\bar{1}3\}$ dominate, while above 20 GPa, PDF orientations parallel to $\{10\bar{1}2\}$ become more abundant. Based on our study, it appears that in order to reach a minimum level of precision and repeatability, at least 50 PDF sets (better 100 PDF sets) per sample should be measured (Fig. 8). We note also that other typical PDF crystallographic orientations in shocked quartz (e.g., $\{10\bar{1}0\}$, $\{11\bar{2}1\}$, $\{21\bar{3}1\}$, $\{51\bar{6}1\}$, $\{11\bar{2}0\}$, etc.; see Table 1) are not included in shock barometry calculations, and it is not clear what additional information these higher index sets may potentially provide.

5. Conclusions and recommendations:

Our study shows that differences in the abundances of PDF set orientations as measured by different operators are rather limited both for dominant and for less common “accessory” orientations. It seems also that the level of ability of the operator (experienced versus inexperienced) is only responsible for modest differences in the number of unindexed planes. However, a recalculation of the data to 100%, excluding unindexed PDF orientations, reduces the minor influence of operator’s ability and permits consistent comparison of the datasets.

The precision of U-stage analysis, which depends mainly on the number of PDF sets investigated, can only be assured by increasing the number of PDF sets measured. When only 25 PDF sets are measured, there is up to 20 percentage points variation (or 81%) in the abundances of dominant PDF sets; by measuring 100 sets, this variation or error can be reduced by nearly two thirds. This finding is especially important when PDF set orientations are being used to calculate shock barometry (cf. Grieve and Robertson 1976). The use of the new stereographic projection template (NSPT; Fig. 1), which includes the positions of four additional typical high-index PDFs, is recommended, as it can allow indexing of up to 8% more PDF planes; these additional PDF sets would remain unindexed using the SPT and potentially regarded as errors of measurement.

Viewing the results, we conclude that by following a strict measurement procedure, the reproducibility of U-stage data is good and that results can be effectively compared. Further, it is critical that published PDF orientation histograms at least clearly define what frequency measurement is used (i.e., relative or absolute frequency), whether or not unindexed PDF sets are included in the frequency calculations, and the numbers of grains and sets analyzed. This information is essential for comparing datasets from different studies or from different workers examining the same samples. In addition, the relative proportions of each PDF set population, which are combined into the published PDF orientation histograms, should also be reported. This information can be useful for detecting variations in shock within a sample and identifying biases due to methodology.

The universal-stage technique will undoubtedly remain a standard method for the measurement of crystallographic orientations of PDF sets in quartz grains, as it is a relatively fast and inexpensive method of investigation, and is currently the only technique that allows large, statistically useful datasets to be readily generated.

Acknowledgments

This work is supported by the Austrian Science Foundation (FWF), grant P18862-N10, and the Austrian Academy of Sciences. Bevan M. French is gratefully acknowledged for his ongoing assistance with this project. We are also grateful to W. Uwe Reimold and Dieter Stöffler for discussion and encouragement.

References

Alexopoulos J. S., Grieve R. A. F., and Robertson P. B. 1988. Microscopic lamellar deformation features in quartz: Discriminative characteristics of shock-generated varieties. *Geology* 16:796–799.

Bloss F. D. 1971. *Crystallography and crystal chemistry: an introduction*. New York: Holt, Rinehart, and Winston. 545 p.

Bohor B. F., Modreski P. J., and Foord E. E. 1987. Shocked quartz in the Cretaceous-Tertiary boundary clays: Evidence for a global distribution. *Science* 236:705–708.

DeCarli P. S., Bowden E., Jones A. P., and Price G. D. 2002. Laboratory impact experiments versus natural impact events. In *Catastrophic events and mass extinction: Impacts and beyond*, edited by Koeberl C. and MacLeod K. G. Boulder: Geological Society of America, Special Paper 356. pp. 595–605.

Dressler B. O., Sharpton V. L., and Schuraytz B. C. 1998. Shock metamorphism and shock barometry at a complex impact structure: State Islands, Canada. *Contributions to Mineralogy and Petrology* 130:275–287.

Emmons R. C. 1943. The universal stage (with five axes of rotation). *Geological Society of America Memoir* 8, 205 p.

Engelhardt W. v. and Bertsch W. 1969. Shock induced planar deformation structures in quartz from the Ries crater, Germany. *Contributions to Mineralogy and Petrology* 20:203–234.

Ferrière L., Morrow J. R., Amgaa T., and Koeberl C. 2008. Systematic comparison of universal stage-indexed planar deformation features in quartz: Implications for statistical significance and representation of results (abstract #3010). Large Meteorite Impacts and Planetary Evolution (LMI IV) Meeting, Johannesburg, South Africa, August 17-21, 2008.

French B. M. 1998. *Traces of catastrophe: A handbook of shock-metamorphic effects in terrestrial meteorite impact structures*. LPI Contribution #954. Houston, Texas: Lunar and Planetary Institute. 120 p.

French B. M. and Short N. M., editors. 1968. *Shock metamorphism of natural materials*. Baltimore: Mono Book Corporation. 644 p.

Goltrant O., Cordier P., and Doukhan J.-C. 1991. Planar deformation features in shocked quartz; a transmission electron microscopy investigation. *Earth and Planetary Science Letters* 106:103–115.

Grieve R. A. F. and Robertson P. B. 1976. Variations in shock deformation at the Slate Islands impact structure, Lake Superior, Canada. *Contributions to Mineralogy and Petrology* 58:37–49.

Grieve R. A. F., Coderre J. M., Robertson P. B., and Alexopoulos J. 1990. Microscopic planar deformation features in quartz of the Vredefort structure: Anomalous but still suggestive of an impact origin. *Tectonophysics* 171:185–200.

Grieve R. A. F., Langenhorst F., and Stöffler D. 1996. Shock metamorphism of quartz in nature and experiment: II. Significance in geoscience. *Meteoritics and Planetary Science* 31:6–35.

Hörz F. 1968. Statistical measurements of deformation structures and refractive indices in experimentally shock loaded quartz. In *Shock Metamorphism of Natural Materials*, edited by French B. M. and Short N. M. Baltimore: Mono Book Corp. pp. 243–253.

Huffman A. R. and Reimold W. U. 1996. Experimental constraints on shock-induced microstructures in naturally deformed silicates. *Tectonophysics* 256:165–217.

Koeberl C., Reimold W. U., Kracher A., Träxler B., Vormajer A., and Körner W. 1996. Mineralogical, petrographical, and geochemical studies of drill core samples from the Manson impact structure, Iowa. In *The Manson impact structure, Iowa: Anatomy of an impact crater*, edited by Koeberl C. and Anderson R. R. Boulder: Geological Society of America, Special Paper 302. pp. 145–219.

Langenhorst F. 2002. Shock metamorphism of some minerals: Basic introduction and microstructural observations. *Bulletin of the Czech Geological Survey* 77:265–282.

Morrow J. R. 2007. Shock-metamorphic petrography and microRaman spectroscopy of quartz in upper impactite interval, ICDP drill core LB-07A, Bosumtwi impact crater, Ghana. *Meteoritics and Planetary Science* 42:591–609.

Müller W. F. and Défourneaux M. 1968. Deformationsstrukturen im Quarz als Indikator für Stosswellen: Eine experimentelle Untersuchung an Quarz-Einkristallen. *Zeitschrift für Geophysik* 34:483–504.

Reinhard M. 1931. *Universaldrehtischmethoden*. Basel, Switzerland: Birkhäuser. 118 p.

Robertson P. B. and Grieve R. A. F. 1977. Shock attenuation at terrestrial impact structures. In *Impact and explosion cratering*, edited by Roddy D. J., Pepin R. O., Merrill R. B. New York: Pergamon Press. pp. 687–702.

Short N. M. and Gold D. P. 1996. Petrography of shocked rocks from the central peak at the Manson impact structure. In *The Manson impact structure, Iowa: Anatomy of an impact*

crater, edited by Koeberl C. and Anderson R. R. Boulder: Geological Society of America, Special Paper 302. pp. 245–265.

Stöffler D. and Langenhorst F. 1994. Shock metamorphism of quartz in nature and experiment: I. Basic observation and theory. *Meteoritics and Planetary Science* 29:155–181.

Whitehead J., Spray J. G., and Grieve R. A. F. 2002. Origin of “toasted” quartz in terrestrial impact structures. *Geology* 30:431–434.

Tables

Table 1. Typical crystallographic orientations of planar deformation features in shocked quartz.

#	Symbol	Miller-Bravais indices $\{hkl\}$	Polar angle (°)*	Azimuthal angle (°)	Crystallographic form	No. of symmetrically equivalent planes
1	c	{0001}	0.00	-	Basal pinacoid	1
2	ω, ω'	{10 $\bar{1}$ 3}, {01 $\bar{1}$ 3}	22.95	30	Rhombohedron	3
3	π, π'	{10 $\bar{1}$ 2}, {01 $\bar{1}$ 2}	32.42	30	Rhombohedron	3
4	r, z	{10 $\bar{1}$ 1}, {01 $\bar{1}$ 1}	51.79	30	Rhombohedron	3
5	m	{10 $\bar{1}$ 0}	90.00	30	Hexagonal prism	3
6	ξ	{11 $\bar{2}$ 2}, {2 $\bar{1}$ 12}	47.73	60	Trigonal dipyramid	3
7	s	{11 $\bar{2}$ 1}, {2 $\bar{1}$ 11}	65.56	60	Trigonal dipyramid	3
8	-	{21 $\bar{3}$ 1}, {3 $\bar{2}$ 11}, {3 $\bar{1}$ 21}, {12 $\bar{3}$ 1}	73.71	50	Trigonal trapezoidron	6
9	x	{5 $\bar{1}$ 61}, {6 $\bar{5}$ 11}, {6 $\bar{1}$ 51}, {15 $\bar{6}$ 1}	82.07	40	Trigonal trapezoidron	6
10	a	{11 $\bar{2}$ 0}, {2 $\bar{1}$ 10}	90.00	60	Trigonal prism	3
11	-	{22 $\bar{4}$ 1}, {4 $\bar{2}$ 21}	77.20	60	Trigonal dipyramid	3
12	-	{31 $\bar{4}$ 1}, {43 $\bar{1}$ 1}, {4 $\bar{1}$ 31}, {1341}	77.91	45	Trigonal trapezoidron	6
13	t	{4041}, {0441}	78.87	30	Rhombohedron	3
14	k	{5 $\bar{1}$ 60}, {6 $\bar{1}$ 50}	90.00	40	Ditrigonal prism	6

Data from Stöffler and Langenhorst (1994).

*angle between the poles to the planar deformation features and the c-axis of quartz.

Table 2. Locations and petrographic descriptions of the investigated samples.

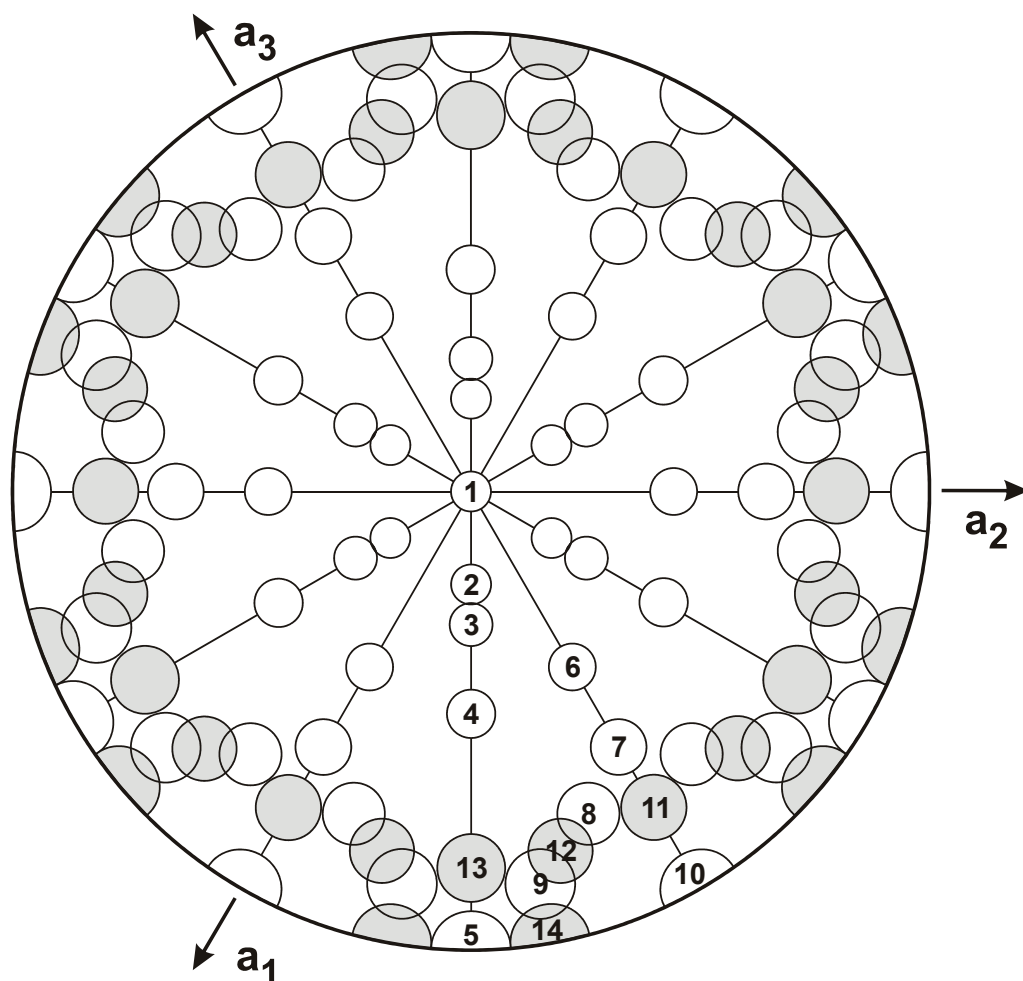
Sample	Meta-greywacke (clast in polymict lithic breccia) BOS-3	Biotite-gneiss M8-427.7	Sandstone (Carmichael sandstone) AUS-90-43-2
Structure name	Bosumtwi, Ghana	Manson, Iowa, USA	Gosses Bluff, Australia
Location	Drill core LB-07A; Deep crater moat; Depth: 341.5 m (see Morrow 2007)	Drill core M8; Eastern slope of the central uplift; Depth: 427.7 ft (129.6 m) (see Koeberl et al. 1996)	From rim of the central uplift ring
Description	Fine-grained meta-greywacke mainly composed of quartz, feldspar, muscovite, chlorite, and biotite. Quartz grains show planar fractures (PFs), planar deformation features (PDFs), and mosaicism. Numerous PDFs are strongly decorated with tiny fluid inclusions. Many quartz grains are toasted. Extremely rare PDFs occur in feldspar.	Well-foliated gneiss composed mainly of quartz, feldspar, biotite, muscovite, and rare opaque minerals. Quartz and feldspar display numerous PDFs. Rare quartz grains show mosaicism. Numerous PDFs in quartz grains are decorated. Most of the quartz grains are toasted. Biotite shows kinkbanding.	Medium-grained sandstone composed of subrounded to subangular quartz grains. Numerous quartz grains display undulatory extinction. Most of the grains show PFs and/or PDFs. The planar microstructures are rarely decorated. A few grains are slightly toasted.

Table 3. Summary of PDF set abundances and indexed PDF crystallographic orientations in quartz grains from BOS-3, M8-427.7, and AUS-90-43-2, as determined using the universal-stage by three operators, two experienced (1, 2) and one inexperienced (3).

Operator	BOS-3			M8-427.7			AUS-90-43-2		
	1	2	3	1	2	3	1	2	3
No. of investigated grains	65	100	49	71	100	52	74	100	55
No. of measured sets	145	198	127	212	262	156	208	267	176
No. of PDF sets/grain (N)	2.2	2.0	2.6	3.0	2.6	3.0	2.8	2.7	3.2
No. of PDF sets/grain (N*) ^a	2.1	1.8	2.3	2.8	2.4	2.5	2.6	2.5	2.9
PDF sets; % relative to total no. of quartz grains examined									
1 set	23	28	14	8.5	11	1.9	19	6.0	15
2 sets	42	49	43	24	37	31	26	41	22
3 sets	26	20	24	35	34	42	27	37	25
4 sets	7.7	3.0	8.2	27	15	17	16	13	20
5 sets	1.5	n.d.	8.2	4.2	3.0	5.8	9.5	2.0	7.3
6 sets	n.d.	n.d.	2.0	1.4	n.d.	1.9	1.4	1.0	9.1
7 sets	n.d.	n.d.	n.d.	n.d.	n.d.	n.d.	1.4	n.d.	n.d.
8 sets	n.d.	n.d.	n.d.	n.d.	n.d.	n.d.	n.d.	n.d.	1.8
Total	100	100	100	100	100	100	100	100	100
Indexed PDF crystallographic orientations; absolute frequency (%) ^b									
PDF crystallographic orientations									
c {0001}	n.d.	2.5	n.d.	1.9	1.1	0.6	28	22	22
ω {1013}	54	48	51	73	67	68	50	51	51
π {1012}	19	19	20	0.9	5.7	3.8	1.0	7.9	4.0
r, z {1011}	3.4	4.5	4.7	6.1	5.7	3.8	4.8	2.2	9.1
m {1010}	0.7	0.5	0.8	n.d.	0.4	n.d.	0.5	n.d.	n.d.
ξ {1122}	2.8	3.0	0.8	1.4	4.6	1.9	2.4	4.5	0.6
s {1121}	1.4	4.5	2.4	n.d.	1.1	0.6	n.d.	1.1	0.6
ρ {2131}	2.1	4.5	0.8	1.4	1.9	2.6	1.4	0.7	1.1
x {5161}	0.7	2.0	1.6	0.5	1.9	0.6	0.5	0.4	n.d.
a {1120}	0.7	1.0	n.d.	n.d.	0.8	n.d.	0.5	n.d.	n.d.
{2241}	4.1	1.0	3.9	4.7	n.d.	1.9	n.d.	2.2	1.7
{3141}	2.1	1.0	1.6	0.9	0.8	n.d.	1.4	n.d.	n.d.
t {4041}	1.4	0.5	0.8	0.9	0.8	0.6	1.0	n.d.	1.1
k {5160}	n.d.	n.d.	n.d.	0.5	0.4	n.d.	0.5	n.d.	n.d.
Unindexed	6.9	7.6	11.8	7.5	8.0	15.4	7.7	7.5	8.5
Total	100	100	100	100	100	100	100	100	100
Indexed PDF crystallographic orientations; relative frequency (%) ^b									
PDF crystallographic orientations									
c {0001}	n.d.	5.0	n.d.	5.6	3.0	1.9	80	60	71
ω {1013}	41	32	44	73	58	68	47	45	55
π {1012}	14	13	17	0.9	5.0	3.8	0.9	7.0	4.2
r, z {1011}	2.6	3.0	4.1	6.1	5.0	3.8	4.5	2.0	9.7
m {1010}	0.5	0.3	0.7	n.d.	0.3	n.d.	0.5	n.d.	n.d.
ξ {1122}	2.1	2.0	0.7	1.4	4.0	1.9	2.3	4.0	0.6
s {1121}	1.0	3.0	2.0	n.d.	1.0	0.6	n.d.	1.0	0.6
ρ {2131}	0.8	1.5	0.3	0.7	0.8	1.3	0.7	0.3	0.6
x {5161}	0.3	0.7	0.7	0.2	0.8	0.3	0.2	0.2	n.d.
a {1120}	0.5	0.7	n.d.	n.d.	0.7	n.d.	0.5	n.d.	n.d.
{2241}	3.1	0.7	3.4	4.7	n.d.	1.9	n.d.	2.0	1.8
{3141}	0.8	0.3	0.7	0.5	0.3	n.d.	0.7	n.d.	n.d.
t {4041}	1.0	0.3	0.7	0.9	0.7	0.6	0.9	n.d.	1.2
k {5160}	n.d.	n.d.	n.d.	0.2	0.2	n.d.	0.2	n.d.	n.d.
Total	67	62	74	94	80	84	138	122	144

^aCalculated only on indexed sets (i.e., unindexed sets excluded).^bMethod described in, e.g., Engelhardt and Bertsch (1969) and Stöfler and Langenhorst (1994). n.d. = none detected.

Figures



Plane	Pole angle to c-axis		
1 {0001}	0.00°	6 {11 $\bar{2}$ 2}	47.73°
2 {10 $\bar{1}$ 3}	22.95°	7 {11 $\bar{2}$ 1}	65.56°
3 {10 $\bar{1}$ 2}	32.42°	8 {21 $\bar{3}$ 1}	73.71°
4 {10 $\bar{1}$ 1}	51.79°	9 {51 $\bar{6}$ 1}	82.07°
5 {10 $\bar{1}$ 0}	90.00°	10 {11 $\bar{2}$ 0}	90.00°
		11 {22 $\bar{4}$ 1}	77.20°
		12 {31 $\bar{4}$ 1}	77.91°
		13 {40 $\bar{4}$ 1}	78.87°
		14 {51 $\bar{6}$ 0}	90.00°

Figure 1. New stereographic projection template (NSPT) used in this study. This is based on the standard stereographic projection of quartz with the c-axis plotted in the center. Each circle (5° radius) marks the position of the most common poles to PDF planes. Modified from the previously used stereographic project template, e.g., Stöffler and Langenhorst (1994) and Langenhorst (2002); four additional PDF orientations (Planes 11-14) are also indicated (gray circles).

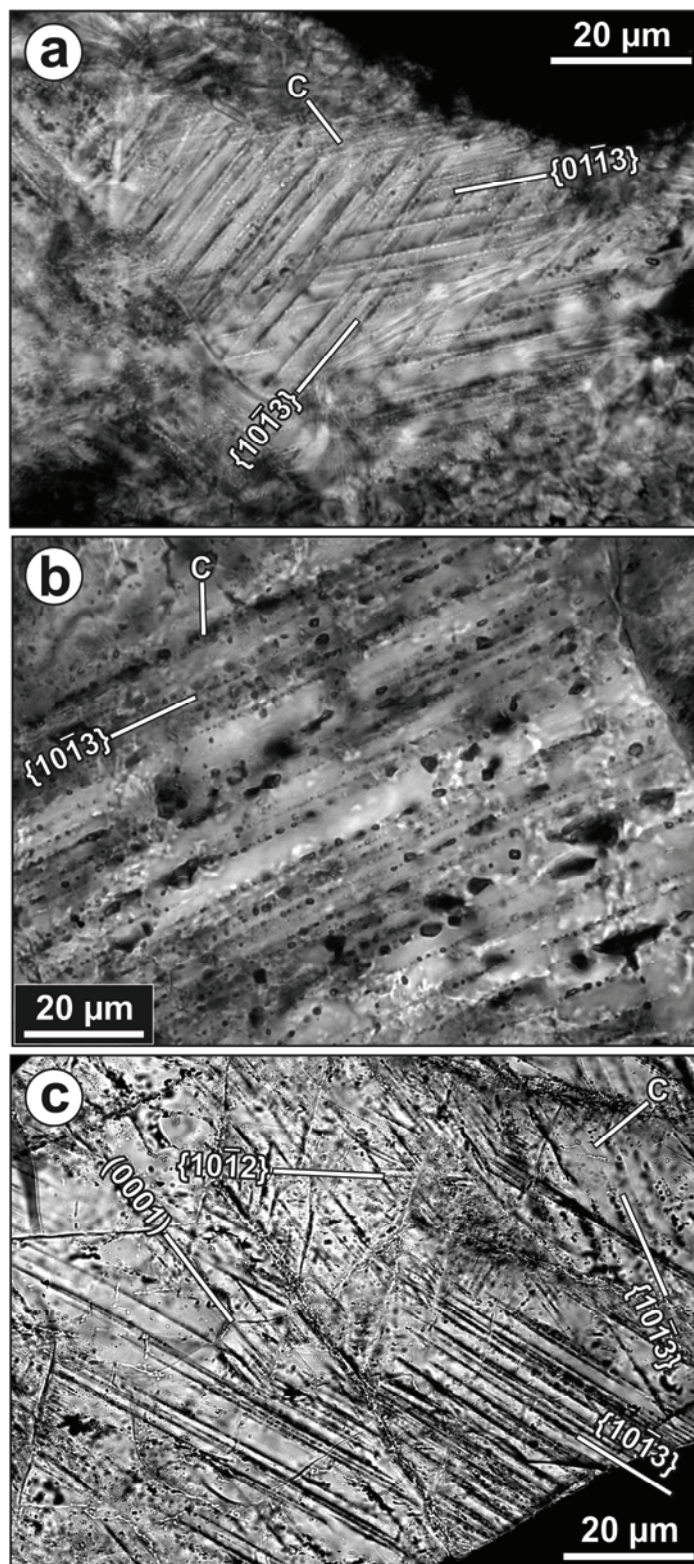


Figure 2. a) Thin section photomicrograph of quartz grain containing two prominent decorated PDF sets with $\omega\{10\bar{1}3\}$ - and $\omega\{01\bar{1}3\}$ -equivalent orientations. Quartz c-axis is indicated. Sample BOS-3, plane-polarized light. b) Thin section photomicrograph of quartz grain containing one decorated PDF set with $\omega\{10\bar{1}3\}$ -equivalent orientation. Quartz c-axis is indicated. Sample M8-427.7, plane-polarized light. c) Thin section photomicrograph of highly shocked quartz grain with at least four orientations of relatively non-decorated planar microstructures, including c(0001), $\omega\{10\bar{1}3\}$, and $\pi\{10\bar{1}2\}$ PDF sets and a second, $\omega\{10\bar{1}3\}$ -equivalent PF set. Quartz c-axis is indicated. Sample AUS-90-43-2, cross-polarized light.

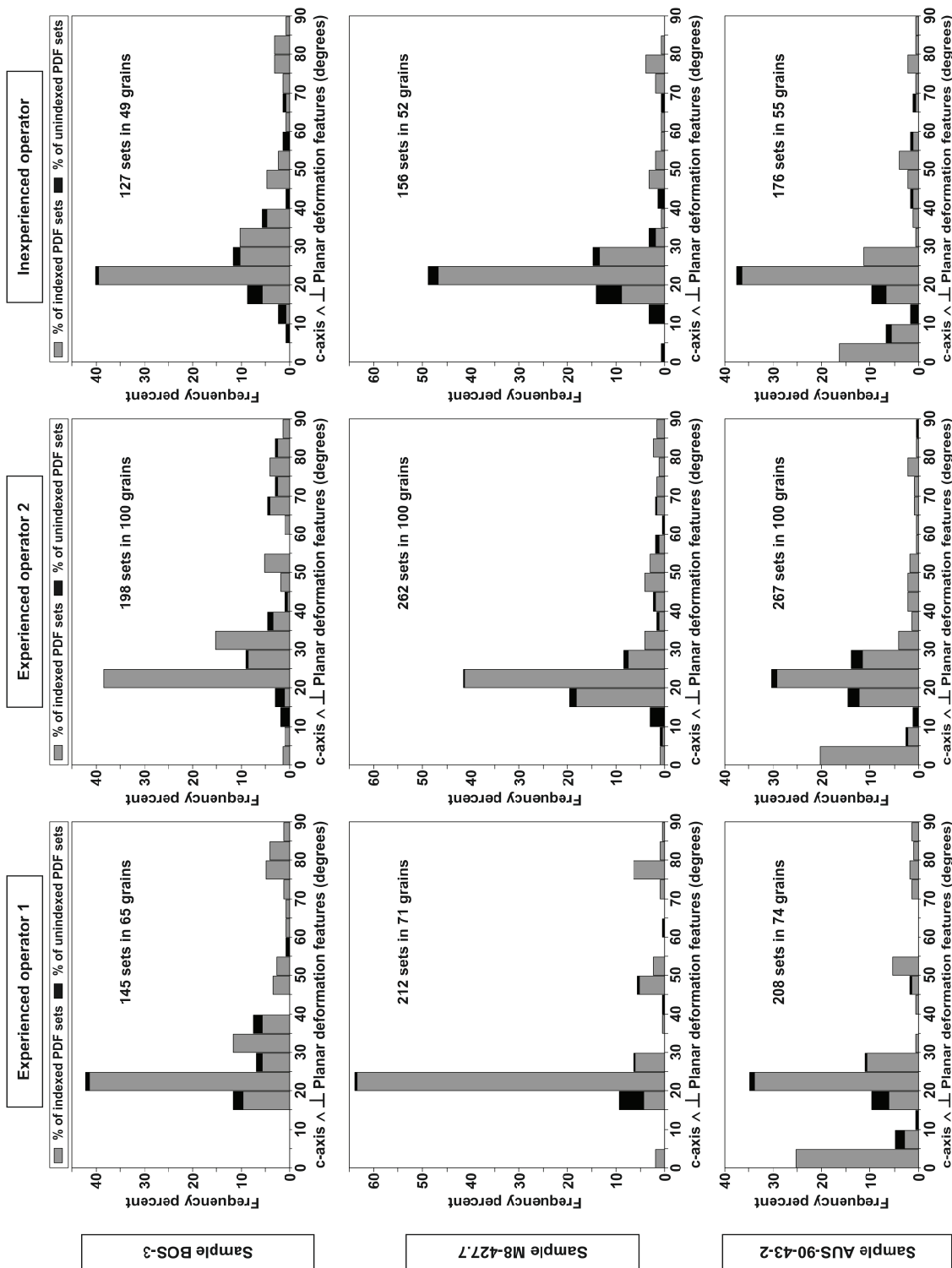


Figure 3. Histograms of angles between c-axis and poles to PDFs, binned by 5°, in quartz grains from samples BOS-3, M8-427.7, and AUS-90-43-2, as determined by the three operators, two experienced and one inexperienced. All measured PDF orientations are reported; “indexed” and “unindexed” portions of the histogram bars are based on measurements using the NSPT (e.g., Fig. 4). Note that the unindexed PDF orientations (in black) are mainly concentrated with angles of 10–30° between c-axis and poles to PDFs.

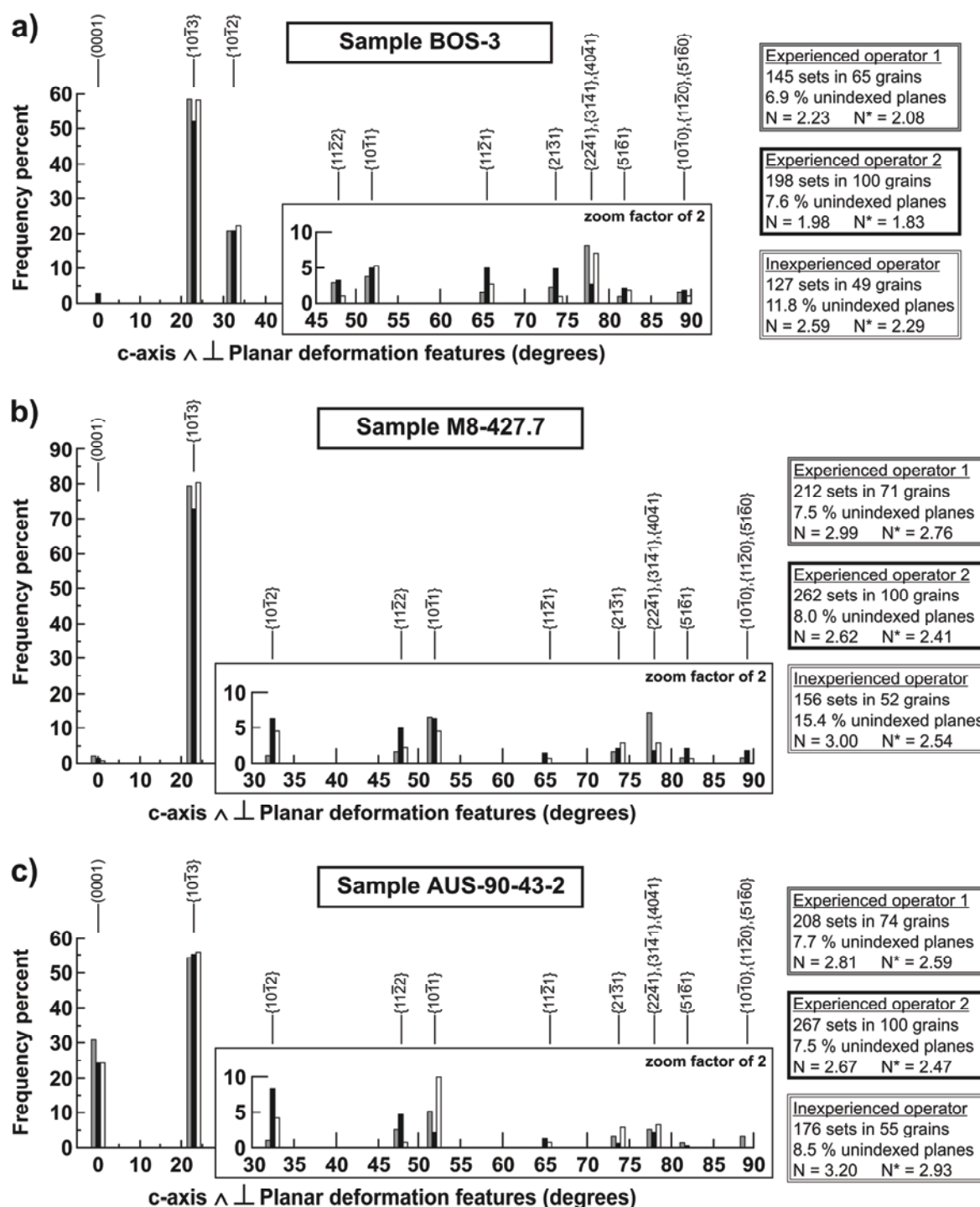


Figure 4. Histograms of absolute frequency percent of indexed PDFs (recalculated to 100% without unindexed PDF orientations) in quartz grains from (a) BOS-3, (b) M8-427.7, and (c) AUS-90-43-2, as determined by the three operators. Recalculation without unindexed PDF orientations, which vary between operators (from 6.9–15.4%; see right column), was performed to allow consistent comparison of the datasets. The average number of PDF sets per grain (denoted N, including all measured PDF orientations, both indexed and unindexed; and N*, including indexed PDF orientations only) varies as well from operator to operator.

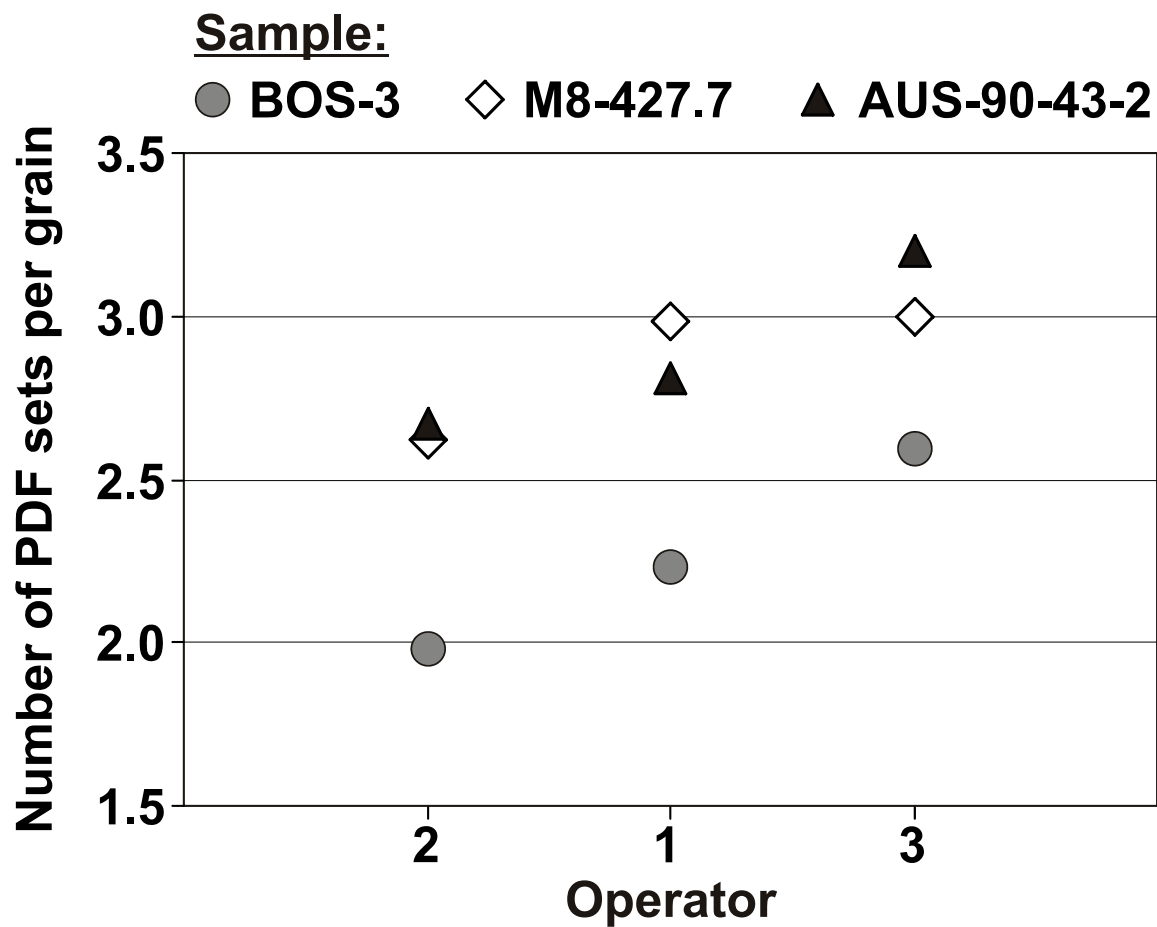


Figure 5. Average number of PDF sets per grain (N) in the three investigated samples (BOS-3, M8-427.7, and AUS-90-43-2), as determined by the three operators, two experienced (1, 2) and one inexperienced (3). Note that the difference in the N values between the operators is of the same magnitude for each investigated thin section (see text for further discussion).

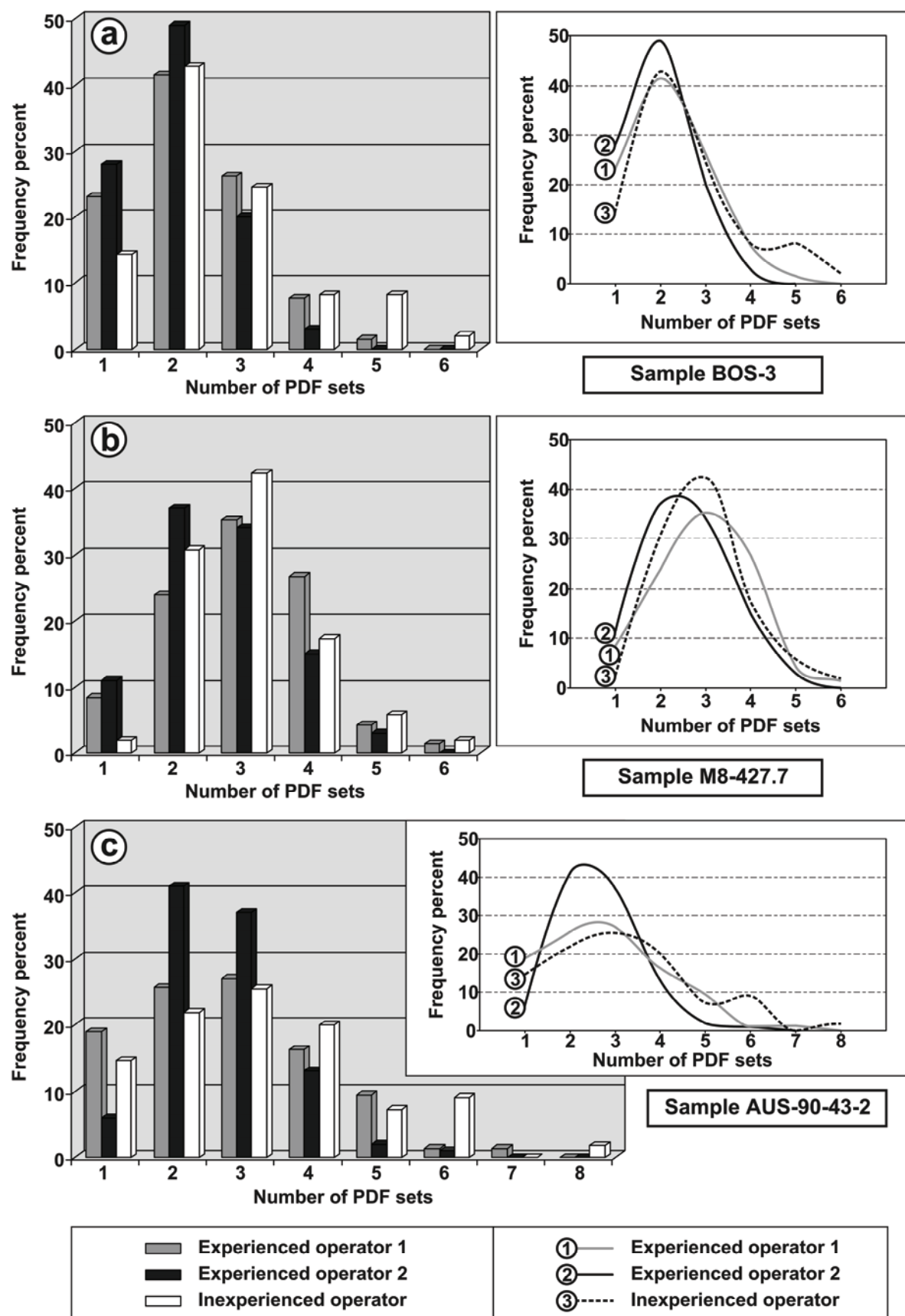


Figure 6. Frequency distribution of the number of PDF sets for the three samples (a) BOS-3, (b) M8-427.7, and (c) AUS-90-43-2, as determined by the three operators. Note the skew or asymmetry in the distribution curve of the number of PDF sets in (a) and (c), and the nearly Gaussian curve in (b). The distribution, notably in (a) and (c), is somewhat “bimodal” for the inexperienced operator.

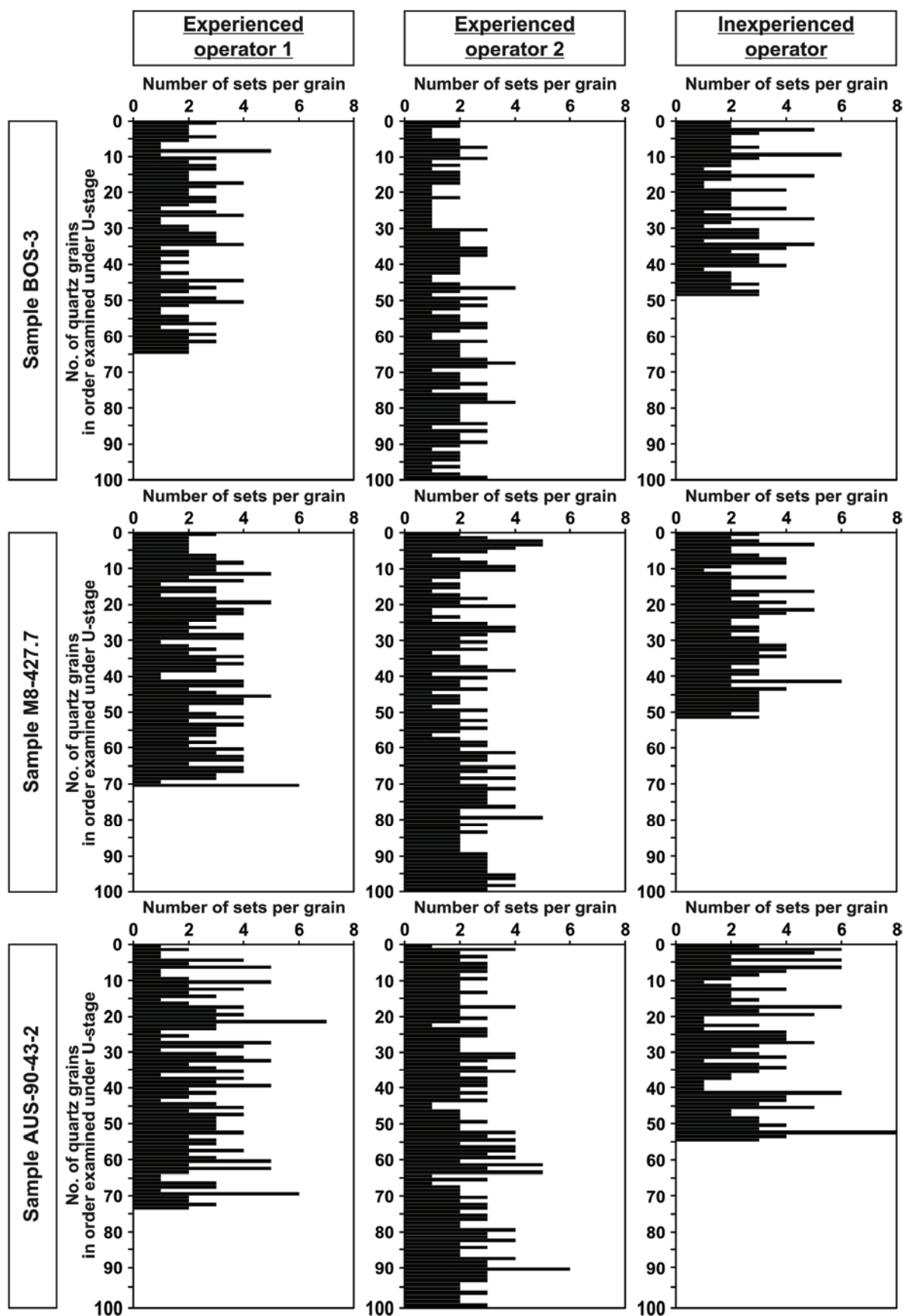


Figure 7. Histogram suites showing the numbers of PDF sets per grain, in the order measured by each operator under the U-stage. Note that no specific concentration of quartz grains with low or high numbers of PDF sets is discernible. A more or less “saw tooth”-shaped distribution is observed.



Figure 8. Absolute frequency distribution of indexed PDFs in quartz grains from BOS-3, M8-427.7, and AUS-90-43-2, as determined by each single operator and compared to the compiled group data (i.e., average of all PDF sets measured by the three operators), which is plotted for reference. Values reported on the x-axis correspond to the different PDF orientations shown in Fig. 1; the relative proportion of unindexed PDF sets (U) is also reported. Only the first 25 measured PDF orientations are reported in the first row, with the first 50 and first 100 measured PDF sets plotted in the second and third rows, respectively.

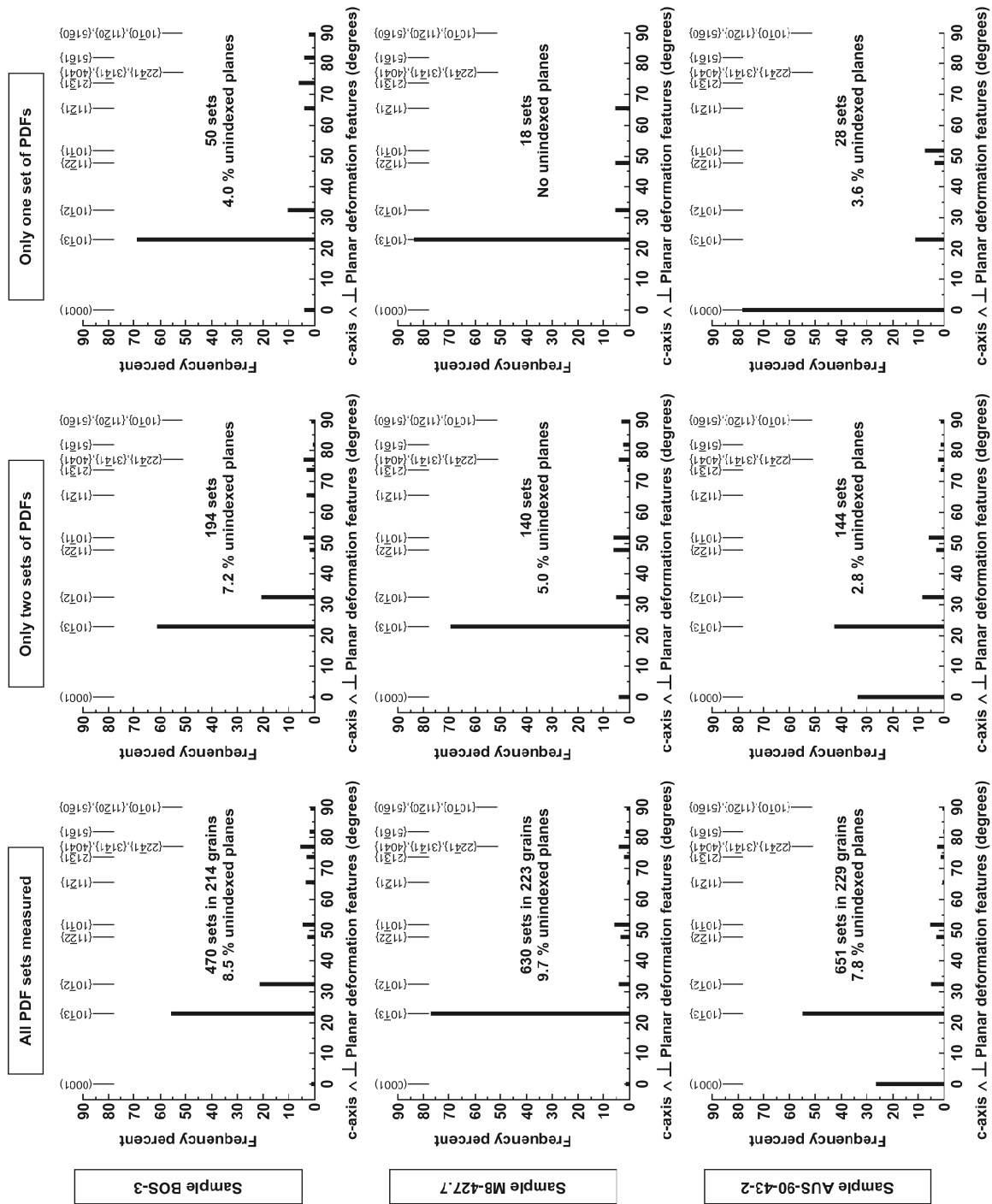
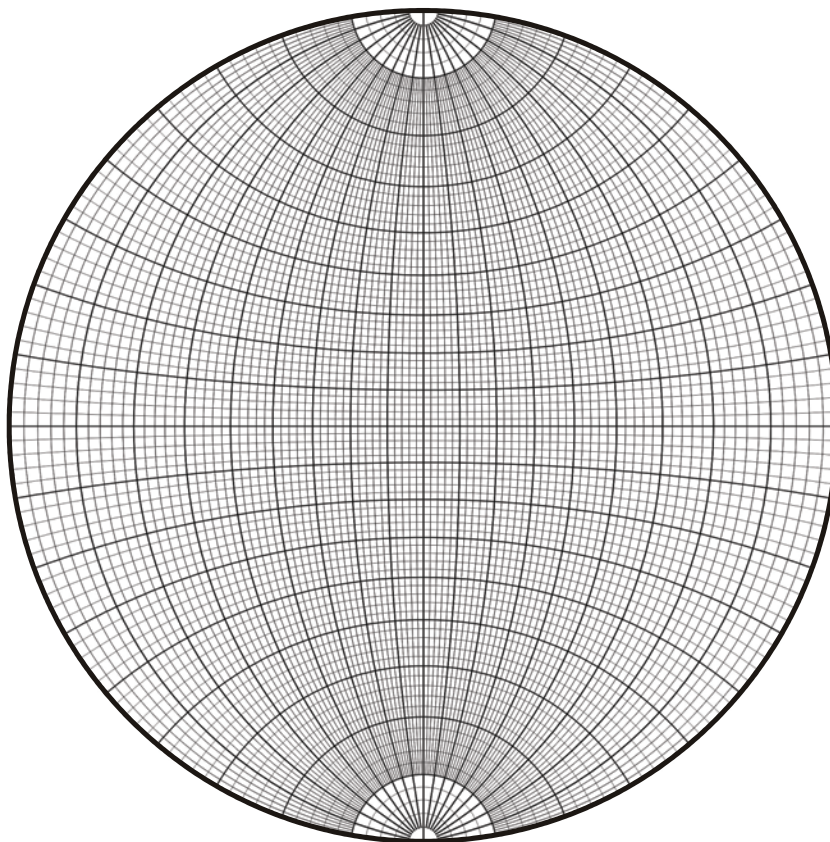


Figure 9. Histograms of the absolute frequency percent of indexed PDFs (recalculated to 100% without unindexed PDF orientations) in quartz grains from BOS-3, M8-427.7, and AUS-90-43-2. A compilation of all PDF orientations measured by the three operators combined (first column) is compared to histograms based on grains containing only two sets and only one set of PDFs (second and third columns, respectively).

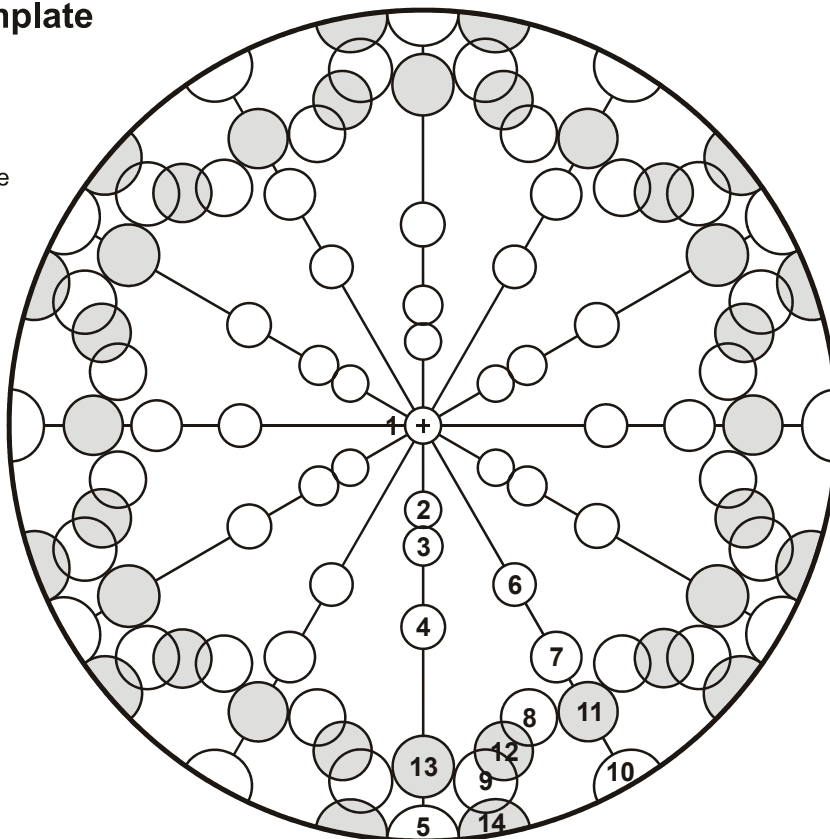
Supporting Online Material

Wulff net



New version of the stereographic projection template

Plane	Pole angle to c-axis
1 (0001)	0.00°
2 {10 $\bar{1}$ 3}	22.95°
3 {10 $\bar{1}$ 2}	32.42°
4 {10 $\bar{1}$ 1}	51.79°
5 {10 $\bar{1}$ 0}	90.00°
6 {11 $\bar{2}$ 2}	47.73°
7 {11 $\bar{2}$ 1}	65.56°
8 {21 $\bar{3}$ 1}	73.71°
9 {51 $\bar{6}$ 1}	82.07°
10 {11 $\bar{2}$ 0}	90.00°
11 {22 $\bar{4}$ 1}	77.20°
12 {31 $\bar{4}$ 1}	77.91°
13 {40 $\bar{4}$ 1}	78.87°
14 {51 $\bar{6}$ 0}	90.00°



CHAPTER 10: Potpourri

This last chapter presents further detailed investigations that were conducted subsequently and to complement the work in the publication chapters 5, 6, 7, 8, and 9; such as SEM investigations of melt particles and calcite clasts from suevite samples, mass spectrometry analyses (including e.g., U-Pb dating of zircons and whole-rock Rb-Sr and Sm-Nd isotope analyses), TEM investigations of PDFs in quartz, and characterization of “toasted” quartz grains and of ballen quartz and ballen cristobalite from several impact structures.

10.1. Geochemistry of various minerals, melt particles, and bulk analyses of samples from the drill core LB-08A:

The geochemistry of the impact breccia and basement rock samples recovered in drill core LB-08A is already discussed in the publication chapter 6, where average compositions of the different lithologies are presented. However, the full results of major and trace element analysis of the 112 samples investigated were not reported and no chemical analysis of melt particles and of lithic and mineral clasts were presented. In order to investigate the possible source rocks of the metasedimentary rocks and to further constrain the mixing of the target rocks involved in the formation of the impact breccias, several diagrams are presented here, including classification diagrams and ternary diagrams. Results of INAA and XRF analyses for the 112 samples investigated are reported in Appendix B.

On both classification diagrams (Figure 10-1a and b), meta-graywacke and phyllite/slate can be clearly distinguished; both lithologies have very low $\text{SiO}_2/\text{Al}_2\text{O}_3$ ratios, typical for immature rocks. Variations of the $\text{Na}_2\text{O}/\text{K}_2\text{O}$ ratios for the meta-graywacke samples are attributed to variations of the abundance of feldspar and/or of micas; samples with high $\text{Na}_2\text{O}/\text{K}_2\text{O}$ ratios contain generally a larger proportion of albite than of orthoclase (and K-micas) compared to meta-graywacke with relatively lower $\text{Na}_2\text{O}/\text{K}_2\text{O}$ ratios, as confirmed by modal analyses of some of the meta-graywacke samples (see supplementary material of the publication chapter 7). However, because the meta-graywacke samples were subject to hydrothermal alteration (see publication chapter 5), secondary minerals, such as muscovite and illite, can induce variations of the $\text{Na}_2\text{O}/\text{K}_2\text{O}$ ratios; thus, the $\text{Na}_2\text{O}/\text{K}_2\text{O}$ ratios can be modified to some extent, and then are not only related to provenance (i.e., source rocks) but also to alteration processes. Most of the investigated meta-graywacke samples have a high Fe_2O_3 content (Figure 10-1b; up to 5.93 wt% for sample KR8-096) which reflects mostly the abundance of chlorite and biotite; the local occurrence of secondary pyrite aggregates, can also influence to some extent the Fe_2O_3 content of some samples. The MgO content is also related to the abundance of chlorite and to the proportion of the matrix; this is well supported by the modal analyses, as samples KR8-036 and KR8-037, which show the highest proportion of chlorite and matrix (representing together about 28 vol%), are also the samples for which the highest MgO content is observed (more than 2 wt%; see Appendix B). The light greenish-gray meta-graywacke samples (LGMG) cannot

be distinguished from the other meta-graywacke samples using the classification diagram by Pettijohn et al. (1972; Figure 10-1a), however, using the classification diagram by Herron (1988; Figure 10-1b), the LGMG, Fe-rich, are easily discriminated from the other metasedimentary rocks. In the $\text{SiO}_2/\text{Al}_2\text{O}_3$ versus $\text{Fe}_2\text{O}_3/\text{K}_2\text{O}$ diagram (Figure 10-1b), all phyllite/slate samples investigated fall in the field of “shale”, only the sample KR8-007

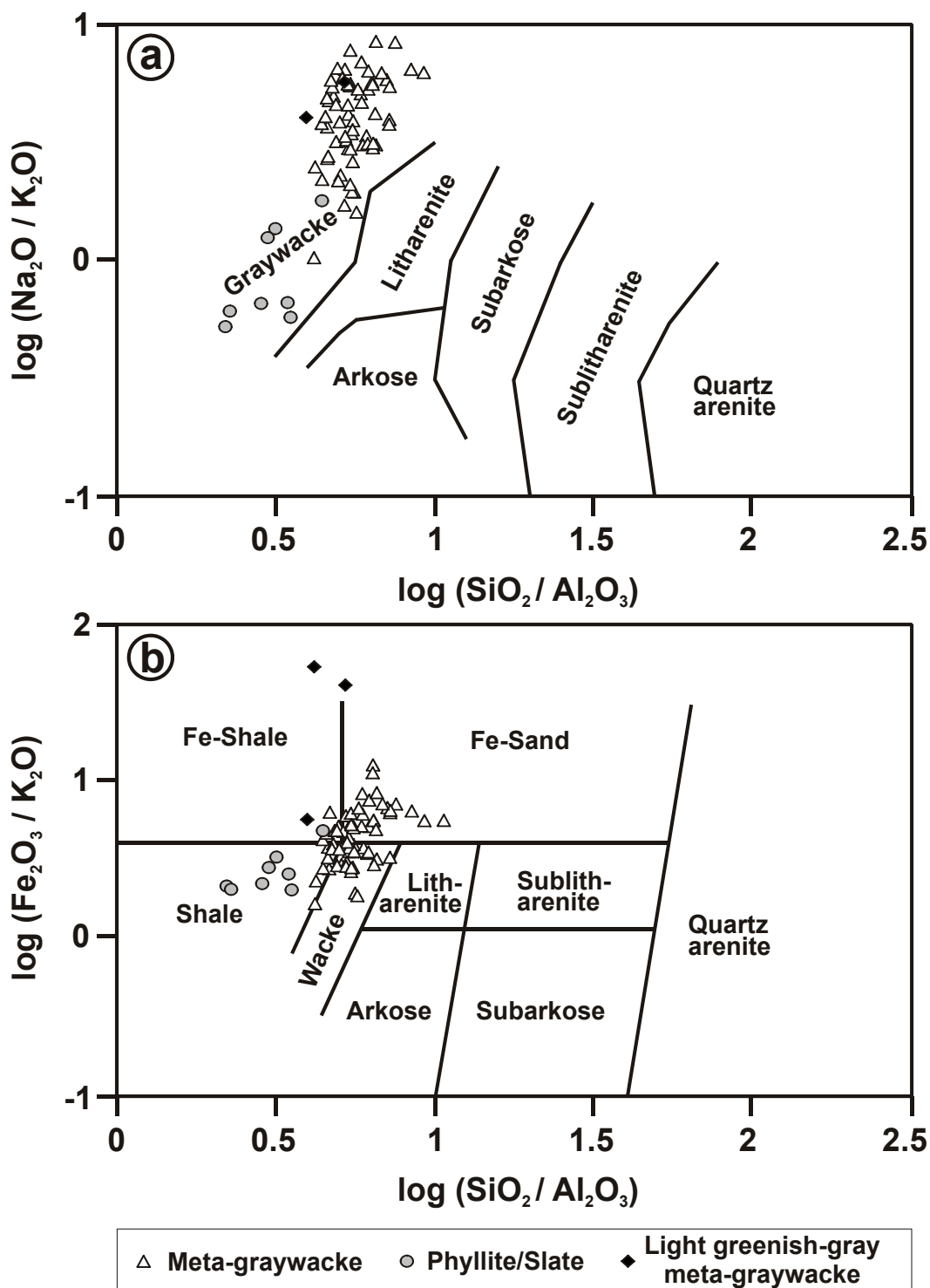


Figure 10-1. Classification diagrams discriminating the metasedimentary rock samples by their logarithmic ratios of (a) $\text{SiO}_2/\text{Al}_2\text{O}_3$ and $\text{Na}_2\text{O}/\text{K}_2\text{O}$ (after Pettijohn et al., 1972) and (b) $\text{SiO}_2/\text{Al}_2\text{O}_3$ and $\text{Fe}_2\text{O}_3/\text{K}_2\text{O}$ (after Herron, 1988).

falls in the field of “Fe-shale”. Most of the meta-graywacke samples are distributed between the fields of “wacke” and Fe-sand” (Figure 10-1b). These results show that the petrographic classification of the samples is further confirmed by their chemical composition.

When plotted in a CaO-Na₂O-K₂O ternary diagram (Figure 10-2), meta-graywacke and phyllite/slate samples are clearly distinct, and both form relatively homogenous groups. On the same ternary diagram, impact breccias from inside and from outside the crater, as well as Ivory Coast tektites, lie on a line (Figure 10-2). Ivory Coast tektites plot into the phyllite/slate field. The average composition of polymict lithic breccia is over-imposed with the average composition of suevite from outside the crater, and both fall at the limit between the meta-graywacke and the phyllite/slate fields. The average composition of suevite from inside the crater plots into the meta-graywacke field. These observations are in agreement with the conclusions of the HMX mixing calculations and petrographic observations reported in the publication chapters 5 and 6, in which it was shown that a higher proportion of phyllite/slate was incorporated in the polymict lithic breccia than in suevite from inside the crater.

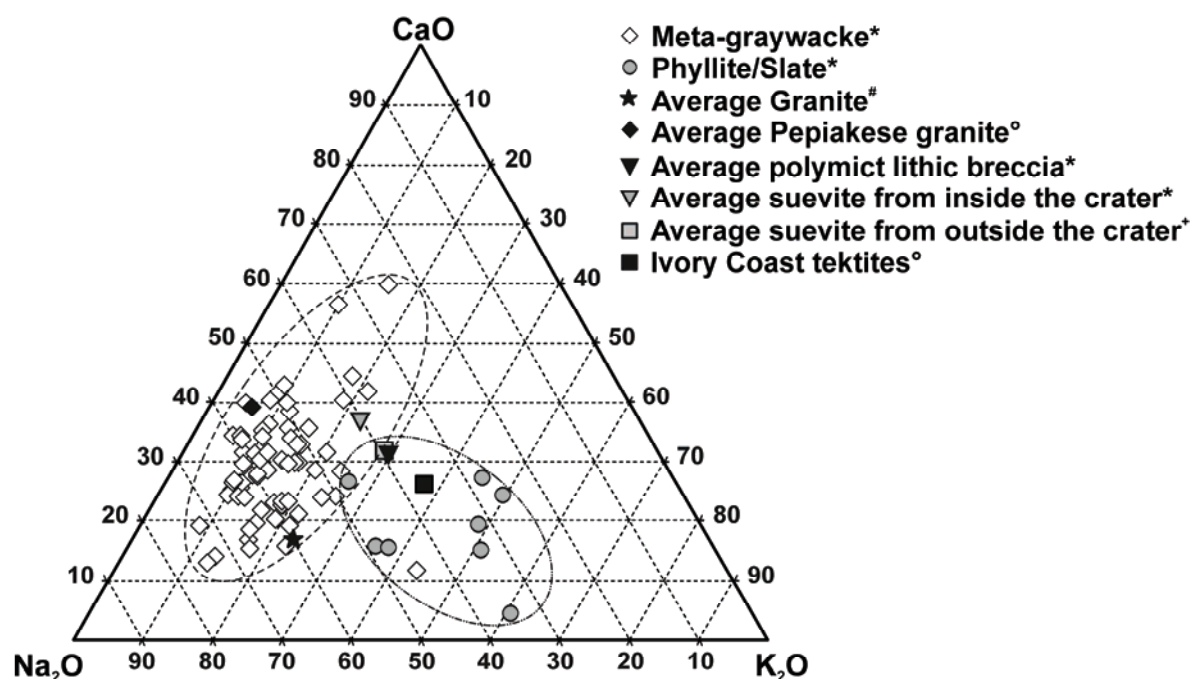


Figure 10-2. CaO-Na₂O-K₂O ternary diagram showing meta-graywacke and phyllite/slate samples from core LB-08A, together with average values for granites, impact breccias, and Ivory Coast tektites. *this study; #from Karikari et al. (2007); °from Koeberl et al. (1998); +from Boamah and Koeberl (2003).

The CaO-Na₂O-K₂O ternary diagram shows also that a majority of the meta-graywacke samples fall between the average composition of the Papiakese granite and the average composition of other granites collected in the near proximity of the Bosumtwi crater. A secondary origin, such as the presence of veinlets of calcite and/or calcite aggregates in some samples, might be responsible for an increase in the CaO content for a few meta-graywacke samples that show a higher CaO content than the Papiakese granite (Figure 10-2). As already mentioned, the chemical composition of the metasedimentary rocks

investigated is mainly function of the source rock composition, but among that, alteration processes and mineral sorting can also be responsible for some variations in major and trace element contents (see, e.g., Taylor and McLennan, 1985). Of particular importance, mineral sorting can modify the proportion of the different rock-forming minerals and consequently the abundance of specific chemical elements. In the case of the meta-graywacke samples, the presence of several accessory minerals was reported in the publication chapter 5, such as epidote, pyrite, sphene, apatite, zircon, rutile, and allanite, based on petrographic observations. The presence of these accessory minerals was confirmed by SEM investigations, and the same accessory minerals were also characterized in suevite samples (see Figure 10-3). In addition, the presence of monazite was also detected in suevite (e.g., in sample KR8-001).

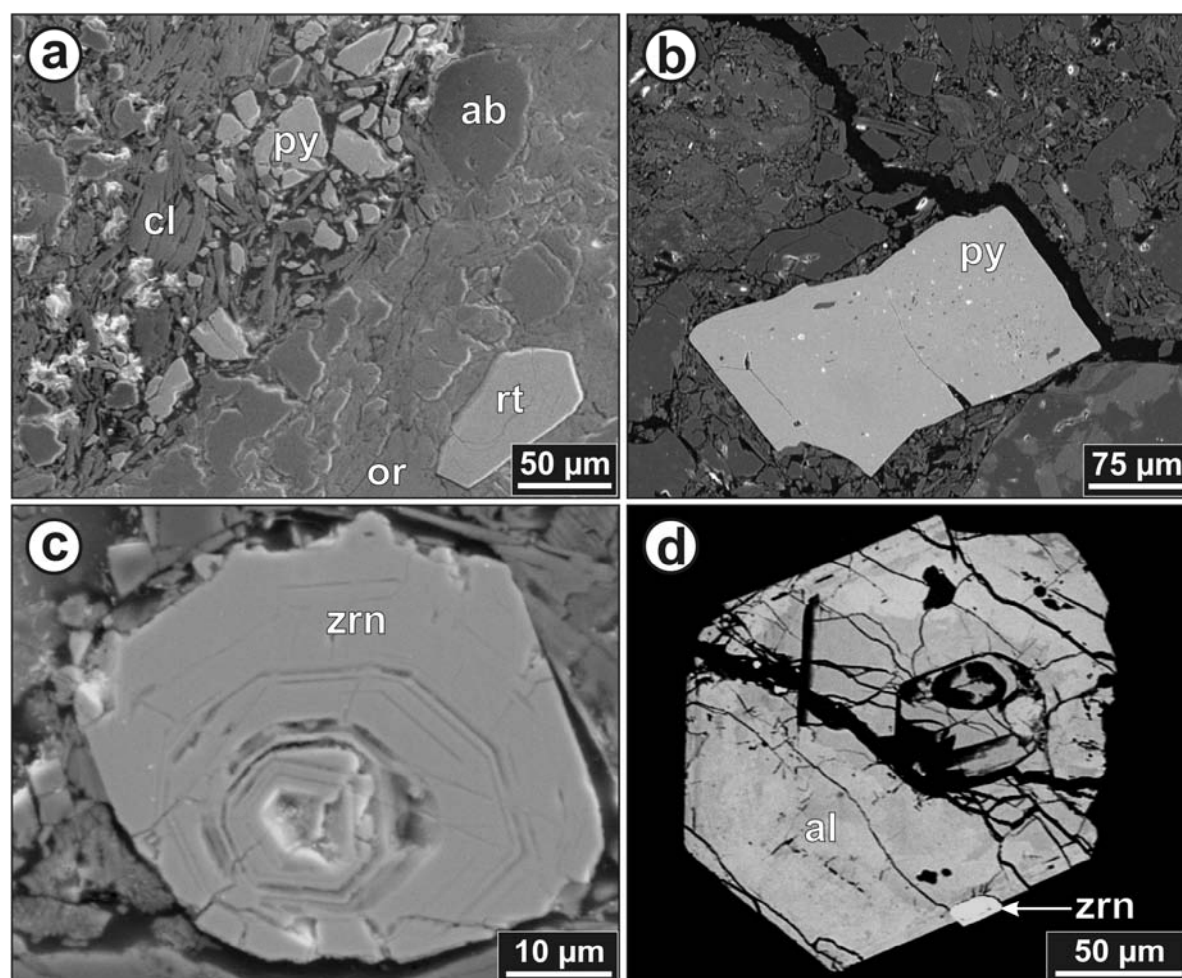


Figure 10-3. Backscattered electron images (except image (d), which is a secondary electron image) of various clasts fragments and minerals present in meta-graywacke and suevite samples: a) Albite (ab), orthoclase (or), chlorite (cl), pyrite (py) and rutile (rt) grains in meta-graywacke; b) Pyrite clast in lithic matrix of suevite; sample KR8-113; depth: 434.59 m; c) Typical zircon grain (zrn) with zonations due to crystal growth; d) Large zoned allanite (al) in contact with a zircon grain in meta-graywacke; Images (a), (c), and (d) are from the meta-graywacke sample KR8-048; depth: 307.30 m.

Allanite grains, such as those observed in the meta-graywacke sample KR8-048 (see Figure 10-3d), typically show a compositional zoning, and frequently, tiny epidote crystals

surround the main crystal of allanite; zircons can be also associated. Allanite usually occurs in granitic rocks and in pegmatites; it is a carrier of rare-earth elements, mainly of cerium and lanthanum, and thorium and uranium are also found in significant amount (Deer et al., 1997). Therefore, the proportion of allanite and also of monazite, a carrier of cerium, lanthanum, neodymium, and thorium (Chang et al., 1998), in the meta-graywacke samples, can influence the whole rock chemical composition, which is especially true for the cerium and lanthanum content.

Usually, Th-Hf-Co and La-Th-Sc ternary diagrams are used to examine the provenance of rocks (see, e.g., Taylor and McLennan, 1985), assuming that the composition of these trace elements in the studied rocks reflects the composition of the source rocks, and that the composition was not changed significantly by alteration processes and/or by mineral sorting. Both ternary plots (see Figure 10-4) show that the investigated samples are derived from a continental source, as most samples fall between average values for the upper continental crust and the bulk continental crust.

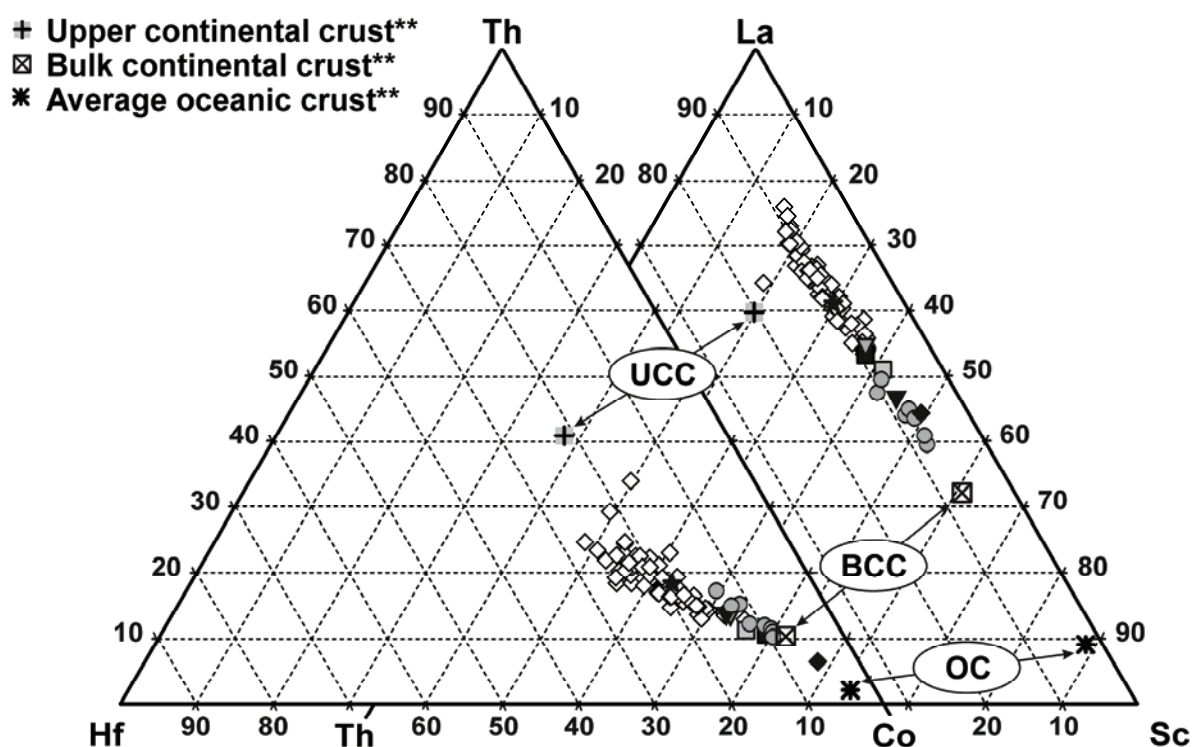


Figure 10-4. Th-Hf-Co and La-Th-Sc ternary diagrams showing meta-graywacke and phyllite/slate samples from core LB-08A, together with averages of different granites, impact breccias, and Ivory Coast tektites. Same legend as in Figure 10-2. **Upper continental crust (UCC), bulk continental crust (BCC), and average oceanic crust (OC) data are from Taylor and McLennan (1985).

Note that in both ternary diagrams (Figure 10-4), meta-graywacke and phyllite/slate samples plot in distinct fields without overlap. All impact breccias plot in the phyllite/slate field in the Th-Hf-Co ternary diagram, whereas they fall exactly between the meta-graywacke and the phyllite/slate fields in the La-Th-Sc ternary diagram (with the exception of the polymict lithic breccia that plots into the phyllite/slate field). Noticeably, the samples show a wide linear distribution, with a higher La content in meta-graywacke than in

phyllite/slate samples, and a higher Co content in phyllite/slate than in meta-graywacke samples. A grain-size effect and/or mineral sorting is possibly responsible for the observed distribution. In addition, the higher Co content in phyllite/slate than in meta-graywacke samples is likely due to the higher proportion of phyllosilicates, such as biotite and chlorite, in the fine-grained metasedimentary rocks. The occurrence of allanite (and/or of monazite), as noted in some meta-graywacke (i.e., in samples KR8-034, 048, 056, 090, and 098; see Appendix C) is probably the cause of the La enrichment observed in some of the meta-graywacke samples (Figure 10-4).

Some geochemical differences were also noted between the LB-08 suevite (i.e., fallback suevite) and fallout suevite. As noted by Ferrière et al. (2007), the MnO content is lower in fallback suevite than in fallout suevite samples, whereas the MgO, CaO, and Na₂O contents are higher in fallback suevite than in fallout suevite. Similarly, Coney et al. (2007a) found significantly higher MgO content (and slightly higher CaO content) in fallback suevite samples from core LB-07A than in fallout suevite. Both authors suggest that these differences in composition can be related to post-impact alteration and/or related to a difference in clast populations in between the two types of suevite. Effectively, calcite clasts occur in fallback breccia and not in fallout suevite, and granite clasts are present in fallout suevite and not in fallback breccia (see publication chapter 5 and Coney et al. 2007b). As mentioned, the presence of calcite clasts (i.e., primary calcite; see Figure 10-5) and aggregates or pods of calcite (i.e., secondary calcite) was noted in most of the fallback suevite samples. To determine if the two generations of calcite have distinct major element

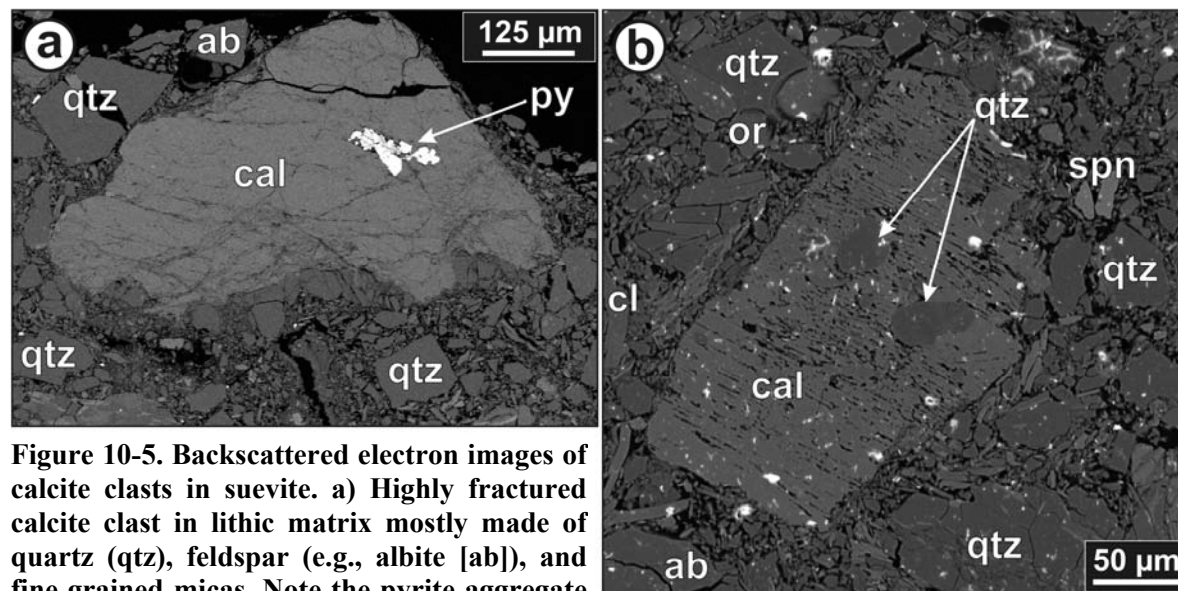


Figure 10-5. Backscattered electron images of calcite clasts in suevite. a) Highly fractured calcite clast in lithic matrix mostly made of quartz (qtz), feldspar (e.g., albite [ab]), and fine grained micas. Note the pyrite aggregate (py) within the clast of calcite; sample CAN-31; depth: 440.32 m; b) Calcite clast showing unusual (dissolution?) features and containing two rounded quartz grains. Several smaller mineral clasts are also identified on the image, including quartz (qtz), orthose (or), albite (ab), chlorite (cl), and sphene (sph); sample KR8-042; depth: 293.97 m.

compositions, several clasts and aggregates of calcite were located in thin sections under optical microscope and subsequently analyzed by SEM. The SEM analyses of calcite grains are reported in Appendix D. As shown in Figure 10-6, calcite contains small fractions of Mn, Fe, and Mg, and, obviously, primary and secondary calcites cannot be discriminated

based on their chemical composition. It cannot be excluded that more than two generations of calcite occur in the investigated samples and/or that the chemical composition of the primary clasts of calcite was modified by the high pressures and temperatures involved in the formation of suevite. Many of the calcite clasts are fractured (shock fracturing?; Figure 10-5a), some others display unusual (dissolution?) features (Figure 10-5b), however, no evidence of shock melting of calcite was observed. It is also not possible, based on this study, to determine if the observed enrichment in CaO in fallback suevite is mainly due to the presence of calcite clasts and/or the result of a hydrothermal addition of CaO.

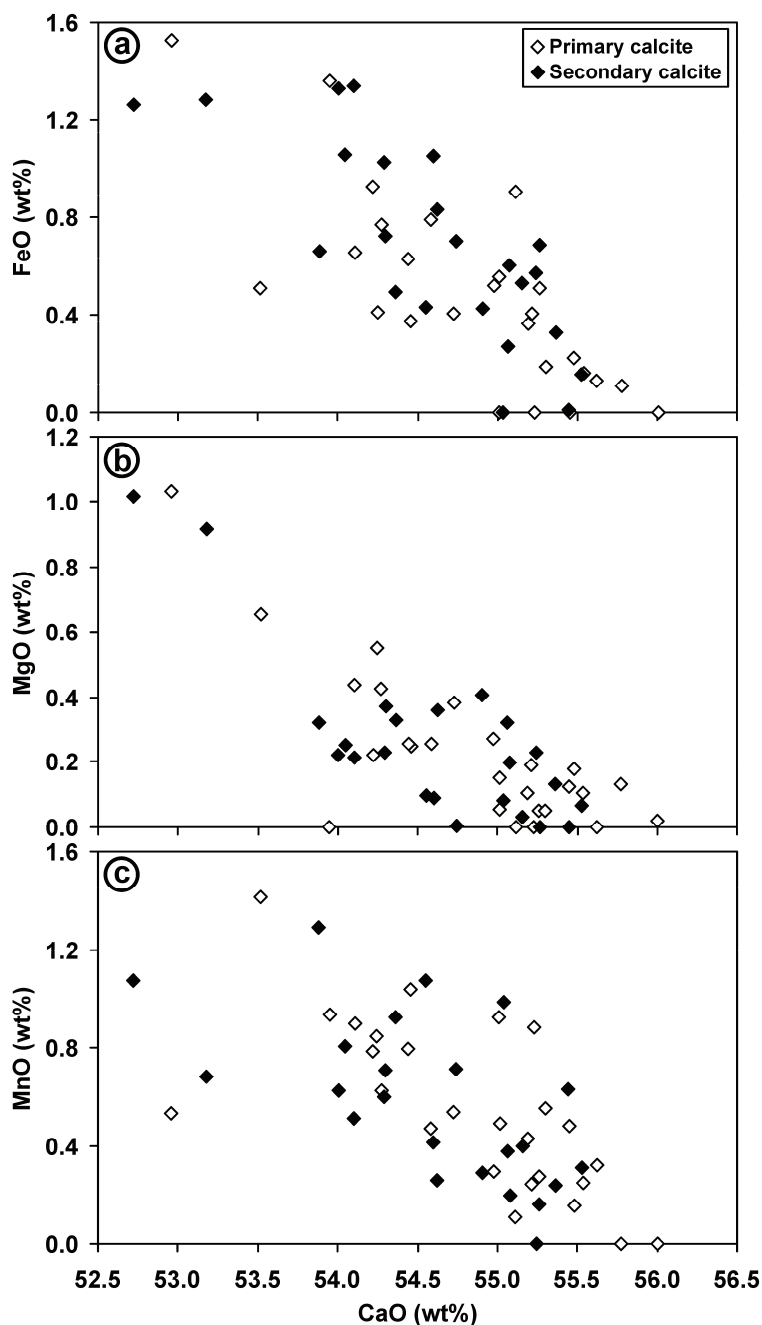


Figure 10-6. Binary diagrams comparing the abundances of FeO, MgO, and MnO with those of CaO (in wt%) in primary calcite (open diamonds) and in secondary calcite (solid diamonds). The complete SEM quantitative energy dispersive X-ray analyses of calcite clasts, aggregates, and veinlets in suevite samples from the drill core LB-08A are reported in Appendix D. Note that primary and secondary calcites cannot be discriminated using only chemical composition.

Furthermore, the major element composition of melt particles was determined using SEM in order to compare their compositions with the composition of the different target lithologies. The SEM investigations have also revealed some characteristics of the

microtexture of the melt particles, and that the groundmass of the suevite is composed mainly of mono-mineral clasts, such as quartz, feldspars, mica, and metasedimentary clasts, essentially meta-graywacke (Figure 10-7). In both cases, for fallback and fallout suevites,

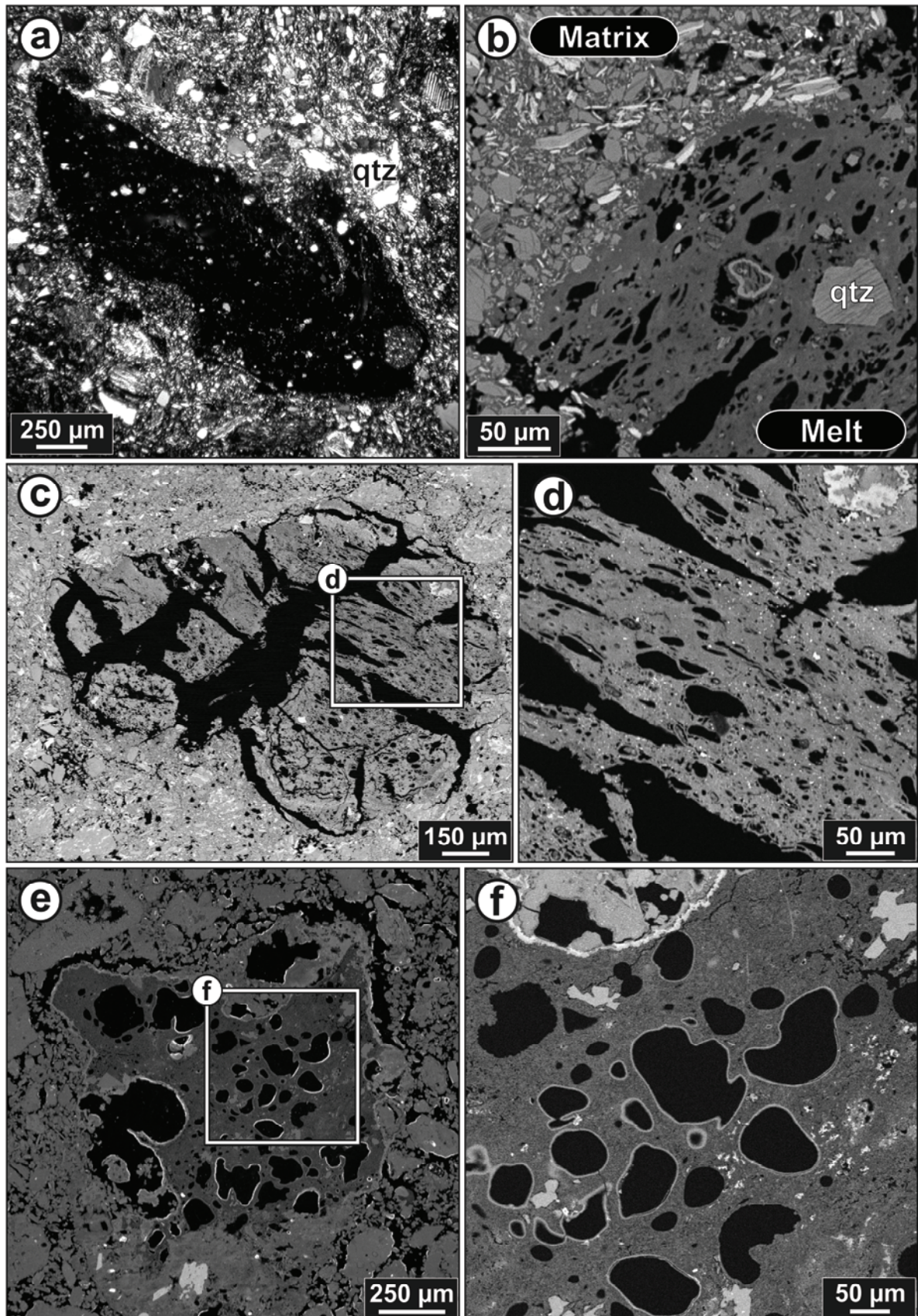


Figure 10-7. Cross-polarized light microphotograph (a) and backscattered electron images (b-f) of melt particles in suevite samples from the Bosumtwi crater. Image (a) is from sample KR8-004 (depth: 239.65 m), images (c-d) are from sample KR8-005 (depth: 240.04 m), and images (e, f) are from sample BH3-0585 (suevite sample from outside the northern crater rim; see Boamah and Koeberl, 2006, for more information on this sample). a) General view of a melt particle containing abundant tiny undigested quartz grains (white spots within the melt particle); b) Closer view of the contact zone between a melt particle and the lithic matrix. Note the presence of abundant elongated vesicles and of a shocked quartz grain (one set of PDFs is barely visible) within the melt; c) General view of a highly cracked and vesiculated melt particle; d) Enlarged part of the general view (c) showing the elongated vesicles (appear black on the image). Note the flow foliation trending NW-SE as indicated by the elongation of the vesicles; e) General view of a highly vesiculated melt particle; f) Enlarged part of the general view (e) showing the irregular shape of the vesicles; Note that most, if not all, vesicles are unfilled by secondary minerals.

melt particles are highly vesicular (Figure 10-7b, d-f) and the presence of undigested shocked quartz grains was noted in most of the investigated melt particles (Figure 10-7a, b). Vesicles have sizes from a few micrometers to hundreds micrometers in melt particles from fallback suevite; vesicles up to several millimeters in diameter were observed in large melt particles from fallout suevite. As noted during optical microscopic observations (see publication chapter 5), the original glass of the melt particles is altered to very fine-grained phyllosilicate minerals. Similar observations were also made for the melt particles in fallout suevite (Figure 10-7f).

Regarding the chemical composition, melt particles show significant differences between the different samples investigated, but also within a given sample (Figure 10-8). The SEM composition for 41 melt particles from fallback suevite, fallout suevite, and suevite dikes is reported in Appendix D. Results are compared with literature data of melt particles from fallout suevite and with average composition of Bosumtwi target rocks and Ivory Coast tektites (Figure 10-8). Most of the melt particles are comparatively more enriched in FeO than the target lithologies; only the melt particles from outside the northern crater rim (i.e., sample BH3-0585) are depleted in FeO (less than 1 wt%), but comparatively enriched in sodium (between 6 and 10 wt%). In the $\text{SiO}_2\text{-Al}_2\text{O}_3\text{-MgO+FeO}$ ternary diagram, most of the melt particles plot, in term of silica, between average composition for meta-graywacke and phyllite/slate, with the notable exception of the melt particles from suevite dikes (i.e., ADE-8A and CAN-31), which are depleted in SiO_2 , and somewhat enriched in MgO+FeO compare to the other investigated melt particles. The higher MgO and FeO content observed for the melt particles from suevite dikes is possibly a result of the intense alteration of these melt particles to phyllosilicate minerals. Macroscopic and petrographic observations of the suevite dikes have shown that these specific samples are extremely altered (see publication chapter 5), possibly due to preferential fluid circulation along dikes. Considering the heterogeneity of the melt particles with regards to their major element composition (Figure 10-8), it seems that most of the melt particles are the result of melting of metasedimentary clasts (i.e., mixture of minerals) than of mono-minerals. In addition, no pure SiO_2 melt particles (i.e., lechatelierite) were detected during our SEM investigations of suevite samples from inside the crater. However, lechatelierite inclusions were reported in suevite sample from outside the northern crater rim (Boamah and Koeberl, 2006).

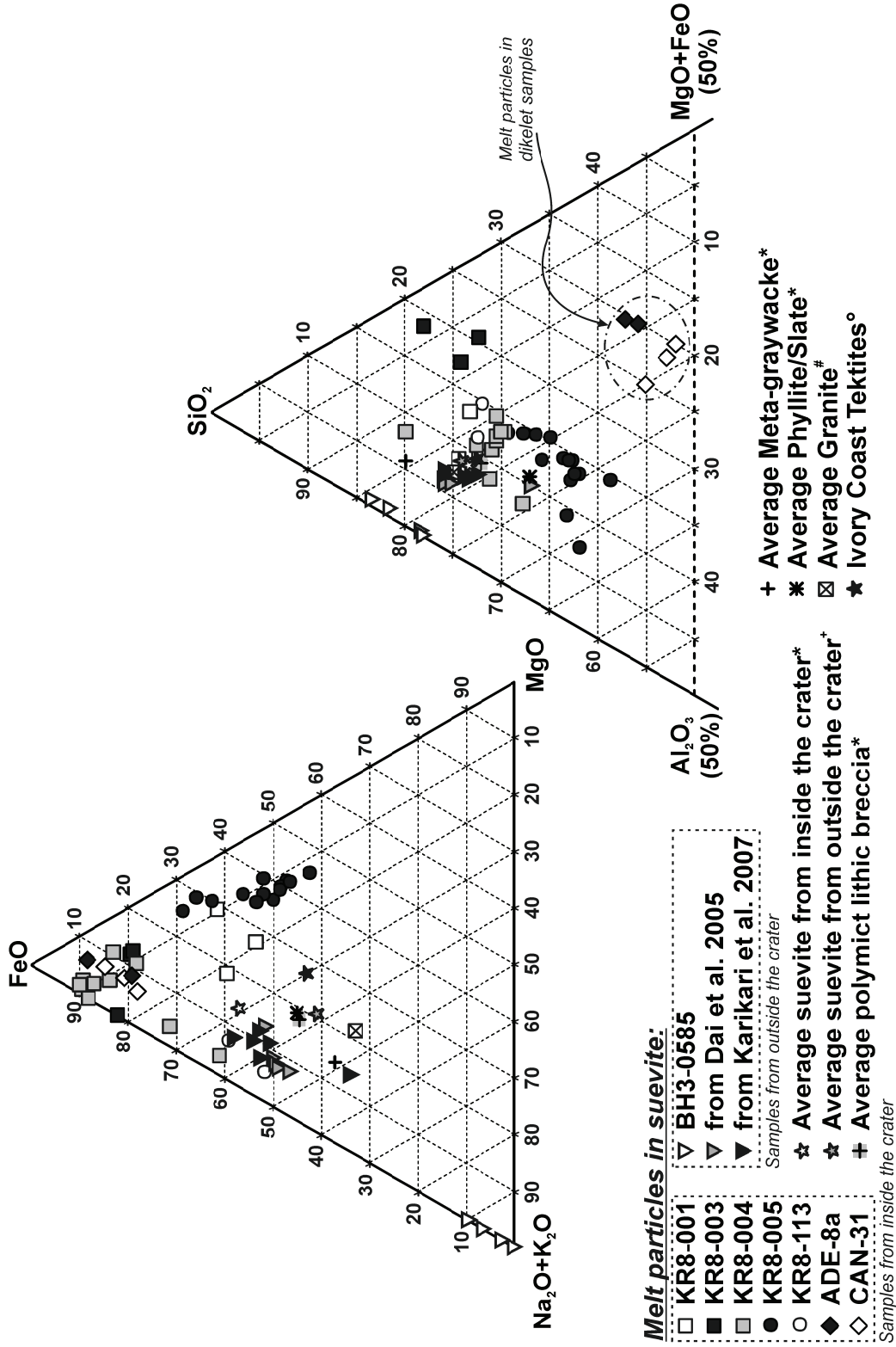


Figure 10-8. Ternary FeO-Na₂O+K₂O-MgO and SiO₂-Al₂O₃-MgO+FeO diagrams showing the chemical composition of melt particles in suevite samples from inside the crater (i.e., from core LB-08A) in comparison to melt in suevite samples from outside the crater [this study, Dai et al. (2005), and Karikari et al. (2007)]. Average values for impact breccia, Bosumtwi target rocks, as well as for Ivory Coast tektites are also plotted for comparison [data from ^{*}Ferrière et al. (2007), [†]Boamah and Koeberl (2003), [#]Karikari et al. (2007), and ^oKoeberl et al. (1998)].

In order to further characterize the extremely fine-grained metasedimentary lithologies, and to compare results for different settings (i.e., shocked basement rocks, clasts in suevite, unshocked samples from outside the crater), the carbon isotopic compositions and carbon contents were determined for 14 samples; including shale, slate, phyllite, and a melt particle from drillcore LB-08A, as well as a graphitic shale from outside the crater. Information on samples and results are reported in Table 10-1. Sample isotope ratios are relative to the Vienna Pee Dee Belemnite (V-PDB) standard. The carbon content against $\delta^{13}\text{C}$ values versus V-PDB standard of the analyzed samples are shown in Figure 10-9.

Table 10-1. Result of the carbon stable isotope analyses of clasts/samples from the Bosumtwi impact structure.

Sample #	Rock/Clast type	$\delta^{13}\text{C}$ (‰)	Carbon content (wt%)	Weight (μg)*	Additional information
KR8-001a	Melt particle	-28.20 \pm 1.39	0.41 \pm 0.02	3720	Dark melt fragment (0.8 mm in size) in suevite
KR8-001b	Slate	-30.42 \pm 1.22	0.28 \pm 0.02	5560	Clast in suevite
KR8-001c	Shale	-27.48 \pm 1.42	0.25 \pm 0.03	2644	Clast in suevite
KR8-001d	Phyllite (or slate?)	-26.86 \pm 2.11	0.27 \pm 0.06	4478	Clast in suevite
KR8-002	Phyllite	-28.61 \pm 1.23	0.25 \pm 0.01	4668	Phyllite with ribbon quartz
KR8-003	Phyllite	-27.12 \pm 1.21	0.30 \pm 0.03	4872	Clast in suevite; phyllite with ribbon quartz
KR8-010	Phyllite/Breccia	-29.48 \pm 1.29	0.26 \pm 0.02	5313	Monomict breccia; phyllite with ribbon quartz
KR8-022	Phyllite/Breccia	-25.64 \pm 1.20	0.26 \pm 0.01	5498	Monomict breccia; phyllite with ribbon quartz
KR8-042	Phyllite (or slate?)	-27.41 \pm 1.50	0.56 \pm 0.03	5057	Clast in suevite
KR8-043	Phyllite (or slate?)	-29.60 \pm 1.27	0.29 \pm 0.01	5654	Clast in suevite
KR8-046	Slate	-30.20 \pm 1.20	0.40 \pm 0.00	5192	
KR8-064	Phyllite	-29.48 \pm 1.23	0.34 \pm 0.02	5063	Phyllite with ribbon quartz
ADE-8a	Phyllite	-27.28 \pm 1.20	0.14 \pm 0.01	5276	
LB-51	Graphitic shale	-23.71 \pm 1.22	2.19 \pm 0.06	938	

All samples are from drillcore LB-08A, except LB-51 sample from outside the crater (see Karikari et al., 2007). $\delta^{13}\text{C}$ values are calculated relative to the Vienna Pee Dee Belemnite (V-PDB).

*Average weight of the three samples analyzed.

All samples from drillcore LB-08A, including the analyzed melt particle, contain <0.5 wt% carbon and have $\delta^{13}\text{C}$ values between -31 and -25 ‰. Only the graphitic shale sample (LB-51; from outside the crater) has a higher carbon content and a higher value of $\delta^{13}\text{C}$ (Table 10-1; Figure 10-9). The values of $\delta^{13}\text{C}$ for all measured samples strongly suggest an origin from biogenically derived carbon (e.g., Coplen et al., 2002). The unique analyzed melt particle plot in the middle of the field of the metasedimentary rocks from core LB-08A, suggesting that the precursor of this melt particle was a phyllite or a shale (Figure 10-9). However, additional carbon isotope analyses of samples from outside the Bosumtwi crater, including fine-grained metasedimentary rocks and clasts and melt particles from fallout suevite samples are necessary for comparison with the results of this preliminary investigation.

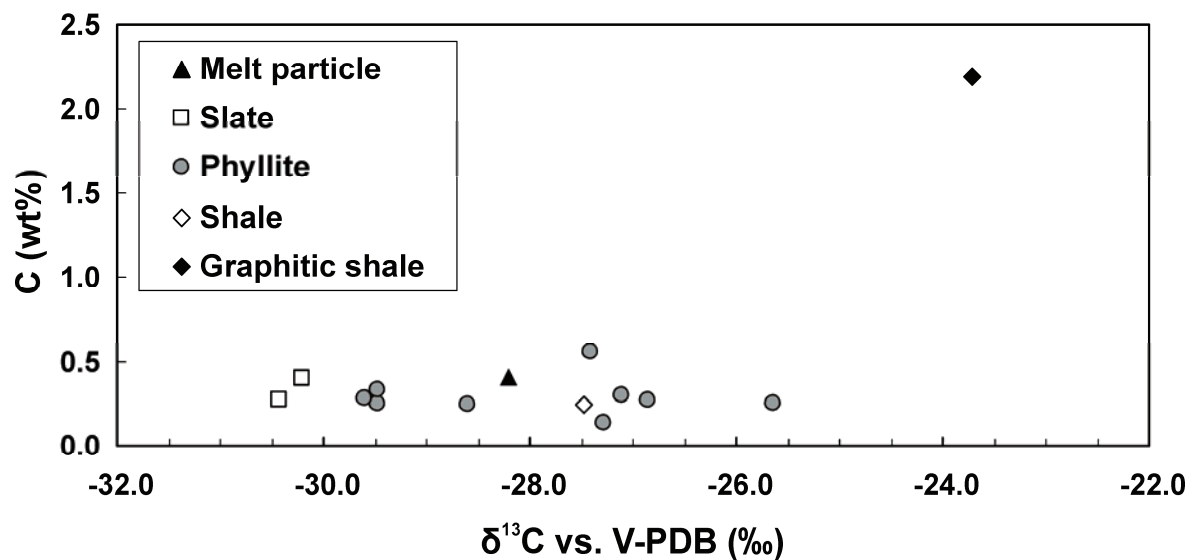


Figure 10-9. Carbon content against $\delta^{13}\text{C}$ values of the analyzed samples from the Bosumtwi impact structure. All analyzed samples have low carbon content (<0.5 wt%) and values of $\delta^{13}\text{C}$ between -31 and -25 ‰; except the graphitic shale sample (LB-51), which has higher carbon content (2.19 wt%) and lower value of $\delta^{13}\text{C}$ (23.71 ‰).

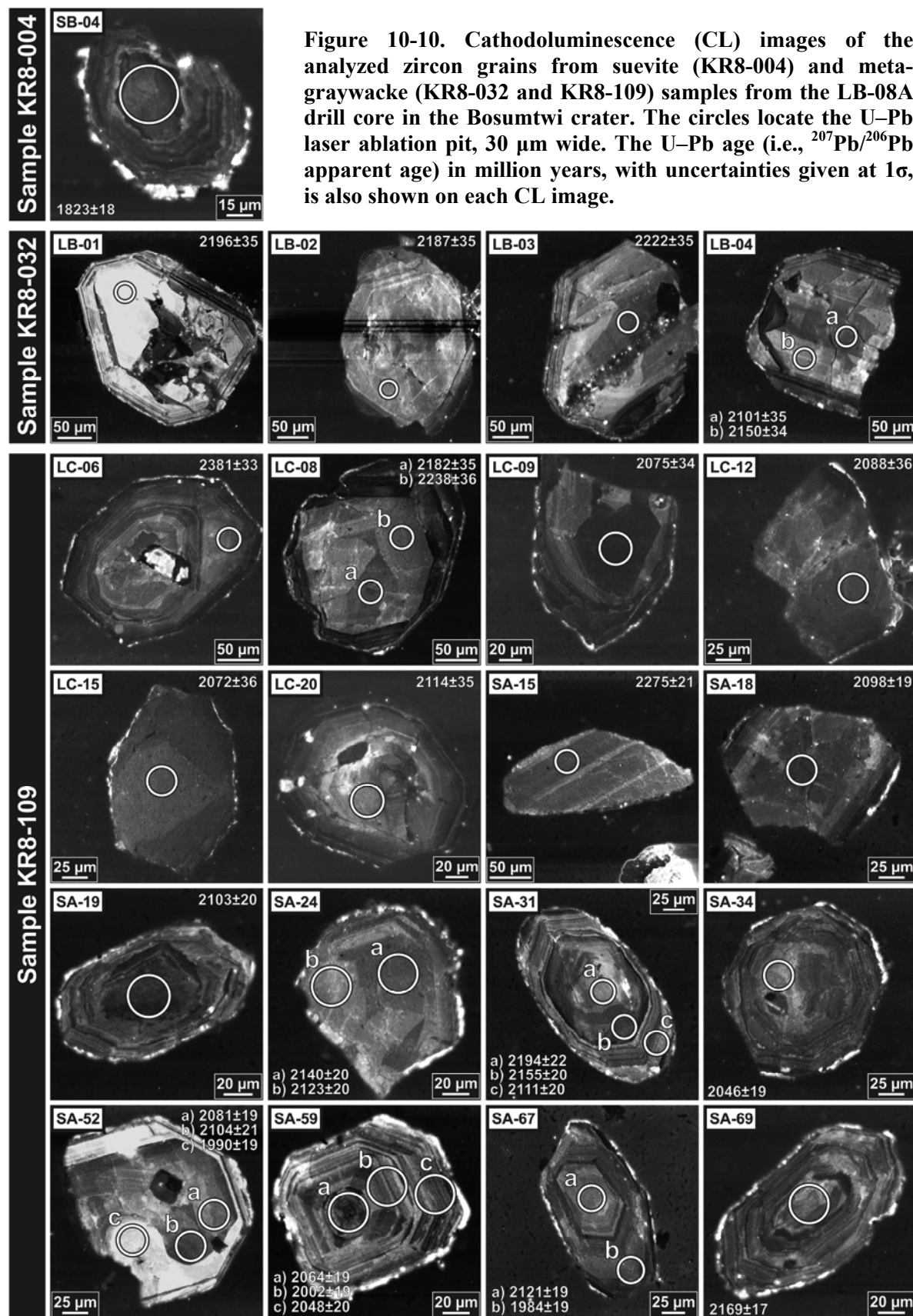
10.2. U-Pb zircon ages and Sr-Nd isotopic composition of samples from drill core LB-08A:

For the first time, U-Pb ages have been measured on single detrital zircon grains from Bosumtwi impactites. In addition, analyses of Sr and Nd isotopic compositions of suevite, phyllite, and meta-graywacke samples from the drill core LB-08A are presented and compared with results previously obtained for samples from outside the crater rim.

A total of 31 laser spot analyses in 21 zircon grains were performed using a LA-ICP-MS at the Northwest University, China (see chapter 4 for details of the method). The investigated zircons from suevite (KR8-004) and meta-graywacke (KR8-032 and KR8-109) samples have dimensions between about 100 and 300 μm . Zircon grains were scanned using cathodoluminescence (CL); CL images of the grains analyzed are presented in Figure 10-10, providing details of the internal structure of the zircon grains investigated. The $^{207}\text{Pb}/^{206}\text{Pb}$ age (the more precise age for old zircons; i.e., from the Proterozoic) for each laser ablation pit is also indicated on each CL image. The full data, including isotope ratios and U-Pb ages are reported in Appendix E.

Some of the zircons display complex internal structures, such as re-crystallized domains (e.g., SA-52; see Figure 10-10) or magmatic zoning with small rims of metamorphic overgrowth around an inherited core/grain (e.g., SA-31). Some zircon grains display also inclusions (e.g., LC-06). Concordia diagrams of the U-Pb isotope data are presented in Figure 10-11 and show discordant ages for the investigated zircons. The $^{207}\text{Pb}/^{206}\text{Pb}$ apparent ages are dispersed over the range ~ 2.38 to ~ 1.82 Ga, with a cluster of ages around 2.1-2.2 Ga. Only three zircon grains show an apparent age less than 2.0 Ga; the laser spot analyses SA-52c and SA-67b for zircons from the meta-graywacke sample KR8-109, corresponding to a re-crystallized domain and to a metamorphic overgrowth, respectively, and SB-04, the only zircon from suevite that was analyzed (see Figure 10-10). It cannot be excluded that the SB-04 zircon grain was not affected by the high pressures and temperatures involved in the formation of suevite. The successive zircon growths and re-crystallized domains, as revealed with CL, are possibly in part responsible for the observed discordant ages.

Using only analyses that are less than 4% discordant, an upper Concordia intercept age of 2145 ± 82 Ma is obtained (Figure 10-11b). This crystallization or magmatic age is in very good agreement with previous geochronological data for rocks from the West African craton, which show that magmatism in this region occurred during a period between 2.1 and 2.2 Ga (e.g., Leube et al., 1990; Hirdes et al., 1992). According to the paleoproterozoic evolution model by Feybesse et al. (2006), an extensive monzonitic magmatism event occurred around 2.16–2.15 Ga, forming the first segments of continental crust in the Ghanaian province. Thus, it is likely that the source rocks contribution of the metasediments excavated by the Bosumtwi crater were formed during this magmatic event. Additionally, a metamorphic age of ~ 1.8 -1.9 Ga can be tentatively derived from the Figure 10-11a.



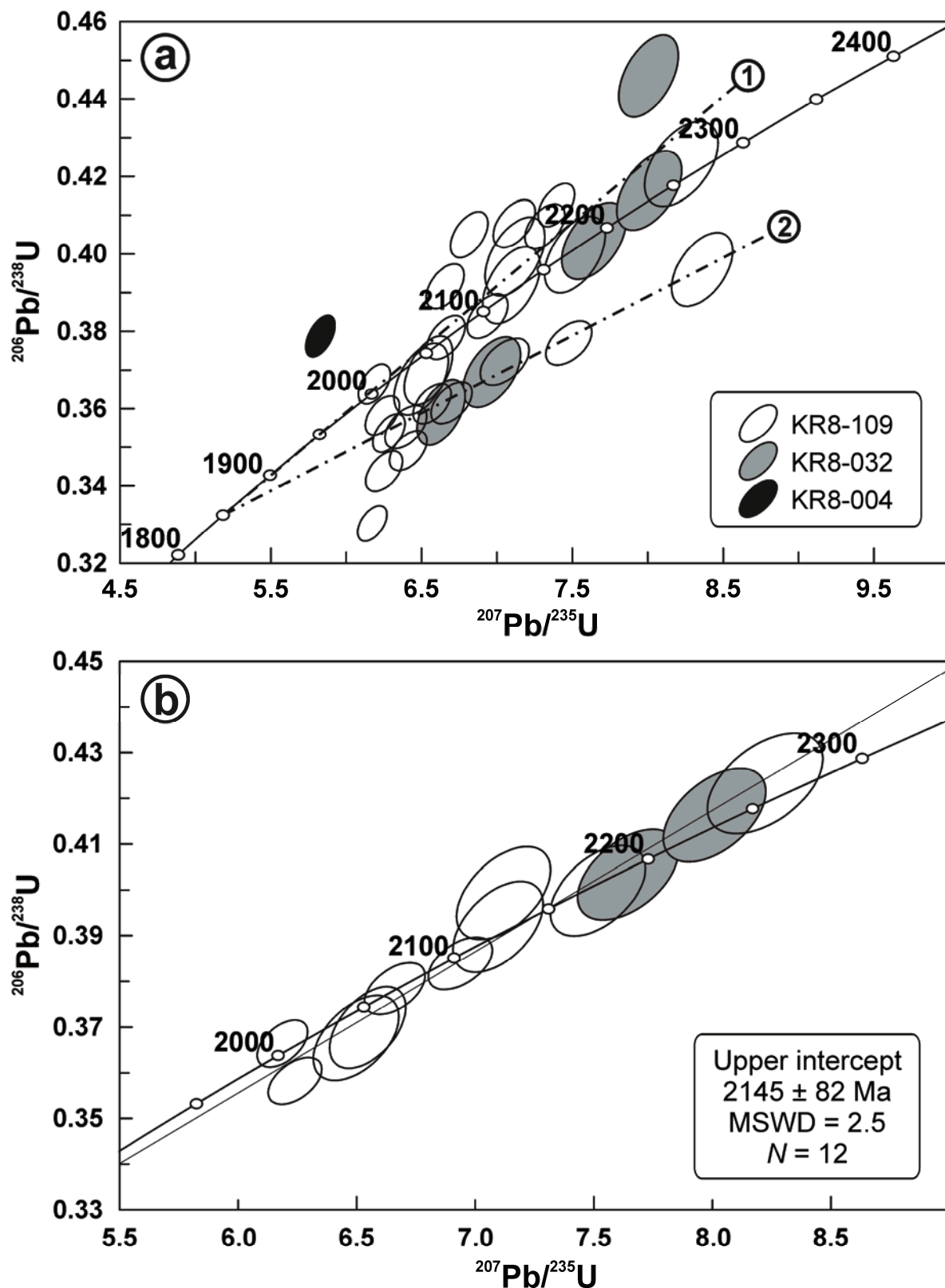


Figure 10-11. U-Pb Concordia diagrams of zircon grains from suevite (KR8-004) and meta-graywacke (KR8-032 and KR8-109) samples from the LB-08A drill core in the Bosumtwi crater. Error ellipses are 2σ . All measured zircons are plotted in (a) and only those analyses that are less than 5% discordant are plotted in (b). Dashed lines (1) and (2) reported in (a) correspond to the two possible different inland contributions or to “magmatic” and “metamorphic” ages, respectively.

In addition to the U-Pb dating of zircons, Rb-Sr and Sm-Nd isotopic analyses of suevite and Bosumtwi basement rocks were performed to better constraint the parent material of the Ivory Coast tektites and to provide further insights into the timing of the metamorphism of the Bosumtwi basement rocks. Whole-rock Rb-Sr and Sm-Nd isotopic compositions of six suevites (5 from inside the crater and one from outside the northern crater rim), three meta-graywacke, and two phyllite samples from core LB-08A were determined at the University of Vienna using an ID-TIMS (see chapter 4 for details on the method used). The results are presented in Table 10-2 and compared with previous Sr and Nd isotopic compositions of country rocks of the Bosumtwi and impactites from outside the crater rim. The new analyses are very comparable to previous data, but for the first time $^{87}\text{Sr}/^{86}\text{Sr}$ and $^{87}\text{Rb}/^{86}\text{Sr}$ ratios for suevite samples are reported (Figure 10-12). Note that very limited differences occur among the suevite samples and that they fall just between meta-graywacke and Ivory Coast tektites. $^{87}\text{Sr}/^{86}\text{Sr}$ and $^{87}\text{Rb}/^{86}\text{Sr}$ ratios vary considerably between the different basement rocks (Figure 10-12); extremely large differences are observed between the phyllite samples, whereas very limited differences occur among the meta-graywacke samples.

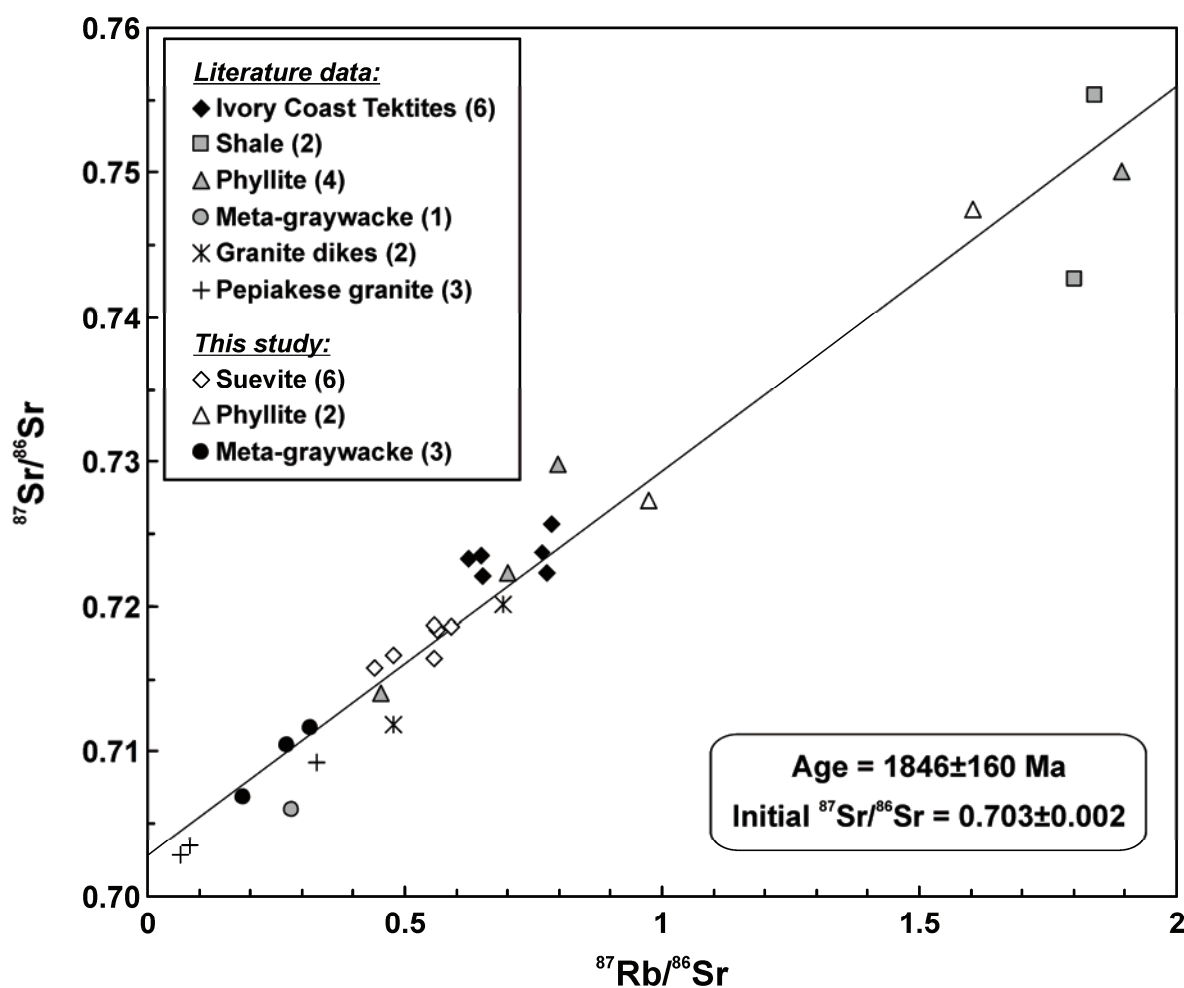


Figure 10-12. Rb-Sr whole rock isochron diagram for Bosumtwi crater target rocks and suevite samples from core LB-08, as well as target rocks samples from outside the crater rim and Ivory Coast tektites (data from Shaw and Wasserburg [1982] and Koeberl et al. [1998]).

It is apparent that the samples plot along a line, with some scatter, when reported on a Rb-Sr isochron diagram (Figure 10-12). The data points of all rock samples define a regression line, whose slope corresponds to an age of 1846 ± 160 Ma, with an initial Sr ratio of 0.703. This age is in good agreement with the “metamorphic” age of ~ 1.8 -1.9 Ga that was tentatively derived from U-Pb dating of zircons (see Figure 10-11a). However, due to the extensive alteration

Table 10-2. Rb, Sr, Sm, Nd, and Sr and Nd isotopic ratios of Bosumtwi crater rocks, compared to those of Ivory Coast Tektites.

Sample	Rb	Sr	$^{87}\text{Rb}/^{86}\text{Sr}$	$^{87}\text{Sr}/^{86}\text{Sr}$ ($\pm 2\sigma$)	ϵ Sr	Sm	Nd	$^{147}\text{Sm}/^{144}\text{Nd}$	$^{143}\text{Nd}/^{144}\text{Nd}$ ($\pm 2\sigma$)	ϵ Nd
<i>Ivory Coast Tektites</i>										
IVC 2069*	50.3	190	0.767	0.723763 (19)	273	3.05	16.3	0.113	n.d.	n.d.
IVC 3396*	56.3	210	0.777	0.722292 (18)	252	3.49	18.2	0.116	n.d.	n.d.
IVC 3398*	78.7	350	0.651	0.722132 (22)	250	4.14	23.2	0.108	0.511583 (21)	-20.6
USNM6011A [†]	62.6	290	0.626	0.72334 (3)	267	3.85	20.5	0.113	n.d.	-20.2
USNM6011B [†]	64.1	286	0.649	0.72357 (4)	270	n.d.	n.d.	n.d.	n.d.	n.d.
USNM6011C [†]	70.4	260	0.785	0.72571 (3)	301	4.00	21.3	0.113	n.d.	-19.5
<i>Suevite</i>										
BCC-5A-64*	n.d.	n.d.	n.d.	0.718064 (20)	192	n.d.	n.d.	n.d.	0.511755 (20)	-17.2
BCC-8A-64*	n.d.	n.d.	n.d.	0.717493 (20)	184	n.d.	n.d.	n.d.	0.511601 (20)	-20.2
LB-44	60.0	295	0.589	0.718659 (4)	201	4.12	22.1	0.113	0.511649 (4)	-19.3
KR8-001	91.1	469	0.562	0.718372 (4)	197	4.11	19.1	0.130	0.511560 (3)	-21.0
KR8-005	55.6	336	0.479	0.716638 (5)	172	3.48	18.7	0.112	0.511565 (5)	-20.9
KR8-026	69.1	360	0.556	0.718762 (4)	202	3.74	17.5	0.129	0.511652 (3)	-19.2
KR8-042	53.8	352	0.443	0.715754 (5)	160	2.57	14.2	0.109	0.511541 (4)	-21.4
CAN-31	73.7	383	0.557	0.716444 (4)	170	3.85	21.0	0.111	0.511486 (3)	-22.5
<i>Shale</i>										
J490*	114	180	1.841	0.755285 (17)	720	3.02	13.5	0.135	0.511691 (24)	-18.5
J497*	92.5	149	1.802	0.742688 (13)	542	4.39	21.8	0.122	n.d.	n.d.
<i>Phyllite</i>										
J491*	94.5	145	1.893	0.750069 (20)	646	6.47	30.1	0.130	0.511661 (20)	-19.1
J494*	41.5	172	0.699	0.722356 (11)	253	5.64	28.5	0.120	n.d.	n.d.
J495*	25.9	165	0.454	0.714000 (19)	134	6.81	38.8	0.106	n.d.	n.d.
J501*	56.3	205	0.796	0.729800 (20)	359	6.62	42.1	0.095	0.511360 (20)	-24.9
KR8-002	127	230	1.605	0.747438 (4)	609	4.08	20.5	0.121	0.511574 (2)	-20.8
KR8-084	128	380	0.974	0.727382 (4)	325	3.97	19.1	0.126	0.511629 (3)	-19.7
<i>Meta-graywacke</i>										
J506*	39.1	402	0.281	0.706011 (11)	21.5	3.03	19.6	0.093	n.d.	n.d.
KR8-032	39.4	360	0.317	0.711632 (4)	101	3.02	15.9	0.115	0.511456 (3)	-23.1
KR8-066	39.3	419	0.272	0.710494 (4)	85.1	3.61	21.0	0.104	0.511465 (3)	-22.9
KR8-109	29.9	467	0.185	0.706893 (3)	34.0	2.98	18.4	0.098	0.511452 (3)	-23.1
<i>Granite dikes</i>										
J493*	51.2	311	0.477	0.711833 (35)	104	3.49	13.4	0.157	n.d.	n.d.
J505*	88.6	372	0.690	0.720106 (14)	221	3.99	26.1	0.092	n.d.	n.d.
<i>Pepiakese granite</i>										
J507*	9.50	335	0.082	0.703523 (27)	-13.8	2.91	17.5	0.100	0.511309 (14)	-25.9
J508*	7.90	359	0.064	0.702850 (10)	-23.4	1.69	6.2	0.165	n.d.	n.d.
J509*	49.9	438	0.330	0.709259 (11)	67.6	6.13	28.7	0.129	n.d.	n.d.

* Data from Koeberl et al. 1998. [†] Data from Shaw and Wasserburg (1982). Rb, Sm, and Nd (in ppm) by INAA. Sr (in ppm) by XRF. 2σ uncertainties refer to the last digits of the measured isotopic ratios. ϵ values are the measured deviation in parts in 10^4 of the $^{143}\text{Nd}/^{144}\text{Nd}$ ratio from the present-day chondritic uniform reservoir (CHUR) value of 0.512638, and of the $^{87}\text{Sr}/^{86}\text{Sr}$ ratio from the inferred unfractionated mantle reservoir (UR) value of 0.7045.

of some of the investigated samples and because, both, the metasedimentary rocks and the suevite samples, represent a mixture of mineral and rock clasts derived from one or several precursors, it is difficult to consider this age as a reliable “metamorphic” age. In addition, the $^{87}\text{Sr}/^{86}\text{Sr}$ and $^{87}\text{Rb}/^{86}\text{Sr}$ ratios show that the suevite samples are mixtures of meta-greywacke and phyllite (and granite), and that Ivory Coast tektites, with somewhat higher $^{87}\text{Sr}/^{86}\text{Sr}$ and $^{87}\text{Rb}/^{86}\text{Sr}$ ratios, are a mixture of metasedimentary rocks (and granite), but with a higher proportion of phyllite (and shale) than for suevite samples. These observations are further supported by the ϵ_{Sr} and ϵ_{Nd} values (Figure 10-13).

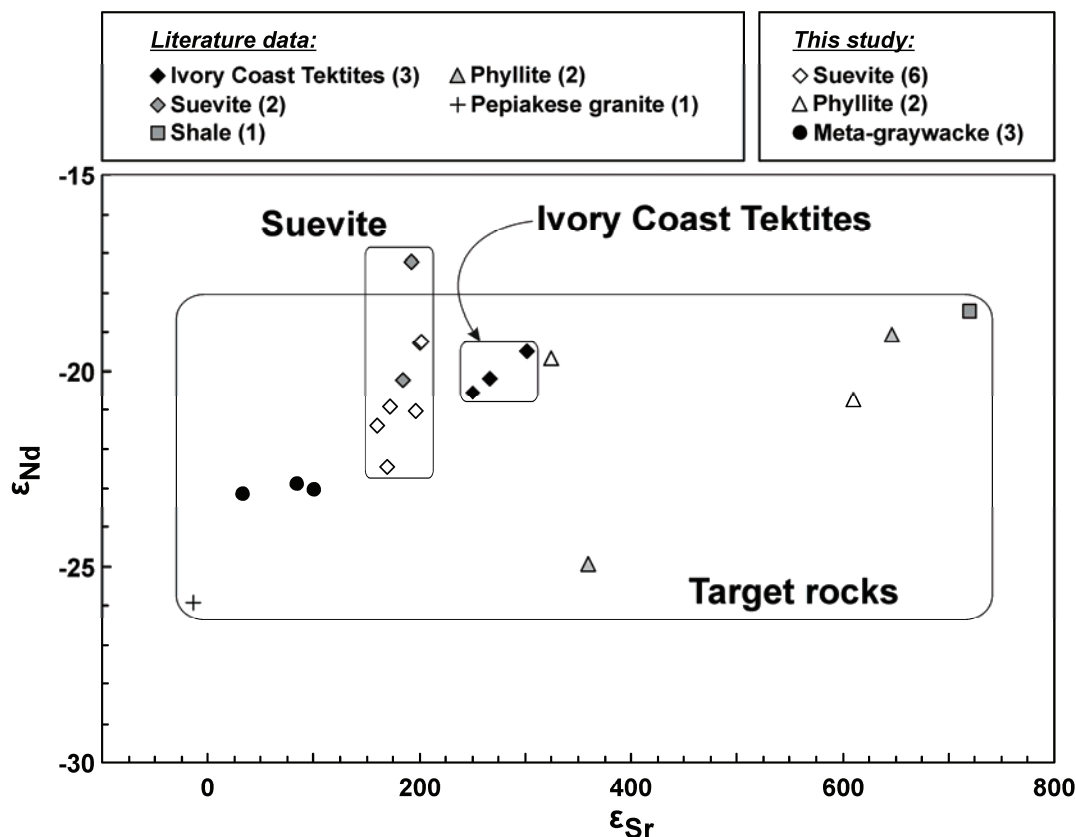


Figure 10-13. Plot of ϵ_{Sr} vs. ϵ_{Nd} for Bosumtwi crater target rocks and suevite samples from core LB-08. These data are compared with values for suevite and target rocks samples from outside the crater rim, as well as Ivory Coast tektites (data from Shaw and Wasserburg [1982] and Koeberl et al. [1998]).

Ivory Coast tektites and meta-graywacke samples show a narrow range of ϵ_{Sr} and ϵ_{Nd} values. In contrast, the fine-grained metasedimentary rocks (i.e., phyllite and shale) show extremely large variations in both, ϵ_{Sr} and ϵ_{Nd} values (Figure 10-13). The suevite samples display similar narrow range of ϵ_{Sr} as observed for Ivory Coast tektites and meta-graywacke, but large range of ϵ_{Nd} values. With the exception of one suevite sample (i.e., sample BCC-5A-64, from Koeberl et al., 1998), suevite and Ivory Coast tektites fall within the range of values of Bosumtwi target rocks (and country rocks). The smaller variations in ϵ_{Sr} and ϵ_{Nd} values, as observed for Ivory Coast tektites, compared to suevite samples, are possibly the result of a smaller variety of different lithologies that were mixed for the production of tektites or, as suggested by Koeberl et al. (1998), due to a better homogenization of the target rock compositions.

10.3. Transmission electron microscope observations of planar deformation features in quartz from the Bosumtwi and the Chesapeake Bay impact structures:

By definition, planar deformation features (PDFs) are narrow planes of amorphous material that are less than 2 μm thick, comprising straight, parallel sets spaced 2-10 μm apart (e.g., Engelhardt and Bertsch, 1969; Stöffler and Langenhorst, 1994). Several microphotographs of PDFs from different impact structures and additional details about PDFs orientations are reported in the chapter 2 and in the publication chapter 9. Detailed investigations of PDFs in quartz, using optical microscope and universal-stage, are reported in the publication chapter 5 and 7 for samples from the Bosumtwi. In this section I report on transmission electron microscope (TEM) observations of PDFs, as PDFs cannot be clearly resolved under the optical microscope. The TEM was used for the characterization of the microstructure of PDFs in quartz grains from suevite (sample KR8-006; depth: 240.36 m) and meta-graywacke (sample KR8-032; depth: 274.99 m) from the Bosumtwi crater, and compared with observations made on a quartz grain with one PDF set of a suevite sample from the Chesapeake Bay crater (CB6-097; depth: 1412.8 m).

The PDFs occurring in samples from the Bosumtwi are generally decorated with tiny fluid inclusions or bubbles which greatly facilitate their detection at the scale of the optical microscope (see Figure 10-14a). Similar decorated PDFs are observed in rocks from many other impact structures, such as in impactites from the ~74 Myr old Manson crater (see Figure 10-14b).

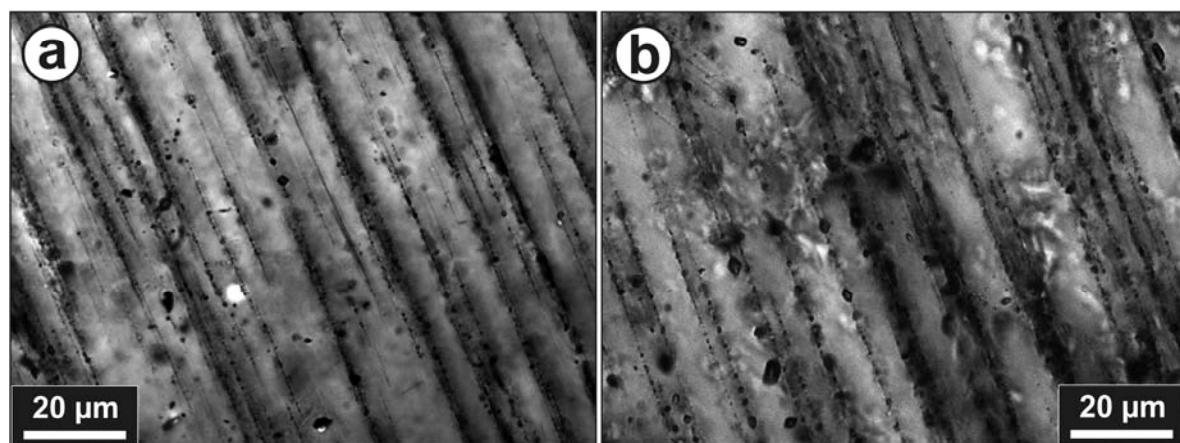


Figure 10-14. Optical microphotographs (in plane-polarized light) of decorated PDFs. a) One set of decorated (with numerous tiny fluid inclusions) PDFs in a quartz grain from a meta-graywacke sample from the Bosumtwi crater (KR8-056; depth: 326.78 m); b) Decorated PDFs in a quartz grain from a granite clast in impact breccia from the Manson crater (sample M8-516.3).

Decorated PDFs are considered secondary features, in which the decorations formed by post-shock annealing and aqueous alteration of non-decorated amorphous PDFs. Fluids can be initially dissolved in the amorphous PDFs and then, during recrystallization of the glass, fluids are pushed out in the form of tiny bubbles (e.g., Goltrant et al., 1991; Leroux and Doukhan, 1996; Leroux, 2005). The fluid inclusions or voids typically display negative

crystal shapes, with a maximum diameter observed of $\sim 1 \mu\text{m}$ in PDFs from the Bosumtwi (see Figure 10-15), and a maximum size of about $0.5 \mu\text{m}$ in PDFs from the Chesapeake Bay impact structure (see Figure 10-16).

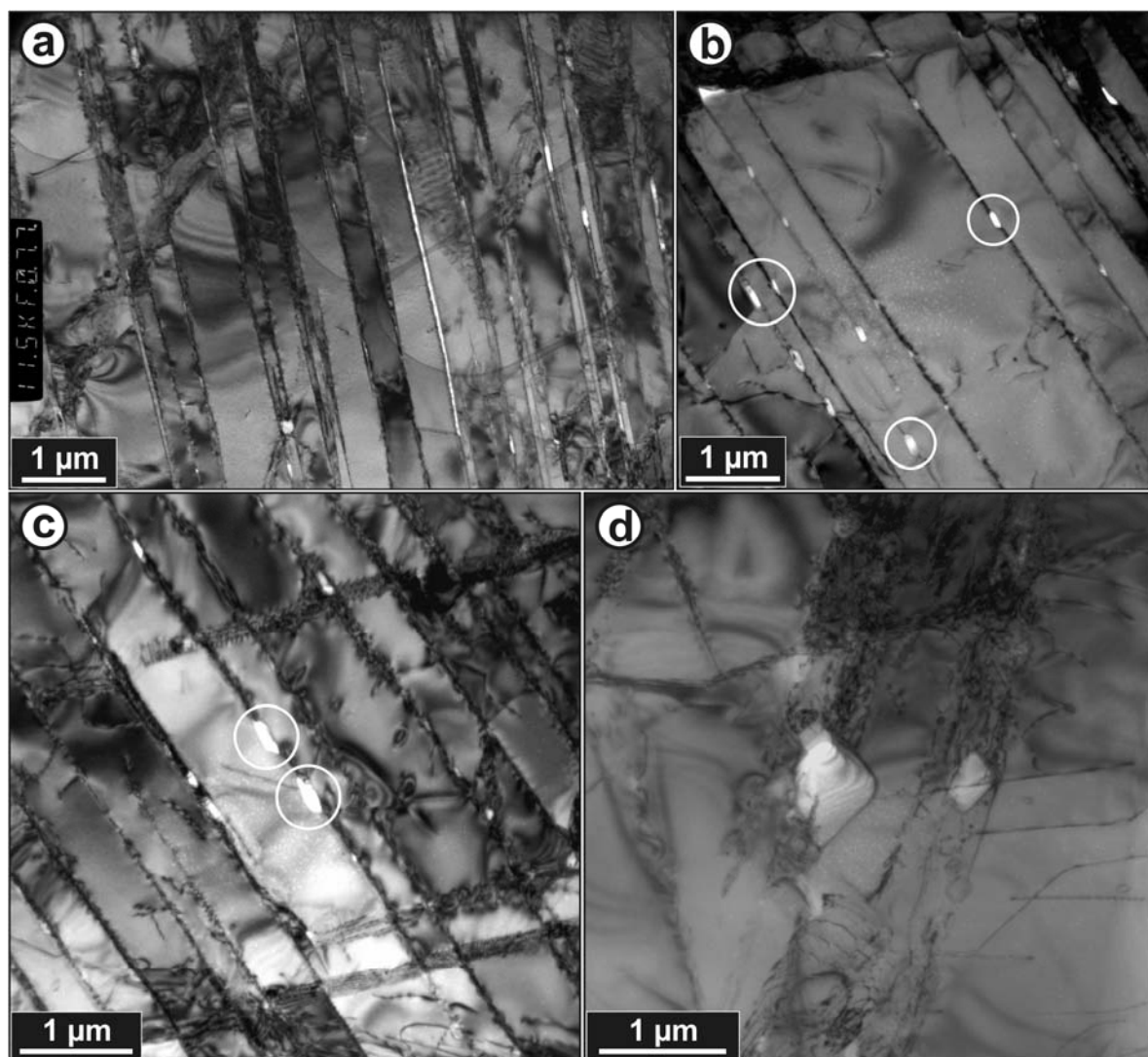


Figure 10-15. TEM bright field photomicrographs of PDFs in quartz. a) General view of one set of irregularly spaced PDFs. Note that the light gray network shown in the background corresponds to the carbon net supporting the specimen; b) One set of decorated (elongated fluid inclusions appear in white) PDFs. Note that PDF planes are irregularly spaced and the presence of dislocation loops; c) Two sets of PDFs with a high density of tiny defects, including dislocations and fluid inclusions; d) Closer view of two inclusions (white in the figure) showing the typical negative crystals shape. A large number of dislocations are also visible; Images (a-c) are from a quartz grain from a quartzite clast in a suevite sample (KR8-006) and image (d) is from a quartz grain from a meta-greywacke sample (KR8-032); both samples are from the Bosumtwi crater.

The PDF planes observed in Bosumtwi samples have a thickness of generally less than $0.1\text{-}0.2 \mu\text{m}$ and spacing between the planes varies from less than $1 \mu\text{m}$ to up to $2 \mu\text{m}$ (Figure 10-15). The PDF planes microstructure consists of a high density of tiny defects, including dislocations and fluid inclusions. Surprisingly, no amorphous phase was detected along the PDF planes. Traditionally, in young impact structures, such as at Meteor Crater,

PDFs consist of amorphous silica (e.g., Kieffer et. al, 1976). In addition, one plane of PDF almost totally dissolved was observed in the meta-graywacke sample (Figure 10-17).

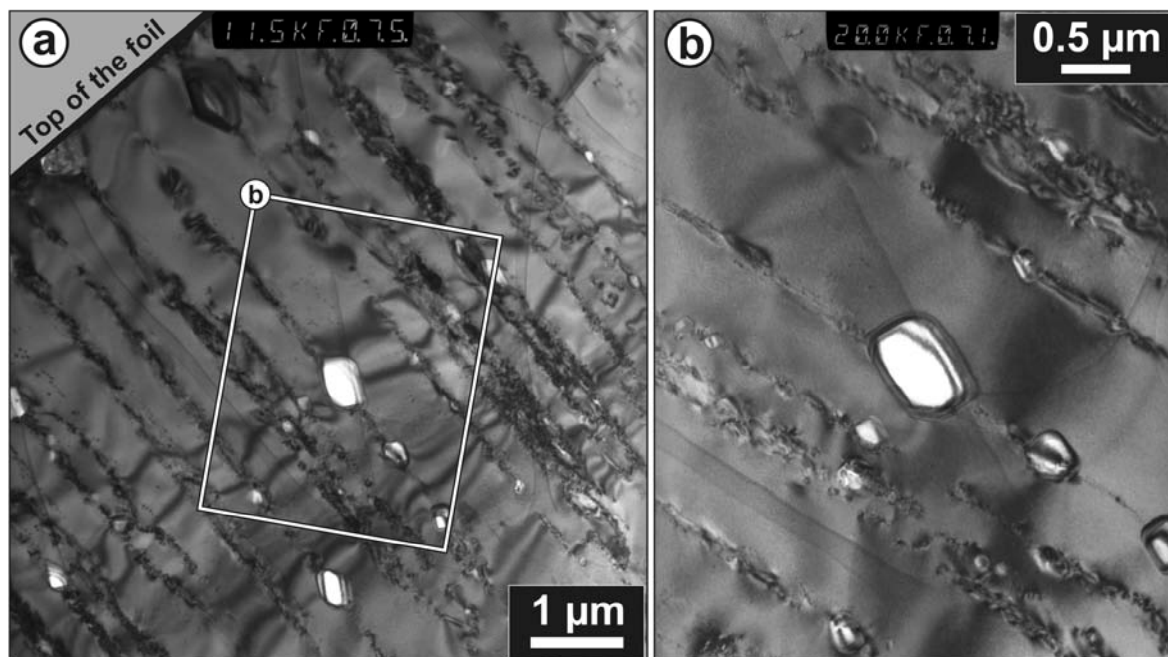


Figure 10-16. TEM bright field photomicrographs of one PDF set in a quartz grain from a suevite sample from the Chesapeake Bay crater (CB6-097). a) General view of the PDF planes which show a high dislocation density and numerous tiny fluid inclusions. b) Enlarged part of the general view (a) showing the typical negative crystals shape of the inclusions (white in the figure). Note that no amorphous phase occurs along the planes. The light gray network shown in the background corresponds to the carbon net supporting the specimen.

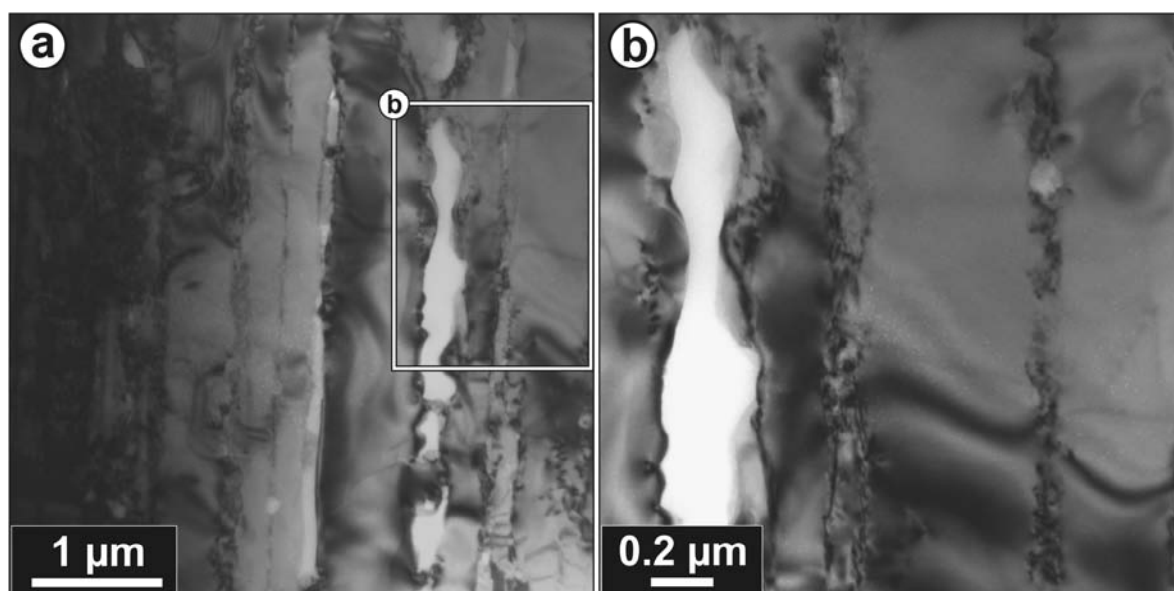


Figure 10-17. TEM bright field photomicrographs of one PDF set in a quartz grain from a meta-graywacke sample from the Bosumtwi crater (sample KR8-032). a) General view; note that one PDF plane is in part dissolved on the right side of the photograph. b) Enlarged part of the general view (a) showing the total dissolution of one lamella and the large density of tiny defects (i.e., dislocations and tiny inclusions) in the other PDF planes visible on the right side of the photograph. Note that the dissolution of the originally amorphous lamellae is indicative of post-impact fluid circulation.

This unusual observation indicates that the Bosumtwi samples were subject to post-impact hydrothermal alteration, with circulation of somewhat “acid” fluids. In comparison, the PDFs, in suevite samples from the Chesapeake Bay structure are represented by planes of high dislocation density and decorated with tiny fluid inclusions (Figure 10-16). The space between PDF planes is generally inferior to 1 μm . The PDFs in the investigated quartz grain did not show any amorphous silica along the rhombohedral planes; the original amorphous phase is totally recrystallized, as for the PDFs from the Bosumtwi crater.

During the TEM observations of PDFs from the Bosumtwi crater, some “micro-fault”-like dislocations, very similar to the ones observed in PDFs from the Charlevoix crater (Goltrant et al., 1992 [Fig. 1]), were detected within PDF planes (Figure 10-18a). Such type of dislocations is particularly interesting, as they occur within PDF planes and, thus, were developed after (re)-crystallization of the originally amorphous material. In addition, elastic deformations were observed along PDF planes in a quartz grain from the meta-greywacke sample from the Bosumtwi (see Figure 10-18b).

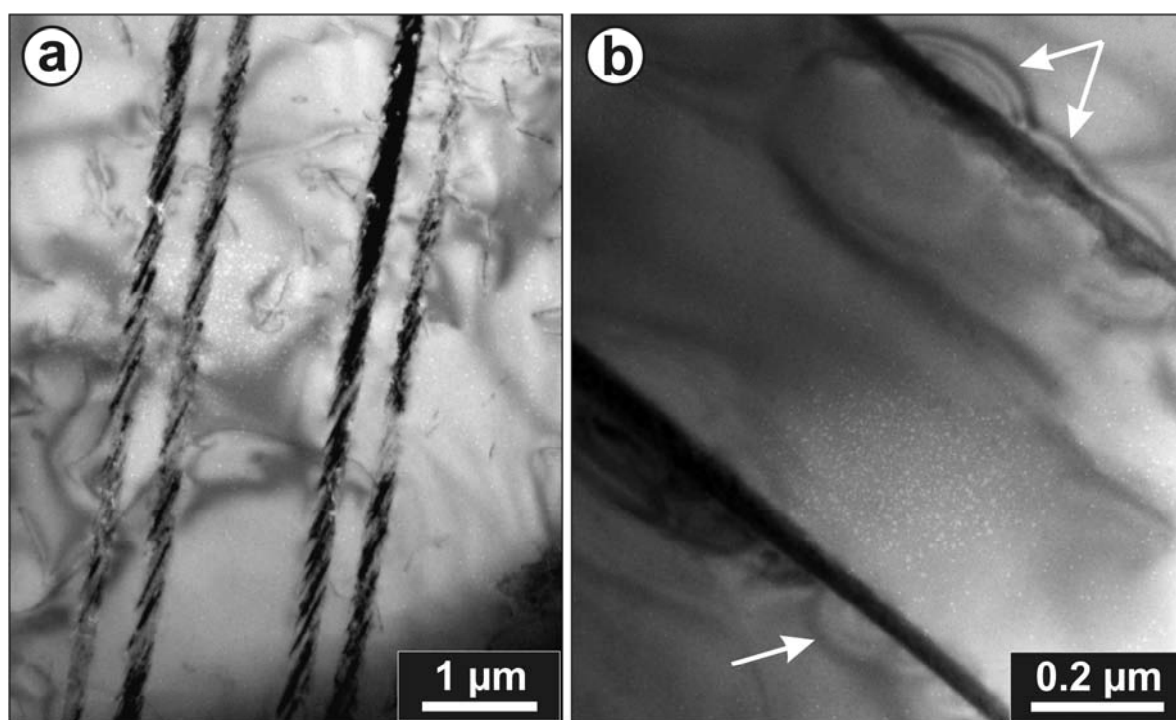


Figure 10-18. TEM bright field photomicrographs of dislocations and deformations within and/or associated with PDFs in quartz grains. a) PDF planes with dislocations (dark lines within the PDFs) in a quartz grain from suevite (sample KR8-006); b) Elastic deformations (arrows) along PDF planes in a quartz grain from a meta-greywacke sample (KR8-032). Note that tiny white spots visible in the middle of the photograph represent electron-beam-induced amorphization of quartz.

Altogether, these TEM observations show that PDFs planes, in quartz from the Bosumtwi suevite and meta-graywacke samples, are defined by dislocations and tiny fluid inclusions (or voids) resulting from the recrystallization of the originally amorphous planes. Thus, as already suggested in the chapter publications 5 and 6, based on petrographic and geochemical investigations, it is clear that the Bosumtwi samples, recovered on the outer flank of the central uplift, were subjected to intense hydrothermal alteration. Our

preliminary TEM observations of PDF planes, with high dislocation density and numerous tiny fluid inclusions, in samples from the 35.3 Myr old Chesapeake Bay crater, also support this hypothesis of fluid circulation in impactites. However, considering the age of the Bosumtwi crater, only 1.07 Myr old, and the abundant decorations of the PDFs, as well as the absence of amorphous phases in the PDF planes, a water-rich metasedimentary target environment might also have accelerated post-impact recrystallization and annealing of the PDFs (see publication chapter 5 and Morrow, 2007).

10.4. “Toasted” quartz in impactites – Origin revisited:

Quartz is one of the most abundant mineral found in rocks at the Earth's surface. Viewed under plane-polarized light with a petrographic microscope, quartz is clear (i.e., transparent) and does not show any cleavage. When viewed in cross-polarized light, quartz displays typically gray to white interference colors. It is now well established that quartz (as other minerals) is deformed and transformed when subject to strong shock waves, as during the impact of a high-velocity projectile. Shock-induced deformations and transformations in quartz include changes in refractive indices, planar fractures (PFs), planar deformation features (PDFs), high-pressure polymorphs (such as coesite and stishovite), diaplectic glass, and fused glass (i.e., lechatelierite). These features are mainly formed during the compression phase of shock waves. However, melting (formation of lechatelierite) and vaporization are temperature dominated processes, which take place during the decompression phase (Langenhorst, 2002). These shock-metamorphic effects have been intensely investigated during the last forty years (see chapter 2 for a review), and shock experiments have permitted to calibrate them as function of pressure. Calibration in terms of temperatures involved is more difficult and not well constrained yet.

A distinctive feature, the called “toasted” quartz (Short and Gold, 1996), which has been so far only reported in rocks produced by shock metamorphism (i.e., impactites), is possibly related to post-shock temperatures, but after investigations by Short and Gold (1996) and by Whitehead et al. (2002), the exact formation mechanism of “toasted” quartz is still unclear. In the intent to provide an up-to-date assessment on this very unique feature, hundreds of thin sections (mostly from the Stöffler's collection) of samples from several known impact structures were scanned under optical microscope. In addition, detailed investigations of rock thin sections from the Bosumtwi and the Chesapeake Bay impact structures were performed using optical and electron microscopy, as well as electron microprobe.

10.4.1. *Previous work*

As already mentioned in chapter 2, the term “toasted” quartz is used to describe quartz grains showing an orange-brown to grayish-reddish brown appearance (Short and Gold, 1993). Such type of quartz is considered to be a post-shock feature, probably the result of “hydrothermal or other post-shock modification” as mentioned by Short and Gold (1996), or resulting of “the exsolution of water from glass, primarily along PDFs, during heat-driven recrystallization”, after Whitehead et al. (2002). Whitehead et al. (2002) noted that “no compositional origin for the browning is evident” and they concluded that the brownish appearance of quartz is caused by a high proportion of very tiny fluid inclusions that are principally located along decorated PDFs. Whitehead et al. (2002) provided also a listing of the impact structures at which toasted quartz have been observed.

10.4.2. *Results and Discussion*

In addition to the 15 impact structures listed by Whitehead et al. (2002) in which toasted quartz have been observed, eleven further craters were added, based on optical

microscopic investigations and updated with the recent published literature in which toasted quartz were reported (see Table 10-3). In addition, the type of rocks in which the toasted grains were observed was also indicated. Some microphotographs of quartz grains toasting in impactite samples from the Chesapeake Bay and Bosumtwi craters are shown in Figure 10-19.

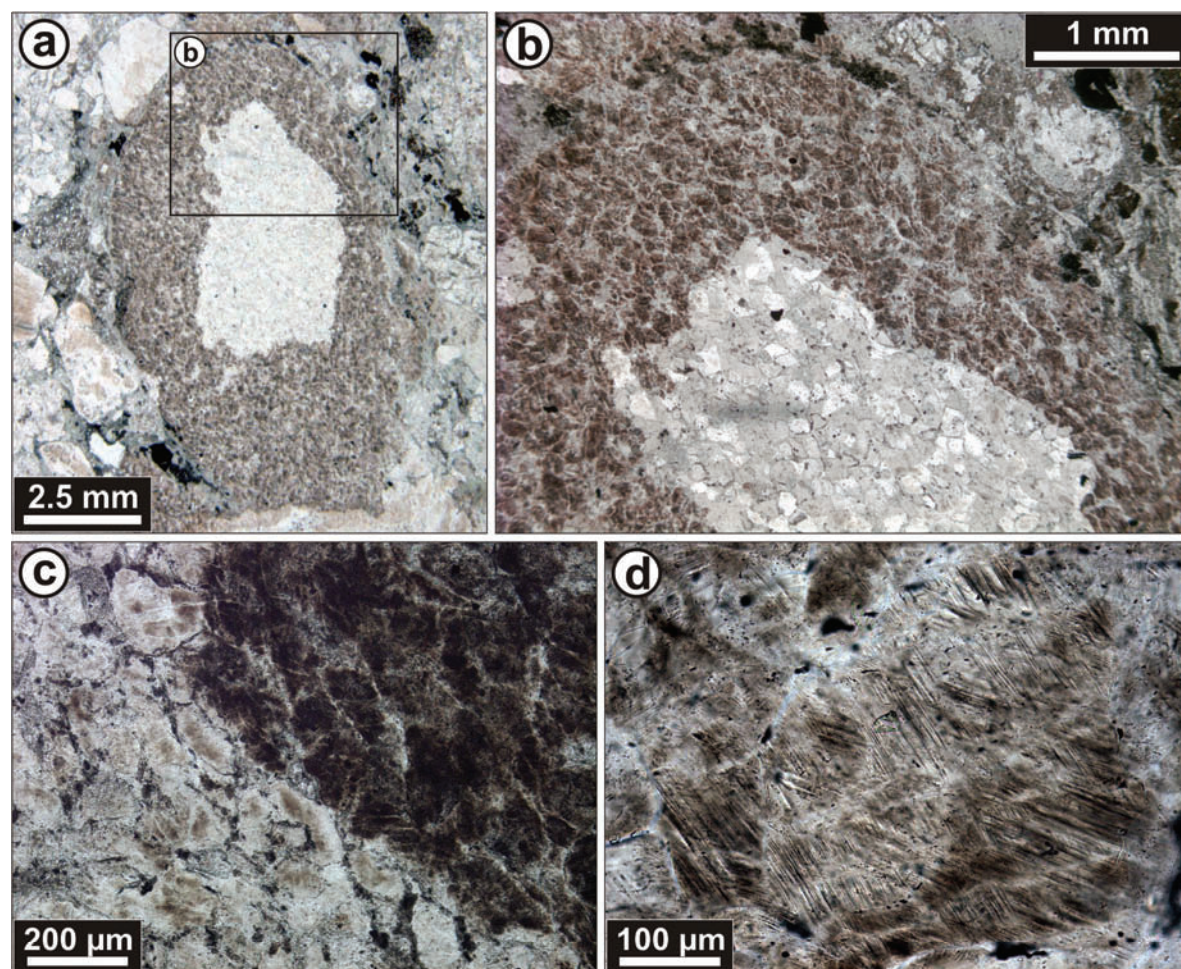


Figure 10-19. Microphotographs (in plane-polarized light) of quartz grains toasting in impactite samples from the Chesapeake Bay (a-c) and Bosumtwi (d) craters. a) General view of a partially toasted sandstone clast in a conglomerate sample from the Chesapeake Bay crater (CB6-125b; depth: 1522.72 m). Note that only the quartz grains from the rim of the sandstone clast are toasted; b) Enlarged part of the general view (a) showing the sharp margin between toasted and untoasted area; c) Closer view of a toasted region (upper right side of the photograph) and untoasted region of a sandstone clast. Note that where the toasting is extreme, quartz grain is quasi opaque; d) Toasted quartz grain with two PDF sets in a quartzite clast in a suevite sample (KR8-006; depth: 240.36 m).

Toasted quartz grains were observed in various lithologies, mainly in impact melt rocks and suevite samples, within lithic rock and mineral clasts, but also in some quartzite, sandstone, and granitoid samples (see Table 10-3). At the Bosumtwi crater, toasting occurs in “up to 41% by volume of the grains” in impact breccia samples recovered in the deep crater moat (Morrow, 2007), and about 20 rel%, on average, of the shocked quartz grains from the basement meta-graywacke samples, are toasted (see publication chapter 7).

Table 10-3. Impact structures at which toasted quartz grains have been observed so far.

Structure name	Location	Diameter (km)	Age (Ma)	Host rock	Reference(s) and notes
Aorounga	Chad	12.6	< 345	orthoquartzite	Koeberl et al. (2005); this study [quartz grains are only slightly toasted]
Boltysh	Ukraine	24	65.17 ± 0.64	migmatite	this study
Bosumtwi	Ghana	10.5	1.07	suevite; polymict lithic breccia; meta-graywacke (i.e., target rocks)	e.g., Ferrière et al. (2007); Morrow (2007); this study
Brent [†]	Ontario, Canada	3.8	396 ± 20		Short and Gold (1996)
Charlevoix [†]	Quebec, Canada	54	342 ± 15		Whitehead et al. (2002)
Chesapeake Bay	Virginia, U.S.A.	85	35.5 ± 0.3	suevite; conglomerate (i.e., clast in impact breccia)	e.g., Bartosova et al. (2007); this study
Clearwater East [†]	Quebec, Canada	26	290 ± 20		Whitehead et al. (2002)
Clearwater West [†]	Quebec, Canada	36	290 ± 20		Whitehead et al. (2002)
Houghton [†]	Numavut, Canada	23	39		Whitehead et al. (2002)
Ilynets	Ukraine	8.5	378 ± 5	impact melt rock	this study
Lappajärvi [†]	Finland	23	73.3 ± 5.3		Whitehead et al. (2002)
Manicouagan [†]	Quebec, Canada	100	214 ± 1		Whitehead et al. (2002); this study
Manson [†]	Iowa, U.S.A.	35	73.8 ± 0.3		Short and Gold (1996); this study
Mistastin [†]	Labrador, Canada	28	36.4 ± 4		Whitehead et al. (2002)
Paasselkä	Finland	10	< 1800	impact melt rock	Schmieder et al. (2008)
Popigai [†]	Russia	100	35.7 ± 0.2	impact melt rock	Whitehead et al. (2002); this study
Puhez-Katunki	Russia	80	167 ± 3	impact breccia dikelet; amphibolite	this study
Ries [†]	Germany	24	15.1 ± 0.1	suevite (in gneiss clasts)	Short and Gold (1996); this study
Rochechouart [†]	France	25	214 ± 8	suevite	Whitehead et al. (2002); this study
Santa Fe	New Mexico, U.S.A.	6-13	< 1200		Fackelman et al. (2008) ["inclusion patches within quartz grains, which appear in part toasted"]
Shoemaker (Teague)	Australia	30	1630 ± 5	granitoid	Pirajno et al. (2003) ["toasted quartz, characterized by a brownish, dirty, speckled appearance"]
Steen River [†]	Alberta, Canada	25	91 ± 7		Short and Gold (1996)
Ternovka (Terny)	Ukraine	11	280 ± 10		this study
Upheaval Dome	Utah, U.S.A.	10	< 170	sandstone	Buchner and Kenkmann (2008) [one grain is described with a "brownish staining of its rim"]
Wanapitei [†]	Ontario, Canada	7.5	37.2 ± 1.2		Whitehead et al. (2002)
West Hawk [†]	Manitoba, Canada	2.44	351 ± 20		Short and Gold (1996)

Impact structures in bold are those for which thin sections were investigated for this study. [†]structures for which toasted quartz were reported in Short and Gold (1996) and Whitehead et al. (2002). Diameter and age data from Earth Impact Database (2008).

Based on detailed investigations of the properties of ~9000 quartz grains in eighteen meta-graywacke samples, it appears that the relative abundances of quartz grains with decorated PDFs and of those with toasted appearance indicate a relatively good correlation ($r = 0.80$; see publication chapter 7). Quartz grains are in part (i.e., only locally) or totally toasted (Figure 10-19d). Even though commonly, as also noted by Morrow (2007), toasted appearance occurs in close association with PDFs, frequently, some toasted quartz grains are barren of any shock-induced PDFs (i.e., no PDFs are detected, either under optical microscope or using universal-stage).

Concerning the toasting of sandstone clasts in samples from the Chesapeake Bay, when partially toasted, only the marginal part of the clast is toasted (Figure 10-19). In contrast, for quartz veins, generally, the inner part of the vein is toasted, whereas the marginal part of the vein is untoasted. For single quartz grains occurring in the matrix of either suevite or impact melt rock samples, marginal, partial, or complete toasting of the grain is observed.

Microprobe examination of the textural and chemical relations of toasted quartz has been performed on a partially toasted sandstone clast in a conglomerate sample from the Chesapeake Bay crater (sample CB6-125b; depth: 1522.72 m). The microprobe study reveal that abundant “vesicles” or “cavities”, with sizes typically from less than 1 μm and up to about 5 μm , occur at the surface of the toasted quartz. Backscattered electron (BSE) images showing the typical vesicular texture (or sponge-like texture) of toasted quartz are shown in Figure 10-20. There is also a tendency that highly toasted regions have a higher volume proportion of vesicles than slightly toasted regions. In addition, in respect to make sure that any geochemical difference occurs between toasted and untoasted quartz, X-ray mapping, as well as high precision and sensitivity spots analysis with a beam diameter of 5 μm (and beam current of 80 nA), were performed. Clearly, as noticeable on the X-ray map of aluminum concentration (Figure 10-20d), the Al content is significantly lower in toasted than in untoasted quartz. On average, Al content is about 5 to 6 times lower in toasted than in untoasted quartz, of ~200 ppm and ~1150 ppm, respectively (Table 10-4; Figure 10-21). Similarly, Na and Ca contents are, on average, about 1.8 and 1.6 times, lower in toasted than in untoasted quartz. In contrast, the Fe content is 2 times higher in toasted than in untoasted quartz. For the other investigated elements, Ti and Mg, respectively, the content was below detection limit in both types of quartz (Table 10-4). In addition, a very strong positive linear correlation is observed between the content in Al, Ca, and Na in untoasted quartz, while only a weak correlation is observed for the content of the same elements in toasted quartz (Table 10-4). This indicates that the content of these elements, which covary together in untoasted quartz, have been heterogeneously substituted from the quartz’s structure during the process that is responsible for the formation of toasted quartz.

Quartz is normally composed of 100% SiO_2 , but small amounts of, e.g., Al, Ti, Fe, Mn, Mg, Ba, Na, Ca, K, and Li can occur (see, e.g., Deer et al., 2004). Those trace elements are mainly structurally bounded within quartz (e.g., cations replacing Si in the silicate tetrahedral and cations squeezed into the lattice) and/or can also be bounded to fluid or mineral inclusions (see, e.g., Götze et al., 2004; and references therein). Thus, based on the microprobe results, it seems that some of the trace elements, originally present in quartz, mostly Al (the dominant trace element in the investigated quartz), were expelled from the

quartz lattice (and/or from inclusions in the quartz) during the formation of toasted quartz. As a result of the expelling of the trace elements, and possibly of fluid (and/or gas phases) inclusions, which were originally occurring in quartz, vesiculation is induced. Toasted quartz may, thus, represent the beginning of quartz breakdown due to heating. Very similar texture, as shown on the BSE images (Figure 10-20), are observed for sinter (i.e., material heated just below its melting point; see, e.g., Coble, 1964 [Fig. 4]).

The orange-brown to grayish-reddish brown appearance of toasted quartz is, however, as already suggested by Whitehead et al. (2002), most probably caused by an increase in light scattering due to the numerous vesicles occurring in toasted quartz. It is unlikely that the minor differences in chemical composition, as observed between toasted and untoasted quartz, can be at the origin of the brownish hue of toasted quartz.

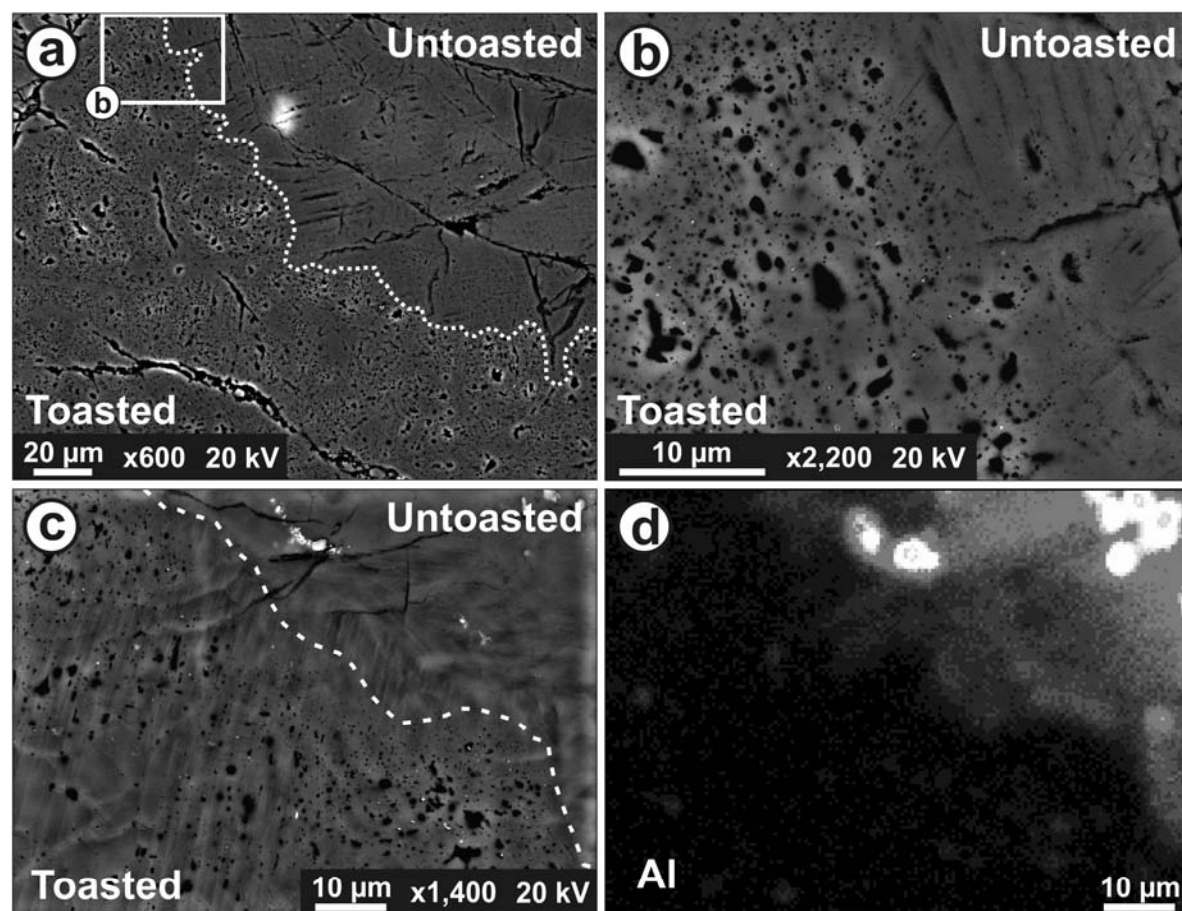


Figure 10-20. Backscattered electron (BSE) images (a-c) and mapping of aluminum concentration (d), performed with electron microprobe, of toasted and untoasted regions in quartz. a) General view of a toasted region (lower left side of the image) and untoasted region. The limit between both regions is indicated with a dashed line. Note the abundant tiny vesicles in the toasted quartz; b) Enlarged part of the general view (a) showing the difference of texture between toasted and untoasted areas. The toasted quartz displays a vesicular texture or sponge-like texture. A few PDF planes are barely visible in the untoasted region; c) Similar view as shown in (a) and (b) for comparison with X-ray mapping of the same area shown in (d). One set of PDFs is visible, especially on the lower left side of the image; d) The untoasted region (upper right side of the image) show a higher aluminum concentration than the toasted area. Note that the white spots represent Al-rich tiny inclusions; Sample CB6-125b (depth: 1522.72 m), sandstone clast in a conglomerate from the Chesapeake Bay crater.

Table 10-4. Average chemical composition of toasted and untoasted quartz (ppm unless otherwise indicated). Limits of detection are indicated. Some correlation coefficients are also reported.

	Untoasted quartz (n = 20)	Toasted quartz (n = 25)	Detection limit
Al	1149	203	25
Mg	b.d.	b.d.	21
Fe	65	129	32
Ca	238	153	20
Ti	b.d.	b.d.	32
Na	307	171	28
Si (wt%)*	46.75	46.75	N.A.
O (wt%)*	53.25	53.25	N.A.
<i>r</i> (Al vs. Na)	0.94	0.72	N.A.
<i>r</i> (Al vs. Ca)	0.98	0.68	N.A.
<i>r</i> (Na vs. Ca)	0.92	0.72	N.A.

n = number of analyses; b.d. = below detection limit; *fixed value; N.A. = not applicable; *r* = correlation coefficient.

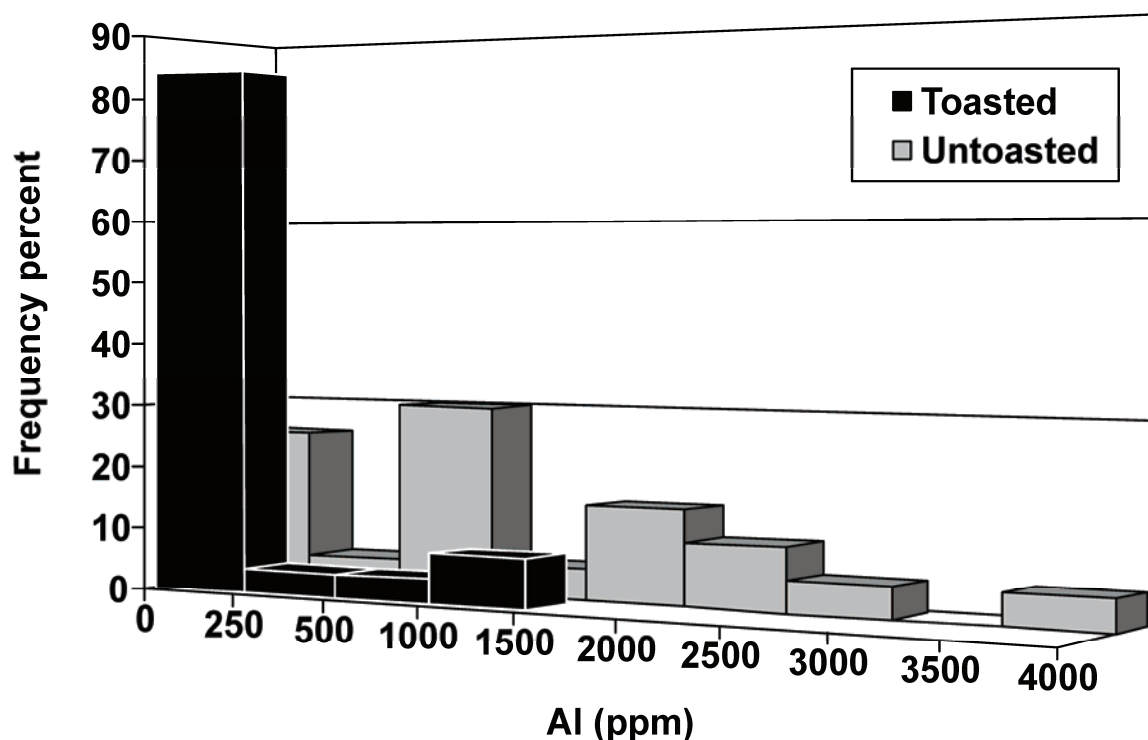


Figure 10-21. Frequency distribution of the aluminum content in toasted (in black) and untoasted quartz (in grey), based on 25 and 20 microprobe analyses, respectively. Note that most of the toasted quartz grains investigated show a lower aluminum content than untoasted grains.

10.4.3. Conclusions

The present study confirms the finding of Whitehead et al. (2002) that toasted quartz contain a high proportion of small vesicles and that these vesicles enhance scattering of transmitted light. However, the vesicles observed in toasted quartz, with highly variable

sizes (from less than 1 μm and up to about 5 μm), are not related to recrystallization of the PDF glass, as suggested by Whitehead et al. (2002). As shown in Figure 10-19, in some sandstone clasts, only the marginal part of the clast is toasted, whereas most of the quartz grains of the clast are shocked, and thus, it would be difficult to explain that only the PDFs occurring in the marginal part of the clast were recrystallized and not the others.

More interestingly, microprobe investigations have shown that some trace elements (and inclusions), originally present in quartz (such as Al), were expelled from the quartz's structure. Therefore, toasted quartz is formed by vesiculation after pressure release, at high post-shock temperatures, and, thus, it represents the beginning of quartz breakdown due to heating.

10.5. New observations of ballen quartz and cristobalite:

Ballen silica, with either α -quartz or α -cristobalite structure, are more or less spheroidal, in some cases elongate, bodies (with sizes up to $\sim 200\ \mu\text{m}$), which occur as independent clasts or within diaplectic quartz glass or lechatelierite inclusions (see Figure 10-22). A review on ballen silica is presented in the publication chapter 8. This section includes only new observations of ballen quartz and cristobalite using optical and transmission electron microscope (TEM), as well as microRaman for the identification of the different polymorphs of silica. Most of the new optical microscopic observations were performed on thin sections from the Stöffler's collection. Furthermore, one focused ion beam (FIB) foil cut across two ballen (one ballen of α -cristobalite and α -quartz structure) occurring within the same silica inclusion, was studied using TEM.

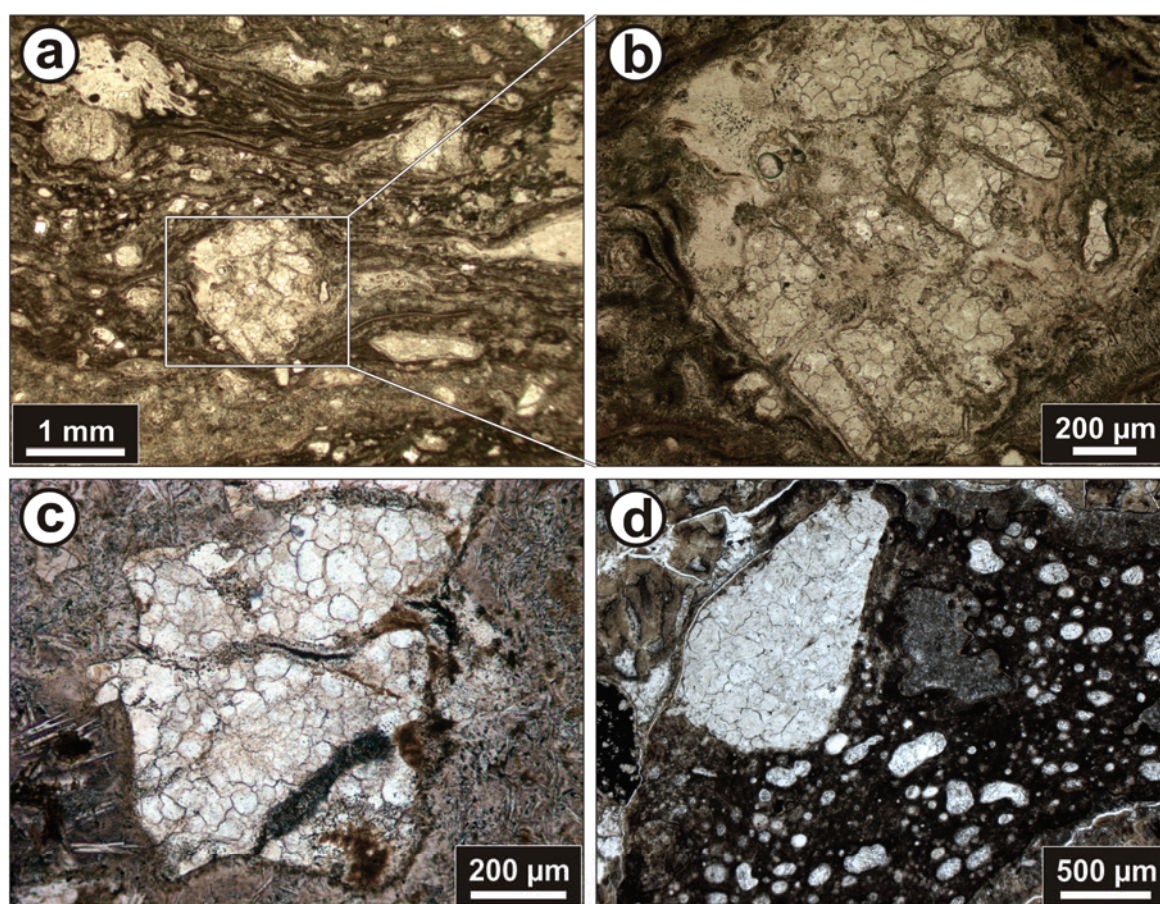


Figure 10-22. Microphotographs of ballen quartz in different petrographic contexts (all microphotographs in plane-polarized light). a) General view of melted clasts (mostly lechatelierite) in a well-defined fluidal glassy matrix (sample RD_01, from Mien crater). b) Enlarged part of (a) showing a porphyroclast with a core that displays typical ballen quartz and tail edges made of feldspar glass. c) Ballen quartz in a lechatelierite clast in a fine-grained melt matrix of impact melt rock from Mien crater. Note the occurrence of a darker (brownish), “glass-rich” halo, surrounding the clast of ballen quartz (sample Mien-02). d) Clast of ballen quartz (center left) in a silicate melt fragment from the lower sorted suevite of the Chicxulub crater (sample Yax-1_808.87 m).

In addition to the 28 impact structures listed in the publication chapter 8 (Table 1) from which ballen silica have been described, ballen were observed and characterized in

impact melt rock from the Logoisk (ballen of types I, II, and III) and Puchezh-Katunki (ballen of types III, IV, and V) craters. Additionally, the presence of ballen silica was recently reported in impactites from the Roter Kamm crater (Hecht et al., 2008) and possibly in some samples from the Wabar crater (M. Schmieder, pers. comm.).

Using both, optical microscope and microRaman, the characterization of the different types of ballen silica was possible for ballen occurring in impact melt rock from Dellen (types I-IV) and from El'gygytgyn (type I), in cryptocrystalline melt breccia from Jänisjärvi (types III and IV) and from Sääksjärvi (types II-V), in impact melt rock from Ternovka (types III and IV), and in glassy impact melt rock from Wanapitei (types I-V) craters. Surprisingly, no coesite inclusions were observed within α -cristobalite ballen (type I) from these impact structures. However, interestingly, cristobalite ballen (type I) were observed together with ballen quartz (types II and III), associated in the same inclusions, in impact melt rocks from Wanapitei and from Popigai craters (Figure 10-23). Additionally, some of the ballen α -quartz from the Popigai crater display a “toasted appearance” (ballen α -cristobalite associated within the same inclusions are not “toasted”; see Figure 10-23).

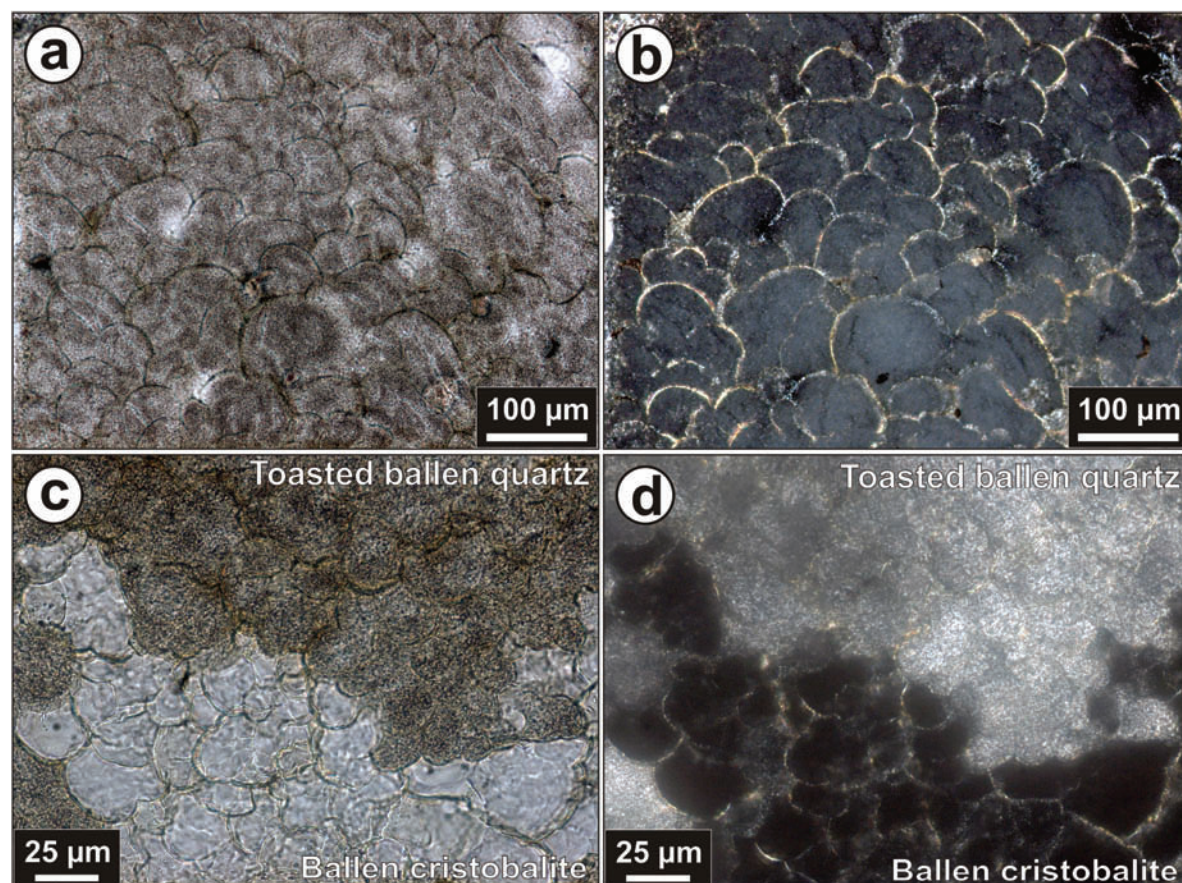


Figure 10-23. Microphotographs of toasted ballen α -quartz and α -cristobalite ballen in impact melt rock from the Popigai crater (sample B99_7-98). (a) Plane-polarized light and (b) cross-polarized light of toasted ballen α -quartz. (c) Plane-polarized light and (d) cross-polarized light of toasted ballen α -quartz (type II) associated with α -cristobalite ballen (type I) in the same lechatelierite inclusion.

“Toasted” ballen quartz was also observed for the first time in impactites from the Rochechouart, Sääksjärvi, and Ternovka craters. Previously, ballen with a “toasted

appearance”, were only reported from Popigai (Whitehead et al., 2002), from Wanapitei (Dressler et al., 1997), and from Dhala (Pati et al., 2008) craters. Raman spectroscopy investigations of these “toasted” ballen show only the typical α -quartz signature. Using SEM, a somewhat similar, vesicular texture, as is present in typical toasted quartz (see previous section; Figure 10-20), was observed.

The TEM investigations of ballen silica in Mien impact melt rock (see Figure 10-24) confirm that α -cristobalite ballen are composed of numerous tiny individual crystals, as already reported in publication chapter 8 for ballen α -cristobalite from the Bosumtwi crater.

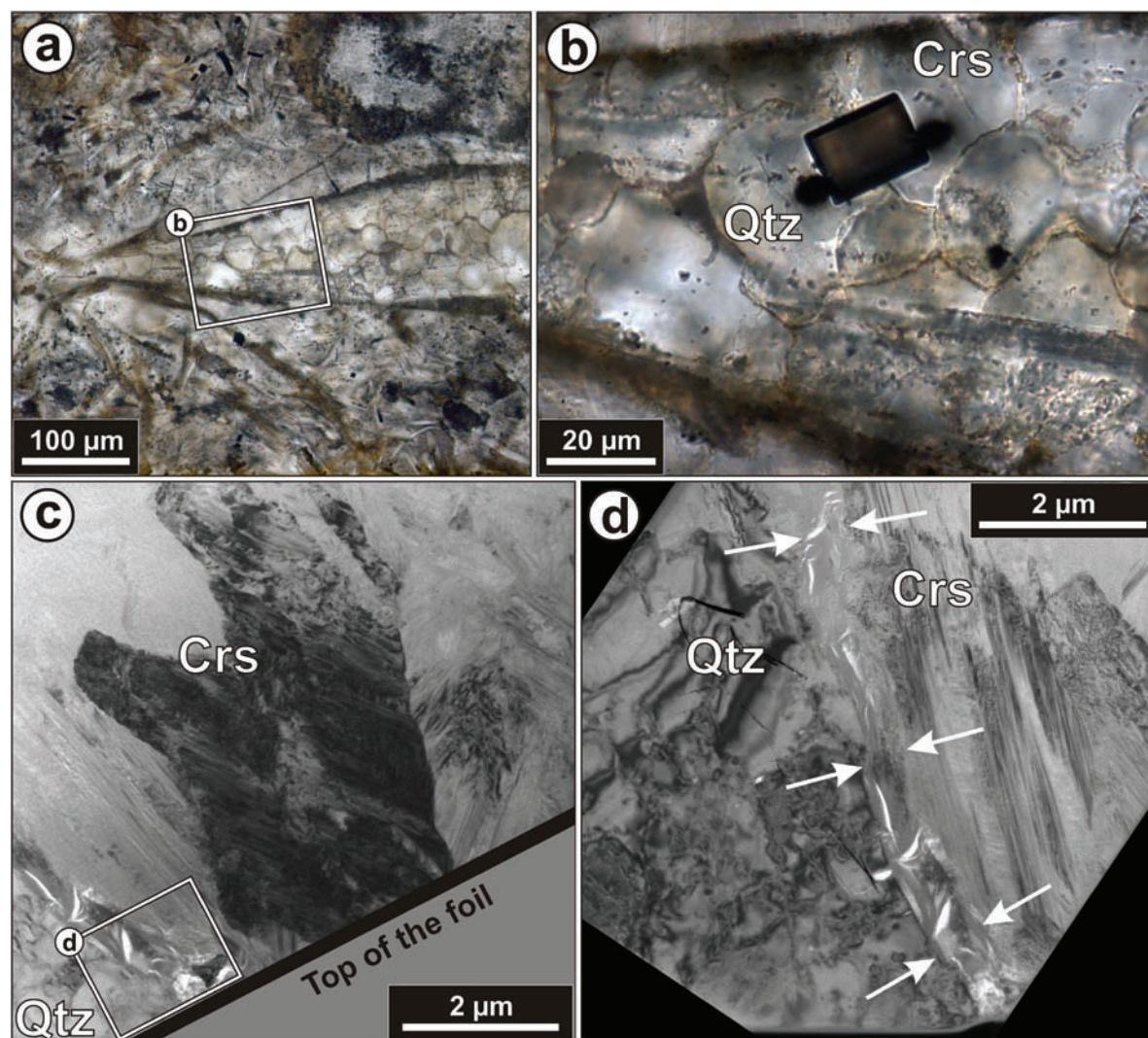


Figure 10-24. Optical microphotographs (a, b; in plane-polarized light) and TEM bright field photomicrographs (c, d) of ballen silica in impact melt rock from the Mien crater (sample Mien-02). a) Microphotograph showing ballen quartz and cristobalite in a lechatelierite clast in a fine-grained melt matrix. b) Enlarged part of the general view (a) showing the exact location of the FIB preparation of the TEM foil. Note that the two ballen in contact are made of different polymorphs of silica, as one is made of α -quartz (Qtz) and the other of α -cristobalite (Crs). c) General view of a part of the prepared TEM foil showing a portion of the α -cristobalite ballen with a large crystal (in dark) and the contact zone between ballen quartz and cristobalite (visible on the lower left side of the photograph). d) Enlarged part of the general view (c) showing fibrous material (i.e., phyllosilicates) that fills the space between the two ballen (arrows set the limits of ballen). Note the twin lamellae of the α -cristobalite crystal and the strong defects in the quartz crystal.

However, individual crystals of α -cristobalite from the Mien crater have sizes up to $\sim 6 \mu\text{m}$, whereas a maximum size of $\sim 2 \mu\text{m}$ was observed for individual crystals in ballen from the Bosumtwi crater. In addition, and for the first time, TEM observations of α -quartz ballen were performed. As for α -cristobalite ballen, α -quartz ballen are composed of numerous tiny crystals (of α -quartz) with sharp angular contacts between them. The contact zone between the investigated α -quartz and α -cristobalite ballen is marked by the occurrence of fibrous material (i.e., phyllosilicates; Figure 10-24d), which probably precipitated in interstices between individual silica ballen or resulted from the aqueous alteration of glass phases, as previously observed between ballen α -cristobalite from the Bosumtwi (see publication chapter 8).

Altogether, these observations of: a) α -cristobalite ballen occurring together with α -quartz ballen in the same inclusion, b) similar microtexture under the TEM for α -cristobalite and α -quartz ballen, and c) the occurrence of α -cristobalite ballen only in the “youngest” impact structures, confirm that α -quartz ballen are the result of back-transformation of β -quartz and/or α -cristobalite with time, as suggested by Carstens (1975), Bischoff and Stöffler (1984), and in publication chapter 8. It needs also to be considered that if α -cristobalite ballen were rapidly quenched, the conversion of α -cristobalite to α -quartz would have been inhibited. Furthermore, α -cristobalite ballen from Bosumtwi, with coesite occurring as tiny intraballen inclusions, is so far unique, as coesite was not detected in α -cristobalite ballen from any other impact structure. It is likely that with time, coesite inclusions in materials from much older structures could have been transformed back to α -quartz; note that the Bosumtwi structure is, at 1.07 Ma age, by far the youngest impact structure investigated for this study.

References

- Bartosova K., Ferrière L., Koeberl C., Reimold W. U., Gibson R., and Schmitt R.-T. 2007. Lithological, petrographical, and geochemical investigations of suevite from the Eyreville core, Chesapeake Bay impact structure (abstract). *GSA Abstracts with Programs* 39(6):A451.
- Bischoff A. and Stöffler D. 1984. Chemical and structural changes induced by thermal annealing of shocked feldspar inclusions in impact melt rocks from Lappajärvi crater, Finland. *Journal of Geophysical Research* 89:B645–B656.
- Boamah D. and Koeberl C. 2003. Geology and geochemistry of shallow drill cores from the Bosumtwi impact structure, Ghana. *Meteoritics and Planetary Science* 38:1137–1159.
- Boamah D. and Koeberl C. 2006. Petrographic studies of “fallout” suevite from outside the Bosumtwi impact structure, Ghana. *Meteoritics and Planetary Science* 41: 1761–1774.
- Buchner E. and Kenkmann T. 2008. Upheaval Dome, Utah, USA: Impact origin confirmed. *Geology* 36:227–230.

Carstens H. 1975. Thermal history of impact melt rocks in the Fennoscandian shield. *Contributions to Mineralogy and Petrology* 50:145–155.

Chang L. L. Y., Howie R. A., and Zussman J. 1998. *Non-silicates: Sulfates, carbonates, phosphates, halides*. Rock-forming minerals. Volume 5B., 2nd edition. London: The Geological Society. 383 p.

Coble R. L. 1964. Ceramic and metal sintering: mechanism of material transport and density-limiting characteristics. In *Fundamental phenomena in the material sciences*. Volume 1, Sintering and plastic deformation, edited by Bonis L. J. and Hausner H. H. New York: Plenum Press. pp. 11–23.

Coney L., Reimold W. U., Gibson R. L., and Koeberl C. 2007a. Geochemistry of impactites from ICDP borehole LB-07A, Bosumtwi impact structure, Ghana. *Meteoritics and Planetary Science* 42:667–688.

Coney L., Gibson R. L., Reimold W. U., and Koeberl C. 2007b. Lithostratigraphic and petrographic analysis of ICDP drill core LB-07A, Bosumtwi impact structure, Ghana. *Meteoritics and Planetary Science* 42:569–589.

Coplen T. B., Böhlke J. K., De Bièvre P., Ding T., Holden N. E., Hopple J. A., Krouse H. R., Lamberty A., Peiser H. S., Revesz K., Rieder S. E., Rosman K. J. R., Roth E., Taylor P. D. P., Vocke Jr. R. D., and Xiao Y. K. 2002. Isotopic abundance variations of selected elements. *Pure and Applied Chemistry* 74:1987–2017.

Dai X., Boamah D., Koeberl C., Reimold W. U., Irvine G., and McDonald I. 2005. Bosumtwi impact structure, Ghana: Geochemistry of impactites and target rocks, and search for a meteoritic component. *Meteoritics and Planetary Science* 40:1493–1511.

Deer W. A., Howie R. A., and Zussman J. 1997. *Disilicates and ring silicates*. Rock-forming minerals. Volume 1B., 2nd edition. London: The Geological Society. 629 p.

Deer W. A., Howie R. A., Wise W. S., and Zussman J. 2004. *Framework silicates: silica minerals, feldspathoids and the zeolites*. Rock-forming minerals. Volume 4B., 2nd edition. London: The Geological Society. 982 p.

Dressler B. O., Crabtree D., and Schuraytz B. C. 1997. Incipient melt formation and devitrification at the Wanapitei impact structure, Ontario, Canada. *Meteoritics and Planetary Science* 32:249–258.

Earth Impact Database 2008. <http://www.unb.ca/passc/ImpactDatabase/> (accessed 29 September 2008).

Engelhardt W. v. and Bertsch W. 1969. Shock induced planar deformation structures in quartz from the Ries crater, Germany. *Contributions to Mineralogy and Petrology* 20:203–234.

Fackelman S. P., Morrow J. R., Koeberl C., and McElvain T. H. 2008. Shatter cone and microscopic shock-alteration evidence for a post-Paleoproterozoic terrestrial impact structure near Santa Fe, New Mexico, USA. *Earth and Planetary Science Letters* 270:290–299.

Ferrière L., Koeberl C., Reimold W. U., and Mader D. 2007. Drill core LB-08A, Bosumtwi impact structure, Ghana: Geochemistry of fallback breccia and basement samples from the central uplift. *Meteoritics and Planetary Science* 42:689–708.

Ferrière L., Koeberl C., and Reimold W. U. 2007. Drill core LB-08A, Bosumtwi impact structure, Ghana: Petrographic and shock metamorphic studies of material from the central uplift. *Meteoritics and Planetary Science* 42:611–633.

Feybesse J.-L., Billa M., Guerrot C., Duguey E., Lescuyer J.-L., Milesi J.-P., and Bouchot V. 2006. The paleoproterozoic Ghanaian province: Geodynamic model and ore controls, including regional stress modeling. *Precambrian Research* 149:149–196.

Goltrant O., Cordier P., and Doukhan J.-C. 1991. Planar deformation features in shocked quartz; a transmission electron microscopy investigation. *Earth and Planetary Science Letters* 106:103–115.

Goltrant O., Doukhan J.-C., Cordier P., and Courtillot V. 1992. An investigation by transmission electron microscopy of planar deformation features in naturally shocked quartz. *Terra Nova* 4:405–412.

Götze J., Plötze M., Graupner T., Hallbauer D. K., and Bray C. J. 2004. Trace element incorporation into quartz: a combined study by ICP-MS, electron spin resonance, cathodoluminescence, capillary ion analysis, and gas chromatography. *Geochimica et Cosmochimica Acta* 68:3741–3759.

Herron M. M. 1988. Geochemical classification of terrigenous sands and shales from core or log data. *Journal of Sedimentary Research* 58:820–829.

Hecht L., Reimold W. U., Sherlock S., Tagle R., Koeberl C., and Schmitt R.-T. 2008. New impact-melt rock from the Roter Kamm impact structure, Namibia: Further constraints on impact age, melt rock chemistry, and projectile composition. *Meteoritics and Planetary Science* 43:1201–1218.

Hirdes W., Davis D. W., and Eisenlohr B. N. 1992. Reassessment of Proterozoic granitoid ages in Ghana on the basis of U/Pb zircon and monazite dating. *Precambrian Research* 56:89–96.

Karikari F., Ferrière L., Koeberl C., Reimold W. U., and Mader D. 2007. Petrography, geochemistry, and alteration of country rocks from the Bosumtwi impact structure, Ghana. *Meteoritics and Planetary Science* 42:513–540.

Kieffer S. W., Phakey P. P., and Christie J. M. 1976. Shock processes in porous quartzite: Transmission electron microscope observations and theory. *Contributions to Mineralogy and Petrology* 59:41–93.

Koeberl C., Reimold W. U., Blum J. D., and Chamberlain C. P. 1998. Petrology and geochemistry of target rocks from the Bosumtwi impact structure, Ghana, and comparison with Ivory Coast tektites. *Geochimica et Cosmochimica Acta* 62:2179–2196.

Koeberl C., Reimold W. U., Cooper G., Cowan D., and Vincent P. M. 2005. Aorounga and Gweni Fada impact structures, Chad: Remote sensing, petrography, and geochemistry of target rocks. *Meteoritics and Planetary Science* 40:1455–1471.

Langenhorst F. 2002. Shock metamorphism of some minerals: Basic introduction and microstructural observations. *Bulletin of the Czech Geological Survey* 77:265–282.

Leroux H. 2005. Weathering features in shocked quartz from the Ries impact crater, Germany. *Meteoritics and Planetary Science* 40:1347–1352.

Leroux H. and Doukhan J.-C. 1996. A transmission electron microscope study of shocked quartz from the Manson impact structure. In *The Manson impact structure, Iowa: anatomy of an impact crater*, edited by Koeberl C. and Anderson R. R. GSA Special Paper #302. Boulder, Colorado: Geological Society of America. pp. 267–274.

Leube A., Hirdes W., Mauer R., and Kesse G. O. 1990. The Early Proterozoic Birimian Supergroup of Ghana and some aspects of its associated gold mineralization. *Precambrian Research* 46:139–165.

Morrow J. R. 2007. Shock-metamorphic petrography and microRaman spectroscopy of quartz in upper impactite interval, ICDP drill core LB-07A, Bosumtwi impact crater, Ghana. *Meteoritics and Planetary Science* 42:591–609.

Pati J. K., Reimold W. U., Koeberl C., and Pati P. 2008. The Dhala structure, Bundelkhand craton, Central India – Eroded remnant of a large Paleoproterozoic impact structure. *Meteoritics and Planetary Science* 43:1383–1398.

Pettijohn F. J., Potter P. E., and Siever R. 1972. *Sand and sandstone*. New York: Springer-Verlag. 618 p.

Pirajno F., Hawke P., Glikson A. Y., Haines P. W., and Uysal T. 2003. Shoemaker impact structure, Western Australia. *Australian Journal of Earth Sciences* 50(5):775–796.

Schmieder M., Moilanen J., and Buchner E. 2008. Impact melt rocks from the Paasselkä impact structure (SE Finland): Petrography and geochemistry. *Meteoritics and Planetary Science* 43:1189–1200.

Shaw H. F. and Wasserburg G. J. 1982. Age and provenance of the target materials for tektites and possible impactites as inferred from Sm-Nd and Rb-Sr systematics. *Earth and Planetary Science Letters* 60:155–177.

Short N. M. and Gold D. P. 1993. Petrographic analysis of selected core materials from the Manson (Iowa) impact structure (abstract). *Meteoritics and Planetary Science* 28:A436–437.

Short N. M. and Gold D. P. 1996. Petrography of shocked rocks from the central peak at the Manson impact structure. In *The Manson impact structure, Iowa: anatomy of an impact crater*, edited by Koeberl C. and Anderson R. R. GSA Special Paper #302. Boulder, Colorado: Geological Society of America. pp. 245–265.

Stöffler D. and Langenhorst F. 1994. Shock metamorphism of quartz in nature and experiment: I. Basic observation and theory. *Meteoritics and Planetary Science* 29:155–181.

Taylor S. R. and McLennan S. M. 1985. *The continental crust: Its composition and evolution*. Oxford: Blackwell Scientific Publications. 312 p.

Whitehead J., Grieve R. A. F., and Spray G. 2002. Mineralogy and petrology of melt rocks from the Popigai impact structure, Siberia. *Meteoritics and Planetary Science* 37:623–647.

Whitehead J., Spray J. G., and Grieve R. A. F. 2002. Origin of “toasted” quartz in terrestrial impact structures. *Geology* 30:431–434.

Appendices

Appendix A:

Table A-1. Details of investigated samples from drill core LB-08A.

Sample no.	Depth (m)	Run number	Box number	Row number	Origin of the measurement*	Starting distance of the measurement (cm)	End distance of the measurement (cm)	Sample dimension (cm)
KR8-001	235.77	1	1	1	TB	17	22	5
KR8-002	236.40	1	1	2	TB	80	86	6
KR8-003	238.90	2	1	4	TR	25	35	10
KR8-004	239.65	2	1	5	TR	100	106	6
KR8-005	240.04	2	2	1	TB	139	146	7
KR8-006	240.36	2	2	1	TB	171	176	5
KR8-007	241.94	2	2	4	TB	329	337	8
KR8-008	244.45	3	3	4	TB	275	285	10
KR8-009	244.87	3	3	5	TB	317	332	15
KR8-010	245.58	4	4	1	TB	83	93	10
KR8-011	247.46	4	4	5	TB	271	278	7
KR8-012	248.00	5	5	1	TR	20	27	7
KR8-013	248.80	5	5	2	TR	100	108	8
KR8-014	249.30	5	5	3	TR	150	158	8
KR8-015	250.74	5	5	5	BR	294	304	10
KR8-016	250.89	6	6	1	TR	5	12	7
KR8-017	251.74	6	6	3	TR	90	98	8
KR8-018	253.04	6	6	5	TR	220	228	8
KR8-019	253.56	6	7	1	TB	272	280	8
KR8-021	255.65	7	7	5	BB	176	181	5
KR8-022	256.81	7	8	2	TB	292	300	8
KR8-023	258.14	8	8	5	TR	120	128	8
KR8-024	259.14	8	9	1	TB	220	228	8
KR8-025	259.74	8	9	2	TB	280	288	8
KR8-026	260.49	9	9	4	TR	50	58	8
KR8-027	263.76	10	10	2	TR	72	80	8
KR8-028	266.18	11	11	1	TR	10	18	8
KR8-029	271.43	12	11	5	TR	230	238	8
KR8-030	272.00	12	12	1	TB	287	292	5
KR8-031	273.99	13	12	5	BB	181	186	5
KR8-032	274.99	13	13	1	TB	281	286	5
KR8-033	277.03	14	13	5	TR	180	185	5
KR8-034	277.89	14	14	2	TB	266	271	5
KR8-035	280.30	15	15	2	TB	202	212	10
KR8-036	281.32	16	15	3	TR	0	5	5
KR8-037	283.50	16	16	2	TB	218	226	8
KR8-038	283.74	16	16	3	TB	242	250	8
KR8-039	286.17	17	17	2	TB	180	188	8
KR8-040	290.47	19	18	1	TR	0	8	8
KR8-041	293.79	20	18	5	TR	27	37	10
KR8-042	293.97	20	19	1	TB	45	53	8

*Origin of the measurement of the core sample, from the top of the box (TB), from the bottom of the box (BR), from the top of the run (TR), or from the bottom of the run (BR).

Table A-1. Continued. Details of investigated samples from drill core LB-08A.

Sample no.	Depth (m)	Run number	Box number	Row number	Origin of the measurement*	Starting distance of the measurement (cm)	End distance of the measurement (cm)	Sample dimension (cm)
KR8-043	296.94	21	19	5	BB	38	50	12
KR8-045	300.41	22	21	1	TB	80	88	8
KR8-046	303.25	23	21	5	BB	59	67	8
KR8-047	305.71	23	22	4	TB	305	313	8
KR8-048	307.30	24	23	3	TB	159	169	10
KR8-049	310.23	25	24	4	TR	147	157	10
KR8-050	310.99	25	24	5	BB	223	233	10
KR8-051	312.40	26	25	4	BB	60	65	5
KR8-052	315.75	27	26	4	BB	90	95	5
KR8-053	316.97	27	27	1	TB	212	217	5
KR8-054	320.62	28	28	3	TB	272	280	8
KR8-056	326.78	30	30	3	TB	278	283	5
KR8-057	330.08	31	31	4	TB	304	309	5
KR8-059	333.51	33	33	1	TB	37	49	12
KR8-060	337.33	34	34	1	TB	114	124	10
KR8-061	341.17	35	35	1	TB	193	198	5
KR8-062	341.86	35	35	3	BR	262	267	5
KR8-063	343.57	36	36	1	TB	129	137	8
KR8-064	348.43	38	37	4	TR	5	13	8
KR8-065	352.31	39	38	5	BB	88	93	5
KR8-066	353.95	39	39	2	TB	252	262	10
KR8-067	356.59	40	40	3	TB	211	216	5
KR8-068	359.44	41	41	3	TB	192	197	5
KR8-069	361.18	42	42	1	TB	61	71	10
KR8-070	364.12	43	43	1	TB	50	60	10
KR8-071	368.97	44	44	5	BB	230	235	5
KR8-072	370.96	45	45	3	TR	124	129	5
KR8-073	371.07	45	45	3	TR	135	140	5
KR8-074	375.24	46	46	4	TB	248	254	6
KR8-075	377.78	47	47	4	TB	197	203	6
KR8-076	379.70	48	48	2	TB	84	90	6
KR8-077	380.98	48	48	4	TB	212	217	5
KR8-078	382.17	49	49	1	TB	26	32	6
KR8-079	384.06	49	49	4	TB	215	220	5
KR8-080	384.54	49	49	5	TB	263	273	10
KR8-081	387.36	50	50	5	TR	240	246	6
KR8-082	387.78	50	51	1	TB	282	288	6
KR8-083	389.25	51	51	4	TR	125	131	6
KR8-084	390.00	51	52	1	TB	200	206	6
KR8-085	392.65	52	52	5	TR	160	170	10
KR8-086	393.07	52	53	1	TB	202	208	6

*Origin of the measurement of the core sample, from the top of the box (TB), from the bottom of the box (BR), from the top of the run (TR), or from the bottom of the run (BR).

Table A-1. Continued. Details of investigated samples from drill core LB-08A.

Sample no.	Depth (m)	Run number	Box number	Row number	Origin of the measurement*	Starting distance of the measurement (cm)	End distance of the measurement (cm)	Sample dimension (cm)
KR8-087	394.30	53	53	4	TR	20	26	6
KR8-088	395.25	53	54	1	TB	115	121	6
KR8-089	397.30	54	54	5	TR	15	21	6
KR8-090	398.80	54	55	2	TB	165	173	8
KR8-091	400.35	55	56	1	TR	15	21	6
KR8-092	403.00	55	56	5	TB	280	288	8
KR8-093	403.64	56	57	1	TR	40	48	8
KR8-094	404.18	56	57	2	TR	94	102	8
KR8-095	405.34	56	57	4	TR	210	218	8
KR8-096	406.31	57	58	2	TR	2	10	8
KR8-097	409.67	57	59	2	TB	338	346	8
KR8-098	410.74	58	59	5	TR	140	148	8
KR8-099	412.92	59	60	2	TB	358	364	6
KR8-100	412.74	59	60	3	TR	35	45	10
KR8-101	414.28	59	61	1	TB	189	197	8
KR8-102	416.84	60	61	5	TR	140	150	10
KR8-103	417.39	60	62	1	TB	195	203	8
KR8-104	417.60	60	62	2	TB	216	226	10
ADE-8a	418.05	60	62	3	BR	257	262	5
KR8-106	421.88	62	63	5	TR	35	45	10
KR8-107	422.36	62	64	1	TB	83	93	10
KR8-108	424.78	63	64	5	TR	20	30	10
KR8-109	425.24	63	65	1	TB	66	78	12
KR8-110	429.31	64	66	3	TR	168	178	10
KR8-111	432.03	65	67	3	TR	135	143	8
KR8-112	434.33	66	68	2	TR	61	67	6
KR8-113	434.59	66	68	2	TR	87	95	8
KR8-114	434.75	66	68	2	TR	103	115	12
KR8-115	437.37	67	69	3	TR	60	68	8
KR8-117	439.87	68	70	2	TR	5	11	6
CAN-31	440.32	68	70	3	TB	50	58	8
KR8-119	441.87	68	70	5	TR	205	213	8
KR8-120	442.11	68	71	1	TB	229	239	10
KR8-121	446.02	70	71	5	TR	10	20	10
KR8-122	446.69	70	72	1	TB	77	89	12
KR8-122a	447.14	70	72	2	TB	122	135	13
KR8-123	447.96	70	72	3	TB	204	214	10
KR8-124	449.12	71	73	1	TB	16	24	8
KR8-125	451.23	71	73	5	TB	250	260	10

*Origin of the measurement of the core sample, from the top of the box (TB), from the bottom of the box (BR), from the top of the run (TR), or from the bottom of the run (BR).

Appendix B:

Table B-1. Major and trace element composition for samples from drill core LB-08A. ^a

Sample no.	KR8-001	KR8-002	KR8-003	KR8-004	KR8-005	KR8-006	KR8-007	KR8-008	KR8-009	KR8-010
Depth (m)	235.77	236.4	238.9	239.65	240.04	240.36	241.94	244.45	244.87	245.58
Lithology	S	P	S	S	S	S	P	B	B	B (S)
SiO ₂	59.37	62.68	62.97	59.76	62.62	68.43	64.41	67.74	58.98	59.85
TiO ₂	0.59	0.68	0.62	0.70	0.68	0.41	0.40	0.63	0.71	0.70
Al ₂ O ₃	16.61	17.82	14.44	16.68	14.61	9.77	14.59	13.58	18.16	15.05
Fe ₂ O ₃	6.50	6.26	6.48	6.48	6.04	4.24	5.25	5.63	8.45	7.05
MnO	0.06	0.04	0.05	0.06	0.06	0.09	0.04	0.03	0.05	0.08
MgO	2.58	2.78	2.40	2.56	2.28	1.57	1.33	2.02	2.86	2.45
CaO	1.79	0.23	1.38	1.51	2.28	4.89	1.10	0.41	0.24	2.70
Na ₂ O	2.85	1.75	2.76	2.94	3.47	1.72	1.93	3.14	2.02	2.66
K ₂ O	2.37	3.06	1.70	1.95	1.24	1.02	1.08	1.32	2.62	1.87
P ₂ O ₅	0.13	0.11	0.10	0.12	0.10	0.07	0.09	0.08	0.12	0.10
LOI	6.14	3.83	5.98	5.71	5.52	6.39	9.99	3.15	4.72	6.21
Total	98.99	99.24	98.88	98.47	98.90	98.60	100.2	97.72	98.93	98.72
Sc	17.1	17.2	15.9	17.3	15.5	10.1	16.9	13.4	24.2	18.6
V	129	148	118	142	127	92	117	117	180	150
Cr	114	101	112	113	110	69	113	101	144	115
Co	20	18	19	21	19	14	17	16	27	27
Ni	60	60	48	52	50	30	56	50	82	59
Cu	43	60	33	36	34	18	43	25	53	34
Zn	84	83	75	80	73	50	82	66	103	83
As	7.50	7.78	5.43	4.59	5.01	2.80	4.62	6.16	15.4	6.10
Rb	91	127	75	76	56	45	97	60	121	83
Sr	469	230	321	350	336	270	203	234	226	312
Y	18	18	16	19	17	14	19	15	19	20
Zr	129	132	133	147	143	96	130	132	135	134
Nb	4	5	5	4	5	3	5	5	4	5
Sb	0.25	0.45	0.22	0.29	0.29	0.25	0.29	0.35	0.48	0.30
Cs	4.85	5.03	3.58	3.21	2.50	1.90	3.74	2.48	4.71	3.52
Ba	700	857	507	573	396	311	612	453	834	599
La	19.3	20.3	18.0	20.3	19.0	16.8	18.9	13.8	19.5	23.1
Ce	40.6	40.9	37.5	41.6	39.0	33.1	39.7	29.8	41.5	48.4
Nd	19.1	20.5	17.4	20.5	18.7	15.6	18.8	14.6	21.3	23.9
Sm	4.11	4.08	3.54	3.77	3.48	3.29	3.96	3.04	4.16	4.45
Eu	1.15	1.04	0.99	1.09	1.04	0.95	1.00	0.79	1.16	1.30
Gd	3.38	2.84	3.06	2.97	3.20	2.86	3.03	2.19	3.86	3.64
Tb	0.52	0.48	0.44	0.45	0.44	0.44	0.53	0.41	0.56	0.59
Tm	0.27	0.22	0.25	0.25	0.21	0.18	0.29	0.20	0.28	0.28
Yb	1.70	1.50	1.53	1.57	1.56	1.30	1.81	1.49	1.80	1.83
Lu	0.27	0.23	0.24	0.24	0.25	0.20	0.30	0.23	0.30	0.28
Hf	3.44	3.06	3.13	3.41	3.40	2.07	3.24	3.00	3.38	3.31
Ta	0.39	0.40	0.37	0.35	0.34	0.23	0.47	0.37	0.44	0.39
W	3.32	4.18	3.71	2.63	2.34	1.19	2.68	2.12	3.89	3.18
Ir (ppb)	<1.3	1.0	0.3	0.2	0.0	0.2	<1.4	<1.2	0.4	<1.9
Au (ppb)	<3.2	1.4	<3.2	0.6	<2.8	<1.5	<2.7	0.8	<2.7	<3.3
Th	3.42	3.68	3.03	3.35	3.23	2.35	4.18	2.87	3.73	3.64
U	2.07	0.68	1.09	0.84	0.71	0.76	1.50	1.01	0.89	0.67
K/U	9,491	37,278	12,986	19,310	14,568	11,097	5,996	10,870	24,309	23,147
Zr/Hf	37.5	43.1	42.4	43.1	42.0	46.4	40.1	44.1	40.0	40.5
La/Th	5.64	5.52	5.93	6.06	5.89	7.14	4.53	4.83	5.24	6.35
Hf/Ta	8.84	7.59	8.56	9.79	9.98	8.92	6.89	8.03	7.60	8.43
Th/U	1.65	5.40	2.79	3.99	4.57	3.08	2.79	2.84	4.17	5.42
La _N /Yb _N	7.68	9.16	7.96	8.72	8.24	8.77	7.05	6.30	7.33	8.52
Eu/Eu*	0.94	0.93	0.92	0.99	0.96	0.94	0.88	0.94	0.88	0.99
CIA	61	73	62	63	57	43	70	65	73	57

^a Major element data (in wt%) by XRF (except Na₂O by INAA and Fe₂O₃, average of INAA and XRF data); All Fe as Fe₂O₃; Trace element data in ppm, except as noted: V, Cu, Sr, Y, Zr, Nb, and Ba by XRF; Ni and Zn: INAA and XRF data; all others by INAA; N = chondrite-normalized (Taylor and McLennan, 1985); Chemical index of alteration (CIA) = (Al₂O₃/[Al₂O₃ + CaO + Na₂O + K₂O]) x 100 in molecular proportions; All ratios are the average of the ratios calculated for each samples.

Abbreviations: S = Suevite; B = Polymict lithic impact breccia; P = Phyllite-Slate; G = Meta-graywacke; LGMG = Light greenish gray meta-graywacke; Gb = Meta-graywacke breccia; LOI = Loss on Ignition.

Table B-1. Continued. Major and trace element composition for samples from drill core LB-08A.^a

Sample no.	KR8-011	KR8-012	KR8-013	KR8-014	KR8-015	KR8-016	KR8-017	KR8-018	KR8-019	KR8-021
Depth (m)	247.46	248	248.8	249.3	250.74	250.89	251.74	253.04	253.56	255.65
Lithology	B	S	B	S	B	B (S)	B	B	B (S)	B
SiO ₂	64.76	61.47	67.72	62.27	54.80	59.24	61.24	58.60	64.57	57.14
TiO ₂	0.57	0.68	0.28	0.62	0.81	0.70	0.71	0.73	0.40	0.75
Al ₂ O ₃	16.33	15.25	9.64	15.70	20.12	17.27	16.30	17.77	11.85	18.16
Fe ₂ O ₃	4.67	6.02	3.31	5.85	7.62	8.64	6.42	7.72	3.99	7.05
MnO	0.04	0.07	0.10	0.06	0.06	0.04	0.09	0.07	0.10	0.09
MgO	1.73	2.25	1.30	2.31	3.04	2.12	2.54	3.02	1.69	2.79
CaO	1.01	2.47	6.14	1.78	0.88	0.20	2.56	0.76	4.93	2.30
Na ₂ O	3.00	2.91	2.18	2.19	4.00	2.66	2.93	2.97	3.45	2.03
K ₂ O	2.49	1.76	0.97	2.28	2.74	2.78	2.02	2.25	0.77	2.93
P ₂ O ₅	0.11	0.12	0.08	0.12	0.21	0.04	0.12	0.15	0.08	0.16
LOI	4.07	5.48	6.81	5.55	4.68	5.91	5.39	4.56	6.45	5.32
Total	98.77	98.48	98.52	98.74	98.96	99.60	100.3	98.60	98.29	98.72
Sc	14.9	16.3	7.15	16.2	25.4	22.5	18.3	22.1	11.0	20.6
V	111	135	63	113	170	153	145	154	79	164
Cr	91	116	46	110	156	115	96	89	76	89
Co	14	18	9	19	19	8	17	20	12	25
Ni	44	52	33	50	61	28	51	55	40	68
Cu	39	36	15	32	63	90	45	48	8	46
Zn	65	78	43	78	103	70	76	86	45	87
As	6.25	4.99	2.30	3.73	8.59	24.9	8.56	4.13	1.35	23.3
Rb	110	79	43	97	111	135	73	87	28	96
Sr	302	314	299	322	322	292	295	286	329	268
Y	15	19	13	22	28	21	26	25	19	28
Zr	149	139	76	141	164	157	143	148	106	149
Nb	4	5	<3	4	6	6	4	5	3	5
Sb	0.33	0.40	0.12	0.26	0.36	1.01	0.30	0.27	0.17	0.48
Cs	4.64	3.63	1.94	4.88	5.92	7.29	4.16	4.77	1.66	5.51
Ba	814	606	340	747	995	1,129	769	786	258	1,088
La	25.4	25.5	15.9	27.0	14.1	9.17	22.7	20.6	18.0	20.4
Ce	51.7	51.3	32.5	59.2	32.0	16.8	47.2	42.5	35.3	45.7
Nd	24.6	26.0	16.3	30.3	11.8	9.38	24.7	21.1	19.4	24.1
Sm	4.44	5.11	3.06	5.63	3.27	1.74	4.76	4.48	4.33	4.55
Eu	1.16	1.35	0.89	1.52	0.90	0.47	1.32	1.15	1.12	1.19
Gd	3.66	3.60	2.29	4.08	3.06	1.87	3.32	3.46	3.66	3.58
Tb	0.48	0.63	0.38	0.66	0.58	0.32	0.65	0.62	0.60	0.64
Tm	0.22	0.28	0.20	0.27	0.36	0.32	0.39	0.45	0.32	0.33
Yb	1.64	1.74	1.26	1.94	3.11	2.35	2.46	2.61	2.04	2.40
Lu	0.26	0.27	0.20	0.31	0.50	0.40	0.37	0.42	0.31	0.38
Hf	4.12	3.36	1.61	3.65	4.29	4.03	3.50	3.76	2.64	3.56
Ta	0.32	0.42	0.17	0.38	0.49	0.47	0.31	0.43	0.25	0.36
W	3.84	2.28	0.73	2.32	2.30	3.99	2.19	3.38	6.11	4.55
Ir (ppb)	<1.3	<1.4	<0.9	<1.3	1.5	0.2	<1.8	<1.9	0.2	0.7
Au (ppb)	3.3	2.5	0.2	<1.7	1.1	3.5	<3.9	1.1	1.5	2.3
Th	3.95	4.11	2.55	4.84	3.80	3.89	3.11	3.17	2.28	3.83
U	1.01	1.23	1.17	0.90	0.92	2.78	0.90	0.61	3.02	2.53
K/U	20,567	11,871	6,863	20,958	24,811	8,308	18,553	30,685	2,117	9,617
Zr/Hf	36.2	41.3	47.1	38.7	38.2	39.0	40.9	39.4	40.1	41.9
La/Th	6.43	6.21	6.25	5.59	3.70	2.36	7.32	6.51	7.90	5.34
Hf/Ta	12.7	8.01	9.78	9.70	8.84	8.65	11.4	8.67	10.4	9.88
Th/U	3.93	3.34	2.17	5.36	4.14	1.40	3.44	5.20	0.76	1.51
La _N /Yb _N	10.5	9.89	8.56	9.42	3.05	2.64	6.26	5.33	5.98	5.76
Eu/Eu*	0.88	0.96	1.03	0.97	0.87	0.80	1.02	0.89	0.86	0.90
CIA	63	58	38	63	64	69	58	67	43	63

^a Major element data (in wt%) by XRF (except Na₂O by INAA and Fe₂O₃, average of INAA and XRF data); All Fe as Fe₂O₃; Trace element data in ppm, except as noted: V, Cu, Sr, Y, Zr, Nb, and Ba by XRF; Ni and Zn: INAA and XRF data; all others by INAA; N = chondrite-normalized (Taylor and McLennan, 1985); Chemical index of alteration (CIA) = (Al₂O₃/[Al₂O₃ + CaO + Na₂O + K₂O]) x 100 in molecular proportions; All ratios are the average of the ratios calculated for each samples.

Abbreviations: S = Suevite; B = Polymict lithic impact breccia; P = Phyllite-Slate; G = Meta-graywacke; LGMG = Light greenish gray meta-graywacke; Gb = Meta-graywacke breccia; LOI = Loss on Ignition.

Table B-1. Continued. Major and trace element composition for samples from drill core LB-08A.^a

Sample no.	KR8-022	KR8-023	KR8-024	KR8-025	KR8-026	KR8-027	KR8-028	KR8-029	KR8-030	KR8-031
Depth (m)	256.81	258.14	259.14	259.74	260.49	263.76	266.18	271.43	272	273.99
Lithology	B (S)	S	B	S	S	G	P	G	G	G
SiO ₂	62.02	64.62	62.05	64.51	61.40	66.92	58.14	79.73	79.27	74.66
TiO ₂	0.63	0.58	0.59	0.51	0.65	0.30	0.73	0.25	0.15	0.37
Al ₂ O ₃	14.87	13.55	14.99	13.70	15.34	10.99	18.46	8.65	7.47	10.39
Fe ₂ O ₃	5.78	5.35	6.11	5.10	5.67	3.22	7.99	2.71	1.64	4.57
MnO	0.09	0.07	0.07	0.08	0.06	0.09	0.06	0.03	0.04	0.05
MgO	2.15	2.02	2.36	2.07	2.30	1.22	3.06	0.59	0.24	1.08
CaO	3.81	2.82	2.56	3.04	2.47	5.17	1.07	1.17	2.36	0.72
Na ₂ O	1.85	2.87	2.59	2.86	3.24	3.09	3.29	2.99	3.25	2.84
K ₂ O	2.31	1.46	1.96	1.52	1.79	0.92	2.42	0.48	0.29	0.72
P ₂ O ₅	0.14	0.12	0.11	0.11	0.12	0.05	0.08	0.05	0.03	0.08
LOI	5.92	4.86	5.05	5.16	5.59	6.10	4.85	2.31	2.81	2.90
Total	99.57	98.32	98.44	98.66	98.63	98.07	100.2	98.96	97.55	98.38
Sc	18.2	14.2	17.0	13.6	16.5	7.67	23.7	4.87	3.13	7.73
V	133	117	139	111	132	64	168	63	50	103
Cr	110	90	106	78	93	42	112	33	21	59
Co	18	15	16	14	16	8	27	6	3	8
Ni	68	51	47	42	49	27	76	19	11	24
Cu	31	27	31	24	18	2	40	10	35	18
Zn	71	60	68	56	64	35	97	21	11	37
As	21.3	19.6	10.7	16.7	19.0	11.4	29.3	4.54	1.62	4.01
Rb	97	55	71	59	69	37	100	21	17	27
Sr	290	339	329	354	360	485	347	265	285	309
Y	23	23	16	21	20	14	16	8	7	12
Zr	132	135	114	127	135	67	112	85	56	132
Nb	5	4	4	4	4	3	5	<3	<3	3
Sb	0.08	0.41	0.48	0.25	0.35	0.16	0.57	0.18	<0.24	0.22
Cs	5.65	3.32	4.23	3.73	4.24	2.26	5.77	1.50	1.13	1.72
Ba	829	724	747	660	743	391	911	388	327	641
La	22.3	20.7	14.6	22.1	17.2	11.6	18.7	16.5	14.9	21.0
Ce	51.8	42.9	30.8	46.1	36.4	23.7	39.8	30.4	28.0	40.4
Nd	26.1	22.6	14.7	22.5	17.5	12.0	18.2	13.0	11.7	17.3
Sm	5.67	3.97	3.72	5.08	3.74	2.41	3.72	1.89	1.86	2.94
Eu	1.54	1.25	0.90	1.30	1.06	0.75	1.08	0.60	0.55	0.85
Gd	5.12	4.00	2.80	3.75	2.93	1.72	4.13	1.63	1.37	2.38
Tb	0.75	0.58	0.44	0.60	0.49	0.34	0.46	0.21	0.19	0.32
Tm	0.42	0.34	0.25	0.33	0.28	0.23	0.25	0.14	0.11	0.18
Yb	2.60	1.99	1.55	1.91	2.11	1.63	1.89	0.87	0.64	1.08
Lu	0.40	0.30	0.24	0.30	0.31	0.27	0.28	0.12	0.10	0.16
Hf	3.56	3.28	2.86	3.31	3.44	1.60	3.15	2.07	1.20	3.68
Ta	0.38	0.29	0.29	0.32	0.35	0.18	0.41	0.18	0.13	0.25
W	1.93	3.49	4.74	2.54	3.80	0.53	3.42	<3.7	0.30	3.93
Ir (ppb)	<1.8	<1.8	0.0	0.1	<1.7	<1.2	0.3	0.1	<0.8	<1.4
Au (ppb)	0.1	1.5	3.1	<3.0	1.4	2.0	1.2	<3.7	1.2	
Th	3.80	3.04	2.40	3.60	3.27	1.58	3.43	4.34	1.65	2.64
U	1.21	2.08	1.79	3.25	1.79	0.53	0.80	0.81	<0.4	0.73
K/U	15,809	5,829	9,112	3,877	8,314	14,334	25,162	4,946		8,198
Zr/Hf	37.0	41.1	39.9	38.3	39.2	41.9	35.6	41.1	46.8	35.9
La/Th	5.88	6.80	6.09	6.14	5.25	7.34	5.45	3.80	9.01	7.96
Hf/Ta	9.28	11.1	9.77	10.5	9.90	9.13	7.75	11.4	9.38	14.8
Th/U	3.13	1.46	1.34	1.10	1.83	2.97	4.29	5.39		3.62
La _N /Yb _N	5.80	7.03	6.37	7.83	5.49	4.82	6.67	12.7	15.7	13.1
Eu/Eu*	0.87	0.96	0.85	0.91	0.98	1.12	0.84	1.05	1.04	0.99
CIA	54	54	58	54	57	42	65	53	43	61

^a Major element data (in wt%) by XRF (except Na₂O by INAA and Fe₂O₃, average of INAA and XRF data); All Fe as Fe₂O₃; Trace element data in ppm, except as noted: V, Cu, Sr, Y, Zr, Nb, and Ba by XRF; Ni and Zn: INAA and XRF data; all others by INAA; N = chondrite-normalized (Taylor and McLennan, 1985); Chemical index of alteration (CIA) = (Al₂O₃/[Al₂O₃ + CaO + Na₂O + K₂O]) x 100 in molecular proportions; All ratios are the average of the ratios calculated for each samples.

Abbreviations: S = Suevite; B = Polymict lithic impact breccia; P = Phyllite-Slate; G = Meta-graywacke; LGMG = Light greenish gray meta-graywacke; Gb = Meta-graywacke breccia; LOI = Loss on Ignition.

Appendices

Table B-1. Continued. Major and trace element composition for samples from drill core LB-08A.^a

Sample no.	KR8-032	KR8-033	KR8-034	KR8-035	KR8-036	KR8-037	KR8-038	KR8-039	KR8-040	KR8-041
Depth (m)	274.99	277.03	277.89	280.3	281.32	283.5	283.74	286.17	290.47	293.79
Lithology	G	G	G	S	G	G	Gb	S	S	S
SiO ₂	72.22	69.85	72.99	66.45	66.99	66.62	57.53	62.51	64.69	66.45
TiO ₂	0.40	0.42	0.34	0.46	0.50	0.53	0.75	0.53	0.55	0.47
Al ₂ O ₃	12.17	12.88	10.36	14.09	14.60	15.99	19.30	14.68	15.37	14.19
Fe ₂ O ₃	4.14	4.06	3.62	4.95	4.47	3.76	6.43	5.95	5.69	4.82
MnO	0.06	0.06	0.05	0.07	0.04	0.04	0.06	0.05	0.06	0.06
MgO	1.18	1.20	1.06	1.92	2.07	2.99	3.92	3.33	2.35	2.43
CaO	1.30	1.69	2.56	2.79	0.99	0.60	1.18	1.55	1.86	2.21
Na ₂ O	3.36	4.15	3.09	3.22	3.86	2.30	2.32	2.75	3.03	3.58
K ₂ O	1.09	0.74	0.53	1.49	1.43	2.25	2.83	1.34	1.92	1.30
P ₂ O ₅	0.08	0.10	0.07	0.13	0.08	0.09	0.12	0.09	0.10	0.10
LOI	2.76	2.94	3.50	4.70	2.82	3.24	4.82	6.41	3.94	4.10
Total	98.75	98.09	98.16	100.3	97.84	98.41	99.26	99.19	99.56	99.71
Sc	9.2	8.4	7.0	12.1	10.8	12.1	21.0	15.0	14.8	11.4
V	106	99	83	96	101	127	175	114	122	104
Cr	57	58	44	72	61	70	145	187	93	109
Co	10	11	9	15	12	12	24	24	17	14
Ni	26	31	23	31	33	37	63	124	57	60
Cu	7	20	12	39	37	11	7	12	32	23
Zn	37	39	32	51	49	43	84	77	66	57
As	11.7	10.9	9.49	18.4	6.05	14.1	35.2			
Rb	39	31	26	53	54	84	111	59	79	53
Sr	360	405	366	438	393	345	363	575	353	334
Y	13	12	10	13	13	11	17	12	14	12
Zr	142	140	115	152	115	130	138	103	110	109
Nb	3	3	<3	3	3	4	6	4	3	3
Sb	0.20	0.32	0.17	0.29	0.25	<0.25	0.29			
Cs	2.59	2.19	1.73	4.71	3.01	4.44	4.92	3.05	4.23	3.05
Ba	972	704	527	322	595	905	1,154	629	676	536
La	18.3	17.0	17.6	17.1	15.5	14.9	21.5	20.1	17.5	16.4
Ce	37.8	34.0	32.7	34.7	33.1	30.5	45.3	43.6	36.5	34.3
Nd	15.9	15.7	14.1	16.8	15.0	12.8	21.3	23.0	17.0	16.2
Sm	3.02	2.78	2.57	3.16	2.88	2.50	4.03	3.77	3.27	2.70
Eu	0.82	0.82	0.72	0.92	0.92	0.86	1.07	1.16	1.00	0.74
Gd	2.60	2.42	2.18	2.80	2.35	2.34	2.78			
Tb	0.32	0.30	0.27	0.37	0.32	0.29	0.47	0.29	0.57	0.27
Tm	0.16	0.18	0.16	0.23	0.20	0.16	0.21	0.15	0.22	0.16
Yb	1.09	1.14	1.07	1.35	1.24	1.21	1.56	1.13	1.50	1.19
Lu	0.16	0.16	0.17	0.21	0.18	0.17	0.25	0.19	0.23	0.18
Hf	3.55	3.36	2.76	2.91	2.73	3.09	3.62	2.71	2.70	2.56
Ta	0.28	0.24	0.25	0.28	0.26	0.26	0.39	0.28	0.30	0.23
W	<4.7	3.71	2.13	0.08	5.13	1.18	4.59			
Ir (ppb)	1.5	0.1	<1.6	<1.5	<1.4	0.1	<1.5	<2.3	2.4	0.9
Au (ppb)	1.9	3.1	0.0	0.4	1.5	0.1	<2.6	2.1	3.8	<5.9
Th	2.85	2.42	2.78	2.75	2.52	2.41	3.48	2.96	2.67	1.95
U	0.47	0.85	0.26	0.88	0.93	0.84	1.50	<2.7	0.83	<2.7
K/U	19,071	7,194	16,877	14,079	12,793	22,291	15,683		19,132	
Zr/Hf	40.0	41.7	41.6	52.2	42.1	42.1	38.1	38.0	40.7	42.5
La/Th	6.44	7.03	6.35	6.23	6.16	6.15	6.17	6.77	6.54	8.40
Hf/Ta	12.8	14.0	11.2	10.3	10.6	11.8	9.26	9.69	9.01	11.3
Th/U	6.00	2.83	10.6	3.13	2.72	2.88	2.32		3.20	
La _N /Yb _N	11.4	10.1	11.1	8.58	8.44	8.30	9.33	12.0	7.87	9.32
Eu/Eu*	0.89	0.97	0.93	0.95	1.08	1.09	0.97			
CIA	57	55	50	54	60	69	68	63	60	56

^a Major element data (in wt%) by XRF (except Na₂O by INAA and Fe₂O₃, average of INAA and XRF data); All Fe as Fe₂O₃; Trace element data in ppm, except as noted: V, Cu, Sr, Y, Zr, Nb, and Ba by XRF; Ni and Zn: INAA and XRF data; all others by INAA; N = chondrite-normalized (Taylor and McLennan, 1985); Chemical index of alteration (CIA) = (Al₂O₃/[Al₂O₃ + CaO + Na₂O + K₂O]) x 100 in molecular proportions; All ratios are the average of the ratios calculated for each samples.

Abbreviations: S = Suevite; B = Polymict lithic impact breccia; P = Phyllite-Slate; G = Meta-graywacke; LGMG = Light greenish gray meta-graywacke; Gb = Meta-graywacke breccia; LOI = Loss on Ignition.

Appendices

Table B-1. Continued. Major and trace element composition for samples from drill core LB-08A.^a

Sample no.	KR8-042	KR8-043	KR8-045	KR8-046	KR8-047	KR8-048	KR8-049	KR8-050	KR8-051	KR8-052
Depth (m)	293.97	296.94	300.41	303.25	305.71	307.3	310.23	310.99	312.4	315.75
Lithology	S	S	G	P	G	G	G	G	G	G
SiO ₂	66.79	60.02	68.02	58.71	68.42	65.49	66.68	71.04	70.21	69.18
TiO ₂	0.44	0.57	0.40	0.70	0.36	0.44	0.50	0.33	0.42	0.49
Al ₂ O ₃	13.47	15.75	14.83	19.70	13.17	12.97	15.14	9.90	13.48	11.21
Fe ₂ O ₃	4.47	6.63	4.47	7.51	4.27	4.26	5.22	3.33	4.31	4.24
MnO	0.06	0.09	0.03	0.07	0.07	0.05	0.06	0.03	0.05	0.03
MgO	2.04	4.75	1.42	2.84	1.90	1.57	1.82	0.99	1.24	1.68
CaO	2.52	4.01	2.39	1.10	2.84	2.19	1.63	0.87	1.70	2.95
Na ₂ O	2.93	2.05	4.29	3.30	2.49	3.30	4.63	3.80	4.58	4.35
K ₂ O	1.47	1.59	1.17	2.65	1.46	1.44	1.22	1.01	0.71	0.82
P ₂ O ₅	0.08	0.14	0.10	0.13	0.07	0.09	0.09	0.07	0.09	0.09
LOI	4.37	3.67	2.67	3.76	4.32	7.44	3.25	9.32	2.49	6.47
Total	98.64	99.27	99.79	100.5	99.37	99.24	100.2	100.7	99.28	101.5
Sc	10.8	18.2	11.4	21.2	8.80	11.1	13.2	8.63	9.18	10.2
V	106	139	109	184	95	106	99	68	99	86
Cr	83	249	68	104	41	63	73	53	60	58
Co	13	26	13	21	8	12	15	10	11	12
Ni	63	165	52	53	46	31	33	31	37	31
Cu	20	15	30	37	9	17	17	10	17	19
Zn	50	84	53	92	52	51	60	39	42	45
As										
Rb	54	72	55	103	54	69	58	40	32	48
Sr	352	468	388	393	324	359	416	546	382	385
Y	12	13	12	20	11	12	13	13	12	13
Zr	104	109	121	126	90	109	107	95	129	119
Nb	3	3	3	5	3	3	4	3	4	4
Sb										
Cs	3.18	6.65	2.68	4.96	2.82	3.39	3.30	2.23	1.70	2.49
Ba	614	642	503	951	582	577	666	449	446	609
La	15.1	23.7	17.6	19.9	14.8	15.8	20.5	17.9	18.5	15.5
Ce	32.0	49.3	36.2	44.9	31.3	34.0	36.9	36.0	37.9	34.0
Nd	14.2	26.2	16.8	21.0	12.8	15.9	17.4	17.9	16.2	13.3
Sm	2.57	4.61	2.91	3.87	2.49	3.02	2.99	3.02	2.96	2.52
Eu	0.84	1.22	0.87	1.29	0.75	0.92	0.92	0.92	0.91	0.87
Gd										
Tb	0.50	0.70	0.32	0.69	0.41	0.31	0.57	0.55	0.48	0.30
Tm	0.18	0.23	0.16	0.29	0.14	0.20	0.21	0.19	0.19	0.18
Yb	1.10	1.29	1.26	1.89	0.87	1.39	1.51	1.21	1.15	1.08
Lu	0.18	0.20	0.21	0.29	0.15	0.21	0.22	0.20	0.18	0.17
Hf	2.49	2.95	3.12	3.13	1.91	3.11	2.88	2.77	3.14	2.78
Ta	0.26	0.26	0.29	0.31	0.19	0.30	0.35	0.24	0.29	0.27
W										
Ir (ppb)	<0.1	2.7	1.3	<2.4	0.2	0.1	1.5	<2.1	2.5	<1.7
Au (ppb)	2.9	6.2	0.3	0.9	<2.0	1.2	2.4	3.6	<3.8	<4.8
Th	2.26	3.02	2.72	3.34	1.66	2.74	2.77	2.35	3.02	2.38
U	2.43	1.42	1.07	1.16	0.71	0.83	1.92	1.04	0.95	0.94
K/U	5,032	9,282	9,063	18,896	17,076	14,389	5,284	8,038	6,186	7,216
Zr/Hf	41.8	37.0	38.8	40.3	47.1	35.1	37.2	34.3	41.1	42.8
La/Th	6.69	7.85	6.49	5.97	8.94	5.75	7.40	7.64	6.12	6.49
Hf/Ta	9.74	11.3	10.7	10.0	10.3	10.2	8.13	11.6	10.8	10.1
Th/U	0.93	2.12	2.54	2.87	2.34	3.30	1.45	2.25	3.17	2.53
La _N /Yb _N	9.30	12.4	9.43	7.12	11.5	7.67	9.20	10.0	10.9	9.72
Eu/Eu*										
CIA	55	56	54	66	55	54	56	53	54	46

^a Major element data (in wt%) by XRF (except Na₂O by INAA and Fe₂O₃, average of INAA and XRF data); All Fe as Fe₂O₃; Trace element data in ppm, except as noted: V, Cu, Sr, Y, Zr, Nb, and Ba by XRF; Ni and Zn: INAA and XRF data; all others by INAA; N = chondrite-normalized (Taylor and McLennan, 1985); Chemical index of alteration (CIA) = (Al₂O₃/[Al₂O₃ + CaO + Na₂O + K₂O]) x 100 in molecular proportions; All ratios are the average of the ratios calculated for each samples.

Abbreviations: S = Suevite; B = Polymict lithic impact breccia; P = Phyllite-Slate; G = Meta-graywacke; LGMG = Light greenish gray meta-graywacke; Gb = Meta-graywacke breccia; LOI = Loss on Ignition.

Table B-1. Continued. Major and trace element composition for samples from drill core LB-08A.^a

Sample no.	KR8-053	KR8-054	KR8-056	KR8-057	KR8-059	KR8-060	KR8-061	KR8-062	KR8-063	KR8-064
Depth (m)	316.97	320.62	326.78	330.08	333.51	337.33	341.17	341.86	343.57	348.43
Lithology	Gb	G	G	G	G	G	G	G	P	P
SiO ₂	61.51	70.91	71.68	71.65	71.81	66.08	70.45	70.39	50.14	61.11
TiO ₂	0.46	0.48	0.40	0.53	0.33	0.50	0.45	0.46	0.95	0.60
Al ₂ O ₃	12.51	12.86	13.11	11.29	12.89	15.75	13.03	14.03	22.86	17.75
Fe ₂ O ₃	6.19	4.72	3.83	5.87	3.08	4.39	4.89	4.25	8.71	7.72
MnO	0.10	0.05	0.04	0.06	0.17	0.04	0.06	0.05	0.07	0.05
MgO	2.34	1.70	1.45	1.76	1.77	2.23	1.66	1.51	3.45	3.06
CaO	5.65	1.15	1.43	1.68	1.48	2.62	1.60	1.33	1.97	0.88
Na ₂ O	1.38	3.11	3.67	2.62	3.07	4.66	4.27	4.31	2.11	1.97
K ₂ O	1.64	1.19	1.07	0.46	1.58	1.88	0.78	1.12	4.03	2.99
P ₂ O ₅	0.19	0.07	0.09	0.09	0.12	0.13	0.11	0.09	0.32	0.11
LOI	6.79	2.67	2.83	2.83	2.06	3.16	2.83	2.54	4.73	3.91
Total	98.76	98.91	99.60	98.85	98.36	101.4	100.1	100.1	99.34	100.2
Sc	12.9	9.93	8.10	8.21	7.34	12.1	9.79	9.71	26.6	17.6
V	122	96	84	118	88	122	106	98	222	137
Cr	61	57	47	64	45	70	67	57	130	86
Co	16	15	9	12	8	14	10	12	27	19
Ni	35	42	24	43	39	33	41	35	75	54
Cu	31	27	16	49	14	23	22	18	64	36
Zn	74	55	45	57	34	52	52	47	111	93
As									<1.86	0.91
Rb	69	49	44	14	53	67	35	51	143	111
Sr	308	308	324	269	225	353	299	333	326	261
Y	18	13	10	13	11	12	11	12	25	20
Zr	87	106	105	161	96	115	150	107	130	118
Nb	3	4	3	3	3	4	3	3	7	5
Sb									0.20	0.28
Cs	3.80	2.49	2.09	1.15	2.58	3.34	1.85	2.33	7.58	5.84
Ba	657	472	481	315	424	567	462	551	1,279	1,106
La	15.7	15.0	14.0	33.0	23.7	18.2	18.9	16.3	19.8	25.2
Ce	32.9	30.9	29.2	64.2	44.5	36.6	40.5	34.4	44.0	53.1
Nd	15.4	12.8	13.1	25.9	17.0	18.8	15.0	14.8	21.4	23.1
Sm	3.37	2.57	2.15	3.39	3.05	3.13	2.90	2.70	4.97	4.62
Eu	1.03	0.86	0.71	1.02	0.79	1.11	0.96	0.89	1.57	1.29
Gd									5.11	4.97
Tb	0.41	0.31	0.21	0.55	0.45	0.55	0.28	0.26	0.68	0.67
Tm	0.23	0.18	0.11	0.19	0.18	0.21	0.16	0.16	0.32	0.26
Yb	1.49	1.18	0.89	1.21	1.05	1.29	1.17	1.11	2.09	1.64
Lu	0.25	0.20	0.15	0.21	0.15	0.21	0.18	0.17	0.36	0.26
Hf	2.01	2.33	2.34	4.14	2.30	3.30	4.26	2.97	3.10	2.82
Ta	0.22	0.20	0.24	0.25	0.28	0.32	0.30	0.27	0.95	0.77
W										
Ir (ppb)	<1.8	<1.8	<1.5	<0.1	<2.0	<1.9	2.1	1.3	<3.5	1.0
Au (ppb)	0.5	3.6	<4.2	0.4	<4.3	2.4	1.9	0.4		
Th	2.19	2.53	2.33	4.12	3.23	2.99	3.30	2.22	3.93	3.84
U	1.08	0.67	0.82	1.48	0.60	0.92	0.84	2.69	0.80	1.45
K/U	12,578	14,729	10,861	2,582	22,013	16,871	7,685	3,458	41,772	17,070
Zr/Hf	43.3	45.4	44.9	38.8	41.8	34.9	35.2	36.1	42.0	41.8
La/Th	7.19	5.91	6.00	8.03	7.33	6.07	5.71	7.33	5.05	6.57
Hf/Ta	9.33	11.5	9.91	16.4	8.08	10.2	14.3	11.0	3.25	3.65
Th/U	2.02	3.78	2.85	2.78	5.42	3.24	3.92	0.83	4.91	2.64
La _N /Yb _N	7.14	8.56	10.6	18.5	15.3	9.55	10.9	9.89	6.41	10.4
Eu/Eu*									0.95	0.82
CIA	47	60	57	59	58	52	55	57	67	69

^a Major element data (in wt%) by XRF (except Na₂O by INAA and Fe₂O₃, average of INAA and XRF data); All Fe as Fe₂O₃; Trace element data in ppm, except as noted: V, Cu, Sr, Y, Zr, Nb, and Ba by XRF; Ni and Zn: INAA and XRF data; all others by INAA; N = chondrite-normalized (Taylor and McLennan, 1985); Chemical index of alteration (CIA) = (Al₂O₃/[Al₂O₃ + CaO + Na₂O + K₂O]) x 100 in molecular proportions; All ratios are the average of the ratios calculated for each samples.

Abbreviations: S = Suevite; B = Polymict lithic impact breccia; P = Phyllite-Slate; G = Meta-graywacke; LGMG = Light greenish gray meta-graywacke; Gb = Meta-graywacke breccia; LOI = Loss on Ignition.

Appendices

Table B-1. Continued. Major and trace element composition for samples from drill core LB-08A.^a

Sample no.	KR8-065	KR8-066	KR8-067	KR8-068	KR8-069	KR8-070	KR8-071	KR8-072	KR8-073	KR8-074
Depth (m)	352.31	353.95	356.59	359.44	361.18	364.12	368.97	370.96	371.07	375.24
Lithology	P (G)	G	G	G	LGMG	G	G	G	G	G
SiO ₂	58.87	67.37	71.77	77.34	59.48	71.88	66.19	69.40	69.40	70.18
TiO ₂	0.68	0.50	0.41	0.32	0.68	n.d.	0.39	0.40	0.43	0.39
Al ₂ O ₃	19.36	14.89	12.29	10.31	15.12	13.52	10.45	14.45	14.05	13.72
Fe ₂ O ₃	6.11	5.02	3.59	3.17	5.05	3.34	4.10	4.29	3.89	3.57
MnO	0.07	0.05	0.04	0.03	0.08	0.05	0.04	0.05	0.05	0.05
MgO	2.37	1.73	1.39	0.92	3.48	1.35	1.20	1.50	1.31	1.14
CaO	1.91	1.24	1.61	0.98	5.06	1.82	2.12	1.64	2.02	2.26
Na ₂ O	3.83	4.34	3.50	3.69	3.54	4.29	3.68	4.36	4.87	4.38
K ₂ O	2.54	1.07	0.69	0.44	0.88	0.77	0.36	0.88	0.75	0.74
P ₂ O ₅	0.13	0.15	0.08	0.06	0.13	0.10	0.08	0.10	0.10	0.09
LOI	3.82	2.53	2.68	1.56	5.78	2.24	9.44	2.11	2.48	2.63
Total	99.69	98.89	98.05	98.81	99.27	99.35	98.05	99.18	99.35	99.14
Sc	16.4	10.5	7.77	5.59	11.9	8.03	6.60	8.13	8.38	7.90
V	168	118	78	76	95	n.d.	68	90	91	85
Cr	103	79	57	41	110	55	57	52	53	48
Co	19	12	9	6	15	7	9	10	10	8
Ni	51	33	24	20	76	14	20	29	23	23
Cu	14	20	29	17	<6	n.d.	42	7	12	20
Zn	62	51	33	26	61	42	42	44	41	39
As	19.4	5.41	0.62	0.91	23.1	0.09	1.82	3.41	2.97	1.08
Rb	90	39	29	22	35	28	20	35	30	31
Sr	465	419	400	354	696	n.d.	307	425	436	413
Y	15	14	12	9	13	n.d.	12	11	11	11
Zr	152	148	120	92	109	132	140	111	124	109
Nb	5	4	3	3	3	n.d.	3	3	3	3
Sb	0.39	0.18	0.46	0.23	4.39	0.14	0.34	0.05	0.05	0.03
Cs	4.80	2.18	1.73	1.00	1.93	1.57	1.00	1.96	1.70	1.65
Ba	1,320	681	369	264	387	279	244	621	519	525
La	22.0	24.8	17.2	15.5	11.8	16.9	20.9	12.7	16.1	14.4
Ce	47.8	51.5	40.5	34.3	27.3	36.9	46.6	32.5	34.6	37.1
Nd	20.4	21.0	16.9	12.9	15.4	14.9	18.4	13.3	13.6	15.9
Sm	3.94	3.61	2.61	2.30	2.82	2.63	3.35	2.22	2.60	2.54
Eu	1.25	1.03	0.86	0.66	0.99	0.86	0.90	0.80	0.84	0.81
Gd	3.60	3.63	3.28	1.78	3.08	2.19	3.44	2.12	2.64	3.03
Tb	0.78	0.65	0.51	0.40	0.60	0.47	0.60	0.51	0.35	0.50
Tm	0.22	0.21	0.16	0.14	0.19	0.15	0.19	0.17	0.17	0.19
Yb	1.51	1.20	1.06	0.92	1.15	1.04	1.13	1.12	1.10	1.01
Lu	0.25	0.21	0.16	0.13	0.17	0.17	0.18	0.17	0.17	0.16
Hf	4.11	4.02	2.67	2.44	2.60	3.03	3.22	2.58	3.00	2.57
Ta	0.70	0.43	0.39	0.23	0.46	0.23	0.47	0.38	0.50	0.37
W										
Ir (ppb)	<3.7	<3.1	<2.4	1.4	1.7	1.0	1.8	<2.4	<2.2	0.4
Au (ppb)										
Th	3.47	3.24	2.62	2.18	1.77	2.56	3.21	2.27	2.49	2.40
U	0.97	1.19	0.85	0.39	5.34	0.89	1.01	0.77	0.57	0.51
K/U	21,722	7,447	6,761	9,430	1,368	7,161	2,970	9,462	10,829	12,060
Zr/Hf	37.0	36.9	44.9	37.6	41.9	43.4	43.5	43.0	41.3	42.4
La/Th	6.34	7.67	6.56	7.10	6.65	6.59	6.50	5.59	6.49	6.01
Hf/Ta	5.86	9.41	6.88	10.5	5.66	13.0	6.88	6.77	6.05	6.97
Th/U	3.57	2.71	3.09	5.63	0.33	2.87	3.19	2.94	4.32	4.71
La _N /Yb _N	9.83	13.9	11.0	11.3	6.91	10.9	12.5	7.66	9.91	9.64
Eu/Eu*	1.01	0.87	0.90	0.99	1.02	1.10	0.81	1.12	0.98	0.89
CIA	61	59	57	55	49	55	50	57	53	53

^a Major element data (in wt%) by XRF (except Na₂O by INAA and Fe₂O₃, average of INAA and XRF data); All Fe as Fe₂O₃; Trace element data in ppm, except as noted: V, Cu, Sr, Y, Zr, Nb, and Ba by XRF; Ni and Zn: INAA and XRF data; all others by INAA; N = chondrite-normalized (Taylor and McLennan, 1985); Chemical index of alteration (CIA) = (Al₂O₃/[Al₂O₃ + CaO + Na₂O + K₂O]) x 100 in molecular proportions; All ratios are the average of the ratios calculated for each samples.

Abbreviations: S = Suevite; B = Polymict lithic impact breccia; P = Phyllite-Slate; G = Meta-graywacke; LGMG = Light greenish gray meta-graywacke; Gb = Meta-graywacke breccia; LOI = Loss on Ignition.

Appendices

Table B-1. Continued. Major and trace element composition for samples from drill core LB-08A.^a

Sample no.	KR8-075	KR8-076	KR8-077	KR8-078	KR8-079	KR8-080	KR8-081	KR8-082	KR8-083	KR8-084
Depth (m)	377.78	379.7	380.98	382.17	384.06	384.54	387.36	387.78	389.25	390
Lithology	Mylonite	G	G	G	G	P	G	G	G	P
SiO ₂	65.84	74.27	69.37	73.75	73.47	50.74	72.67	69.32	70.57	56.85
TiO ₂	0.55	0.37	0.43	0.36	0.41	0.70	0.47	0.38	0.40	0.73
Al ₂ O ₃	15.66	12.09	15.03	11.31	11.51	22.38	12.34	12.99	13.44	20.01
Fe ₂ O ₃	4.72	3.67	4.04	3.29	5.15	8.04	4.65	4.27	3.75	7.67
MnO	0.05	0.04	0.04	0.05	0.05	0.08	0.05	0.06	0.05	0.10
MgO	1.91	1.25	1.51	1.21	1.49	3.00	1.58	1.73	1.24	3.04
CaO	1.86	1.24	1.30	2.04	1.55	2.35	1.61	2.62	1.56	1.37
Na ₂ O	2.92	3.21	3.99	3.15	2.72	2.37	3.50	3.54	3.89	2.24
K ₂ O	2.07	1.03	1.45	1.02	0.91	3.90	0.75	1.19	1.22	3.42
P ₂ O ₅	0.11	0.08	0.11	0.09	0.09	0.44	0.11	0.12	0.09	0.16
LOI	3.08	1.95	2.11	2.55	2.53	4.32	2.50	3.20	2.40	3.84
Total	98.77	99.20	99.39	98.81	99.88	98.32	100.23	99.41	98.61	99.44
Sc	12.3	8.14	10.1	7.42	7.44	22.5	8.21	8.38	8.09	18.5
V	119	88	102	80	124	196	108	76	85	153
Cr	75	55	63	52	64	103	64	51	48	94
Co	13	9	11	8	10	22	10	10	9	24
Ni	33	24	31	25	25	58	36	28	22	59
Cu	36	33	31	20	58	44	21	12	22	28
Zn	57	38	48	36	45	82	49	54	44	110
As	1.49	1.82	2.74	1.85	0.77	1.27	2.87	3.41	1.83	21.8
Rb	67	41	54	41	37	128	26	41	39	128
Sr	409	430	477	403	384	522	401	440	523	380
Y	15	10	12	10	13	24	14	11	11	18
Zr	126	110	113	102	142	114	119	93	103	112
Nb	5	3	4	3	3	6	3	<3	3	6
Sb	0.12	0.33	0.20	0.08	<0.3	0.32	<0.4	<0.3	0.54	0.52
Cs	3.68	2.28	2.89	2.06	1.80	6.62	1.48	2.11	2.25	6.52
Ba	761	456	582	407	382	1,235	724	442	477	1,233
La	15.0	16.7	14.2	17.0	22.7	19.9	21.3	14.4	15.6	17.1
Ce	34.4	35.9	32.5	34.6	40.7	48.3	48.2	31.6	31.7	38.8
Nd	16.6	14.0	15.0	13.9	19.4	25.5	17.9	13.2	14.9	19.1
Sm	2.69	2.89	2.63	2.56	3.10	4.81	3.09	2.35	2.54	3.97
Eu	0.94	0.84	0.91	0.78	0.94	1.42	0.97	0.77	0.82	1.08
Gd	2.70	3.03	2.65	2.24	4.08	5.87	3.72	1.04	2.95	3.07
Tb	0.57	0.50	0.50	0.46	0.59	0.84	0.60	0.48	0.48	0.50
Tm	0.19	0.19	0.19	0.17	0.22	0.32	0.21	0.14	0.17	0.26
Yb	1.25	1.14	1.11	1.04	1.24	2.13	1.30	1.01	1.12	1.69
Lu	0.21	0.17	0.18	0.16	0.17	0.34	0.19	0.16	0.17	0.26
Hf	2.69	2.71	2.76	2.45	3.97	2.75	4.25	2.41	2.66	2.79
Ta	0.45	0.37	0.40	0.24	0.47	0.75	0.58	0.31	0.39	0.45
W										1.73
Ir (ppb)	<3.1	<2.8	<2.9	<2.5	<2.5	<4.8	2.6	1.3	0.7	<1.6
Au (ppb)										0.5
Th	2.55	2.64	2.44	2.16	3.86	3.41	3.52	2.12	2.21	3.27
U	0.66	1.36	0.98	1.14	3.36	0.65	1.94	2.59	0.74	1.09
K/U	26,127	6,274	12,313	7,452	2,245	49,525	3,208	3,817	13,666	26,031
Zr/Hf	46.8	40.6	41.0	41.7	35.8	41.5	28.0	38.5	38.7	40.1
La/Th	5.89	6.34	5.80	7.84	5.90	5.85	6.04	6.82	7.04	5.23
Hf/Ta	5.99	7.27	6.92	10.3	8.36	3.67	7.28	7.68	6.90	6.26
Th/U	3.88	1.94	2.50	1.90	1.15	5.21	1.82	0.82	2.99	3.00
La _N /Yb _N	8.11	9.91	8.60	11.1	12.4	6.33	11.1	9.65	9.41	6.84
Eu/Eu*	1.06	0.87	1.05	0.99	0.81	0.82	0.88	1.51	0.92	0.94
CIA	60	58	59	53	58	64	57	52	56	67

^a Major element data (in wt%) by XRF (except Na₂O by INAA and Fe₂O₃, average of INAA and XRF data); All Fe as Fe₂O₃; Trace element data in ppm, except as noted: V, Cu, Sr, Y, Zr, Nb, and Ba by XRF; Ni and Zn: INAA and XRF data; all others by INAA; N = chondrite-normalized (Taylor and McLennan, 1985); Chemical index of alteration (CIA) = (Al₂O₃/[Al₂O₃ + CaO + Na₂O + K₂O]) x 100 in molecular proportions; All ratios are the average of the ratios calculated for each samples.

Abbreviations: S = Suevite; B = Polymict lithic impact breccia; P = Phyllite-Slate; G = Meta-graywacke; LGMG = Light greenish gray meta-graywacke; Gb = Meta-graywacke breccia; LOI = Loss on Ignition.

Table B-1. Continued. Major and trace element composition for samples from drill core LB-08A.^a

Sample no.	KR8-085	KR8-086	KR8-087	KR8-088	KR8-089	KR8-090	KR8-091	KR8-092	KR8-093	KR8-094
Depth (m)	392.65	393.07	394.3	395.25	397.3	398.8	400.35	403	403.64	404.18
Lithology	G	G	G	G	G	G	G	G	G	G
SiO ₂	71.17	69.26	68.70	66.72	73.47	70.89	73.03	69.69	73.46	74.44
TiO ₂	0.45	0.43	0.39	0.30	0.36	0.37	0.41	0.38	0.35	0.39
Al ₂ O ₃	12.12	14.55	12.86	11.78	11.49	12.82	11.82	13.09	11.54	11.48
Fe ₂ O ₃	4.94	4.05	3.76	2.99	3.35	3.52	4.34	3.83	3.90	4.21
MnO	0.05	0.04	0.06	0.07	0.04	0.05	0.05	0.05	0.04	0.04
MgO	1.12	1.32	1.43	1.17	0.95	1.33	1.27	1.09	1.04	1.00
CaO	2.17	1.07	3.19	6.14	1.98	2.66	1.77	3.20	2.08	1.76
Na ₂ O	4.08	5.47	4.11	2.54	3.53	3.81	3.61	3.96	3.84	3.55
K ₂ O	0.59	1.01	0.99	1.59	1.13	0.98	0.57	0.87	0.69	0.85
P ₂ O ₅	0.10	0.12	0.10	0.08	0.09	0.10	0.09	0.09	0.08	0.09
LOI	1.85	2.13	3.72	5.93	2.32	3.11	1.60	2.75	1.90	1.75
Total	98.64	99.45	99.31	99.31	98.71	99.64	98.56	99.00	98.91	99.56
Sc	7.83	8.14	7.84	6.83	6.22	6.99	6.57	6.92	6.55	7.10
V	112	98	76	85	92	82	97	78	85	102
Cr	59	53	49	38	44	46	49	46	46	54
Co	10	10	10	7	8	9	8	8	8	9
Ni	26	29	22	23	16	26	16	33	21	25
Cu	23	20	41	<6	24	17	61	12	19	21
Zn	46	43	48	34	34	37	42	36	37	40
As	0.09	10.4	7.73	6.64	0.65	6.08	0.17	3.82	1.20	0.90
Rb	31	32	39	54	43	35	19	34	24	31
Sr	588	503	553	513	308	531	612	559	542	570
Y	12	11	10	9	11	10	11	10	9	11
Zr	139	125	114	79	128	112	123	111	106	114
Nb	3	4	3	<3	3	3	4	3	3	3
Sb	0.98	0.28	0.30	0.23	0.32	0.41	0.53	0.53	0.57	0.60
Cs	3.79	1.71	2.24	3.08	2.32	1.89	1.08	2.09	1.36	1.75
Ba	364	821	545	706	522	592	341	537	418	570
La	25.1	18.8	18.6	13.4	22.7	18.5	28.8	18.6	21.6	24.8
Ce	47.1	37.8	37.8	26.2	43.3	36.9	53.5	37.2	40.9	47.3
Nd	20.7	17.7	16.7	12.9	17.5	15.4	21.1	14.7	17.2	21.7
Sm	3.63	3.17	3.10	2.38	3.21	2.74	3.36	3.36	3.14	3.52
Eu	0.99	0.92	0.85	0.68	0.89	0.82	0.91	0.85	0.85	0.89
Gd	2.45	2.57	2.16	1.50	2.10	2.26	2.38	2.40	2.08	2.25
Tb	0.37	0.34	0.33	0.25	0.33	0.29	0.31	0.33	0.31	0.36
Tm	0.20	0.16	0.16	0.13	0.14	0.14	0.15	0.15	0.14	0.15
Yb	1.24	1.10	1.11	0.93	1.02	1.01	1.09	1.04	1.01	1.11
Lu	0.18	0.17	0.17	0.16	0.16	0.16	0.16	0.16	0.15	0.18
Hf	3.69	3.39	2.98	1.86	3.07	2.69	3.32	3.13	2.79	2.91
Ta	0.32	0.30	0.28	0.19	0.30	0.25	0.29	0.30	0.28	0.30
W	0.07	1.22	<1.7	3.03	1.59	<1.5	1.76	0.08	1.78	1.59
Ir (ppb)	<0.9	<1.2	0.1	0.1	<0.9	0.1	0.1	<1.1	<1.6	<1.2
Au (ppb)	2.4	0.3	1.0	0.0	<1.5	<1.6	1.1	0.7	0.3	0.6
Th	3.84	3.23	2.92	1.80	3.47	3.03	3.38	2.89	2.87	3.35
U	1.20	0.87	0.64	0.46	1.11	1.01	1.08	1.18	1.37	2.18
K/U	4,075	9,633	12,914	28,896	8,487	8,026	4,394	6,137	4,195	3,243
Zr/Hf	37.6	36.8	38.3	42.4	41.7	41.6	37.1	35.4	37.9	39.2
La/Th	6.53	5.83	6.36	7.45	6.54	6.09	8.52	6.44	7.52	7.40
Hf/Ta	11.6	11.4	10.5	9.58	10.2	10.9	11.5	10.4	9.97	9.67
Th/U	3.20	3.71	4.59	3.95	3.14	2.99	3.14	2.45	2.10	1.54
La _N /Yb _N	13.6	11.6	11.3	9.77	15.1	12.3	17.9	12.1	14.5	15.1
Eu/Eu*	1.01	0.99	1.01	1.09	1.05	1.01	0.99	0.92	1.01	0.97
CIA	52	55	49	41	52	51	55	50	52	54

^a Major element data (in wt%) by XRF (except Na₂O by INAA and Fe₂O₃, average of INAA and XRF data); All Fe as Fe₂O₃; Trace element data in ppm, except as noted: V, Cu, Sr, Y, Zr, Nb, and Ba by XRF; Ni and Zn: INAA and XRF data; all others by INAA; N = chondrite-normalized (Taylor and McLennan, 1985); Chemical index of alteration (CIA) = (Al₂O₃/[Al₂O₃ + CaO + Na₂O + K₂O]) x 100 in molecular proportions; All ratios are the average of the ratios calculated for each samples.

Abbreviations: S = Suevite; B = Polymict lithic impact breccia; P = Phyllite-Slate; G = Meta-graywacke; LGMG = Light greenish gray meta-graywacke; Gb = Meta-graywacke breccia; LOI = Loss on Ignition.

Appendices

Table B-1. Continued. Major and trace element composition for samples from drill core LB-08A.^a

Sample no.	KR8-095	KR8-096	KR8-097	KR8-098	KR8-099	KR8-100	KR8-101	KR8-102	KR8-103	KR8-104
Depth (m)	405.34	406.31	409.67	410.74	412.92	412.74	414.28	416.84	417.39	417.6
Lithology	G	G	G	G	G	G	G	Gb	G/S	G
SiO ₂	69.51	67.54	72.02	76.24	66.20	71.50	74.35	69.21	67.95	68.33
TiO ₂	0.44	0.52	0.47	0.33	0.39	0.40	0.33	0.42	0.39	0.41
Al ₂ O ₃	12.15	14.55	13.08	10.58	14.98	13.04	11.40	14.01	14.51	14.94
Fe ₂ O ₃	4.95	5.93	5.03	3.80	4.39	4.29	3.74	3.98	3.67	3.50
MnO	0.06	0.06	0.05	0.05	0.04	0.05	0.06	0.06	0.05	0.05
MgO	1.27	1.69	1.18	1.05	2.35	1.47	1.41	1.37	1.52	1.34
CaO	3.46	2.07	2.32	1.94	1.57	1.76	2.19	2.92	2.72	2.73
Na ₂ O	3.87	4.41	3.53	3.16	3.42	2.94	3.72	4.47	4.40	5.21
K ₂ O	0.73	0.93	0.99	0.58	1.56	1.51	0.44	1.00	1.55	1.07
P ₂ O ₅	0.09	0.13	0.09	0.09	0.06	0.10	0.10	0.11	0.10	0.12
LOI	2.57	2.17	1.79	1.53	4.96	2.21	1.91	2.64	3.34	2.62
Total	99.10	100.0	100.6	99.35	99.93	99.27	99.65	100.2	100.2	100.3
Sc	7.87	10.1	8.23	6.02	6.30	7.87	6.45	8.28	7.64	8.02
V	112	121	112	88	90	107	81	84	77	78
Cr	68	78	64	42	47	57	46	52	50	51
Co	10	12	10	6	8	9	6	10	10	9
Ni	20	27	22	24	28	31	25	23	32	21
Cu	49	29	18	<6	83	24	<6	10	25	19
Zn	49	62	53	38	38	50	43	42	45	41
As	0.49	0.63	3.28	3.20	1.96	4.59	0.60	9.34	7.88	4.76
Rb	27	35	33	25	34	50	22	37	54	39
Sr	595	638	510	462	548	491	477	552	502	454
Y	13	14	13	10	10	12	9	11	10	10
Zr	167	171	146	103	119	118	109	115	114	123
Nb	3	4	4	3	3	4	3	3	<3	4
Sb	0.89	0.53	0.73	0.67	0.89	0.49	0.46	0.75	0.39	0.66
Cs	1.52	1.95	2.06	2.19	5.74	3.49	1.35	2.38	4.00	2.63
Ba	439	510	690	521	363	861	284	664	835	547
La	31.5	28.2	29.5	17.2	24.6	21.0	17.8	21.3	20.7	17.9
Ce	60.0	55.6	55.7	34.0	47.4	41.5	35.4	41.9	39.2	35.5
Nd	24.6	24.5	23.2	15.0	19.1	17.5	15.3	13.6	17.6	16.7
Sm	4.25	4.19	4.16	2.78	2.90	3.01	3.10	3.36	3.29	3.02
Eu	1.17	1.20	1.11	0.79	0.91	0.85	0.83	0.97	0.93	0.93
Gd	3.38	2.86	2.61	2.10	2.23	2.23	2.46	2.73	2.57	2.43
Tb	0.42	0.46	0.41	0.28	0.31	0.32	0.31	0.38	0.32	0.32
Tm	0.18	0.23	0.21	0.13	0.15	0.16	0.15	0.17	0.16	0.16
Yb	1.31	1.52	1.29	0.90	1.00	1.10	1.01	1.20	0.94	1.04
Lu	0.23	0.24	0.19	0.15	0.16	0.17	0.15	0.19	0.14	0.16
Hf	5.07	5.09	3.86	2.79	3.00	3.03	3.08	3.45	3.33	3.30
Ta	0.33	0.37	0.38	0.25	0.28	0.29	0.30	0.33	0.28	0.28
W	1.60	3.48	0.40	<1.8	0.51	<1.5	0.11	2.95	2.54	0.05
Ir (ppb)	<1.5	<0.1	0.1	0.1	<1.1	<1.4	<1.1	0.9	1.0	0.4
Au (ppb)	0.7	<0.1	<1.6	0.2	0.8	1.4	0.5	0.3	<1.6	0.6
Th	4.36	4.36	4.42	2.67	3.19	2.82	2.84	3.35	2.99	3.00
U	1.95	1.58	1.90	0.67	1.72	1.00	1.23	1.35	1.40	1.21
K/U	3,102	4,886	4,336	7,208	7,522	12,491	2,974	6,168	9,176	7,357
Zr/Hf	32.9	33.6	37.8	37.0	39.7	39.0	35.4	33.4	34.2	37.3
La/Th	7.21	6.46	6.68	6.44	7.70	7.44	6.25	6.36	6.92	5.98
Hf/Ta	15.2	13.7	10.0	11.2	10.8	10.3	10.2	10.5	12.0	11.6
Th/U	2.23	2.76	2.33	4.00	1.85	2.81	2.31	2.49	2.13	2.48
La _N /Yb _N	16.2	12.5	15.4	12.9	16.6	12.9	11.9	12.0	14.8	11.6
Eu/Eu*	0.94	1.06	1.03	1.00	1.09	1.00	0.92	0.98	0.98	1.05
CIA	47	55	54	53	60	57	52	50	51	50

^a Major element data (in wt%) by XRF (except Na₂O by INAA and Fe₂O₃, average of INAA and XRF data); All Fe as Fe₂O₃; Trace element data in ppm, except as noted: V, Cu, Sr, Y, Zr, Nb, and Ba by XRF; Ni and Zn: INAA and XRF data; all others by INAA; N = chondrite-normalized (Taylor and McLennan, 1985); Chemical index of alteration (CIA) = (Al₂O₃/[Al₂O₃ + CaO + Na₂O + K₂O]) x 100 in molecular proportions; All ratios are the average of the ratios calculated for each samples.

Abbreviations: S = Suevite; B = Polymict lithic impact breccia; P = Phyllite-Slate; G = Meta-graywacke; LGMG = Light greenish gray meta-graywacke; Gb = Meta-graywacke breccia; LOI = Loss on Ignition.

Appendices

Table B-1. Continued. Major and trace element composition for samples from drill core LB-08A.^a

Sample no.	ADE-8a	KR8-106	KR8-107	KR8-108	KR8-109	KR8-110	KR8-111	KR8-112	KR8-113	KR8-114
Depth (m)	418.05	421.88	422.36	424.78	425.24	429.31	432.03	434.33	434.59	434.75
Lithology	P (S)	LGMG	S	G	G	G	Quartz	S	S	S
SiO ₂	58.91	55.99	59.01	70.08	73.55	68.91	96.97	63.44	64.28	64.76
TiO ₂	0.61	0.58	0.54	0.39	0.39	0.47	0.01	0.43	0.47	0.45
Al ₂ O ₃	18.30	10.78	13.33	14.88	10.82	14.10	n.d.	13.60	13.88	14.31
Fe ₂ O ₃	8.09	6.97	5.40	3.61	3.89	4.69	n.d.	4.44	4.69	4.61
MnO	n.d.	0.10	0.08	0.04	0.05	0.05	n.d.	0.06	0.06	0.06
MgO	3.97	9.48	5.16	1.21	1.06	1.26	n.d.	1.68	2.24	1.62
CaO	0.82	5.53	4.61	0.99	2.64	2.46	0.05	4.72	3.02	3.76
Na ₂ O	0.89	0.96	2.76	5.61	3.35	4.38	n.d.	2.93	2.97	3.33
K ₂ O	3.96	n.d.	0.87	0.97	0.54	0.96	n.d.	1.72	1.68	1.88
P ₂ O ₅	0.08	0.19	0.15	0.11	0.09	0.11	0.01	0.11	0.12	0.10
LOI	4.01	8.79	7.01	1.76	1.84	2.37	0.12	5.77	5.65	4.99
Total	99.64	99.37	98.92	99.66	98.23	99.77	97.16	98.89	99.06	99.87
Sc	20.9	16.2	12.3	7.78	6.49	8.10	n.d.	10.5	9.72	11.2
V	159	129	122	80	96	104	<12	101	101	105
Cr	97	531	238	49	47	54	20	79	101	81
Co	35	41	20	9	7	10	<6	13	15	13
Ni	68	386	156	23	17	26	<6	46	58	47
Cu	32	<6	11	<6	7	19	<6	22	19	22
Zn	108	88	64	40	42	51	<6	53	59	58
As	29.2	161	51.9	10.6	2.53	0.21	n.d.	12.5	25.6	12.2
Rb	136	13	39	31	30	36	<1	64	58	83
Sr	139	328	523	473	467	568	9	393	364	384
Y	18	11	12	11	10	13	<3	15	15	16
Zr	110	90	118	119	115	130	22	117	117	124
Nb	5	<3	3	4	3	3	<3	3	4	4
Sb	0.70	1.15	0.57	0.18	0.46	0.66	n.d.	0.56	0.65	0.69
Cs	7.65	1.04	2.50	1.76	3.45	2.46	n.d.	6.16	4.63	7.31
Ba	1,522	48	493	859	351	482	<20	691	715	743
La	16.5	15.8	19.0	19.7	19.3	23.1	n.d.	23.2	20.1	25.1
Ce	36.4	37.2	40.7	38.3	38.3	44.3	n.d.	45.1	40.6	50.5
Nd	18.6	22.5	22.4	17.3	18.4	20.1	n.d.	22.9	18.2	24.0
Sm	3.58	4.17	4.10	3.04	2.98	3.65	n.d.	3.88	3.32	4.48
Eu	1.11	1.06	1.12	0.88	0.85	1.11	n.d.	1.29	1.07	1.36
Gd	3.62	3.01	2.74	2.41	2.36	3.48	n.d.	3.38	3.23	4.09
Tb	0.54	0.47	0.44	0.34	0.32	0.45	n.d.	0.47	0.42	0.56
Tm	0.31	0.15	0.19	0.17	0.16	0.18	n.d.	0.23	0.18	0.19
Yb	1.88	0.98	1.17	1.09	1.05	1.18	n.d.	1.33	1.14	1.41
Lu	0.31	0.15	0.19	0.17	0.17	0.19	n.d.	0.21	0.19	0.23
Hf	2.89	2.25	3.08	3.34	3.02	3.57	n.d.	2.93	2.72	3.39
Ta	0.41	0.17	0.28	0.27	0.25	0.35	n.d.	0.28	0.26	0.38
W	2.17	<2.1	1.07	4.45	0.74	1.55	0.02	1.59	4.20	0.97
Ir (ppb)	0.3	<1.8	0.1	0.5	<0.9	0.2	<0.3	<1.1	<1.1	<1.4
Au (ppb)	0.7	0.1	0.0	0.4	0.8	0.3	0.1	1.1	0.8	<1.2
Th	3.21	2.01	2.66	2.68	2.88	3.88	n.d.	3.01	2.61	3.68
U	1.20	1.14	0.88	0.70	0.75	1.31	0.12	1.19	1.03	1.40
K/U	27,317		8,220	11,498	6,013	6,089		11,961	13,570	11,145
Zr/Hf	38.0	40.0	38.3	35.7	38.0	36.4		40.0	43.0	36.6
La/Th	5.14	7.86	7.12	7.37	6.69	5.94		7.71	7.68	6.83
Hf/Ta	7.13	13.1	10.9	12.5	12.1	10.1		10.6	10.4	8.87
Th/U	2.67	1.76	3.03	3.82	3.86	2.97		2.52	2.54	2.63
La _N /Yb _N	5.95	10.8	11.0	12.3	12.4	13.2		11.8	11.9	12.0
Eu/Eu*	0.94	0.92	1.02	1.00	0.98	0.95		1.09	1.00	0.97
CIA	72	48	49	55	50	53		47	53	50

^a Major element data (in wt%) by XRF (except Na₂O by INAA and Fe₂O₃, average of INAA and XRF data); All Fe as Fe₂O₃; Trace element data in ppm, except as noted: V, Cu, Sr, Y, Zr, Nb, and Ba by XRF; Ni and Zn: INAA and XRF data; all others by INAA; N = chondrite-normalized (Taylor and McLennan, 1985); Chemical index of alteration (CIA) = (Al₂O₃/[Al₂O₃ + CaO + Na₂O + K₂O]) x 100 in molecular proportions; All ratios are the average of the ratios calculated for each samples.

Abbreviations: S = Suevite; B = Polymict lithic impact breccia; P = Phyllite-Slate; G = Meta-graywacke; LGMG = Light greenish gray meta-graywacke; Gb = Meta-graywacke breccia; LOI = Loss on Ignition.

Appendices

Table B-1. Continued. Major and trace element composition for samples from drill core LB-08A.^a

Sample no.	KR8-115	KR8-117	CAN-31	KR8-119	KR8-120	KR8-121	KR8-122	KR8-122a	KR8-123	KR8-124	KR8-125
Depth (m)	437.37	439.87	440.32	441.87	442.11	446.02	446.69	447.14	447.96	449.12	451.23
Lithology	G	G	S	G	G	LGMG	G	LGMG	G	G	G
SiO ₂	69.74	67.94	65.89	77.60	66.21	53.49	69.15	54.68	68.51	68.38	70.49
TiO ₂	0.42	0.46	0.48	0.32	0.57	0.67	0.39	0.65	0.44	0.40	0.39
Al ₂ O ₃	14.26	12.91	14.51	9.23	13.33	12.12	13.24	13.22	12.64	12.63	13.00
Fe ₂ O ₃	4.17	4.98	4.69	3.31	5.39	7.34	3.73	6.43	3.40	3.91	3.82
MnO	0.05	0.05	0.06	0.03	0.07	0.11	0.04	0.10	0.06	0.07	n.d.
MgO	1.33	1.43	1.62	0.68	1.94	8.54	1.22	6.38	1.46	2.08	1.28
CaO	1.53	2.50	2.81	1.40	3.10	6.28	2.37	7.19	2.85	3.61	1.63
Na ₂ O	4.55	3.90	3.04	3.28	3.14	2.05	4.32	3.62	4.96	3.05	3.99
K ₂ O	1.43	1.21	2.07	0.51	1.45	n.d.	1.29	0.12	0.64	1.46	1.35
P ₂ O ₅	0.08	0.10	0.12	0.06	0.12	0.14	0.09	0.14	0.10	0.10	0.10
LOI	2.47	3.95	4.38	1.95	4.35	8.82	3.28	8.90	3.99	4.37	3.26
Total	100.0	99.43	99.67	98.37	99.67	99.56	99.11	101.4	99.05	100.1	99.31
Sc	9.11	8.96	11.1	5.34	9.56	20.4	6.90	20.3	9.93	7.75	7.83
V	85	105	108	80	116	143	72	142	113	94	86
Cr	57	67	71	36	74	442	48	272	57	50	52
Co	11	12	12	6	12	41	9	28	9	9	8
Ni	28	31	38	20	33	193	18	120	27	28	28
Cu	17	32	32	9	14	6	74	19	11	20	12
Zn	49	53	62	30	64	82	35	72	36	45	48
As	7.09	2.66	6.81	4.27	11.2	121	7.54	33.5	7.13	0.73	0.51
Rb	58	48	74	25	49	5	44	13	23	44	53
Sr	427	352	383	348	462	554	436	854	619	562	554
Y	11	12	14	9	17	12	11	12	12	13	10
Zr	104	140	120	92	151	81	114	78	116	112	100
Nb	3	3	3	3	4	<3	3	<3	<3	<3	3
Sb	0.37	0.48	0.57	0.12	0.21	0.52	0.35	0.30	0.11	0.12	0.06
Cs	3.34	3.44	6.51	1.76	2.99	0.48	2.77	0.85	1.42	2.37	2.86
Ba	798	752	803	403	769	46	688	137	518	664	557
La	18.0	24.7	23.1	21.3	25.5	10.5	18.9	12.7	18.4	17.1	19.8
Ce	36.1	49.2	46.8	40.7	50.2	23.8	38.1	26.9	37.7	34.1	39.9
Nd	17.2	20.8	21.0	18.1	20.7	12.5	16.3	15.0	16.8	15.2	18.1
Sm	3.01	3.63	3.85	2.72	3.83	2.81	2.74	3.30	3.09	2.81	3.33
Eu	0.91	1.09	1.21	0.75	1.19	0.78	1.02	0.98	1.17	0.94	0.97
Gd	1.96	2.71	3.23	2.73	3.63	2.18	2.23	2.35	3.27	2.50	2.74
Tb	0.36	0.43	0.48	0.53	0.48	0.40	0.31	0.43	0.39	0.38	0.37
Tm	0.16	0.17	0.19	0.13	0.20	0.16	0.14	0.20	0.16	0.17	0.15
Yb	1.14	1.11	1.32	0.86	1.53	1.07	0.96	1.30	1.16	1.22	1.03
Lu	0.18	0.19	0.22	0.14	0.25	0.17	0.16	0.21	0.19	0.21	0.17
Hf	2.97	4.03	3.47	3.28	4.29	2.14	2.82	2.38	3.07	2.57	3.83
Ta	0.31	0.32	0.33	0.25	0.36	0.18	0.29	0.20	0.21	0.22	0.32
W	1.45	3.28	6.17	4.27	0.67	3.84	1.53	3.93	0.18	1.22	5.45
Ir (ppb)	0.8	<1.5	<1.2	0.1	0.1	0.1	0.4	1.5	0.1	0.0	0.3
Au (ppb)	1.0	<1.5	<1.3	<1.5	0.6	1.3	<1.3	1.2	<1.8	<1.4	<1.3
Th	2.79	3.80	3.85	2.99	4.24	1.54	2.82	1.70	3.20	2.88	2.90
U	0.77	0.77	1.03	0.83	0.87	0.85	0.72	0.76	0.81	0.70	0.91
K/U	15,397	13,082	16,705	5,096	13,789		14,923	1,306	6,575	17,324	12,253
Zr/Hf	35.1	34.7	34.6	28.0	35.2	37.9	40.4	32.8	37.7	43.5	26.1
La/Th	6.46	6.51	5.99	7.14	6.00	6.86	6.71	7.47	5.76	5.95	6.85
Hf/Ta	9.59	12.5	10.4	13.2	11.9	11.7	9.58	11.7	15.0	11.6	11.8
Th/U	3.62	4.95	3.75	3.59	4.86	1.81	3.94	2.23	3.96	4.12	3.17
La _N /Yb _N	10.7	15.1	11.8	16.8	11.2	6.63	13.3	6.63	10.7	9.50	13.0
Eu/Eu*	1.14	1.06	1.04	0.84	0.97	0.96	1.26	1.08	1.12	1.08	0.98
CIA	55	51	54	52	52	45	51	41	47	49	54

^a Major element data (in wt%) by XRF (except Na₂O by INAA and Fe₂O₃, average of INAA and XRF data); All Fe as Fe₂O₃; Trace element data in ppm, except as noted: V, Cu, Sr, Y, Zr, Nb, and Ba by XRF; Ni and Zn: INAA and XRF data; all others by INAA; N = chondrite-normalized (Taylor and McLennan, 1985); Chemical index of alteration (CIA) = (Al₂O₃/[Al₂O₃ + CaO + Na₂O + K₂O]) x 100 in molecular proportions; All ratios are the average of the ratios calculated for each samples.

Abbreviations: S = Suevite; B = Polymict lithic impact breccia; P = Phyllite-Slate; G = Meta-graywacke; LGMG = Light greenish gray meta-graywacke; Gb = Meta-graywacke breccia; LOI = Loss on Ignition.

Appendix C: Petrographic descriptions of LB-08A drill core samples

Detailed petrographic descriptions of the 176 thin sections (i.e., 153 standard thin sections and 23 polished thin sections), prepared from the 121 samples taken from drill core LB-08A, are reported. Note that when more than one thin section was available for a given sample, observations are usually combined; in rare cases specific observations, made on a given thin section, are reported, and the exact reference of the thin section is indicated (e.g., KR8-XXX [A]).

KR8-001 (depth = 235.77 m) – Suevite

Suevite with a variety of lithic and mineral clasts; including meta-graywacke, phyllite, slate, melt particles (partially or completely devitrified), carbon-rich organic shale, diaplectic quartz glass, and calcite clasts. One clast of a lithology similar to e.g., sample KR8-069, i.e., chloritoid-rich meta-graywacke with granophyric material, also occurs. Minerals identified include quartz, K-feldspar, plagioclase, muscovite, chlorite, calcite, rutile, sphene, and opaque minerals. In addition, monazite was characterized using SEM. All the biotite is altered to chlorite and most of the feldspar to sericite (some feldspars are cloudy). Quartz grains show undulatory extinction, irregular microfractures, and some PFs and PDFs occur (1 or 2 sets, one quartz grains with 3 sets). A few quartz grains are isotropic. An interesting shear fracture with different types of planar microdeformations occurs in a large quartz grain. Calcite aggregates are present in the matrix.

KR8-002 (depth = 236.40 m) – Phyllite with quartzitic laminae/ribbon quartz (clast)

Well-banded and folded phyllite with quartzitic laminae/ribbon quartz (clast in the impact breccia section). Composed mainly of quartz, muscovite, chlorite, rutile, opaque minerals, and zircon. Quartz grains show microfractures and display undulatory extinction. Local development of crenulation cleavage (in the most micaceous layers). A few microfractures transect the section; some of them are filled with iron oxides. No obvious shock effects, such as PDFs in quartz. The sample is very similar to KR8-007.

KR8-003 (depth = 238.90 m) – Suevite

Suevite with a variety of lithic and mineral clasts; including meta-graywacke, phyllite, slate, melt particles (partially or completely devitrified; brown and black in color), carbon-rich organic shale (partially melted?), quartzite, and calcite clasts. The sample is very similar to KR8-001 in composition and appearance (but no diaplectic quartz glass seen). Minerals identified include quartz, K-feldspar, plagioclase, muscovite, chlorite, amphibole, and a few rutile and opaque minerals. All the biotite is altered to chlorite and most of the feldspar to sericite (some feldspars are cloudy). Some of the quartz grains show undulatory extinction, irregular microfractures, and a few display PDFs (1 or 2 sets). A few quartz grains are isotropic. Calcite aggregates are present in the matrix.

KR8-004 (depth = 239.65 m) – Suevite

Suevite with a variety of lithic and mineral clasts; including phyllite and slate (with development of crenulation cleavage), mylonitic meta-graywacke, quartzite, melt particles (in a few cases with flow structure and vesicles) brown or black in color (one large melt particle in the center of the section is about 1 cm in the longest dimension), and carbon-rich organic shale. Many melt particles occur. Minerals identified include quartz, K-feldspar, plagioclase, muscovite, chlorite, biotite, rutile, and opaque minerals. Most of the biotite is altered to chlorite. Some quartz grains show undulatory extinction and some PFs and PDFs (1 or 2 sets). Feldspar grains are altered to sericite and display a cloudy appearance. Microfractures filled with iron oxides transect the section. Calcite aggregates occur in the matrix.

KR8-005 (depth = 240.04 m) – Suevite

Suevite with a variety of lithic and mineral clasts; including phyllite (similar to KR8-002, with large ribbon quartz) and slate, melt particles (brown or black in color and with vesicles), mylonitic meta-graywacke, carbon-rich organic shale, quartzite, calcite, and diaplectic quartz glass. Many melt particles occur. Minerals identified include quartz, K-feldspar, plagioclase, muscovite, rutile, and opaque minerals. All the biotite is altered to chlorite and most of the feldspar to sericite (feldspar are cloudy). Quartz grains show undulatory extinction and some display PFs and PDFs (1 or 2 sets; one quartz grains with 3 sets). Calcite aggregates occur in the matrix.

KR8-006 (depth = 240.36 m) – Quartzite clast in suevite

Quartzite clast in suevite with numerous calcite veinlets. Minerals identified include quartz, calcite, and a few opaque minerals (such as pyrite). Quartz grains show microfractures and undulatory extinction. There are abundant PDFs (1, 2, 3, and 4 sets) in quartz grains, partially or totally toasted. A small part of the section comprises suevite with lithic and mineral clasts of mylonitic meta-graywacke, phyllite and slate, quartzite, melt particle (only one; with tiny undigested quartz grains), and a few carbon-rich organic shale. Minerals identified include quartz, K-feldspar, plagioclase, chlorite, muscovite, and opaque minerals (pyrite). A few quartz grains show PFs (no PDFs seen). Feldspar grains are partially altered to sericite. A few calcite aggregates occur in the matrix of the suevite portion.

KR8-007 (depth = 241.94 m) – Phyllite with quartzitic laminae/ribbon quartz (clast)

Well-banded and folded phyllite with quartzitic laminae/ribbon quartz (clast in the impact breccia section). Composed mainly of quartz, muscovite, chlorite, and opaque minerals. Quartz grains show microfractures and display undulatory extinction. Chlorite veinlets, aligned parallel to the foliation of the rock, occur. A few microfractures transect the section; some of them are filled with iron oxides. No trace of shock deformation seen. The sample is very similar to KR8-002.

KR8-008 (depth = 244.45 m) – Strongly altered polymict lithic breccia (clast-supported)

Strongly altered polymict lithic breccia (clast-supported) with a variety of lithic and mineral clasts: meta-graywacke (some mylonitic), phyllite and slate, and quartzite. Minerals identified include quartz, K-feldspar, plagioclase, muscovite, chlorite, biotite, opaque minerals, and

zircon. Some of the quartz grains show undulatory extinction, microfractures, and few PDFs (1 or 2 sets) have also been observed. Most of the biotite is altered to chlorite and feldspar to sericite (some feldspar grains are cloudy).

KR8-009 (depth = 244.87 m) – Altered polymict lithic breccia (clast-supported)

Altered polymict lithic breccia (clast-supported) with lithic and mineral clasts; including faulted clasts of phyllite and slate with quartzitic laminae, quartzite, and meta-graywacke clasts. Minerals identified include quartz, K-feldspar, muscovite, chlorite, and tabular opaque minerals. All the biotite is altered to chlorite. Some of the quartz grains show undulatory extinction. A few PFs and PDFs (1 or 2 sets) occur in quartz grains.

KR8-010 (depth = 245.58 m) – Altered polymict lithic breccia with injected suevitic breccia

Altered polymict lithic breccia (one part of the section is very similar to sample KR8-009 and one other part to KR8-008) with injected suevitic breccia (veinlets). One part of the section show faulted clasts of phyllite and slate with quartzitic laminae and breccia veinlets (matrix poor), and a few quartzite and meta-graywacke clasts. The second part of the section display mylonitic meta-graywacke, phyllite and slate, and quartzite clasts. Minerals identified include quartz, K-feldspar, muscovite, chlorite, and tabular opaque minerals. All the biotite is altered to chlorite and some of the feldspar to sericite. Some of the quartz grains show undulatory extinction. A few PFs and PDFs (1 or 2 sets) occur in quartz grains.

KR8-011 (depth = 247.46 m) – Altered polymict lithic breccia

Altered polymict lithic breccia composed mainly of mylonitic meta-graywacke, quartzite, and phyllite and slate clasts. Minerals identified include quartz, K-feldspar, plagioclase, muscovite, calcite, chlorite, opaque minerals and a few biotite. Quartz grains show microfractures and undulatory extinction. Many quartz grains show PFs and/or PDFs (1 or 2 sets, one grain with 3 sets). Calcite aggregates occur in the matrix.

KR8-012 (depth = 248.00 m) – Suevite

Suevite with a variety of lithic and mineral clasts; including mylonitic meta-graywacke, phyllite and slate (fine-grained, well-foliated and with locally development of crenulation cleavage), melt particles (devitrified), quartzite, carbon-rich organic shale, and rare calcite clasts. Minerals identified include quartz, K-feldspar, plagioclase, chlorite, muscovite, calcite, and opaque minerals. Most of the biotite is altered to chlorite and feldspar to sericite (feldspar grains are cloudy). Some of the quartz grains show microfractures and undulatory extinction. A few quartz grains display PDFs (1 or 2 sets). Calcite aggregates are present in the matrix.

KR8-013 (depth = 248.80 m) – Altered polymict lithic breccia

Altered polymict lithic breccia composed mainly of mylonitic meta-graywacke, quartzite, and phyllite and slate clasts. Minerals identified include quartz, K-feldspar, plagioclase, muscovite, calcite, chlorite, and a few rutile, opaque minerals (such as pyrite), biotite, and sphene. Quartz grains show microfractures and undulatory extinction. Many PFs and PDFs (1 or 2 sets) in quartz grains (locally toasted). Calcite aggregates are present in the matrix. The sample is similar to KR8-011.

KR8-014 (depth = 249.30 m) – Suevite (matrix dominate)

Suevite with a variety of lithic and mineral clasts; including altered meta-graywacke, phyllite and slate, melt particles (gray to brown in color), quartzite, and calcite. Minerals identified include quartz, K-feldspar, plagioclase, chlorite, muscovite, calcite, biotite, rutile, and opaque minerals. Most of the feldspar is altered to sericite and biotite to chlorite. Quartz grains show microfractures and undulatory extinction. A few quartz grains show PFs and PDFs with 1 set (only 3 quartz grains with 2 sets of PDFs each). Calcite aggregates are present in the matrix.

KR8-015 (depth = 250.74 m) – Altered polymict lithic breccia (clast-supported)

Altered polymict lithic breccia (clast-supported) composed of two different clast types, phyllite (and/or slate) and mylonitic meta-graywacke. Minerals identified include quartz, K-feldspar, muscovite, calcite, chlorite, biotite, opaque minerals, and a few plagioclases. Most of the biotite is altered to chlorite and feldspar to sericite. Phyllite shows locally development of crenulation cleavage in the most micaceous layers. Quartz veinlets transect the section (aligned parallel or sub-parallel to the foliation of the rock). Lots of the quartz grains are fractured, a few show undulatory extinction, and a few others PFs and PDFs (1 or 2 sets). Many microfractures transect the section and are filled with clay minerals as alteration products. Mylonitic meta-graywacke clasts display veinlets and aggregates of calcite.

KR8-016 (depth = 250.89 m) – Strongly altered polymict lithic breccia with injected suevitic breccia (veinlet)

Strongly altered polymict lithic breccia with injected suevitic breccia veinlet; composed of a variety of clasts, including phyllite and slate (with development of crenulation cleavage), mylonitic meta-graywacke, melt particles (brown in color) that are completely devitrified, and quartzite clasts. Minerals identified include quartz, K-feldspar, plagioclase, muscovite, biotite, chlorite, and opaque minerals. Most of the biotite is altered to chlorite and feldspar to sericite (some feldspars are cloudy). Some of the quartz grains show microfractures, undulatory extinction, and a few PDFs (1 or 2 sets). Isotropic quartz grains also occur. The alteration is localized mainly around the suevitic breccia veinlet; several microfractures filled with iron oxides transect the suevitic breccia veinlet.

KR8-017 (depth = 251.74 m) – Altered polymict lithic breccia (clast-supported)

Altered polymict lithic breccia (clast-supported) composed of two different clast types, phyllite (and/or slate) and mylonitic meta-graywacke. Minerals identified include quartz, K-feldspar, muscovite, plagioclase, calcite, chlorite, biotite, and opaque minerals. Most of the biotite is altered to chlorite and feldspar to sericite. Phyllite shows locally development of crenulation cleavage in the most micaceous layers. Some of the quartz grains show microfractures and/or PFs and PDFs (1 or 2 sets). Mylonitic meta-graywacke clasts display veinlets and aggregates of calcite. Many microfractures transect the section. The sample is very similar to KR8-015.

KR8-018 (depth = 253.04 m) – Altered polymict lithic breccia (clast-supported)

Altered polymict lithic breccia (clast-supported) composed of two different clast types, phyllite (and/or slate) and mylonitic meta-graywacke. Minerals identified include quartz, K-feldspar, muscovite, plagioclase, calcite, chlorite, biotite, and opaque minerals. Most of the biotite is

altered to chlorite and feldspar to sericite. Phyllite shows locally development of crenulation cleavage. Some of the quartz grains show microfractures and/or PFs and PDFs (1 or 2 sets). Aggregates of tiny opaque minerals and tabular opaque crystals occur. A few calcite aggregates are present in the matrix. The sample is very similar to KR8-015 and KR8-017.

KR8-019 (depth = 253.56 m) – Altered polymict lithic breccia with injected suevitic breccia (veinlets)

Altered polymict lithic breccia with injected suevitic breccia veinlets; composed of meta-graywacke clasts (dominant), a few melt particles (altered), phyllite and slate, and calcite clasts. Minerals identified include quartz, K-feldspar, calcite, plagioclase, muscovite, chlorite, and a few opaque minerals, sphene, biotite, and epidote. Most of the biotite is altered to chlorite. Some of the quartz grains show microfractures and undulatory extinction. Very few quartz grains display PFs (no PDFs seen). Some feldspar grains are altered to sericite and display a cloudy appearance. Abundant calcite aggregates and veinlets. Aggregates of tiny opaque minerals are present in the section. Microfractures transect the section and are filled with calcite or locally with iron oxides.

KR8-021 (depth = 255.65 m) – Altered polymict lithic breccia (clast-supported)

Altered polymict lithic breccia (clast-supported) composed of two different clast types, phyllite (and/or slate) and mylonitic meta-graywacke. Phyllite clasts show development of crenulation cleavage. Minerals identified include quartz, muscovite, calcite, chlorite, opaque minerals, a few feldspar (partially altered to sericite), and very few biotite. Most of the biotite is altered to chlorite and feldspar to sericite. Some of the quartz grains show microfractures, undulatory extinction, and a few grains are isotropic. A few quartz grains show PFs (no PDFs seen). Many calcite aggregates and veinlets occur. A few microfractures transect the section and are filled with iron oxides. The sample is very similar to KR8-015, KR8-017, and KR8-018.

KR8-022 (depth = 256.81 m) – Altered polymict lithic breccia (clast-supported)

Altered polymict lithic breccia (clast-supported) composed of two different clast types, phyllite (and/or slate) and mylonitic meta-graywacke. Some phyllite clasts show development of crenulation cleavage. Minerals identified include quartz, muscovite, calcite, K-feldspar, plagioclase, chlorite, opaque minerals (tabular crystals and aggregates), and a few biotite and epidote. Most of the biotite is altered to chlorite. Quartz grains show undulatory extinction and some grains are isotropic. Some feldspar grains are altered to sericite (preferentially plagioclase grains). A tiny suevitic veinlet mostly composed of melt particles, isotropic quartz grains, and quartz grains with undulatory extinction, is present in the thin section. Several calcite veinlets and aggregates occur. No PDFs seen. The sample is very similar to KR8-015, KR8-017, KR8-018, and KR8-021.

KR8-023 (depth = 258.14 m) – Suevite

Suevite with a variety of lithic and mineral clasts; including meta-graywacke (medium-grained meta-graywacke dominant) to mylonitic meta-graywacke, slate and phyllite, melt particles (brown in color; with tiny undigested grains, mainly quartz grains), quartzite, and minor calcite clasts. Minerals identified include quartz, K-feldspar, plagioclase, muscovite, chlorite, opaque

minerals, and a few biotite, epidote, and sphene. Most of the biotite is altered to chlorite. Some of the quartz grains show microfractures and undulatory extinction. A few isotropic quartz grains occur. A few quartz grains (some partially toasted) show PFs (no PDFs seen). Feldspar and especially plagioclase grains are altered to sericite and display a cloudy appearance. A few feldspar crystals are recrystallized (myrmekitic intergrowths of quartz and feldspar). Some calcite and opaque minerals aggregates occur in the matrix.

KR8-024 (depth = 259.14 m) – Altered polymict lithic breccia (clast-supported)

Altered polymict lithic breccia (clast-supported) composed of two different clast types, mylonitic meta-graywacke faulted phyllite (and/or slate). Some phyllite clasts show development of crenulation cleavage. Unusual outline (step-like; possibly result of faulting?) of phyllite in contact with mylonitic meta-graywacke. Minerals identified include quartz, K-feldspar, plagioclase, muscovite, chlorite, and opaque minerals. All the biotite is altered to chlorite. Quartz grains show microfractures and undulatory extinction. Isotropic quartz grains have been seen in the section. Very few quartz grains show PFs (no PDFs seen). Feldspar and especially plagioclase grains are partially altered to sericite. A few fine-grained breccia veinlets (suevite?) occur. Calcite aggregates and veinlets occur. Many opaque grains occur in the matrix.

KR8-025 (depth = 259.74 m) – Suevite

Suevite with a variety of lithic and mineral clasts; including meta-graywacke (fine- to medium-grained; some are mylonitic or sheared), quartzite, slate, phyllite, melt particles brown to black in color, and a few calcite clasts. Minerals identified include quartz, K-feldspar, plagioclase, muscovite, chlorite, calcite, opaque minerals, and a few sphene and epidote. All the biotite is altered to chlorite. Quartz grains show microfractures and undulatory extinction. A few isotropic quartz grains occur. Very few quartz grains with PFs occur (no PDFs seen). Feldspar grains are partially altered to sericite and display a cloudy appearance. Some calcite and opaque minerals aggregates occur in the matrix.

KR8-026 (depth = 260.49 m) – Suevite

Suevite with a variety of lithic and mineral clasts; including phyllite, fine- to medium-grained meta-graywacke (some are mylonitic), melt particles (brown or black in color), quartzite, slate, and calcite clasts. Minerals identified include quartz, K-feldspar, plagioclase, chlorite, muscovite, opaque minerals, and some sphene. All the biotite is altered to chlorite. Some of the quartz grains show microfractures, undulatory extinction, and/or mosaicism. Many quartz grains show PDFs (1 or 2 sets), generally decorated, and some quartz grains are partially toasted. Feldspar grains are partially altered to sericite. A few feldspar crystals are recrystallized with spherulitic texture (myrmekitic intergrowths of quartz and feldspar). Calcite aggregates occur, as well as large opaque minerals (such as pyrite), opaque aggregates, and opaque minerals with a rim of iron oxides.

KR8-027 (depth = 263.76 m) – Sheared, fine-grained meta-graywacke

Sheared, fine-grained meta-graywacke composed mainly of quartz, K-feldspar, plagioclase, muscovite, chlorite, epidote, sphene, and opaque minerals (such as pyrite). Quartz grains show

microfractures and undulatory extinction; a few grains are partially isotropic. Some quartz grains show PFs and PDFs (a few grains with 2 sets of PDFs each). Feldspar grains are altered to sericite and display a cloudy appearance. Calcite aggregates and veinlets occur.

KR8-028 (depth = 266.18 m) – Very fine-grained metasediment (slate)

Well-banded and folded very fine-grained metasediment (slate). Minerals identified include quartz, K-feldspar, plagioclase, muscovite, biotite, and opaque minerals (such as pyrite). Quartz grains show microfractures and undulatory extinction. A few quartz grains contain PDFs (1 set). Quartz veinlets and calcite aggregates occur. The sample is very similar to KR8-046.

KR8-029 (depth = 271.43 m) – Gritty meta-graywacke

Gritty meta-graywacke, composed mainly of quartz, K-feldspar, plagioclase, chlorite, muscovite, calcite, opaque minerals, sphene, and rare biotite. Most of the biotite is altered to chlorite. Quartz grains show numerous microfractures, undulatory extinction, and mosaicism. There are abundant PDFs in quartz (1, 2, rarely 3 sets; one grain with 4 sets); many PDFs are decorated; some quartz grains are toasted. Feldspar grains show numerous microfractures, undulatory extinction, and are commonly altered to sericite (feldspars are cloudy). Polysynthetic twinning in plagioclase has been displaced along tiny faults. Some quartz and feldspar grains are partially isotropic. Calcite aggregates occur. The sample is very similar to KR8-030 and KR8-065.

KR8-030 (depth = 272.00 m) – Gritty meta-graywacke

Gritty meta-graywacke, composed mainly of quartz, K-feldspar, plagioclase, muscovite, epidote, zircon, sphene, opaque minerals (such as pyrite), and rare biotite. Most of the biotite is altered to chlorite and feldspar to sericite. Quartz grains show microfractures, undulatory extinction, and mosaicism. There are abundant PDFs in quartz (1, 2, and 3 sets; rarely 4 sets); many PDFs are decorated; some quartz grains are toasted. Feldspar grains show many microfractures and undulatory extinction; some feldspar grains are partially isotropic. Calcite aggregates occur. The sample is very similar to KR8-029.

KR8-031 (depth = 273.99 m) – Gritty meta-graywacke

Gritty meta-graywacke, very similar to KR8-029 and KR8-030; composed mainly of quartz, K-feldspar, plagioclase, muscovite, chlorite, opaque minerals (mostly pyrite), epidote, zircon, and sphene. Most of the feldspar grains are altered to sericite and display a cloudy appearance. Quartz grains show microfractures, undulatory extinction, and mosaicism. There are abundant PDFs in quartz (1, 2, rarely 3 sets). Feldspar grains show abundant microfractures and undulatory extinction. Some quartz and feldspar grains are partially isotropic. Calcite aggregates occur.

KR8-032 (depth = 274.99 m) – Medium-grained to gritty meta-graywacke

Gritty to medium-grained meta-graywacke; composed mainly of quartz, K-feldspar, plagioclase, muscovite, chlorite, sphene, and opaque minerals. Most of the feldspar grains are altered to sericite and display a cloudy appearance. Quartz grains show microfractures and undulatory extinction. There are abundant PDFs (1, 2, or 3 sets) in quartz grains; PDFs are

decorated; some quartz grains are partially or totally toasted. Feldspar grains show abundant microfractures and undulatory extinction. Some quartz and feldspar grains are partially isotropic. Calcite aggregates occur.

KR8-033 (depth = 277.03 m) – Medium-grained meta-graywacke

Medium-grained meta-graywacke composed mainly of quartz, K-feldspar, plagioclase, muscovite, chlorite, sphene, and opaque minerals. Quartz grains show microfractures, undulatory extinction, and some grains are partially isotropic. Lots of PDFs in quartz (1 or 2 sets); PDFs are commonly decorated; some quartz grains are toasted. Feldspar grains show many microfractures and are partially altered to sericite (some feldspars are cloudy). Shock-induced twinning in plagioclase. Aggregates of calcite occur.

KR8-034 [B] (depth = 277.89 m) – Mylonitic, medium-grained to gritty meta-graywacke (locally brecciated)

Mylonitic meta-graywacke composed mainly of quartz, K-feldspar, plagioclase, muscovite, chlorite, calcite, opaque minerals, epidote, and a few biotite, zircon, and allanite. Rare chert clasts also occur. Quartz grains show microfractures and undulatory extinction. Lots of PDFs in quartz (1 or 2 sets), some decorated, and some grains are partially toasted. Feldspar grains show microfractures and are partially altered to sericite (some feldspars are cloudy). Locally, polysynthetic twinning in plagioclase has been displaced along tiny faults. A large veinlet of calcite transects the section; calcite aggregates also occur.

KR8-035 (depth = 280.30 m) – Altered suevite (dikelet)

Altered suevite with a variety of lithic and mineral clasts: meta-graywacke (sheared or mylonitic), quartzite, phyllite and slate (some clasts displays crenulation cleavage), altered melt particles (gray to brown in color; commonly with tiny undigested quartz grains), and calcite clasts. Minerals identified include quartz, K-feldspar, plagioclase, muscovite, chlorite, epidote, sphene, and opaque minerals (mostly pyrite). Biotite is altered to chlorite. Quartz grains show microfractures, some grains display PDFs (1 or 2 sets), and a few grains are toasted. Feldspar grains are partially altered to sericite and display a cloudy appearance. Calcite aggregates occur.

KR8-036 (depth = 281.32 m) – Mylonitic, medium-grained meta-graywacke

Mylonitic, medium-grained meta-graywacke composed mainly of quartz, K-feldspar, plagioclase, muscovite, biotite, chlorite, epidote, opaque minerals, rutile, and rare zircon. Some quartz grains show microfractures and undulatory extinction. Abundant PDFs in quartz (1 or 2 sets, rarely 3 sets), some decorated (~50 rel%); a few quartz grains are partially toasted (less than 15 rel%). Feldspar grains are partially or totally altered to sericite (some grains are cloudy) and some show microfractures. Calcite veinlets and aggregates occur.

KR8-037 (depth = 283.50 m) – Mylonitic, medium-grained meta-graywacke

Mylonitic, medium-grained meta-graywacke composed mainly of quartz, K-feldspar, plagioclase, chlorite (representing more than 10 vol% of the section), muscovite, biotite, epidote, sphene, rutile, zircon, and opaque minerals. A clast of organic dark matter occurs as

well. Some quartz grains show microfractures and undulatory extinction; rarely quartz grain mosaicism. Many PDFs in quartz (1 or 2 sets, rarely 3 sets); about 60 rel% of the PDFs are decorated; 25 rel% of the quartz grains are toasted. Most of the feldspar grains are totally altered to sericite (some are cloudy) and some show microfractures. A few calcite aggregates occur. Muscovite grains display rarely kink bands.

KR8-038 [A1, A2, B, and C] (depth = 283.74 m) – Brecciated meta-graywacke locally mylonized

Brecciated meta-graywacke, locally mylonized, composed mainly of quartz, K-feldspar, plagioclase, muscovite, epidote, rutile, a few biotite and opaque minerals, and rare zircon. Quartz grains show microfractures. Lots of PDFs in quartz (1 or 2 sets); some quartz grains are partially toasted. Feldspar grains show microfractures and are partially altered to sericite (some are cloudy). In rare cases, polysynthetic twinning in plagioclase has been displaced along tiny faults. Calcite aggregates occur.

KR8-039 [A1, A2, B, and C] (depth = 286.17 m) – Strongly altered suevite (dikelet)

Strongly altered suevite with a variety of lithic and mineral clasts: abundant melt particles (gray to brown in color; with tiny undigested quartz grains), meta-graywacke (some mylonitic), quartzite, phyllite and slate, and calcite clasts. Minerals identified include quartz, K-feldspar, plagioclase, muscovite, chlorite, calcite, amphibole, and a few biotite, apatite, and sphene. Biotite is mostly altered to chlorite. Feldspar grains are partially altered to sericite and display a cloudy appearance. Calcite aggregates occur.

KR8-040 [A and B] (depth = 290.47 m) – Suevite (dikelet)

Suevite with a variety of lithic and mineral clasts: meta-graywacke clast (altered, weakly sheared fine-grained meta-graywacke principally), phyllite, melt particles (mostly brown in color), and calcite clasts. Minerals identified include quartz, K-feldspar, plagioclase, muscovite, chlorite, opaque minerals, and a few biotite, sphene, and epidote. Some quartz grains show undulatory extinction and very few quartz grains display PFs (only one grain with 1 set of PDFs). Feldspar grains are partially or totally altered to sericite and display a cloudy appearance. Calcite aggregates occur.

KR8-041 [A1, A2, and B] (depth = 293.79 m) – Suevite (dikelet)

Suevite with a variety of lithic and mineral clasts: phyllite, slate, medium-grained meta-graywacke, chloritoid-rich meta-graywacke, melt particles (brown in color; commonly with tiny undigested quartz grains), quartzite, and calcite clasts. Minerals identified include quartz, K-feldspar, plagioclase, muscovite, chlorite, calcite, opaque minerals, epidote, and sphene. Some quartz grains show undulatory extinction and a few grains display microfractures. A few quartz grains show PFs or PDFs (1 set). Feldspar grains are partially or totally altered to sericite (some are cloudy). Calcite aggregates occur. Locally, muscovite display kink bands.

KR8-042 [A1 and A2] (depth = 293.97 m) – Suevite with a prominent phyllite clast (dikelet)

Suevite with a variety of lithic and mineral clasts: phyllite and slate, meta-graywacke (mainly mylonitic and some chloritoid-rich meta-graywacke), brown melt particles (commonly with

tiny undigested quartz grains), quartzite, and calcite clasts. Minerals identified include quartz, muscovite, K-feldspar, plagioclase, chlorite, calcite, sphene, opaque minerals (mainly pyrite), rutile, apatite, and rare zircon. Some quartz grains show undulatory extinction. Only a few quartz grains show PDFs (1 or 2 sets); some quartz grains are partially toasted. Feldspar grains are partially or totally altered to sericite (some feldspars are cloudy). A few calcite aggregates are present in the matrix.

KR8-043 (depth = 296.94 m) – Strongly altered suevite (dikelet)

Strongly altered suevite with a variety of lithic and mineral clasts: phyllite and slate, meta-graywacke (mylonitic, fine- to medium-grained meta-graywacke, and some chloritoid-rich meta-graywacke), melt particles (brown in color; commonly with tiny undigested quartz grains), quartzite, and calcite clasts. Minerals identified include quartz, K-feldspar, plagioclase, muscovite, chlorite, calcite, epidote, opaque minerals, rutile, and rare zircon. Most of the feldspar grains are altered to sericite and display a cloudy appearance. A few quartz grains show PDFs (1 or 2 sets). Calcite aggregates occur in the matrix. A few muscovite clasts display kink bands.

KR8-045 (depth = 300.41 m) – Weakly sheared, heterogranular meta-graywacke (fine- to medium-grained)

Weakly sheared, heterogranular meta-graywacke composed mainly of quartz, K-feldspar, plagioclase, muscovite, calcite, biotite, chlorite, epidote, sphene, amphibole, apatite, and opaque minerals. Quartz grains display microfractures and some grains are partially isotropic. Some quartz grains show PDFs, generally decorated (1 or 2 sets); some quartz grains are partially toasted; a few grains display broad, occasionally planar fluid inclusion trails. Feldspar grains are partially altered to sericite and display a cloudy appearance. Calcite veinlets and aggregates occur. Microfractures partially filled with iron oxides transect the section.

KR8-046 (depth = 303.25 m) – Very fine-grained slate

Well-banded and folded very fine-grained slate; composed mainly of quartz, muscovite, K-feldspar and few plagioclase, biotite, sphene, epidote, and opaque minerals. A small quartz veinlet with few quartz grains with PFs and PDFs occur. Microfractures partially filled with iron oxides transect the section. The sample is very similar to KR8-028.

KR8-047 (depth = 305.71 m) – Alternating slate and sheared, fine-grained meta-graywacke

Alternating slate and sheared, fine-grained meta-graywacke composed mainly of quartz, K-feldspar, muscovite, plagioclase, chlorite, and a few biotite, sphene, epidote, and calcite. Quartz grains show microfracturing, some PFs, and a few PDFs (1 set) that are generally decorated. Feldspar grains are partially altered to sericite and display a cloudy appearance. One large clast of an unknown mineral, with a distinct blue polarization color, occurs.

KR8-048 [A, B, and C] (depth = 307.30 m) – Altered protomylonitic medium-grained meta-graywacke, locally cataclastic

Altered protomylonitic medium-grained meta-graywacke, composed mainly of quartz, K-feldspar, plagioclase, muscovite, chlorite, epidote, sphene, rutile, and opaque minerals (mainly

pyrite). Allanite occur in KR8-048 [B] and also zircon in KR8-048 [C]. Quartz grains show microfractures, some display undulatory extinction, and a few PFs and PDFs were observed. Feldspar grains are partially altered to sericite and display a cloudy appearance. Calcite aggregates occur. Numerous penetrative fractures filled by iron oxides and/or by chlorite occur (principally in KR8-048 [A]).

KR8-049 [A and B] (depth = 310.23 m) – Medium-grained meta-graywacke breccia, locally sheared or cataclastic

Medium-grained meta-graywacke breccia composed mainly of quartz, K-feldspar, plagioclase, muscovite, chlorite, epidote, sphene, and opaque minerals. Quartz grains show microfractures and a few grain display undulatory extinction. Some PFs and a few PDFs (1 set) occur in quartz grains. Feldspar grains are partially altered to sericite and display a cloudy appearance. Several clasts are crushed *in situ*. Abundant calcite aggregates occur.

KR8-050 (depth = 310.99 m) – Heterogranular meta-graywacke

Heterogranular meta-graywacke composed mainly of quartz, calcite, K-feldspar, plagioclase, muscovite, biotite, chlorite, sphene, and a few epidote and opaque minerals. Quartz grains show microfractures and some display undulatory extinction; some quartz grains are partially isotropic. A few PFs (no PDFs seen) in quartz grains have been seen in the section. Feldspar grains are partially altered to sericite and display a cloudy appearance. Abundant calcite aggregates occur.

KR8-051 (depth = 312.40 m) – Medium-grained to gritty meta-graywacke

Medium-grained to gritty meta-graywacke composed mainly of quartz, K-feldspar, plagioclase, muscovite, chlorite, epidote, sphene, and opaque minerals. All the biotite is altered to chlorite. Quartz and feldspar grains show a lot of microfractures. Quartz grains displays undulatory extinction and some grains are partially isotropic. Very few quartz grains show decorated PFs and only one grain with 1 set of decorated PDFs has been seen in the thin section. Feldspar grains are partially altered to sericite (some are cloudy). Calcite aggregates occur. Microfractures partially filled with iron oxides transect the section.

KR8-052 (depth = 315.75 m) – Weakly sheared medium-grained meta-graywacke

Weakly sheared medium-grained meta-graywacke composed mainly of quartz, K-feldspar, plagioclase, muscovite, chlorite, epidote, opaque minerals, and a few biotite and sphene. Some quartz grains show microfractures, undulatory extinction, and a few are partially isotropic. A few quartz grains show decorated PFs (only one toasted quartz grains with 2 sets of PDFs). Feldspar grains are partially altered to sericite and display a cloudy appearance. Fractures filled with iron oxides and calcite aggregates occur.

KR8-053 [A1, A2, and B] (depth = 316.97 m) – Sheared medium-grained meta-graywacke breccia

Sheared medium-grained meta-graywacke breccia composed mainly of quartz, feldspar, plagioclase, calcite, muscovite, chlorite, opaque minerals (pyrite), a few epidote, and rare zircon. Some quartz grains show undulatory extinction. Many decorated PFs and PDFs (1 or 2

sets) in partially or totally toasted quartz grains. Rare feldspar grains are slightly altered to sericite; a few feldspar grains show fracturing. A large calcite veinlet transects the section; calcite aggregates occur.

KR8-054 (depth = 320.62 m) – Altered, fractured, mylonitic medium-grained meta-graywacke

Mylonitic medium-grained meta-graywacke composed mainly of quartz, K-feldspar, plagioclase, muscovite, chlorite, opaque minerals, and a few epidote and sphene (only one biotite seen). Quartz and feldspar grains show abundant microfractures. Quartz grains display undulatory extinction. A few decorated PFs and PDFs (1 set, only one grains with 2 sets) in partially toasted quartz grains. Feldspar grains are partially or totally altered to sericite (some are cloudy). Many microfractures partially filled with iron oxides transect the section. Calcite aggregates occur. The sample is very similar to KR8-070.

KR8-056 [A1, A2, and B] (depth = 326.78 m) – Medium-grained meta-graywacke (locally sheared)

Medium-grained meta-graywacke (locally sheared) composed mainly of quartz, K-feldspar, plagioclase, muscovite, chlorite, biotite, epidote, amphibole, sphene, apatite, opaque minerals, calcite, allanite, and rare zircon. Quartz grains show microfractures. Many quartz grains partially or totally toasted with decorated PFs and PDFs (1 or 2 sets). Feldspar grains are partially altered to sericite and display a cloudy appearance. Penetrative fractures filled with iron oxides occur.

KR8-057 (depth = 330.08 m) – Altered, weakly sheared, medium-grained meta-graywacke, locally cataclastic

Altered, weakly sheared medium-grained meta-graywacke composed mainly of quartz, K-feldspar, plagioclase, muscovite, chlorite, epidote, opaque minerals, and sphene (only one biotite seen). Quartz grains show microfractures, undulatory extinction, and a few grains are partially isotropic. A few quartz grains with PFs and PDFs (1 set); low shock degree (~10 GPa). Some feldspar grains are altered to sericite and display a cloudy appearance. Local cataclasis and veining filled with chlorite and epidote occur in the section. Many fractures are filled with iron oxides. Calcite aggregates occur.

KR8-059 [A and B] (depth = 333.51 m) – Mature heterogranular meta-graywacke, locally annealed, and brecciated

Mature heterogranular meta-graywacke composed mainly of quartz, K-feldspar, plagioclase, muscovite, chlorite, opaque minerals, epidote, and sphene. Quartz grains show microfractures and some grains are partially isotropic. A lot of quartz grains show PDFs (1, 2, and 3 sets) and some are partially toasted. Some feldspar grains are altered to sericite and display a cloudy appearance. Polysynthetic twinning in plagioclase has been displaced along tiny faults. Some penetrative fracturing. Several calcite aggregates occur.

KR8-060 (depth = 337.33 m) – Sheared, fine-grained meta-graywacke (locally brecciated)

Sheared, fine-grained meta-graywacke composed mainly of quartz, K-feldspar, plagioclase, muscovite, biotite, chlorite, sphene, opaque minerals, and epidote. Quartz grains display

microfractures. A few quartz grains show decorated PFs and only two grains with PDFs (1 set) have been seen in the section; low shock degree (ca. 5-6 GPa). A few feldspar grains are partially altered to sericite (some are cloudy). Calcite veinlets and aggregates occur in the section.

KR8-061 (depth = 341.17 m) – Unshocked heterogranular meta-graywacke

Unshocked heterogranular meta-graywacke composed mainly of quartz, K-feldspar, plagioclase, muscovite, chlorite, calcite, biotite, opaque minerals, and rutile. Some quartz grains show undulatory extinction. Some feldspar grains are partially altered to sericite and display a cloudy appearance. One penetrative microfracture filled by iron oxides cut through the section. Calcite aggregates occur. No diagnostic shock indicators.

KR8-062 (depth = 341.86 m) – Sheared medium-grained meta-graywacke

Sheared medium-grained meta-graywacke composed mainly of quartz, K-feldspar, plagioclase, chlorite, muscovite, opaque minerals, and a few biotite, epidote, and sphene. Some quartz grains show undulatory extinction. A few quartz grains show decorated PFs and only one grain with PDFs (1 set). Some feldspar grains are partially altered to sericite (some are cloudy). Small calcite aggregates occur.

KR8-063 (depth = 343.57 m) – Well-banded, fine-grained metasediment (bands of phyllite, slate, and fine-grained meta-graywacke)

Well-banded, fine-grained metasediments composed mainly of quartz, muscovite, chlorite, opaque minerals, and rutile. A lot of quartz grains with PFs and some with PDFs (1 or 2 sets) occur; a few quartz grains are slightly toasted. Microfractures transect the section and are filled with clay minerals as alteration products. Tabular opaque crystals and calcite pods occur.

KR8-064 (depth = 348.43 m) – Phyllite with shocked quartz veinlets

Phyllite with shocked quartz veinlets and crenulation cleavage. Composed mainly of muscovite, quartz, biotite, and opaque minerals (such as pyrite; abundant). Quartz veinlets transect the section (aligned parallel to the foliation of the rock). Quartz grains display undulatory extinction and some grains are partially isotropic. Many quartz grains show decorated PDFs (1 or 2 sets). Microfractures partially filled with iron oxides are present in the section. Calcite aggregates occur.

KR8-065 [A] (depth = 352.31 m) – Gritty meta-graywacke (partially brecciated)

Gritty meta-graywacke composed mainly of quartz, K-feldspar, plagioclase, muscovite, chlorite, epidote, opaque minerals, and a few biotite and sphene. Quartz grains show abundant microfractures and undulatory extinction. Many decorated PFs and PDFs (1 or 2 sets) in quartz grains. Feldspar grains show microfractures, undulatory extinction, and are commonly altered to sericite (some feldspar grains are cloudy). Some quartz and feldspar grains are partially isotropic. Many microfractures filled with iron oxides and chlorites occur. Calcite aggregates occur. The sample is very similar to KR8-029 and KR8-030.

KR8-065 [B and C] (depth = 352.31 m) – Weakly sheared, heterogranular meta-graywacke

Weakly sheared, heterogranular meta-graywacke composed mainly of quartz, K-feldspar, plagioclase, muscovite, chlorite, epidote, opaque minerals, biotite, and sphene. Quartz grains show abundant microfractures and undulatory extinction. Only a few PFs occur in quartz grains (no PDFs seen). Feldspar grains show microfractures and are partially altered to sericite (some grains are cloudy). Some quartz and feldspar grains are partially isotropic. Some microfractures filled with iron oxides occur. Calcite aggregates occur.

KR8-066 (depth = 353.95 m) – Altered, sheared, fractured, heterogranular meta-graywacke

Altered, sheared, heterogranular meta-graywacke composed mainly of quartz, K-feldspar, plagioclase, muscovite, chlorite, calcite, epidote, opaque minerals, and rare sphene and zircon. Most of the biotite is altered to chlorite. Quartz grains show abundant microfractures and undulatory extinction. Many PDFs (1 or 2 sets) in quartz grains, some are decorated; a few grains are toasted. Some quartz grains are partially isotropic. Feldspar grains are altered to sericite and display a cloudy appearance. A large quartz veinlet cut through the section. Penetrative fractures filled with iron oxides and chlorites occur. Calcite aggregates occur.

KR8-067 (depth = 356.59 m) – Weakly sheared, fractured, heterogranular meta-graywacke

Weakly sheared, heterogranular meta-graywacke composed mainly of quartz, K-feldspar, plagioclase, chlorite, calcite, muscovite, biotite, epidote, opaque minerals, sphene, and zircon. Most of the biotite is altered to chlorite. Quartz grains show abundant microfractures and some grains display undulatory extinction. Many decorated PFs and PDFs (1 or 2 sets, rarely 3 sets) in quartz grains, some partially toasted. Feldspar grains are partially altered to sericite and display a cloudy appearance. Many fractures filled with iron oxides occur. Calcite aggregates occur.

KR8-068 (depth = 359.44 m) – Altered, gritty meta-graywacke, locally cataclastic

Altered gritty meta-graywacke composed mainly of quartz, K-feldspar, plagioclase, muscovite, chlorite, epidote, opaque minerals, and sphene. All the biotite is altered to chlorite. Many microfractures occur in quartz and feldspar grains. Quartz grains show undulatory extinction. A lot of PDFs (1 or 2 sets) in quartz grains (some partially toasted). Feldspar grains are partially altered to sericite (some are cloudy). Polysynthetic twinning in plagioclase has been displaced along tiny faults. Many penetrative fractures filled with iron oxides and chlorites occur. Calcite aggregates occur.

KR8-069 (depth = 361.18 m) – Shocked (and somewhat brecciated) light greenish gray (chloritoid-rich), medium-grained meta-graywacke with granophyric material

Shocked light greenish-gray (chloritoid-rich) meta-graywacke with granophyric material; composed mainly of K-feldspar, plagioclase, calcite, quartz, muscovite, chloritoid, sphene, rutile, and opaque minerals. Quartz grains show abundant microfractures and undulatory extinction. Some quartz grains show PDFs (1 or 2 sets) and some grains are toasted. Many graphic intergrowths of quartz and feldspar. Calcite aggregates occur. The sample is very similar to KR8-106, KR8-121, and 122a, but shocked.

KR8-070 (depth = 364.12 m) – Mylonitic medium-grained meta-graywacke

Mylonitic medium-grained meta-graywacke composed mainly of quartz, K-feldspar, plagioclase, muscovite, biotite, chlorite, epidote, and opaque minerals. Some quartz grains show undulatory extinction. A lot of PDFs (1 or 2 sets) in quartz grains (some partially toasted). Feldspar grains are altered to sericite and display a cloudy appearance. Calcite aggregates occur in the section.

KR8-071 [A and B] (depth = 368.97 m) – Mylonitic, medium-grained to gritty meta-graywacke

Mylonitic, medium-grained to gritty meta-graywacke, locally brecciated (annealed), and weakly shocked; composed mainly of quartz, K-feldspar, plagioclase, chlorite (filling the pore-space), calcite, muscovite, epidote, apatite, sphene, biotite, opaque minerals (such as pyrite), and a few zircons. Quartz grains show microfractures and undulatory extinction. Some decorated PFs and PDFs (1 or 2 sets) in quartz grains, some partially toasted. Several quartz grains are partially isotropic. Feldspar grains are partially or totally altered to sericite (some are cloudy). Some fractures filled with iron oxides and chlorites occur. Calcite veinlets and a few calcite aggregates occur.

KR8-072 [A and B] (depth = 370.96 m) – Sheared, fine- to medium-grained meta-graywacke

Sheared, weakly shocked fine- to medium-grained meta-graywacke composed mainly of quartz, K-feldspar, plagioclase, muscovite, chlorite, biotite, epidote, sphene, and a few opaque minerals. Some quartz grains display undulatory extinction. Some quartz grains show sub-planar fractures and/or PFs and a few grains with PDFs (1 set) occur. Feldspar grains are partially altered to sericite and display a cloudy appearance. Calcite aggregates occur.

KR8-073 (depth = 371.07 m) – Medium-grained meta-graywacke

Medium-grained and weakly shocked meta-graywacke composed mainly of quartz, K-feldspar, plagioclase, muscovite, chlorite, biotite, epidote, sphene, and a few opaque minerals. Some quartz grains show undulatory extinction. Some quartz grains with PFs and a few with PDFs (1 set) occur in the section. Feldspar grains are partially altered to sericite (some are cloudy). Calcite aggregates occur.

KR8-074 (depth = 375.24 m) – Medium-grained meta-graywacke

Medium-grained meta-graywacke composed mainly of quartz, K-feldspar, plagioclase, muscovite, chlorite, biotite, sphene, epidote, and a few opaque minerals and rutile. Some quartz grains show undulatory extinction and others are partially isotropic. A lot of quartz grains show PFs and PDFs (1 or 2 sets). Feldspar grains are partially altered to sericite and display a cloudy appearance. Calcite aggregates occur in the section. The sample is very similar to KR8-073, but shocked to a higher degree.

KR8-075 (depth = 377.78 m) – Mylonite

Quartz-rich mylonite composed mainly of quartz, K-feldspar, muscovite, chlorite, epidote, and opaque minerals. Feldspar grains are partially or totally altered to sericite (some grains are cloudy). Unshocked sample.

KR8-076 (depth = 379.70 m) – Weakly sheared medium-grained to gritty meta-graywacke (locally cataclastic)

Weakly sheared and weakly shocked meta-graywacke composed mainly of quartz, K-feldspar, plagioclase, muscovite, chlorite, epidote, sphene, opaque minerals, and rare biotite. Quartz grains show abundant microfractures and some grains display undulatory extinction. A few quartz grains show PDFs (1 set) and some are partially toasted. Feldspar grains are partially or totally altered to sericite (some are cloudy). Calcite aggregates occur. Many fractures filled with secondary phyllosilicate minerals occur in the section.

KR8-077 (depth = 380.98 m) – Sheared fine-grained meta-graywacke

Sheared, fine-grained meta-graywacke composed mainly of quartz, K-feldspar, plagioclase, muscovite, chlorite, epidote, sphene, and a few biotite and opaque minerals. Some quartz grains show undulatory extinction. Some quartz grains show decorated PFs and PDFs (1 or 2 sets), partially toasted. Feldspar grains are partially or totally altered to sericite (some are cloudy). A few calcite aggregates occur. One mylonitic intercalation is present in the section. Minor fracturing. The sample is relatively similar to KR8-072.

KR8-078 (depth = 382.17 m) – Medium-grained to gritty meta-graywacke, partially annealed, and locally cataclastic

Medium-grained to gritty meta-graywacke composed mainly of quartz, K-feldspar, plagioclase, muscovite, chlorite, epidote, sphene, opaque minerals, and rare biotite. Quartz grains display abundant microfractures and some grains show undulatory extinction. Feldspar grains are partially or totally altered to sericite (some are cloudy). Calcite aggregates occur in the section. No obvious shock effects, such as PDFs in quartz.

KR8-079 [A, B, and C] (depth = 384.06 m) – Weakly sheared heterogranular meta-graywacke

Weakly sheared, heterogranular meta-graywacke composed mainly of quartz, K-feldspar, plagioclase, biotite, muscovite, epidote, sphene, and opaque minerals. Quartz grains show abundant microfractures and a few grains are partially isotropic. Feldspar grains are partially or totally altered to sericite (some are cloudy). Microfractures mostly filled with opaque minerals, phyllosilicate minerals, and calcite are present. A few calcite aggregates also occur. No obvious shock effects, such as PDFs in quartz.

KR8-080 [A and B] (depth = 384.54 m) – Alternation of fine-grained metasediments (phyllite, slate, and meta-graywacke) with a wide quartzitic vein

Alternation of phyllite (with development of crenulation cleavage), slate, and meta-graywacke with a wide quartzitic vein (~1 cm thick). Minerals identified include quartz, calcite, muscovite, and a few chlorite, K-feldspar, plagioclase, opaque minerals (mainly pyrite), and rutile. Quartz grains show numerous microfractures and some grains display undulatory extinction. Many decorated PFs and PDFs in quartz (1 or 2 sets). There are abundant calcite veinlets and aggregates.

KR8-081 [A and B] (depth = 387.36 m) – Weakly shocked and weakly sheared medium-grained meta-graywacke

Weakly shocked (a few PDFs) and weakly sheared medium-grained meta-graywacke composed mainly of quartz, K-feldspar, plagioclase, muscovite, chlorite, epidote, sphene, and opaque minerals. Some quartz grains show microfractures and a few display undulatory extinction. A few quartz grains show PFs and/or PDFs (1 set, only 1 quartz grain seen with 2 sets). Feldspar grains are partially altered to sericite and display a cloudy appearance. A large calcite veinlet and some calcite aggregates occur. A few microfractures filled with chlorite and others with opaque material are present.

KR8-082 (depth = 387.78 m) – Altered, sheared, weakly shocked, fine- to medium-grained meta-graywacke

Altered, sheared, weakly shocked, meta-graywacke composed mainly of quartz, K-feldspar, plagioclase, muscovite, chlorite, epidote, sphene, opaque minerals, and a few biotite. Most of the biotite is altered to chlorite. Some quartz grains show microfractures and undulatory extinction. Some decorated PFs and PDFs (1 set, only one quartz grain seen with 2 sets) in quartz grains (some partially toasted). Feldspar grains are partially (a few totally) altered to sericite (some are cloudy). Many microfractures (more or less penetrative) filled by calcite, iron oxides, and chlorite are present in the section. Some calcite aggregates occur.

KR8-083 (depth = 389.25 m) – Altered, fractured, medium-grained to gritty meta-graywacke

Altered, fractured meta-graywacke composed mainly of quartz, K-feldspar, plagioclase, chlorite, muscovite, epidote, sphene, and opaque minerals (such as pyrite). All the biotite is altered to chlorite. Some quartz grains show undulatory extinction. Only two quartz grains seen with 1 set of PFs each. Feldspar grains are partially altered to sericite and display a cloudy appearance. Several large penetrative fractures filled by iron oxides are present. Some calcite veinlets and aggregates occur in the section. No obvious shock effects, such as PDFs in quartz.

KR8-084 (depth = 390.00 m) – Slate/Phyllite

Slate/phyllite, composed mainly of muscovite, quartz, K-feldspar, chlorite, tabular opaque minerals, and a few sphene and biotite. No trace of shock deformation.

KR8-085 (depth = 392.65 m) – Altered, fractured, medium-grained to gritty meta-graywacke

Altered, fractured, meta-graywacke composed mainly of quartz, K-feldspar, plagioclase, chlorite (abundant), muscovite, opaque minerals, calcite, epidote, and sphene (only one biotite seen). All the biotite is altered to chlorite. Quartz grains show abundant microfractures and undulatory extinction. A few quartz grains show decorated PFs and PDFs (1 or 2 sets); some quartz grains are toasted. Feldspar grains are partially (some totally) altered to sericite (some are cloudy) and show numerous microfractures. Many microfractures transect the section and are filled with iron oxides and chlorite. Very few calcite aggregates occur.

KR8-086 (depth = 393.07 m) – Altered, weakly shocked, heterogranular meta-graywacke

Altered, weakly shocked, heterogranular meta-graywacke composed mainly of quartz, K-feldspar, plagioclase, chlorite, muscovite, epidote, sphene, opaque minerals, and a few biotite.

Most of the biotite is altered to chlorite. Quartz grains show undulatory extinction. Many quartz grains display decorated PFs (only 2 grains with decorated PDFs, 1 and 2 sets, respectively). Feldspar grains are partially altered to sericite and display a cloudy appearance. Some calcite aggregates occur in the section.

KR8-087 [A and B] (depth = 394.30 m) – Altered medium-grained meta-graywacke

Altered medium-grained, moderately shocked meta-graywacke; composed mainly of quartz, K-feldspar, plagioclase, muscovite, chlorite (abundant), biotite, epidote, sphene, and opaque minerals. Quartz grains show microfractures and some grains display undulatory extinction. Many PFs and some decorated PDFs (1 or 2 sets) in quartz grains (some partially toasted). Feldspar grains are partially altered to sericite (some are cloudy). A large penetrative microfracture with halo of secondary calcite is present in the section. Calcite aggregates occur.

KR8-088 (depth = 395.25 m) – Fine- to medium-grained meta-graywacke

Weakly shocked meta-graywacke composed mainly of quartz, calcite, plagioclase, K-feldspar, muscovite, and a few epidote. Quartz and feldspar grains display microfractures. Some quartz grains are partially isotropic and a few others show undulatory extinction. A few quartz grains show irregular fluid inclusion trails. A lot of calcite veinlets and aggregates occur as well as a few sphene aggregates. No obvious shock effects, such as PDFs in quartz.

KR8-089 [A and B] (depth = 397.30 m) – Medium-grained meta-graywacke partially brecciated

Medium-grained meta-graywacke composed mainly of quartz, K-feldspar, plagioclase, calcite, chlorite, muscovite, opaque minerals (such as pyrite), epidote, biotite, sphene, apatite, and zircon. Several quartz grains show microfractures and a few display undulatory extinction; some grains are partially isotropic. Quartz grains display some decorated PFs and PDFs (1 or 2 sets; rarely 3 sets), some grains are partially toasted. Feldspar grains are partially altered to sericite and display a cloudy appearance. Calcite veinlets and aggregates occur. Several microfractures filled with iron oxides are present in the section. A few quartz grains contain rutile fibers.

KR8-090 (depth = 398.80 m) – Weakly sheared, fine- to medium-grained meta-graywacke

Weakly sheared, fine to medium-grained meta-graywacke composed mainly of quartz, K-feldspar, plagioclase, muscovite, epidote, chlorite, opaque minerals, and rare allanite. Some quartz grains show microfractures and some grains display undulatory extinction. Feldspar grains are partially altered to sericite and display a cloudy appearance. Calcite aggregates occur in the section. No trace of shock deformation.

KR8-091 (depth = 400.35 m) – Altered gritty meta-graywacke, fractured, and locally brecciated

Altered gritty meta-graywacke composed mainly of quartz, K-feldspar, plagioclase, muscovite, chlorite, epidote, and opaque minerals (only one biotite seen). Biotite is altered to chlorite. Quartz grains show microfractures and some display undulatory extinction; a few grains are partially isotropic. Some quartz grains with decorated PFs and/or PDFs (1 or 2 sets) occur.

Feldspar grains are partially altered to sericite (some are cloudy). Many microfractures filled with chlorite and iron oxides occur in the section.

KR8-092 [A, B, and C] (depth = 403.00 m) – Altered medium-grained meta-graywacke

Altered medium-grained meta-graywacke composed mainly of quartz, K-feldspar, plagioclase, muscovite, chlorite, sphene, epidote, apatite, a few opaque minerals, and rare zircon. Some quartz grains show microfractures and undulatory extinction. A few quartz grains with decorated PFs and/or PDFs (1 set; only 2 grains seen with 2 sets) occur. Feldspar grains are partially altered to sericite and display a cloudy appearance. Minor fracturing occurs. A calcite veinlet transects the section (KR8-092 [A]); Calcite aggregates occur.

KR8-093 (depth = 403.64 m) – Altered gritty meta-graywacke locally cataclastic and fractured

Altered gritty meta-graywacke composed mainly of quartz, K-feldspar, plagioclase, muscovite, chlorite, calcite, epidote, opaque minerals, and rare biotite. Most of the biotite is altered to chlorite. Some quartz grains show microfractures and undulatory extinction. Only two quartz grains with PFs (1 set) seen. Feldspar grains are partially altered to sericite (some are cloudy). Numerous penetrative microfractures are filled with iron oxides and chlorite. Calcite aggregates occur in the section. No obvious shock effects, such as PDFs in quartz.

KR8-094 (depth = 404.18 m) – Gritty meta-graywacke

Gritty meta-graywacke composed mainly of quartz, K-feldspar, plagioclase, muscovite, chlorite, epidote, sphene, and opaque minerals (such as pyrite). Many quartz grains display undulatory extinction; one quartz grain show mosaicism. A few quartz grains with PFs (1 set) occur. Feldspar grains are partially altered to sericite and display a cloudy appearance. Calcite aggregates occur. No PDFs seen.

KR8-095 [A and B] (depth = 405.34 m) – Altered, fractured, and mylonitic fine-grained meta-graywacke

Altered, mylonitic, weakly shocked meta-graywacke composed mainly of quartz, K-feldspar, plagioclase, chlorite, muscovite, epidote, sphene, and a few opaque minerals. A few quartz grains display undulatory extinction. A few quartz grains with PFs and/or PDFs (1 set) occur. Two quartz grains show shear fractures and associated planar microdeformations in the thin section KR8-095 [B]. Feldspar grains are partially altered to sericite. The mica-rich shear bands are cut by a veinlet of impact breccia? Several microfractures filled with iron oxides and/or secondary calcite occur. Calcite aggregates are also present.

KR8-096 (depth = 406.31 m) – Medium-grained meta-graywacke, locally brecciated, and fractured

Medium-grained meta-graywacke composed mainly of quartz, K-feldspar, plagioclase, chlorite, calcite, muscovite, epidote, opaque minerals, sphene, zircon, and rare biotite. Numerous quartz grains show microfractures more or less penetrative. Some quartz grains show undulatory extinction. Some PFs and a few PDFs (1 or 2 sets) have been seen in quartz grains; a number of PDFs are decorated; a few quartz grains are toasted. Feldspar grains are

partially altered to sericite (some are cloudy). Several microfractures (shock compression resulted?) transect the section.

KR8-097 (depth = 409.67 m) – Altered sheared medium-grained to gritty meta-graywacke (locally annealed)

Altered sheared medium-grained to gritty meta-graywacke composed mainly of quartz, K-feldspar, plagioclase, muscovite, chlorite, epidote, sphene, and a few biotite and opaque minerals. Most of the biotite is altered to chlorite. Some quartz grains show microfractures and undulatory extinction. Some feldspar grains are partially altered to sericite and display a cloudy appearance. A few quartz and feldspar grains are partially isotropic. Small calcite aggregates occur in the section. No obvious shock effects, such as PDFs in quartz.

KR8-098 (depth = 410.74 m) – Medium-grained meta-graywacke (fractured)

Medium-grained meta-graywacke composed mainly of quartz, K-feldspar, plagioclase, chlorite, muscovite, epidote, sphene, zircon, opaque minerals, apatite, and a few calcite and allanite. Most of the biotite is altered to chlorite. Quartz grains show microfractures and undulatory extinction. Quartz grains (partially toasted) display decorated, curved or sub-planar fractures, occasionally PFs and PDFs (1 or 2 sets). Feldspar grains are partially altered to sericite (some are cloudy). Several microfractures occur in the section. A few quartz grains contain rutile fibers.

KR8-099 (depth = 412.92 m) – Gritty meta-graywacke (fractured, locally brecciated, and weakly sheared)

Gritty meta-graywacke composed mainly of quartz, K-feldspar, plagioclase, muscovite, biotite, chlorite, epidote, sphene, and opaque minerals (such as pyrite). Quartz grains show microfractures and undulatory extinction; some quartz grains display sets of sub-planar fractures (some decorated), some PFs, and very few PDFs (1 set). Feldspar grains are partially altered to sericite (some are cloudy). Many microfractures filled with iron oxides occur in the section.

KR8-100 (depth = 412.74 m) – Sheared, heterogranular meta-graywacke

Sheared, heterogranular meta-graywacke composed mainly of quartz, K-feldspar, plagioclase, muscovite, chlorite, biotite, calcite, sphene, zircon, and rare opaque minerals. Rare quartz grains show PFs (1 set). Feldspar grains are partially altered to sericite and display a cloudy appearance. Calcite aggregates occur. No trace of shock deformation.

KR8-101 (depth = 414.28 m) – Altered gritty meta-graywacke

Altered gritty meta-graywacke composed mainly of quartz, K-feldspar, plagioclase, chlorite, epidote, sphene, apatite, zircon, calcite, opaque minerals, and a few muscovite. All the biotite is altered to chlorite. Some quartz grains show, more or less penetrative, microfractures; some grains show undulatory extinction. Only a few quartz grains show PFs and/or PDFs (1 set; rarely 2 sets); some PDFs are decorated; a few quartz grains are toasted. Feldspar grains are partially altered to sericite (some are cloudy). Minor fractures filled with iron oxides are present in the section. A few calcite aggregates also occur.

KR8-102 (depth = 416.84 m) – Monomict meta-graywacke breccia (sheared, medium-grained meta-graywacke)

Monomict meta-graywacke breccia composed mainly of quartz, K-feldspar, plagioclase, muscovite, biotite, chlorite, sphene (some with overgrowth of a second generation of sphene), and a few epidote and opaque minerals. Quartz grains show abundant microfractures and undulatory extinction. Quartz grains display rare decorated PFs and PDFs (1 set). Feldspar grains are partially altered to sericite and display a cloudy appearance. Microfractures transect the section. Some secondary calcite veinlets and aggregates occur.

KR8-103 (depth = 417.39 m) – Heterogranular (from medium-grained to gritty) meta-graywacke and suevite

Heterogranular meta-graywacke and suevite; composed mainly of quartz, K-feldspar, plagioclase, biotite, chlorite, muscovite, epidote, sphene, and opaque minerals. Suevite with variety of lithic and mineral clasts, including meta-graywacke (altered meta-graywacke dominant), quartz, feldspar, melt particles, and calcite clasts. Quartz grains display undulatory extinction. A few quartz grains show decorated PFs (only one grain with 1 set of PDFs seen). Feldspar grains are partially altered to sericite (some are cloudy). Calcite aggregates occur in the section.

KR8-104 (depth = 417.60 m) – Altered, fine-grained meta-graywacke (locally cataclastic)

Altered, fine-grained meta-graywacke composed mainly of quartz, K-feldspar, plagioclase, chlorite, muscovite, sphene, and a few epidote, biotite, and opaque minerals. Quartz grains show microfractures. A few quartz grains are partially toasted and display decorated PFs (only three grains with 1 set of PDFs seen). Feldspar grains are partially altered to sericite and display a cloudy appearance. Calcite aggregates occur.

ADE-8A (depth = 418.05 m) – Altered suevite veinlet in fine metasediment (from phyllite to fine-grained meta-graywacke, locally mylonitic)

Altered suevite veinlet (~1 cm thick) in fine metasediment, from phyllite with development of crenulation cleavage to fine-grained meta-graywacke. A variety of lithic and mineral clasts are present: fine- to medium-grained meta-graywacke (altered), melt particles (brown in color), quartz, and calcite clasts. Minerals identified include quartz, K-feldspar, plagioclase, biotite, chlorite, muscovite, amphibole, sphene, epidote, and opaque minerals (mainly pyrite). In addition, sphalerite was characterized using SEM. Most of the feldspar grains are altered to sericite. Some quartz grains show undulatory extinction. A few quartz grains display PFs and only two quartz grains with decorated PDFs (1 set) have been seen in the section. Calcite aggregates occur. Locally, small suevite injections in meta-graywacke clasts are noted.

KR8-106 [A and B] (depth = 421.88 m) – Light greenish gray (chloritoid-rich), medium-grained meta-graywacke with granophyric material

Light greenish-gray (chloritoid-rich), meta-graywacke with granophyric material; composed mainly of chloritoid, calcite, quartz, calcite, K-feldspar, opaque minerals, rutile, sphene, and a few muscovite (only one biotite seen). Cuneiform-shaped intergrowths of quartz in feldspar.

Several calcite veinlets and aggregates occur. No distinct shock deformation. Lithology very similar to KR8-069, KR8-121, and KR8-122a.

KR8-107 [A1, A2, B, and C] (depth = 422.36 m) – Altered suevite (dikelet)

Altered suevite with a variety of lithic and mineral clasts: melt particles (brown in color, very heterogeneous in shape, from sub-angular to rounded), light gray (chloritoid-rich) medium-grained meta-graywacke (similar to sample KR8-106), meta-graywacke, quartz, slate and phyllite, and calcite slats. Minerals identified include quartz, K-feldspar, plagioclase, chloritoid, biotite, chlorite, muscovite, opaque minerals, and sphene. A few quartz grains display decorated PFs and PDFs (1 set). Several calcite aggregates occur.

KR8-108 [A and B] (depth = 424.78 m) – Shocked heterogranular (from fine-grained to gritty) meta-graywacke (partially sheared) with a thick (~1.5 cm) quartz veinlet

Heterogranular meta-graywacke composed mainly of quartz, K-feldspar, plagioclase, biotite, chlorite, muscovite, sphene, epidote, and opaque minerals (such as pyrite). Some quartz grains show undulatory extinction. Several decorated PFs and PDFs (1 or 2 sets) in quartz grains (some are partially toasted) occur. Feldspar grains are partially altered to sericite (some are cloudy). A large shocked quartz vein, cross-cut by calcite veinlets and aggregates, occur (chlorite is also associated; very abundant in sample KR8-108 [A]). A large pyrite pod is present. Minor fracturing occurs.

KR8-109 (depth = 425.24 m) – Gritty meta-graywacke

Gritty meta-graywacke composed mainly of quartz, K-feldspar, plagioclase, muscovite, chlorite, biotite, chlorite, calcite, epidote, sphene, apatite, zircon, and a few opaque minerals (such as pyrite). Some quartz grains show microfractures and undulatory extinction; some other grains are partially isotropic. One quartz grain display shear fractures. A few quartz grains show curved and sub-planar fractures; a few PFs and PDFs (1 or 2 sets) in quartz grains (some are partially toasted) occur. Feldspar grains are partially altered to sericite. Fractures filled with iron oxides are present. Pyrite infill of a cataclastic zone. A few calcite aggregates occur.

KR8-110 [A and B] (depth = 429.31 m) – Altered, brecciated, medium-grained meta-graywacke

Altered, medium-grained meta-graywacke composed mainly of quartz, K-feldspar, plagioclase, chlorite (abundant), muscovite, epidote, sphene, and opaque minerals. All the biotite is altered to chlorite. Some quartz grains show undulatory extinction. Several decorated PFs and PDFs (1 or 2 sets) in quartz grains (a few are partially toasted) occur. Feldspar grains are partially or totally altered to sericite (some are cloudy). Calcite veinlets and aggregates are present. Many fractures filled with calcite or chlorite also occur.

KR8-111 (depth = 432.03 m) – Quartz, shocked, fractured, and locally cataclastic (large vein)

Shocked and fractured quartz, locally cataclastic (sample of a large vein of quartz). Several fractures occur and show preferential orientations (sub-parallel fractures). Many PFs and PDFs (1 or 2 sets) occur in quartz grains (locally toasted). Some part of the thin section display

cataclastic quartz (angular quartz fragments; crushed *in situ*). Minor calcite veinlets occur. At macroscopic scale, this quartz sample shows cleavages (impact effect or crystallization under pressure?).

KR8-112 [A, Abis, and B] (depth = 434.33 m) – Suevite (dikelet)

Suevite with a variety of lithic and mineral clasts, including meta-graywacke (altered), slate and phyllite, quartz, calcite clasts, and melt particles. Clasts are small in size (2 mm maximum). Minerals identified include quartz, K-feldspar, plagioclase, muscovite, chlorite, and opaque minerals. Some quartz grains show undulatory extinction. Only two quartz grains show PFs. Feldspar grains are partially or totally altered to sericite (some are cloudy). Some calcite aggregates occur.

KR8-113 [A1, A2, and B] (depth = 434.59 m) – Suevite (dikelet)

Suevite with a variety of lithic and mineral clasts, including fine- to medium-grained meta-graywacke (dominant, more or less altered, some clasts showing calcite veinlets and/or microfractures filled with iron oxides), melt particles (brown in color; large variety of shape), slate and phyllite, quartz, and calcite clasts. Minerals identified include quartz, K-feldspar, plagioclase, muscovite, chlorite, biotite, opaque minerals (pyrite and ilmenite), sphene, rutile, apatite, and a few epidote, allanite, and zircon. Some quartz grains show microfractures and undulatory extinction. A few quartz grains show decorated PFs and/or PDFs (1 set). Feldspar grains are partially altered to sericite. Some calcite aggregates occur.

KR8-114 [A and B] (depth = 434.75 m) – Suevite (dikelet)

Suevite with a variety of lithic and mineral clasts, including fine- to medium-grained meta-graywacke (more or less altered), melt particles (brown in color), slate and phyllite, quartz, and calcite clasts. Minerals identified include quartz, K-feldspar, plagioclase, muscovite, chlorite, opaque minerals, and a few biotite. Some quartz grains display undulatory extinction. A few quartz grains show decorated PFs and only 2 grains seen with decorated PDFs (1 set). Feldspar grains are partially altered to sericite. Some calcite aggregates occur. The sample is very similar to sample KR8-113, but with meta-graywacke clasts less abundant.

KR8-115 (depth = 437.37 m) – Altered, fine- to medium-grained meta-graywacke

Altered meta-graywacke composed mainly of quartz, K-feldspar, plagioclase, muscovite, chlorite, opaque minerals, epidote, zircon, and a few biotite and rutile. Two dark clasts (organic matter?) occur as well. Most of the quartz grains show microfractures and some grains display undulatory extinction. Feldspar grains are partially or totally altered to sericite and display a cloudy appearance. Calcite aggregates occur. No distinct shock deformation has been seen in the section.

KR8-117 [A and B] (depth = 439.87 m) – Altered medium-grained to gritty meta-graywacke

Altered meta-graywacke composed mainly of quartz, K-feldspar, plagioclase, muscovite, chlorite (abundant), sphene, and many opaque minerals (such as pyrite). Several quartz grains display undulatory extinction. Some quartz grains show PFs and/or PDFs (1 or 2 sets). Feldspar grains are partially altered to sericite and display a cloudy appearance. A sliver of

impact breccia (suevite veinlet?) is present in the section. Microfractures filled with iron oxides or chlorite and calcite aggregates occur.

CAN-31 (depth = 440.32 m) – Altered suevite (dikelet)

Altered suevite with a variety of lithic and mineral clasts: fine- to medium-grained altered meta-graywacke, melt particles (brown in color; commonly with tiny undigested quartz grains; a large particle of ~1 cm occur), slate and phyllite, quartz, and calcite clasts. Two dark clasts (shale?, or melted organic matter?) also occur. Minerals identified include quartz, K-feldspar, plagioclase, chlorite, biotite, amphibole, rutile, apatite, muscovite, and opaque minerals (pyrite and ilmenite). Most of the feldspar is altered to sericite. Quartz grains show microfractures and a few grain display undulatory extinction. A few quartz grains show PFs; no PDFs seen.

KR8-119 (depth = 441.87 m) – Altered gritty meta-graywacke

Altered gritty meta-graywacke composed mainly of quartz, K-feldspar, plagioclase, chlorite, calcite, opaque minerals, muscovite, and rare epidote. Some quartz grains show undulatory extinction and others grains are partially isotropic. A few quartz grains with PFs and rarely with decorated PDFs (1 set; rarely 2 sets) occur. Feldspar grains are partially or totally altered to sericite (some are cloudy). Penetrative fracturing filled with iron oxides, chlorite, or calcite is present in the section. Calcite aggregates also occur.

KR8-120 [A and B] (depth = 442.11 m) – Altered mylonitic medium-grained meta-graywacke

Altered mylonitic meta-graywacke composed mainly of quartz, K-feldspar, plagioclase, muscovite, chlorite (abundant), epidote, and opaque minerals. Several quartz grains display undulatory extinction. Some quartz grains show PDFs (1 or 2 sets). Feldspar grains are partially altered to sericite and display a cloudy appearance. Many microfractures filled with chlorite, calcite, or clay minerals (as alteration products) are present. A breccia veinlet transects the section. Calcite aggregates occur.

KR8-121 (depth = 446.02 m) – Light greenish gray (chloritoid-rich), medium-grained meta-graywacke, partially sheared, and with granophyric material

Light greenish-gray (chloritoid-rich), meta-graywacke, partially sheared (chloritoid in shear bands), and with granophyric material; composed mainly of K-feldspar, plagioclase, chloritoid (abundant), calcite, quartz, muscovite, rutile, and opaque minerals. Cuneiform intergrowths of quartz and feldspar. Calcite aggregates occur. Unshocked sample; very similar to sample KR8-069, KR8-106, and KR8-122a.

KR8-122 (depth = 446.69 m) – Altered, weakly shocked, medium-grained meta-graywacke with intense cataclasis (locally brecciated)

Altered, weakly shocked (fracturing), medium-grained meta-graywacke composed mainly of quartz, K-feldspar, plagioclase, muscovite, chlorite, and opaque minerals. Quartz grains show microfractures and some grains display undulatory extinction. Feldspar grains are partially altered to sericite (some are cloudy). A few roundish plagioclase clasts occur in the brecciated part of the section. A lot of calcite aggregates occur. No PDFs seen; only shock fracturing (shock pressure <8 GPa).

KR8-122a [A and B] (depth = 447.14 m) – Light greenish gray (chloritoid-rich), medium-grained meta-graywacke, partially sheared, and with granophyric material

Light greenish-gray (chloritoid-rich), meta-graywacke, partially sheared (chloritoid in shear bands), and with granophyric material; composed mainly of K-feldspar, plagioclase, chloritoid, calcite, quartz, muscovite, rutile, and a few opaque minerals. Cuneiform-shaped intergrowths of quartz in feldspar (or poikiloblastic nature). Abundant calcite aggregates and chloritoid occur. No distinct shock deformation. The sample is very similar to KR8-069, KR8-106, and KR8-121.

KR8-123 (depth = 447.96 m) – Altered medium-grained to gritty meta-graywacke (partially annealed)

Altered, partially annealed, meta-graywacke composed mainly of quartz, K-feldspar, plagioclase, muscovite, sphene, and a few biotite, rutile, opaque minerals, and zircon. Quartz grains show microfractures and undulatory extinction; a few grains are partially isotropic. Only 4 quartz grains with PFs (no PDFs seen) have been seen in the section. Feldspar grains are partially altered to sericite (some are cloudy). Many microfractures filled with calcite and chlorite are present. Calcite aggregates occur.

KR8-124 [A1, A2, and B] (depth = 449.12 m) – Altered, sheared, heterogranular, meta-graywacke (in part brecciated)

Altered, sheared, heterogranular, meta-graywacke composed mainly of quartz, K-feldspar, plagioclase, muscovite, chlorite, a few biotite, and opaque minerals (pyrite). Some quartz grains show undulatory extinction; most of the quartz grains display microfractures. Extremely rare PFs (1 set) in quartz grains; only one partially toasted quartz grain with PDFs (1 set) seen. Feldspar grains are partially or totally altered to sericite and display a cloudy appearance. Many calcite veinlets and aggregates occur. Microfractures filled with iron oxides are present.

KR8-125 (depth = 451.23 m) – Weakly sheared medium-grained to gritty meta-graywacke

Weakly sheared meta-graywacke composed mainly of quartz, K-feldspar, plagioclase, chlorite, calcite, muscovite, opaque minerals, epidote, and rare biotite and zircon. Matrix-poor sample (representing less than 3 vol% of the section). Some quartz grains show microfractures and a few grains display undulatory extinction. Feldspar grains are partially altered to sericite. Calcite aggregates occur. No diagnostic shock indicators.

Appendix D:

Table D-1. SEM quantitative energy dispersive X-ray analyses of calcite clasts, aggregates, and veinlets in suevite samples from the LB-08A drill core in the Bosumtwi crater (Ghana).

Sample no.	Depth (m)	Calcite type	Calcite generation	Oxides composition (wt. %)					Numbers of ions on the basis of six (O)				
				CaO	MgO	FeO	MnO	CO ₂	Ca	Mg	Fe	Mn	C
KR8-003	238.90	Clast	P	52.96	1.03	1.53	0.53	43.95	1.891	0.051	0.043	0.015	2.000
KR8-003	238.90	Veinlet	S	54.55	0.10	0.43	1.07	43.85	1.953	0.005	0.012	0.030	2.000
KR8-003	238.90	Veinlet	S	52.72	1.02	1.26	1.07	43.92	1.884	0.051	0.035	0.030	2.000
KR8-005	240.04	Clast	P	55.54	0.10	0.16	0.25	43.95	1.983	0.005	0.004	0.007	2.000
KR8-005	240.04	Clast	P	55.48	0.18	0.22	0.15	43.97	1.981	0.009	0.006	0.004	2.000
KR8-005	240.04	Clast	P	54.73	0.39	0.40	0.53	43.95	1.955	0.019	0.011	0.015	2.000
KR8-005	240.04	Aggregate	S	53.18	0.92	1.29	0.68	43.94	1.899	0.046	0.036	0.019	2.000
KR8-005	240.04	Aggregate	S	54.30	0.37	0.72	0.70	43.90	1.941	0.019	0.020	0.020	2.000
KR8-005	240.04	Aggregate	S	54.29	0.23	1.02	0.60	43.86	1.943	0.011	0.029	0.017	2.000
KR8-005	240.04	Aggregate	S	55.24	0.23	0.57	n.d.	43.96	1.973	0.011	0.016	---	2.000
KR8-005	240.04	Aggregate	S	54.91	0.41	0.43	0.29	43.97	1.960	0.020	0.012	0.008	2.000
KR8-005	240.04	Aggregate	S	54.60	0.09	1.05	0.42	43.85	1.955	0.004	0.029	0.012	2.000
KR8-005	240.04	Aggregate	S	54.00	0.22	1.33	0.62	43.82	1.934	0.011	0.037	0.018	2.000
KR8-039	286.17	Clast	P	54.27	0.43	0.77	0.62	43.91	1.940	0.021	0.021	0.018	2.000
KR8-039	286.17	Clast	P	54.25	0.55	0.41	0.84	43.95	1.937	0.027	0.011	0.024	2.000
KR8-039	286.17	Clast	P	53.95	n.d.	1.36	0.93	43.75	1.935	---	0.038	0.027	2.000
KR8-039	286.17	Clast	P	54.46	0.25	0.37	1.04	43.88	1.948	0.012	0.010	0.029	2.000
KR8-039	286.17	Clast	P	54.22	0.22	0.92	0.79	43.85	1.941	0.011	0.026	0.022	2.000
KR8-039	286.17	Clast	P	53.52	0.66	0.51	1.41	43.90	1.913	0.033	0.014	0.040	2.000
KR8-042	293.97	Clast	P	55.21	0.19	0.41	0.24	43.94	1.972	0.010	0.011	0.007	2.000
KR8-042	293.97	Clast	P	54.11	0.44	0.65	0.90	43.90	1.935	0.022	0.018	0.025	2.000
KR8-042	293.97	Clast	P	55.45	0.12	n.d.	0.48	43.95	1.980	0.006	---	0.014	2.000
KR8-042	293.97	Clast	P	54.59	0.26	0.79	0.47	43.89	1.952	0.013	0.022	0.013	2.000
KR8-042	293.97	Clast	P	56.01	0.02	n.d.	n.d.	43.97	1.999	0.001	---	---	2.000
KR8-042	293.97	Veinlet	S	55.53	0.07	0.16	0.31	43.94	1.984	0.003	0.004	0.009	2.000
KR8-042	293.97	Veinlet	S	55.36	0.13	0.33	0.24	43.94	1.978	0.007	0.009	0.007	2.000
KR8-042	293.97	Veinlet	S	55.04	0.08	n.d.	0.99	43.89	1.968	0.004	---	0.028	2.000
KR8-042	293.97	Veinlet	S	55.06	0.32	0.27	0.38	43.97	1.966	0.016	0.008	0.011	2.000
KR8-042	293.97	Veinlet	S	55.45	n.d.	0.01	0.63	43.91	1.982	---	0.000	0.018	2.000
KR8-042	293.97	Veinlet	S	54.36	0.33	0.49	0.92	43.89	1.944	0.016	0.014	0.026	2.000
ADE-8a	418.05	Clast	P	55.19	0.11	0.36	0.43	43.91	1.973	0.005	0.010	0.012	2.000
ADE-8a	418.05	Clast	P	55.26	0.05	0.51	0.27	43.91	1.976	0.003	0.014	0.008	2.000
ADE-8a	418.05	Clast	P	55.01	0.06	0.56	0.49	43.88	1.968	0.003	0.016	0.014	2.000
ADE-8a	418.05	Clast	P	55.11	n.d.	0.90	0.11	43.87	1.972	---	0.025	0.003	2.000
ADE-8a	418.05	Clast	P	55.01	0.15	n.d.	0.93	43.91	1.966	0.008	---	0.026	2.000
ADE-8a	418.05	Aggregate	S	54.05	0.25	1.06	0.80	43.84	1.935	0.013	0.030	0.023	2.000
ADE-8a	418.05	Aggregate	S	54.74	0.01	0.70	0.71	43.84	1.960	0.000	0.020	0.020	2.000
ADE-8a	418.05	Aggregate	S	55.16	0.03	0.53	0.39	43.89	1.973	0.002	0.015	0.011	2.000
ADE-8a	418.05	Flake in melt	S	54.10	0.21	1.34	0.51	43.83	1.937	0.011	0.038	0.015	2.000
CAN-31	440.32	Clast	P	54.98	0.27	0.52	0.30	43.94	1.964	0.013	0.014	0.008	2.000
CAN-31	440.32	Clast	P	55.78	0.13	0.11	n.d.	43.98	1.990	0.007	0.003	---	2.000
CAN-31	440.32	Clast	P	55.62	n.d.	0.13	0.32	43.93	1.987	---	0.004	0.009	2.000
CAN-31	440.32	Clast	P	54.44	0.26	0.63	0.79	43.88	1.947	0.013	0.018	0.022	2.000
CAN-31	440.32	Clast	P	55.30	0.05	0.19	0.55	43.91	1.977	0.002	0.005	0.016	2.000
CAN-31	440.32	Clast	P	55.23	n.d.	n.d.	0.88	43.89	1.975	---	---	0.025	2.000
CAN-31	440.32	Aggregate	S	54.62	0.36	0.83	0.26	43.93	1.952	0.018	0.023	0.007	2.000
CAN-31	440.32	Aggregate	S	53.88	0.32	0.66	1.29	43.84	1.929	0.016	0.019	0.037	2.000
CAN-31	440.32	Flake in melt	S	55.26	n.d.	0.69	0.16	43.89	1.976	---	0.019	0.005	2.000
CAN-31	440.32	Flake in melt	S	55.08	0.20	0.60	0.19	43.93	1.968	0.010	0.017	0.006	2.000

Analysis are normalized to 100% where the CO₂ content was calculated from stoichiometry; All depths are below Bosumtwi lake's level; P = Primary; S = Secondary; n.d. = not detected.

Table D-2. Mineral chemistry by SEM quantitative energy dispersive X-ray analyses of orthoclase clasts in suevite samples from drill core LB-08A, Bosumtwi (Ghana).

Sample no.	Depth (m)	Host	SiO ₂	TiO ₂	Al ₂ O ₃	FeO	MnO	MgO	CaO	Na ₂ O	K ₂ O	Cr ₂ O ₃
KR8-001	235.77	Matrix	53.03	0.34	35.04	1.17	0.22	n.d.	0.12	0.11	9.70	0.27
KR8-001	235.77	Melt	54.33	0.28	34.59	1.52	0.05	0.90	0.11	0.05	8.04	0.13
KR8-001	235.77	LGMG	51.34	0.38	37.87	0.58	0.10	0.26	0.06	0.19	8.80	0.42
KR8-001	235.77	LGMG	51.93	0.97	35.15	1.56	0.10	0.79	0.09	0.09	9.13	0.19
KR8-001	235.77	LGMG	53.86	0.66	34.01	1.51	0.21	0.14	0.08	0.14	9.17	0.22
KR8-003	238.90	Mc	49.71	0.30	35.33	3.53	n.d.	n.d.	0.35	0.61	10.17	n.d.
KR8-005	240.04	Matrix	52.43	0.27	36.74	1.42	n.d.	0.53	0.08	0.58	7.86	0.10
KR8-005	240.04	Matrix	51.77	0.21	37.30	1.09	n.d.	1.06	0.12	0.65	7.81	n.d.
KR8-005	240.04	Matrix	51.90	0.39	36.43	1.93	n.d.	0.89	0.04	0.66	7.63	0.12
KR8-005	240.04	Matrix	50.00	0.35	36.96	3.09	n.d.	1.44	0.04	0.61	7.45	0.05
KR8-005	240.04	Matrix	51.94	0.06	37.03	1.60	n.d.	0.69	0.02	0.68	7.87	0.12
KR8-005	240.04	Matrix	52.65	0.45	36.69	1.09	0.08	0.90	0.06	0.56	7.38	0.13
KR8-042	293.97	Matrix	50.68	0.16	36.74	0.76	0.16	n.d.	0.34	0.55	10.61	n.d.
KR8-005	240.04	Melt	51.21	0.19	37.60	1.33	0.11	0.92	0.13	0.68	7.81	n.d.
KR8-005	240.04	LGMG	50.24	0.44	38.48	1.01	0.29	1.14	0.08	0.87	7.10	0.35

Analysis (in wt%) are normalized to 100%. All depths are below Bosumtwi lake's level. Melt = Melt particle; LGMG = Light greenish gray meta-graywacke clast; Mc = Metasedimentary clast; n.d. = not detected.

Table D-3. Mineral chemistry by SEM quantitative energy dispersive X-ray analyses of albite clasts in suevite samples from drill core LB-08A, Bosumtwi (Ghana).

Sample no.	Depth (m)	Host	SiO ₂	TiO ₂	Al ₂ O ₃	FeO	MnO	MgO	CaO	Na ₂ O	K ₂ O	Cr ₂ O ₃
KR8-001	235.77	Matrix	70.44	0.08	21.44	0.45	0.32	n.d.	0.06	6.94	0.14	0.12
KR8-001	235.77	Matrix	69.58	0.13	20.87	0.23	0.15	0.36	0.28	8.14	0.08	0.19
KR8-001	235.77	LGMG	69.12	0.08	22.25	0.13	0.07	n.d.	0.35	7.87	0.07	0.06
KR8-003	238.90	Matrix	72.02	0.26	15.43	0.35	0.03	n.d.	0.29	11.34	0.09	0.18
KR8-003	238.90	Matrix	74.06	n.d.	13.60	0.29	0.14	n.d.	0.11	10.47	1.33	n.d.
KR8-003	238.90	Matrix	72.81	0.01	14.88	0.19	0.08	n.d.	0.21	11.82	n.d.	n.d.
KR8-003	238.90	Melt	73.72	n.d.	14.57	n.d.	0.09	n.d.	0.16	9.78	1.67	0.01
KR8-004	239.65	Melt	69.09	0.18	20.99	0.31	0.07	0.20	0.34	8.57	0.14	0.11
KR8-004	239.65	Melt	68.50	0.32	20.86	0.24	0.18	0.25	0.32	8.96	0.14	0.23
KR8-005	240.04	Matrix	69.17	n.d.	20.75	n.d.	n.d.	n.d.	0.25	9.72	0.10	0.01
KR8-005	240.04	Matrix	68.95	0.06	21.17	0.29	n.d.	n.d.	0.64	8.65	0.18	0.06
KR8-005	240.04	Melt	69.13	0.12	20.48	0.09	0.07	n.d.	0.21	9.88	n.d.	0.01
KR8-042	293.97	Matrix	72.32	n.d.	15.56	0.13	n.d.	n.d.	0.09	11.65	n.d.	0.24
KR8-042	293.97	LGMG	75.01	n.d.	13.90	0.54	n.d.	n.d.	0.44	10.03	0.07	n.d.
ADE-8a	418.05	Matrix	72.97	0.07	14.89	n.d.	n.d.	n.d.	n.d.	11.81	0.01	0.26
ADE-8a	418.05	Matrix	73.57	n.d.	14.43	n.d.	n.d.	n.d.	0.27	11.66	n.d.	0.07
ADE-8a	418.05	Melt	72.76	0.15	14.99	0.21	0.18	n.d.	0.12	11.57	0.03	n.d.
CAN-31	440.32	Matrix	72.42	0.39	15.34	0.23	0.21	n.d.	0.26	10.79	0.09	0.28
CAN-31	440.32	Matrix	72.40	n.d.	15.22	0.09	n.d.	n.d.	0.51	11.76	n.d.	0.03

Analysis (in wt%) are normalized to 100%. All depths are below Bosumtwi lake's level. Melt = Melt particle; LGMG = Light greenish gray meta-graywacke clast; n.d. = not detected.

Table D-4. Mineral chemistry by SEM quantitative energy dispersive X-ray analyses of chlorite in suevite samples from drill core LB-08A, Bosumtwi (Ghana).

Sample no.	Depth (m)	Host	SiO ₂	TiO ₂	Al ₂ O ₃	FeO	MnO	MgO	CaO	Na ₂ O	K ₂ O	Cr ₂ O ₃
KR8-001	235.77	Matrix	33.83	0.30	25.34	25.86	0.53	13.28	0.29	0.10	0.24	0.23
KR8-001	235.77	Matrix	32.11	0.20	26.18	27.83	0.32	12.62	0.36	n.d.	0.17	0.21
KR8-001	235.77	Matrix	29.66	0.36	25.59	32.31	0.79	10.46	0.29	n.d.	0.10	0.42
KR8-001	235.77	Matrix	29.35	0.21	26.57	28.18	0.43	14.97	0.03	n.d.	0.04	0.20
KR8-001	235.77	Matrix	30.64	0.30	26.72	26.26	0.34	15.01	0.23	0.07	0.23	0.20
KR8-001	235.77	LGMG	31.55	0.32	26.74	22.23	0.27	18.33	0.11	0.02	0.18	0.26
KR8-001	235.77	LGMG	32.07	0.24	27.00	22.67	0.11	17.69	0.08	n.d.	0.06	0.09
KR8-001	235.77	LGMG	31.19	0.35	26.38	22.88	0.41	18.02	0.23	n.d.	0.13	0.40
KR8-005	240.04	Matrix	29.63	0.70	26.63	25.34	n.d.	16.87	n.d.	0.71	0.02	0.10
KR8-005	240.04	Matrix	29.88	0.35	26.73	25.75	0.07	16.39	n.d.	0.63	0.08	0.12
KR8-005	240.04	Matrix	29.83	0.07	28.02	25.64	0.20	15.45	n.d.	0.52	n.d.	0.28
KR8-005	240.04	Matrix	29.39	n.d.	27.15	24.83	0.30	17.14	0.06	0.86	0.11	0.17
KR8-005	240.04	Matrix	30.22	0.01	26.87	24.79	n.d.	17.04	0.08	0.78	0.09	0.11
KR8-005	240.04	Matrix	32.29	0.22	26.25	23.50	0.18	16.40	0.18	0.92	0.07	n.d.
KR8-005	240.04	Matrix	30.37	0.12	26.95	24.36	0.08	17.23	n.d.	0.88	0.03	n.d.
KR8-005	240.04	Matrix	31.02	n.d.	26.90	26.83	0.01	14.16	0.05	0.70	0.18	0.14
KR8-005	240.04	Matrix	28.94	0.07	26.97	27.56	0.26	15.32	n.d.	0.85	0.02	n.d.
KR8-005	240.04	Matrix	30.57	0.08	26.95	26.03	0.18	15.34	0.10	0.67	0.03	0.03
KR8-005	240.04	Matrix	29.85	n.d.	27.75	25.87	n.d.	15.87	n.d.	0.38	0.15	0.13
KR8-005	240.04	Matrix	29.11	0.26	26.49	26.62	n.d.	16.36	n.d.	1.02	n.d.	0.15
KR8-005	240.04	Matrix	28.93	0.09	27.14	27.15	n.d.	15.61	0.02	0.91	0.13	0.02
KR8-005	240.04	Matrix	31.08	0.26	26.12	26.20	0.24	15.23	n.d.	0.68	0.13	0.06
KR8-005	240.04	Melt	34.85	0.09	26.97	23.38	0.22	12.72	0.15	0.83	0.77	0.02
KR8-005	240.04	LGMG	33.38	0.04	26.37	16.39	n.d.	22.65	0.25	0.77	0.15	n.d.
KR8-005	240.04	LGMG	33.36	n.d.	25.40	16.88	0.29	23.66	0.08	0.27	n.d.	0.08
KR8-005	240.04	LGMG	31.78	n.d.	26.95	16.70	0.18	23.17	0.07	1.10	n.d.	0.04
KR8-042	293.97	Matrix	33.70	0.16	13.54	27.43	0.13	24.74	n.d.	n.d.	0.04	0.26
KR8-042	293.97	Matrix	34.04	0.30	13.70	23.90	0.40	27.17	0.01	n.d.	0.02	0.46
KR8-042	293.97	Matrix	31.98	n.d.	17.05	29.03	0.42	21.10	0.42	n.d.	n.d.	n.d.
KR8-042	293.97	LGMG	33.12	n.d.	14.53	25.64	0.15	26.16	n.d.	n.d.	0.26	0.14
KR8-042	293.97	LGMG	33.12	n.d.	16.47	22.99	0.84	26.03	0.39	n.d.	0.17	n.d.
CAN-31	440.32	Matrix	31.54	0.17	15.32	29.92	0.45	22.29	0.32	n.d.	n.d.	n.d.

Analysis (in wt%) are normalized to 100%. All depths are below Bosumtwi lake's level. Melt = Melt particle; LGMG = Light greenish gray meta-graywacke clast; n.d. = not detected.

Table D-5. Mineral chemistry by SEM quantitative energy dispersive X-ray analyses of muscovite in suevite samples from drill core LB-08A, Bosumtwi (Ghana).

Sample no.	Depth (m)	Host	SiO ₂	TiO ₂	Al ₂ O ₃	FeO	MnO	MgO	CaO	Na ₂ O	K ₂ O	Cr ₂ O ₃
KR8-003	238.90	Melt	52.99	0.33	33.41	1.25	n.d.	n.d.	0.28	0.73	10.88	0.14
KR8-113	439.59	Matrix	51.22	0.02	32.46	4.36	0.47	n.d.	0.45	n.d.	10.68	0.34
ADE-8a	418.05	Matrix	52.33	0.13	30.65	4.01	n.d.	n.d.	0.47	0.17	12.24	n.d.
CAN-31	440.32	Matrix	52.36	0.23	34.21	1.41	0.37	n.d.	0.18	0.58	10.48	0.17
CAN-31	440.32	Matrix	49.90	2.87	31.66	3.75	0.04	n.d.	0.54	0.28	10.95	n.d.

Analysis (in wt%) are normalized to 100%. All depths are below Bosumtwi lake's level. Melt = Melt particle; n.d. = not detected.

Table D-6. Mineral chemistry by SEM quantitative energy dispersive X-ray analyses of amphibole in suevite samples from drill core LB-08A, Bosumtwi (Ghana).

Sample no.	Depth (m)	Host	SiO ₂	TiO ₂	Al ₂ O ₃	FeO	MnO	MgO	CaO	Na ₂ O	K ₂ O	Cr ₂ O ₃
KR8-003	238.90	Matrix	28.85	n.d.	17.82	42.03	0.47	10.73	n.d.	n.d.	0.10	n.d.
KR8-003	238.90	Matrix	26.89	0.14	16.97	45.12	n.d.	10.64	n.d.	n.d.	0.11	0.14
KR8-003	238.90	Matrix	26.82	0.29	19.17	43.46	0.40	9.69	0.14	n.d.	n.d.	0.04
KR8-003	238.90	Matrix	29.10	0.32	16.49	41.86	0.16	11.94	0.08	n.d.	0.05	n.d.
KR8-003	238.90	Matrix	28.54	0.16	18.97	39.84	0.24	11.80	0.08	n.d.	0.06	0.32
KR8-003	238.90	Matrix	30.56	0.18	16.09	40.70	0.80	11.33	0.21	n.d.	n.d.	0.13
KR8-003	238.90	Matrix	31.41	0.13	16.39	41.31	n.d.	10.54	0.06	n.d.	0.17	n.d.
KR8-003	238.90	Matrix	35.26	0.03	14.21	40.75	0.61	8.61	0.34	n.d.	0.19	n.d.
KR8-003	238.90	Mc	27.27	n.d.	17.79	43.92	0.52	10.22	0.09	n.d.	0.06	0.13
KR8-039	286.17	Matrix	31.38	0.36	18.11	34.69	n.d.	15.05	0.15	n.d.	0.27	n.d.
ADE-8a	418.05	Matrix	25.33	n.d.	18.23	50.49	0.24	5.69	0.02	n.d.	n.d.	n.d.
ADE-8a	418.05	Matrix	26.59	n.d.	17.63	46.22	0.04	9.36	0.11	n.d.	n.d.	0.05
ADE-8a	418.05	Matrix	26.33	0.11	20.28	50.38	0.42	2.15	0.17	n.d.	0.03	0.13
ADE-8a	418.05	Melt	24.89	0.19	21.32	49.63	0.26	3.60	n.d.	n.d.	n.d.	0.10
CAN-31	440.32	Matrix	38.19	0.13	13.91	41.02	0.10	6.44	0.03	n.d.	0.15	0.03
CAN-31	440.32	Matrix	28.46	0.23	15.70	40.47	1.01	14.06	0.08	n.d.	n.d.	n.d.
CAN-31	440.32	Matrix	25.10	0.40	20.19	48.83	n.d.	4.80	0.17	0.28	n.d.	0.23

Analysis (in wt%) are normalized to 100%. All depths are below Bosumtwi lake's level. Melt = Melt particle; Mc = Metasedimentary clast; n.d. = not detected.

Table D-7. Mineral chemistry by SEM quantitative energy dispersive X-ray analyses of sphene in suevite samples from drill core LB-08A, Bosumtwi (Ghana).

Sample no.	Depth (m)	Host	SiO ₂	TiO ₂	Al ₂ O ₃	FeO	MnO	MgO	CaO	Na ₂ O	K ₂ O	Cr ₂ O ₃
KR8-039	286.17	Matrix	33.22	38.33	0.74	0.72	n.d.	n.d.	26.79	n.d.	0.19	n.d.
KR8-039	286.17	Matrix	32.23	38.90	n.d.	n.d.	0.46	n.d.	27.93	0.46	0.01	n.d.
KR8-039	286.17	Matrix	32.06	39.27	n.d.	0.17	n.d.	n.d.	28.50	n.d.	n.d.	n.d.
KR8-042	293.97	Matrix	32.17	39.91	n.d.	0.09	0.25	n.d.	27.30	0.07	0.22	n.d.
KR8-042	293.97	Matrix	34.18	38.12	0.41	0.57	0.26	n.d.	26.18	n.d.	0.29	n.d.
KR8-113	439.59	Mc	32.52	38.34	n.d.	2.35	0.63	n.d.	26.02	n.d.	0.13	n.d.
KR8-113	439.59	Mc	31.34	38.40	n.d.	1.70	0.47	0.25	27.61	0.20	0.03	n.d.

Analysis (in wt%) are normalized to 100%. All depths are below Bosumtwi lake's level. Mc = Metasedimentary clast; n.d. = not detected.

Table D-8. SEM quantitative energy dispersive X-ray analyses of melt particles in suevite samples from the Bosumtwi crater (Ghana). All samples are from drill core LB-08A (i.e., impact breccia deposits within the crater), with the exception of the sample BH3-0585, from outside the northern crater rim.

Sample no.	Depth (m)	SiO ₂	TiO ₂	Al ₂ O ₃	FeO	MnO	MgO	CaO	Na ₂ O	K ₂ O	Cr ₂ O ₃
KR8-001	235.77	71.02	0.28	12.80	8.93	0.40	4.18	0.69	n.d.	1.35	0.34
KR8-001	235.77	65.94	0.53	16.21	5.92	0.16	3.02	5.97	0.21	1.90	0.14
KR8-001	235.77	67.38	0.47	15.45	5.97	0.17	1.88	6.18	0.24	1.93	0.34
KR8-003	238.90	74.41	0.14	3.29	17.71	n.d.	n.d.	0.40	1.62	2.18	0.25
KR8-003	238.90	71.89	0.24	8.36	14.60	0.44	2.22	0.75	n.d.	1.51	n.d.
KR8-003	238.90	70.00	0.05	7.08	17.04	0.36	2.82	0.70	n.d.	1.73	0.22
KR8-004	239.65	68.05	0.62	16.35	12.47	0.24	0.38	0.61	0.03	1.09	0.16
KR8-004	239.65	68.08	0.55	16.28	12.19	0.22	0.13	0.90	0.02	1.26	0.37
KR8-004	239.65	68.61	0.59	16.74	11.50	0.17	0.40	0.52	0.04	1.26	0.18
KR8-004	239.65	71.92	8.35	10.68	6.61	0.37	0.85	0.37	n.d.	0.50	0.36
KR8-004	239.65	67.95	0.70	19.49	7.71	0.32	0.37	0.45	0.21	2.53	0.26
KR8-004	239.65	68.24	0.94	17.26	9.53	0.30	1.36	0.80	0.02	1.27	0.29
KR8-004	239.65	70.24	0.58	16.17	10.55	0.33	n.d.	0.46	0.20	1.20	0.27
KR8-004	239.65	64.13	0.49	22.88	7.30	0.09	0.41	0.29	0.15	4.09	0.17
KR8-004	239.65	66.78	0.66	16.20	12.26	0.35	0.79	1.03	0.26	1.32	0.35
KR8-004	239.65	68.76	0.38	14.65	13.85	0.21	0.24	0.40	0.08	1.21	0.23
KR8-005	240.04	65.69	n.d.	17.40	8.21	0.14	6.03	0.32	1.06	1.14	0.03
KR8-005	240.04	64.35	0.26	18.11	8.85	0.19	5.72	0.41	0.76	1.25	0.10
KR8-005	240.04	62.90	0.19	19.26	8.00	n.d.	7.06	0.55	1.19	0.77	0.09
KR8-005	240.04	67.48	0.13	16.82	7.82	n.d.	5.52	0.49	0.79	0.94	n.d.
KR8-005	240.04	61.46	0.31	21.62	8.62	0.06	5.57	0.40	0.63	1.33	n.d.
KR8-005	240.04	64.21	0.38	20.88	8.73	0.06	4.21	0.51	n.d.	1.01	n.d.
KR8-005	240.04	61.18	0.19	24.11	7.07	0.01	5.36	0.83	0.81	0.38	0.04
KR8-005	240.04	60.10	0.42	23.85	8.26	n.d.	5.09	0.79	0.64	0.74	0.12
KR8-005	240.04	60.10	0.57	23.30	7.23	0.11	5.98	0.86	0.77	1.00	0.08
KR8-005	240.04	60.82	0.40	22.04	7.70	0.09	6.24	0.74	0.94	1.02	n.d.
KR8-005	240.04	60.23	0.46	22.00	7.51	0.15	6.73	0.95	0.83	1.14	n.d.
KR8-005	240.04	60.83	0.15	30.64	3.44	n.d.	3.67	0.10	0.69	0.32	0.16
KR8-005	240.04	57.41	0.18	26.18	10.18	0.20	4.50	0.55	n.d.	0.79	0.02
KR8-005	240.04	62.05	0.26	27.16	6.77	0.33	2.51	0.30	n.d.	0.60	n.d.
KR8-113	439.59	63.48	0.82	11.74	11.70	0.57	1.44	2.95	0.54	6.13	0.63
KR8-113	439.59	64.98	n.d.	14.37	9.48	0.09	0.99	2.24	0.23	7.62	n.d.
ADE-8a	418.05	53.64	0.16	13.74	26.93	n.d.	2.00	2.01	0.62	0.90	n.d.
ADE-8a	418.05	54.10	0.56	12.59	25.55	0.01	2.74	0.45	1.02	2.97	n.d.
CAN-31	440.32	46.54	0.02	16.69	23.17	0.51	2.09	7.20	n.d.	3.43	0.35
CAN-31	440.32	48.99	0.57	17.94	20.57	n.d.	1.66	5.98	n.d.	4.12	0.17
CAN-31	440.32	45.91	1.00	15.97	24.63	n.d.	2.12	8.08	n.d.	2.29	n.d.
BH3-0585	5.85	73.65	0.32	14.04	0.57	n.d.	n.d.	3.09	6.15	1.94	0.25
BH3-0585	5.85	71.89	0.45	15.66	0.74	0.03	n.d.	4.26	6.20	0.78	n.d.
BH3-0585	5.85	67.26	n.d.	18.89	n.d.	0.03	n.d.	3.10	9.20	1.23	0.28
BH3-0585	5.85	67.40	0.26	18.39	0.24	0.17	n.d.	4.06	8.26	1.20	0.03

Analysis (in wt%) are normalized to 100%. All depths are below Bosumtwi lake's level, with the exception of sample BH3-0585 for which the depth is below the ground surface; n.d. = not detected.

Table E-1. Isotope ratios and U-Pb ages of zircons from suevite (KR8-004) and meta-graywacke (KR8-032 and KR8-109) from the LB-08A drill core in the Bosumtwi crater (Ghana).

Sample and spot no.	Isotope ratios and errors					
	$^{207}\text{Pb}/^{206}\text{Pb}$		$^{207}\text{Pb}/^{235}\text{U}$		$^{206}\text{Pb}/^{238}\text{U}$	
		1σ		1σ		1σ
Sample KR8-004						
SB-04	0.11142	± 0.00114	5.82762	± 0.04045	0.37873	± 0.00219
Sample KR8-032						
LB-01	0.13746	± 0.00282	7.64273	± 0.08625	0.40337	± 0.00404
LB-02	0.13676	± 0.00281	6.96431	± 0.07872	0.36943	± 0.00372
LB-03	0.13955	± 0.00285	8.00911	± 0.08880	0.41636	± 0.00419
LB-04-a	0.13019	± 0.00259	8.00371	± 0.08064	0.44599	± 0.00434
LB-04-b	0.13394	± 0.00266	6.62879	± 0.06542	0.35900	± 0.00347
Sample KR8-109						
LC-06	0.15313	± 0.00303	8.36005	± 0.08279	0.39597	± 0.00388
LC-08-a	0.13636	± 0.00276	7.51715	± 0.08200	0.39981	± 0.00404
LC-08-b	0.14090	± 0.00294	8.22268	± 0.09961	0.42323	± 0.00448
LC-09	0.12833	± 0.00254	6.54637	± 0.06552	0.36991	± 0.00365
LC-12	0.12926	± 0.00264	7.11928	± 0.08094	0.39930	± 0.00415
LC-15	0.12812	± 0.00262	6.49731	± 0.07367	0.36764	± 0.00381
LC-20	0.13122	± 0.00265	7.09600	± 0.07776	0.39194	± 0.00406
SA-15	0.14392	± 0.00174	7.47611	± 0.06254	0.37700	± 0.00232
SA-18	0.13003	± 0.00143	7.39368	± 0.04926	0.41262	± 0.00228
SA-19	0.13039	± 0.00148	7.31758	± 0.05417	0.40710	± 0.00236
SA-24-a	0.13316	± 0.00155	6.41118	± 0.05079	0.34910	± 0.00209
SA-24-b	0.13183	± 0.00152	6.56971	± 0.05149	0.36129	± 0.00214
SA-31-a	0.13732	± 0.00171	7.05102	± 0.06611	0.37218	± 0.00246
SA-31-b	0.13430	± 0.00157	6.69865	± 0.05548	0.36152	± 0.00223
SA-31-c	0.13095	± 0.00150	6.93734	± 0.05521	0.38395	± 0.00233
SA-34	0.12622	± 0.00139	6.23961	± 0.04622	0.35822	± 0.00209
SA-52-a	0.12874	± 0.00137	6.28391	± 0.04359	0.35362	± 0.00202
SA-52-b	0.13043	± 0.00155	6.39534	± 0.05675	0.35522	± 0.00228
SA-52-c	0.12231	± 0.00130	6.18633	± 0.04341	0.36640	± 0.00211
SA-59-a	0.12749	± 0.00141	6.66062	± 0.05225	0.37843	± 0.00230
SA-59-b	0.12310	± 0.00135	6.65573	± 0.05131	0.39163	± 0.00236
SA-59-c	0.12634	± 0.00141	7.11392	± 0.05691	0.40782	± 0.00252
SA-67-a	0.13168	± 0.00146	6.25155	± 0.04995	0.34381	± 0.00212
SA-67-b	0.12189	± 0.00130	6.81589	± 0.05075	0.40496	± 0.00242
SA-69	0.13536	± 0.00135	6.17312	± 0.03968	0.33026	± 0.00187

Table E-1. Continued. Isotope ratios and U-Pb ages of zircons from suevite (KR8-004) and meta-graywacke (KR8-032 and KR8-109) from the LB-08A drill core in the Bosumtwi crater (Ghana).

Sample and spot no.	Apparent ages (Ma) and errors						Discordance (%)
	$^{207}\text{Pb}/^{206}\text{Pb}$	1σ	$^{207}\text{Pb}/^{235}\text{U}$	1σ	$^{206}\text{Pb}/^{238}\text{U}$	1σ	
Sample KR8-004							
SB-04	1823	± 18	1951	± 6	2070	± 10	-14
Sample KR8-032							
LB-01	2196	± 35	2190	± 10	2185	± 19	1
LB-02	2187	± 35	2107	± 10	2027	± 18	7
LB-03	2222	± 35	2232	± 10	2244	± 19	-1
LB-04-a	2101	± 35	2231	± 9	2377	± 19	-13
LB-04-b	2150	± 34	2063	± 9	1977	± 16	8
Sample KR8-109							
LC-06	2381	± 33	2271	± 9	2151	± 18	10
LC-08-a	2182	± 35	2175	± 10	2168	± 19	1
LC-08-b	2238	± 36	2256	± 11	2275	± 20	-2
LC-09	2075	± 34	2052	± 9	2029	± 17	2
LC-12	2088	± 36	2127	± 10	2166	± 19	-4
LC-15	2072	± 36	2046	± 10	2018	± 18	3
LC-20	2114	± 35	2124	± 10	2132	± 19	-1
SA-15	2275	± 21	2170	± 7	2062	± 11	9
SA-18	2098	± 19	2160	± 6	2227	± 10	-6
SA-19	2103	± 20	2151	± 7	2202	± 11	-5
SA-24-a	2140	± 20	2034	± 7	1930	± 10	10
SA-24-b	2123	± 20	2055	± 7	1988	± 10	6
SA-31-a	2194	± 22	2118	± 8	2040	± 12	7
SA-31-b	2155	± 20	2072	± 7	1989	± 11	8
SA-31-c	2111	± 20	2103	± 7	2095	± 11	1
SA-34	2046	± 19	2010	± 6	1974	± 10	4
SA-52-a	2081	± 19	2016	± 6	1952	± 10	6
SA-52-b	2104	± 21	2032	± 8	1960	± 11	7
SA-52-c	1990	± 19	2003	± 6	2012	± 10	-1
SA-59-a	2064	± 19	2067	± 7	2069	± 11	0
SA-59-b	2002	± 19	2067	± 7	2130	± 11	-6
SA-59-c	2048	± 20	2126	± 7	2205	± 12	-8
SA-67-a	2121	± 19	2012	± 7	1905	± 10	10
SA-67-b	1984	± 19	2088	± 7	2192	± 11	-10
SA-69	2169	± 17	2001	± 6	1840	± 9	15

List of Publications:

Papers published or submitted in refereed journals

1. **Ferrière L.**, Koeberl C., and Reimold W. U. 2007. Drill core LB-08A, Bosumtwi impact structure, Ghana: Petrographic and shock metamorphic studies of material from the central uplift. *Meteoritics and Planetary Science* 42:611–633.
2. **Ferrière L.**, Koeberl C., Reimold W. U., and Mader D. 2007. Drill core LB-08A, Bosumtwi impact structure, Ghana: Geochemistry of fallback breccia and bedrock samples from the central uplift. *Meteoritics and Planetary Science* 42:689–708.
3. Karikari F., **Ferrière L.**, Koeberl C., Reimold W. U., and Mader D. 2007. Petrography, geochemistry, and alteration of country rocks from the Bosumtwi impact structure, Ghana. *Meteoritics and Planetary Science* 42:513–540.
4. McDonald I., Peucker-Ehrenbrink B., Coney L., **Ferrière L.**, Reimold W. U., and Koeberl C. 2007. Search for a meteoritic component in drill cores from the Bosumtwi impact structure, Ghana: Platinum group element contents and osmium isotopic characteristics. *Meteoritics and Planetary Science* 42:743–753.
5. **Ferrière L.**, Koeberl C., Ivanov B. A., and Reimold W. U. 2008. Shock metamorphism of Bosumtwi impact crater rocks, shock attenuation, and uplift formation. *Science* (in press).
6. **Ferrière L.**, Koeberl C., and Reimold W. U. 2009. Characterization of ballen quartz and cristobalite in impact breccias: New observations and constraints on ballen formation. *European Journal of Mineralogy*, in press, DOI: 10.1127/0935-1221/2009/0021-1898.
7. **Ferrière L.**, Morrow J. R., Amgaa T., and Koeberl C. 2009. Systematic study of universal-stage measurements of planar deformation features in shocked quartz: Implications for statistical significance and representation of results. *Meteoritics and Planetary Science* (in review).
8. Bartosova K., **Ferrière L.**, Koeberl C., Reimold W. U., and Gier S. 2009. Petrographic and shock metamorphic studies of the impact breccia section (1397–1551 m depth) of the Eyreville drill core, Chesapeake Bay impact structure, USA. Geological Society of America – Special Paper “Chesapeake Bay Impact Structure Deep Drilling Project” (in press).
9. Bartosova K., Dieter M. Schmitt R.-T., **Ferrière L.**, Koeberl C., Reimold W. U., and Brandstaetter F. 2009. Geochemistry of the impact breccia section (1397–1551 m depth) of the Eyreville drill core, Chesapeake Bay impact structure, USA. Geological Society of America – Special Paper “Chesapeake Bay Impact Structure Deep Drilling Project” (in press).

Publications (not peer-reviewed)

1. Koeberl C., Milkereit B., Overpeck J. T., Scholz C. A., Reimold W. U., **Ferrière L.**, Coney L., and Peck J. A. 2007. Results of the 2004 ICDP Bosumtwi impact crater, Ghana, drilling project. *DOSECC Journal* 5:1–4.

Abstracts published

1. Devouard B., **Ferrière L.**, Zanda B. and Messaoudi M. 2005. Mineralogy and petrology of TAN057 (C4) and comparison to the CV and CK groups (abstract). 4th Colloque International 3MA. Agadir, Maroc. p.1.
2. Hanova J., Lawton D. C., Visser J., Hildebrand A. R., and **Ferrière L.** 2005. 3D Structural interpretation of the Eagle Butte impact structure, Alberta, Canada (abstract #2355). 36th Lunar and Planetary Science Conference. CD-ROM.
3. **Ferrière L.** and Robin E. 2005. Zoning in K/T boundary spinel (abstract #5263). *Meteoritics and Planetary Science* 40:A47.
4. **Ferrière L.**, Koeberl C., Reimold W. U., and Gibson R. L. 2006. First mineralogical observations and chemical analyses of core LB-08A from the central uplift of the Bosumtwi impact structure, Ghana: Comparison with suevite from outside the crater(abstract #1845). 37th Lunar and Planetary Science Conference. CD-ROM.
5. **Ferrière L.**, Koeberl C., Reimold W. U., and Gibson R. L. 2006. Mineralogical and geochemical observations on core LB-08A from the central uplift of the Bosumtwi impact structure, Ghana (abstract #05692). *Geophysical Research Abstracts* 8. CD-ROM.
6. Koeberl C., Milkereit B., Reimold W. U., **Ferrière L.**, and Coney L. 2006. First results from the 2004 ICDP Bosumtwi impact crater, Ghana, drilling project: Impact and geophysical aspects (abstract). Workshop on Impact Craters as Indicators for Planetary Environmental Evolution and Astrobiology. Östersund, Sweden. p. 2.
7. **Ferrière L.**, Koeberl C., and Reimold W. U. 2006. Shock-metamorphic effects in samples from core LB-08A: First material recovered from the central uplift of the Bosumtwi impact crater, Ghana (abstract). Workshop on Impact Craters as Indicators for Planetary Environmental Evolution and Astrobiology. Östersund, Sweden. p. 2.
8. Coney L., Reimold W. U., **Ferrière L.**, Koeberl C., and Gibson R. L. 2006. The ICDP drillcores through the breccia fill of the Bosumtwi impact structure, Ghana. *Berichte der Dtsch. Mineral. Ges., Beiheft zu European Journal of Mineralogy* 18(1):A25.
9. Devouard B., **Ferrière L.**, Zanda B., and Messaoudi M. 2006. Mineralogy and petrology of TAN057 (C4) and comparison to the CV and CK groups (abstract #9025). *Meteoritics and Planetary Science* 41:A203.
10. **Ferrière L.**, Koeberl C., and Reimold W. U. 2006. Ballen quartz in impact glass from the Bosumtwi impact crater, Ghana (abstract #5097). *Meteoritics and Planetary Science* 41:A54.
11. **Ferrière L.** and Robin E. 2006. Zonations in spinel from meteorite fusion crusts and their relevance to impact spinel formation (abstract #5048). *Meteoritics and Planetary Science* 41:A55.

12. **Ferrière L.**, Koeberl C., Reimold W. U., and Coney L. 2006. Drilling into the Bosumtwi impact crater, Ghana: Investigating the crater fill of a well-preserved complex impact structure (abstract). *GSA Abstracts with Programs* 38(7):A296.
13. Koeberl C., **Ferrière L.**, and Reimold W. U. 2006. Shock levels in fallback and fallout impact breccias at the Bosumtwi impact structure, Ghana: Results of drill core studies(abstract #MR54A-02). American Geophysical Union Fall Meeting.
14. Reimold W. U., Koeberl C., Coney L., **Ferrière L.**, and Gibson R. L. 2007. Results of recent petrographic and geochemical studies of the ICDP drill cores from the interior of the Bosumtwi impact structure, Ghana (abstract #1137). 38th Lunar and Planetary Science Conference. CD-ROM.
15. Coney L., **Ferrière L.**, Reimold W. U., Koeberl C., and Gibson R. L. 2007. Geochemical characteristics of the LB-07A and LB-08A cores from the Bosumtwi impact structure, Ghana (abstract). *Geochimica et Cosmochimica Acta* 71(15S):A185.
16. **Ferrière L.** and Koeberl C. 2007. Ballen quartz, an impact signature: New occurrence in impact melt breccia at Rochechouart-Chassenon impact structure, France (abstract #5079). *Meteoritics and Planetary Science* 42:A46.
17. **Ferrière L.**, Koeberl C., and Reimold W. U. 2007. Distribution of shocked quartz grains with depth in central uplift of the Bosumtwi impact crater, Ghana (abstract #5078). *Meteoritics and Planetary Science* 42:A47.
18. **Ferrière L.**, Koeberl C., and Reimold W. U. 2007. Distribution of shocked quartz grains along the LB-08A core through the central uplift of the Bosumtwi impact crater, Ghana – Implications for numerical models (abstract #8035). Bridging the Gap II: The effect of target properties on the impact cratering process. Montreal, Canada. CD-ROM.
19. Bartosova K., **Ferrière L.**, Koeberl C., and Reimold W. U. 2007. Investigations of melt particles in suevite from the Eyreville B core, Chesapeake Bay impact structure (abstract). *GSA Abstracts with Programs* 39(6):A314.
20. Bartosova K., **Ferrière L.**, Koeberl C., Reimold W. U., Gibson R., and Schmitt R.-T. 2007. Lithological, petrographical, and geochemical investigations of suevite from the Eyreville core, Chesapeake Bay impact structure (abstract). *GSA Abstracts with Programs* 39(6):A451.
21. Bartosova K., Koeberl C., Schmitt R.-T., Reimold W. U., and **Ferrière L.** 2008. A petrographical, geochemical, and shock metamorphic study of suevite from the Eyreville drillcore, Chesapeake Bay impact structure, USA (abstract #1065). 39th Lunar and Planetary Science Conference. CD-ROM.
22. **Ferrière L.**, Koeberl C., and Reimold W. U. 2008. Drilling at impact structures: The case of the Bosumtwi impact structure, Ghana (abstract #01581). *Geophysical Research Abstracts* 10. CD-ROM.
23. **Ferrière L.**, Morrow J. R., Amgaa T., and Koeberl C. 2008. Systematic comparison of Universal stage-indexed planar deformation features in quartz: Implications for statistical

significance and representation of results (abstract #3010). Large Meteorite Impacts and Planetary Evolution (LMI IV) Meeting, Vredefort Dome, South Africa. pp. 76–77.

24. **Ferrière L.**, Koeberl C., Reimold W. U., Libowitzky E., and Greshake A. 2008. Ballen quartz and cristobalite in impact breccias: Types, occurrence, and possible origin (abstract #3011). Large Meteorite Impacts and Planetary Evolution (LMI IV) Meeting, Vredefort Dome, South Africa. pp. 74–75.

25. **Ferrière L.**, and Koeberl C. 2008. The 2004 ICDP Bosumtwi impact crater (Ghana) drilling project: A review (abstract). *Journal of Alpine Geology* 49:A223.

26. Bartosova K., **Ferrière L.**, Mader D., Koeberl C., Schmitt R.-T., and Reimold W. U. 2008. Petrographic and geochemical studies of impact breccia from the Eyreville drill core, Chesapeake Bay impact structure, USA (abstract). *Journal of Alpine Geology* 49:7.

27. Bartosova K., **Ferrière L.**, Koeberl C., and Brandstaetter F. 2008. Melt particles from the impact breccia section, Eyreville B drill core, Chesapeake Bay impact structure, USA (abstract). *GSA Abstracts with Programs* 40(6):A407.

28. **Ferrière L.**, Morrow J. R., Amgaa T., and Koeberl C. 2008. Universal stage determination of crystallographic orientations of planar deformation features in quartz: Quality, precision, repeatability, and representativeness of measurements (abstract). *GSA Abstracts with Programs* 40(6):A409.

Curriculum Vitae

Name: Ludovic FERRIERE
Date of birth: October 21, 1982.
Nationality: French
Marital status: Single
Home address: 4 Chemin des Gouvaisons 41120 Feings, France

Education

- 1999-2000: High School Diploma in Earth Sciences.
- 2000-2003: Bachelor's degree in Earth Sciences, University of Tours, France (ranked 1st).
Exchange year at University Laval, Quebec, Canada.
- 2003-2005: Master, Planetology (Earth and Planetary Sciences):
* University Pierre and Marie Curie, Paris, France.
* University of Nantes, France.
Thesis title: Zoning in K/T boundary spinel and in spinel from meteorite fusion crusts.
Supervisors: Dr. Eric Robin and Dr. Francois Robert.
- 2005-2008: Ph.D., Petrography-Geochemistry, University of Vienna, Vienna, Austria.
Supervisor: Ao. Univ. Prof. Dr. Christian Koeberl.

Research activity – Professional Experience

- 25/08–18/09/2003: Research internship at the CEREGE (Aix en Provence, France) with Pierre Rochette. Magnetic characterization of various materials including meteorites. Chemical analyses (majors and traces by ICP AES) and magnetic properties (VSM, Kappabridge, Cryogenic magnetometer, SM30...).
- 03/05–04/06/2004: Internship at the National Museum of Natural History, Paris and University Blaise Pascal, Clermont-Ferrand with Brigitte Zanda and Bertrand Devouard. Classification of the Tanezrouft 057 meteorite in the metamorphic series of CV/CK chondrite classes. SEM/EDS assembly, electronic microprobe (CAMECA SX50 and SX100).
- Summer 2004: Field trip to Eagle Butte crater, Alberta, Canada with Alan Hildebrand. Discovery of an outcrop of shatter cones (LPSC abstract, 2005).
- 01/03–30/06/2005: Research internship at the National Museum of Natural History, Paris and Commissariat à l'Énergie Atomique (CEA), Gif sur Yvette, with François Robert and Eric Robin. Composition and characterization of K/T boundary spinel (and spinels from meteorite

fusion crusts). Magnetic separator, SEM/EDS assembly, and SIMS Microprobe (NanoSIMS 50).

01/07–30/09/2005: Internship at GDF (Saint-Denis, Exploration Production Department). Auzance 8 drilling core samples study, France. Optical microscope, SEM/EDS assembly, Raman, and TEM.

Award(s)

07–2008 Barringer Family Fund for Meteorite Impact Research

Participation in Conferences/Workshops – Lectures

2006 Lunar and Planetary Science Conference, LPSC XXXVII, Houston, USA, March 12–16, 2006.

European Geosciences Union (EGU) General Assembly, Vienna, Austria, April 2–7, 2006.

40th ESLAB, First International Conference on Impact Cratering in the Solar System, ESA, Noordwijk, The Netherlands, May –12, 2006.

Workshop - Impact Craters as Indicators for Planetary Environmental Evolution and Astrobiology, Östersund, Sweden, June 8–14, 2006. **Student Abstract Award.**

69th Annual Meeting of the Meteoritical Society, Zürich, Switzerland, August 6–11, 2006. **Student Travel Award.**

Workshop - Signatures of an Impact – the K/T boundary in Denmark, organized by NIR, Copenhagen, Denmark, September 18–25, 2006.

2007 European Geosciences Union (EGU) General Assembly, Vienna, Austria, April 15–20, 2007.

Workshop – How impact cratering affects local geology, geochemistry, and geophysics, organized by NIR, Rättvik, Sweden, May 28–June 2, 2007.

Workshop – Kobe International School of Planetary Sciences 2007 – The origin and evolution of planetary materials, Maiko Villa Kobe, Hyogo, Japan, July 16–20, 2007. **Student Travel Award.**

70th Annual Meeting of the Meteoritical Society, Tucson, Arizona, USA, August 13–17, 2007. **Student Travel Award.**

Bridging the Gap II workshop – Effect of target properties on the impact cratering process, Saint-Hubert, Quebec, Canada, September 22–26, 2007. **Student Travel Award.**

ICDP Scientific Drilling - Training Course, Windischeschenbach, Germany, November 5–9, 2007.

2008 European Geosciences Union (EGU) General Assembly, Vienna, Austria, April 13–18, 2008.

Large Meteorite Impacts and Planetary Evolution (LMI IV) Meeting, Johannesburg, South Africa, August 17–21, 2008. **Student Travel Award.**

PANGEO AUSTRIA 2008 conference, Vienna, Austria, September 22–25, 2008.

Recent invited lectures

Shock effects in rocks at the Bosumtwi crater, Ghana – Optical and TEM observations. (Invited lecture at the Museum für Naturkunde of the Humboldt University Berlin, Germany) Wednesday, April 25, 2007, 10 a.m.

Géologie des cratères d'impact météoritiques et intérêts économiques (Exemples de structures Canadiennes). (Invited lecture at the University Laval, Quebec, Canada) Friday, September 28, 2007, 11:30 a.m.

Shock transformation and deformation of quartz: Example of PDFs from Bosumtwi and review on ballen quartz/cristobalite. (Invited lecture at the Museum für Naturkunde of the Humboldt University Berlin, Germany) Thursday, February 7, 2008, 10 a.m.

Journal Reviewer

Canadian Journal of Earth Sciences (1 review; 2005).

Geochimica and Cosmochimica Acta (1 review; 2007).

Geological Society of America Special Paper (2 reviews; 2008).

Meteoritics & Planetary Science (1 review; 2006).